ISSN 0915-6348

NATIONAL INSTITUTE FOR FUSION SCIENCE

Proceedings of the 13th International Symposium on LASER-AIDED PLASMA DIAGNOSTICS 18-21 September, 2007 Hida Hotel Plaza, Takayama, Japan

(Ed.) K. Kawahata

(Received - Aug. 22, 2007)

NIFS-PROC-68 Sep. 2007

RESEARCH REPORT
NIFS-PROC Series

TOKI, JAPAN

Proceedings of the 13th International Symposium on
LASER-AIDED PLASMA DIAGNOSTICS
18-21 September, 2007
Hida Hotel Plaza, Takayama, Japan

(Ed.) K. Kawahata

(Received - August 22, 2007)

NIFS-PROC-68 September 2007

Proceedings of the 13th International Symposium on LASER-AIDED PLASMA DIAGNOSTICS

18-21 September, 2007
Hida Hotel Plaza, Takayama, Japan

Edited by K. Kawahata
National Institute for Fusion Science,
Oroshi-cho, Toki 509-5292, Japan

The 9th international symposium on LASER-AIDED PLASAMA DIAGNOSTICS was held from 18th November to 21st September, 2007 at Takayama, Japan. This symposium was organized by the National Institute for Fusion Science, Toki, Japan. The topics of the symposium include laser diagnostics and diagnostics aided by lasers for fusion plasmas, industrial process plasmas, environmental plasmas as well as for other plasma applications and processes related to plasmas. Hardware development related to laser-aided plasma diagnostics is another topic. Over 80 participants attended this international symposium. 1 Akazaki lecture, 10 general talks, 10 topical talks, 12 short oral talks and 45 posters were presented.

Key Words: plasma diagnostics, coherent Thomson scattering, fast ion collective Thomson scattering, laser spectroscopy, laser interferometry, laser polarimetry, laser and related hardware, electric field measurement, microwave reflectometry

PREFACE

This book of Proceedings is a compilation of papers presented at the Thirteenth International Symposium on Laser-Aided Plasma Diagnostics (LAPD-13), held from 18th till 21th September 18-21, 2007 at Hida Hotel Plaza in Takayama, Japan. The Symposium is the continuation of a biennial series which was originally inaugurated at Kyushu University in 1983 and which has been alternatively organized in Japan, Europe and the United States. and has traveled around the world four times (1983: Fukuoka; 1985: Oxford: 1987: Lake Arrowhead, 1989: Fukuoka; 1991 Ban Honnef; 1993: Bar Harbor; 1995: Fukuoka; 1997: Doorwerth; 1999: Lake Tahoe; 2001: Fukuoka; 2003: Les Houches; 2005: Snowbird; 2007: Takayama).

The Symposium brings together physicists from different disciplines including laser physics, low-temperature plasma chemistry and physics, and nuclear fusion. The Symposium is an important and fruitful source for cross-fertilization between these fields. The topics of the Symposium include laser diagnostics and diagnostics aided by lasers for fusion plasmas, industrial process plasmas, environmental plasmas as well as for other plasma applications and processes related to plasmas. Hardware development related to laser-aided plasma diagnostics is another topic that is emphasized. The scope of the Symposium is very broad, including any techniques related to coherent probe of plasmas: laser induced fluorescence, laser absorption spectroscopy, laser photodetachment spectroscopy, cavity ringdown spectroscopy, Raman scattering, incoherent and coherent Thomson scattering, polarimetry, interferometry, reflectometry and related laser hardware developments.

I hope that this book of Proceeding will serve as a valuable record of the present Symposium to all workers in the field.

On behalf of the local Organizing Committee, I would like to thank all participants for their contributions to this symposium. I also thank all members of the international scientific committee for their support and cooperation, and Inoue Foundation for Science for their financial support. I am grateful to Director General Prof. Motojima and all stuff members of the National Institute for Fusion Science for their supports.

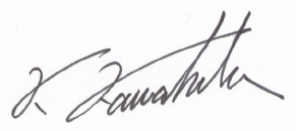

Kazuo Kawahata
(Local Organizer)

INTERNATIONAL SCIENTIFIC COMMITTEE:

- A. J. H. Donné, FOM-Institute voor Plasmafysica, The Netherlands (Chairperson)
- K. Kawahata, National Institute for Fusion Science, Japan
- N. C. Luhmann, Jr., University of California, Davis, USA
- K. Muraoka, Chubu University, Japan
- N. Sadeghi, University Joseph Fouvier-Grenoble and C. N. R. S., France
- H. Soltwisch, Ruhr-Universität Bochum, Germany
- P. P. Woskov, Massachusetts Institute of Technology, USA
- B. Graham, The Queen's University, Belfast

FORMER CHAIRMEN:

- M. Akazaki (1983 - 1989)
- D. E. Evans (1989 - 1993)
- H. F. Döbele (1993 - 1999)
- K. Muraoka (1999 - 2003)
- A.J.H. Donné (2003 -)

LOCAL ORGANIZERS:

K. Kawahata, National Institute for Fusion Science: Chairperson

K. Tanaka, National Institute for Fusion Science: Secretary

T. Tokuzawa, National Institute for Fusion Science,

T. Akiyama, National Institute for Fusion Science,

K. Muraoka, Chubu University

K. Sasaki, Nagoya University

PREVIOUS LAPD MEETINGS

1983- Fukuoka, Japan:	K. Muraoka	(Organizer)
1985- Oxford, U.K.:	D. Evans	(Organizer)
1987- Lake Arrowhead, USA:	N. C. Luhmann, Jr.	(Organizer)
1989- Fukuoka, Japan:	K. Muraoka	(Organizer)
1991- Bad Honnef, Germany:	F. Döbele	(Organizer)
1993- Bar Harbor, USA:	P. Woskov	(Organizer)
1995- Fukuoka, Japan:	K. Muraoka	(Organizer)
1997- Doorwerth, Netherlands:	A. J. H. Donné	(Organizer)
1999- Lake Tahoe, USA:	N. C. Luhmann, Jr.	(Organizer)
2001- Fukuoka, Japan:	K. Muraoka	(Organizer)
2003- Les Houches, France:	N. Sadeghi	(Organizer)
2005- Snowbird, USA:	N. C. Luhmann, Jr.	(Organizer)
2007- Takayama, Japan:	K. Kawahata	(Organizer)

Table of Contents

Session 18PM1:

(Chairperson: N. Sadeghi)

Pre-poster (PⅠ) : 16:55-18:00 (3min.for each presentation)

(Chairperson: H. Soltwisch)

Session 18PM2: Poster Presentation (P Ⅰ) : 20:00-22:00

PI-1, PI-2, PI-3, PI-4, PI-5, PI-6, PI-7, PI-8, PI-9, PI-10, PI-11, PI-12, PI-13, PI-14, PI-15, PI-16, PI-17, PI-18, PI-19, PI-20 , PI-21, PI-22

SEPTEMBER 19, 2007 Wendsday

Session 19AM1:

(Chairperson: H. Park)

– Coffee Break –

Session 19AM2: Poster Presentation (P Ⅱ) : 10:50-12:00

(Chairperson: J. Fujita)

Excursion (12:30 – 19:30)

Session 19PM2: Poster Presentation (PⅡ) : 20:00-22:00
PII-1, PII-2, PII-3, PII-4, PII-5, PII-6, PII-7, PII-8, PII-9, PII-10, PII-11, PII-12, PII-13, PII-14, PII-15, PII-16, PII-17, PII-18, PII-19, PII-20, PII-21, PII-22, PII-23

SEPTEMBER 20, 2007 Thursday

Session 20AM1:
(Chairperson: K. Muraoka)

– Coffee Break –

Session 20AM2:

(Chairperson: N. C. Luhmann, Jr)

– Lunch / Break –

Session 20PM1:

(Chairperson: K. Sasaki)

Banquet (18:30 – 21:30)

SEPTEMBER 21, 2007 Friday

Session 21AM1:

(Chairperson: P. P. Woskov)

– Coffee Break –

Session 21AM2:

(Chairperson: A. Mase)

Measuring Electric Fields in Plasmas: What can we know? What ought we do? For what may we hope?

U. Czarnetzki

Institute for Plasma and Atomic Physics, Ruhr University Bochum, 44790 Bochum, Germany

Laser spectroscopic electric field measurements have become a versatile tool for the diagnostics of low-temperature plasmas. High spatial and temporal resolutions can be achieved and from the measured field structures other important quantities like voltage, displacement current, or even the plasma density can be inferred directly. A variety of different techniques has been developed over the past two decades since the first experiments were performed by Gottscho in 1987. One of the most successful and sensitive techniques is fluorescence-dip spectroscopy. This general technique has been applied to Hydrogen, Helium, Argon, Krypton, and Xenon discharges and gas mixtures containing theses gases. In this paper an introduction to the technique with special emphasis to results obtained in Hydrogen and Argon is presented. Further a brief review on the general field of laser electric field measurement in low-temperature plasmas and related questions on use of the Stark effect is provided.

1. Introduction

Electric fields play a fundamental role in plasmas. Particle transport, power coupling, and wave propagation are all related to electric field structures and dynamics. At the edge of plasmas, ions and secondary electrons can be accelerated to high energies in the sheaths. Moreover, in high frequency RF sheaths the dynamics of electron and electric fields are strongly coupled. Finally, even if there is no electric field on a macroscopic scale, quasi neutral plasmas can develop rather strong fields by the random ion charge distribution on scale lengths shorter than the Debye length. These microfields can lead to a substantial broadening of optical transitions and lowering of the ionization energy in atoms and molecules and are a measure of the plasma density.

A variety of different techniques have been developed for the measurement of electric fields in plasmas. Ambipolar fields can be measured rather conveniently with Langmuir or emissive probes [1, 2]. Induction or B-dot probes can be used for the detection of induced RF electric fields, or wave fields in general [3]. Optical emission spectroscopy allows the determination of microfields, especially at high plasma densities as they are found in e.g. pinches or arcs [4]. Over the past two decades substantial effort has been made on the development of sensitive laser techniques for electric field measurement in plasmas. This development has been motivated mostly by the investigation of the electric field structure in static and RF sheaths. Electric fields in sheaths are very important for the understanding of power coupling to the plasma, the transport of electrons and ions, and the ion-surface interaction. Laser techniques are non-intrusive and have the additional advantage of high spatial and temporal resolution which is ideal for sheaths with typical spatial extensions in the mm range and dynamics on a ns timescale.

The paper first gives an overview on existing techniques for laser electric field measurements and their basic properties. Within the limited frame of this work the overview can only be a rough sketch and the intention is more on introducing the general ideas, problems, and techniques than to go very much into detail. For work before 1994 the reader might refer to the excellent review paper by Lawler and Doughty [5]. The main focus is on the application of fluorescence dip spectroscopy to laser electric field measurement. In recent years this technique has applied successfully in a number of atomic systems and has allowed investigations on plasma and sheath phenomena that were not possible otherwise. In particular it has enabled the measurement of plasma parameters directly linked with the electric field, like voltages, charge densities, displacement current densities, and plasma densities. Finally, it will be investigated what further challenges and developments can be expected in the near future.

2. Principles of Laser Electric Field Measurement

Neutral atoms or molecules are naturally present in low-temperature plasmas and often certain traces can be added without altering the discharge characteristic. These neutral particles can serve as probes for electric field measurements. In highly excited Rydberg states the electrons are on large orbits and the electric field of the core is relatively weak. Therefore, already small external fields can change the eigenstates and eigenfunctions of the electron and states are shifted and mixed by the Stark effect. Generally, the Stark effect increases with the principle quantum number n approximately like n^2. The related optical line shifts or the amplitude of otherwise forbidden transitions can be measured with high sensitivity by laser spectroscopy. These investigations were started by R. Gottscho in 1987 on BCl in a BCl_3 discharge [6] and since then a large variety of different atomic (H, He, Ne, Ar, Kr, Xe) and bi-molecular systems (BH, CS, NaK) as well as laser spectroscopic techniques has been applied [5-37]. Depending on the particular scheme the lowest detectable fields range from a few V/cm to several 100 V/cm. All these techniques are limited to low pressures where quenching is weak. A so far unique exception is the technique developed by Ochkin and co-workes in 1995 which is based on a CARS like four-wave mixing technique and allows in principle single shot electric field measurement [35, 36]. It requires molecular probes like H_2 and works at atmospheric pressures or above. In fact, it is the only technique that can work at atmospheric pressures and seems ideal for application in micro-discharges. Although more than ten years have passed since its fist introduction, which was actually on the LAPD 7 in Fukuoka, so far no one except the Ochkin group has ever taken advantage of this great opportunity. Here, however, further on only low-pressure applications of typically less than a few 100 Pa where quenching is weak or can be neglected [38] are considered.

The Stark effect usually couples different angular momentum states of the same principal quantum number n. These states are energetically close and mixing can be strong. States at different principal quantum number that are further away, contribute substantially less. However, this clear order is present only in atomic hydrogen and certain deviations can occur in many electron atoms like e.g. Krypton. Since n is larger, also the number of angular momentum states is large and the spectrum can become quite complex. In order to understand the basic physics one can concentrate on a simple model system consisting of only two states with wavefunctions $\Psi_{1/2}$ which are located symmetrically at energies $E_{1/2} = \pm\Delta$. Due to selection rules only one of these states might be connected to a lower state by an optical dipole transition. Here the Ψ_1 state is chosen. If an electric field F is applied new eigenfunctions $\varphi_\pm$ with new energies $E_\pm$ result that are a superposition of the undisturbed eigenfunctions. In this simple case it is easy to calculate exactly the solution from Schrödinger's equation:

$$\varphi_\pm = a_\pm \Psi_1 + b_\pm \Psi_2 \quad \text{and} \quad E_\pm = \pm\sqrt{1+|W|^2}$$

$$\text{with} \quad W = \left\langle \Psi_1 \middle| \vec{d}\cdot\vec{F} \middle| \Psi_2 \right\rangle / \Delta$$

$$\text{and} \quad a_\pm = \left[1 + \left|\frac{W}{E_\pm}\right|^2\right]^{-1}, \quad |b_\pm|^2 = 1 - |a_\pm|^2$$

Here W is the matrix element normalized to Δ where d = -e r is the dipole operator. W can be viewed as a normalized field strength. The results depend only on the absolute value of W, i.e. they are independent of sign of the electric field that has to be inferred otherwise. A plot is shown in Fig. 1. At vanishing field strength, the undisturbed energies result (Fig. 1b) but at final but small values $0 < W < 1$ the energies are shifted approximately quadratically with W and for $W >> 1$ the shift is linear. This means that the Stark effect is quadratic as long as the additional energy of the electron in the external field is smaller than the separation between the states involved. In hydrogen all states are effectively degenerate ($\Delta = 0$) and a linear Stark effect is observed at all field strengths. In multi-electron atoms the fine-structure shift is much stronger and only states with high angular momentum are degenerate, i.e. Δ can be quite large. The quadratic Stark effect leads to very small shifts at low field strengths and, therefore, has a lower sensitivity than the linear Stark effect.

The state mixing becomes obvious in Fig. 1a. At zero field the new eigenfunctions are identical

to the initial eigenfunctions. With increasing field strength, the upper state φ_+ receives a growing admixture of the Ψ_2 state while the contribution of the initial Ψ_1 state decreases. The lower state develops just oppositely. Since it has been assumed initially that only the Ψ_1 state has an allowed optical transition, the observed intensity is directly proportional to the coefficients $|a_\pm|^2$. This means that the initially allowed transition to the upper state becomes weaker with increasing fieldstrength and the initially forbidden transition to the lower state grows in strength. In this example both states show equal intensity at infinite field strength. At very low field strength the quadratic Stark shift might be difficult to observe. However, the intensity ratio of the initially allowed and forbidden transition is often much easier observed. Especially at low field strength, this ratio varies strongly with the field strength. In fact, this is the way the Stark effect is measured in diatomic molecules. The higher angular momentum states (f, g, …) in Rydberg levels of multi-electron atomic systems are often approximately degenerate and show a linear Stark effect. However, due to selection rules transitions to these states are forbidden from commonly accessible lower states like ns or np. Only at higher field strengths the increasing admixture of the s and p states makes an observation of the linear Stark effect possible.

In more realistic atomic systems the calculation works very similar [39, 40]. However, the increasing number of states does no longer allow for an analytical solution and the related sets of linear algebraic equations have to be solved numerically. This can be performed relatively easily for atomic hydrogen. In multi-electron atoms an increasing complexity in the coupling of the different angular moments arises and often reliable matrix elements are not available. Especially for low angular momentum states, the wave functions show non-vanishing amplitudes at the core and are strongly influenced by the nucleus and the core electrons which makes calculations quite difficult. Nevertheless, there has been substantial progress in recent years in the calculation of the Stark effect in noble gases and also in molecules [9, 11, 15, 23, 25, 27, 30, 32].

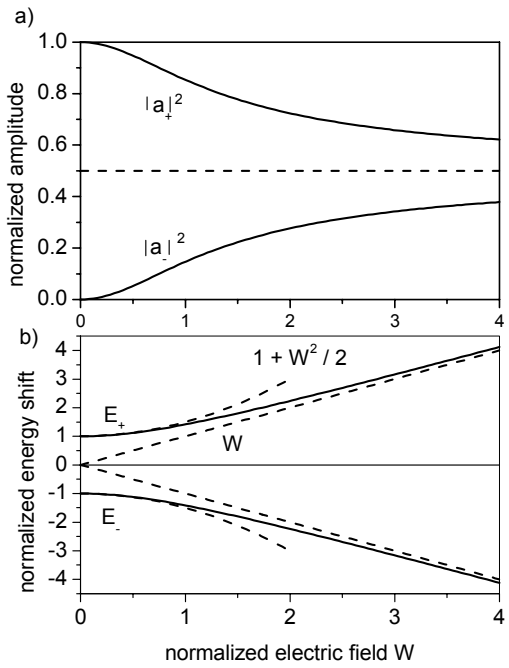

Fig. 1: Stark effect in a two-level system: a) amplitudes for dipole-transition to lower state, b) shift of the new eigenstates. The broken lines indicate the approximate behavior at low (quadratic) and high (linear) field strengths.

Additional to calculations calibration measurements are usually performed. Here the probe atoms are placed in a homogeneous electric field which is typically generated between two planar electrodes. In order to avoid electrical breakthrough and collisional quenching, the pressure is normally chosen well on the left side of the Paschen curve. For schemes which require population in metastable states, these states have to be prepared in an external discharge like in a flow-tube system. Care has to be taken to keep the calibration region free from residual charges generated in the external discharge. This can be achieved by placing mesh electrodes or perpendicular magnetic fields in the gas flow between the discharge and the calibration region.

Laser spectroscopic techniques for the measurement of the Stark effect in plasmas can be divided into two categories: optogalvanic detection and fluorescence detection. In optogalvanic detection, the ionization probability of an atom is changed by laser excitation to a Rydberg state. This leads then to a change of the discharge current by charge multiplication, that can be easily detected as a short AC signal if the laser is pulsed, typically on a ns timescale. The

electric field is inferred by measuring the detailed spectrum of a particular transition by tuning the laser frequency over the resonance. These techniques are very sensitive and ideal for DC or low frequency discharges over small electrode areas. The laser beam is focussed in order to achieve the required spatial resolution and the entire beampath in the sheath contributes which leads to a limit on the electrode size. The optogalvanic signal is usually on a much longer timescale than the laser pulse and does not allow the temporal resolution required for RF discharges. The spatial structure of the electric field in the sheath is obtained by successive measurements at different sheath positions.

The detection of fluorescence light emitted from the excited Rydberg state provides the opportunity of direct spatial resolution within the laser beam cross section by adequate imaging. Thereby the need of focussing is avoided. Further, and maybe even more important, it allows high temporal resolution since the limiting factor is now only the laser pulse width. The electric field and the related Stark effect on the atom are only probed during the short interaction time between the laser radiation and the atomic transition, although the subsequent fluorescence light might be emitted on a much longer timescale. Typically Nd:YAG pumped dye or OPO systems with subsequent frequency doubling or tripling are used which have pulsewidths of about 5 ns. This is short compared to the period of 74 ns of typical RF discharges at 13.56 MHz. In principle even shorter pulsewidths could be used. The laser systems mentioned above all operate on a number of spectral modes with a total spectral width of typically about 0.1 cm^{-1}. Therefore, with the same spectral resolution a single mode laser could have a pulsewidth of the order of 0.1 ns. However, such systems are not easily available.

The laser excitation of Rydberg states is a general problem for both techniques. By definition, Rydberg states have a high excitation energy and this usually does not allow direct excitation from the ground state by radiation in the visible or UV. For this reason the use of most atomic probe systems is based on a sufficient population of metastable states by collisional processes in the plasma, i.e. mostly by electrons. From this elevated initial state further excitation to the Rydberg state becomes feasible, as is the case for He, Ne, and Ar. Alternatively, an intermediate state can also be populated temporarily from the ground state by a two-photon excitation using a second pulsed laser system. Both laser pulses need to be synchronized since the lifetime of the intermediate state is typically of the order of 10 ns. The advantage is that now the much higher population of the ground state can be accessed and the technique becomes independent from sufficient excitation by the plasma. The former point provides the opportunity to admix small amounts of the probe gas as a tracer to complex molecular gas mixtures and the latter point becomes important at low electron densities or high quenching of the metastable state by collisions. However, the available photon energy for the two-photon excitation is limited ($\lambda > 203$ nm) and only H, Kr, and Xe have been used so far. It should be noted that also N, O, C, and Cl can be two-photon excited, although they have not been applied as atomic probes for electric field measurement yet.

A general problem of fluorescence light detection is that the long lifetime of Rydberg states leads to very small emission amplitudes. This is especially troublesome since the lifetime increases with the principle quantum number approximately like n^3 while the Stark effect increases only like n^2. This limits the maximum n and thereby the field sensitivity. Nevertheless, in atomic hydrogen, Stark splitting in sheaths has been measured by direct fluorescence spectroscopy with states ranging from $n = 2$ to $n = 6$. In order to overcome this general shortcoming Greenberg and Hebner used successfully a collisonal population transfer from the singlet to the triplet system in He [10, 11]. The laser excitation is between a metastable 2s and an np Rydberg state (typically $n = 11$) in the singlet system. At high n, the singlet states are energetically very close to the triplet states and electron and neutral collisions can both lead to a population transfer. The advantages are that the lifetime of the triplet system is much shorter (but still of the order of several 100 ns) and that the emission wavelength is different from the laser wavelength.

In atomic hydrogen an interesting alternative has been developed by de la Rosa and

Grützmacher et al. [37]. This polarization spectroscopic technique is effectively a kind of four-wave mixing. It requires rather high atomic hydrogen densities as can be found in arcs or hollow cathode discharge where the method has been applied. The technique is based on a two-photon transition between the 1s ground state and the 2s state and the polarization of a probe beam is measured. The electric field strength is inferred from the spectral width of the absorption profile and a lower limit for the resolved field of about 2 kV/cm was achieved. The advantage is that background emission from the plasma is strongly suppressed by detecting light only within the small solid angle of the probe beam. Polarization techniques have been applied also by Oda et al. in He under the presence of a magnetic field [33, 34].

3. Laser-Induced Fluorescence-Dip Spectroscopy

One of the main problems related to fluorescence spectroscopy is the long lifetime of Rydberg states that setting limits to the maximum quantum states. In order to overcome this limit fluorescence dip spectroscopy was introduced for electric field measurements in 1997 [16]. The technique was first applied to atomic Hydrogen and has been adopted for Xenon, Krypton, and in modified versions also to Helium and Argon. It is similar to scheme applied earlier for the measurement of excited states in molecular Nitrogen [41]. A general scheme is shown in Fig. 2. The basic idea is to excite first with one laser beam from a lower state (1) a short living intermediate state (2) from where fluorescence light emitted by a transition to a lower state (3) can be observed conveniently. Then a second laser beam is tuned in resonance between this intermediate state (2) and a highly excited Rydberg state (4). If both lasers are pulsed, the second excitation can efficiently transfer a substantial part of the population of the intermediate state to the Rydberg state. Consequently, fluorescence from the intermediate state will decrease. The Rydberg spectrum can now be measured by keeping the first laser frequency fixed on resonance between the lower and the intermediate state and tuning the second laser frequency. The various resonances are observed as dips in the fluorescence originating from the intermediate state. Therefore, the lifetime of the Rydberg state does not affect the observed signal. Nevertheless, with increasing lifetime also the transition moment decreases and the energy necessary for depletion of the population of the intermediate state increases. With ns pulses and energies up to some mJ Rydberg states up to n = 50 can be observed readily.

Care might also be taken with respect to the population of the intermediate level 2. Amplified stimulated emission can occur along the axis of the beam of the first laser if the population exceeds a certain threshold N_{2C}. For the Balmer-α transition in atomic hydrogen, a Doppler width Δ_D at room temperature, and a amplification (focal) length of L = 1 cm, the critical density is about $N_{2C} = 1x10^{13}$ cm^{-3}. Generally, such a high population leads also to strong fluorescence signals and the pumping laser intensity can easily be adjusted.

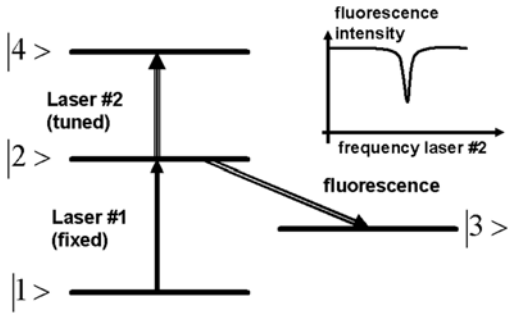

Fig. 2: General scheme for fluorescence-dip spectroscopy.

In atomic hydrogen, level 1 is the ground state n = 1, intermediate level 2 is n = 3, level 3 is n = 2, and level 4 is a Rydberg state with n >> 3. The excitation from the ground state to the intermediate level is provided by two-photon excitation at λ = 205 nm. In order to achieve a better efficiency, two counter propagating UV beams allow Doppler-free two-photon excitation. Florescence light is observed at Balmer-α (656 nm). The near IR radiation for the excitation to the Rydberg level can be generated conveniently by Raman shifting laser radiation in the visible to the first Stokes component in a high pressure cell filled with molecular hydrogen at typically 30 bar to 40 bar. This has the advantage of operating the laser in the visible between about 600 nm and 660 nm instead of near IR and it extends the wavelength tuning range by about a factor two from approximately 800 nm to 910 nm.

The hydrogen ground state is 1s and the magnetic quantum number is m = 0. With linearly polarized radiation in the two-photon excitation only m = 0 states are populated in the intermediate n = 3 state. Then, with radiation from the second laser polarized parallel to the electric field, again only m = 0 states are populated in the Rydberg state. This allows a total number of Stark split states of n + 1, corresponding to the number of states with different angular momentum. For the above case of n = 6 this gives the observed number of seven. If n is even a central line appears and if n is odd the centre shows a void. With the second laser polarized perpendicular to the electric field, only m = ±1 states can be reached and the total number of lines is n. Then for even n the centre shows a void and for odd n a central line appears. This provides a convenient way for measuring the direction of the electric field by rotating the polarization of the second laser and detecting the relative strength of the central component. This is demonstrated in Fig. 3 where the experimental result is compared to the expected scaling proportional to $\sin^2(\phi)$.

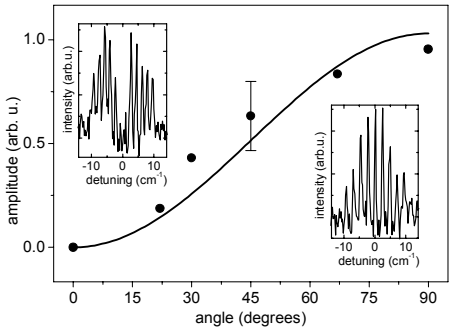

Fig. 3: Polarization dependence of the central line at n = 14 and an electric field of 950 V/cm. The solid line represents the theoretically expected dependence and the inserts show the spectra at $\phi = 0°$ and $\phi = 90°$ [16].

.In atomic systems other than hydrogen the situation is more complex. There, the angular momentum states for a given principal quantum number n are no longer degenerate. Since the lower state is typically an s-state, the intermediate state is either a s- or d-state after two-photon excitation and a p-state in case of single photon excitation. This allows excitation in the Rydberg state to f-states or lower angular momentum states. The lower the angular momentum, the more pronounced is in general the deviation from degeneracy due to the fine structure. Further, the lower states receive a relative strong disturbance by the core electrons since the wave functions have a non-vanishing amplitude at the core. This leads to a quadratic Stark effect at low field strengths and a more complex polarization dependence. However, the higher angular momentum states are mostly degenerate and so at very high electric fields when they are admixed to the lower angular momentum states at observable amplitudes, a linear Stark effect spectrum similar to hydrogen can be observed. An example in case of Krypton is given in Fig. 4 [32].

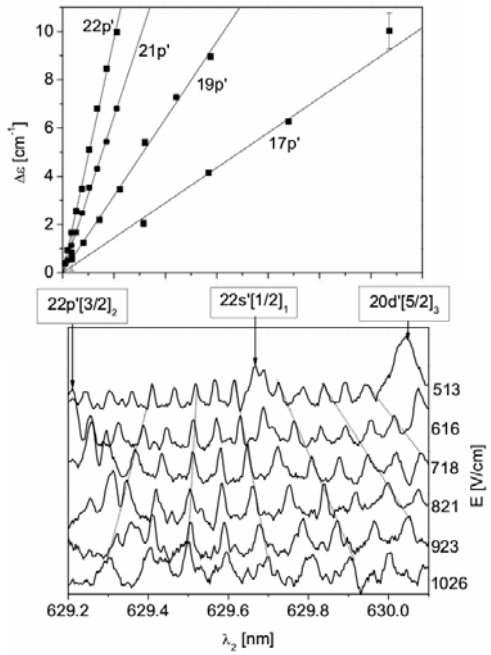

Fig. 4: Stark effect measured by fluorescence-dip spectroscopy in Krypton: Quadratic Stark shift of the 17p' to 22p' levels (upper figure). The straight lines represent ab-initio calculations. Linear Stark effect spectrum for the 19(l' > 3) levels which spectrally overlap with the 22s', 22p', and 20d' levels (lower figure). The 19(l' > 3) lines become visible only at fields above about 500 V/cm [32].

Highly excited states in the hydrogen atom all show a linear Stark effect which makes it ideal for electric field measurement. Even with the very low state n = 3 electric field measurements are possible. Using a single mode Fourier limited bandwidth laser system ($\Delta\nu = 0.004$ cm^{-1}) and Doppler-free two-photon excitation at 205 nm with counter propagating beams Booth et al. achieved a sensitivity of about 100 V/cm [12]. However, this required a very specialized

non-commercial laser system. With more standard systems, as ours, the bandwidth is usually larger and a smaller sensitivity results of about 1 kV/cm. Here the Stark effect is strongly influenced by the fine structure splitting which is about the same order for fields at 1 kV/cm. This gives the spectrum a strong dependence on the polarization of the laser radiation relative to the electric field and the broadening is much more pronounced with parallel polarization as predicted by calculation [12]. The figure represents the lower limit of electric field measurement at about. A similar sensitivity was found by de La Rosa and Grützmacher et al. by applying a kind of two-photon polarization spectroscopy technique [37].

Much higher sensitivities can be achieved by using Rydberg states with a principal quantum number n >> 3. Here the fluorescence-dip technique allows probing of states up to about n = 50. The minimum detectable field in mostly limited by the finite bandwidth of the laser radiation and a slight broadening by the saturation introduced in order to observe easy detectable dip of typically a few 10 % reduction of the fluorescence intensity. An upper limit is set by the overlap of Stark spectra from states with neighboring quantum numbers, i.e. n-1 and n+1. While the upper limit can be calculated, the lower limit depends on the experimental spectral resolution. One of the main limitations in resolution are fluctuations of the fluorescence intensity introduced by power, spatial beam profile, and especially spectral mode profile variations in the pump beam for the two-photon excitation. The related noise requires a certain dip strength for detection and this again is related to a certain saturation and line broadening. An experimental result is shown in Fig. 5 where the spectral resolution is about Δ_0 = 0.57 cm^{-1}. Typical error bars are indicated. The minimum electric field is then given for n >> 1 by $E_{min} \approx \Delta_0 / \alpha n^2$ and the maximum electric field by $E_{max} \approx 2R / \alpha n^5$ where α = 1.28x10^{-4} V^{-1} is the Stark constant for atomic hydrogen and R = 1.097x10^5 cm^{-1} the Rydberg constant. The theoretical curve for the minimum field fits very well to the experimental data and also the maximum field is confirmed for the higher quantum numbers where the corresponding field strength is realized in the experiment.

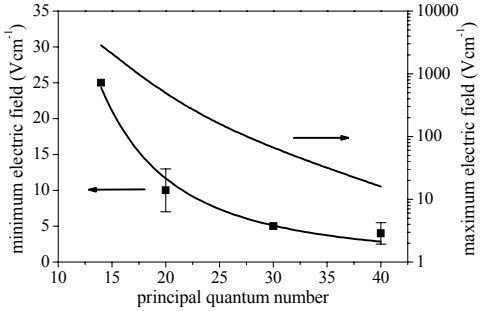

Fig. 5: Experimentally determined minimum detectable electric field strength and calculated maximum unambiguously detectable field strength in atomic hydrogen as a function of the principal quantum number n. The minimum electric field is also represented by the theoretical curve including the experimental spectral resolution.

4. Summary and Outlook

A rather broad spectrum of experimental techniques and atomic probes has been established for laser electric field measurement. The most sensitive and successive schemes are based on fluorescence-dip spectroscopy. This allows high field sensitivity down to about 10 V/cm to 100 V/cm, depending on the atomic system, high spatial resolution of a few 10 mm, and high temporal resolution of about 4 ns at the same time. Especially the use of noble gases provides the opportunity to admix them to other gases without altering the discharge properties. This extends substantially the range of applicability. All these applications are limited to pressures ranging from about 1 Pa to several 100 Pa, which is the typical regime for low-pressure discharges.

In recent time an increasing interest has developed in the study of micro-discharges at pressures close to or even above atmospheric pressure, providing a special diagnostic challenge. Small spatial dimensions, high pressure and related quenching, and often bright emission background are all contributing to an environment unfavourable for most standard diagnostics. So far the CARS technique seems to be the only option and even that is not yet fully exploited. Therefore, a strong demand still exists for further development and novel ideas originating from a healthy mixture of laser spectroscopy, atomic physics, and plasma physics.

References

[1] F.F. Chen in M.N. Hirsch and H.J. Oskam (edit.), Gaseous Electronics, Vol. 1, Academic Press, New York 1978

[2] T. Lho, N. Hershkowitz, G.H. Kim, Rev. Sci. Instrum. 71, 403 (2000)

[3] R. Piejak, V. Godyak, B. Alexandrovich, Rev. Sci. Instrum. 72, 4002 (2001)

[4] H. R. Griem, Spectral Line Broadening by Plasmas, Academic Press, New York (1974)

[5] J.E. Lawler and D.A. Doughty, Advances in Atomic, Molecular, and Optical Physics 34, 171 (1994)

[6] R.A. Gottscho, Phys. Rev. A 36, 2233 (1987)

[7] B.N. Ganguly, J. Appl. Phys. 60, 571 (1986)

[8] E.A. Den Hartog, D.A. Doughty, J.E. Lawler, Phys. Rev. A 38, 2471 (1988)

[9] M.P. Alberta, H. Debontride, J. Derouard, N. Sadeghi, J. Phys. III (France), 3, 105 (1993)

[10] Greenberg K E and Hebner G A 1993 Appl. Phys. Lett. 63 3282

[11] G.A. Hebner, K. Greenberg, M.E. Riley, J. Appl. Phys. 76, 4036 (1994)

[12] J.P. Booth, M. Fadlallah, J. Derouard, N. Sadeghi, Appl. Phys. Lett. 65, 819 (1994)

[13] J.P. Booth, M. Fadlallah, J. Derouard and N. Sadeghi, Appl. Phys. Lett. 69, 1361 (1994)

[14] Y.W. Choi, M.D. Bowden, and K. Muraoka, Appl. Phys. Lett. 69, 1361 (1996)

[15] S. Maurmann, V.P. Gavrilenko, H.J. Kunze, E. Oks, J. Phys. D: Appl. Phys. 29, 1525 (1996)

[16] Czarnetzki, D. Luggenhölscher, and H.F. Döbele, Phys. Rev. Lett. 81 (21), 4592 (1998)

[17] J.B. Kim, K. Kawamura, Y.W. Choi, M.D. Bowden, K. Muraoka, V. Helbig, IEEE Trans. Plasma Sci. 26, 1556 (1998)

[18] U. Czarnetzki, D. Luggenhölscher, and H.F. Döbele, Plasma Sources Sci. Technol. 8, 230 (1999).

[19] U. Czarnetzki, D. Luggenhölscher, and H.F. Döbele, Appl. Phys. A 72, 509 (2001)

[20] U. Czarnetzki, G.A.Hebner, D. Luggenhölscher, and H.F. Döbele, M.E. Riley, IEEE Trans. Plasma Sci. 27, 70 (1999)

[21] U. Czarnetzki, D. Luggenhölscher, V.A. Kadetov, and H.F. Döbele, Pure Appl. Cem. 77 (2), 345 (2005)

[22] J.B. Kim, T. Ikutake, M.D. Bowden, K. Muraoka, and U. Czarnetzki, Jap. J. Appl. Phys. Part 1, 39 (1), 299 (2000)

[23] V.P. Gavrilenko, H.J. Kim, T. Ikutake, J.B. Kim, Y. Y. W. Choi, M.D. Bowden and K. Muraoka, Phys. Rev. E 62, 7201 (2000)

[24] V.P. Gavrilenko, Instr. Exp. Tech. 49 (2), 149 (2006)

[25] E.K. Cherkasova, V.P. Gavrilenko, A.I. Zhuzhunashvili, J. Phys. D: Appl. Phys. 39 (3), 477 (2006)

[26] Z. Altug, J. Neumann, T. Rieper, and V. Helbig, in Proc. Xth Laser Aided Plasma Diagnostics, edited by K. Muraoka, Fukuoka/Japan (2001)

[27] E. Wagenaars, G.M.W. Kroesen, M.D. Bowden, Phys. Rev. A, 74 (3), 033409 (2006)

[28] K. Takizawa, K. Sasaki, and K. Kadota, Jpn. J. Appl. Phys. 41, L1285 (2002)

[29] K. Takizawa, K. Sasaki, and A. Kono, Appl. Phys. Lett. 84, 185 (2004)

[30] T. Jiang, M.D. Bowden, E. Wagenaars, E. Stoffels, and G.M. Kroesen, New J. Phys. 8, 202 (2006)

[31] E.V. Barnat and G.A. Hebner, Appl. Phys. Lett. 85, 3393-95 (2004)

[32] T. Kampschulte, J. Schulze, D. Luggenhölscher, M.D. Bowden, and U. Czarnetzki, New J. Phys. 9, 18 (2007)

[33] M. Watanabe, K. Takiyama, T. Oda, Rev. Sci. Instr. 70 (1), 903 (1999)

[34] Watanabe M, Takiyama K and Oda T 2000 Japan. J. Appl. Phys. 39 L116

[35] O.A. Evsin, E.B. Kupryanova, V.A. Ochkin, S.Yu. Savinov, and S.N. Tskhai, Quant. Electr. 25, 278 (1995)

[36] V.N. Ochkin, S.Y.Savinov, S.N. Tskhai, U. Czarnetzki, V. Schulz-von der Gathen, and H.F. Döbele, IEEE Trans. Plasma Science 26, 1502 (1998)

[37] M.I. de la Rosa, C. Perez, K. Grützmacher, A.B. Gonzalo, A. Steiger, Plasma Sources Sci. Technol. 15, 105 (2006)

[38] N. Sadeghi, D.W. Setser, A. Francis, U. Czarnetzki , H.F. Döbele, J. Chem. Phys. 115 (7), 3144 (2001)

[39] R.D. Cowan, The theory of atomic structure and spectra, University of California Press, London 1981

[40] H.A. Bethe E.E. Salpeter, Quantum Mechanics of One- and Two-Electron Atoms, Berlin, Springer Verlag (1957)

[41] T. Ebata, N. Mikami, and M. Ito, J. Chem. Phys. 78, 1132 (1983)

Recent fast ion measurements by collective Thomson scattering (CTS) at the TEXTOR tokamak

S.K.Nielsen[1,2], H.Bindslev[1], J.A.Hoekzema[3], S.B.Korsholm[1], F.Leipold[1], F.Meo[1], P.K.Michelsen[1], H. Oosterbeek[3], E.Westerhof[4], P.Woskov[2] and the TEXTOR Team.

[1]*Association EURATOM-Risø National Laboratory, Technical University of Denmark, DK-4000 Roskilde, Denmark, www.risoe.dk/fusion*
[2]*MIT Plasma Science and Fusion Center, Cambridge, MA 0213,USA*
[3]*Forschungszentrum Jülich GmbH, Institut für Energieforschung 4 - Plasmaphysik, EURATOM Association, Trilateral Euregio Cluster, D-52424 Jülich, Germany*
[4]*FOM-Institute for Plasma Physics Rijnhuizen, Association EURATOM-FOM, Trilateral Euregio Cluster, The Netherlands, www.rijnhuizen.nl*

Fast ions created in the fusion processes will provide up to 70% of the heating in ITER. In the TEXTOR tokamak 110 GHz, 150 kW gyrotron radiation is used to diagnose the fast ion behaviour by Collective Thomson scattering (CTS). The diagnostic allows measurements of confined fast ions resolved both in space and pitch angle with a temporal resolution of 4ms. The fast ions in TEXTOR are mainly created by neutral beam injection and measurements of the heating start-up and turn-off phases show good agreement with numerical simulations. Also the fast ion distribution function during co- and counter-current neutral beam injection is studied. CTS is expected to play an important role in understanding the dynamics of energetic alpha particles in ITER.

1. Introduction

In future tokamak experiments, such as ITER, and in future fusion power plants, the main source of heating will come from the plasma itself in the form of fast alpha particles produced in D-T fusion reactions. These fast alpha particles must transfer their energy to the bulk plasma before they are expelled from the plasma. Populations of fast particles represent a source of free energy. This may drive instabilities and plasma modes which in some cases may react back on the fast ions and expel them from the plasma [1-6]. This will reduce the plasma heating and the driven modes may furthermore degrade the general confinement.

As a challenge to current theory and as a guidance for the further development of our understanding of fast ion dynamics, experimental measurements of confined fast ions resolved in time, space and velocity are needed. Collective Thomson scattering (CTS) can provide such measurements [7-12]. In CTS high power mm waves are scattered off fluctuations in the electron distribution. For the right choice of scattering geometries, and when the resolved fluctuation, $\boldsymbol{k}^{\delta} = \boldsymbol{k}^{s} - \boldsymbol{k}^{i}$, is smaller than $1/\lambda_D$, the received scattered radiation yields information of the projected 1d distribution function $g(u) = \int \delta(\boldsymbol{v} \cdot \hat{\boldsymbol{k}}^{\delta} - u) f(\boldsymbol{v}) d^3v$. Here $\boldsymbol{k}^{s}$ and $\boldsymbol{k}^{i}$ refers to the wave vector of the scattered and incident wave, respectively. λ_D is the debye length. The frequency, ν^{δ}, of a particular wave vector component, $\boldsymbol{k}^{\delta}$, of the fluctuations driven by a particular ion is approximately given by $\nu^{\delta} = \boldsymbol{v}_{ion} \cdot \boldsymbol{k}^{\delta} / 2\pi$, where $\boldsymbol{v}_{ion}$ is the velocity of the ion setting up the fluctuation.

CTS has previously been applied to measure the fast ion distribution at JET [13] and CTS measurements of the fast ion dynamics was recently measured at TEXTOR [14]. An overview of CTS activity can be found in [15]. Here we present resent fast ion measurements from TEXTOR (R=1.75 m, a=0.45 m). In section 2 the experimental setup is described. Section 3 deals with evidence of CTS data. Section 4 and 5 deal with measured distribution functions. Section 6 describes the CTS future plans for ITER. Conclusions are drawn in section 7.

2. Experimental setup

The TEXTOR CTS system uses a 110 GHz gyrotron operated at 100-150 kW to scatter off the fluctuations in the electron distribution. A Catia drawing of the CTS transmission line is shown in figure 1. As shown in figure 2, the

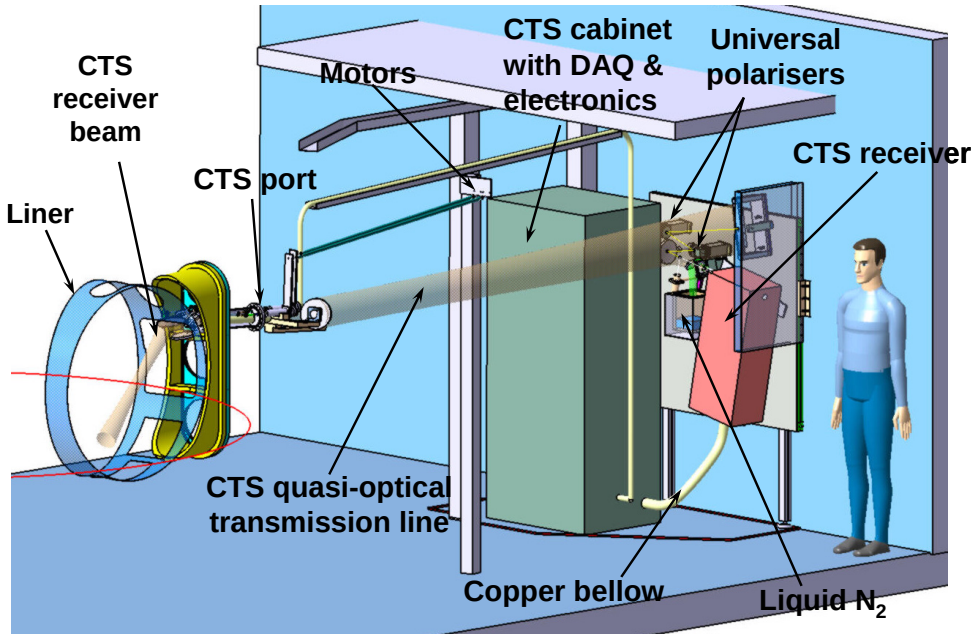

Fig. 1: Catia drawing of the CTS transmission line at TEXTOR. The tokamak cross section is shown at the left. The CTS receiver is shown at the right, and the receiver horn defines the CTS receiver beam pattern.

gyrotron probe beam enters the tokamak in the horizontal midplane. The receiver beam enters the plasma ~20 cm above the probe beam. The radiation scattered from the region where the receiver and probe beam overlap is transmitted to a receiver through a quasi-optical transmission line, shown in figure 1. The transmission line includes a universal polariser to optimize the signal to noise ratio. The CTS receiver is a hetrodyne radiometer with 42 spectral channels covering the frequency range from ~107 to ~113 GHz. Seven synchronised NI-4472 data acquisition cards, each with 8 ADCs, sample the data with a sample rate of 100 k samples/sec.

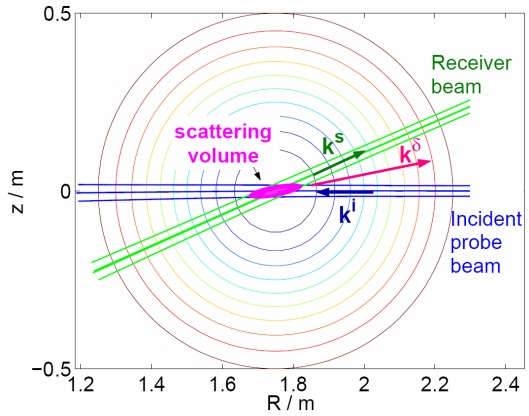

Fig. 2: CTS scattering geometry in the TEXTOR tokamak shown in the poloidal plasma cross section. The probe enters the plasma in the horizontal midplane and the first receiver mirror is located ~ 20 cm above. Both beams enter from the high field side.

Two 60 dB notch filters with a width of 200 MHz are used to attenuate gyrotron stray radiation. A voltage controlled variable attenuator is used to attenuate the received radiation during the gyrotron switching phases. More details on the CTS diagnostic can be found in [16-17].

During CTS experiments the magnetic field on axis is operated at 2.6T. This keeps the cold 110 GHz resonances outside the plasma. In order to separate the CTS fast ion signal level, which is in the order of 1-10 eV, from the background ECE level, which is in the order of 10-100 eV, the gyrotron is modulated. The gyrotron is modulated with a 2 ms on/2 ms off 50% duty cycle, resulting in a time resolution of 4 ms.

3. Evidence of CTS data

In order to verify that the received signal is indeed CTS scattered radiation reflecting the ion motion, a number of experiments have been performed. In figure 3 the received scattered radiation in six selected channels is shown while the receiver beam is being swept toroidally. A clear signal is seen to emerge with a maximum at 2.1 s when the receiver beam intersects the probe beam, confirming that the received radiation is spatially localised from the scattering volume.

A set of discharges have been made where a co-current neutral beam injection (NBI) heated plasma was observed for two different scattering

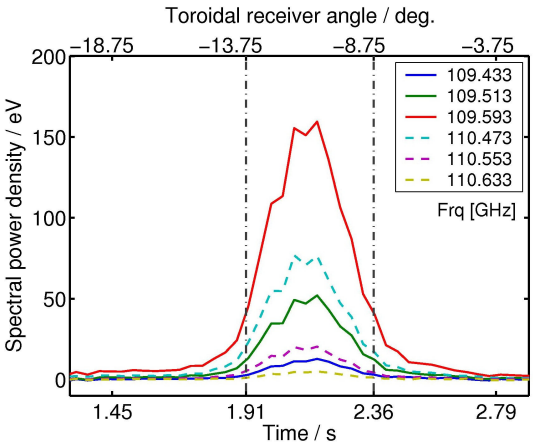

Fig. 3: TEXTOR shot #100467. Toroidal scan of the receiver beam viewing direction. The probe beam was injected in the horizontal midplane with a toroidal angle of -10 degrees and the gyrotron was modulated with a duty cycle of 5%. The receiver beam is seen to intersect the gyrotron beam in the time from 1.91 s to 2.36 s corresponding to a toroidal receiver angle of -13.75 degrees to -8.75 degrees.

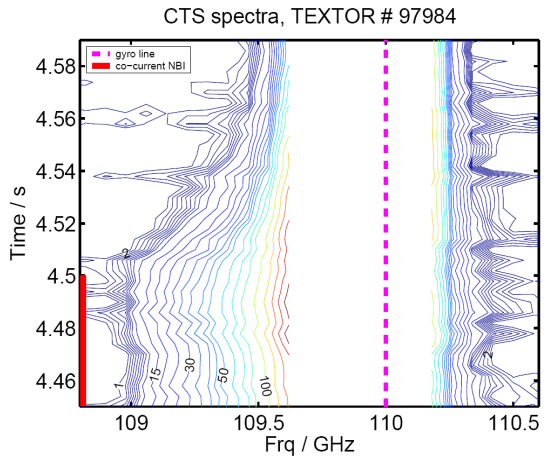

Fig. 5: Contour plot of CTS spectra from TEXTOR discharge #97984. The co-NBI was injected until t = 4.5 s giving rise to a pronounced signal at frequencies lower than the gyrotron frequency. This corresponds to counter passing ions with $v_{ion} \cdot k^{\delta} < 0$ (see scattering geometry in fig 4).

geometries. In both cases the scattering volume was located in the plasma centre but the resolved fluctuation vector was altered. In plasma shot #97984 (figure 4 and 5) the resolved fluctuation wave vector, k^{δ}, had an angle to the static magnetic field of ~45 degrees. It is seen than the CTS spectra are unsymmetrical during the heating phase (until t = 4.5 s), extending to frequencies lower than the gyrotron frequency indicating that $v_{fast\ ions} \cdot k^{\delta} < 0$ (see geometry in figure 4). This agrees with the fact that the birth velocity of the beam injected fast ions is antiparallel to the magnetic field. Likewise, in plasma shot #100911 (figure 6 and 7), the resolved angle is $\angle (k^{\delta}, B) \sim 135$ degrees and a positive frequency shift is dominating the CTS spectra during the beam heating phase until t = 4.0 s.

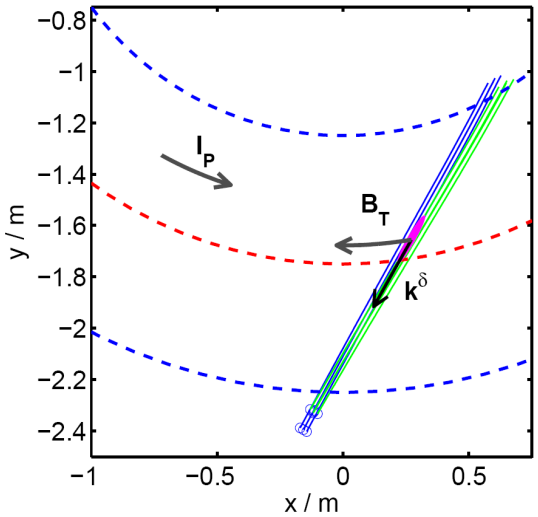

Fig. 4: Scattering geometry of TEXTOR #97984. The overlap is located in the plasma centre and the resolved fluctuation was resolved with an angle to the magnetic field of ~45 degrees.

4. Measured velocity distributions

The measured CTS spectra are used to infer the projected 1D ion velocity distribution, g(u) [18, 19]. The forward model used in the inference is a fully electromagnetic model of

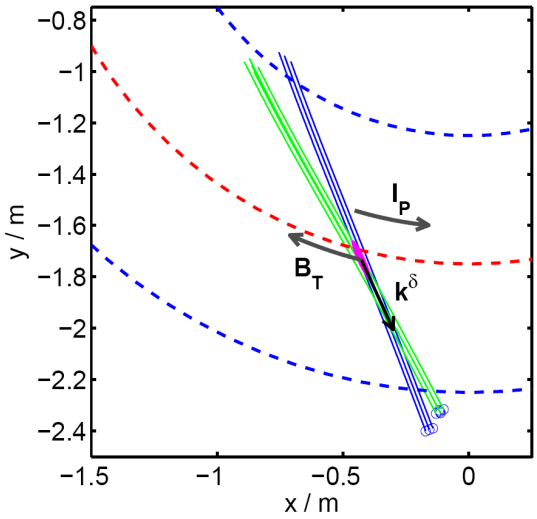

Fig. 6: Scattering geometry of TEXTOR #100911. The overlap is located in the plasma centre and the resolved fluctuation was resolved with an angle to the magnetic field of ~135 degrees.

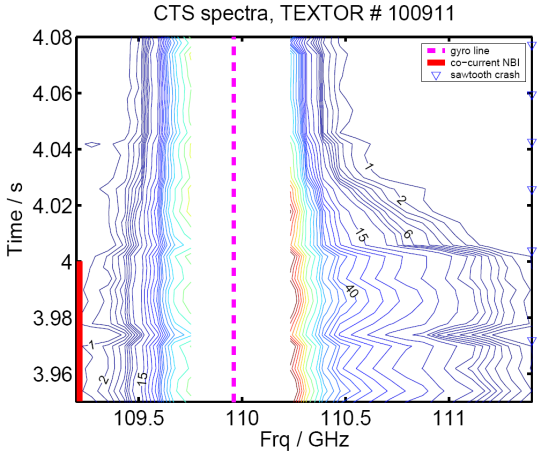

Fig. 7: Contour plot of CTS spectra from TEXTOR discharge #100911. The co-NBI was injected until t = 4.0 s giving rise to a pronounced signal at frequencies higher than the gyrotron frequency. This corresponds to counter passing ions with $v_{in} \cdot \boldsymbol{k}^{\delta} > 0$ (see scattering geometry in fig 6).

CTS with magnetised thermal ions while the fast ions are treated as un-magnetised [11].

The fast ion distribution function has been measured in a TEXTOR discharge where the co- and the counter-current NBI were injected subsequently. In this discharge the CTS scattering geometry was such that the measuring volume was located in the horizontal midplane at R = 1.87 m, and the resolved fluctuation, $\boldsymbol{k}^{\delta}$, made an angle to the magnetic field of 123 degrees. The co-NBI was injected until t = 2.15 s at which point the counter-NBI was turned on. A contour plot of the logarithm of the ion distribution is shown in figure 8. The figure

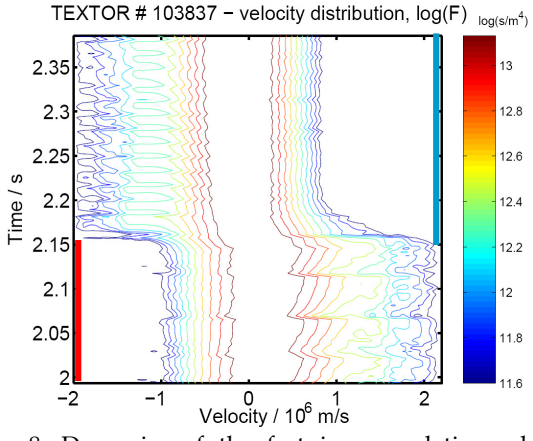

Fig. 8: Dynamics of the fast ion population when switching from co– to counter–injection of NBI. The switch occurs at t = 2.15 s. NBI power was 1.35 MW for co–injection and 1.32 MW for counter injected. $\angle(\boldsymbol{k}^{\delta}, \mathbf{B}) = 123$. Scattering volume at R = 1.87 ± 0.05 m and z = 0 ± 0.03 m.

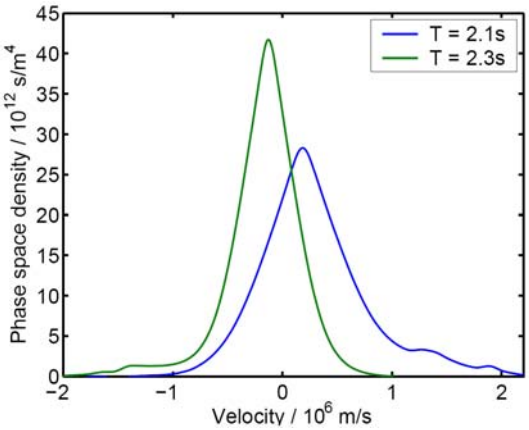

Fig. 9: TEXTOR #103837. Time slices from figure 8 at t = 2.1 s (during co-NBI) and t = 2.3 s (during counter-NBI).

shows a clear fast ion population at positive velocities prior to the switch in NBI. At t = 2.15, when the NBI is switch from co to counter, the fast ion population at positive velocities are seen to decay on the time scale of 50 ms while a population at negative velocities grows up. Both populations of fast ions are seen to be sensitive to sawtooth oscillation. In figure 9 the inferred distribution function is shown at t = 2.1 s and t = 2.3 s during the co- and the counter-NBI phase, respectively.

5. Neutral beam switch-on and switch-off

In order to change the slowing down rate of the fast ions, a scan in electron density prior to the NBI switch on has been made. The scattering geometry in these discharges was such that the measuring position was located on the high field side, R = 1.63 m, and the resolved fluctuation, $\boldsymbol{k}^{\delta}$, made an angle to the magnetic field of 113 degrees. The co-NBI start-up phase was measured in five discharges with different density. An example of the inferred velocity distribution is shown in figure 10 (bottom) as a logarithmic contour plot for a mid density discharge. Here the co-NBI was turned on at t = 2 s. The measured data are compared to Fokker-Planck simulations for a homogeneous plasma [19] which is shown in the top of figure 10. Good agreement is found. The time trace of the fast ion density at the ion velocity 1.2 10^6 m/s is shown in figure 11 for both the measured distribution (green squares) and the simulated distribution (green solid line). On the same graph the

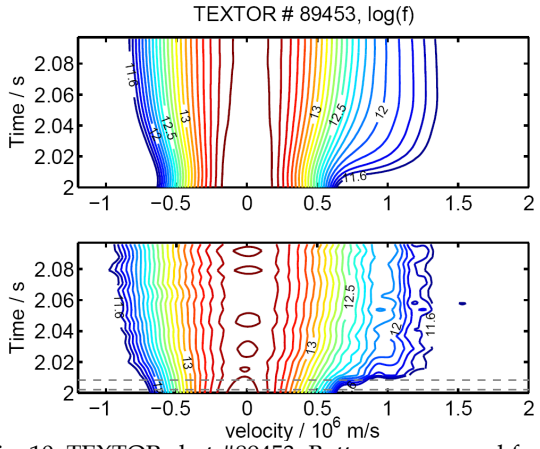

Fig. 10: TEXTOR shot #89453. Bottom: measured fast ion velocity distribution. Scattering geometry: R = 1.63 m, $\angle(\boldsymbol{k}^{\delta}, \mathbf{B}) = 113$ degrees. Co-NBI was injected from t = 2.0 s. Top: Fokker-planck simulation of fast ion population projected onto $\boldsymbol{k}^{\delta}$. Good agreement between simulation and measurements is found.

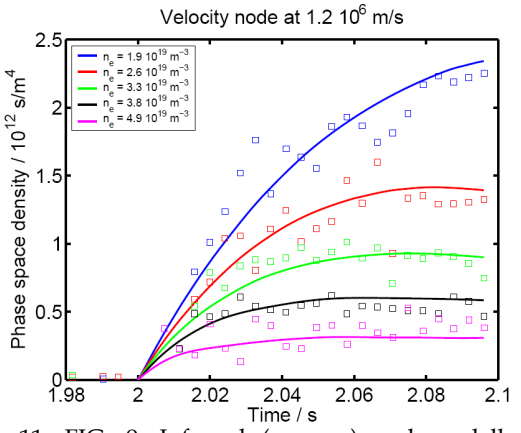

Fig. 11: FIG. 9: Inferred (squares) and modelled (continuous lines) fast ion density at an ion velocity of 1.2 × 10⁶ m/s as a function of time for a range of electron densities. 1.3 MW Co–injected NBI switched on at t = 2 s. $\angle(\boldsymbol{k}^{\delta}, \mathbf{B}) = 113$. Scattering volume at R = 1.63 m and z = 0 m. Values in figure legend refer to electron densities in scattering volume prior to switch on of NBI.

time traces have been added for four other discharges with a different electron density. The density prior to the beam turn-on is displayed in the legend. All five time traces shown good agreement between measured (squares) and simulated (solid lines) velocity distributions.

Tree discharges have been performed where the fast ion distribution was measured during the switch off of co-NBI for different densities. Figure 12 shows the evolution of the measured fast ions (squares) and the simulated fast ions (solid lines) at a projected velocity of 1.2 10^6 m/s. Here the co-NBI was turned on at t = 1.8 s and switched off at t = 2 s. The scattering geometry is

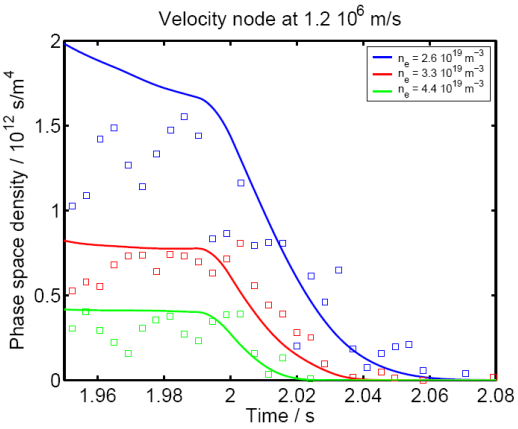

Fig. 12: Figure caption as in fig 10. Here the NBI is turned off at t = 2.0 s.

as in figure 10 and 11. Reasonable agreement is found.

6. Plans for ITER CTS.

The current CTS experiments are the stepping stones for a CTS system on ITER to measure fast fusion alphas in a burning plasma. A comprehensive feasibility study was carried out [20] to identify the CTS design, including choice of probe frequency, which would satisfy ITER measurement requirements for confined fusion alphas. The study concluded that a dual forward and back scattering system with a probe frequency around 60 GHz is the only CTS system that satisfies all criteria with present or near term technologies. A summary of the feasibility and conceptual design study can be found in reference [21] and [22]. The proposed design was optimised to satisfy requirements on accuracy and detail of the inferred fast ion velocity distribution, spatial resolution, time resolution and robustness over a broad range of plasma parameters. The system would measure the fast ion velocity distribution parallel and perpendicular to the magnetic field at 10 different radial locations simultaneously. It would bring out the dynamics of fast ions on passing orbits, on trapped orbits and would measure the bulk ion toroidal drift velocity across the plasma. In an expanded version it is predicted also to be able to provide measurements of the fuel ion ratio.

7. Conclusions

In conclusion, measurements of the temporal evolution of the fast ion velocity distribution function obtained by collective

Thomson scattering (CTS) have been presented. Examples of data are presented which give good evidence that the signals are indeed due to CTS. The ion velocity distribution after switch-on of co-current NBI heating was inferred from CTS for a number of electron densities and agrees remarkably well with simple Fokker-Planck simulations. Also the measured relaxation of the fast ion distribution after NBI turn off can be described by simple simulation. Fast ion measurements during injection of both co- and counter-NBI (subsequently) have been presented and the inferred fast ion dynamics is currently being analysed. All these results represent a breakthrough for the use of mm-wave collective Thomson scattering for diagnosing dynamics of confined fast ions in fusion plasmas, and is an important milestone in preparing this diagnostic technique for use at ITER. More information on CTS may be obtained from the website www.risoe.dk/fusion/cts.

Acknowledgements

This work was supported by EURATOM and U. S. DoE

References

[1] W. W. Heidbrink and G. Sadler, Nucl. Fusion, 34, 535 (1994).
[2] J. Jacquinot et al., Nucl. Fusion, 39, 2471 (1999).
[3] S. D. Pinches et al., Plasma Phys. Controlled Fusion, 46, B187 (2004).
[4] M. Rosenbluth and P. H. Rutherford, Phys. Rev. Lett. , 34, 1428 (1975).
[5] C. Cheng and M. Chance, Phys. Fluids, 29, 3695 (1986).
[6] K. Wong, Plasma Phys. Controlled Fusion, 41, R1 (1999).
[7] H. Bindslev, J. Plasma and Fusion Research, 76, 878 (2000).
[8] A. Sitenko and Y. Kirochkin, Sov. Phys. Usp. , 9, 430 (1966).
[9] R. Aamodt and D. Russel, Nucl. Fusion, 32, 745 (1992).
[10] H. Bindslev, Plasma Phys. Controlled Fusion, 35, 1615 (1993).
[11] H. Bindslev, J. Atmos. Terr. Phys. 58, 983 (1996).
[12] H. Bindslev Strong microwaves in plasmas (Russian Academy of Sciences, Institute of Applied Physics, Nizhny Novgorod 1996), vol. 1, p. 109.
[13] H. Bindslev et al, Phys. Rev. Lett., 83, 3206 (1999).
[14] H. Bindslev et al, Phys. Rev. Lett., 97, 205005 (2006).
[15] P. Woskov, proceeding of the 12th International Symposium of Laser Aided Plasma Diagnostics (LAPD-12), Snowbird, UT, September 26-29, 2005
[16] S. Michelsen et al., Rev. Sci. Instrum. , 75, 3634 (2004).
[17] S. Korsholm et al., Rev. Sci. Instrum. , 77, 10E514 (2006).
[18] H. Bindslev, Rev. Sci. Instrum. , 70, 1093 (1999).
[19] S. K. Nielsen et al., submitted to Physical Review E. (2007)
[20] H. Bindslev, F. Meo and S. B. Korsholm, Iter fast ion collective Thomson scattering-feasibility study, report, efda contract 01.654 (2003), available at www.risoe.dk/fusion/cts/iter.
[21] H. Bindslev et al., Rev. Sci. Instrum. , 75, 3598 (2004).
[22] F. Meo et al., Rev. Sci. Instrum., 75, 3585 (2004)

Microwave imaging for plasma diagnostics and its applications

A. Mase[1], Y. Kogi[1], N. Ito[1], Y. Yokota[1], T. Sakoda[1], N. Tateishi[1], K. Ogawa[1], K. Miyazaki[1], S. Takaichi[1], H. Hojo[2], S. Yamaguchi[3], T. Tokozawa[3], Y. Nagayama[3], K. Kawahata[3], C. W. Domier[4], N. C. Luhmann, Jr.[4], H. K. Park[5], A. J. H. Donne[6]

[1]*Art, Science and Technology Center for Cooperative Research, Kyushu University, Kasuga 816-8580, Japan*
[2]*Plasma Research Center, University of Tsukuba, Tsukuba 305-8577, Japan*
[3]*National Institute for Fusion Science, Toki 509-5292, Japan*
[4]*Department of Applied Science, University of California, Davis, CA 95616, U.S.A.*
[5]*Plasma Physics Laboratory, Princeton University, Princeton, NJ 08543, U.S.A.*
[6]*FOM-Instituut voor Plasmafysica Rijnhuizen, Associate EURATOM-FOM, Trilateral Euregio Cluster, 3430 BE, Nieuwegein, The Netherlands*

Microwave to millimeter-wave diagnostic techniques such as interferometry, reflectometry, scattering, and radiometry have been powerful tools for diagnosing magnetically confined plasmas. Important plasma parameters were measured to clarify the physics issues such as stability, wave phenomena, and fluctuation-induced transport. Recent advances in microwave and millimeter-wave technology together with computer technology have enabled the development of advanced diagnostics for visualization of 2D and 3D structures of plasmas. Microwave/millimeter-wave imaging is expected to be one of the most promising diagnostic methods for this purpose. We report here on the representative microwave diagnostics and their industrial applications as well as application to magnetically-confined plasmas.

1. Introduction

Transmission, reflection, scattering, and radiation processes of electromagnetic waves due to dielectric materials are utilized as diagnostic tools. In magnetically-confined plasmas, since various specific frequencies such as the cut offs and resonances in plasmas determined by confining magnetic fields and electron densities are in the range of 30-300 GHz, the optimum probing wavelengths are in the range of microwave to millimeter-wave. The diagnostic techniques are interferometry, reflectometry, scattering, and radiometry (electron cyclotron emission: ECE). The parameters obtained by these diagnostic techniques are the equilibrium and fluctuation components of electron density, electron and ion temperatures, and magnetic field.

Significant advances in microwave to millimeter wave technology have enabled the development of a new generation of imaging diagnostics as a visualization tool of the plasmas. Microwave imaging is expected to be one of the most promising diagnostic methods that measure profiles and fluctuations of plasmas. The physics issues of magnetically-confined plsamas have been studied by use of the microwave diagnostics. The microwave imaging diagnostics have also been applied to the other industrial applications. In this paper are reported the representative microwave diagnostics and their applications.

2. Plasma imaging diagnostics

2.1. Interferometry

Interferometry is a well-utilized method for measurement of plasma density profiles. A sufficient number (8-12) of probing chords is needed to perform a reconstruction of density profiles. When enough power is obtained as an incident source, power splitters can be used to divide the incident signal into a number of independent probing beams, otherwise, separate oscillators have to be employed for each probing beam. Different intermediate frequencies (IFs) for each channel are also employed to avoid the crosstalk between adjacent chords.

Instead of multichord system, phase-imaging interferometers have been used in several plasma experiments in order to measure multichord line-integrated electron densities. This technique uses a single set of optics and multichannel detector array instead of using multichannel optical paths with a single detector for each chord. The first example was a CO_2 laser interferometer using a 15-element PbSnTe detector array, which was applied to a high-density arc plasma. An FIR laser interferometer with a 20-element micro-bolometer array has been applied to a tokamak plasma [1]. A millimeter-wave phase-imaging interferometer using a Schottky barrier diode array has been applied to the GAMMA 10 tandem mirror [2].

2.2. Radiometry

The measurement of electron cyclotron emission (ECE) has become a main diagnostic to determine temporal and spatial behaviors of electron temperature. When the plasma density and temperature are sufficiently high, the plasma becomes optically thick specifically at the first and second harmonic of electron cyclotron frequency. The radiation intensity of optically thick ECE harmonics reaches that of black body radiation. Therefore, the electron temperature and its fluctuations can be diagnosed by measuring the intensity of ECE. In tokamak plasmas, the ECE frequency is often a monotonically decreasing function of plasma radius towards the outboard side. Therefore, time resolved 1D temperature profiles can be obtained by a conventional radiometer.

On the other hand, ECE imaging (ECEI) is a method whereby two-dimensional (2D) to three-dimensional (3D) images of temperature fluctuations as well as temperature profiles can be obtained. An ECEI system was at first applied to TEXT-U, and subsequently developed for the RTP tokamak, and more recently implemented on TEXTOR-94 [3,4] and LHD [5]. A CAD drawing of the microwave imaging system is shown in Fig.1. The system is capable of simultaneously measuring density and temperature fluctuations in the plasma core with ~1 cm^2 resolution in the poloidal plane. The ECEI system yields the temperature and its fluctuation in an 8×16 matrix of sample volumes, while the MIR system measures density fluctuations at 16 points along the density cutoff surface. Both systems view the plasma through a large

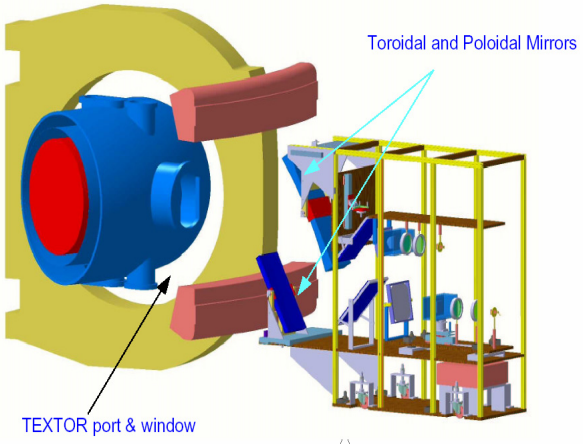

Fig. 1 TEXTOR-U ECEI/MIR system [3].

42×30 cm^2 quartz window. The two large-sized toroidal and poloidal collection mirrors are shared by the ECEI and MIR system. An electroformed metal mesh beam splitter is employed to separate the radiation at the ECE range of frequencies (95–140 GHz) from the frequencies used in the reflectometer (70–90 GHz). Each system utilizes a dedicated high-resolution multi-channel detector array based dual dipole antenna.

2.3. Reflectometry

Reflectometry has been expected to be one of the key diagnostics to measure density profiles and density fluctuations in large fusion devices. It provides good spatial and temporal resolutions, while requiring a single viewing chord and minimal vacuum access in contrast to interferometry and Thomson scattering. One of the most serious problems in density profile measurement using conventional frequency-modulation (FM) reflectometer is caused by the existence of density fluctuations in plasmas, since the multifringe phase changes produced by a reflectometer are easily masked by those due to density fluctuations. Several methods have been proposed to avoid this problem such as amplitude-modulation (AM) reflectometry or dual-frequency differential reflectometry and pulsed-radar reflectometry using moderate short pulse or ultrashort pulse as well as advanced data processing techniques based on sliding fast Fourier transform (FFT) algorithm, maximum entropy method (MEM), wavelet transform, and Wigner distribution.

If the amplitude of fluctuations is small or the width of their wavenumber spectrum is narrow, the reflected waves bear phase information on a large distance and interpretation of the signal is straightforward. The interference of the scattered wavefronts destructs the shape of the phase already close to the cutoff position making difficult extraction of the information from the reflectometer signal. One of the possible ways to solve the problem is to use microwave imaging reflectometry (MIR) with large aperture optics to restore the wavefronts at the receiver position. This technique can record time history of the density fluctuations and estimate value and spectrum of the fluctuations. In Fig. 2 is shown the schematics of MIR system in LHD [6].

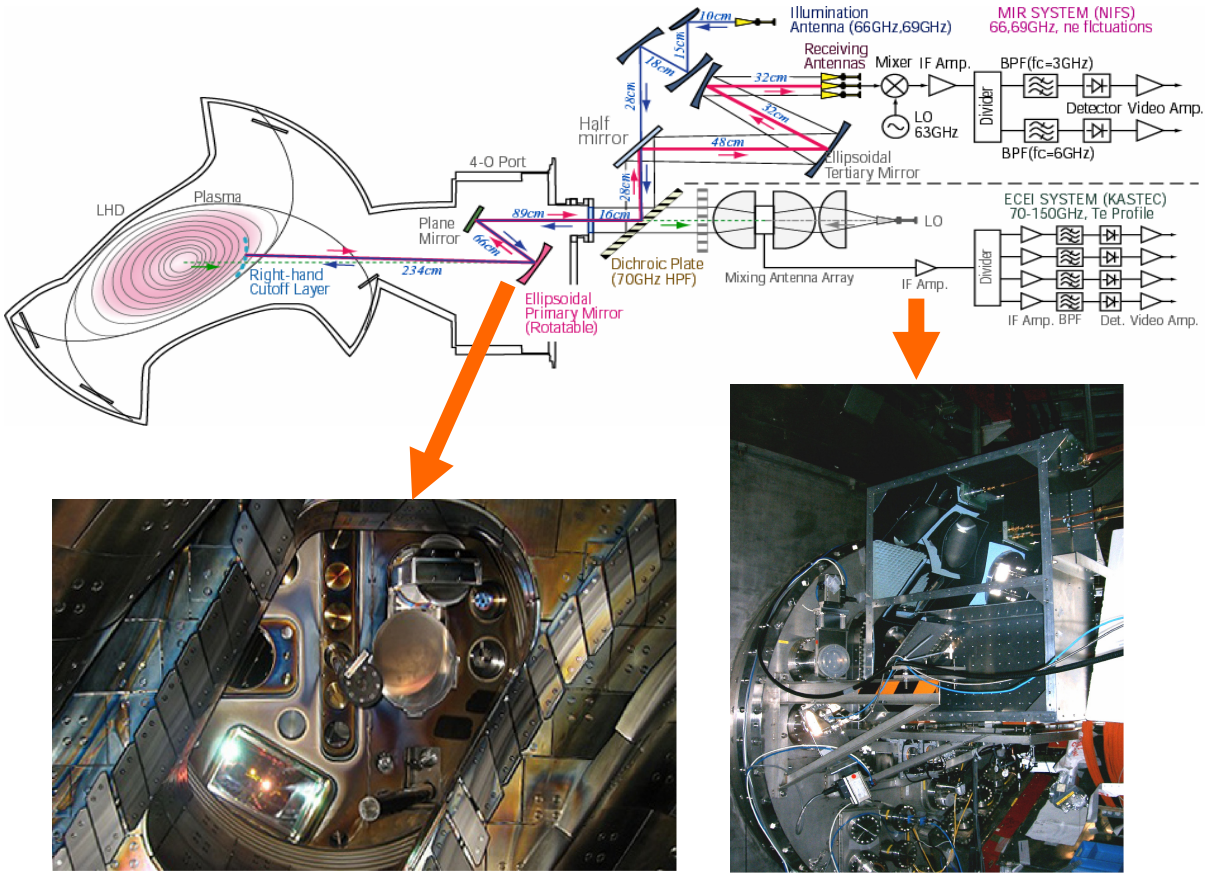

Fig. 2. LHD MIR/ECEI system [6].

3. Imaging diagnostics using an ultrashort-pulse radar

The reflectometry (radar) techniques are utilized in various industrial applications as well as in plasma diagnostics. Recently ultra-wide-band (UWB) radar has become popular for the time- and spatially-resolved measurements which give the dynamic structure of internal behavior of the object. There are two methods to perform the UWB radar, which are an ultrashort-pulse as a probe beam. We have tried an ultrashort-pulse radar (USPR) for the imaging measurements. The outputs of impulse generator are 3V, 22 ps, 8V, 65 ps and 10V, 130 ps full-width half-maximum (FWHM) pulses. An impulse is fed to a planar antenna or waveguide antenna, and irradiated to an object. The reflected wave detected by an identical antenna is amplified by a low-noise amplifier and recorded by a sampling scope or fed to a constant fraction discriminator (CFD) and time-to-amplitude converter (TAC) for the data processing. The CFD generates a timing output pulse at the optimum timing point (peak) of the input pulse. The timing pulse from the CFD is used as the stop trigger for the TAC; the output trigger from the impulse generator is used as the start trigger. The TAC output, which is a 0-10 V rectangular pulse with amplitude proportion ally to the time delay between the start and stop triggers, is sampled and recorded using high-resolution memory scope.

In this section, we describe the simulation study of the USPR for human-body imaging. We have solved full-wave Maxwell equations describing millimeter-wave propagation and its scattering and reflection by an object. The numerical scheme is based on the finite-difference time-domain (FDTD) scheme, and the simulations were done in two-dimensional space. As an example, we investigate human breast with tumor inside.

The optical property of matter is generally characterized by the complex permittivity. A

foreign object having a permittivity different from an object to be inspected causes a wave reflection and scattering. The breast has simple structure and lower dielectric constant than other parts, and loss tangent than the other part of body. In addition, dielectric properties of breast tumors are much higher than the normal breast tissue. Half circle with radius equal to 10 cm is used as a breast model. A breast tumor is located at 2-10 cm depth from the breast surface. We assume that the dielectric property of normal breast tissue is ε_r = 9, σ= 0.4 S/m and the malignant breast tissue is ε_r = 50, σ= 4 S/m, where σ is the conductivity. Here, a Gaussian-shape pulse with a 100 ps FWHM is irradiated to the breast through an antenna located at the position of 10 cm apart from the breast surface. The antenna is moved every 10 degree around the breast from 0 to 180 degrees. The reflected waves from the skin and the tumor are received by an identical antenna.

Hagness *et al.* recently proposed a confocal microwave imaging (CMI) approach to breast cancer detection [8]. The CMI is the reconstruction method based on synthetic aperture radar (SAR). In our FDTD simulation, the numbers of antenna array correspond to *M*=19. The calculation process is repeated for each antenna position. Although the incident wave and the reflected wave from the skin are much larger than that from the breast tumor, it is not difficult to distinguish those waves due to the difference of the TOF. Therefore, the spurious signals can be removed at the data processing.

To reconstruct the image, a point is focused. First, the distances between the focal point and each antenna position are determined and converted to the time delays. The reflected waves obtained by each antenna are summed up, and the square of this sum is assigned as

$$I(\vec{r}) = \left[\sum_{m=1}^{M} B_m(\tau_m(\vec{r})) \right]^2 ,$$

$$\tau_m(\vec{r}) = 2\left|\vec{r} - \vec{r}_m\right| / (v\Delta t) ,$$

where B_m is the back scattering waveform at the *m*th antenna located at $\vec{r}_m$, and $\tau_m(\vec{r})$ is the time delay from the *m*th antenna to the synthetic focal point at $\vec{r}$. Here, the propagation velocity inside the breast is calculated by using the assumed dielectric constant of the breast tissue, $\varepsilon_r = 9$. Figure 3 shows the reconstructed images by CMI. White line indicates the breast skin. Note that the tumor located at 7 cm depth from the skin can be detected when the size is 1 cm×1 cm. Also the tumor size of 2 mm×2 mm can be detected when it is located at 3 cm depth from the breast skin, which is considered to be very early stage.

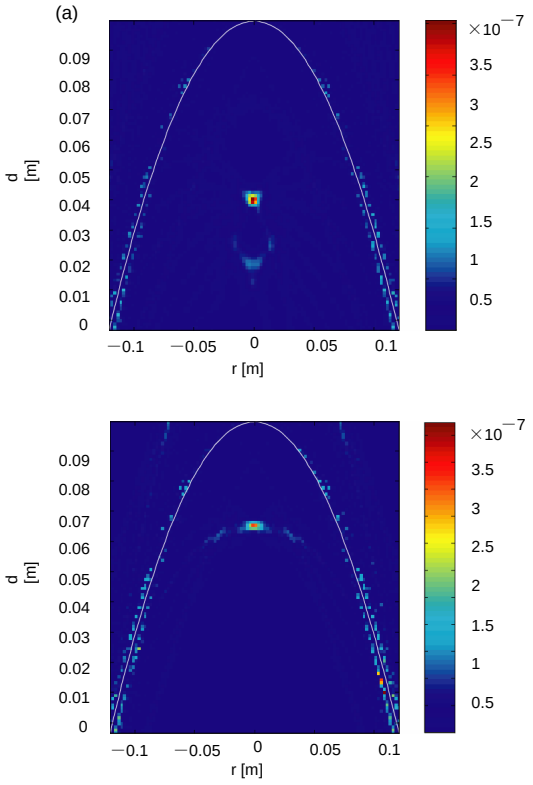

Fig. 3. Reconstructed image of the breast with tumor. The tumor located at (a) 7 cm depth from the breast skin (the size of tumor is 1 cm×1 cm), (b) 3cm depth (the size is 2 mm×2 mm).

4. Conclusion

In conclusion, the microwave/millimeter-wave imaging diagnostics have been applied to magnetically-confined plasmas in order to solve the physics issues. The methods are also useful to other fields including biomedical imaging, remote sensing using airborne synthetic aperture radar (SAR), nondestructive detection, and etc.

Acknowledgments
This work is partly supported by the Grant-in-Aid for Scientific Research, the Ministry of Education, Science, Sports and Culture (No. 16082205 and No. 17656134), and also by the U.S. DOE, Contracts No. DE-AC02-76-CH0-3073, No. DE-FG03-95ER-54295.

References

[1] P. E. Young et al., Rev. Sci. Instrum. **56** (1985) 903.
[2] N. Oyama, A. Mase et al., Rev. Sci. Instrum. **70** (1993)1003; K. Hattori, A. Mase et al., Rev. Sci. Instrum. **62** (1991) 2857.
[3] H. Park, C. C. Chang et al., Rev. Sci. Instrum. **74** (2003) 4239.
[4] H. Park, N. C. Luhmann, Jr. et al., Phys. Rev. Lett. **96** (2006) 195003; H. Park, A. J. H. Donne et al., Rev. Sci. Instrum. **96** (2006) 195004.
[5] A. Mase, Y. Kogi et al., Rev. Sci. Instrum. **74** (2003) 1445.
[6] S. Yamaguchi, Y. Nagayama et al., Rev. Sci. Instrum. **77** (2006) 10E930-1.
[7] S. C. Hagness, A. Taflove, and J. E. Bridges, IEEE Trans. Biomed. Eng. **45** (1998) 1470; E. C. Fear, Xu Li, and S. C. Hagness, IEEE Trans. Biomed. Eng. **49** (2002) 812.

Wideband ECEI Upgrade for Increased Plasma Coverage

P. Zhang[1], C.W. Domier[1], Z. Shen[1], N.C. Luhmann, Jr.[1], H.K. Park[2] , A.J.H. Donné[3] , N. Ito[4], A. Mase[4]

[1] *Dept. of Applied Science, University of California at Davis, Davis, CA 95616, U.S.A.*
[2] *Princeton Plasma Physics Laboratory, Princeton Universiry, Princeton, NJ 08543 , U.S.A.*
[3] *FOM-Institute for Plasma Physics Rijnhuizen, PO Box 1207, 3430 BE Nieuwegein, The Netherlands*
[4] *Art, Science and Technology Center for Cooperative Research, Kyushu University, Kasuga, Fukuoka 816-8580, Japan*

A 128 channel 2-D Electron Cyclotron Emission Imaging (ECEI) instrument has been employed to study MHD physics such as the m=1 and m=2 modes on the TEXTOR tokamak. This system was upgraded in February 2007 with new wideband electronics which increased the instantaneous frequency coverage by >50% from 4.0 to 6.4 GHz with a corresponding increase in plasma coverage. Details regarding the diagnostic upgrade and recent physics results from TEXTOR will be presented together with a discussion of diagnostic development activities underway at UC Davis to implement ECEI on other plasma devices including KSTAR and DIII-D.

1. Introduction

Electron Cyclotron Emission (ECE) Imaging (ECEI) has been routinely employed to study the dynamics of electron temperature T_e fluctuations in TEXTOR tokamak plasmas [1-3]. In a tokamak, the cyclotron frequency, f_{ce}, depends on the major radius R of the device, leading to a 1:1 mapping between f_{ce} and R. The ECE frequency in plasmas with sufficiently high density and temperature is proportional to the local T_e value and thus yields information regarding the electron temperature and its fluctuations [4].

ECEI systems began as single emission frequency systems, enabling 1-D spatially resolved measurements along a vertical chord of the plasma. This technique was subsequently extended to 2-D by allowing each array element to collect broad bandwidth radiation that is then frequency resolved into bands [5].

A 128 channel ECEI instrument has been routinely used to study MHD physics on the TEXTOR tokamak [1, 2]. Each array element of the 16 element Schottky diode mixer array measures electron cyclotron emission at 8 simultaneous frequencies to form 16×8 images of $\boldsymbol{T_e}$ profiles and fluctuations over an extended area of the TEXTOR plasma.

2. Overview of the ECEI Diagnostic Upgrade

An upgraded ECEI diagnostic system with a redesigned array and new wideband electronics was installed in February, 2007 on TEXTOR and increases the plasma coverage to 17 cm (v) × 9 cm (h) from 16 cm (v) × 6 cm (h) by both array modifications and development of new wideband IF electronics. The new arrangement offers increased temperature resolution together with new gain and video bandwidth controls in a modular configuration for ease of maintenance as well as ease of future upgrades, both in frequency coverage as well as number of channels.

An overview of the ECEI scheme is presented in Fig. 1. Large aperture optics are employed to image the ECE radiation onto a multichannel mixer array. A quasi-optical, square loop, notch filter has been developed to shield the array from the 800 kW, 140 GHz gyrotron heating source. Unlike waveguide filters, these frequency selective surface filters must retain their filtering characteristics over a wide range of incident angles to provide adequate shielding. The filter shown in Fig. 1 has a measured 35 dB rejection at normal incidence, and only drops to 25 dB at incidence angles of ±15° [6].

The ECEI optical layout remained unchanged during the upgrade, and thus will not be discussed herein. Modifications to the mixer array are described in Sec. 3, while the new wideband IF electronics are described in Sec. 4 with results presented in Sec. 5. We conclude in Sec. 6 with a discussion of the planned implementation schedule together with a number of possible additional upgrades.

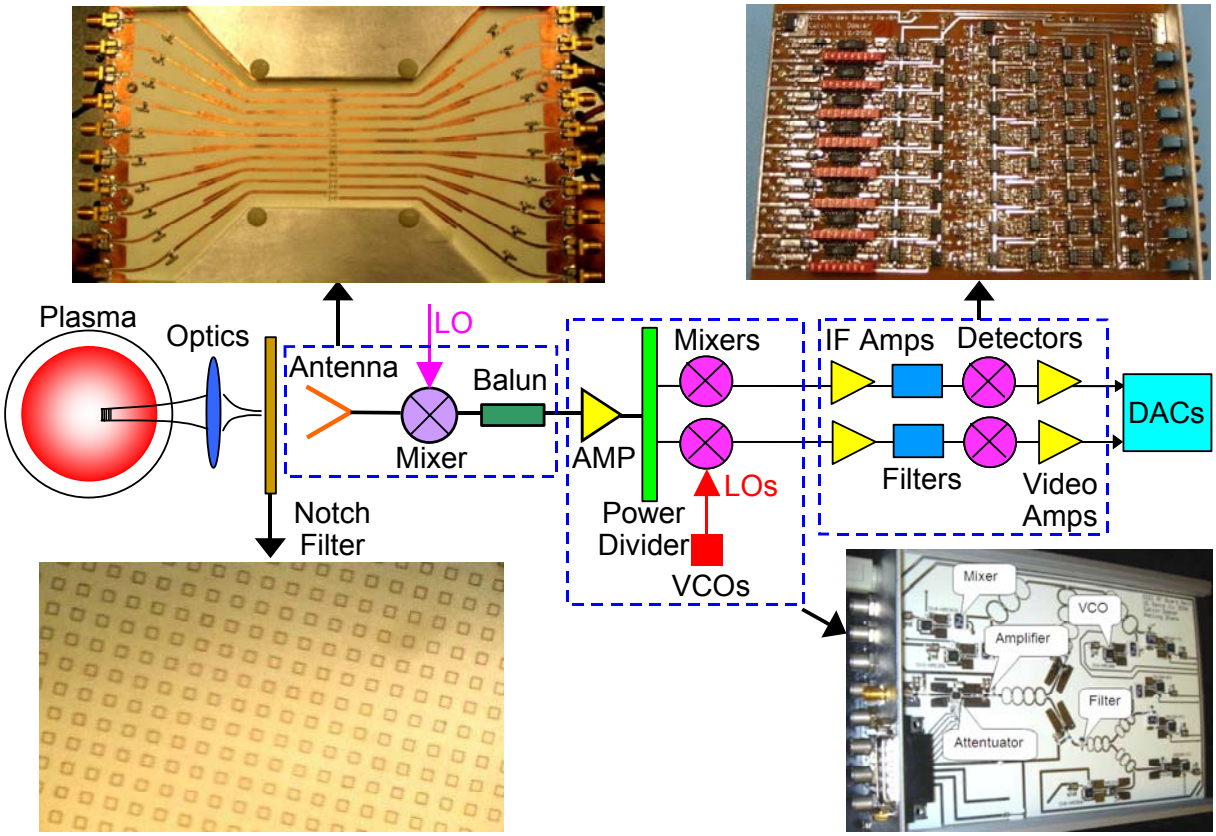

Fig. 1. Schematic diagram of the ECEI detection scheme employed on TEXTOR, illustrating the steps required to convert wideband ECE radiation into 2.0-8.4 GHz IF signals and then to generate 16×8 channel ECEI output signals.

3. ECEI Mixer array

The new mixer array shown in Fig. 1 employs dual dipole antennas similar to those in the current system, but with an antenna spacing of 2.44 mm (increased from 2.29 mm). This extends the vertical plasma coverage by 1 cm, retaining the same vertical spot size while reducing the signal overlap between adjacent channels from ~65% to ~55% [7].

Microwave baluns, which convert the microwave signals from balanced (at the antenna) to unbalanced (at the output SMA connector) format, have been reduced in size while simultaneously increased in bandwidth. A unique feature of this design is the ability to supply DC bias to the mixers while maintaining an extremely wide IF bandwidth. The new baluns achieve a 2 dB insertion loss bandwidth (4 dB for back-to-back baluns) that extends from DC to 16 GHz, and a 3 dB loss bandwidth that extends past 30 GHz as shown in Fig. 2.

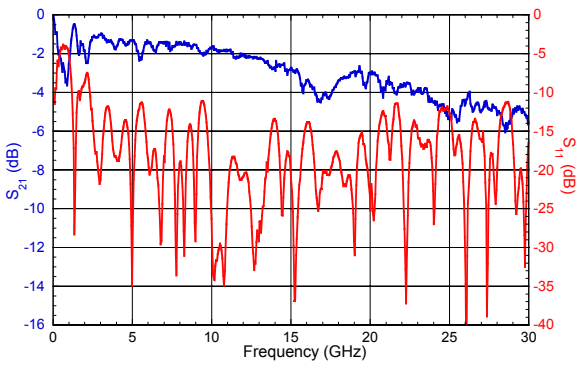

Fig. 2. Measured insertion loss (S_{21}) and reflection loss (S_{11}) through a pair of back-to-back microwave baluns.

4. ECEI Electronics

As in the previous implementation, down-converted ECE radiation from each antenna element is amplified by ~35 dB using low noise preamplifiers. Microwave cables transmit these signals out of the TEXTOR bunker to the new wideband IF electronics modules. Each of the new modules is comprised of two printed circuit boards mounted within a shielded enclosure box. The first board is a radio frequency (RF) circuit which splits each 2.0-8.4 GHz input signal into 8 portions, each of which is down-converted a second time using surface mount balanced mixers fed with 2.4-8.0 GHz LO signals spaced 800 MHz apart. The second board consists of an

array of 8 circuits which rectify the IF signals from the RF circuit board to form 8 video signals whose amplitude is proportional to the ECE signal level strength over each of the 8 RF frequency bands. Both of the boards are shown in Fig. 1.

The RF circuit board layout is shown schematically in Fig. 3. The input signal is amplified using a low noise gain block, split into two parts, and then amplified and split a second time. Each of these signals is high-pass filtered with a distinct cutoff frequency, and then split one last time to form 8 RF signals which are fed to balanced mixers for the second down-conversion process. These high-pass filters serve to eliminate spurious mixer byproducts arising from higher harmonic RF components, as well as to eliminate low frequency (< 1 GHz) noise arising from the RF amplifier chain that feeds the mixers.

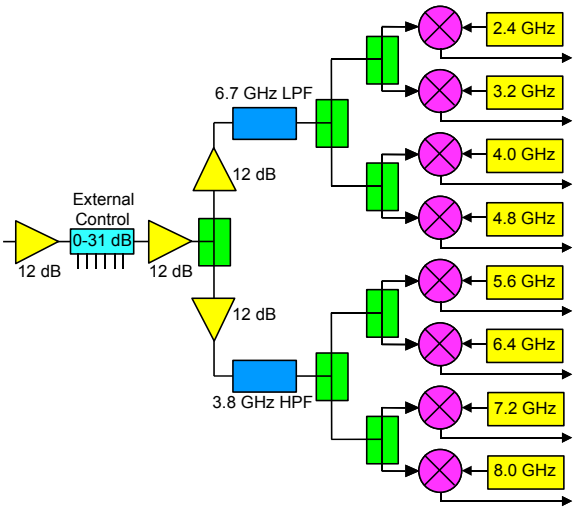

Fig. 3. Schematic layout of the ECEI RF electronics.

Each of the mixer LO signals are generated onboard from voltage-controlled oscillators (VCOs). Previously, the 8 LO signals were generated off-board in separate VCO modules, split into 16 portions, and routed to the RF mixers via 16×8=128 microwave cables. This had the undesirable effect of making detection module access difficult and time-consuming, as roughly half of these cables had to be disconnected on the detection module end before a given module could be removed for modification, repair, or replacement.

Each of the 8 IF signals from the RF circuit board are coupled to detection circuits on the IF circuit board where the signals are amplified and band-pass filtered (5-350 MHz), detected or rectified, and then video amplified and low-pass filtered shown in Fig. 4 [7]. Since this last mixing process is a double sideband down-conversion process, collecting power on both sides of the LO signal, this translates to an effective RF bandwidth of ~700 MHz. This is more than twice the RF bandwidth of the current system, and translates to a 1.5× improvement in temperature resolution.

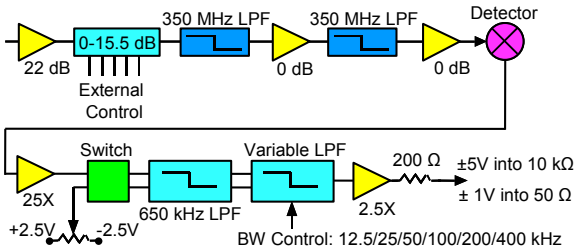

Fig. 4. Schematic layout of the ECEI IF electronics.

Video bandwidth control in the current system is set by a tunable single order RC low-pass filter. This has been replaced by a tenth order, low-pass switched capacitor filter (Linear Technology model LTC1569-7) whose cutoff frequency may be selected between 12.5, 25, 50, 100, 200, and 400 kHz. Filter selection on all channels is simultaneously set using front-panel DIP switches or via computer control. Note that the frequency of the lowest filter setting, 12.5 kHz, is set by the use of a seventh order, 650 kHz low-pass prefilter (Linear Technology model LTC1565-31) which prevents high frequency noise (at ≥64 times the filter cutoff frequency) from being aliased down by the switched capacitor filter.

In the new electronics, a pair of digital step attenuators is employed. The first provides up to 31.5 dB attenuation under external control, applied equally to all 128 ECEI channels. This provides a way to adjust the system gain to account for variations in T_e or in receiver sensitivity (by, for example, tuning the ECEI array to operate well outside its optimum RF bandwidth). The second provides up to 15.5 dB of gain control set via DIP switches within the module. These switches are adjusted to compensate for fixed cable losses and variations in the frequency-gain response of individual ECEI channels. Finally, new controls individually set the polarity and dc offsets on each channel to accommodate a wide variety of transient digitiz-

ers, with the capability of driving ±1 V into 50 Ω loads and ±5 V into high impedance loads.

5. ECEI Physics Studies

The TEXTOR ECEI system employs a 16 element array with 8 frequency bands spaced 800 MHz apart, generating time-resolved 16×8 images of T_e profiles and fluctuations of the TEXTOR plasma [1, 2]. The system is wide-band tunable from 100 to 130 GHz, and the focus location may be shifted horizontally by translating one of the optical imaging elements. The ECEI measurements illustrated in Fig. 6 provide a 2-D movie of the magnetic field perturbation, and make it possible to directly compare the measurements with predictions from various theoretical models. These and other recent studies into tearing mode suppression [8] are expected to benefit greatly from the increased plasma coverage achieved by this upgrade.

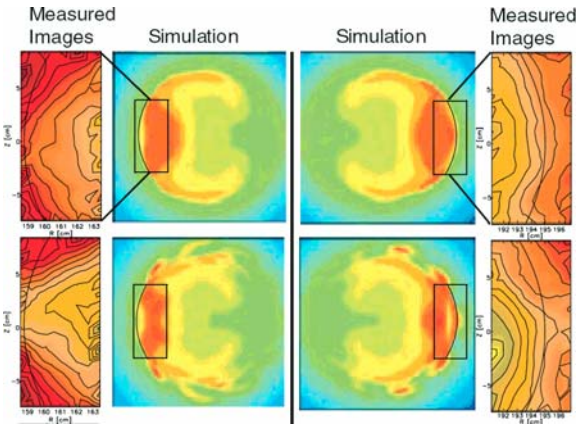

Fig. 5. Experimental 2-D images of hot spot and island formation are directly overlaid for comparison with ballooning mode model images (from [1]).

6. Possible Future ECEI Upgrades

A second ECEI system has been proposed for TEXTOR which would employ similar wideband electronics but with 24×8 channels, a 1.0 GHz channel spacing, and a tunable RF bandwidth extending from 130 to 153 GHz.

The number of ECEI channels in the present ECEI system could also be easily increased from 16×8 to 20×8. This can be done simply by fabricating 4 additional IF electronics modules and the installation of an additional 4×8=32 digitizers, as the current array already encompasses 20 elements. Other related diagnostic development activities underway at UC Davis include the extension of the ECEI diagnostic technique to other plasma devices such as KSTAR, EAST and DIII-D.

Acknowledgements

This work was supported in part by the U.S. Department of Energy under Grants DE-FG02-99ER54518, DE-FG02-99ER54531 and DE-AC02-76-CHO-307, and by NWO and the Association EURATOM-FOM.

References

[1] H.K. Park, N.C. Luhmann, Jr., A.J.H. Donné, I.G.J. Classen, C.W. Domier, E. Mazzucato, T. Munsat, M.J. van de Pol, Z. Xia and TEXTOR team, Phys. Rev. Lett. **96**, 195004 (2006).

[2] H.K. Park, E. Mazzucato, N.C. Luhmann, Jr., C.W. Domier, Z. Xia, T. Munsat, A.J.H. Donné, I.G.J. Classen, M.J. van de Pol, and TEXTOR team, Phys. Plasmas **13**, 055907 (2006).

[3] H. Park, E. Mazzucato, T. Munsat, C.W. Domier, M. Johnson, N.C. Luhmann, Jr., J. Wang, Z.G. Xia, I.G.J. Classen, A.J.H. Donné, M.J. van de Pol, Rev. Sci. Instrum. **75**, 3787 (2004).

[4] I.H. Hutchinson, Principles of Plasma Diagnostics, Cambridge University Press, New York, 1987.

[5] J. Wang, C.W. Domier, Z.G. Xia, Y. Liang, N.C. Luhmann, Jr., H. Park, T. Munsat, E. Mazzucato, M.J. van de Pol, I.G.J. Classen, A.J.H. Donné, Rev. Sci. Instrum. **75**, 3875 (2004).

[6] Z. Shen, N. Ito, E. Sakata, C.W. Domier, Y. Liang, N.C. Luhmann, Jr., A. Mase, *2006 IEEE Antennas and Propagation Society International Symposium*, July 9-14, 2006, Albuquerque, NM, 4191 (2006).

[7] C.W. Domier, Z.G. Xia, P. Zhang, N.C. Luhmann, Jr., H.K. Park, E. Mazzucato, M.J. van de Pol, I.G.J. Classen, A.J.H. Donné, R. Jaspers, *16th Topical Conference on High-Temperature Plasma Diagnostics*, May 7 - 11, 2006, Williamsburg, Virginia.

[8] I.G.J. Classen, E. Westerhof, C.W. Domier, A.J.H. Donné, R.J.E. Jaspers, N.C. Luhmann, Jr., H.K. Park, M.J. van de Pol, G.W. Spakman and TEXTOR Team, Phys. Rev. Lett. **98**, 35001 (2007).

LTS Diagnostics for the Study of Detached Divertor Plasmas

S. Kado[1] and F. Scotti[2]

[1] *High Temperature Plasma Center, The University of Tokyo, Kashiwa, Chiba, 277-8568, Japan*
[2] *School of Engineering, The University of Tokyo, Bunkyo, Tokyo, 113-8656, Japan*

A laser Thomson scattering (LTS) system developed in the MAP (material and plasma) -II steady-state linear divertor/edge plasma simulator at the University of Tokyo, intended for the study of low-temperature recombining plasmas (referred to as the *detached plasma* in the divertor region of the magnetically confined fusion devices), is presented. The electron temperature (T_e) at the entrance of the recombination front of He electron-ion recombining (EIR) plasma was determined to be as low as 0.15 eV. An electron temperature of 0.05 eV, which was previously determined based on the Rydberg series spectra of He I at the brightest point of the recombining front, can be considered to be a plausible value. Possible effects leading to an error in the estimation of the parameters in low-temperature plasma were evaluated, leading to the conclusion that these effects are negligible.[1]

1. Introduction

In the so-called recombining plasmas, since the electron temperature is so low, the excited state populations are governed by volumetric recombination processes such as electron-ion recombination (EIR) consisting of radiative and three-body recombinations, and molecular assisted recombination (MAR) induced by hydrogen (H_2-MAR)[1] or hydrocarbons (C_xH_y-MAR)[2]. Recombining plasma in the divertor/edge region in magnetically confined fusion-relevant plasma can be a sink of particle and energy due to the neutralization of the plasma before reaching the divertor plate (this phenomenon being referred to as "detachment"), so that the production and the control of the recombining plasma are key issues in future fusion devices.

Investigation of detached recombining plasmas requires efficient methods of electron temperature measurement, since the atomic and molecular processes depend strongly on the electron temperature, T_e. Typically, for example, T_e < 6-8 eV is required for C_xH_y-MAR [3], T_e < 2-3 eV for H_2-MAR, while T_e can be much lower than 1 eV for EIR. Common knowledge holds, however, that conventional diagnostic methods tend to give ambiguous results for recombining plasmas.

A problem involved in applying a single probe to recombining plasmas is that the electron current exhibits values anomalously lower than those expected from the ion saturation current (known as an anomalous current-voltage characteristic). As a result, the electron temperature is overestimated if one *believes* the probe characteristics to be valid, and in turn the electron density become immeasurable [4,5,3]. The atomic Boltzmann plot method applied to the Rydberg spectra from the highly excited states, being in partial local thermal equilibrium (p-LTE), can be simply applied to determine the electron temperature. However, the spectroscopic measurement always reflects the brightest point, which makes it difficult to analyze the spatial distribution and dynamic behavior of the detachment. It is also noteworthy that between the ionizing and EIR regions there exists a layer where the excitation rates are so low that the line emissivity is small. This transition region cannot be measured either by a probe (due to the anomaly) or by passive spectroscopy (due to the absence of emissions).

Also for MAR plasmas, analysis of the atomic spectra is influenced to a considerable degree by the contribution of the molecular dissociation. Therefore, we have developed a more direct way of measuring the electron temperature, i.e., the Thomson scattering method [6].

[1] This proceeding is the extended version of the paper presented in the *28th International Conference on Phenomena in Ionized Gases (ICPIG), July 15-20, 2007, Prague, Czech Republic*, **4P06-32**, "*Development of the laser Thomson scattering method intended for the study of low-temperature recombining plasmas in the MAP-II divertor simulator*", S. Kado, F. Scotti, T. Shikama, Y. Kuwahara, K. Kurihara and S. Tanaka. Note that small corrections are made in the optical system.

Obtaining the Doppler-broadened Thomson scattering spectra of free electrons in low-temperature recombining plasmas can pose a challenge since the stray light at the laser wavelength interferes with the narrow Doppler spectra, this effect being attributable to scattering from the chamber walls as well as due to the Rayleigh scattering caused by residual neutral gas. This led us to use a double-monochromator having a stray-light rejection capability.

This article reviews our LTS system which was initially developed for MAR plasmas and has recently been upgraded with the intention of gaining access to the EIR regime in the MAP (material and plasma)-II steady-state linear divertor/edge plasma simulator at the University of Tokyo.

2. Experimental setup

The configuration of the laser Thomson scattering (LTS) system is schematically shown in Fig. 1. A frequency-doubled Nd:YAG laser beam (532 nm in wavelength, a 10 Hz repetition rate, 7 ns pulse duration, and typically 400 mJ of energy per pulse, 8 mm in diameter) is directed to a plasma by means of a mirror located beneath the chamber. A lens with a focal length of 900 mm focuses the beam in the center of the plasma through a Brewster window and three baffle plates. This lens is sometimes removed for easier optical alignment when the scattering signal is high enough. An object lens with a 150-mm focal length and a diameter of 100 mm is used to image the 12 mm vertical scattering region onto an optical fiber array with a magnification of 2/3, which transfers the light to a spectrometer.

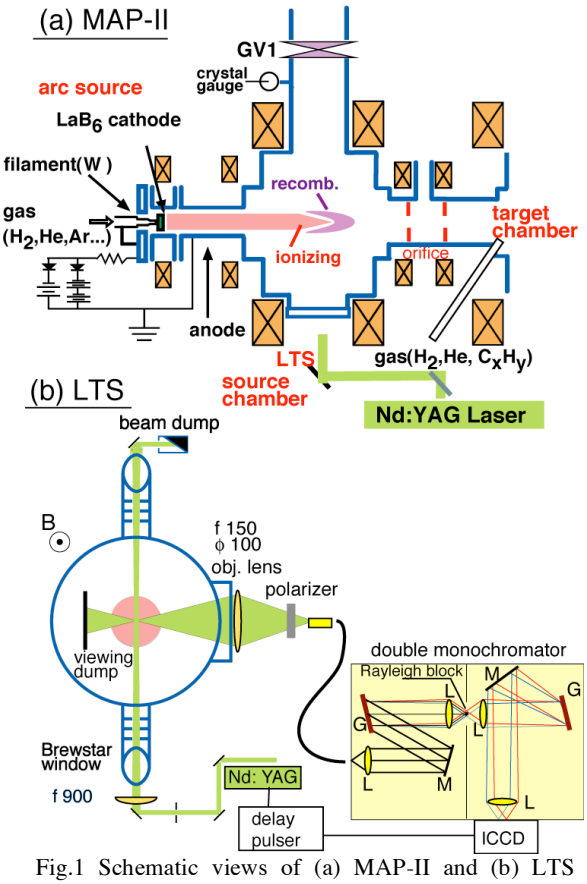

Fig.1 Schematic views of (a) MAP-II and (b) LTS system. The target chamber is omitted.

Since the 1 eV electron temperature corresponds to about 1.5 nm in the Doppler half-width at 1/e maximum at 532 nm for an orthogonal viewing chord, it is difficult for commercially available narrow-band interference filters (which typically have a pass band broader than about 1 nm) to resolve the Doppler profiles. For this reason, we have assembled a double monochromator equipped with four commercial camera lenses (Nikon, 135 mm F/2.8), a pair of gratings with 1800 grooves/mm, and an image-intensified charge-coupled device (ICCD) detector (Hamamatsu C4078+C4742, 1344x1024 pixels). The first grating produces a dispersed Thomson spectrum in the image plane, where a spatial stray-light filter, called a Rayleigh-block, is located and filters out the stray light which also contains a Rayleigh scattering component. The second grating then disperses the notch-filtered Thomson spectrum, which is imaged on the photocathode of an ICCD detector.

The wavelength resolution (instrumental width) is 0.13 nm full width at half maximum (FWHM) for a slit width of 0.085 mm. A Rayleigh-block 0.35 mm in diameter, applied in the initial case [6], corresponds to the lower limit of the measurable electron temperature of about 0.3 eV. This was applicable to MAR plasmas, but was not sufficient for application to EIR plasmas in the MAP-II device. Recently, the original block has been replaced with one 0.2 mm in diameter, which allows us to perform measurements as low as 0.13 eV (after considering the margin for the Gaussian fitting area)[7].

The absolute intensity necessary for the electron density measurement was calibrated using the dependence of the Rayleigh scattering spectrum on the filled gas pressure of N_2 according to the cross section ratio of the

Thomson to Rayleigh scatterings. The offset signal of this Rayleigh scattering at 0 pressure is attributable to the stray light originating in the reflection from the windows or the chamber wall. The typical level of the stray light is equivalent to a Rayleigh scattering signal of approximately 1-10 Torr for N_2 depending on the alignment condition, which is much higher than that from the Rayleigh scattering at the working gas pressure of 10-150 mTorr of He or H_2. Note that the Doppler width of the Rayleigh signal is governed by the thermal motion of the neutral gas, and thus the line width of the stray light and Rayleigh components can be regarded as identical to the instrumental width.

3. Results

The MAP-II [8] is a dual-chamber linear device consisting of a first chamber in the upstream (called the source chamber) and a second chamber in the downstream (called the target chamber) connected to each other by means of a drift tube having two diaphragms 50 mm in diameter. A longitudinal magnetic field of about 20 mT suppresses the radial diffusion, forming a plasma stream of approximately 50 mm in core diameter and about 2 m in length, which is terminated at the target plate at the second chamber. Typical discharge conditions are: discharge voltage of 60 - 80 V, a current of 30 - 45 A, and filled helium gas pressure of about 4 - 20 mTorr. However, in order to produce EIR plasma at the first chamber where the LTS system is installed, the neutral pressure is increased up to 120 mTorr by puffing the additional helium gas into the second chamber.

Photos of the He EIR plasma are shown in Fig. 2. One can see that the bright recombining "front" is formed surrounding the tip of the plasma stream (ionizing plasma). As the neutral pressure increases the recombining front moves across the fixed observation point, 4.5 mm in vertical (along the laser path) and 0.2 mm in the horizontal direction (along the plasma stream). This operation changes only the length of the plasma stream (approximately 1m from the plasma source) and the recombining front can be

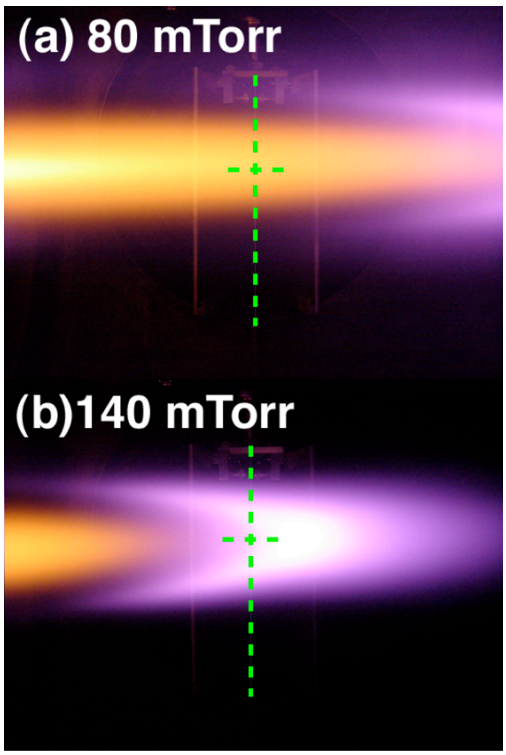

Fig. 2 Photos of the He EIR plasmas in MAP-II. Cross points of the broken lines represent the viewing points.

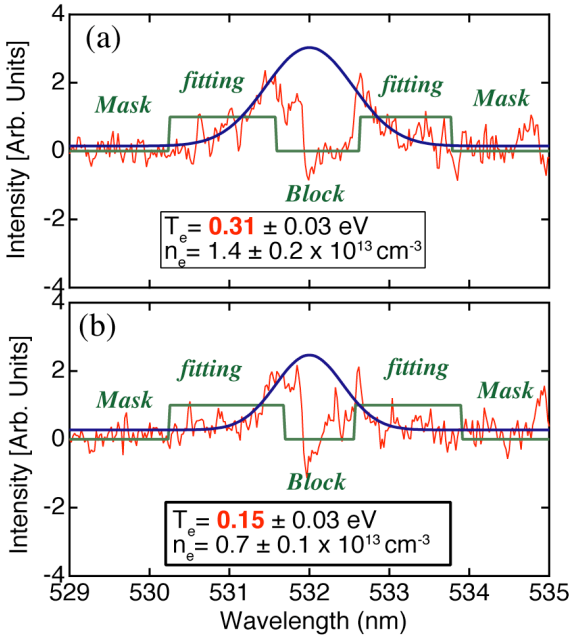

Fig. 3. Typical Thomson scattering spectra for low temperature regime corresponding to the transition region between ionizing and recombining plasmas. (a) and (b) were obtained at the neutral pressure of 140 and 144 mTorr, respectively, which can interpreted as the ones at the relative distances from the observation point for 84 mTorr. Then, these spectra, respectively, can be regarded as the equivalent ones at 25.5 and 27.4 cm from the central position for 84 mTorr

regarded as having the same parameters - a kind of nature of the optical emissions of recombining plasmas. The spatial profiles along the plasma stream was thus obtained by relating the position (0 – 27.4 cm) to the neutral pressure (82 – 144 mTorr).

Typical Thomson scattering spectra for the lowest two temperature conditions, 25.5 cm (140 mTorr) and 27.4 cm (144 mTorr) are shown in Fig. 3. The spectrum without plasma was subtracted from that with plasma to eliminate the stray light, which remained even after the suppression at the Rayleigh block. As mentioned in the previous section, the fitting to a Gaussian curve was performed avoiding the wavelength region corresponding to the Rayleigh block with, in reality, a little wider safety margin.

Fig. 4 shows the electron temperature and density as a function of the neutral pressure, interpreted as the distance along the plasma stream. The electron temperature monotonously decreases from left to right until reaching the rightmost data point, 0.15 eV, at the immediate entrance of the recombining front. This is the measurable lower temperature limit of the current system. We evaluated the collisional mean free path of the electrons and revealed that the change

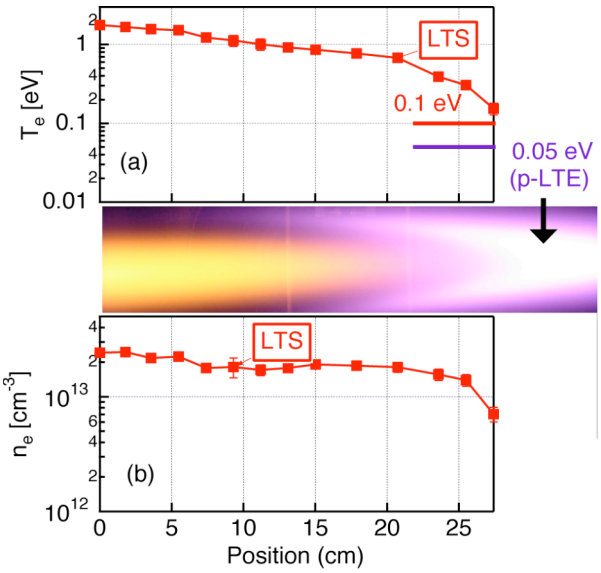

Fig. 4 Electron temperature and density measured using LTS. The picture in the middle indicates the measured position. The brightest point of He EIR exhibits 0.05 eV from spectroscopy, while 0.1 eV is the lower measurable limit of the current LTS system.

in the electron temperature in the upstream region was due to the elastic collision with neutrals, while in the region of interest in the present study this change is due to the collision with ions. This fact supports the invariance of the shape of the recombining front as the neutral pressure increases.

Our previous results regarding the electron temperature in He EIR plasma show 0.05 - 0.06 eV based on the atomic Boltzmann plot [9], on the collisional-radiative (CR)-model for Rydberg series spectra [8] , and on the CR-model for the principal quantum numbers n = 3 and 4 [10]. Although the discharge condition is not identical to the previous one, the brightest point, around 32 cm, is expected to have such temperature. A further major upgrade in the double monochromator, now being planned, is necessary to access that temperature regime. However, it can be supposed, from the decay of the electron temperature toward the recombining front shown in Fig. 4(a), that such a low temperature exists.

4. Discussion

Here we evaluate possible perturbations that could lead to measurement errors.

Plasma heating by absorption of the laser energy through inverse bremsstrahlung can be described based on Kunze [11] as

$$\frac{\Delta T_e}{T_e} \approx 5.32 \cdot 10^{-7} \frac{n_e Z}{(T_e)^{3/2}} \lambda_i^3 \times \left\{1 - \exp\left(-\frac{h\nu_i}{eT_e}\right)\right\} \cdot Q_i \ . \qquad (1)$$

The simulated results as a function of T_e are shown in Fig. 5. The typical theoretical optical condition using 900-mm focusing lens for the laser beam, where, in the unit used in the equation, the electron density $n_e = n_i Z = 7 \times 10^{12}$ cm^{-3} (Z = 1), $T_e \geq 0.15$ eV, the wavelength of the incident laser photon, $\lambda_i = 5.32 \times 10^{-5}$ cm ($h\nu_i / e$ = 2.33 eV) and its power density Q_i = 400 mJ / ($0.04^2 \pi$) mm^2 = 5 kJ cm^{-2}, yields at most 7.5% of T_e. This value is within the range of error. Note that the measurements in the present paper were conducted without focusing the laser beam in the measurement point. Therefore, this effect causes no problem. If one applies the 900-mm focusing lens below the chamber to yield more photons for the T_e = 0.05 eV case, however, the theoretical disturbance can be up to 40 %. Even in that situation, the laser beam radius at the focal point

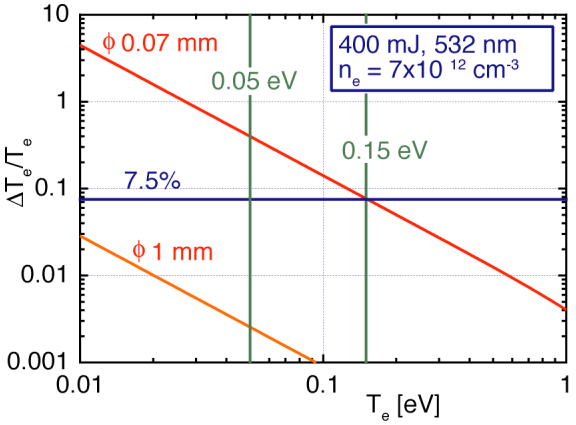

Fig. 5 Degree of the plasma heating by high power laser absorption. Theoretically calculated beam diameter based on the Gaussian optics is 0.1 mm. In the real situation, the beam spot can be more or less defocused.

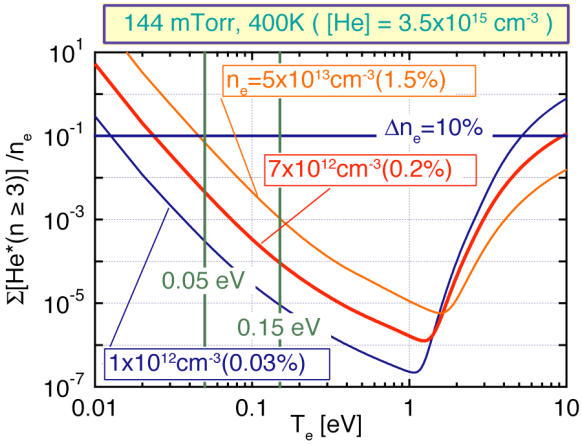

Fig. 6. Excited state population of the neutral helium that can be ionized by the photoionization process for 532-nm laser. The typical parameter condition in the present work is adopted in the CR-model considering the radiation trapping. The round brackets indicate the degree of ionization.

of the convex lens can be larger than the ideal value of 0.035 mm. Moreover, one can replace the convex lens with a cylindrical lens focusing only in the direction perpendicular to the viewing line, which further mitigates the criteria without losing so much signal intensity. Experimentally, this effect can be checked by varying the laser power and observing if the obtained temperature changes or not. For the former case, the real value can be evaluated by extrapolating to the laser power of zero.

It has been pointed out that photoionization from the exited state can affect electron density measurement.For He having the first ionization potential of 24.59 eV, states with the principal quantum number $n \geq 3$ need to be considered since the ionization threshold for the single photon processes in these states is less than 2.33 eV (532 nm photon). We have confirmed, as shown in Fig. 6, based on the CR model of He I - developed by Goto [12] and modified by Iida including radiation trapping for our condition [13] - that the $n \geq 3$ population is smaller than 0.01% even for T_e = 0.15 eV and n_e = 7 x10^{12} cm^{-3}. The contribution starts to be significant only for $T_e \leq 0.02$ eV, where the increase in the density is 20%. This temperature is considerably smaller than that expected for the brightest recombining front of 0.05 eV. For T_e = 0.05 eV, the 10 % disturbance in n_e can be induced when the n_e is increased up to 5 x10^{13} cm^{-3}, which corresponds to the degree of ionization of 1.5 %. It may worthwhile to mention that at the transition region where the emissivity is small exhibits low population density in the excited state. Therefore, the disturbance in the transition regime is negligible for all cases of interest, which further indicates the effectiveness of applying the LTS method in the transition region where the spectroscopy and the probe cannot be applied.

5. Conclusion

We have developed an LTS system intended for the study of low-temperature recombining plasmas. A recent upgrade has allowed the measurements as low as approximately 0.1 eV. The position at the entrance of the recombination front was revealed to have a very low electron temperature (0.15 eV).

In the transition region between ionizing and recombining plasmas, where n_e and T_e cannot be measured by the use of a probe and/or by the spectroscopy, these parameters vary smoothly from ionizing to the entrance of the recombining regions. Therefore, it is very likely that the T_e from the Rydberg series spectra of He I, about 0.05 eV, is a plausible value. A further major upgrade to access to the brightest region in the EIR plasmas is planned in the near future.

Acknowledgements

This work was supported in part by a NIFS Collaborative Research Program (NIFS04KOAB009).

References

[1] S. I. Krasheninnikov, A. Yu. Pigarov and D.J. Sigmar, Phys. Lett. **A 214** (1996) 285.
[2] R.K. Janev, D.E. Post, W.D. Langer, *et al*., J. Nucl. Mater. **121** (1984)10.
[3] S. Kado, H. Kobayashi, T. Oishi and S. Tanaka, J. Nucl. Mater. **313-316** (2003)754.
[4] R.D. Monk *et al*., J. Nucl. Mater. **241-243**(1997)396.
[5] N. Ohno *et al*., Contrib. Plasma Phys. **41**(2001), 473.
[6] A. Okamoto, S. Kado, S. Kajita and S. Tanaka, Rev. Sci. Instrum. **76** (2005) 116106.
[7] F. Scotti, S. Kado, A. Okamoto, T. Shikama and S. Tanaka, Plasma Fusion Res. **1** (2006) 054 .
[8] S. Kado, Y. Iida, S. Kajita *et al*., J. Plasma Fusion Res. **81** (2005) 810.
[9] S. Kado, S. Kajita, Y. Iida, *et al*., Plasma Sci. Tech. **6** (2004) 2451.
[10] F. Scotti, S. Kado, A. Okamoto, *et al*., to be published in Plasma Fusion Res.
[11] H.J. Kunze, The Laser as a Tool for Plasma Diagnostics, In *Plasma Diagnostics (ed. W. Lochte-Holtgraven), p. 550, North-Holland Publishing Company, Amsterdam* (1968).
[12] M. Goto, J. Quant. Spectrosc. and Radiat. Tranf. **76** (2003) 331.
[13] Y. Iida, S. Kado *et al*., J. Plasma Fusion Res. SERIES **7**(2006)123 .

Examination of scattering volume alignment in Thomson scattering off of a shock front in argon

A.B. Reighard[1], D.H. Froula[1], R.P. Drake[2], J.S. Ross[1], L. Divol[1]
[1] *Lawrence Livermore National Laboratory, 7000 East Ave, Livermore, CA, 94550, USA*
[2] *AOSS Department, University of Michigan, 2455 Hayward St, Ann Arbor, MI, 48109, USA*

Thomson scattering in argon gas successfully probed the region of plasma just behind the shock front. The instantaneous shock velocity can be inferred from the duration of the signal, taking into account the size and shape of the scattering volume. Possible misalignment of the probe beam and spectrometer slits greatly affects the size and shape of the scattering volume, and therefore affects the calculation of the instantaneous shock velocity.

1. Introduction

Thomson scattering is a powerful technique for plasma diagnosis. Thomson-scattering measurements use a coherent light source with an initial wavelength and wavenumber (λ_o and k_o) to scatter light from plasma electrons with a scattering wavevector $\boldsymbol{k}$ [1],[2]. In the collective regime, where the scattered light probes many Debye lengths (λ_D) in a plasma (so $1/(k\lambda_D)=\alpha>1$), strong signals are observed when the probed electrons have a resonant collective response (e.g. from ion-acoustic waves, when $T_i/ZT_e<\alpha$, or from electron plasma waves) [3]. Many experiments have used Thomson scattering (TS) to extract fundamental plasma properties from the scattered frequency spectrum, and TS is now widely used as a diagnostic in fusion research [4-6].

Thomson scattering was successfully implemented to measure flow velocity and electron temperature in a driven shock in argon gas [7]. Careful analysis showed that the size and shape of the scattering volume significantly affected conclusions made about other parameters in the system.

A shock velocity was calculated based on the duration of the scattered light signal. However, the following calculations show that the estimate of the shock velocity depends heavily on the alignment of the system. Without better understanding of the relative alignment of the probe beam with the collection diagnostic slits, the error bars on the shock velocity calculation will be very large.

2. Experimental Design

Figure 1 shows the setup of the experiment, the scattering vector diagram, and a three-dimensional image of the scattering volume and shock front. A more detailed description can be found in Reighard et al. [8].

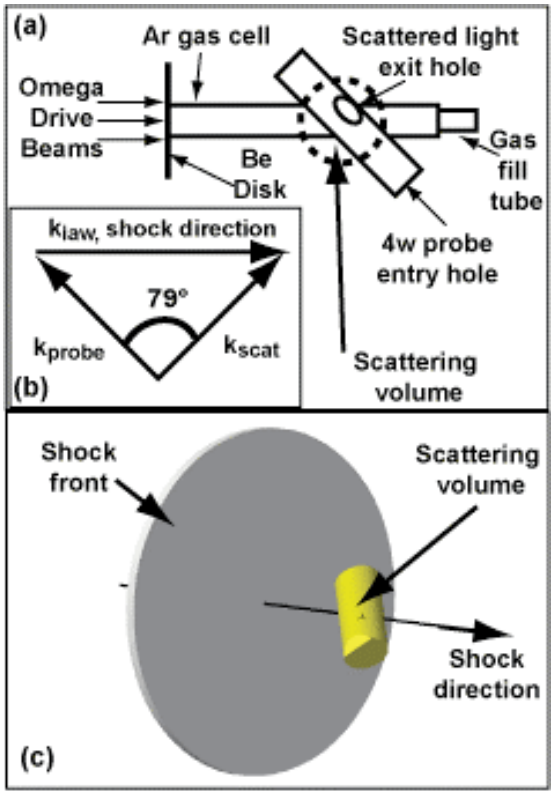

Figure 1: Target geometry and setup. a) 2D drawing of target features. This gas-tight target was filled with 1.1 ATM argon gas shortly before the shot. b) Scattering vector diagram. The probed ion-acoustic wave was parallel to the shock propagation direction. c) 3D image of scattering volume, showing the relative size and direction of the shock.

A 20 μm thick, 2 mm diameter beryllium disk was attached to the end of a 574 μm ID, 625 OD polyimide tube, 6 mm in length. This cylinder was gas tight, and filled with argon via a hypodermic tube in other end of the cylinder. A polyimide tube was mounted on this main assembly, pointed in the direction of the probe beam when the target was aligned, and had a 725 μm ID, 875 μm OD. The entrance hole of the larger tube was 2 mm from the axis of the main target assembly, was covered with 3000 Å of polyimide, and opened into a hole drilled into the main target wall at 4 mm from the beryllium disk down the cylinder's axis. The other end of this tube was filled with epoxy to keep the target gas tight. A second hole pointed in the direction of the collection spectrometer when the target was aligned, and was also covered with 3000 Å of polyimide.

These experiments were performed on the Omega laser at Rochester, NY [9]. We focused 10 smoothed laser beams with a wavelength of $\lambda = 0.35$ μm (3ω) into a 1 mm spot in a 1-ns, flat-topped, square pulse centered on the beryllium disk, with the midpoint of the rising edge defining time $t = 0$. This laser pulse shocked the disk, and then accelerated it into the argon gas cell, driving a shock. The total drive intensity on target was 5×10^{14} W/cm^2. At $t = 16$ ns a single, unsmoothed, defocused 3ω beam at an intensity of 1.5×10^{14} W/cm^2 removed the polyimide cover on the scattered light exit hole in a 2-ns square pulse. At $t = 19$ ns, a 4ω probe beam fired in a 2-ns square pulse with a wavelength of $\lambda_0 = 0.2633$ μm, an energy of 175 J, and a best focus spot size of 80 μm. The Thomson-scattered light was gathered at a scattering angle $\theta = 101°$ using a 1-m UV imaging spectrometer with a 3600 lines/mm grating and a 500 μm spectral slit width, giving a spectral resolution of 0.9 Å at FWHM. It was recorded on a UV streak camera with a sweep window duration of 5 ns centered at $t = 20$ ns, and a 500 μm temporal slit width[10]. The scattered light was collected and imaged to the spectrometer with an optical magnification of 2.

3. Scattering Volume

The scattering volume was defined by the overlap of 2 sets of orthogonal slits in the plane of the scattered light collection diagnostic and the 4-ω probe beam. The scattered light diagnostic was located at $\theta = 79.19$, $\phi = 90.0$ in the Omega chamber. The slits were both 250 μm wide. An image of a grid at target chamber center showed that the slits are rotated to a 66 degree angle from the view of the chamber port [11] in the plane of the spectrometer. This volume is shock with the shock front in Figure 1c.

The probe beam issued from port P9 in the Omega target chamber, at $\theta = 116.57$, $\phi = 18.0$. It was an f/6.67 beam with an 80 μm diameter at it's best focus. When perfectly aligned, these overlapping features produce a skew cylinder that was approximately 80 μm x 300 μm x 300 μm in size.

4. Scattered Power

Using Hyades [12], a 1D, Lagrangian radiation hydrodynamics code, we estimated the power scattered by the argon around the shock. Though the unshocked gas was preheated to a few eV, it scattered a negligible amount of light. The scattered power had a local peak at the peak of the electron temperature, just behind the shock front. Then, the scattered power continued to increase as the electron density increased, even as the shocked gas cooled radiatively. The electron density continued to rise despite cooling temperatures because of increased compression of the gas due to radiative losses [13].

This scattered power was attenuated by bremsstrahlung absorption, which was significant in the shocked argon. This absorption limited the scattered power to about 50 μm behind the shock front. Details of the absorption profile, as well as the scattered light profile, will be published elsewhere [7]. This result was convolved with the calculated signal as a function of space, resulting in a simulated instrument function.

5. Simulated instrument function

We used the above parameters to simulate the instrument function. We defined a scattering volume based on the direction and best focus size of the probe beam (80 μm diameter). Using the orientation and size of the slits, the probe beam was truncated to the volume the

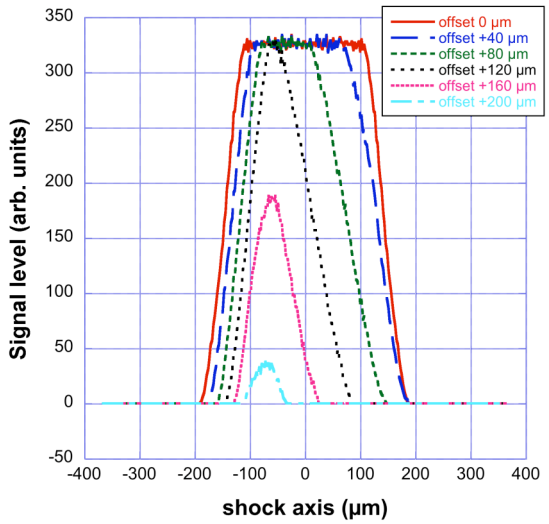

Figure 2: Calculated signal levels as a function of space. Each curve represents a different offset of the probe beam with respect to the place of the target axis and spectrometer slits. The signal is reduced to zero when the beam is offset by more than 220 µm.

collection diagnostic could detect. A delta function was then passed through the volume in the shock direction, and the signal from each step recorded. This overall response function was then convolved with the scattered-power profile. This gave the instrument function as a function of position of the shock.

Figure 2 shows the calculated signal as a function of space. Each curve shows a different offset from perfect alignment. In these cases, the probe beam was offset in a direction perpendicular to the plane made by the collection diagnostic and the probe beam.

Notice that the signal peak stays as high as the perfectly aligned case until the probe beam is misaligned by more than 120 µm. The signal did not disappear completely until the beam was offset by more than 220 µm.

Our relatively dim signal at high probe laser beam power suggests that the probe beam was significantly offset from the plane of the collection slits and the target axis. Note that other Thomson scattering experiments had stronger signal than ours using a 20 J or less probe beam [8],[10], whereas our probe beam energy was 175 J.

Assuming a constant shock velocity through the scattering volume, we then calculated how fast a shock would have to move through our calculated profile to give the same duration as the scattered light data. The duration of the collected signal in the experiment at FWHM was 350 ps.

Figure 3 shows the duration at FWHM as a function of the offset of the probe beam. Each curve assumes a different constant shock velocity through the scattering volume. The solid, horizontal line marks the duration of the collected data, at 350 ps. Note that all the curves cross this line, meaning the offset must be better characterized to use this method to determine the shock velocity through the scattering volume. As a comparison to the actual data, Figure 4 shows the velocity as a function of offset that would give a calculated duration of 350 ps, as a direct comparison to the data. From this, it is likely our experiment was offset more than 150 µm.

6. Conclusion and Acknowledgements

The orientation of the collection slits with respect to the shock volume has a large effect when correlating the observed signal duration with a constant shock velocity through the scattering volume.

Better measurements of the instantaneous shock velocity through the scattering volume would give a better

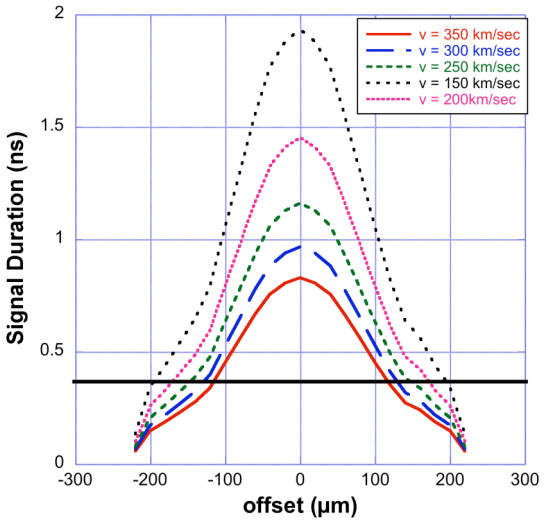

Figure 3: Signal duration as a function of probe beam offset. Each curve represents a different shock velocity through the scattering volume. The dark, horizontal line at 350 ps marks the duration of the measured signal. Each shock velocity curve crosses the horizontal line, giving a wide range of possible shock velocities, given a possible experimental misalignment.

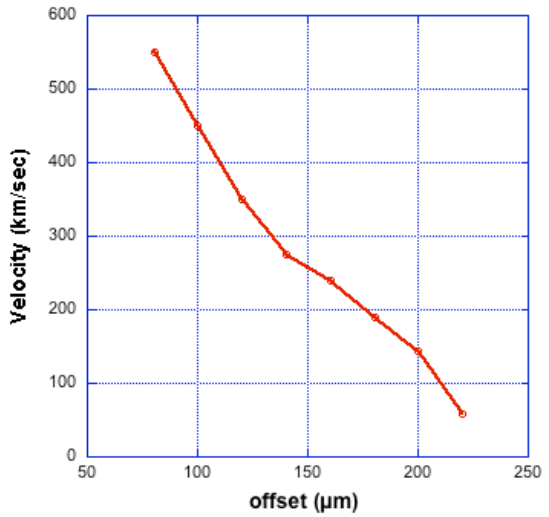

Figure 4: Calculated velocity for a given offset between the spectrometer slit and probe beam, given that the detected signal lasted 350 ps. The offset direction is perpendicular to the plane made by the slit and beam when they are perfectly aligned. Note that the signal disappears when the slit and beam are offset by more than 220 μm.

measurement of the compression of the probed gas, when measured simultaneously with the plasma flow velocity. The compression of a radiatively collapsed shock in gas has not yet been directly measured.

These experiments were supported by the National Nuclear Security Agency under DOE grants DE-FG03-99DP00284 and DE-FG03-00SF22021, and by other grants and contracts. This work was performed under the auspices of the U.S. Department of Energy by University of California, Lawrence Livermore National Laboratory under Contract W-7405-Eng-48.

7. References

[1] H.-J. Kunze *et al.*, Phys. Letters **11**, 42 (1964).
[2] A. A. Offenberger *et al.*, Phys. Rev. Lett. **71**, 3983 (1993).
[3] J. Sheffield, *Plasma scattering of electromagnetic radiation* (Academic Press, Inc., New York, 1975).
[4] D. H. Froula *et al.*, Phys. Rev. Lett. **95**, 195005/1 (2005).
[5] S. H. Glenzer *et al.*, Phys. Rev. Lett. **79**, 1277 (1997).
[6] S. H. Glenzer *et al.*, Phys. Rev. Lett. **82**, 97 (1999).
[7] A. B. Reighard *et al.*, Phys. Rev. Lett. (in submission).
[8] A. B. Reighard *et al.*, Rev. Sci. Instrum. **77**, 10E504 (2006).
[9] T. Boehly *et al.*, Rev. Sci. Instrum. **66**, 508 (1995).
[10] D. H. Froula *et al.*, Rev. Sci. Instrum. **77**, 10E522 (2006).
[11] J. S. Ross *et al.*, Rev. Sci. Instrum. **77**, 10E520/1 (2006).
[12] J. T. Larsen, and S. M. Lane, J. Quant. Spectrosc. Radiat. Transfer **51**, 179 (1994).
[13] R. P. Drake, and A. B. Reighard, in Shock Compression of Condensed Matter, AIP Conference Proceedings, edited by M. D. Furnish *et al.* (American Institute of Physics, 2006), pp. 1417.

Development of a two color laser interferometer

K. Kawahata[1)], T. Akiyama[1)], R. Pavlichenko[1)], K. Tanaka[1)]
K. Nakayama[2)], and S. Okajima[2)]

[1] *National Institute for Fusion Science, 322-6 Oroshi-cho, Toki-shi, 509-5292, Japan*
[2] *Chubu University, 1200 Matsumoto-cho, Kasugai-shi, Aichi 487-8501, Japan*

This paper describes an innovative laser diagnostic instrument, a two color FIR laser interferometer, under development at the National Institute for Fusion Science, aiming for the establishment of reliable density measurement techniques in the next step magnetically confined fusion devices. In the process of searching for new laser oscillation lines, we have successfully achieved the powerful laser lines simultaneously oscillating at 57.2 and 47.6 μm, which lead to the construction of a new type of two color laser interferometer. A two color laser interferometer has been developed and its original function, vibration subtraction, was confirmed in a test stand.

1. Introduction

Measurements of the refractive index of the plasma by using electromagnetic waves are a well-established tool for measuring electron density profiles in high temperature plasmas. In the Large Helical Device (LHD) [1], a 13-channel far infrared laser interferometer [2] has been constructed and routinely operated for the precise measurements of the electron density profile almost every shot except in the case of a high-density plasma produced by an ice pellet injection. In the latest experimental campaign of the LHD, a super dense core plasma as high as 5 x 10^{20} m^{-3} has been achieved [3] by an internal diffusion barrier created by the use of the local island divertor and multiple pellets injection. In these high density plasmas, steep density gradient is formed leading to the fringe jumps on the density traces measured by fringe counters. In order to overcome this difficulty we have been developing new laser sources in the wave length region of 40 to 70 μm, which is optimum value from view points of the S/N for an expected phase shift and the plasma refraction effect.

In the interferometry, we need to develop short wavelength laser diagnostics to avoid the beam bending effect caused by the density gradient. However, it is also necessary to equip a second wavelength interferometer to compensate for a fringe shift due to mechanical vibrations of the optical components since the fringe shift caused by the vibrations is inversely proportional to the wavelength. In the LHD, a CO_2 laser imaging interferometer [4] has been developed for detailed profiled measurements of density and density fluctuation. For the sake of vibration compensation a 1.06-μm YAG laser interferometer is employed. In this way, the conventional two color laser interferometer systems use two independent laser interferometers [5-7] as is schematically shown in Fig.1. Probing laser beams (ω_1 and ω_2) are combined and made coaxial at the DM_1 dichromatic mirror, and divided into two beams at BS_1, a probe beam and a beam which is used in the reference arm for a heterodyne signal detection. The probe beam is combined with the local beam which also contains two laser beams (with angular frequency $\omega_1 + \Delta\omega_1$ and $\omega_2 + \Delta\omega_2$) at BC_1 after passing through the plasma, and then separated into two laser components by using the DM_4 dichromatic mirror, and finally

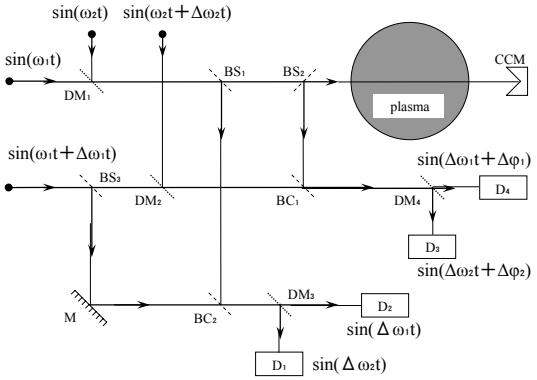

Fig. 1: Schematic drawing of the conventional two color laser interferometer of the Michelson type. Two laser oscillation lines are combined and separated with the dichromatic mirrors (DM).

detected by the appropriate detectors (D_3 and D_4). By using 4 output signals we can get information about the fringe shifts caused by the plasma and by the mechanical vibrations. In this type of the two color system, the fringe shift caused by the mechanical vibrations cannot be canceled out completely since the optical path difference between two independent interferometers remains and effects due to optically dispersive components are significant when the wavelength of two laser sources is different largely.

In order to overcome these difficulties, new types of two color interferometers [4-6] have been developed to establish more reliable two color laser interferometers. At NIFS, we have been developing new laser sources operating in the wavelength region of 40 to 70 μm, which is suitable for high density operation of LHD and for future fusion devices. In the process of searching for new laser oscillation lines, we have successfully achieved many oscillation lines around 40 to 70 μm by the use of a CO_2 laser pumped far-infrared laser [8]. Among these oscillation lines a unique laser operation was found by using CH_3OD molecular gas excited by the 9R(8) CO_2 laser line. This laser operation provides two laser oscillation lines (57.2 and 47.6 μm) simultaneously, which lead to the construction of a new type of two color laser interferometer [9]. The new system has some excellent features as follows:(i) the wavelength of 57.2 μm is optimum value to avoid refractive effects in high density operation of LHD and future fusion devices, (ii) the optical components such as windows, beam combiners and beam splitters can be optimized at both frequencies, (iii) an additional laser instrument is not needed to compensate the fringe shift due to mechanical vibrations, (iv) both laser beams pass the same optical path in the interferometer without optical path difference, and (v) one detector simultaneously detects the beat signals of both oscillation lines, and each interference signal can be separated electrically.

2. Two color FIR laser Interferometer

Figure 2 shows the conceptual drawing of a new type of two color laser interferometer system of the Michelson type, which is a rather simple system compared with Fig.1. The optical

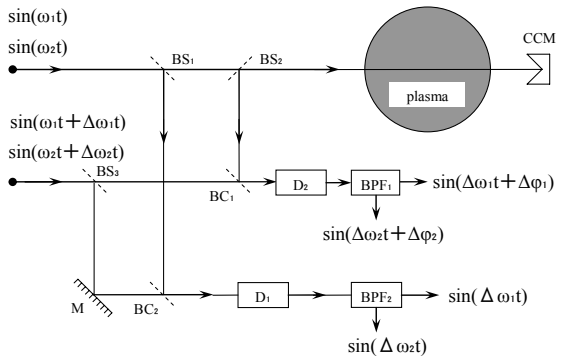

Fig. 2: Schematic drawing of a new type of the two color laser interferometer of the Michelson type. The optical components are the same as a conventional heterodyne interferometer with single laser oscillation line. The detector output includes two heterodyne beat signals, $\Delta\omega_1$ and $\Delta\omega_2$.

arrangement is similar to a single heterodyne interferometer system. The laser source is a twin optically-pumped CH_3OD laser, which simultaneously oscillates at 57.2 and 47.6 μm in wavelength, which are pumped by the 9R(8) CO_2 laser line. Each laser line has different polarization, so that a Martin-Puplett diplexer is used to make a co-polarized beam [9]. By tuning the cavity lengths, the beat frequency of each heterodyne interferometer can be set at an optimum value, around 500 kHz for 57.2 μm and 1.2 MHz for 47.6 μm, which is determined considering detector IF frequency band width, laser tunability and frequency characteristics of band-pass filters to separate beat signals of each laser interferometer. The main components to construct the system are beam splitters and beam combiners made of a silicon etalon with high resistivity, which is a low absorption material (absorption coefficient α = 0.56 cm^{-1} at 47.6 μm) in the short wavelength FIR regime compared with quartz (α_o, α_e = 6.6 cm^{-1}, 4.9 cm^{-1}). Visible light is not transmitted through silicon so that an YAG laser beam of 1.06 μm in wavelength is used for alignment of the optical axis with infrared sensor cards.

One of the key issues to realize this diagnostic instrument is the development of high quality detectors with fast and sensitive heterodyne detection. There are three candidates used in FIR wavelength regime, a GaAs Schottky barrier diode mixer, a InSb He-cooled detector and a gallium-doped germanium detector. The GaAs Schottky barrier diode mixer has widely been used in many FIR laser diagnostics since the detector can be operated at room temperature with high sensitivity. The sensitivity of the detector, however, decreases with operating frequency due to the cut-off frequency bellow several THz, and difficult to make tuning of the detector simultaneously to both frequencies. The InSb He-cooled detector with magnetic tuning [10] has been applied on JET tokamak to simultaneously detect a 195-μm DCN laser and a 118.8-μm CH_3OH laser. The spectral responsivity of the detector, which is normally limited in the frequency region of 60 to 600 GHz, can be tuned in the specified frequency up to about 3 THz by means of magnetic field, but not over than 3THz. Then we finally chose a gallium-doped germanium detector operating at liq.He temperature. Figure 3 shows the interference signals detected by Ge:Ga photoconductive detectors, D_1 and D_2. The observed signal-to-noise ratio is excellent to be about 40 dB. This high signal-to–noise ratio was achieved when the input power to the detector was reduced by 30 dB. So, we can achieve a good signal-to-noise ratio even when the multi-channel system is constructed.

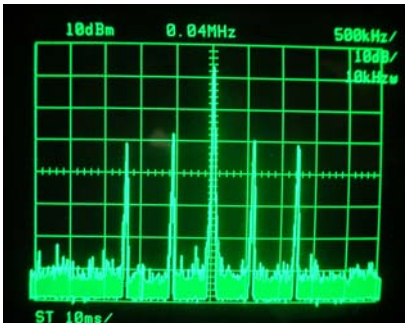

500 kHz, 10dB/div.

Fig. 3: Two color beat signals detected by the gallium-doped germanium photoconductor.

The Ge:Ga detector has almost the same sensitivity at both laser frequencies (Fig. 4), and the detected signals are separated electronically into two wavelength components. Each frequency component is fed into a phase comparator for phase measurement.

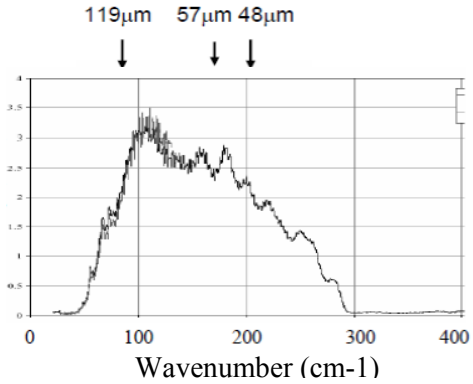

Fig. 4: The overall response function of the detector system.

The variations of the phase of the two color interferometer, ϕ_1 and ϕ_2, (for the wavelengths λ_1 and λ_2, respectively) caused by variation in the plasma density n_e and by optical path length variation ΔL are given by following equations,

$$\phi_{1,2} = 2.82\times10^{-13}\lambda_{1,2}\int n_e dl + 2\pi\Delta L/\lambda_{1,2} \qquad (1)$$

By using two color interferometer ($\lambda_1>\lambda_2$), we can compensate for the mechanical vibrations by using the following equation,

$$\phi_p = \frac{\phi_1 - \gamma\phi_2}{1-\gamma^2} \qquad (2)$$

where ϕ_p is the phase shift due to the plasma in the interferometer of λ_1, and $\gamma$is the ratio of the wavelengths, λ_2/λ_1.

In order to develop new type of two color interferometer, a single channel two color interferometer system is constructed (Fig.5) and operated in the laboratory, where main key issues to establish this innovative diagnostics are as follows; 1) development of laser control

system to achieve stable simultaneous oscillation at 57 and 48 μm, 2) development of optical components to construct short wavelength FIR laser diagnostics such as beam combiner/splitter, polarizer, beam optics to compromise with two different frequencies and detectors. An example of vibration subtraction test is shown in Fig.6. In this case the reflecting mirror is placed on a piezo-electric transducer to confirm the idea of the two color laser interferometer and to find out what kind of problems need to be solved. The position of the mirror is modulated in a triangular waveform (Fig.6(a)) at 10 Hz with the amplitude of ~118 μm to change the optical path length. The displacements of the mirror measured by 57 and 48 μm laser interferometers are shown in Fig. 6(b). The difference of these displacements measured is also plotted in Fig. 6(b), which shows the effectiveness of the vibration compensation using two color laser oscillations. At the present the phase noise level of the interferometer is about 1/25 fringes, which is mainly caused by cross talk of each beat frequency component and will be reduced by the use of more proper electric filter and by setting the beat frequencies at proper different frequencies to attenuate the unwanted frequency component**.**

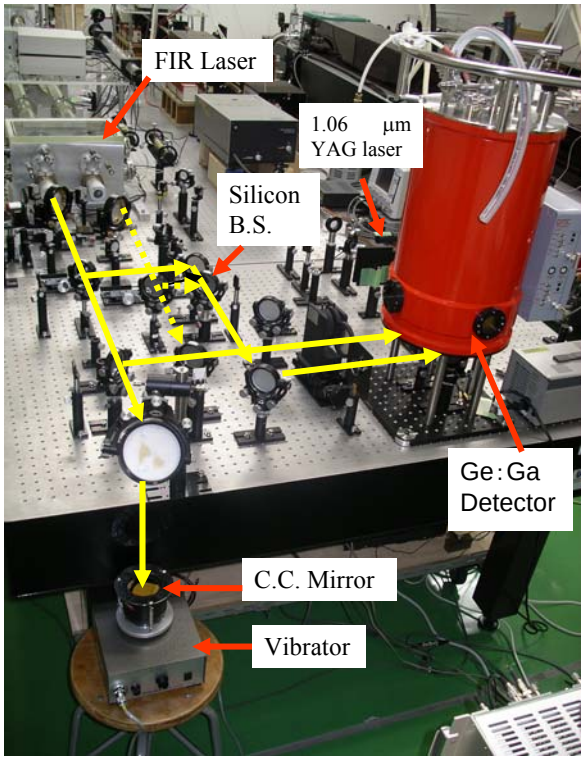

Fig. 5: Photograph of the test stand under development for application of the two color laser.

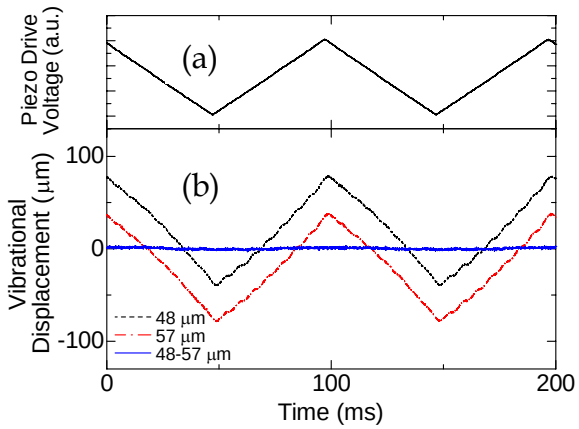

Fig. 6: (a) Waveform of the applied voltage on the piezo-electric transducer. (b) The measured displacements of the vibration mirror by a 57 μm and 48 μm CH_3OD laser interferometers, and their subtraction. The mechanical vibration is simulated by using a piezo-electric transducer.

References

[1] O. Motojima, *et al.*, Nucl. Fusion **43**, 1674 (2003).

[2] K. Kawahata, *et al.*, Rev. Sci. Instrum.**70**, 707 (1999).

[3] N. Ohyabu, *et al.*, Phys. Rev. Lett. **97**, 055002 (2006).

[4] K. Tanaka, *et al.*, Rev. Sci. Instrum. **75**, 3429 (2004).

[5] J. Irby, *et al.*, Rev. Sci. Instrum. **70**, 699 (1999).

[6] V. P. Drachev, *et al.*, Rev. Sci. Instrum. **64**, 1010 (1993).

[7] P. A. Bagryansky, *et al.* , Rev. Sci. Instrum. **77**, 053501 (2006).

[8] K. Nakayama, *et a*l., Elect. Eng. in Japan **153**, 1 (2005).

[9] K. Kawahata, *et al.*,Rev. Sci. Instrum. **75**, 3508 (2004).

[10] G. Braithwaite, N. Gottardi, G. Magyer, J. Rourke, J. Ryan, and D. Veron, Rev. Sci.Instrum. **60**, 9 (1989) 2825.

Notch Filter Options for ITER Stray Gyrotron Radiation

Paul Woskov

MIT Plasma Science & Fusion Center, Cambridge, MA 02139, U. S. A.

ITER will have multi megawatt gyrotron systems at 170, 120, and potentially at 60 GHz for ECH, current drive, NTM control, start up, and CTS diagnostics. The ITER environment will therefore have significant background levels of stay radiation at these frequencies that can pose a problem to a number of diagnostic systems. Several deep, narrowband reject filter approaches have been examined. These include fundamental mode waveguide filters, quasi-optical resonance filters, and molecular absorption gases.

1. Introduction

The current plans for ITER include twenty-four 1 MW 170 GHz gyrotrons for electron cyclotron heating (ECH), current drive, and neoclassical tearing mode (NTM) control [1], three 1 MW 120 GHz gyrotrons for start up [1, 2], and two proposed 1 MW 60 GHz gyrotrons for fast ion collective Thomson scattering (CTS) diagnostics [3]. Consequently there will be significant stray radiation at these frequencies and ITER diagnostics [4] with detectors having sensitivities to this radiation will be adversely affected. Diagnostics that operate at higher frequencies in the infrared such as density interferometry/ polarimetry and thermal emission bolometry can be shielded by high pass meshes [5] or dichoric filters [6]. However, millimeter-wave to terahertz diagnostics such as reflectometry, refractometry, electron cyclotron emission (ECE), and collective Thomson scattering (CTS) which operate around these frequencies will require narrow band notch filters with stop bands wide enough to block multiple drifting gyrotron frequencies [7] and at the same time have wide, low loss pass bands outside the notches.

Several notch filter approaches are possible. Fundamental mode rectangular waveguide filters with many side coupled resonator cavities have been successfully used up to 140 GHz with rejection depths of up to -100 dB [8, 9]. Quasi-optical resonance cavities with rejections up to -40 dB in the 100 – 140 GHz have also been reported [10, 11] and a molecular absorption gas (N_2O) has been used at 778 GHz with a rejection of over -60 dB [12]. The relative merits of each of these technologies is briefly discussed here along with a new compact, rugged quasi-optical resonator notch filter design and candidate absorption gases for the ITER gyrotron frequencies.

2. Fundamental Waveguide Filters

Narrow stop band filters fabricated in standard rectangular waveguide with a dozen or more cylindrical side cavities tuned to the reject frequency are a well established technology [8, 9] and have been successfully used at many fusion plasma experiments in the 70 to 140 GHz range. Extending this technology to 170 GHz will be challenging because the dimensions for the waveguide and resonators become very small, making them difficult to fabricate and increasing ohmic losses with frequency will reduce resonator q and increase insertion losses. Another difficulty is that the pass bands on either side of the notch frequency are narrower that the waveguide band in which the filter is built.

This limitation is illustrated in Figure 1 where a measured transmission spectrum for one of the 110 GHz notch filters used on the TEXOR fast ion CTS system [13] is shown. The measurement was made with a millimeter-wave extended

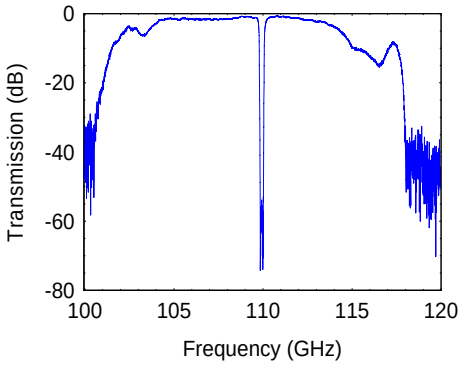

Fig. 1: Transmission through TEXTOR CTS Notch B WR08 waveguide filter with 16 resonators. Central notch at 109.95 GHz is 200 MHz wide below 60 dB.

Agilent Model E8363B Network Analyzer. The deep notch at 110 GHz is flanked by low insertion loss (< 3 dB) pass bands that extent only about 6 GHz on the low frequency side and 3.6 GHz on the high side due to other cavity modes in the filter. Such pass band limits would be a problem for very wide band diagnostics such as ECE and reflectometry.

3. Quasi-Optical Resonance Filters

Resonance filters based on optics are more easily extended to higher frequencies, but are more difficult to mechanically and thermally stabilize and to achieve high q in free space propagation. There are many possible configurations [11]. One that is easily implemented is a variation on the Fabry-Perot resonator [10] as illustrated in Fig. 2. The transmission for such a filter is given by:

$$T = \frac{t(1-l)^2 + 4l\sin^2 \delta/2}{(1-tl)^2 + 4tl\sin^2 \delta/2} \qquad (1)$$

where t is the transmission through the beamsplitter, l is the single pass transmission factor between the mirrors, and $\delta = 4\pi L/\lambda$ for wavelength λ. The transmission characteristic has a series of notches separated by the free spectral range (FSR) of $c/2L$ with the depth and spectral width depending on the beamsplitter transmission and single pass factor.

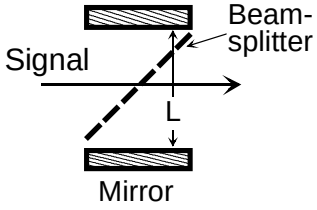

Fig. 2: Design of quasi-optical resonance notch filter

The realization of this type filter in corrugated waveguide is shown in Fig. 3. The use of HE_{11} corrugated waveguide makes it possible to avoid free space diffraction making it compact and mechanically rugged. This filter has an internal diameter of 20 mm with a corrugation depth and pitch for the 90 – 140 GHz range. The side mirror pugs are tuneable and both polyethylene and quartz beamsplitters have been used. Measurements with a quartz beamsplitter with a transmission t = 0.46 at 120 GHz for the E-field

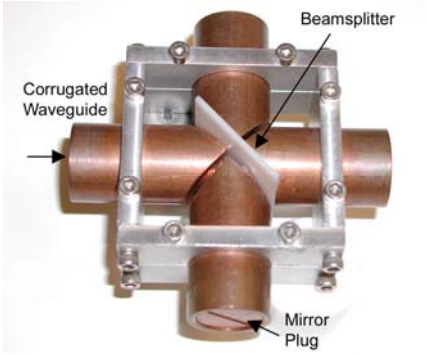

Fig. 3: Quasi-optical notch filter range in corrugated waveguide shown with polyethylene beamsplitter. Internal dia. is 20 mm.

perpendicular to the plane of Fig. 2 are shown in Fig. 4. The mirror separation in this case was about 26 mm corresponding to a FSR of 5.7 GHz. The repetitive notches have rejections of > -30 dB over bandwidths of 56 MHz with a peak rejection approaching -40 dB, and 3 dB pass bands of 4.4 GHz with a minimum insertion loss of -0.7 dB. A plot of Eq. (1) shown overlaid on the measurement fits the data for single pass factor of l = 0.996. Measurements with a polyethylene beamsplitter with t = 0.69 at 110 GHz resulted in l = 0.921 and peak notch depths of only -17 dB and minimum insertion losses of -0.2 dB. In another test the mirror separation was decreased closer to the diameter of the waveguide to increase the FSR to 6.7 GHz.

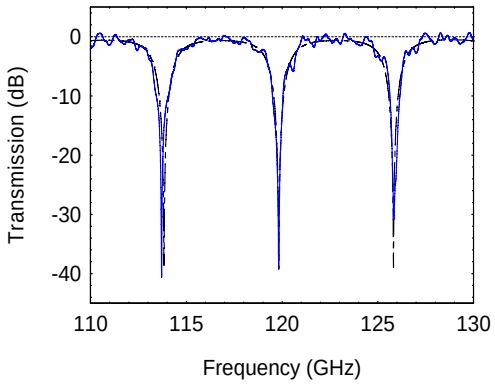

Fig. 4: Measured (solid line) and calculated for l = 0.996 (dashed line) transmission through quasi-optical interference filter with 1.5 mm thick quartz beamsplitter for E-field polarization perpendicular to the plane of Fig. 2

This type filter could be used as a building block in units of two or more to tailor the stop band to the needed rejection depth and bandwidth.

Care would need to be taken in the spacing between such resonators since they reject by reflection and the potential for mutual interference would need to be considered. Also novel arrangements where additional filters of this type with different FSR are used as the mirrors for the main filter could be used to eliminate the repetitive pattern of notches at the expense of increasing the insertion loss to the beamsplitter transmission.

4. Molecular Absorption Gases

The rotational energy levels of many molecules occur in the millimeter-wave wavelength range. A successful notch filter molecule should be small (diatomic or triatomic) to minimize additional absorptions outside the notch frequency. A survey of the JPL NASA molecular absorption data base [14] revealed two common molecules with relatively strong transitions and simple spectra near the ITER gyrotron frequencies.

4.1. OCS Molecule

The millimeter-wave absorption spectrum in the 40 – 250 GHz range for the carbon sulphide (OCS) molecule is shown in Figure 5 for three different pressures assuming Lorentzian line broadening with a half width of 6.22 MHz/torr [15] and summing over all transitions between 24 and 280 GHz. It has a series of rotational absorptions separated by 12.16 GHz with peaks at 60.8, 121.6, and 170.3 GHz having peak absorptions of 0.4, 3.2, and 8.0 dB/m, respectively, occurring close to the ITER gyrotron frequencies. Thus in principle this one gas could be used as a notch filter for all the ITER gyrotrons.

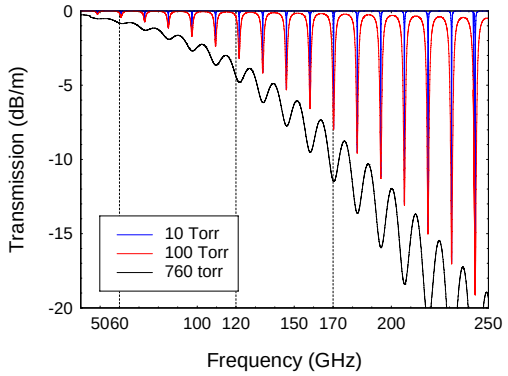

Fig. 5: Absorption spectrum of the OCS molecule at various pressures.

In practice this gas filter would need to be used at low pressure (< 100 torr) to minimize the insertion loss between the absorbing lines. The trade off between gas pressure and path length for a minimum rejection of -60 dB over a 500 MHz wide notch at the 170 GHz transition is illustrated in Fig. 6. A path length of about 10 m at a pressure of 70 torr would achieve this specification with an insertion loss < 1 dB in the adjacent pass band centered at 163.6 GHz. However, with these parameters the filter cell would only have a peak rejection of 4.3 dB at the 61 GHz frequency so it may be difficult to use this gas to simultaneously reject all the gyrotron frequencies. Also the many absorption peaks in this rotational band that come to a peak at 474 GHz and extend well into the THz frequency range may not be a desirable feature for some diagnostics.

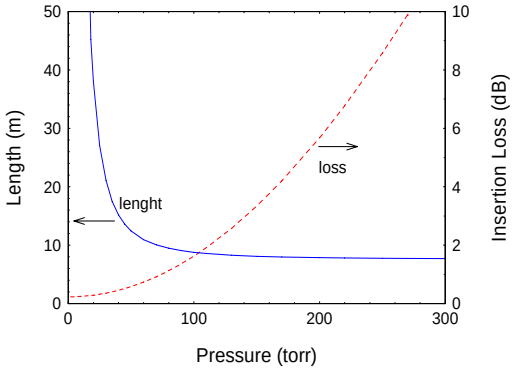

Fig. 6: OCS pressure - path length dependence for -60 dB minimum rejection over 500 MHz bandwidth at 170.3 GHz and insertion loss at 163.6 GHz (dashed line).

4.2. H_2S Molecule

The hydrogen sulfide (H_2S) molecule has only two prominent features in the 40 – 250 GHz range with one at 168.8 GHz near the 170 GHz gyrotron frequency. The H_2S absorption spectrum is shown in Fig. 7 for three pressures assuming Lorentzian broadening with 7.18 MHz/torr half width [16] and summing over all transitions up to 370 GHz. At atmospheric pressure the 168.8 GHz transition is sufficiently broadened to have an absorption strength of 8.6 dB/m at 170 GHz. A 7 m long path length would achieve 60 dB attenuation at 170 GHz with an insertion loss of < 3 dB below 144 GHz.

The required pressure for a given attenuation could be lowered with longer path lengths or with

a gyrotron frequency closer to 168.8 GHz. Lowering the pressure would increase the pass bandwidth closer to the 168 GHz frequency and reduce insertion losses.

Like OCS there are many stronger absorption lines in H_2S above 250 GHz so this molecule would not be useful for diagnostics such as ECE requiring a broad pass band to over one THz. In addition, the infrared absorption bands of these molecules would need to be carefully examined to determine if they could be used as gyrotron blocking filters for infrared interferometry/ polarimetry or bolometer diagnostics.

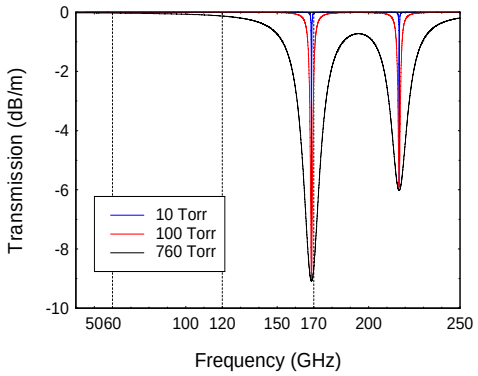

Fig. 7: Absorption spectrum of the H_2S molecule at various pressures.

5. Conclusions

Filtering stray gyrotron radiation in ITER will be a challenging problem for ITER diagnostics. The need to filter up to three gyrotron bands with deep rejection in narrow bands, but not too narrow to accommodate multiple drifting gyrotron frequencies in each band, while at the same time having broad low insertion loss pass bands will be a difficult requirement to meet in many cases. The fundamental mode waveguide filters, quasi-optical resonance filters, and molecular absorption gases described here all have limits in terms of their rejection and pass band capability. Each diagnostic will need to customize its stray gyrotron radiation rejection approach. For example, the fast ion CTS diagnostic could use a combination of a fundamental waveguide notch filter at 60 GHz, H_2S fill in the receiver waveguide for 170 GHz rejection and a blocking switch during start up for 120 GHz. Refectrometry diagnostics which will operate below 160 GHz could also use a combination of rejection filter technologies described here. On the other hand ECE diagnostics that need to cover a broad range of spectrum from 100 to over 1000 GHz will likely need to operate in low and high bands since none of the notch filter approaches described here have efficient transmission at 1000 GHz.

Acknowledgments

The author thanks R. J. Temkin and J. R. Sirigiri at MIT PSFC for access to the Agilent network analyzer and F. Meo and J. Holm of Risø National Lab., Denmark for providing and assisting with the TEXTOR filter measurements.

References

[1] G. Bosia, Proceedings of the 12th Joint Workshop on Electron Cyclotron Emission and Electron Cyclotron Heating, World Scientific, Singapore (2003) 571.

[2] K. Takahashi, N. Kobayashi, A. Kasugai and K. Sakamoto, J. Phys. Conf. Series **25** (2005) 75-83, www.iop.org/EJ.

[3] H. Bindslev, F. Meo, E. L. Tsakadze, S. B. Korshlom, P. Woskov, Rev. Sci. Instrum. **75**, part II, (2004) 3598-3600.

[4]A. J. H. Donné *et al*, Nucl. Fusion **47**, (2007) S337-S384.

[5] R. Ulrich, Appl. Optics **9**, (1977) 2511.

[6] C. Winnewisser, IEEE Trans. Microwave Theory and Tech. **48**, (2000) 744.

[7] P.Woskov *et al*, Rev. Sci. Instrum.**77**,(2006) 10E524.

[8] T. Geist and M. Bergbauer, Int. J. Infrared and Millimeter Waves **15**, (1994) 2043.

[9] Yu. Dryagin, N. Scalyga, and T. Geist, Int. J. Infrared and Millimeter Waves, **17**, (1996) 1199.

[10]P.F.Goldsmith & H.Schlossberg, IEEE Trans. Microwave Theory and Tech. **28**, (1980) 1136.

[11] G. G. Denisov, S.V. Kuzikov, M. Yu. Shmelov, Proc. 18th Int. Conf. Infrared and Millimeter Waves, (1993) 353.

[12] P. Woskoboinikow, W J. Mulligan, and R. Erickson, IEEE J. Quantum Electronics, **19**, (1983) 4.

[13] H. Bindslev *et al*, Phys. Rev. Lett., **97**, (2006) 205005.

[14] http://spec.jpl.nasa.gov/

[15]J.Doose *et al*, Molecular Phys. 81, (1994) 20.

[16]P. Helminger and F.DeLucia, J. Quant. Spect. and Radiative Transfer 17, (1977) 751.

Development of Microwave Imaging Reflectometry in LHD

S. Yamaguchi[1], Y. Nagayama[1], Z. Shi[2],Y. Kogi[2] and A. Mase[2]

[1] *National Institute for Fusion Science, 322-6 Oroshi-cho, Toki-shi, 509-5292, Japan*
[2] *Graduate University for Advanced Studies, 322-6 Oroshi-cho, Toki-shi, 509-5292, Japan*
[3] *Art Science and Technology Center for Cooperative Research, Kyushu Univ., Kasuga 816-8580, Japan*

Microwave Imaging Reflectometry (MIR) is under development for 2-D/3-D measurement of the electron density fluctuations in Large Helical Device (LHD). An adjustable ellipsoidal mirror has been installed inside the vacuum chamber of LHD in order to optimize the illumination beam angle vertically and horizontally. The illumination and reflected beam paths near the reflection surface are calculated by using the ray-tracing code. The illumination angles are optimized in the plasma experiment. A novel MHD mode with harmonics is observed by using MIR during ICRH and NBI heated discharge in LHD.

1. Introduction

Microwave reflectometry is a radar technique for the measurement of the electron density profiles and its fluctuations by probing the density-dependent cut-off layer in the plasma [1]. A multi-channel reflectometry system equipped with the imaging optics has been developed for the microwave imaging reflectometry (MIR) [2-6]. The MIR has a potential to obtain the 2-D/3-D image of the turbulences and instabilities with good time and spatial resolutions. The MIR system is under development in the Large Helical Device (LHD), which is a superconducting heliotron-type fusion device [7]. This paper describes the recent development of MIR system in LHD. The system design will be presented in Section II, and the system performance is described in Section III, the recent experimental result is shown in Section IV, and followed by the conclusion in Section V.

2. System Design

Figure 1 shows a schematic view of the MIR system of LHD. Illumination sources with frequency of 69, 66 and 53 GHz are utilized to probe beams. The beam is launched from port 4-O to the plasma center in the X-mode or the O-mode. In the case of X-mode it is reflected at the right-hand cut-off layer in the peripheral plasma as shown in Fig. 1. In the case of O-mode it is reflected at the plasma cut-off layer in the plasma core. The cut-off layers of X-mode and is less bent and the wavelength of X-mode is shorter than O-mode. The X-mode illumination is better than the O-mode in the low density LHD plasma, because the X-mode cut-off layer is determined by both the density profile, which is sometimes hollow, and the magnetic field profile, which is parabolic. The reflected beam is focused by the imaging optical system, and it is detected by the heterodyne receivers.

The MIR system is combined with the Electron Cyclotron Emission Imaging (ECEI)

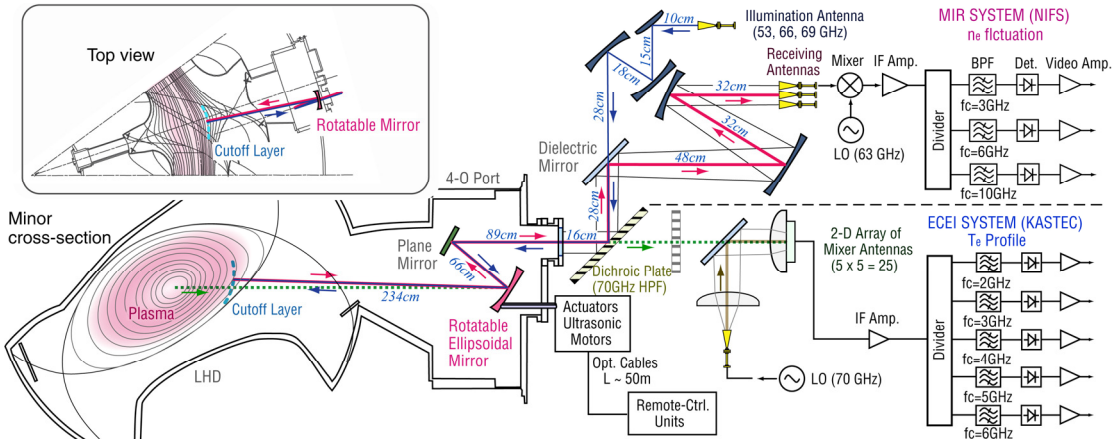

Fig.1 Schematic of the microwave imaging system combined with MIR and ECEI in LHD.

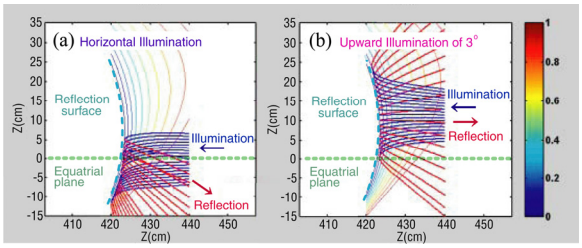

Fig.2 Simulation result of the ray-tracing nearby the right-hand cut-off layer.

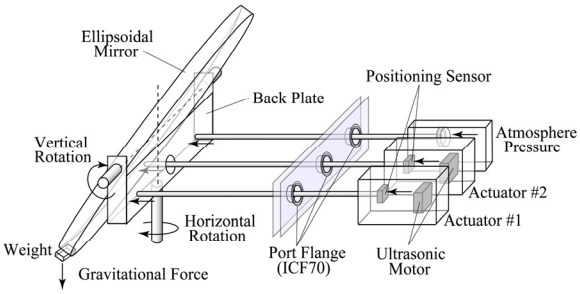

Fig.3 Schematic of the adjustable ellipsoidal mirror with the three pushrods.

[8-9] system for the measurement of the electron temperature profile. The MIR/ECEI system share the same optical imaging system in vacuum, and their beam paths are separated by an 8 mm thick dichroic plate, which works as an optical high pass filter. The optical layout enables to measure the cross-correlation between the MIR and ECEI signals at the same measurement point.

The dichroic plate has a clear cut-off feature at 70 GHz, so that it can separate the operational frequency band for MIR (50 - 70 GHz) and for ECEI (70 - 140 GHz). The dichroic plate contains close-packed circular holes with 2.5 mm in diameter and separated by 2.8 mm (center-to-center). This configuration provides the cut-off frequency of 70 GHz. The large size of the dichroic plate (300 mm x 260 mm, with 45 degree incident angle) preserves the wave fronts of both illumination and reflected beams.

The illumination beams are generated by high-power IMPATT oscillators (Quinstar QIO-5327CZ, QIO-6627CZ and QIO-6927CZ with output power of 0.5W). They are combined to one beam with two 3 dB directional couplers and it is launched from a scalar horn antenna. The polarization of the illumination beam can be changed by using twisted or straight fundamental waveguide behind the antenna. The launched beam is firstly diverged by a convex parabolic mirror (size of 110 mm x 80 mm, focal length of 102 mm) and it is reflected by a plane mirror (size of 190 mm x 120 mm). And it is focused by an ellipsoidal mirror (size of 290 mm x 216 mm, focal length of 310 mm). And then it passes through a beam splitter (acrylic plate with size of 260 mm x 200 mm) and it is reflected by the dichroic plate. The launched beam converges at the fused quartz window (the diameter of 192 mm) in order to enter the vacuum vessel. Finally the launched beam becomes parallel and illuminate the plasma by using the oval plane mirror (size of 300 mm x 257 mm) and an ellipsoidal mirror (size of 500 mm x 430 mm, focal length of 1064.7 mm), which are mounted in vacuum. All mirrors are made of aluminium alloy by using a numerically controlled milling machine with the cutting pitch of 0.2 mm. The mirror finish is necessary to check the beam focusing and the stray light by using of a bright halogen lamp.

The LHD plasma has a twisted elliptical or triangular cross-section, so the elliptical cross-section is tilted downward near the equatorial plane at the port 4-O as shown in Fig. 1. Therefore, the optimum illumination angle is different between O-mode and X-mode. For example, as the density is higher, the right-hand cut-off layer is more tilted. And as the magnetic axis shifts to outboard, the illumination beam should be more tilted upward. The illumination angle should be adjusted according to the inclination of the reflection surface. The illumination and the reflection paths in the X-mode are simulated by using a ray-tracing code [10]. Figure 2(a) shows the simulation results in the previous setup. The horizontally illuminated beams are reflected downwards as shown in Fig. 2(a). To obtain considerable reflected power, the ellipsoidal primary mirror should be tilted by 3 degrees upward as shown in Fig. 2(b).

In the new setup, the angle of the ellipsoidal primary mirror can be adjusted by using remote-controlled actuators with ultrasonic motors (Shinsei USR60-S3N). Since the ultrasonic motor is non-magnetic, it doesn't disturb the magnetic fields of plasma. Figure 3 shows the schematic of the rotating mechanism with three pushrods and one weight. The ellipsoidal mirror is connected to a rectangular back plate with a horizontal rotation axis. The back plate is connected to the base plate with a

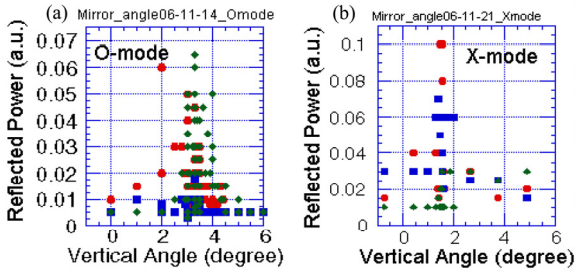

Fig.4 Optimized illumination angle in the case of O-mode (a) and X-mode (b) measured in the plasma experiment.

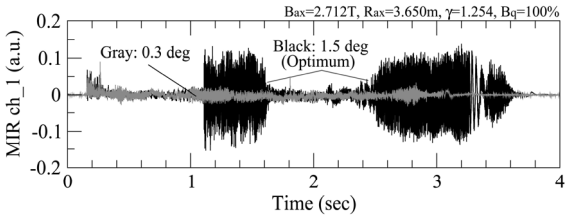

Fig.5 MIR signals before and after the optimization of the mirror angle.

vertical rotation axis. Both the horizontal axis and the vertical axis pass the center of the concave surface of the ellipsoidal mirror. The left hand side of the back plane is pushed by the actuator rod #1. The right hand side of the back plane is pushed by a free rod, which is connected with an ICF70 flange. This flange is guided by two bars and is connected to the LHD vacuum vessel with a bellows. The free rod can move freely in one direction and the atmosphere pressure pushes the ellipsoidal mirror with the free rod. So the ellipsoidal mirror can be rotated around the vertical axis by controlling the actuator #1.

The lower part of the ellipsoidal mirror is pushed by the actuator rod #2. A weight is attached at the bottom of the mirror. Since the gravitational force due to the weight pushes the mirror to the actuator rod #2, the ellipsoidal mirror can be rotated around the horizontal axis by controlling the actuator #2. The thrust bearings are coated with the titanium nitride so that the friction is fairly reduced in vacuum. Non-magnetic stainless-steel (SUS304) ball bearings are used as well. These mechanisms allow the smooth mirror rotation by one degree per second with the allowance of the mirror angle less than 0.1 degree.

3. System Performance

The mirror angle is optimized during the LHD plasma experiment. The time-averaged amplitude of fluctuations in the MIR signal is plotted by scanning the mirror angle in the vertical direction as shown in Fig. 4. The optimum illumination angle is about 3 degree upward in the O-mode, as shown in Fig.4 (a) and that it is about 1.5 degree upward in the X-mode, as shown in Fig.4 (b). Since the profile is very narrow with half width of about 1 degree, the optimization of the illumination angles is required to detect the reflected beam power from the twisted reflection surface.

The wave number vector of the electron density fluctuation is measured with three receiving antennas, which correspond to three reflection points. The first one is centrally positioned at the intersection of the optical axis with the reflection surface. The second one is separated from it by about 8 cm in the direction parallel to the field line. And the third one is separated from the central antenna by about 10 cm in the direction perpendicular to the field line. The two cut-off surfaces of 66 and 69 GHz are separated about 4 cm in typical in the radial direction.

The reflected power is measured by a multi-channel heterodyne receiver (Figure 1). The received signal is down converted by the wide band balanced mixer (Millitech MXP-15-RSXSL) to the intermediate frequency (IF) of 3, 6 and 10 GHz with the local oscillator signal of 63 GHz. The resultant signal splits into 3 ways by the power divider and they are amplified by 23 dB. They are band-pass filtered with the central frequency of 3, 6, 10 GHz and the -3 dB bandwidth of 300 MHz, and then they are detected by Schottky-barrier diodes (Herotek DHM185AA). The signal is amplified with the variable gain up to 40 dB in order to match the signal level to the input range of the PXI digitizer (National Instruments PXI-6133). It has a resolution of 14 bits maximum time resolution is 3 M-samples/sec, real-time recording. Since the time resolution is usually set to 1 M-samples/sec. The total time resolution of the MIR system is about 2.4 μsec.

The beams pattern near the reflection surface are measured by using a metal rod and a vector-network-analyzer (ANRITSU 37397C). The rod is scanned along the toroidal direction or

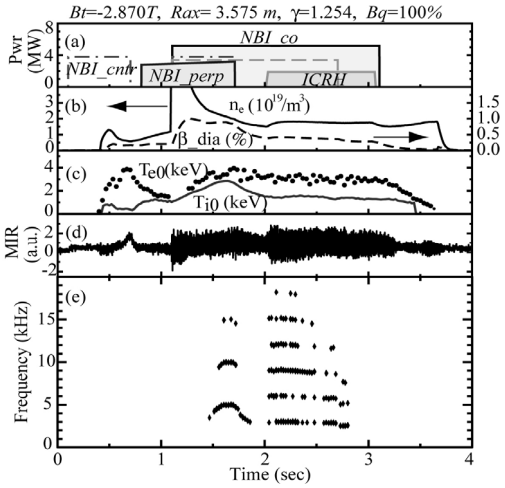

Fig.6 A novel MHD mode with harmonics during NBI and ICRH heating plasma.

the radial direction around the reflection center. The wave reflected on the narrow region (with width of a few millimeters) of the rod surface reaches to the receiving antenna. This profile is almost identical in the frequency range between 45 - 60 GHz. The beam waist of the reflected wave that is received by the antenna is about 3.3 cm and the focal depth is about 1 m near the reflection surface.

Typical MIR signals before and after the optimization is shown in Fig. 5. By optimizing the beam direction, the MIR signal becomes high enough to measure the density fluctuation.

4. Experimental Result

By using the MIR system, a novel MHD instability is observed in LHD. A typical example is shown in Fig. 6. The LHD configuration is as follows: R_{ax} = 3.575 m, a = 0.6 m, B_t = 2.870 T, γ = 1.254 and B_q = 100 %. The plasma is heated by the co-injected NBI with the power of 8.6 MW and the counter-injected NBI with the power of 3.8 MW. Fig. 6 shows time evolutions of the heating power, the beta β_{dia} measured by the diamagnetic diagnostics, the line averaged electron density n_e, the central electron temperature T_{e0}, the central ion temperature T_{i0} and the MIR signal. Fig.6 (e) shows the time evolution of the FFT power spectrum of the MIR signal. A mode appears at t=1.5 sec.

This mode has equally separated several harmonics. The mode frequency looks depending on the ion temperature. The frequency decreases after turning off the perpendicular injected NBI with the power of 3.2 MW, and this mode disappears 0.2 sec after the perpendicular NBI turning off. Right after turning on the ICRH with the power of 1.9 MW, a mode with equally separated several harmonics appears. In this case, the number of harmonics is double of the former mode. So, the heating of perpendicular ion component looks important to destabilize this mode. By the improvement of the MIR system the notable MHD mode has been observed in the MIR signals for the first time.

5. Conclusion

In conclusion, we have found that the optimization of the direction of microwave beam is a key of the microwave imaging reflectometry, which is expected to be a powerful tool to study the turbulence in plasmas. The illumination and reflected beam paths near the reflection surface are calculated with the ray tracing code. We have developed a mirror rotation mechanism using three rods and two actuators driven by ultra-sonic motors. The mirror angle is changed shot by shot. The experimentally obtained optimum illumination angle in LHD is 3 degree upward in the case of O-mode and 1.5 degree upward in the case of X-mode. These angles are similar to the simulation. By optimizing the beam direction, the MIR signal becomes high enough to measure the density fluctuation. The novel MHD mode with harmonics is observed by using the new setup of MIR system in ICRH and NBI heated plasma of LHD.

References

[1] C. Laviron et al., Plasma Phys. Control. Fusion, 38, (1996) 905.
[2] E. Mazzucato, Nuclear Fusion, 41, (2001) 203.
[3] E. Mazzucato, Plasma Phys. Control. Fusion, 46, (2004) 1271.
[4] T. Munsat et al., Rev. Sci. Instrum. 74, (2003) 1426.
[5] H. Park et al., Rev. Sci. Instrum. 75, (2004) 3787.
[6] H. Park et al., Rev. Sci. Instrum. 74, (2003) 4239.
[7] O. Motojima et al., Nuclear Fusion, 45, (2005) S255.
[8] A. Mase et al., Rev. Sci. Instrum. 72, (2001) 375.
[9] A. Mase et al., Rev. Sci. Instrum. 74, (2003) 1445.
[10] M. Ignatenko et al., Rev. Sci. Instrum. 75, (2004) 3810.

Proposal of *in situ* Density Calibration for Thomson Scattering Measurement by Microwave Reflectometry

Takashi Minami[1]

[1]*National Institute for Fusion Science, Oroshi-cho 322-6, Toki 509-5292, Japan*

An *in situ* density calibration for a Thomson scattering measurement by a microwave reflectometry based on Bayesian estimation is proposed. A simultaneous calibration with a plasma experiment is feasible, because it is not necessary for a vacuum vessel to be filled with N_2, Ar or H_2 gases. The Bayesian estimation provides an accurate density calibration factor from a few reflectometer measurements, which is confirmed by a Monte-Carlo simulation.

1 Introduction

The electron temperature and density profiles measurement with the Thomson scattering method is a basic diagnostic for the high temperature plasma experiment. It is especially a crucial tool for the estimation of the thermal and particle diffusivities for the transport study. Though the Thomson scattering method is classical in the plasma diagnostics, the several problems that should be resolved are remained. One of the problems is the absolute calibration for the density measurement.

Because the density measurement with the Thomson scattering is to measure an amount of the scattered light, the calibration factor is affected by the misalignment of a laser path and a collective system of the scattered light, the sensitivity of polychromators and detectors, a laser beam profile and so on. Most popular method for the Thomson density calibration is a gas scattering method, which utilizes Raman or Rayleigh scattering of molecule[1]. However, the gas scattering method has a drawback: a vacuum vessel needs to be filled with N_2, Ar or H_2 gases to an atmospheric pressure level[1]. Thus the calibration in parallel with the density measurement is difficult, although the calibration factor is modified during the plasma experiment after the gas scattering calibration. Consequently, another *in situ* calibration method is required for the precise measurement of the plasma density.

A preferable technique for the *in situ* calibration is a method using plasma density values measured with the other plasma diagnostic. In this paper, the method of the density calibration by the microwave reflectometer for the multipoint Thomson scattering system is proposed. The specification of the reflectometer for the density calibration is discussed. The density calibration factor is estimated on the Bayesian theorem. The Bayesian technique is simulated by a Monte-Carlo method.

2 Density calibration using the microwave reflectometer

The Thomson scattering calibration factor C^T for the density measurement is defined as $n_e = C^T S$, where n_e is the plasma density, S is an amount of the Thomson scattered light. The factor depends on the laser alignment, the collective system alignment and so on. Though the calibration factor is stable, the factor have decades of continuous change. The purpose of the calibration method by the microwave reflectometry is improving the calibration factor to the real value by the reflectometer measurement. The reflectometer utilize a laws of physics that a wave propagating in the plasma is reflected at the cut off point. The plasma density can be measured by detecting the reflected wave from the cut-off layer, because the location of the cut-off layer depends on the plasma density. The calibration is performed by the simultaneous density measurement with both the multi point Thomson scattering system and the reflectometer, as shown in figure 1.

The compact and simple system is preferable as the reflectometer due to the small space around the thomson scattering device. Thus, I choose the FM type reflectometer, which is the simplest one. The FM reflectometer consists of a launching antenna, a receiving antenna, a direct coupler, a mixer, waveguides and a oscillator with frequency swept over wide

ranges[2]. The required sweep time is less that 10-100μsec. The FM reflectometer measures phase delay ϕ of the reflected wave at the cut-off layer. Because of the phase delay at lots of different frequencies by the sweep oscillator so that the function $\phi(\omega)$ can be constructed. When the injected wave is ordinary mode, the location of the cut-off layer is derived from the following equation[3].

$$r_c(\omega) = a - \frac{c}{\pi}\int_0^{\omega} \frac{d\phi}{d\omega'}\frac{d\omega'}{\omega^2 - \omega'^2} \qquad (1)$$

, where the 'a' is a location of the plasma surface, 'c' is a speed of light. The FM reflectometer has drawback that the measurement accompany a error that is caused by a fringe jump[2]. However, this drawback can be resolved by the Bayesian estimation, which is explained in the next section. An another candidate is AM type reflectometer, in which the fringe jump problem is resolved using the two oscillators that have two different frequencies[2].

The density range that can be measured with the reflectometer is the determined by the frequency of the injected wave, because the cut-off density depends on the wave frequency. If the calibration is performed only once, the calibrated thomson channels of the profile measurement are limited to the region that determined by the frequencies of the injected wave and the plasma density. Avoiding this situation, the calibration is repeated more than once for different density plasmas.

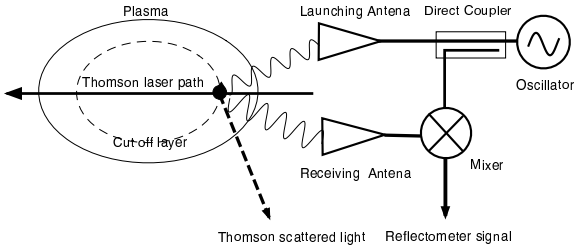

Fig.1 Conceptual diagram of Thomson density calibration by microwave reflectometry.

Figure 2 shows the result of the estimation of a plasma frequency for the typical LHD plasma[4]. I assume the density profile is parabolic: $n_e = n_e(0)(1-\rho^2)^{\alpha}$. In this estimation, I choose 0.3 as the factor α, because the LHD density profile is typically flatten. The central electron density $n_e(0)$ is swept form $1 \times 10^{13} cm^{-3}$ to $4 \times 10^{13} cm^{-3}$. If the oscillator frequency is swept from 30 GHz to 50 GHz, the Thomson channels that corresponds to the almost half region of the plasma cross section can be calibrated by measuring the different density plasmas, as shown in figure 2(a). However, a peaked density profile is more preferable, because the accuracy of the location of the cut-off layer is better than the flatten profile. The peaked density profile is produced by a pellet injection or a magnetic structure control in the LHD[4].

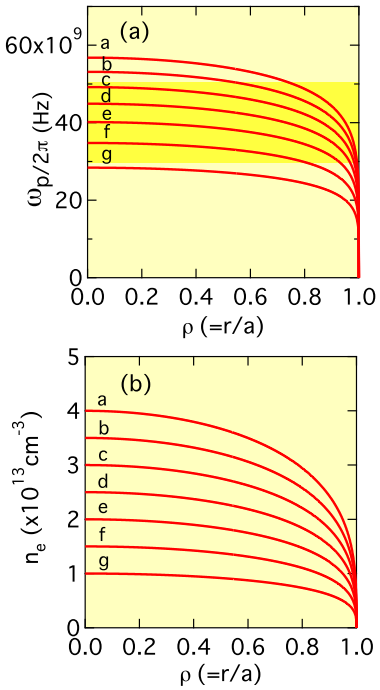

Fig.2 Estimation of the plasma frequency profiles (a) with corresponding density profiles (b). The profile shape is assumed as the typical LHD one. The central electron density $n_e(0)$ is swept form $1 \times 10^{13} cm^{-3}$ to $4 \times 10^{13} cm^{-3}$ (a). The yellow zone shows the frequency range from 30GHz to 50GHz.

3 Density calibration method based on Bayesian estimation

The Bayesian estimation is a probabilistic approach for estimating an unknown probability density function. The Bayesian theorem is defined as

follows[5].

$$P(x|d) = \frac{P(d|x)P(x)}{P(d)} \tag{2}$$

, where $P(x)$ is a prior probability, $P(x|d)$ is a posterior probability and a conditional probability of x given d, $P(d|x)$ is a conditional probability of d given x, $P(d)$ is a normalized constant, and $P(d|x)/P(d)$ is a likelihood. The $P(d)$ is defined as follows.

$$P(d) = \int_0^\infty P(d|x)P(x)dx \tag{3}$$

For the purpose of the Thomson density calibration, the parameter 'd' is the calibration factor derived from the reflectometer measurement, and is defined as follows.

$$d = \frac{n_e^{ref}}{S} \tag{4}$$

,where n_e^{ref} is a plasma density measured with the reflectometer, and the S is the amount of the scattered light measured with the Thomson scattering device.

I assume that the prior probability function of the calibration factor C^T for the density measurement is a gaussian destribution. The prior probability P(x) is defined as follows.

$$P(x) = \frac{1}{\sqrt{2\pi}w_{prior}} exp\Big\{ -\frac{1}{2}(\frac{x - C^T_{prior}}{w_{prior}})^2 \Big\} \tag{5}$$

, where C^T_{prior} is a prior calibration factor, and w_{prior} is a error range of the calibration factor. The first prior calibration factor (the initial value) can be determined from the gas scattering experiment or the estimation taking the solid angle of the scattering light and the transmission efficiency of the collective optics and the spectrometer into account. It is no problem that the first prior calibration factor includes an error, because the primal error is corrected with the reflectometer measurement.

The probability function $P(d|x)$ is derived form the reflectometer measurement. I also assume that $P(d|x)$ is a gaussian distribution, and the $P(d|x)$ is defined as follows.

$$P(d|x) = \frac{1}{\sqrt{2\pi}w_d} exp\Big\{ -\frac{1}{2}(\frac{x - d}{w_d})^2 \Big\} \tag{6}$$

, where w_d is a error range of the 'd'.

The modified calibration factor to the real value after the one reflectometer measurement is calculated as the posterior value ,which is derived from the posterior probability function $P(x|d)$ (eq.(2)). The posterior calibration factor $C^T_{posterior}$ and that error range $w_{posterior}$ are derived from the following formulas.

$$C^T_{posterior} = \int_0^\infty xP(x|d)dx \tag{7}$$

$$w_{posterior} = \sqrt{\int_0^\infty x^2 P(x|d)dx - (C^T_{posterior})^2} \tag{8}$$

The Bayesian estimation provides a sequential analysis for the calibration factor determination taking the accuracy of the reflectometer measurement into account. The simultaneous measurement of the Thomson scattering and the reflectometer is repeated. The posterior value of the C^T and w are used as the prior one of the next step, and the derivation of the posterior probability function is repeated recursively. The calibration factor is modified and come close to the real value with the number of the times of the simultaneous measurements.

4 Monte-Carlo simulation for the density calibration by the reflectometer

For confirming the effectiveness of the density calibration by the reflectometer based on the Bayesian estimation, a Monte-Carlo simulation is carried out. The calibration factor 'd' derived form the reflectometer measurement is simulated using a random function based on a Gauss distribution. I assume the reflectometer and the Thomson scattering measurements include no systematic error. First, w_d is determined by a random value from the Gaussian distribution that is determined by the given standard deviation, then the calibration factor 'd' is determined from the random function of which standard deviation corresponds with the w_d.

I assume the worse situation as the calibration experiment, such that the derived factors from eq.(4) are considerably scattered due to the measurement error caused by the reflectometer and the Thomson scattering diagnostics: the standard deviation of the Gaussian distribution is larger. The result of the simulated calibration factor eq(4) form the reflectometer is shown in figure 3 (a). In this simulation, number of

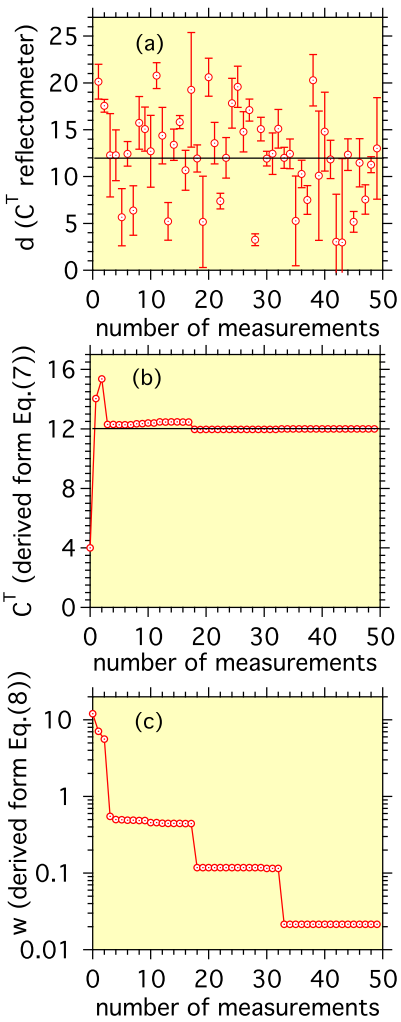

Fig.3 Monte-Carlo simulation of Thomson density calibration by microwave reflectometry. (a)Simulated 50 calibration factors of eq(4) from the random function based on the Gaussian distribution. (b) Estimated calibration factors C^T using eq.(7). (c) Estimeted error ranges w using eq.(8).

times of the reflectometer measurements is assumed as 50, and the real value of calibration factor C^T is assumed as 12. As a result, the average of the 50 simulated reflectometer data is 12.22.

The estimated calibration factor C^T using the eq.(7) is shown in the figure 3 (b). I assume the case that the initial value of C^T is considerably different from the real value of 12 (C^T_{prior}=4). After a few steps of measurements, however, the C^T converge to the close value of 12, then the value is stabilized near the real value, though the simulated data of the reflectometer is far from the real value, because the estimated error range (w) is sharply reduced, as shown in figure 3 (c). The final value of the C^T after the 50 measurements is 11.99 ± 0.02, of which value is close to the real value of 12 compared with the average (12.22) of the simulated reflectometer data shown in figure 3 (a). When the other seed of the random function is given, the same tendency is observed. When a type of laser on Thomson scattering device is a high repetition Nd:YAG laser (10Hz), the 10-20 simultaneous measurements for the calibration is possible during one discharge. Consequently, expected number of discharges for the density calibration is below 10.

5 Summary

I propose that the *in situ* density calibration for the Thomson scattering measurement by the microwave reflectometry. The procedure of deriving the calibration factor is based on the Bayesian estimation. The FM sreflectometer used for the calibration is compact compared to the Thomson scattering device. The simultaneous calibration with the plasma experiment is feasible, because it is not necessary for the vacuum vessel to be filled with the gas. The Monte-Carlo simulation shows that the Bayesian estimation provides the accurate density calibration factor from a few reflectometer measurements.

References

[1] J.Howard et.al., J. Phys. D: Appl. Phys., Vol.12 (1979) p.1435-1440

[2] A.Ejiri J. Plasma and Fusion Res. vol. 79 No.9 (2003) p.921-928

[3] I.H.Hutchinson, "Principles of plasma diagnostics second edition" Cambridge Univ. Press. p.146

[4] K. Tanaka et.al., Fusion Sci. and Tech. **51** (2007) p.97.

[5] A lot of references about "Bayesian theorem" are available.
(e.g. http://en.wikipedia.org/wiki/Bayes'_theorem)

Recent Progress of the LHD Thomson Scattering

I. Yamada, K. Narihara, H. Funaba, T. Minami, H. Hayashi, and LHD experimental group

National Institute for Fusion Science, 322-6 Oroshi-cho, Toki, 509-5292, Japan

We developed the LHD Thomson scattering about ten years ago, and have made many improvements on it. The LHD Thomson scattering measures electron temperature and density profiles of LHD plasmas along with the LHD major radius at a horizontally elongated section. The LHD Thomson scattering has two kinds of YAG lasers, three 10 Hz/2.3 J lasers and four 50 Hz/0.5 J lasers, and various operational modes are possible. Thomson scattered light is collected with a large gold-coated spherical mirror, and analyzed by conventional polychromators with five wavelength channels. In this paper, we describe recent progress of the LHD Thomson scattering.

1. Introduction

Thomson scattering is one of the most reliable diagnostics for measuring electron temperature and density profiles of fusion plasmas. We constructed the LHD YAG Thomson scattering about ten years ago [1][2]. The LHD Thomson scattering has worked well routinely and obtained a huge number of electron temperature and density profile data in the LHD plasma experiments. In the past one decade, we have continued our efforts to improve the performance and reliability of it.

The LHD Thomson scattering measures electron temperature and density profiles of LHD plasmas along with the LHD major radius at a horizontally elongated section, as shown in Fig.1. It consists of several subsystems, laser system, light collection optics, polychromators, and data acquisition system. Typical specifications of the LHD Thomson scattering are summarized in table 1. The number of spatial points and typical spatial resolution are 144 and 25 mm, respectively. The temporal resolution is determined by laser repetition rate. In following sections, we describe the recent progress of the LHD Thomson scattering.

Table 1: Typical specifications of the LHD Thomson scattering.

Scattering angle	167°
Solid angle	16 msr
Number of spatial points	144
Spatial resolution	25 mm
Temporal resolution	10-200 Hz
T_e range	20 eV – 20 keV
N_e range	10^{18} – 10^{21} m^{-3}

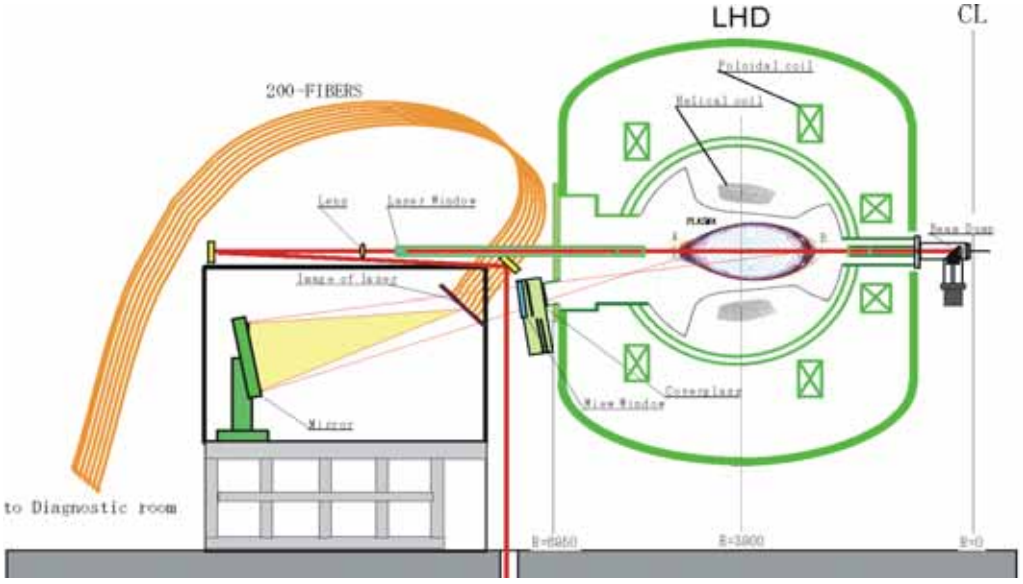

Fig. 1: Overview of the LHD Thomson scattering.

2. LHD Thomson Scattering

2.1. Scattering Configuration

The LHD Thomson scattering has an oblique backward scattering configuration, in which typical scattering angle is 167^o as shown in Fig.1. In such backward scattering configuration, Thomson scattering spectrum width becomes wider than those in conventional right angle scattering configuration. Then, it suits for low temperature region, while the spatial resolution is not as good as that of right angle scattering configuration. The lowest measurable temperature is about 20 eV in the LHD Thomson scattering.

2.2. Laser System

The LHD Thomson scattering has two kinds of lasers, high-energy low-repetition 2.3 J/10 Hz lasers (Thales SAGA 230) and low-energy high-repetition 0.5 J/50 Hz (Continuum NY-50). In the LHD Thomson scattering, flexible multilaser operations are possible [3][4]. For examples, four 0.5 J/50 Hz lasers can be used as a 2 J/50 Hz laser by firing the lasers simultaneously. They can be also used as a 0.5 J/200 Hz laser by firing them at intervals of 5 msec. Figure 2 shows comparison of electron temperature profiles obtained from the simultaneous firing mode of four lasers and one laser operation. The plasma performances of the two discharges were almost same under a fixed discharge operation. In the high-energy mode, both of the number of detected photons and signal-to-noise ratio are increased, resulting in higher data quality [4].

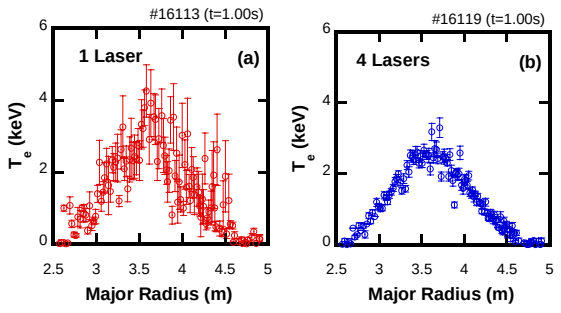

Fig.2: Comparison of T_e profiles obtained by (a) single laser, and (b) four lasers.

2.3. Light Collection and Polychromator

Thomson scattered light is collected with a large 1.5 m x 1.8 m Au-coated spherical mirror onto 144 optical fibers with the core diameter of 2.0 mm, and then transmitted to 144 polychromators [5]. Each Polychromator has five wavelength channels for Thomson scattering measurements, and additional sixth channel for Rayleigh calibration [6]. Figure 3 shows the schematics of the polychromator. The Thomson scattered light is separated by bandpass filters and detected with avalanche photo diode (APD) detectors. An example of the spectral responsibility of a polychromator is shown in Fig. 4, together with Thomson spectrum at 50 eV, 500 eV, and 5 keV. Since both of the characteristics of the bandpass filter and APD strongly depend on temperature, the temperature of polychromators is stabilized by temperature-controlled chilled water.

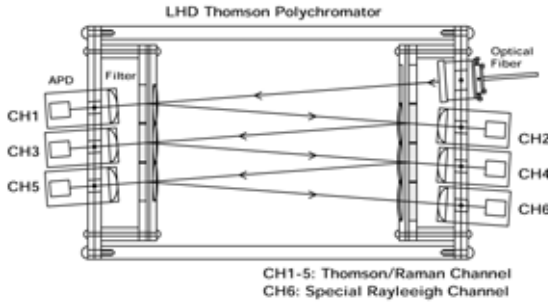

Fig.3: Schematic diagram of the 6-channel polychromator. The 6th channel is used for Rayleigh calibration.

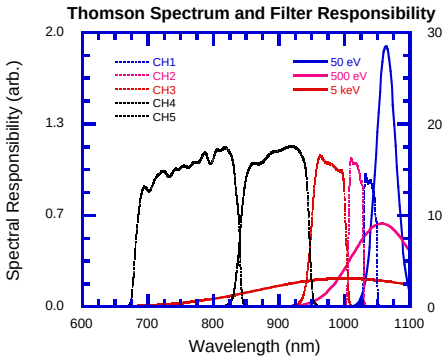

Fig.4: Spectral responsibility of a polychromator. Solid lines are Thomson spectrum, 50 eV, 500 eV, and 5 keV.

2.4. Data Acquisition

Detected Thomson scattering signals are digitized with the FASTBUS based data acquisition system, which includes extremely fast

analog-to-digital converters. The system has a low cut filter, and then only fast components (>1 MHz) can pass through. The method is good for eliminating slow plasma light influence efficiently, but we could not know plasma light intensity on the APDs. When APD is irradiated by intense plasma light, the performance of APDs is degraded and the detectors may be broken at the worst [7]. Then, we installed a new system for monitoring plasma light intensity on all APDs, which is based on the Lab VIEW PXI system. The plasma light monitor system has worked since the 10th LHD experimental campaign.

Figure 5 shows an example of raw data of Thomson scattering signals and plasma radiation detected by five wavelength channels in a polychromator. The upper and lower rows of circles are Thomson signals from high and low energy lasers, respectively, and the dots are plasma radiation. At the middle stage of the discharge, strong plasma light appeared suddenly, and the APD outputs were saturated completely in the wavelength channel #3, #4 and #5. In the period, Thomson signals disappeared due to the detector saturation. We have found that the intense background light is observed by only specific polychromators that see divertor plates. Therefore, we believe that the background light is originated from divertor plasma related phenomena. Although it is not easy to suppress the divertor light influence efficiently, we can properly judge the data reliability, and provide only reliable Thomson data [8].

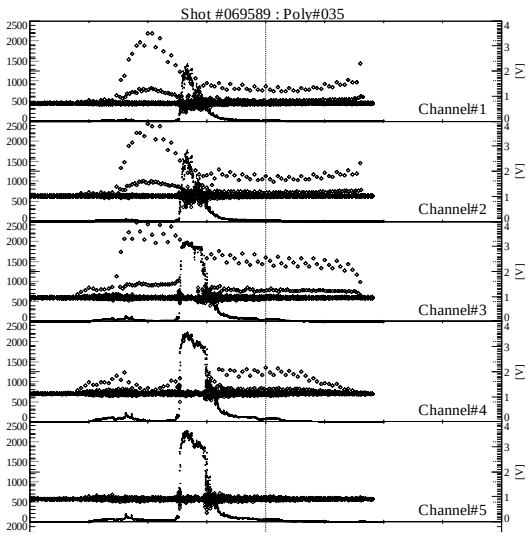

Fig. 5: Raw signal detected by 5 wavelength channels in a polychromator.

2.5. Calibrations

In order to obtain absolute electron densities, the Thomson scattering device should be calibrated absolutely whereas only relative calibration is required for electron temperature measurement. For absolute electron density measurement, we have tried Raman and Rayleigh calibrations [6][9]. In both of the calibrations, pure gaseous nitrogen or dry air was introduced into the LHD vacuum vessel up to 50 kPa. The calibration factors obtained from the Raman and Rayleigh calibrations show good agreements. However, we believe that Rayleigh calibration may be suitable to the LHD YAG Thomson scattering because more accurate calibration factors can be obtained. Figure 6 shows an example of measured electron temperature and density profiles of a super dense core (SDC) plasma discharge. The electron densities are calibrated absolutely by using Raman scattering.

Next, We have checked long-term stability of the Thomson scattering through the 10th LHD experimental campaign by comparing electron line densities obtained from Thomson scattering and measured by the MMW diagnostics. Both of them measure electron density at LHD horizontally elongated sections, so the data can be compared directly without any assumption and/or additional analytical procedure. The ratio of the two line densities obtained from Thomson scattering and MMW shows some variations through the 10th LHD experimental campaign. Typical variation during a plasma discharge is

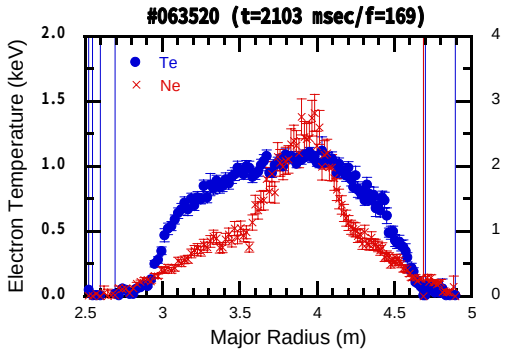

Fig.6: Example of T_e and N_e profiles of the LHD SDC plasmas measured by the LHD Thomson scattering. A narrow peaked N_e profile and bell-shaped T_e profile were observed in the SDC discharge.

less than a few percents, typical weekly variation is estimated to be less than 6 %, and then overall variation in the 10^{th} experimental campaign is less within 24 %. Therefore, we can conclude that the short-term stability of the LHD Thomson scattering is good, and weekly or monthly recalibration is recommended.

3. Summary

The LHD Thomson scattering, which is constructed about ten years ago, has worked routinely and obtained a huge number of electron temperature and density data of LHD plasmas. In the past one decade, we have continued our efforts to improve the performance and reliability. The LHD plasma performance has grown step-by-step, then measurable temperature and density ranges of the LHD Thomson scattering should be further improved so as to cover the LHD plasma performance.

Acknowledgements

This work was supported by the NIFS LHD project budgets (NIFS04ULHH502, NIFS05ULHH502 and NIFS06ULHH502), and partially supported by the Grant-in-Aid for Scientific Research (C), No. 16540456.

References

[1] K. Narihara *et al.*, Fusion Eng. Design **34-35**, 67 (1997).

[2] K. Narihara *et al.*, Rev. Sci. Instrum. **72**, 1122 (2001).

[3] I. Yamada *et al.*, NIFS Ann. Rep. 1993-1994, 80 (1994).

[4] I. Yamada *et al.*, Rev. Sci. Instrum, **72**, No.1, 1126 (2001).

[5] K. Narihara *et al.*, Rev. Sci. Instrum., **74**, No.10, Part II, 3878 (2004).

[6] I. Yamada *et al.*, JPFR SERIES, 9, in press (2007).

[7] K. Narihara *et al.*, JPFR SERIES, 9, in press (2007).

[8] I. Yamada *et al.*, NIFS Ann. Rep. 2006-2007, in press (2007).

[9] I. Yamada *et al.*, Rev. Sci. Instrum., **74**, No.3, 1675 (2003).

Two color Poloidal Interferometer / Polarimeter for ITER

R. Pavlichenko[1], K. Kawahata[1], T. Akiyama[1], S. Okajima[2]

[1] *National Institute for Fusion Science, 322-6 Oroshi-cho, Toki-shi, 509-5292, Japan*
[2] *Chubu University, 1200 Matsumoto-cho, Kasugai-shi, Aichi 487-8501, Japan*

The determination of the profile of the toroidal plasma current (safety factor) has been considered as essential diagnostic for ITER. In absence of neutral beam, the only reliable diagnostics which can provide the information on the q-profile is polarimetry. About ten viewing chords could cover significant part of the poloidal cross section of the plasma in a fan-like arrangement at the equatorial port. The probing beams enter the vacuum vessel through a penetration in the blanket modules at the low-field side. The four additional quasi-vertical viewing chords are inserted through the upper port. Retroreflectors at the high field side mirror the laser beams back towards the initial penetrations and allowed to measure Faraday rotation and phase shift. The present work considered the combined interferometer / polarimeter configuration for laser wavelength of about 50 μm. At this wavelength the ellipticity is small but has to be taken for account. Thus, the promising Cotton-Mouton effect, which is considered as an alternative for plasma density measurements, will be difficult to implement. The initial optimization of the viewing chords arrangement for several ITER plasma scenarios (sensitivity to the toroidal current profiles) has been done. The additional issue of delivering laser radiation to the plasma will be addressed. The advantages of the waveguide approach for beam focusing in the long (more than 50 m) optical path are shown..

1. Introduction

Control of the current density profile becomes a paramount issue for the future tokamak experiments. Polarimetry can provide information on the density and magnetic field from which current profile could be reconstructed. Previous system [1] was design to operate at λ =118.8 μm CH_3OH oscillation line. It is well known that there are two main approaches to build the polarimetry system. To obtained information about magnetic field one have to measure the value of Faraday rotation angle α_F, which is proportional to poloidal magnetic field $B_{p\|}$ and electron density n_e.

$$\alpha_{\mathrm{F}} = 2.62\times10^{-13}\lambda^2\int_Z n_e(z)B_{p\|}(z)\,dz \quad (1)$$

From α_F values profile of the poloidal component of the magnetic field could be calculated. It became obvious that the electron density along same beam line have to be known. For this purpose along beam chord a phase measurements by interferometer or measurements of the ellipticity angle α_{CM} (Cotton-Mouton effect (CM)) have to be performed.

$$\alpha_{\mathrm{CM}} = 2.62\times10^{-11}\lambda^3\int_Z n_e(z)B_t^2(z)\,dz \quad (2)$$

2. System discription

Maximum number of twelve probing beams comes into the plasma through the diagnostic plug at the low-field side (LFS). At the high field side (HFS) of the blanket shield module (BSM) small (∅ 37 mm) corner retroreflectors (CRR) are placed to reflect backwards the laser beams. Recently for ITER-scale experiments and for the plasma experiments on Large Helical Device (LHD) we have been developing short wavelength FIR laser. These research activities are carried out to overcome the common ‘fringe jumps’ phenomena which occurs because of electron density increasing during pellet injection experiments. On LHD 13-channel 119 μm laser interferometer has routinely operated to provide information on the electron density profile.

The wavelengths of the new two-color interferometer are 57.2 μm (1.6 W) and 47.6 μm (0.8 W) in a twin optically pumped CH_3OD laser [2].

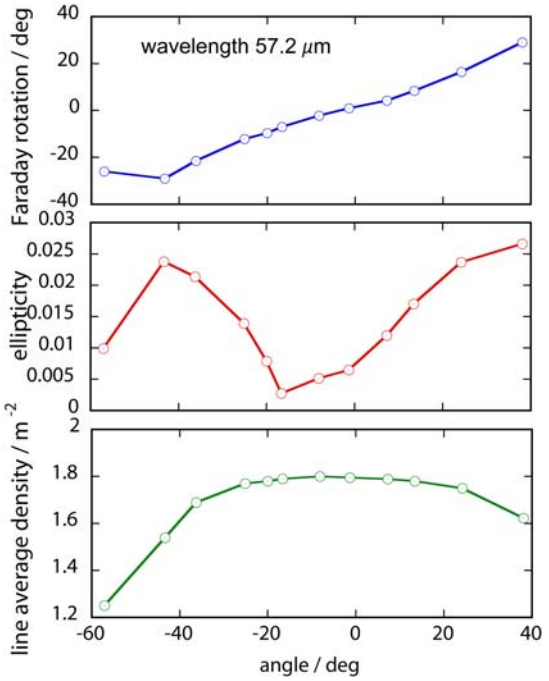

Fig. 1: Calculated Faraday rotation (top) and ellipticity (center), line density (bottom) 57 μm.

For ITER experiments we advocate the classical dual interferometer / polarimeter approach for its considerable simplicity to reconstruct experimental data. We consider the propagation of polarimeter beams through a thin layer of plasma (thickness z_0) in the presence of a magnetic field. This calculation takes into account both the Faraday rotation and the Cotton-Mouton effect.

3. Alternated transmission line and numerical simulation of the expected values of the rotation angle and ellipticity

The calculation of the expected values of Faraday rotation angle and ellipticity for chosen ITER 'plasma burn' scenario #2 (plasma current I_p=15.0197 MA, q_0 = 0.99, 'flat' electron density profiles are shown at the Fig. 1. One can see that for the chosen wavelength of 57.2 μm Faraday rotation angle is about 25−30°, which is still large enough.

Recently for ITER-scale experiments and for the plasma experiments on Large Helical Device (LHD) we have been developing short wavelength FIR laser. These research activities are carried out to overcome the common 'fringe jumps' phenomena because of rapid raise of the plasma electron density, which occurs during pellet injection experiments. On LHD 13-channel 118.8 μm CH_3OH laser interferometer has routinely operated to provide information on the electron density profile. The wavelengths of the new two-color interferometer are 57.2 μm (power 1.6 W) and 47.6 μm (power 0.8 W) in a twin optically pumped CH_3OD.

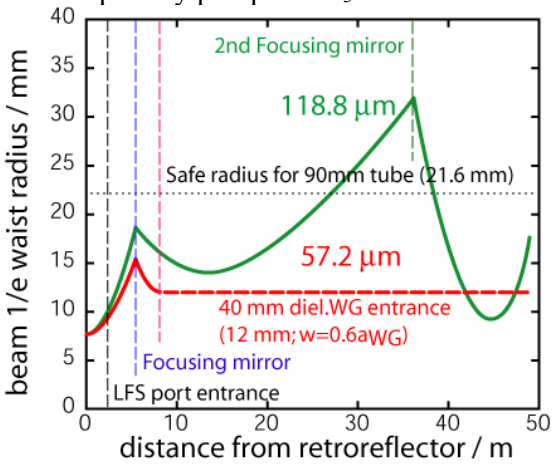

Figure 2: Calculated Gaussian beam radius (waist of 1/e intensity value) for wavelength 118 and 57 μm.

Since 47.6 μm and 57.2 μm have different polarization a Martin-Puplett diplexer is placed in front of the laser output. One of the most important issues is the developing of high quality heterodyne detection system with fast and sensitive characteristics. One of the main differences from 118.8 μm system is that instead of using quasi-optical transmission line (evacuated tubes of 90-120 mm in diameter) 40 mm dielectric waveguides become an attractive candidate. Those waveguides were made from Pyrex® borosilicate glass (with relative dielectric constant ε_r = 4.6−5.0) or acrylic resin (ε_r = 2.7−6.0)). From the other hand an oversized waveguides offer an attractive practical solution to transport light through the complicated geometry surrounding the fusion reactor.

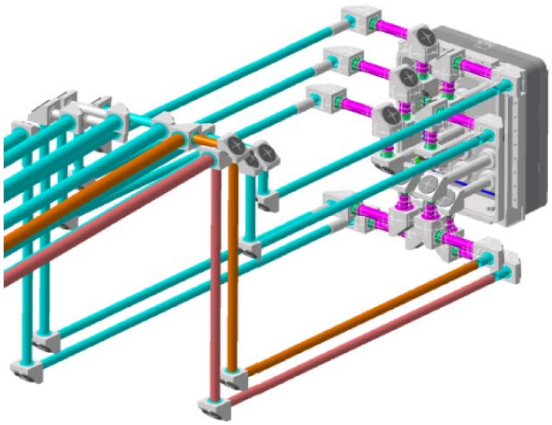

Figure 3: Poloidal polarimetry transmission lines and port plug to tokamak.

However, they can suffer from serious radiation-induced optical absorption and radioluminescence. Special fabrication and glass hardening techniques must be developed before suitable radiation -resistance dielectric waveguides can be used in ITER. By switching from pure quasi-optical (QO) beam free space propagation to 'waveguide ideology' for the transmission line that lies outside port plug (transmission line that correspond to the straight line at the Fig. 2) we can resolve several obstacles such as: mode matching / mode conversion, misalignment in the 'middle part' of the polarimeter optical path, which will be very difficult to maintain.

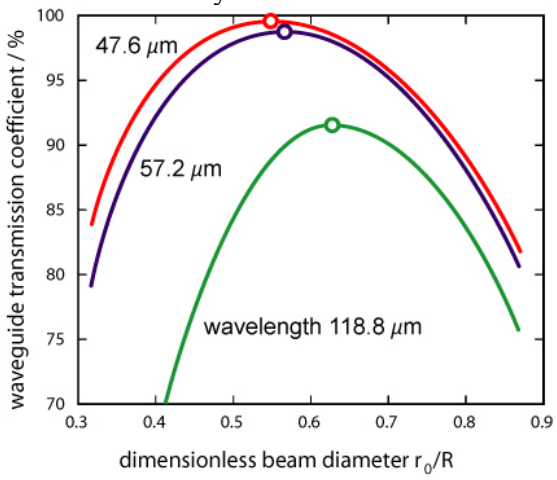

Figure 4: Coupling of Gaussian beam at the entrance of the dielectric waveguide. The inside diameter of the waveguide is 40 mm

From other hand waveguide system has precise mode matching (Fig. 2) (defined by waveguide diameter), easy alignment and more robust to mechanical vibrations. To deliver radiation from / to plasma each laser beam line is equipped with up to 8 miter-bends, with small conversion losses (Fig. 3). To avoid beam power dissipation Gaussian beam must enter the waveguide hawing optimized diameter. The calculation of waveguide transmission coefficient have been done for λ=48, 57, 118.8 μm

$$T = \left(1 - \exp\left(-F\frac{R^2}{r_0^2}\right)\right)F^{-1} \qquad (3)$$

where $F = 1 + \frac{\varepsilon_r + 1}{\sqrt{\varepsilon_r - 1}}\frac{L}{R}\frac{1}{k^2 r_0^2}$ and R, L - waveguide radius and length, $k = 2\pi/\lambda$ - laser beam wavelength, r_0-radius of the 1/e beam intensity level at the waveguide entrance, ε_r-waveguide material (relative dielectric constant) was chosen such as: $\sqrt{\varepsilon_r} = 2.1$. The calculation (refer to Fig. 4) shows that transmission coefficient values for 47.6 and 57.2 coupling into 40 mm diameter waveguide are about 99.6−98.42%, which is 7−8% higher than that for 118.8 μm.

The beam propagation inside the oversized dielectric waveguide have the same efficiency as for the free space, thus, preserves its polarization (99.6%). It was already confirmed by the long-term operation of FIR interferometer at LHD [5] (acrylic resin waveguide, length about 40m) and from several reports on JET polarimeter diagnostic (Pyrex® glass waveguide, length about 30m) that polarization of the laser beam in the waveguide remains almost constant. It was already shown [1, 3] by other research groups mechanical and optical properties of the corner retroreflectors became ultimately 'Achilles heel' of the system. The positions of the retroreflectors are limited by mechanical design of blanket shield modules on HFS inner wall (see Fig. 5). It was found that for wavelength 118.8 μm previously,

which CRR can cope with misalignment up to 15 - 20 mm in poloidal plane without any serious effect on the reflectivity. For the shorter wavelength those values become twice smaller: up to 7.5 mm (see Fig. 6).

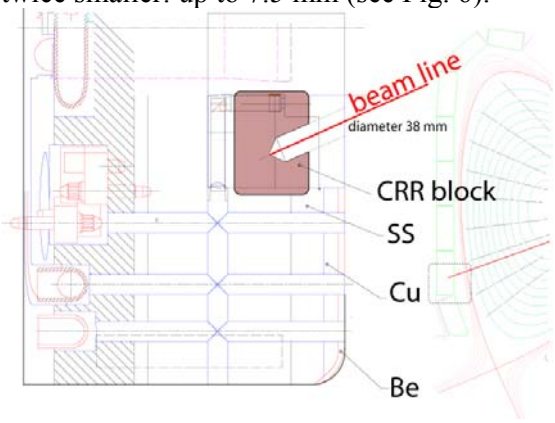

Figure 5: Outline of the retroreflector block incorporated into the blanket shield module. Initially (without the plasma the beam is aimed at the center of the retroreflector.

This gives us much more freedom to cope with beam displacement caused by mechanical vibrations and due to refraction in plasma. Present level of CRR manufacturing could deal with 'ideal' sharp corner to sustain desirable sharpness which is about 5% from the laser beam width.

4. Final remarks

Recently proposed poloidal high power polarimeter will operate at 47.6 μm, 57.2 μm infrared oscillation. The output power of 57.2 μm laser is estimated to be over 1.6W and that of 47.6 μm is about 0.8W. Two color beat signals are simultaneously detected by a Ge:Ga detector with success. It was shown that preferable polarimeter-interferometer configuration will unveil some extra advantages in respect of 'full-polarimetric' system. Shorter wavelength laser will significantly improve (diminish) refraction problems. For present chord alignments and beam wavelength caused considerably small Cotton-Mouton effect. Alternated waveguide transmission line (with miter bends included) showed better focusing and tuning as well as much simple further maintenance, the Cotton-Mouton polarimeter becomes clear only in the case when the viewing chords are orientated in the equatorial plane, where the poloidal component of the magnetic field B_p is zero (pure toroidal polarimetry). Under some plasma condition there is a possibility of coupling Faraday and Cotton-Mouton effects.

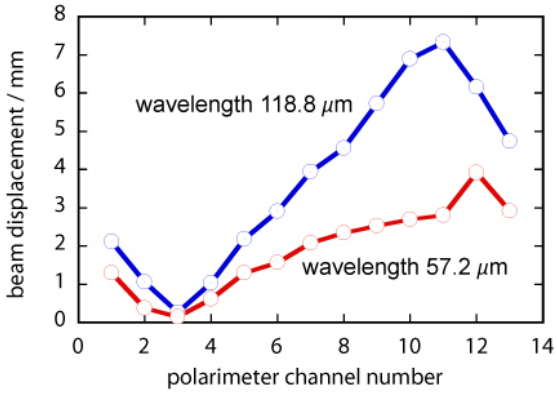

Figure 6: Beam displacement characteristics for the vertical fan of the chords at the position of the center of the correspondent corner retroreflectors.

Small Faraday rotation angle along some central chords suggests that placing additional beam lines must be done to improve spatial resolution of the system. Promotion of the dielectric waveguide addresses the issue of the radiation effect on those components. The appropriate additional 'shielding' of the waveguides studies now under the consideration. Further research is needed to define the most adapted materials for dielectric waveguides for FIR polarimetry.

References

[1] A. J. H. Donné, et.al, Rev. Sci. Instrum., **75**, (2004) 4701.

[2] K. Kawahata, et.al, Rev. Sci. Instrum., **77**, (2006) 10F132.

[3] V. S. Voitsenya, et.al, Rev. Sci. Instrum., **76**, (2005) 083502.

[4] H. Soltwich, Plasma Phys. Control. Fusion, **35**, (1993) 1777.

[5] K. Kawahata, et.al, Rev. Sci. Instrum., **71**, (1999) 707.

A two-dimensional Thomson Scattering Diagnostic on LHD

K. Narihara, I. Yamada, H. Hayashi

National Institute for Fusion Science, 322-6 Oroshi-cho, Toki-shi, 509-5292, Japan

In this paper we show the feasibility of a 2D Thomson scattering diagnostic on the Large Helical Device. Nearly parallel four laser beam paths are set on the plane formed by the currently used laser beam path and the center of the observation window. The distance between the adjacent laser beams, which is limited by the focus depth of the light collection optics, is 5 mm. On a ribbon like region of 15 mm width and length longer than 250 mm, 4 x 19 scattering points are distributed. The four lasers are fired successively every 60 ns. The scattered lights from different laser beams are captured by a common fiber and transported to a polychromator, where they are spectrum-analyzed and detected. The output-signals from the polychromator are fed in parallel to four ADC modules (Lecroy FASTBUS:1885F 96ch, 15bit) gated by pulse signal from the corresponding laser. The maximum time difference among the lasers is 180ns, which is short enough to see a fast MHD phenomenon.

1. Introduction

Time resolved two- and three-dimensional diagnostics is becoming more and more important in fusion plasma experiments [1]. In the case of Thomson scattering diagnostic (TS), a combination of laser beam paths and light collection optics gives arbitrary one-, two- or even three-dimensional *Te* (electron temperature) and *ne* (density) profiles, provided that the necessary number of lasers, collection optics, photo-diodes and ADCs are given. However, because these TS components are expensive, the cost of such a system will be tremendously high. Then, for the design to be realistic, we need ideas to reduce, for example, the number of detectors and ADC or to replace them with something like a CCD. The simplest one is to sweep the laser beam path transversely, with the focusing conditions of the collection optics being synchronously altered [2]. In this case, the plasma should be in a steady state during the sweeping, which is hardly the case for the phenomena of interest. The ASDEX Upgrade group firstly performed a quasi-simultaneous 2D-TS measurement to investigate dynamics of ELM behaviors [3]. They aligned five laser beams along z-direction on a R-z plane with 2.7 mm separation and fired them successively with 0.5 μs interval. Over full time interval of 2μs 'exposure time', the interested profiles are almost frozen. Recently, further advanced idea was proposed and tested in reference [4], in which equally separated five-times-folded beam-path is used for 2D-TS. Digital oscilloscopes sampling at a few GHz can separate the signals scattered from different beam-positions. In this paper, we examine the feasibility of operating a 2D-TS similar to that on the ASDEX Upgrade on LHD.

2. Magnetic field structures of LHD

Cross sectional view of a set of magnetic field lines cut at the toroidal angle $\phi=108^{\circ}$(4O port), where 1D-TS measurement is done, is shown in Fig.1 [5]. The last closed flux surface (LCFS) is defined literally as the outermost flux surface from inside of which no field line leaks outside. Outside LCFS, there is the so-called stochastic region where many magnetic islands overlap. In the further outside, a slender bundle of field lines appears and extends to the wall. Inside the LCFS, there is a nested magnetic surfaces with intrinsic small islands embedded. Although *Te* and *ne* profiles are complex outcomes of heating, fuelling and transport, they, we expect, largely reflect magnetic structures described above. Considering that the present TS data is valid for $ne > 3 \cdot 10^{18}\,\mathrm{m}^{-3}$, we expect that rich structures may be measured around LCFS, the neighborhood of which contains both the nested magnetic flux surfaces and the stochastic region with measurable value of *ne*. Zoomed-in cut-views of magnetic field lines at the inner and outer regions

where we expect some interesting structure to exist are shown together with supposed laser beams for 2D-TS in Fig. 1(b) and (c), respectively.

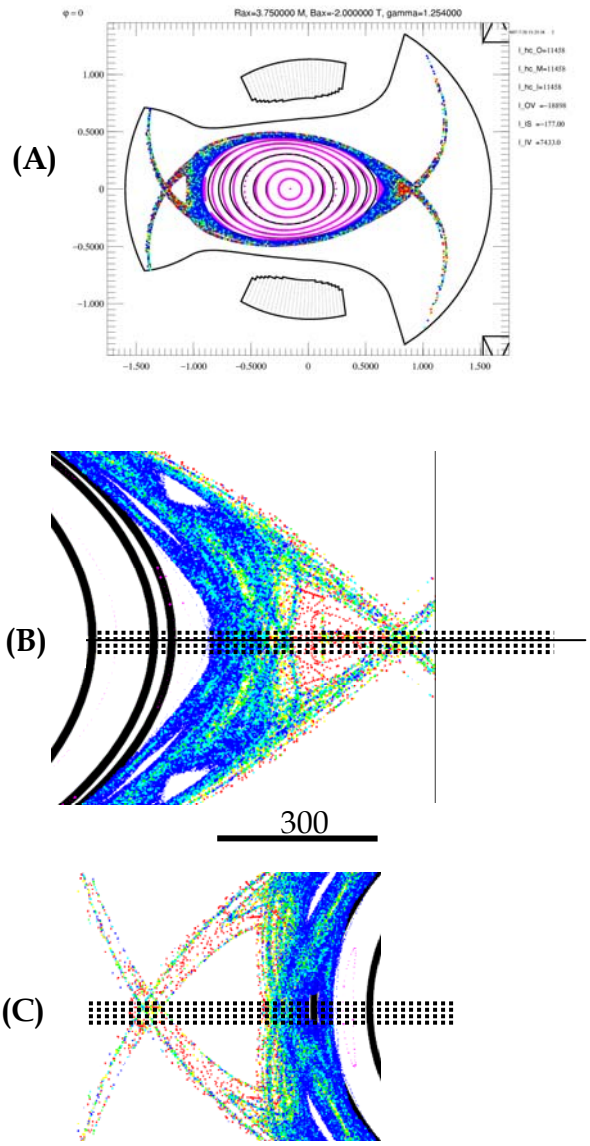

Fig. 1. (A): Cross sectional view of magnetic field lines at the toroidal angle ϕ=108°. Magnetic axis position R_{ax}=3.75 m, γ=1.254, B_q=100%. (B): Zoom-in view around the R=4.5 m, where the LCFS interfaces the inner nested-flux-surfaces with the stochastic region. (C) The same as the above around R= 2.5m. Note that the distance between the adjacent laser beams is not correctly scaled.

3. The 1D LHD Thomson scattering system and extension to 2D-TS

The outstanding features of the LHD-TS [6], shown in Fig.2, are: (1) It adopts a highly back-backscattering configuration; (2) it uses a mosaic mirror for light collection. The image of

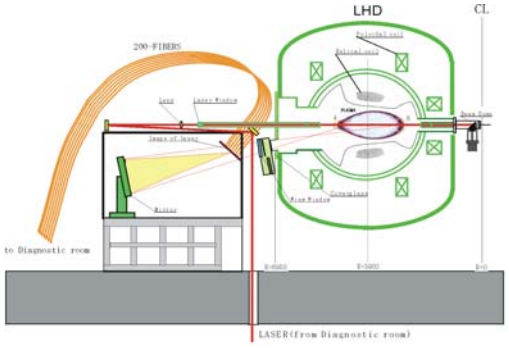

Fig.2. Thomson scattering system on LHD. The laser beam runs along a major radius at ϕ=108°. A large area mirror (1.5m x 1.8m) collects the scattered light onto an array of 200-tip of 2mm-dia optical fibers.

the laser beam (reference beam) that runs along a major radius passing the magnetic axis, is formed onto the end surface of arrayed optical fibers of 2mm in diameter. The tips of the optical fiber are cut at 55° so that they tightly contact to the image. Scattered light collected on a fiber tip is transported to a polychromator, and then divided in five spectra, each of which is detected by an avalanche photodiode and then analog-to-digital converted by charge ADC (Lecroy:1881M). Laser beams from four lasers are steered to run a reference beam path as closely as possible. For this purpose a compact elliptical mirror system was developed [7]. Although, in the present setting, the deviations of the beam paths from the reference path are small enough in the central plasma region, this is not the case in the edge region. This gives us a hint to developing a 2D-TS on the present LHD-TS with small modifications: In the edge region, in which we are now interested, the laser beam paths from different lasers distribute two-dimensionally and yield 2D-TS naturally if we properly set the laser beam directions and discriminate scattering signals from different lasers. In this line of thinking, our first concern is how widely laser-beam-paths can be distributed. This depends on how the efficiency of collecting scattered light drops as the laser beam path departs from the reference beam path. The diameter of blurred image of a point source as a

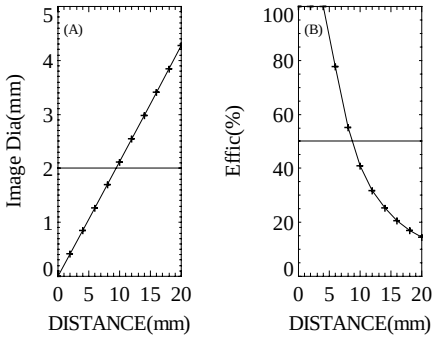

Fig. 3. (A): Diameter of the blurred image of a point source as a function of the deviation from the reference path. (B): The efficiency of collecting light from the blurred image as a function of the deviation from the reference path.

function of the separation ξ from the reference path is shown in Fig. 3(A). If the blurred image size is less than the fiber diameter (2mm), the light collection efficiency is 100%: Otherwise, the efficiency is η= (fiber dia/ blurred image dia)^2. The η as a function of ξ is plotted in Fig. 3(B). Here we assume that the clearly focused image size is 50% of the fiber diameter. Here we permit the loss of light due to blurring down to η=50%, then the laser beam can be located 9 mm apart from the reference path. We would like to make 4 laser beams run in almost equally distributed within ±9 mm from the reference beam path. The parameters to be used for controlling the laser beam are the position (x0) and inclination (x0´) of the beam at the laser exit, and the position of lens and the focal length f_L. The distance between the laser exit and the focusing lens $D_{\text{Laser-Lens}}$=40m. The transverse beam position x as a function of the distance z measured from the lens is given by

$$x(z) = x_0(1-\frac{z}{f_L}) + \left[D_{LASER-LENS}(1-\frac{z}{f_L}) + z \right] x_0'$$

If we tune the first mirror so that $x_0' = -x_0 / D_{\text{Laser-Lens}}$, $x(z) = x_0 / D_{\text{Laser-Lens}}\, z$. The present 'combining' mirror system has x0=±40 mm and ± 20 mm, which gives x(z)= ±1/2000z, and x(z)= ±1/1000z, which are shown in Fig. 4. These laser beam paths are close to the reference path enough to yield intense signals.

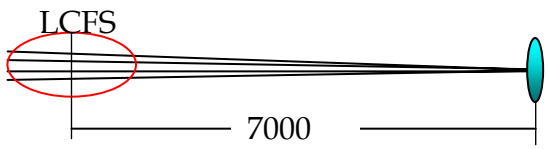

Fig. 4: Laser beam paths. Transverse direction is magnified 150 times.

5. Analog-to-digital converters

As in other modern measurement instruments, analog-to-digital converter (ADC) is one of the key elements. We have two kinds of charge-ADC: 16-1881M (@64ch, total 1024ch, 13bit), 4-1885F (@96ch, total 384ch, 15 bit). The currently operating ADC, 1881M, allows burst mode operation, in which up to 64 events are recorded every 12 μs. If this burst mode is used for the 4-laser 2D-TS, the overall delay time is 36 μs, which is short enough for observing a phenomenon with characteristic frequency less than 30kHz. For observing much higher frequency phenomena, we will use four 1885F ADCs with each gated independently by the delayed pulses generated by the related laser. Ninety-five signals (19*5=95) from 19 polychromators are fed to 4-1885F tightly packed together in parallel, as shown in Fig. 4.

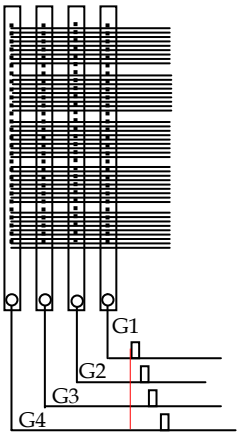

Fig. 4: Wire-connections to four 1885F ADCs. The related laser gates each module.

In considering the pulse width of the laser, the bandwidth of the detector amplifier (30MHz), and the minimum settable gate width of 1885F (50ns), we will fire the lasers every 60 ns. The

resultant overall delay-time of 180 ns is short enough even for MHz phenomena.

6. Discussions

We considered the easiest and most cost-effective way of extending the present 1D-TS to 2D-TS. Three laser beams are added in the depth-direction within the range of focal-depth. A combination of a fiber and polychromator can be used for all channels in depth-direction, thus saving the fibers and polychromators that would be necessary otherwise. The available number of lasers, 4, limits the number of usable channels in depth-direction. If we are satisfied with a slow observation (~ 20 KHz), full channels in R-direction can be used. Otherwise, dedicated ADC gated by each laser is necessary, which for now limits the channel numbers in R-direction to 19. The plane on which the 2D-TS grids lie makes angle 30º with z-axis. Scattering points along R-direction is almost the same as that of the currently used 1D-TS, which covers the region 2.1m<R<5m, while in the other direction ($\hat{z}\cos 30^\circ + \hat{\varsigma}\sin 30^\circ$), scattering points of 4 cover 12-16mm, which depends on the scattering position. Thus the observational domain is very slender ribbon. This 2D-TS may miss a large 2D structures such as islands, but will detect a slender or blob-like structures such as ELM.

In conclusion, we showed that a 2D-TS on narrow ribbon-like region is possible with a small modification on the currently operating 1D-TS on LHD. This will, we hope, capture a blob-like structure that is supposed to occasionally appear in LHD as in tokamaks.

References

[1] *Proc. Time Resolved Two- and Three-Dimensional Plasma Diagnostics, Nagoya, Japan. (International Atomic Energy Agency, Vienna, 1991).*

[2] J.A. Casey, et al., Rev. Sci. Instrum. **63**, 4950 (1992).

[3] B. Kurzan, H.D. Murmann, and J. Neuhauser (ASDEX Upgrade Team) Phy. Rev. Lett. **95**, 145001 (2005).

[4] T. SUMIKAWA, et al. Plasma and Fusion Research: Rapid Comm.**1** 014(2006).

[5] T.Watanabe *et.al*., Nucl. Fusion **46** 291 (2006)

[6] K. Narihara, et al., Rev. Sci. Instrum.72, 1122, (2001).

[7] K. Narihara, et al., Rev. Sci. Instrum.66, 4607 (1995).

Divertor density measurements using mm-wave interferometer in JT-60U

H. Takenaga , N. Oyama , N. Asakura , Y. Sakamoto , S. Sakata

Japan Atomic Energy Agency, 801-1 Mukouyama, Naka, Ibaraki 311-0193, Japan

A mm-wave interferometer has been developed for divertor density measurements in JT-60U. The measurements performed for several plasma phases indicated the feasibility of the system except for the ELMy H-mode phase. In the ELMy H-mode phase, the signal intensity was significantly reduced probably due to refraction. A sharp drop in the divertor plasma density was found during a transition to the ELM free H-mode phase concomitant with a sharp drop in Dα emission intensity. Low frequency fluctuation of ~1.5 kHz was observed in the divertor plasma density during the quiescent H-mode phase. Feedback control of the divertor plasma density was successfully demonstrated using the mm-wave interferometer as a real-time monitor and the gas-puffing from the bottoms of the W-shaped divertor as an actuator.

1. Introduction

One of the most important issues on fusion plasma research is an optimization of divertor plasma performance for effective heat and particle control. Measurements of the divertor plasma density provide precious information to resolve the divertor physics and to control the divertor plasma actively. Several methods have been applied for the measurement of the electron density in the divertor plasma. Reciprocating probes have been installed in the divertor region of several tokamaks [1, 2] together with Langmuir probes mounted on the divertor plates. In the lower DIII-D divertor, a laser Thomson scattering system was also installed [3]. These diagnostics have a high spatial resolution. However, it is difficult to measure transient response of the divertor plasma density such as response during a transition from an L-mode to an H-mode confinement phase. Also, it is difficult to use them as a monitor for the real-time control. On the other hand, interferometer can measure time evolution of the line integrated density, which enables us to study fast response of the divertor plasma density and to demonstrate the real-time feedback control. In the W-shaped divertor of JT-60U, laser diagnostics are not suitable, because it is difficult to pass a laser beam due to its complicated divertor geometry. In contrast, the waveguide system allows flexible access of mm-wave to the divertor plasma. Therefore, a mm-wave interferometer has been developed in JT-60U [4] for measuring the line-integrated electron density in the divertor plasma.

In this paper, we describe the system and the measurement results to show the feasibility of the system. The system is described in section 2 together with other diagnostics used in this paper. The measurement results are presented in section 3, followed by a summary in section 4.

2. System description

JT-60U is a large tokamak device with a major radius of ~3.4 m and an aspect ratio of ~4. A W-shaped divertor has been installed with the divertor pumping from both the inner and outer private flux regions [5].

The waveguide system has been installed in the divertor region as shown in Fig. 1. The sight line passes horizontally near the X-point. A transmitter and receiver unit with a frequency of 183 GHz was employed. A cut-off density of 4.1×10^{20} m^{-3} is higher than the divertor plasma density expected using a 2D fluid divertor code (~$1\text{-}2\times10^{20}$ m^{-3}). The transmitter/receiver was attempted to be unified not by using quasi-optical transmission but by using waveguide transmission. Thus, the *G* band frequency was chosen. The electromagnetic and vibration

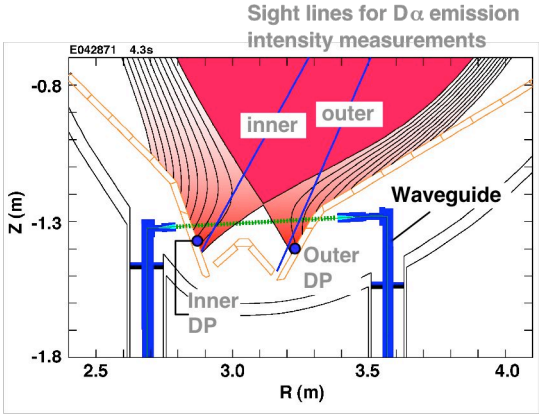

Fig. 1 : Schematic drawing of the waveguide system of the mm-wave interferometer and typical divertor configuration. Slight lines for Dα emission intensity measurements and positions of the divertor probe (DP) used in this paper are also indicated.

analyses results indicated that the phase shift due to the mechanical movement is not a serious problem in the routine plasma discharge. The error due to the mechanical movement was estimated to be about 0.1 fringe, because it is expected that the movement of the antenna in the plasma discharge is one order of magnitude smaller than that during the disruption (~1 mm). Therefore, the vibration compensation using the two different frequencies was not adopted. The waveguide and antenna were made of stainless steel inside the vacuum vessel because of its feasibility against the stress due to thermal expansion and electromagnetic force. The antenna size is 20x16 mm, and the 1.3x1.3 mm square waveguide is basically used around the divertor region owing to flexible use for the transmission in both O and X modes. The X band oversize waveguides made of brass pass through the vertical ports and are connected to windows at about 4 m below the vacuum vessel. The vacuum window was made of sapphire and welded to the waveguide with a metallized ring. Due to the complexity of the transmission line inside the tokamak and the low electrical conduction in stainless steel, the insertion loss is as large as 65 dB.

The source consists of a gun oscillator and a doubler, and produces 15.4 mW. The output of the source is divided into the signal and reference waves by the coupler. The receiver system (RX) comprises radio frequency (RF) unit and intermediate frequency (IF) unit, and a super heterodyne detection is adopted. In the RX-RF unit, the signal and reference waves are mixed with second harmonic wave of the local oscillator with frequency of 91 GHz. The RF frequency of 1.5 GHz is produced. Forward tracking detection is adopted in the IF unit, and IF frequency is selected to be 2 MHz. By suppressing the leak of the reference wave to the signal detection line, the low equivalent input noise of -90 dBm was achieved. S/N ratio of about 20 dB was consequently obtained.

The phase difference between the signal and reference waves with 2 MHz is detected in the fast digital phase detection circuitry with a clock frequency of 200 MHz. For the monitor of feedback control, the analogue phase detector is used. The data is recorded at a sampling time of 1-5 μs.

In Fig. 1, the diagnostics related to this study also indicated. The Dα emission intensities were measured using a fiber array. In the present study, measuring chords covering the inner and outer divertor regions, as shown in Fig. 1, were used. The data was recorded at a sampling time of 5-40 μs. The Dα emission intensity signal from the outer divertor was synchronized with the divertor plasma density signal using the same data acquisition system. Langmuir divertor probes (DPs) placed on the divertor plates near the strike points were used for the measurement of the particle flux to the divertor plates with a high constant voltage of -150 V. The data was recorded at a sampling time of 40 μs.

3. Measurement results

3.1. Measurements in several plasma phases

In order to demonstrate the feasibility of the system, the divertor density measurements were performed in several plasma phases. Figure 2 shows typical waveforms of the discharge with a plasma current of I_p = 1.08 MA at flat top started from t = 3.3 s and a toroidal magnetic field of B_T = 2.7 T. During the limiter phase with the configuration (I) (t = 0-0.8 s), the divertor plasma density was almost zero, and it started to increase when formation of the divertor configuration was started at t = 0.8 s. The Dα emission intensity from the outer divertor also started to increase together with the divertor plasma density. With configuration (II), the divertor plasma density reached its peak value at t = 1.2 s. During the ohmic heating phase with the configuration (III), the divertor plasma density decreased as well as the main plasma density and the Dα emission intensity with a small rate of the gas-puffing from the plasma top. From t = 3.6 s, the gas-puffing rate was increased to get the higher target density for the NB injection. The divertor plasma density increased together with the main plasma density and the Dα emission intensity.

A constant neutral beam (NB) heating power of P_{NB} = 12 MW was applied from t = 4.05 s. The divertor plasma density and the Dα emission intensity largely increased during the L-mode confinement phase. During the transition to the ELM free H-mode confinement phase, a sharp drop of the divertor plasma density was observed together with a sharp drop of the Dα emission intensity, as shown by arrows in Fig. 2. The detailed behavior during the transition is discussed in 3.2.

The divertor plasma density cannot be measured during the ELMy H-mode phase as shown by the hatched region in Fig. 2, because the signal intensity was reduced significantly. Refraction can be considered as a candidate for the physical procedure for reducing the signal.

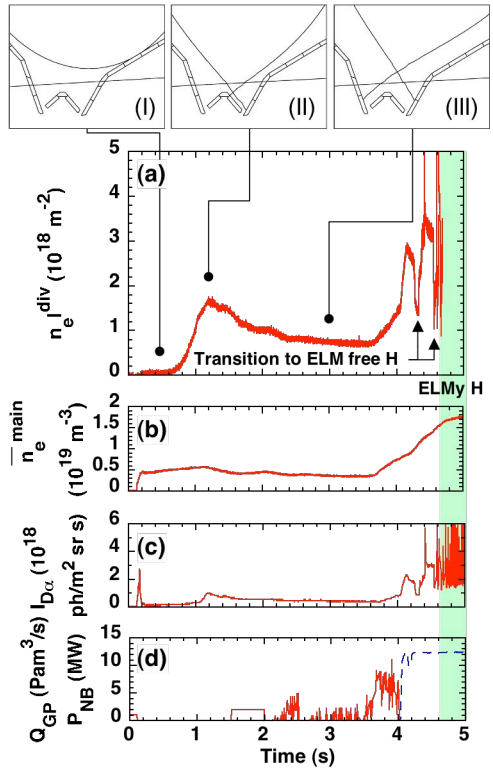

Fig. 2 : Waveforms of (a) line-integrated divertor plasma density, (b) main plasma density, (c) Dα emission intensity from the outer divertor and (d) gas-puffing rate (solid) and NB power (dashed). The hatched region indicates ELMy H-mode phase. Plasma configurations are shown in upper part of the figure.

3.2. Time evolution of the divertor plasma during transition to ELM free H-mode

Figure 3 shows an expanded view of the divertor plasma density during the transition from the L-mode phase to the ELM free H-mode phase (t = 4.545-4.56 s) together with the Dα emission intensities and the absolute value of the ion saturation currents. The Dα emission intensities from the inner and outer divertor regions were simultaneously reduced as shown in Fig. 3 (b). The ion saturation current was also reduced at the same time for the outer divertor region. The ion saturation current for the inner divertor region seems to slightly increase at the immediate start of the reduction of Dα emission intensity. This increase might be related to behavior of non-thermal electron flux to the divertor plate during the transition. The divertor plasma density began to decrease ~0.5 ms after the reduction of the Dα emission intensities on a time scale of ~8 ms. The delayed reduction of divertor plasma density indicated that the reduction of the heat and particle fluxes escaping from the main plasma decreases the divertor plasma density through the change of the recycling and/or the divertor plasma parameters, but it does not decrease the divertor plasma density directly. This transient behavior was reproduced using a 2D fluid divertor code, when the recycling coefficient was assumed to decrease with a decrease in heat flux and increase with a decrease in particle flux [6].

3.3. Fluctuation of divertor plasma density in quiescent H-mode phase

The operation region with small ELMs is attractive due to the reduction of transient heat load to the divertor plates. Quiescent H-mode (QH-mode) [7] is considered to be one of such attractive operation regions. In the QH-mode plasmas, edge harmonic oscillation (EHO) with a base frequency of ~10 kHz has been observed, and EHO is considered to be related with the disappearance of large ELMs.

The time evolution of the divertor plasma density during the QH-mode with EHO was investigated with I_p = 1.0 MA and B_T = 2.6 T. Figure 4 shows (a) Dα emission intensity and (b) the spectrogram of the divertor plasma density. During t = 3.7-4.5 s, the Dα drop was frequently observed, indicating a mixture phase. After t = 4.5 s, stable QH-mode phase was obtained. The fluctuation with a frequency of ~1.5 kHz was fragmentary observed in the divertor plasma density as shown in Fig. 4 (b). This frequency is lower than the base frequency of EHO (~10 kHz in electron temperature). The expanded view (Fig.

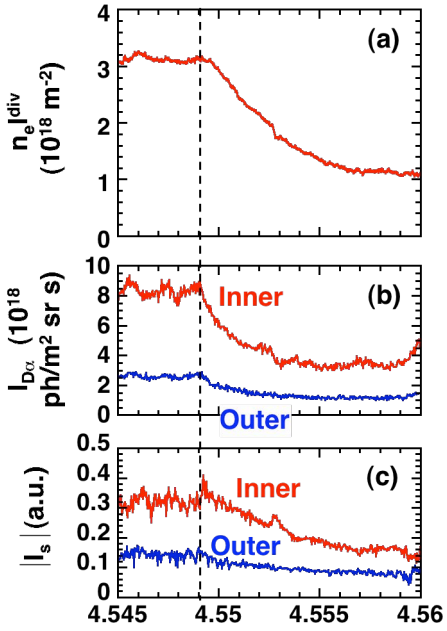

Fig. 3 : Expanded view of (a) line-integrated divertor plasma density, (b) Dα emission intensities and (c) ion saturation currents during the transition to ELMy free H-mode phase.

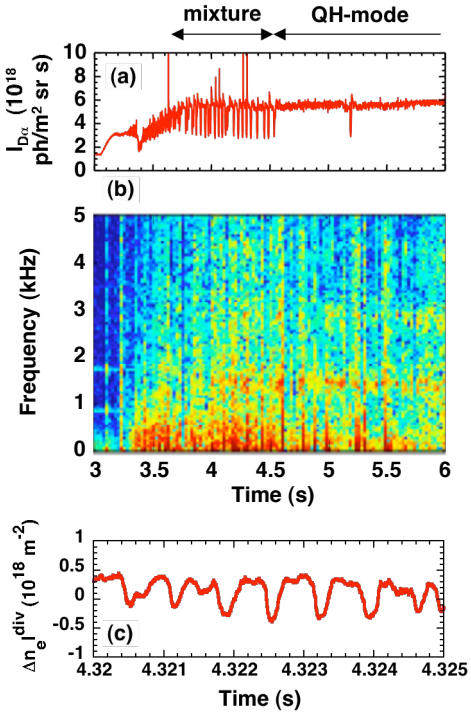

Fig. 4 : (a) Dα emission intensity in the QH-mode discharge. (b) Spectrograph of the divertor plasma density. (c) Expanded view of the divertor plasma density from t = 4.32 s to 4.325 s.

4 (c)) of the divertor plasma density clearly shows the fluctuation. Spikes were also observed in the ion saturation current measured using inner DP with the same frequency. A 2D fluid divertor code indicated that the divertor plasma density slightly decreased with a time scale of ms when a thermal diffusivity was instantly reduced [6]. However, relation to the time evolution of the edge temperature was not found in this discharge. Physical mechanisms for the low frequency fluctuation should be investigated in future.

3.4. Feedback control of divertor plasma density

The mm-wave interferometer can be used for a monitor of feedback control of the divertor plasma density. The divertor gas-puffing rate (Q_{div}) was determined using proportional and differential gains (α_p and α_d) as

$$Q_{div} = \alpha_p(n_el^{sig}-n_el^{ref})+\alpha_d\Delta(n_el^{sig}-n_el^{ref})/\Delta t,$$

where n_el^{sig} is the measured line integrated divertor plasma density and n_el^{ref} is the preprogrammed reference value. The divertor gas-puffing was applied from bottoms of W-shape configuration.

The feedback control of the divertor plasma density was demonstrated in hydrogen OH plasma. Figure 5 shows typical waveforms with $I_p = 1.2$ MA and $B_T = 3.5$ T, where α_p and α_d were set to be 1.5×10^{-13} and 3×10^{-15}, respectively.

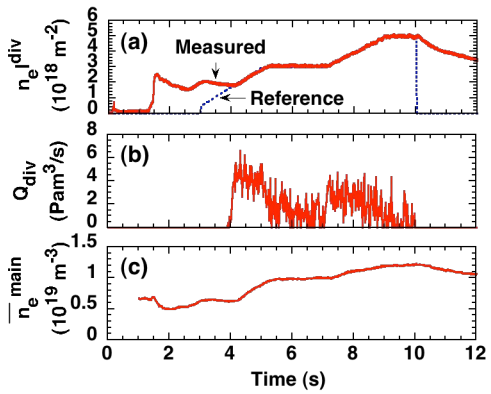

Fig. 5 : Typical waveforms of feedback control for the divertor plasma density : (a) line integrated divertor plasma density for measurement and reference, (b) divertor gas-puffing rate, (c) main plasma density.

The feedback control was applied from $t = 3$ s to 10 s. The reference value was set to be 3×10^{18} m^{-2} during $t = 5$-7 s and 5×10^{18} m^{-2} during $t = 9$-10 s. It can be seen from this figure that the divertor plasma density was well controlled by the feedback control system. The main plasma density was also varied. Control scheme including actuators should be developed for the divertor plasma density control separated from the main plasma density control in future.

4. Summary

The mm-wave interferometer has been developed for divertor density measurements in JT-60U. The system showed its feasibility for the studies on transient response of the divertor plasma against the change of the main plasma edge. The system also indicated its feasibility for active control of the divertor plasma.

Acknowledgement

This work was partly supported by JSPS, Grant-in-Aid for Scientific Research (B) No. 17360447.

References

[1] S. Sakurai et al., J. Nucl. Mater. **266-269**, (1999) 1191.
[2] C.S. Pitcher et al., J. Nucl. Mater. **220-222,** (1995) 213.
[3] D.G. Nilson et al., Fusion Eng. Des. **34-35,** (1997) 609.
[4] H. Takenaga et al., Rev. Sci. Instrum. **69,** (1998) 3181.
[5] H. Takenaga et al., Nucl. Fusion **41,** (2001) 1777.
[6] H. Takenaga et al., Plasma and Fusion Res. **1,** (2006) 046.
[7] N. Oyama et al., Nucl. Fusion **45,** (2005) 871.

Design optimization of microwave reflectometry using Kirchhoff integral

A. Ejiri[1], T. Yamada[2], Y. Adachi[1], O. Watanabe[1], Y. Takase[1]

[1] *The University of Tokyo, Kashiwa 277-8561, Japan*
[2] *Research Institute for Applied Mechanics, Kyushu University, Kasuga 816-8580, Japan*

Effect of fluctuations on microwave reflectometry has been studied, using Kirchhoff integral, under parameterized configuration, including Gaussian launching and receiving beams, and sinusoidal cutoff surface deformation. Analytic expressions for the measured field responses to fluctuations were obtained. It was found that beam waist size, effective curvature of the waves on the cutoff surface, amplitude and wavelength of the fluctuations, and vertical plasma shift affect the linear and nonlinear responses. On the other hand, miss-alignment of the beam axis reduces the measured amplitude, but they do not affect the responses.

1. Introduction

Microwave reflectometry launches microwaves into plasmas, and uses reflection of the microwaves at a cutoff layer in the plasma. Since the phase of the reflected wave is a function of the optical distance, density fluctuations can be derived from the phase fluctuations. Although one-dimensional wave behaviour is well understood, two- or three-dimensional configuration causes complicated diffraction, and the relationship between the fluctuations and the measured complex electric field is not straightforward. In some cases, fringe jumps, phase runaway and nonlinear responses arise from fluctuations [1]. In order to design and construct microwave reflectometer which does not suffer from these effects, it is necessary to understand behaviour of measured complex electric field under generalized configurations.

Since microwave reflectometry is sensitive to local fluctuations near the cutoff, basic features of wave reflection can be described by the Kirchhoff integral on deformed reflection surface. The Kirchhoff integral can describe scalar wave propagation and reflection in vacuum with finite number of discrete optics, including mirrors, lens, antennas and a cutoff layer [2]. This paper presents analytic expressions for measured electric field as a function of configuration parameters. In addition, guidelines for optimizing the design of microwave optics are presented.

2. Analytical expression for measured wave

2.1. Kirchhoff integral

The Kirchhoff integral can be derived from the Helmholtz equation for scalar wave, and Green's theorem. The Kirchhoff integral represents electric field at a specific point as a surface integral of wave field. Figure 1 shows a basic configuration, where wave is launched from a source O and the wave passes through a surface and detected (received) at a point-like detector Q. The field at Q can be written as

$$v(\mathrm{Q}) = -\frac{ik}{4\pi}\int u\frac{e^{ikr}}{r}\left(\frac{\mathbf{k}_1\cdot\mathbf{n}}{k}+\frac{\mathbf{k}_2\cdot\mathbf{n}}{k}\right)dS\,, \qquad (1)$$

where k is the wavenumber of the wave, u is the local field of the launched wave, $\mathbf{k}_1$ and $\mathbf{k}_2$ are launched and received local wavenumber vectors.

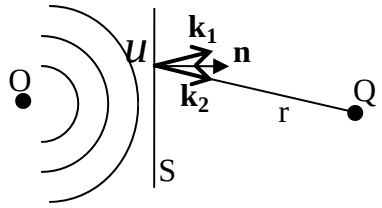

Fig. 1 : Basic configuration of the Kirchhoff integral.

We consider a launching antenna and a receiving antenna instead of the source O and the detector Q. Then the transmitted field is proportional to

$$\frac{1}{2}\int uv\left(\frac{\mathbf{k}_1\cdot\mathbf{n}}{k}+\frac{\mathbf{k}_2\cdot\mathbf{n}}{k}\right)dS\,, \qquad (2)$$

where u and v are local fields of the launching and receiving antenna patterns. More specifically, u is the field emitted from launching antenna, and v is the virtual field when waves are emitted from the receiving antenna. The field can be normalized by the integral

$$\int uu^{*}\left(\frac{\mathbf{k}_1\cdot\mathbf{n}}{k}\right)dS\,. \qquad (3)$$

When we set this integral as one, we can calculate the field transmission efficiency by Eq. (2).

Choosing the cutoff layer as the integration surface and by changing the direction of $\mathbf{k}_1$ to the vector symmetric to the surface, we can calculate the configuration of a reflectometer. Note that $\mathbf{k}_1 \cdot \mathbf{n}$ is replaced by $-\mathbf{k}_1 \cdot \mathbf{n}$ and u is the same.

2.2. Configuration

We consider the configuration shown in Fig. 2. The x, y and z axes correspond to toroidal, vertical and radial axes for the case of a toroidal plasma. Let us define a cutoff surface $z(x,y)$ with curvatures R_x in x-z and R_y in y-z planes. Then, the surface is written as

$$z(x,y) = -\frac{x^2}{2R_x} - \frac{(y-y_s)^2}{2R_y} + \Delta \sin(k_p y + \tilde{\phi}) \quad , \quad (4)$$

here the last term in the R.H.S represents a sinusoidal density fluctuations with wavenumber k_p along y. y_s denotes the vertical shift of the cutoff surface.

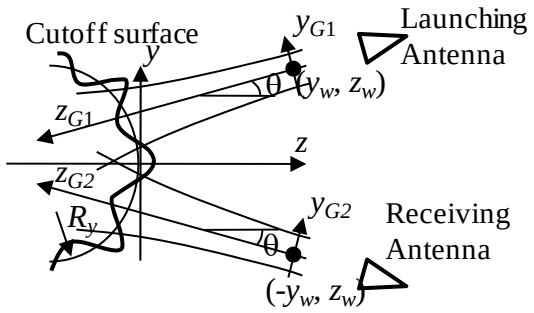

Fig. 2 : Configuration of the cutoff surface, the launching and the receiving antennas.

Launching and receiving waves are represented by a Gaussian beam with the same parameters, except that the position and direction are symmetric with respect to xz-plane. A Gaussian beam field is written as

$$u(x_i, y_{Gi}, z_{Gi}) = \sqrt{\frac{2}{\pi}} \frac{1}{w(z_{Gi})} Exp\left(-\frac{x_i^2 + y_{Gi}^2}{w^2(z_{Gi})} \right) \times Exp\left(ikz_{Gi} + \frac{ik}{2R(z_{Gi})}(x_i^2 + y_{Gi}^2) \right) \quad , (5)$$

where the subscript i denotes a coordinate attached with the launching (i=1) and receiving (i=2) beams. $w(z_{Gi})$, $R(z_{Gi})$ are the waist and curvature of the Gaussian beam. z_{Gi} is the coordinate along the beam axis with the origin $(0, \pm y_w, z_w)$ at the beam waist. y_{Gi} is the perpendicular coordinate. The coordinate transformation from (y, z) to (y_{G1}, z_{G1}) is

$$\begin{aligned} y_{G1} &= -(y_W - y)\cos\theta + (z_W - z)\sin\theta \\ &= y\cos\theta - z\sin\theta - h, \\ \text{where } h &= y_w \cos\theta - z_W \sin\theta. \end{aligned} \quad (5)$$

$$z_{G1} = (y_W - y)\sin\theta + (z_W - z)\cos\theta,$$

where h represents the tangency radius of the Gaussian beam, and it is a measure of miss-alignment of the beam. The coordinate transformation from (y, z) to (y_{G2}, z_{G2}) is

$$\begin{aligned} y_{G2} &= y\cos\theta + z\sin\theta + h, \\ z_{G2} &= (y_w + y)\sin\theta + (z_W - z)\cos\theta. \end{aligned} \quad (6)$$

2.3. Analytic expression

Using these transformations, terms $y_{G1}^2 + y_{G2}^2$, $z_{G1} + z_{G2}$ which are used in later are written as

$$\begin{aligned} y_{G1}^2 + y_{G2}^2 &= 2\left(y^2\cos^2\theta + h^2 + z^2\sin^2\theta + hz\sin\theta\right) \\ &\sim 2\left(y^2\cos^2\theta + h^2\right). \end{aligned} \quad (7)$$

$$\begin{aligned} z_{G1} + z_{G2} &= 2(z_W - z)\cos\theta = 2z_W\cos\theta - 2z\cos\theta \\ &= 2(y_W\sin\theta + z_W\cos\theta) \\ &\quad - 2\cos\theta\left(-\frac{x^2}{2R_x} - \frac{y^2}{2R_y} + \Delta\sin\left(k_p y + \tilde{\phi}\right)\right) \\ &\sim \cos\theta\left(\frac{x^2}{R_x} + \frac{(y-y_S)^2}{R_y} - 2\Delta\sin\left(k_p y + \tilde{\phi}\right)\right), \end{aligned}$$

here $z\sin\theta$ and $2(y\sin\theta + z\cos\theta)$ are neglected, because the former does not change largely on the cutoff surface, and the latter causes a constant phase shift.

Using Eq. (2) with the opposite sign for $\mathbf{k}_1 \cdot \mathbf{n}$ the measured electric field E can be written as

$$E = \iint dxdy u(x,y)v(x,y)\frac{(\mathbf{k}_2 - \mathbf{k}_1)\cdot\mathbf{n}}{2k}\frac{dS}{dxdy}. \quad (8)$$

The launching field u and the receiving field v in this integration are represented by Gaussian beam fields defined by Eq. (5) with coordinate transformation given by Eqs. (6,7). In the following calculation, we assume effective perpendicular extent in xy-plane is small and the fluctuations are small, so that the cutoff surface is nearly perpendicular to z-axis. Then, $dS/dxdy \sim 1$. We also assume $(\mathbf{k}_2 - \mathbf{k}_1)\cdot\mathbf{n}/2k \sim \cos\theta$, which is valid when the beam waists are located far from the cutoff surface. Note that, these assumptions do not

modify the phase of the integrand, and they do not affect the results qualitatively.

The measured electric field E can be rewritten as

$$E = \iint dxdy \cos\theta \frac{2}{\pi} \frac{1}{w(z_{G1})w(z_{G2})} \times Exp\left(-\frac{x^2+y_{G1}^2}{w^2(z_{G1})} - \frac{x^2+y_{G2}^2}{w^2(z_{G2})} \right) \times Exp\left[ik\left(z_{G1}+z_{G2} + \frac{x^2+y_{G1}^2}{2R(z_{G1})} + \frac{x^2+y_{G2}^2}{2R(z_{G2})} \right) \right]. \quad (8)$$

Usually, w and R vary slowly with z_G. In addition, we have assumed fluctuations and perpendicular extent are small as described above. Therefore, we can approximate w and R are constant on the cutoff surface, that is $w(z_{G1}) \sim w(z_{G2}) \sim w$ and $R(z_{G1}) \sim R(z_{G2}) \sim R$. In this case, Eq. (8) can be split into x-integral E_x and y-integral E_y,

$$E_x = \sqrt{\frac{2}{\pi}} \frac{1}{w} \int dx Exp\left[-\frac{2x^2}{w^2} + ikx^2\left(\frac{1}{R} + \frac{\cos\theta}{R_x} \right) \right]$$

$$E_y = \sqrt{\frac{2}{\pi}} \frac{1}{w} e^{-2h^2/w^2 + ikh^2/R} \int \cos\theta dy Exp\left[-\frac{2y^2\cos^2\theta}{w^2} \right] \times Exp\left[ik\left(\frac{y^2\cos^2\theta}{R} + \frac{(y-y_S)^2\cos\theta}{R_y} \right) \right] \times Exp\left[-i2k\Delta\cos\theta\sin(k_p y + \tilde{\phi}) \right] \quad (9)$$

E_x is independent of fluctuation parameters (i.e., $\Delta, k_p, \tilde{\phi}$), and $|E_x|$ approaches one when the curvatures R, R_x become large. Therefore, we consider only E_y. Changing the integration variable from y to $y'=y\cos\theta$, and introducing a corrected (poloidal) wavenumber $k_p' = k_p/\cos\theta$ and corrected fluctuation amplitude $\Delta' = \Delta\cos\theta$, E_y is written as

$$E_y = \sqrt{\frac{2}{\pi}} \frac{1}{w} e^{-2h^2/w^2} \int dy' Exp\left[-\frac{2y'^2}{w^2} \right] \times Exp\left[ik\frac{(y'-y_S')^2}{R_{eff}} - i2k\Delta'\sin(k_p' y' + \tilde{\phi}) \right], \quad (10)$$

here we omit a constant phase shift $kh^2/R + ky_S^2\cos^2\theta/(R + R_y\cos\theta)$. $y_S' = y_S R_{eff}/R_y$ represents the effective vertical shift of the cutoff surface. Curvature $R_{eff} = \left(1/R + 1/R_y\cos\theta\right)^{-1}$ represents the effective wave front curvature along the cutoff surface. R_{eff} can be infinite when we adjust the Gaussian beam curvature to satisfy $R = -R_y\cos\theta$. This condition is termed phase matching condition. h is the miss-alignment of the Gaussian beams, and it varies with the movement of the cutoff surface, and E_y decreases with h.

Equation (10) yields the response of electric field on the fluctuations represented by the phase shift $2k\Delta'\sin(k_p' y' + \tilde{\phi})$. This is expected to be the same as the phase of E_y under an ideal condition. Figure 3 illustrates the integrand in Eq. (10) as a function of y. Gaussian beam width limits the y-extent to ~w, and phase iky^2/R_{eff} causes a rapid phase oscillation at large y. The latter can be represented by $Exp(i2y^2/R_F^2)$, where $R_F = \sqrt{2R_{eff}/k}$ is proportional to the Fresnel zone radius $\sqrt{\pi/2}R_F$. When w is small or R_F is small, integrand around y~0 contribute to the integration. The ideal condition, described by $w << R_F$, $k_p' w << 1$ yields $E_y \sim Exp(-i2\Delta k\cos\theta\sin\tilde{\phi})$, and the phase fluctuation is proportional to the density fluctuation. In this case, the linear phase sensitivity is (defined to be) one. $|E_y|$~1 and amplitude efficiency is one.

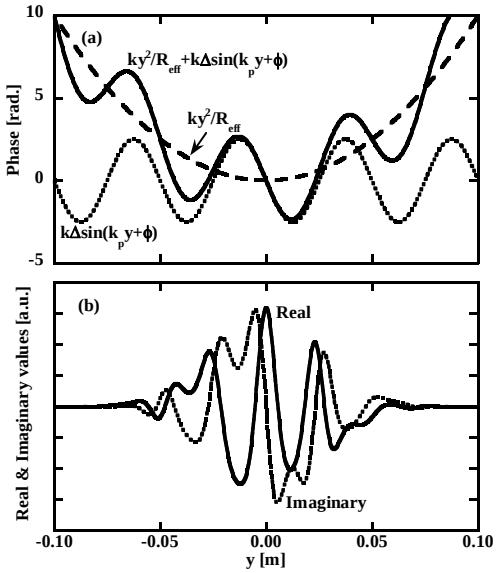

Fig. 3 : Example of integrand in Eq. (10). Figure (a) shows the phase terms, and figure (b) shows the real and the imaginary components. Parameters are k=2π/0.01 m^{-1}, w=0.05 m, R_{eff}=0.1 m, y'_S=0, k'_p=2π/0.05 m^{-1}, Δ=0.002 m.

2.4. Evaluation of response

Here we consider a small fluctuation amplitude case: $k\Delta$<1, and expand E_y in series of $\sin n\tilde{\phi}$,

$\cos n\tilde{\phi}$, where n is integer. Eq. (10) is rewritten as

$$E_y = \sqrt{\frac{2}{\pi}}\frac{e^{-2h^2/w^2}}{w}\int dy Exp\left[-2qy^2 - i\frac{4y_S}{R_F^2}y - \frac{2y_S^2}{R_F^2}\right] \times Exp\left[-i2k\Delta\sin(k_p y + \tilde{\phi})\right] \quad (11)$$

$$= \sqrt{\frac{2}{\pi}}\frac{e^{-2h^2/w^2}e^{i2y_S^2/R_F^2}}{w}\int dy\sum_n J_n(2k\Delta)\times Exp\left(-in\tilde{\phi}\right) \times Exp\left[-2q\left(y + \frac{i}{q}\left(\frac{y_S}{R_F^2} + \frac{nk_p}{4}\right)\right)^2 - \frac{2}{q}\left(\frac{y_S}{R_F^2} + \frac{nk_p}{4}\right)^2\right],$$

where $q = \frac{1}{w^2} - \frac{i}{R_F^2}$,

J_n is the nth order Bessel function. To simplify the expression, y', k'_p are denoted by y, k_p. Performing the integration and removing a phase offset, Eq. (11) is rewritten as

$$E_y = \frac{Exp\left(-\frac{2y_S^2w^2}{w^4+R_F^4} - \frac{2h^2}{w^2}\right)}{\left(1+w^4/R_F^4\right)^{1/4}} \times\sum_n J_n(2k\Delta)Exp\left[-n\sigma - n^2\kappa^2\right] \times Exp\left(-in\tilde{\phi} - in\sigma' - in^2\kappa'^2\right), \quad (12)$$

where $\sigma = \frac{y_S k_p w^2 R_F^2}{w^4+R_F^4}$, $\sigma' = \sigma\frac{w^2}{R_F^2}$

$$\kappa^2 = \frac{k_p^2 w^2 R_F^4}{8\left(w^4+R_F^4\right)}, \quad \kappa'^2 = \kappa^2\frac{w^2}{R_F^2}$$

Miss-alignment h reduces the amplitude, but it does not change the ratio between different orders.

When the fluctuation amplitude is small (i.e., $k\Delta$<<1), higher order terms become small, and analytic formulas can be derived. Summing negative and positive order terms, 0th order and the ratio of higher order terms are

$$E_{y0} = \frac{J_0 Exp\left(-\frac{2y_S^2w^2}{w^4+R_F^4} - \frac{2h^2}{w^2}\right)}{\left(1+w^4/R_F^4\right)^{1/4}},$$

$$\frac{E_{y1}}{E_{y0}} = -\frac{2J_1e^{-\kappa^2}}{J_0}\left(i\sin\tilde{\phi}_1\cosh\sigma + \cos\tilde{\phi}_1\sinh\sigma\right),$$

$$\frac{E_{y2}}{E_{y0}} = \frac{2J_2e^{-4\kappa^2}}{J_0}\left(\cos\tilde{\phi}_2\cosh 2\sigma + i\sin\tilde{\phi}_2\sinh 2\sigma\right), \quad (13)$$

$$\frac{E_{y3}}{E_{y0}} = -\frac{2J_3e^{-9\kappa^2}}{J_0}\left(i\sin\tilde{\phi}_3\cosh 3\sigma + \cos\tilde{\phi}_3\sinh 3\sigma\right).$$

where $\tilde{\phi}_n = n\left(\tilde{\phi} + \sigma'\right) + n^2\kappa'^2$.

Here we discuss two analyses: one is phase analysis, and the other is complex amplitude analysis. We assume that $\sigma << 1$. When we analyze the phase, fringe jumps and phase runaway should be avoided. This is achieved by the condition $|E_{y1}/E_{y0}|$<<1, which is rewritten as $2J_1e^{-\kappa^2}/J_0 \sim 2k\Delta e^{-\kappa^2} << 1$. In this case, the linear phase sensitivity decreases as $J_1e^{-\kappa^2}/J_0 k\Delta \sim e^{-\kappa^2}$, and the third order distortion ratio, representing nonlinear phase response, is $\left|E_{y3}/E_{y1}\right| = J_3e^{-8\kappa^2}/J_1 \sim e^{-8\kappa^2}k^2\Delta^2/6$. Note that the second order does not contribute to the phase. In order to achieve a linear phase sensitivity of around one, κ^2<<1. Two extreme cases satisfy this condition, those are (i) $w << R_F, w << 1/k_p$ and (ii) $R_F << w, R_F << \sqrt{wk_p}$. Case (i) corresponds to a focused beam configuration. More precisely, large R_F is achieved by a phase matching wave front and small w is achieved by a small illuminating spot. Case (ii) corresponds to a divergent beam configuration. Note that 0th order absolute field $|E_{y0}|$ is reduced significantly in the latter case. In addition, $k\Delta$<<1 is require to reduce the nonlinear phase response.

When we analyse the complex amplitude, the first condition $|E_{y1}/E_{y0}|$<<1 is not required. The linear sensitivity is $\sim e^{-\kappa^2}$. The second order distortion $\left|E_{y2}/E_{y1}\right| = J_2e^{-3\kappa^2}/J_1 \sim e^{-3\kappa^2}k\Delta/2$ arises as the nonlinear response. As in the phase analysis case, the conditions κ^2<<1 and $k\Delta$<<1 should be satisfied. Therefore, the same two extreme cases exist also in this complex amplitude analysis.

3. Summary

Effect of fluctuations on microwave reflectometry has been studied, using Kirchhoff integral, under parameterized configuration. Normalized parameters $k\Delta$, $\kappa^2(w,R_F,k_p)$, $\sigma(y_S,w,R_F,k_p)$ affect the linear and nonlinear responses, while h/w only reduces the whole field. Two extreme configurations, those are focused beam and divergent beam configurations, are found to achieve large linear response and small nonlinear response to fluctuations.

References

[1] A. Ejiri, *et al.*, Plasma Phys. Contr. Fusion **39**, (1997) 1963.

[2] T. Yamada, *et al.*, to be published in J. Plasma Fusion Res. SERIES (2007).

Extraction of velocity fluctuations from density dynamics using CO2 laser phase-contrast imaging on LHD

C.A. Michael[1], L. N. Vyacheslavov[2], K. Tanaka[1], A. Sanin[2], K. Kawahata[1], S. Okajima[3]

[1] *National Institute for Fusion Science, 322-6 Oroshi-cho, Toki-shi, 509-5292, Japan*
[2] *Budker institute of Nuclear Physics, Novosibirsk, Russia*
[3] *Chubu University, 1200 Matsumoto-cho, Kasugai-shi, Aichi 487-8501, Japan*

Probing plasmas using electromagnetic radiation allows only direct measurement of density fluctuations; however the deduced phase velocity can deliver information about potential fluctuations, which may reveal dynamics associated with zonal flows (ZF) and possibly the turbulent flux. We consider the use of temporal and spatial wavelet/Fourier cross-correlation techniques for the extraction of edge poloidal velocity fluctuations from a 2D CO_2 laser phase contrast imaging system, having a sightline passing normal to the edge of the plasma, and using an appropriate digital image filtering to localize along the line of sight, and radial velocity dynamics from a 1D phase contrast imaging system, having its sightline tangent to the edge of the plasma. A broad spectrum of poloidal velocity and density fluctuations is found. Because of insufficient spatial resolution, no clear signature of a ZF or geodesic acoustic modes is present in the frequency spectrum of either field. However, a clear negative relationship between density fluctuation amplitude and velocity fluctuation amplitude is found, suggesting turbulence modulation by zonal flows. Radial phase velocity fluctuations are analyzed in an attempt to calculate the turbulent particle flux (product of density and velocity). While the link between the measured "flux" (product of line-integrated density and deduced radial velocity) and line integrated turbulent particle flux is unclear at this stage because of line integration effects, changes of the "flux" are found concomitant with changes in heating power in spite of little change in the density fluctuation level.

1. Introduction

Fluctuation diagnostics probing with electromagnetic radiation have the capability of measuring the properties of density fluctuations. However, in the last decade, attention has been drawn to the turbulent potential field which can reveal structures associated with non-linear processes, such as the inverse cascade, zonal flows and geodesic acoustic modes (GAMs) [1]. Zonal flows have no direct signature in the density field (apart from their interaction, such as through envelope modulation. Such structures are detectible through fluctuation of the poloidal velocity component. Moreover, radial velocity fluctuation characteristics may give further information about the radial flux transport, as well as statistical properties such as intermittency. With sufficient localization, in principle the turbulent particle flux could be determined.

Fluctuation diagnostics intrinsically measure the phase velocity; a strong contribution of the phase velocity comes from ExB flows in the plasma, both consisting of DC part and fluctuating part, which may arise from potential fluctuations at all spatial scales, from gyro-radius scale associated with the turbulence through to macro-scales such as Zonal flow and GAM structures. Treatment of the fluctuating part requires caution that the spatial resolution of the deduced phase velocity fluctuation is at least several times larger than that of the density fluctuations, because by definition, phase velocity can only be measured by identifying wave-like structures. An additional caution is that since the phase velocity has higher statistical confidence with a higher level of density fluctuations, the statistics of the velocity fluctuations are intrinsically biased by those of the density. This will certainly bias any measurement of the (bi)coherence between density and velocity fluctuations. To properly clarify what physical process can be measured with this technique (e.g. zonal flows, turbulent flux), for a given resolution and measurement SNR is beyond the treatment of this proceeding, however, we have started to approach this problem by performing simple 2D non-linear turbulence simulation results using the Hasegawa-Wakatani equation, described briefly in Sec 2b.

The extraction of velocity fluctuations from density dynamics is not a new principle; Doppler reflectometry has been used to demonstrate the existence of GAMS [2]. Moreover, many density diagnostics have the capability of phase velocity determination. By reducing the time window, the fluctuating part of the signal can be determined. A great deal of attention has been given to the algorithms for extracting velocity fluctuations [3,4] from local data such as Beam Emission Spectroscopy and Gas-Puff Imaging; for line integrated data here, similar techniques are used however, in the case of 2D PCI, the additional analysis step of spatial localization is necessary.

The CO2 laser imaging interferometer and 2D PCI system is installed on LHD [5]. The system has a set of sight lines spanning the entire vertically elongated cross-section. For these experiments, the outermost set of chords was converted to a 1D imaging PCI system to be more sensitive to edge line-integrated density fluctuations for R~4.05-4.12. Also, routinely the 2D PCI system also measures line-integrated density dynamics, along a chord passing close to the plasma core (R=3.63m), thereby having contributions from both edges of the plasma as well as the core. For both drift and MHD instabilities with m/n ~ 1, the toroidal wavelength is much longer than the poloidal wavelength owing to the high aspect ratio and number of field periods of LHD (l=10). Additionally, difference in the direction of the field lines on the top and bottom edges of the plasma is large (~80°). Therefore, along a vertical line of sight, contributions from the core and either edge can be separated on the basis of their propagation direction [6,7]. The 2D PCI uses a 6x8 element detector array to simultaneously detect waves propagating in different directions within the image – which can then be mapped to different positions along the line of sight. Spatial resolution of about dρ~1/(10k) where k is in cm^{-1}, and the detectible wavenumber range is between ~1cm^{-1} and 9cm^{-1} [8].

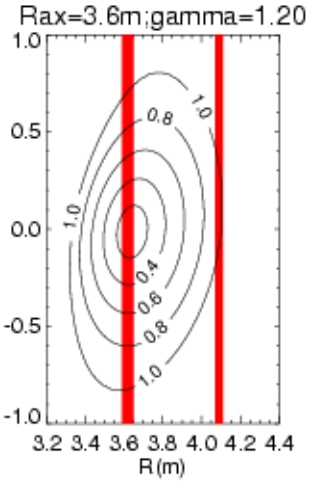

Fig. 1: Sightlines of core 2D PCI and edge 1D PCI relative to flux surfaces

Sight lines are shown in Fig. 1. The line integration effect results in only components of fluctuations propagating perpendicular to the sight line appearing in the signals. For the 2D system, this consists of predominantly poloidal components at the edge and radial components in the core, while for the 1D PCI this is radial components at the edge. The fluctuation amplitude profile extracted from the 2D PCI is peaked around the edge of the plasma as shown in Fig. 3. Therefore, with this combined system, both the radial and poloidal dynamics of edge velocity fluctuations can be diagnosed. For this analysis, different discharges are analysed with either system, however, in the future, it will be possible to analyze these simultaneously.

2. Principle of velocity extraction

Because the beam size and measurable k range is different between the 2D and 1D systems, different analysis techniques have been applied to diagnose velocity fluctuations. In simple terms, a velocity can be measured either by looking at the time delay between wavefronts at fixed locations

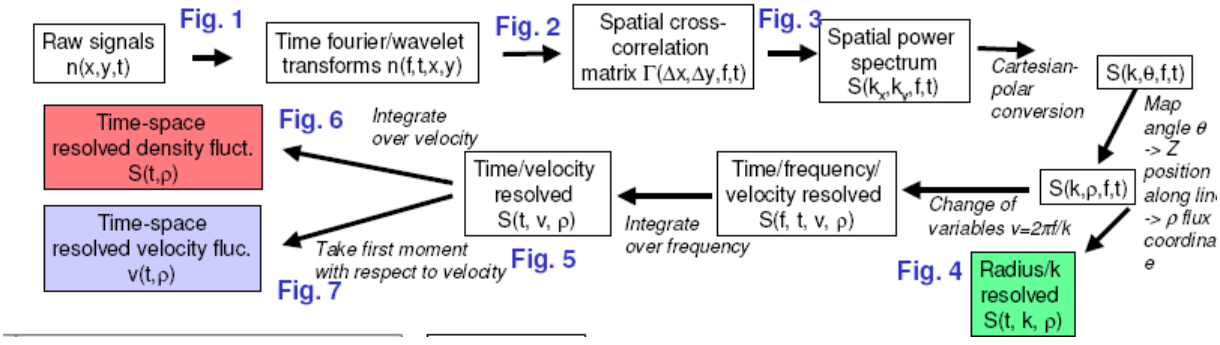

Figure 2: Flowchart for analysis velocity fluctuations from 2D PCI

(time-domain technique) or at the spatial separation between frames with fixed time delay (spatial domain technique). We choose to use a time domain technique for analyzing data from the 2D PCI, because it is a general extension of the analysis technique previously used [8]. For the 1D system, with no spatial localization, a larger number of channels (32) are available in a single direction, and the spacing many times smaller than the peak wavelength, meaning that the spatial propagation can be easily followed. To follow the dynamics of line integrated fluctuations, with only moderate sampling rate (generally ~500kHz), a spatial cross-correleation technique is used. It has been reported [4] that for time domain techniques, very high sampling rate is necessary to follow the fluctuating dynamics. We employ the opposite approach here: to use very high spatial sampling.

(2a) Poloidal Velocity fluctuations from 2D PCI analysis technique

The analysis technique is briefly summarized as a flowchart in Fig. 2. This technique is used for extraction of DC phase velocity. Signals are first pre-processed using the 6th order Morlet wavelet transform to give a time/frequency dependent signal for each channel. (Under conventional analysis, this is done simply using a windowed FFT method). The wavelet technique allows for adaptive time resolution, giving high time resolution for high frequencies, and low time resolution for low frequencies. By forming pairs of channels, the cross-phase and cross-amplitude is calculated, though is not smoothed in time. The cross-correlation is averaged over different pairs of channels with equivalent spatial separation. This generates a 2D cross-correlation matrix, which is then Fourier analysed to determine wave propagation directions, which can be associated with different spatial positions. (When analysing larger time averaging intervals with a fixed time window using FFT-based temporal Fourier transforms, we use a maximum entropy method, to improve the angular (spatial) resolution however, for wavelet analysis here with a large number of time/frequency points, we use a simple FFT-based method for computational simplicity and better statistical stability). Then, mapping k, ω to velocity via v=ω/k, the distribution of velocities can be obtained. A spatial profile of the distribution of velocities, S(ρ,v) (under FFT time and maxent spatial analysis) is shown in Fig. 3. The velocity reverses about the core because of ExB and drift rotation in the lab-frame poloidal electron-diamagnetic direction. The fluctuation power is also strongest towards the edges. The spatial resolution is at best ~ 0.2a (where a is the minor radius), since the strongest amplitude is at lower k, even with the Maximum entropy method. With wavelet time and FFT spatial analysis, the spatial resolution is at least a factor of 2-3 worse ~0.5a. This means at best we can distinguish top and bottom fluctuations only with the present wavelet analysis since bleeding from the edge to the core cannot be separated from intrinsic core

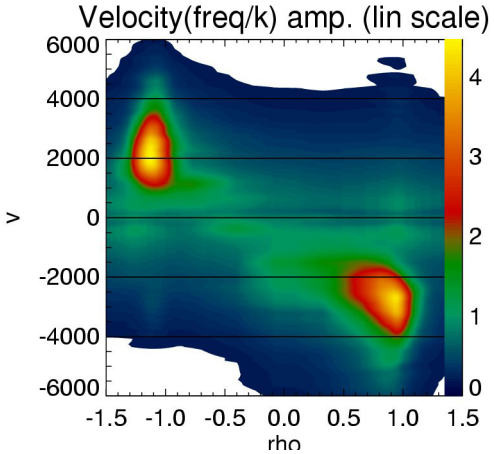

Figure 3: Velocity and spatial distribution of density fluctuation amplitude from Max. Ent. Spatial analysis.

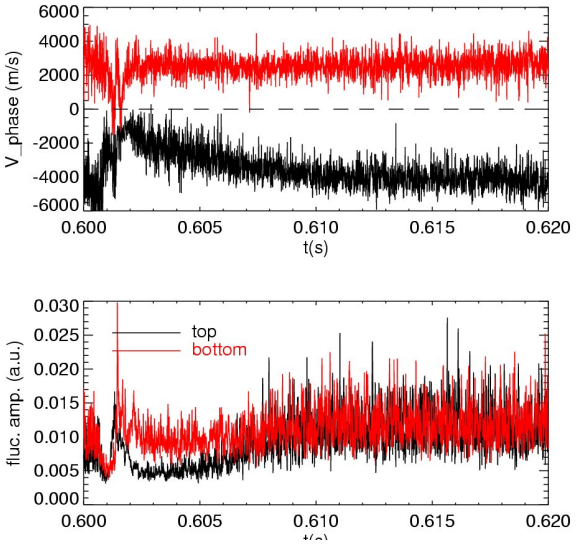

Figure 4: Evolution of top & bottom velocity and density fluctutation amplitude after TESPEL pellet injection at t=0.6s.

fluctuations.

For each spatial position ρ, the first velocity moment is taken as a measure of the average velocity. Finally, for each spatial position (for which we consider only top and bottom of the plasma), the time series $|\tilde{n}(t)|_{env}$ and v(t) are formed; higher frequency components contributing to faster changes by the nature of the wavelet-based temporal analysis at the first step of the analysis. The density fluctuation signal obtained is the envelope, i.e. $|\tilde{n}(t)|_{env}=<\tilde{n}(t)^2+H(\tilde{n}(t))^2>^{1/2}$, where H denotes the Hilbert transform.

A typical time-series of velocities, on both the top and bottom edges of the plasma, are plotted in Fig. 4. At t=0.60 a TESPEL impurity pellet is introduced for a heat pulse experiment [9]. A corresponding change in velocity and density can

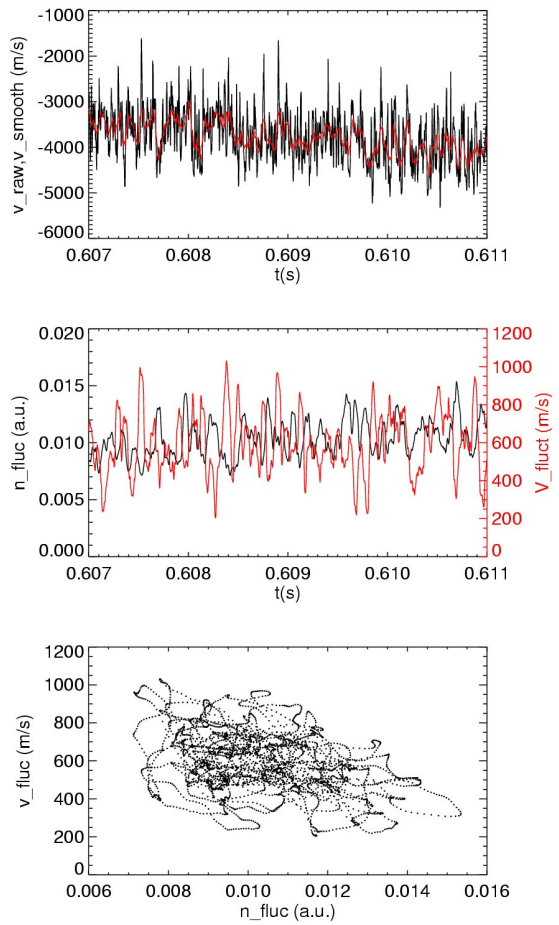

Figure 5: (a) time series of raw velocity and smoothed velocity; (b) time series of fluctuating component of velocity compared with density fluctuation amplitude; (c) link between density and velocity fluctuations

be observed. In this discharge, a core temperature rise is observed which cannot be explained by a diffusive or even local transport model. Therefore, it is hypothesized that the action of inverse cascade and zonal flow/GAM activity may be important for this phenomenon.

The FFT based spectrum of velocity fluctuations shows no clear peaks and has a broad spectrum (~200kHz bandwidth) similar to that of the spectrum of density fluctuations. However, both the density and the velocity fluctuations exhibit strong burst-like intermittency. There is no clear characteristic frequency of bursting, since the frequency spectrum is very broad, but there seems to be a link between the phase velocity and the density fluctuation level. To compare density and velocity fluctuation amplitude, firstly a smoothed velocity time trace is calculated $v_{smooth}(t)=<v(t)>_\tau$, where τ is the averaging time. The fluctuating component is then associated with $v_{fluc}(t)=v(t)-v_{smooth}(t)$, and an rms is taken $v_{fluc,sm}^2(t)=<v_{fluc}^2(t) + H(v_{fluc}(t))^2>_\tau$. Time traces of v(t) and $v_{smooth}(t)$ are plotted in Fig. 5a. A smoothing window of τ=50μs is used, however the results do not depend strongly on the value used. From this, $v_{fluc,sm}(t)$ is extracted and plotted in Fig. 5b, on the right hand axis. This is compared with the density fluctuation level (averaged) $<|n_{env}(t)|>_\tau$ on the left axis in the same graph. Immediately it is striking that there is a noticeable degree of anti-correlation between density and velocity fluctuations. An anti-correlation between drift-wave energy and zonal flow energy is at the basic idea behind fluctuation mitigation by zonal flows, and has been observed, e.g. [10]. To show this anti-correlation more clearly, $|\tilde{n}(t)|_{env}$ is plotted against $v_{fluc,sm}(t)$ in Fig. 5c. The curve clearly has a negative slope, with high $|\tilde{n}(t)|_{env}$

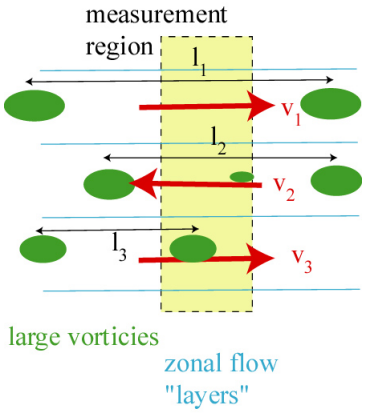

Figure 6: illustration of line-integration effects on velocity fluctuations

corresponding to low $v_{fluc,sm}$. At low $|\tilde{n}(t)|_{env}$, a the distribution of $v_{fluc,sm}$ is broader, however the statistical distribution clearly favours higher $v_{fluc,sm}$.

The contribution to the quantitity $v_{fluc,sm}$ due to the self generated ExB field of the measured fluctutations (with $k\sim2cm^{-1}$) is likely to be small, since only velocity fluctuations of larger scale structures can be diagnosed. The velocity fluctuations therefore would correspond to structures with $k<k_{min}/2\sim0.5cm^{-1}$, which may include zonal flow activity.

Zonal flows are known to have a radial wave/correlation length of the order of several cm, and oscillate in space and in time at low frequency (DC up to a few kHz) [1]. However, here, these velocity fluctuations persist up to high frequencies characteristic of the drift-wave turbulence. However, this is not inconsistent with the action of zonal flows; since the statistics of density fluctuations, combined the limited spatial resolution (~0.6m compared with the ZF structure of 2cm), imply that the temporal dynamics of the zonal flows themselves are not detectible. This illustrated in Fig 6, showing the line-integrated region passing through many layers whose flow velocity (relative to the steady-state ExB rotation) has opposite sign in each layer. As vortices pass through the line of sight, they contribute a velocity characteristic of the layer which they are in. However, since the integrated signal consists of vortices from all layers, and the drift-wave timescale ($l_{1,2,3}/v_{1,2,3}$ as defined in Fig. 6) is much shorter than the ZF correlation time, the determined velocity may take on the value from any layer (e.g. v_1,v_2,v_3), including positive or negative sign. This means that $v_{fluc,sm}(t)$ will have an amplitude characteristic of the spatially averaged ZF, but the time dynamics will be determined by the density fluctuations (lifetime and poloidal rotation velocity and wavelength).

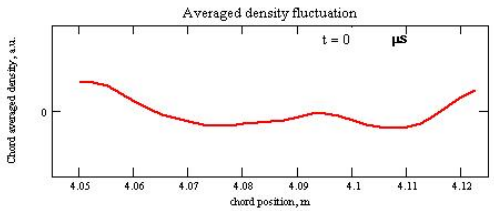

Figure 7: Single time-snapshot of edge 1D fluctuation image

(2b) Radial velocity fluctuations from a 1D PCI analysis technique

A spatial cross-correlation technique is used to compare 1D fluctuation images in successive frames. The difference between frames can deliver the propagation velocity via cross-correlation techniques. The spatial signal for a fixed time is plotted in Fig 7. The spectrum is dominated by lower k components. The evolution between successive frames motivates the use of a cross-correlation technique for identifying a propagation direction and dispacement, which can give the velocity directly via $v=\Delta x/\Delta t$.

The motivation for the analysis is to extract density N(t), velocity v(t) and $\Gamma(t)=<N(t)\ v(t)>$. Because of strong oscillation, the average value of gamma to the rms value is of the order of 1%, and it does show a dynamic change associated with changes in heating power, as shown in Fig 8.

To relate the determined value of Γ to the

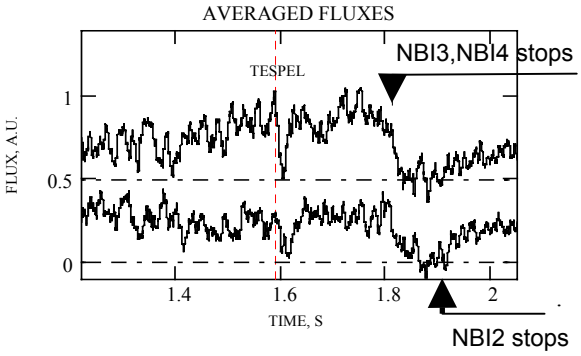

Fig 8: Particle flux $\overline{\Gamma}a$ calculated from measurements on high β discharges #74926 (upper trace) and #74937 (lower trace)

anomalous flux, it is necessary to consider how line integration effects the signal. To pursue this, we have performed simple non-linear 2 dimensional turbulence simulations using the Haswegawa-Wakatani equations [11] using an approach similar to [12]. The simulation evolves self-consistently the density and potential (vorticity) fields based on resistive drift wave equations. Although the model is simplified, it does include the non-linear ExB term, which is responsible for the dynamical evolution of turbulence and turbulent particle flux. Though more advanced models may include more effects

(which may produce inward flux for example), only the ExB non-linearity is necessary to understand this diagnostic technique. Simulation results show that, due to particle flux, positive density fluctuations move outward and negative density fluctuations move inwards (in response to a prescribed negative density gradient). This is the motivation for associating the determined Γ with the anomalous flux, since this method essentially looks at the motion of such structures. However, the flux calculated from line integral measurements can be inward or outward, whereas the line integrated local flux is always strictly outwards owing to poloidal phase separation between density and potential due to gradient drive. This suggests that line-integration erases some of the local dynamics (ExB rotation around vortices) which are essential for producing anomalous flux. Further work is necessary to make a more rigorous physical interpretation.

Nevertheless, the changes in the mean value of Γ are relevant to changes in turbulent properties. The PDF of Gamma also has highly non-Gaussian wings associated with strong intermittency, as shown in Fig 9.

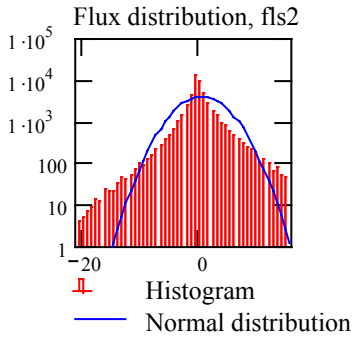

Figure 9: PDF of "flux "calculated from line integrated density and its velocity

.

3. Conclusions

Analysis of velocity fluctuations from density dynamics has revealed oscillating poloidal velocity, which appears to regulate the density fluctuation level. Further checking of the instrumental effects relating to this trend are necessary to show that this is not an instrumental artifact, however, this is unlikely.

Analysis of the radial flux has revealed interesting dynamics. Further theoretical modelling is necessary to ascertain what physical conclusions can be obtained.

[1] P. Diamond et al., PoP 13, 055502 (2006)
[2] G.D. Conway et al., PPCF 47, 1165 (2005)
[3] T. Munstat et al., RSI 77, 103501 (2006)
[4] M. Jakubowski et al., RSI 70, 874 (1999)
[5] T. Akiyama et al., RSI 74, 1638 (2003)
[6] A. Sanin et al, RSI 75, 3439 (2004)
[7] L. Vyacheslavov, IEEE trans. Plas. 33, 464 (2005)
[8] C.A. Michael et al., RSI, 77, 10E923 (2006)
[9] N. Tamura et al., Nuc. Fus. 47, 449 (2007)
[10] T. Ido et al., Nuc. Fus. 46, 512 (2006)
[11] Hasegawa and Watatani, PRL 50, 682 (1983)
[12] R. Numata et al. in "Frontiers in Turbulence and Coherent Structures" [Proceedings of the COSNet/CSIRO Workshop] (World Scientific, 2007, eds. J.P. Denier and J.S. Frederiksen), pp. 431-442, (http://www.arxiv.org/abs/physics/0703274)

High Resolution Thomson Scattering diagnostic for JET

M. Kempenaars[1], A. Alfier[2], M. Beurskens[1], E. Giovanozzi[3], C. McKenna[1], R. Pasqualotto[2], M. Walsh[1] and JET-EFDA contributors*

[1] *EURATOM/UKAEA Fusion Association, Culham Science Centre, Abingdon, Oxon, OX14 3DB, UK*
[2] *Associazione EURATOM-ENEA sulla Fusione, Consorzio RFX Padova, Italy*
[3] *Associazione Euratom-ENEA, ENEA Centro Ricerche Frascati C.P. 65, 00044 Italy*
* *Appendix of M. Watkins et al., Fusion Energy 2006 (Proc. 21st Int. Conf. Chengdu, 2006) IAEA, Vienna (2006)*

The new High Resolution Thomson scattering system entered its operational phase during the 2006 and 2007 JET experimental campaigns. The system measures electron Temperature and Density along the full outboard chord covering both the core and pedestal plasma region with a spatial resolution of up to 1.5cm ($\Delta r/a$=1.5%). The system's performance is illustrated with a demonstration of raw data, first profile measurements and examples of the capabilities of this powerful new diagnostic.

1. High Resolution Thomson Scattering at JET

During the large EP1 shutdown at JET many new diagnostics were installed, including a High Resolution Thomson Scattering (HRTS) system [1] and [2], this new system is based on a conventional 90° scattering geometry, see figure 1. HRTS is the first conventional Thomson Scattering system on JET since the installation of the Core LIDAR system in 1986. It is designed to measure electron temperature and density profiles at 63 points along the outer radius (R = 2.9-3.9 m) close to the equatorial plane of the machine ($Z \approx +0.1$m). The laser system is a commercial Nd:YAG laser, which produces a dual output of 15ns, 20Hz pulses of 3J each, 6J total. This determines the sampling rate of 20Hz. The collection system is made out of 21 interference filter polychromators with Avalanche Photodiodes; in the design specifications each polychromator would be fed by three delay lines, which accounts for the 63 spatial points. The polychromators are divided into two groups, a set of seven with filters suitable for low T_e (50eV – 5keV) and the rest for high T_e (0.5 – 20keV): they are respectively used for edge ($R > 3.6$m, $r/a < 0.6$) and core region ($R < 3.6$m, $r/a > 0.6$). Simulations have predicted that T_e profiles can be measured with an accuracy better than 15% at $n_e = 1 \cdot 10^{19} m^{-3}$. Measurements of Raman scattering in N_2 have been used for density calibration, spectral calibrations have been performed by illuminating each collection fibre and stepping through the wavelengths.

During the last JET campaign the system was still in a commissioning phase, which meant it was limited to firing a maximum of 1 second, i.e. 20 laser pulses, during a JET pulse, corresponding to a maximum of 20 HRTS profiles per JET pulse. A reduced number of delay lines meant that the system had 37 spatial points with a spatial resolution of about 45mm in the core, 25mm close the edge, and 15mm in the pedestal region. However, since in most plasma configurations the axis is above the equatorial plane, the effective resolution in the centre after mapping on to the midplane is better then 25mm due to flux surface expansion, but this does vary from JET pulse to JET pulse.

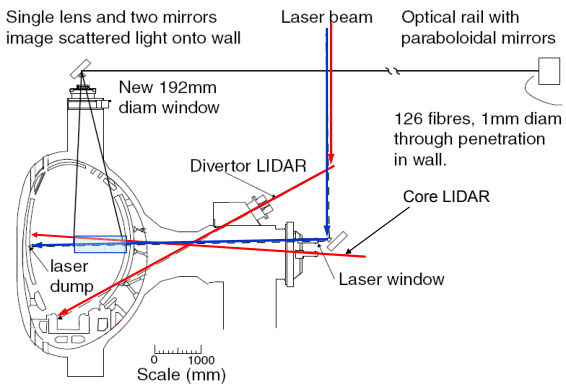

Figure 1: Layout of the JET HRTS system beam path (blue). In red the JET core (horizontal) and edge LIDAR (diagonal) Thomson scattering systems are indicated.

2. Demonstration of raw signal

The first measurements with the system were performed in October 2005, and the initial results showed a good signal to noise ratio promising a good diagnostic capability. Some improvements were made over time to reduce the amount of stray light produced by various sources; a) The laser power density on the machine inner wall was high enough to create a laser induced plasma on the stainless steel, knife edge blade, beam dump, this light is a broad band light source which can be seen on several channels and lasts for many nanoseconds. This was reduced by vertically enlarging the laser beam to reduce the power density to below the ablation threshold of the beam dump and to not affect the spatial resolution and collected light level. b) The lay-out of all spectrometers was improved so that the channel closest to the laser wavelength became the last channel and the angle of the filter was adjusted to improve rejection. And c) Because of the lay-out of the system in the JET Torus Hall, the laser beam passes in between the collection optics on the machine and the collection optics on the Torus Hall wall. This produces a Raman scattering from the air in the Torus Hall that is visible in a few spectrometers. This signal is at a different time to the actual Thomson Scattering signal. Because this signal is highly reproducible and only depends on the laser energy and air pressure it can be used as a laser energy monitor. All the mentioned adjustments result in an improvement in raw signal trace as shown in figure 2 and figure 3. The order of the channels has been swapped between figure 2 and 3 because of step b) mentioned above.

This setup was used for the rest of the experimental campaigns in 2006 and 2007, C15-C19. Several of the diagnostics at JET can measure similar plasma properties, which makes it possible to compare and, if needed, cross calibrate diagnostics. The diagnostics the HRTS system can be compared to for electron density are the Core LIDAR and Edge LIDAR systems, see figure 4, and for the electron temperature measurements the ECE systems can be added to this, see figure 5. These graphs show that the HRTS measurements match the measurements from the ECE and two LIDAR systems very well.

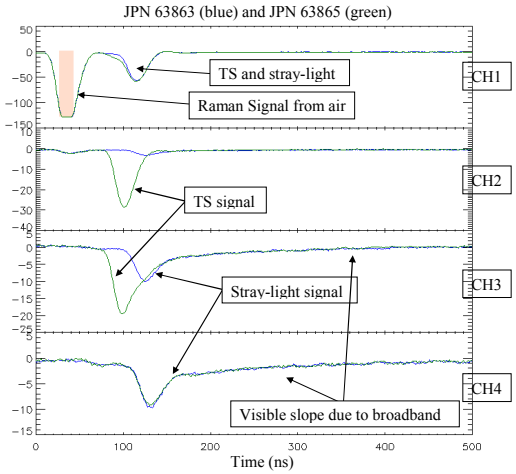

Figure 2: The signals before the improvements mentioned in paragraph 2, showing the long tail of the broadband light produced by the laser induced plasma, blue line is in empty vessel, green line is with plasma

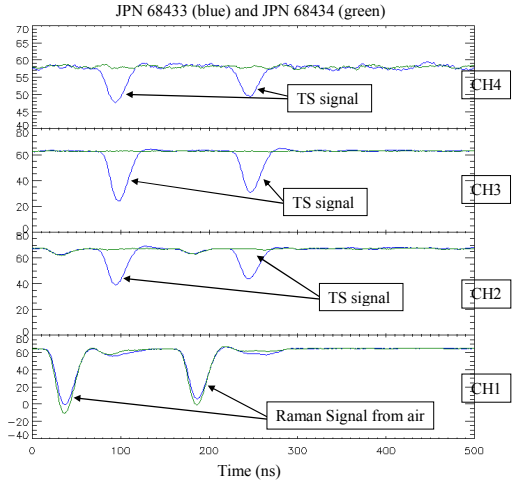

Figure 3: The signals as they are after the improvements, still showing the Raman from air, but clearly the white light from the beam dump has disappeared. Green line is in empty vessel, blue is in plasma

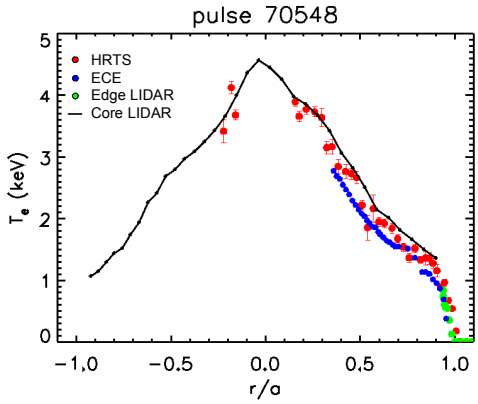

Figure 4: JET electron temperature profiles, showing the comparison between HRTS, ECE, Edge LIDAR and Core LIDAR

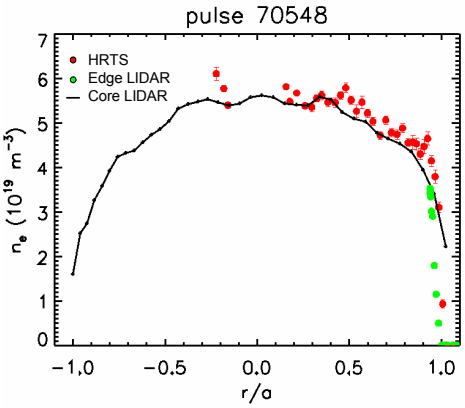

Figure 5: JET electron density profiles, showing the comparison between HRTS, Edge LIDAR and Core LIDAR

3. Examples of recently obtained results

3.1 Error Field Correction Experiments

A new JET scenario was tested, during which external magnetic perturbation (edge ergodisation) fields were applied to the plasma, in order to mitigate large type-I ELMs [3] and [4] in H-mode plasmas. Four ex-vessel error field correction coils (EFCC) have been placed around the JET machine each at 90º angles to each other. By applying currents to pairs of coils different phases of perturbation can be achieved. Figure 6 shows the result of such an EFCC experiment on the ELM size and frequency.

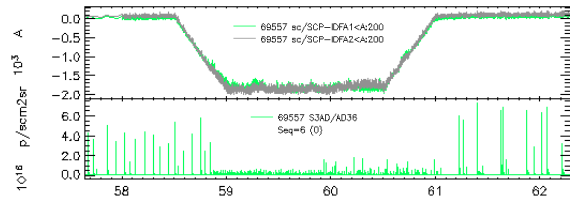

Figure 6: In the top graph the EFCC is displayed, while the bottom graph shows the effect on the ELM size.

Figure 7 show the effect this perturbation field has on the plasma edge as measured by the HRTS system. Because these fields are machine area (octant) dependant it does matter in which section of the machine the diagnostics is located, in our case the HRTS system is at Octant 5. The system takes measurements at 20Hz and that these measurements are taken as the perturbation field is applied. In figure 7, it is clearly visible how the field moves the plasma pedestal inwards by as much as 3cm, it also reduces the pressure by up to 30%. Linear ELM theory [5] predicts that ELM mitigation correlates to an edge pressure gradient reduction, due to a reduced height and an increased width of the edge pressure transport barrier. Measurements like this shows this correlation and is only possible with a high rep-rate, high spatial resolution diagnostic like the HRTS system. The examples shown here are by no means a detailed analysis of the EFCC experiment, but merely serve to show the capabilities of the HRTS diagnostic system.

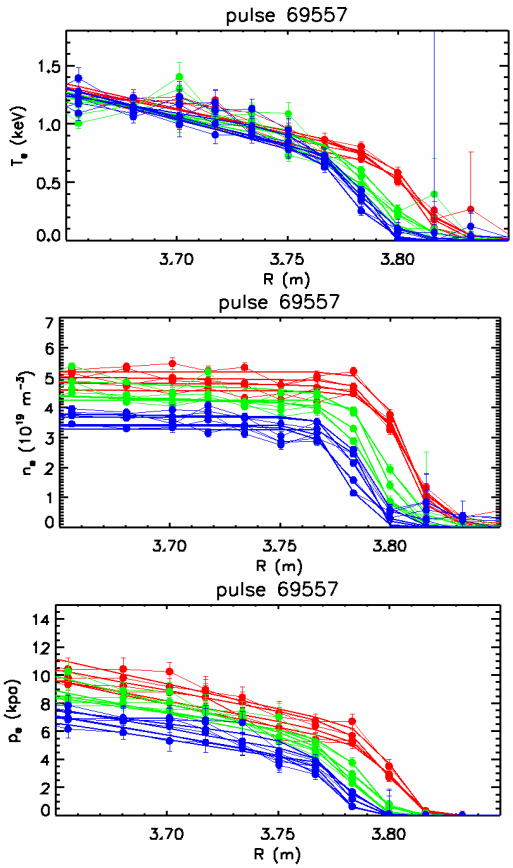

Figure 7: Electron Temperature at the top, Electron Density in the middle and Electron Pressure at the bottom. For an EFCC of 45º. Red is before EFCC, green is during the ramp and blue when it is fully on.

3.2 Filamentation of the plasma edge

Something previously observed at other fusion machines, first on MAST [6], [7], [8] and later on ASDEX-Upgrade [9], [10], is a phenomenon called ELM filamentation. At JET, this phenomenon has never been directly observed, only the result of filaments hitting the vessel wall was seen by the Infra Red camera diagnostics in 2006. Using the HRTS an effort was made to try to measure this phenomenon [4] and to try to measure their size and energy content, which is highly relevant when scaling to ITER.

Using the HRTS 20Hz capability, a picture of the ELM behaviour was built up over several laser pulses during a JET discharge. ELMs have been hit by a laser pulse during different phases of their life. Figure 8 shows just such a JET pulse, where the HRTS coincides with two ELMs.

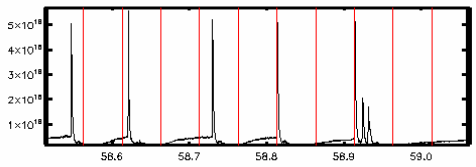

Figure 8: Shows a typical section of a Type-I ELM Dα trace of a JET pulse. The red vertical lines are to indicate when the HRTS made a measurement.

Two of these measurements occured during the first 100μs of the onset of the ELM. Figure 9 shows the electron Density as measured by HRTS for 4 of the measurements of this plasma.

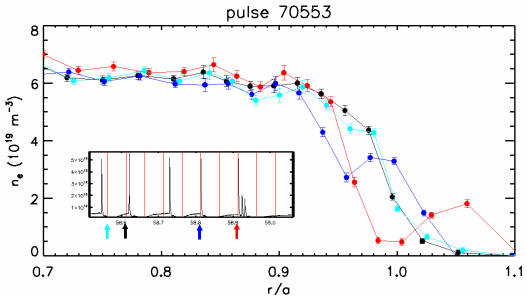

Figure 9: The turquoise line shows the pedestal region just after an ELM, see inset. The black line represents the pedestal just before an ELM, the dark blue and the red lines show the ELM filament during different phases.

As can be seen in figure 9, the ELM filament detaches from the plasma and then moves outward. In figure 10 it can clearly be seen that the signal arrives at the detectors at exactly the right time for a Thomson Scattering signal and it is very clearly distinguishable from the background noise signal.

During the following campaigns more measurements like these will be performed and the statistics will be improved.

5. Conclusions

During the last campaigns, C15-C19, the new HRTS diagnostic at JET has shown to be powerful tool for measurement and analysis of fusion scenarios. It has shown to measure plasma edge parameters down to and accuracy of 1.5cm with error bars smaller than 15% for T_e and 10% for n_e. The system is expected to become fully operational during the next JET campaign.

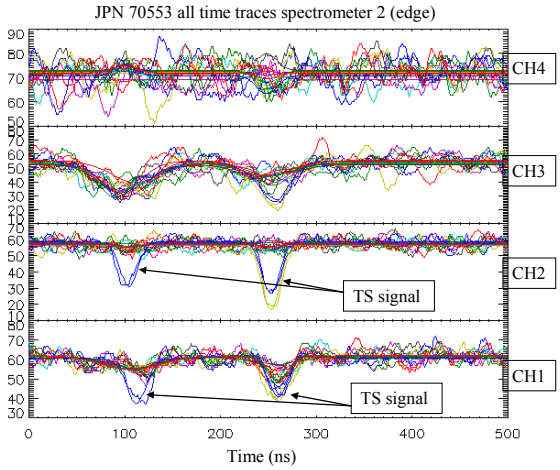

Figure 10: This figure displays the raw data for the ELM filament measurements, clearly showing the signals and the fit to the raw data.

6. Acknowledgements

The authors would like to acknowledge the major contributions of Per Nielsen and Chris Gowers, without whom this system would not have been what it is today.

References

[1] R.Pasqualotto et al., Rev. Sci. Instrum., **75** 3891 (2004)

[2] R.Pasqualotto, et al., Laser-Aided Plasma Diagnostics, Snowbird, Utah, USA, 26th September 2005

[3] Y.Liang at al, Phys. Rev. Lett. **98** (2007) 265004

[4] M.Beurskens, et al.,Joint Pedestal/SOL ITPA Meeting, Garching, Germany 7–10 May 2007

[5] J.W. Connor, Plasma Phys. Control. Fusion **40**, 531 (1998)

[6] E.R. Arends, Density gradients in spherical tokamak plasmas (Ph.D. thesis), Eindhoven University of Technology, The Netherlands (2003)

[7] A.Kirk et al., 2004 PRL **92** 245002-1

[8] R.Scannell et al., Plasma Phys. Control. Fusion **49** (2007) 1431–1446

[9] T.Eich et al, Plasma Phys. Control. Fusion **47** (2005) 815-842

[10] B.Kurzan et al., 2005, Phys. Rev. Lett. **95** 145001

Development of IF system for ECE radiometer on KSTAR tokamak

Y. Kogi[1], T. Sakoda[1], A. Mase[1], S. Yamaguchi[2], Y. Nagayama[2], and K. Kawahata[2]

[1]*Art, Science and Technology Center for Cooperative Research, Kyushu University, 6-1 Kasuga-koen, Kasuga-shi, Fukuoka, 816-8580, Japan*
[2]*National Institute for Fusion Science, 322-6 Oroshi-cho, Toki-shi,509-5292, Japan*

We have developed ECE radiometer system for KSTAR plasma. In this paper, we describe mainly the IF system development utilized in the radiometer. We have constructed the down conversion module by using commercial components, and confirmed that the module is satisfied with required performances. The detector module has been able to constructed on the compact substrate by using MIC technology.

1. Introduction of ECE radiometer system on KSTAR

Electron cyclotron emission (ECE) radiometer is an essential diagnostics that is widely utilized in the fusion experimental devices [1-3]. Amplitude of ECE from optically thick plasma can be treated as black body radiation, ECE radiometer is able to measure electron temperature and its fluctuations. Frequency of ECE is proportional to the magnetic field strength, radial temperature distribution can be measured by resolving frequency component of ECE and its harmonics. In the recent study, this diagnostics has been expanded to not only radial resolved measurement but also poloidal resolved measurement by utilizing ECE detector array [4-6]. This study and development have been performed as a part of Japan Korea collaboration to develop the ECE radiometer system on KSTAR tokamak. Figure 1 shows block diagram of the signal flow of the ECE radiometer system. We utilize second harmonic frequency of the ECE, which frequency ranges from 110 to 196GHz. In the pre-down conversion box, the detected signal is down converted to four signals by using power dividers, frequency mixers, and LO waves. In the box, the signals with frequency from 110 to 162GHz(T-band) and 164 to 196GHz(G-band) are converted to two sets of the signal with frequency up to 26.5GHz and 16GHz, respectively by using LO wave with frequency of 136 and 180GHz. These signals are then fed to 2nd down conversion modules in order to make the signals up to 9GHz. Then these signals are resolved by the band-pass filter bank with center frequencies from 2 to 9GHz by 1GHz step, and detected by the video detector in the detector module. In order to achieve the frequency-resolved measurement from 110 to 196 GHz by 1 GHz step, we prepare two pre-down conversion modules, four 2nd down conversion modules, and twelve detector modules. In this article, we will describe system development after the stage of pre-down conversion box.

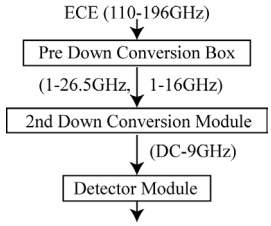

Fig. 1 Signal flow of the ECE radiometer

2. Development of IF system and evaluation

Figure 2 shows block diagram of the 2nd down conversion module. These components are composed from commercial components. First, signal from the pre-down conversion module is divided into 4 signals by the power divider. One of the four signals directly passes through to output of the module with same bandwidth to the input. This channel corresponds to most right branch in the figure. The other three signals are injected into the frequency mixers through high-pass filters with each cutoff frequency of 9, 15, 19 GHz.

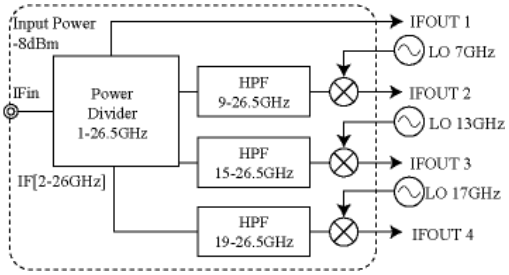

Fig. 2 Block diagram of the 2nd down conversion module

Then each signals are mixed with LO wave, which frequencies are 7, 13, 17 GHz. Resultant IF bandwidth of each mixer output is from DC to 9 GHz. We have evaluated the 2nd down conversion module by utilizing frequency synthesizer instead of pre-down conversion module output. Here, input power is fixed to –8 dBm, which is considered to be almost same situation to real application (Te=5keV). Power from the IF outputs (IFOUT 1-4 in Fig. 2) are plotted versus input frequency as shown in figure 3. Power loss at port IFOUT1 is consistent with insertion loss of the power divider. Power losses at port IFOUT2-4 are consisted from insertion loss of the power divider and conversion loss of the mixer. Monotonic output power decrement with input frequency observed in each output channel is considered to be due to insertion loss of the coaxial cables connected between the components. Signals from 2nd down conversion module are then fed to the detector modules.

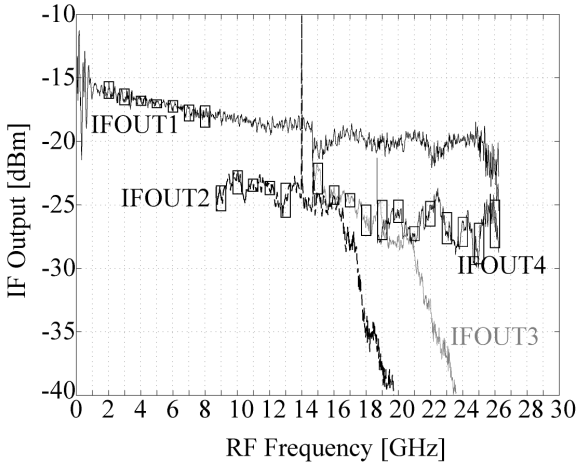

Fig. 3 Power of the IF output is plotted as a function of input frequency.

Figure 4 shows block diagram of the detector module. First, signal is amplified by 10 dB amplifier, and is then fed to low-pass filter. The low-pass filter is installed in order to reject the frequency component over 10GHz. This filter is especially important when the detector module receives signal from IFOUT1 with frequency range up to 26GHz. The filtered signal is divided into 8 channels by the power divider. Each signal is then fed to band-pass filters with center frequency from 2 to 9 GHz by 1GHz step. Bandwidth of each filter is 500 MHz. After the filter, the video detector detects the filtered signal. Here, we intend to construct these components utilized in the detector module by

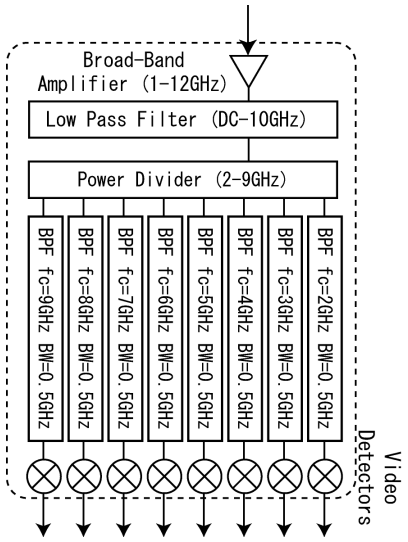

Fig. 4 Block diagram of the detector module

using microwave integrated circuit technology （MIC）. We have employed the MIC technology to construct the detector module, because it has advantages like optimum performance, compact size and low cost system. Figure 5 shows the layout of the detector module designed by electro magnetic simulator (Microwave office, AWR inc.). This layout is fabricated on Teflon substrate (NPC-F220A, NIPPON PILLAR PACKING CO., LTD.) with relative dielectric constant of 2.2 and thickness of 254 um. Thickness of the copper foils on the substrate is 9 um. Here, it has a distinctive in layout of the power divider and the band-pass filter region located in the center of the substrate. That is, the power divider is just replaced by a simple micro strip line, which end is terminated by 50 ohm resistor. The band-pass filters are arranged besides the micro strip line with proper gap. We employed inter-digital type filter as the band-pass filter [7]. The center frequency and the bandwidth are adjusted by changing coupled line length and number of the coupled line stage, respectively. By using this new layout type, broad-band and compact filter bank can be achieved. Then each band-pass filtered signal is fed to the video detector. We have designed these video detectors in order to achieve optimum impedance matching between the band-pass filters and the video detectors only within bandwidth of each band-pass filter [8]. This design policy has the advantage that we can acquire the high-sensitive detector, however, we have to design the individual detector for each band-pass filter.

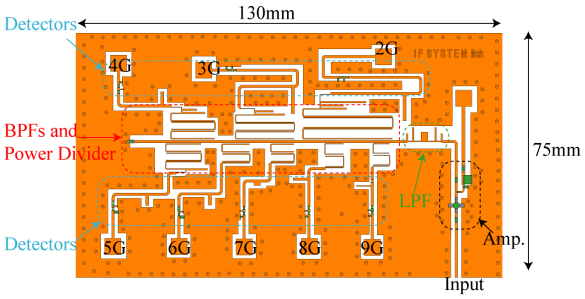

Fig. 5 layout of the detector module substrate

Figure 6 shows transmission and return loss performances of the amplifier, low-pass filter, and band-pass filters combined with the power divider, and detection characteristics of the video detectors. These characteristics have been evaluated by making individual microwave functional component into an unit substrate, e.g., an amplifier substrate etc. Major specifications of each component are described briefly as follows. The gain of the amplifier is about 10dB from 1.5 to 11 GHz with return loss below –10dB. Cutoff frequency of the low-pass filter is 10GHz. Insertion loss under –1.5dB and return loss over –9dB has been achieved within the pass range. While, signal attenuation attains over –20dB from 11 to 26GHz range. Transmission of the band-pass filter within the pass-band ranges from –13 to –9dB. Return loss is kept under –9dB within the pass-band. By adjusting the gap between the band-pass filter and the micro strip line, return loss performance is compatible with transmission performance. This is one of the advantages of employing this type of band-pass filter. Generally, return loss at input port of the power divider deteriorates significantly (about -3dB) when low-pass filters are simply connected to the power divider. Sensitivity of the video detectors ranges from 4V/mW up to 10V/mW. Tangential signal sensitivity is under –50dBm, which limits minimum temperature. We can estimate that amplitude range of the detector output is between 15 and 80 mV from ECE with temperature of 5 keV. The dynamic range of the system is estimated to be about 30dB, which indicates that minimum measurable temperature is about 5 eV.

3. Summary and future work

In summary, we have developed the IF system for ECE radiometer system on KSTAR. The 2nd down conversion module has been composed by using commercial components.

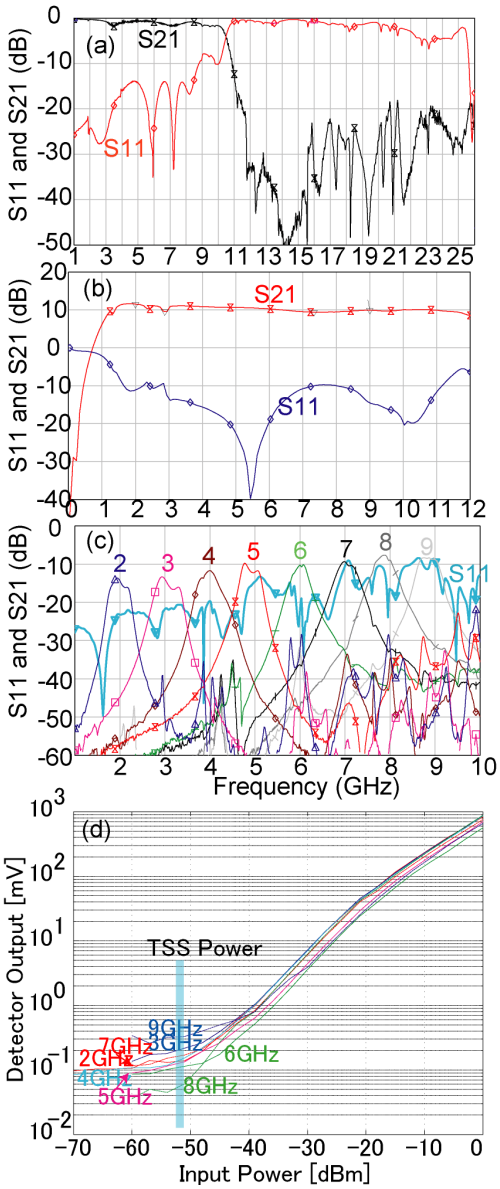

Fig. 6 Characteristics of the low-pass filter (a), the broadband amplifier (b), the band-pass filter bank (c), and the video detectors are plotted from top to bottom.

We have confirmed that this module works properly according to the catalogue specifications. The detector module has been fabricated by using MIC technology on the substrate. We have also confirmed that the performances of individual functional components.

. In the present filter, difference in transmission within 500MHz is at most 3dB as shown in figure 6. We have been working on flattening transmission performance of the band-pass filter bank within the bandwidth of 500MHz under 1dB. In order to adapt tiny amplitude of

the detector output to a digitizer (10 V peak to peak), we prepare video amplifiers. We also plan to apply our IF system to LHD plasma before installation of ECE radiometer system to KSTAR in order to confirm applicably of our system to the fusion experimental device.

Acknowledgements

This work is performed as a collaborating research program at National Institute for Fusion Science (NIFS07KCHP009), and is also partly supported by the Grant-in-Aid for Scientific Research, the Ministry of Education, Science, Sports and Culture ("Advanced Diagnostics for Burning Plasma" No. 16082205)

References

[1] Nagayama Yoshio, et.al., J. Plasma Fusion Res. **79**, 601 (2003)
[2] V. S. Udintsev, et.al., Rev. Sci. Instrum. **72**, 359 (2001)
[3] B. H. Deng, et.al., Phys. Plasmas **5,** 4117 (1998)
[4] A. Mase, et.al., Fusion Eng. Des. **53**, 87 (2001)
[5] J. Wang, et.al., Rev. Sci. Instrum. **75**, 3875 (2004)
[6] B. H. Deng, et.al., Rev. Sci. Instrum. **72**, 368 (2001)
[7] G. Matthaei, et.al., "Microwave filters, impedance-matching networks, and coupling structures", Artech House Publishers
[8] S. A. Maas, "The RF and Microwave Circuit Design Cookbook", Artech House Publisers

Quantum-dot-array diffraction grating with single order diffraction property

Chuanke Wang[1], Longyu Kuang[1], Zhebin Wang[1], Leifeng Cao[1], Shenye Liu[1], Yongkun Ding[1], Deqiang Wang[2], Changqing Xie[2], Tianchun Ye[2]

[1]*National Key Laboratory of Laser Fusion, Research Center of Laser Fusion, China Academy of Engineering Physics, Mianyang, Sichuan 621900, P. R. China*

[2]*Key Laboratory of Nano-Fabrication and Novel devices integrated technology, Institute of Microelectronics, China Academy of Sciences, Beijing, 100029, P. R. China*

A new dispersive element named as quantum-dot-array diffraction grating (QDADG) [L. F. Cao, Chinese patent, 2004, 200410081499.X] for visible light has been developed and characterized experimentally. A large number of quantum dots distributed on a substrate as sinusoidal function can be used to diffract x-rays without higher-order diffraction. The experimental patterns show that the higher-order diffractions which inevitably exist in the spectrum recorded using traditional diffraction gratings can be eliminated effectively by this newly designed element. It indicates that quantum-dot-array diffraction grating could be an attractive alternative of presently used diffraction grating in soft x-ray spectroscopy application to get rid of the higher-order diffractions distortion.

1. Introduction

Diagnoses of soft x-ray emissions from laser-heated targets are vital to understanding laser-plasma interactions.[1, 2] For many years, transmission gratings (TGs) have been widely used in soft x-ray spectroscopy. The straightforward construction and ease of alignment of TG spectrometers led to their wide spread usage in the areas of plasma spectroscopy and x-ray lasers.[3-8] Unfortunately, the inherent higher-order diffractions of so-called black-white TGs commonly used lead to distortions in the recorded spectra which are the main source of errors in spectral analysis.[9,10] To eliminate the higher-order diffractions disturbance from the experimental data, it is necessary to perform an unfolding process which should be validated carefully. By introducing sinusoidal TGs, higher-order diffractions can be avoided.[11] However, sinusoidal TGs with high spatial frequency (≥1000 line/mm) has not been fabricated so far.

Recently, a new concept of x-ray dispersive element named as quantum-dot-array diffraction grating (QDADG) has been proposed by L. F. Cao *et al.*[12, 13] A large number of quantum dots distributed on a substrate as sinusoidal function can be used to diffract x-rays without higher-order diffraction. Based on the concept, a QDADG for visible light is developed for the first time as described in this paper. The diffraction properties of this element are characterized by using a wavelength-adjustable visible monochromatic light source. It shows good agreement with the theoretical prediction.[12, 13]

2. Development of DADG

Black-white TGs consist of a series of parallel slits on an opaque screen. When a plane wave normally incident to a space-infinite black-white TGs, the transmission function of the grating can be written as:

$$t(x)=\begin{cases}1 & when \quad nd-a<x<nd\\ 0\end{cases} \tag{1}$$

Where $n=0,\pm1,\pm2,\pm3,\cdots$, a is the width of a transparent bar of the grating, and d is the grating's period width. Equation (1) can be expanded into Fourier series in infinite space:

$$t(x)=t_0+\sum_{n\neq0}t_n\exp(2\pi i f_n x) \tag{2}$$

where $t_0=a/d$, $t_n=(a/d)(\sin(n\pi a/d)/(n\pi a/d))$, and $f_n=n/d$ is the n[th] space frequency of the grating.

If the plane wave is $A_0\exp(2\pi iz/\lambda)$, the transmitted wave can be written as:

$$\begin{aligned}u(x,z)&=A_0\exp(2\pi iz/\lambda)t(x)\\&=A_0\exp(2\pi iz/\lambda)\left[t_0+\sum_{n\neq0}t_n\exp(2\pi i f_n x)\right]\\&=A_0t_0\exp(2\pi iz/\lambda)+A_0\sum_{n\neq0}t_n\exp[2\pi i(z+\lambda f_n x)/\lambda]\end{aligned}$$

. (3)

From equation (3), one can see that after modulating by the black-white TG the incident plane wave changes into $2n+1$ plane waves.

Different from black-white TGs, the transmission function of the sinusoidal transmission grating can be written as:

$$t(x)=\frac{a}{d}+\frac{a}{d}\frac{\sin(n\pi a/d)}{n\pi a/d}\left(\exp(2\pi jx/d)+\exp(-2\pi jx/d)\right) \quad (4)$$

When a plane wave $A_0\exp(2\pi iz/\lambda)$ is incident to a sinusoidal TG, the transmitted wave can be written as:

$$U(x,z)=A_0\exp(2\pi iz/\lambda)t(x)$$
$$=A_0\exp(2\pi iz/\lambda)\left[\frac{a}{d}+\frac{a}{d}\frac{\sin(n\pi a/d)}{n\pi a/d}\left(\exp(2\pi jx/d)+\exp(-2\pi jx/d)\right)\right] \quad (5)$$

From equation (5), one can see that after modulating by the sinusoidal TG only the 0th and the 1st order diffraction exist, while there are no higher-order diffractions.

Fig. 1 The microstructure of QDADG as seen through a microscope with a magnification factor of 1000

Sinusoidal TGs are of great benefit to X-ray diagnostics. However, sinusoidal TGs with high spatial frequency (≥1000 line/mm) have not been developed so far due to the limitation of fabrication technologies.

QDADGs for the visible light region can be more easily fabricated due to much larger dimension of such quantum dots than that for the X-ray region. A QDADG is developed by depositing a large number of Au dots on a quartz substrate. Fig.1 shows the microstructure of such a grating as seen by a microscope with a magnification factor of 1000. The dot density obeys sinusoidal distribution periodically along horizontal axis with the same period of the black-white TG. Along the vertical axis, the dot density is quasi-randomly distributed. For visible light, the quartz substrate is transparent and dots are opaque. The quantum dot is 2 μm×2 μm square, and the space frequency of QDADG is 25 lines / mm.

3. Diffraction properties of QDADG

The design of the experiment conforms to two conditions. First, the light source must be monochromatic; and second, the detector needs to be sensitive enough. The first is achieved by coupling a tungsten lamp to an optical multi-channel analyzer (OMA) as monochromatic light source, while the second is realized by using a scientific charge coupled device (CCD). In this experiment, the OMA is equipped with a grating of 600 lines / mm, and the CCD is a PID1100 chip manufactured by Princeton Instruments Co., which is back-illuminated, with 1100×330 pixels (each pixel is 24 μm-square).

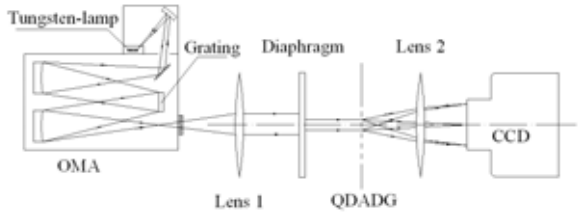

Fig. 2 Experimental arrangement for the characterization of the QDADG.

Experimental arrangement is shown in Fig. 2. Entrance and exit slits width of the OMA are adjustable to ensure the intensity of emissive light is suitable. Lens-1 is placed between the OMA and a diaphragm in order to collimate the incident light. The grating diffraction pattern is imaged on the CCD by the lens-2. Both lense-1 and lens-2 are 300 mm foci. A coded computer controls the scanning stage, the shutter, and triggers of the CCD. The TG efficiency is defined as the ratio of transmitted flux to incident one and the sensitivity factor of the CCD detector is included in the calculations, where the flux is conveniently expressed in units as the counts per second per pixel.

In order to reduce the influence of background noise, the calibration experiment was carried out in a darkroom. The wavelength of monochromatic light with a bandwidth of 1nm can be varied from 460nm to 1100nm with 20nm step. Diffraction patterns were acquired by the CCD, and the intensity and position of the 0th and 1st order diffraction spectrum could be read easily.

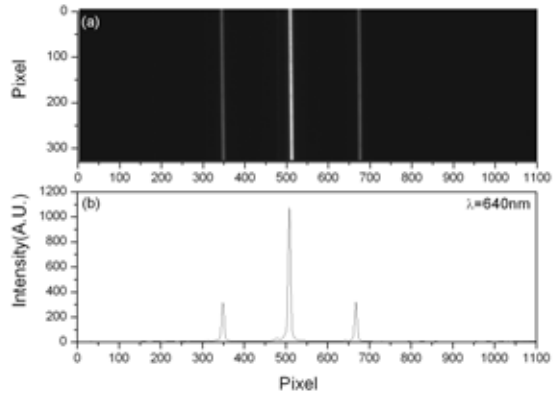

Fig. 3 (a) Diffraction pattern recorded on the CCD and (b) the corresponding intensity profile when the incident light is 640nm.

A typical diffraction pattern recorded using the QDADG and the corresponding intensity profile are shown in Fig. 3 (a) and (b) respectively. Obviously, the QDADG can get rid of the puzzle of high order diffraction, and only the 0^{th} and 1^{st} order diffractions exist which is consistent with theoretical prediction. The spectra from the QDADG offers much higher S/N ratio compared to black-white TGs. Fig 4 shows the intensity profiles of the recorded diffraction pattern at different wavelengths with their 0th order intensities are normalized to the same level. It clearly shows the intensity ratio of the 1^{st} order to the 0^{th} order diffraction varies little.

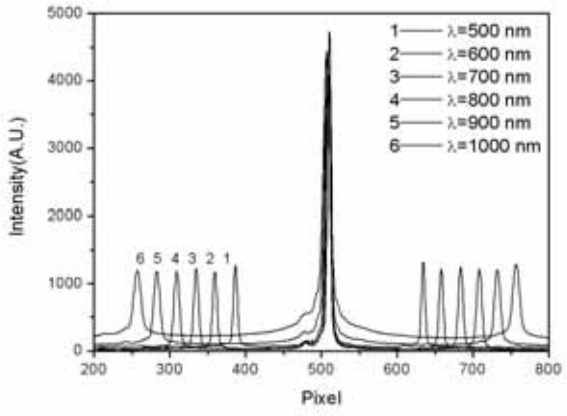

Fig. 4 X-ray line intensities .vs. axial position (all normalized by 0th order peak values)

We define the relative diffraction efficiency as the ratio of the flux in one wing of the first order diffraction spectrum to that of the transmitted light, and the absolute efficiency is the ratio of the flux of one wing of the first order diffraction spectrum to that of the incident light. Fig. 5 shows the variation in the relative and absolute diffraction efficiencies of the QDADG in the wavelength range between 460 nm to 1100 nm. From the figure, it can be seen that both the relative and absolute efficiencies of the QDADG are nearly constant within the measurement errors in the wavelength region of interest.

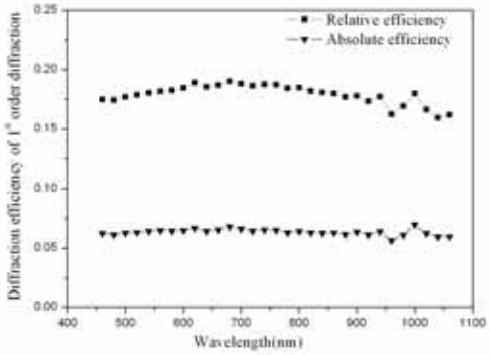

Fig. 5 The relative and absolute diffraction efficiencies of the QDADG vs. wavelength.

IV Conclusion

Based on the concept of x-ray dispersive element named as quantum-dot-array diffraction grating, a QDADG for visible light is developed for the first time, and the diffraction properties of this element are characterized in detail. The results show that this element can suppress higher orders of diffraction; only the 0^{th} and the 1^{st} order diffraction exist, which shows good agreement with the theoretical prediction. The transmission efficiency of QDADG has an attractive flat curve over the whole investigated region, and the diffraction position rises linearly with wavelength. Both these properties are convenient in the spectrum analysis. The emission spectral lines of Hg light have also been measured by using the element which shows superior properties in the spectrum analysis.

The QDADG for visible light can be used to disperse light without higher-order diffractions in optical range, and it can become a potential alternative for x-ray, extreme ultraviolet, or microwave diagnosis. As the fabrication technology improves it may become possible to deposit smaller dots and optimize the dot distribution. If so, QDADGs can be used to replace black-white TGs for soft-x-ray diagnostics.

Acknowledge

This work is supported by the Natural Science Foundation of China (No. 10375055), and Innovation Foundation of National Key Laboratory of Laser Fusion, CAEP (No. 200201).

References

1 E. Fill, K.-H. Stephan, P. Predehl, G. Pretzler, K.

Eidmann, and A. Saemann, Rev. Sci. Instrum.**70**, 2597 (1999)
2 R. T. Eagleton and S. F. James, Rev. Sci. Instrum.**75**, 3969 (2004)
3 H. Gursky and T. Zehnpfennig, Appl. Opt. **5**, 875 (1966).
4 K. P. Beuermann, R. Lenzen, and H. Bra¨uninger, Appl. Opt. **16**, 1425 (1977).
5 K. P. Beuermann, H. Bra¨uninger, and J. Tru¨mper, Appl. Opt. **17**, 2304 (1978).
6 K. Eidmann and T. Kishimoto, Appl. Phys. Lett. **49**, 377 (1986).
7 K. Eidmann and W. Schwanda, Laser Part. Beams **9**, 551 (1991).
8 Y. Li, G. Pretzler, P. Lu, and E. E. Fill, Phys. Plasmas **4**, 479 (1997).
9 G. Schriever, R. Lebert, A. Naweed, S. Mager, W. Neff, S. Kraft, F. Scholze, and G. Ulm, Rev. Sci. Instrum. **68**, 3301 (1997)
10 L. E. Ruggles, M. E. Cuneo, J. L. Porter, D. F. Wenger, and W. W. Simpson, Rev. Sci. Instrum.**72**, 1218 (2001)
11 M. Born and E. Wolf, *Principle of Optics*, (Pergamon, London, 1980)
12 L. F. Cao, *Quantum Dot Array Diffraction Grating*, patent, [China, 2004, 200410081499.X]
13 L. F. Cao, E. Förster, A. Fuhrmann, C. K. Wang, L. Y. Kuang, S. Y. Liu and Y. K. Ding, Appl. Phys. Lett. **90**, 053501 (2007)

Measurements of Sputtered Particles in Surface Discharge Using Laser Induced Fluorescence Technique

T. Sakoda, S. Takagi, Y. Tanaka and C. Honda

[1] *Dept. of Electrical and Electronic Engineering, University of Miyazaki, 1-1 GakuenKibanadai-Nishi, Miyazaki 889-2192, Japan*

Spatiotemporal distributions of Mg atoms emitted from an MgO surface during the surface discharges operated at He 50 torr were directly measured using the laser induced fluorescence (LIF) technique. The results showed the existence of diffused Mg atoms sputtered intermittently during the surface discharge, and the complicated spatial distribution due to the diffusion of the intermittently emitted Mg atoms was observed. Based on the results, we evaluated the sputter and the diffusion processes during the surface discharge, which is useful for understanding of the degradation process of the MgO protective layer used in the plasma display panel electrodes.

1. Introduction

The beginning of the digital terrestrial broadcasting has provided an opportunity to popularize the plasma display panels (PDPs), rapidly. However, further efforts are required to enhance luminous efficiency and lifetime, and to decrease power consumption. We focused on the improvement of the life time. One of factors which influence the lifetime is sputtered particles from the electrode materials. The sputtered particles deposited on phosphors whereby the luminous intensity decreases and the life time is gradually shortening.

An MgO layer in PDP cell plays a very important role for the protection of the electrode layer and for the promotion of the discharge efficiency. Although the sputter yield of MgO is relatively lower than those of other materials for the protective layer of PDP, the sputtering due to discharges can't be avoided.

In this study, measurements of spatiotemporal behaviours of Mg atoms sputtered from an MgO layer during surface discharges operated with the repetition rate of 20 kHz were performed by the laser induced fluorescence (LIF) technique. The general operating gas for PDPs is a mixed gas of Xe and Ne, and the operating gas pressure is around 500 torr. However, we operated the surface discharges at He 50 torr. This allows us to simplify the evaluation of sputtering phenomenon although the further computer simulations at 50 and 500 torr are required to fully understand the actual sputter and deposition phenomena for PDP.

2. Experimental methods

A schematic arrangement of experimental apparatus with better optical accesses is shown in Fig. 1. A chamber with a series of baffles and Brewster windows for reducing the stray light level was made of stainless steel, and its inner diameter and height were 286 mm, 400 mm, respectively. An electrode system for formation of the surface discharge was arranged at the center of the chamber filled with He at 50 Torr. The typical operating gas for PDP discharge is a mixed gas of Xe and Ne; however, we used only He to simplify the evaluation of Mg sputtering phenomenon.

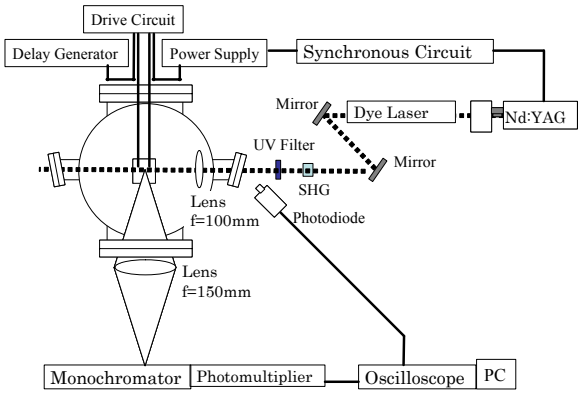

Fig. 1:Schematic arrangement of the experimental apparatus.

A two-level system, in which Mg atoms at the ground state of 3^1S_0 are excited to an upper metastable state of 3^1P_1 by the excitation laser beam with a wavelength of 285.2 nm and then the fluorescence form 3^1P_1 to 3^1S_0 are detectable, was used for the LIF measurements. The light

source was a dye laser pumped by a Nd:YAG laser with a pulse duration of about 7 ns, a repetition rate of 10 Hz and a line-width of 2.5pm. The excitation wavelength of 285.2 nm was obtained through a SHG crystal and an UV filter, and was calibrated with optogalvanic signals. The light injection was controlled by a synchronous circuit to synchronize the laser injection with the surface discharge. The laser beam was injected into the chamber at right angles to the chamber axis using a 100-mm-focal-length lens, and focused 1 mm above the MgO layer. The focal spot size was estimated as about 0.2 mm. The fluorescence light was collected by a 150-mm-focal-length lens (detection solid angle 0.06sr), and was directed into a double monochromator connected to a photomultiplier (PMT). The observation volume was 0.2 × 0.6 × 10 mm^3, determined by the laser beam diameter, the slit height and the width of the double monochromator. A PIN photodiode was placed near a Brewster window to make external triggers for a digital oscilloscope and a photomultiplier. The signal intensity increased linearly against the power of excitation beam and reached an obvious saturation value when the laser power was higher than 400 μJ. Therefore, the laser power was kept at 400 μJ in all experiments reported here.

Figure 2 shows an electrode configuration and measurement loci. The MgO with thickness of 500 nm and the surface area of 4 × 37 mm^2 was formed on an electrode layer made of Cr of 4 μm thickness and the quartz glass of 3 mm thickness. The surface discharge was sustained over the whole area of the MgO layer by a drive circuit whose maximum voltage and output frequency were 270 V and 20 kHz, respectively. Measurements of spatial profiles were carried out from the center (l_h = 0 mm) of the electrode gap to l_h = 0.8 mm at intervals of 0.2 mm.

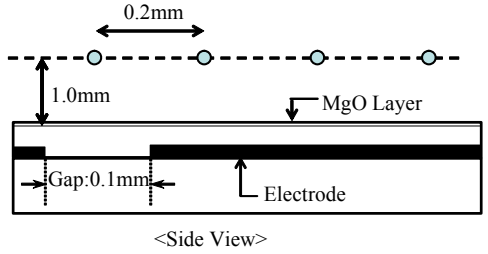

Fig. 2: Electrode configuration and measurement loci.

3. Experimental results

Figure 3 shows waveforms of the driving voltage of 270 V and the discharge current. In this figure, "t = 0 μs" denotes the supply time of the repetitive driving voltage. The discharge current consists of the displacement current due to capacitance of dielectric electrode and the pulse current due to the surface discharge which is delayed from the voltage application. As can be also seen from Fig. 3, the discharge terminated within 5 μs. The surface discharge propagates on the dielectric surface, and the accumulated charges on the dielectric surface lead to the reduction in the electric field in the discharge region. Then, the discharge terminated within a short time. The sputtering of Mg atom might be caused at the initial stage of the short-lived surface discharge.

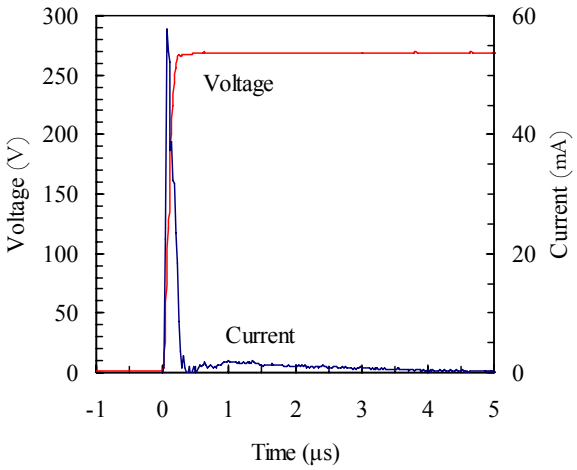

Fig. 3:Waveforms of the discharge voltage and the discharge current.

The temporal profiles of LIF signals and the driving voltage pulse are shown in Fig. 4. The LIF signal was obtained at l_h = 0 mm. The LIF signal increases with the time elapsed from the voltage supply and reaches a peak at t = 1.5 μs and thereafter gradually decreases. Additionally, it should be noted that LIF signals are also observed even before the voltage supply, i.e., at t = -3.0 and -1.5 μs. Because the surface discharge was chocked within 5 μs from the voltage supply, the signals might be due to Mg atoms emitted at former discharge periods.

The spatial profile of LIF signals obtained at t = -1.5 μs is shown in Fig. 5. The profile has peak at l_h = 0.2 mm, i.e., at around electrode edge where the electric field is higher than those at

other regions. In addition, the profile at t = -1.5 μs was relatively flat as comparison with that at 3.0 μs. The reason why the profile has a peak at the electrode edge will be treated later.

Figure 6 shows a temporal variation of LIF signals at l_h = 0.2 mm after the final supply of driving voltage. Mg atoms gradually decreases and observed until t = 600 μs, which indicates the minimum required time for the diffusion of Mg atoms from the MgO layer to the LIF measurement point. From Figs. 4, 5 and 6, it was found that Mg atoms existed around the MgO surface for a relatively long time.

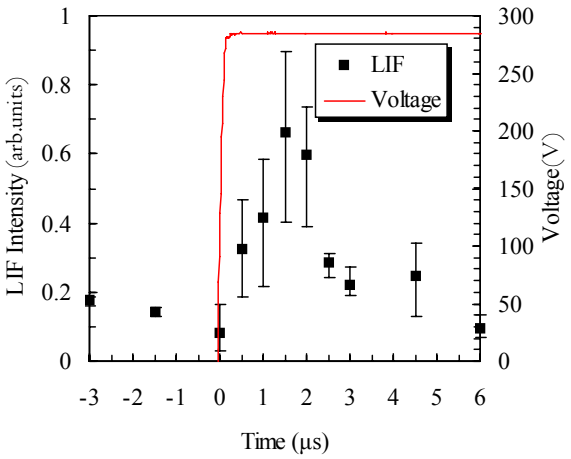

Fig. 4: Temporal profiles of LIF signals and the driving voltage pulse.

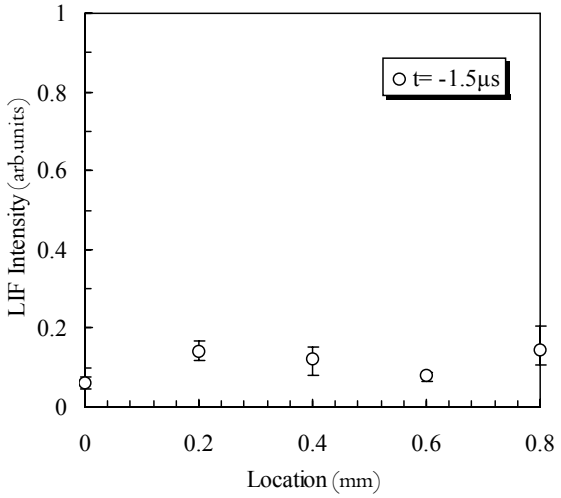

Fig. 5: Spatial profiles of LIF signals obtained at t = -1.5 μs.

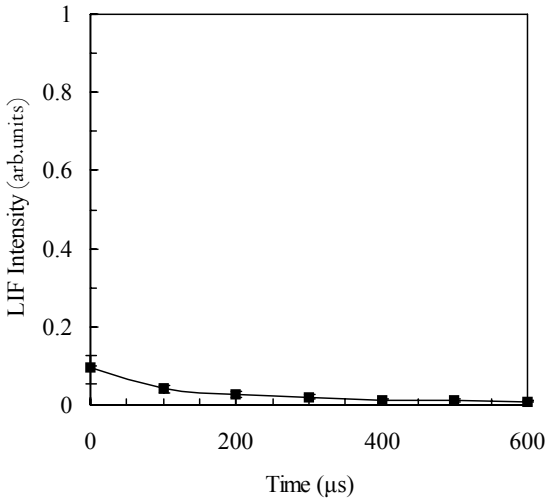

Fig. 6: Temporal variation of LIF signals at l_h = 0.2 mm after the final supply of driving voltage.

4. Discussions

The surface discharge was produced at He 50 torr; therefore, collisions between sputtered Mg atoms with He and Mg atoms play the main role of diffusion process. The energy loss for the collision process is characterized by the relative velocity of the colliding particles. In the case of collision between Mg atoms, the ratio of kinetic energy after collision to that before was 0.5. For the case of collision between Mg and He, the ratio of kinetic energy is 0.76. Even if the energy of sputtered Mg atoms is around 10 eV, it immediately becomes low as that of gas atom after the Mg atoms experienced collisions of 10 - 20 times. That is, the sputtered atom was immediately thermalized and would experience about 1000 collisions from the sputtered point to the observation point. Taking into account that the sputtered Mg atom has collisions with atoms of another species, the mean free path (λ) of the atom can be expressed as follows [1]:

$$\lambda = \frac{M_g v_{rel}^{\ 2}}{2\sqrt{\pi}\rho^2 P}\frac{1}{\Psi(x)},$$

$$\Psi(x) = x\exp(-x^2) + (2x^2+1)\sqrt{\pi}/2erf(x), \quad (1)$$

$$x = v_{rel}\sqrt{\frac{M_g}{2kT_g}}.$$

M_g is the mass of the gas atom (He), v_{rel} is the relative speed of the colliding atoms, ρ is the

radius corresponding to the collision cross section, P is the gas pressure of He, k is Boltzmann's constant, T_g is the gas temperature, erf(x) is the error function. Following Eq. (1), λ was calculated as 2.8 μm. The diffusion coefficient could be calculated with the collision frequency obtained for the calculation process of λ, and the time required for the diffusion from the surface of MgO layer to the LIF measurement point was calculated as 1.1 ms. Therefore, the detected signals reflect the floating Mg atoms sputtered at former discharge periods.

Incidentally, it is considered that the LIF peak shown in Fig. 4 is brought by another fact. Figure 7 shows temporal variations of optical emission at 388.8 nm (He), 631.1 nm (MgO), and 285.2 nm (Mg). The optical emissions were observed with the slit width of 0.2 mm and the slit height of 10 mm of the monochromator. The central axis of optical observation system was set to the center of the electrode gap. The supply voltage to a photomultiplier was kept at 1400 V. An optical emission of Mg has a peak at t = 1.5 μs just as the temporal variation of LIF signal shown in Fig. 4. As mentioned above, some sputtered Mg atoms are thermalized through collisions and diffuse; however, others recombine with O atoms. In Fig. 7, the obvious emission due to MgO is seen and has peaks at t = 1.1 μs. The optical emission due to He has a peak at t = 0.9 μs. That is, emission peaks appear in the order, He, MgO, Mg. This indicates that some MgO molecules produced by recombination of sputtered Mg and O are dissociated by high energy electrons in the surface discharge. The laser beam for LIF measurements was focused 1 mm above the MgO layer, and the focused point was in the surface discharge. The detected LIF signals were considered to be due to diffused Mg atoms from the sputtered point and ones re-dissociated by the surface discharge.

Additionally, the electric field at around the edges of electrodes is higher than those at other areas. The sputtering and the dissociation of MgO due to high energy electrons at the edges of electrodes become remarkable. Therefore, the LIF signals at the edge of the electrode gap becomes relatively larger than those at other regions.

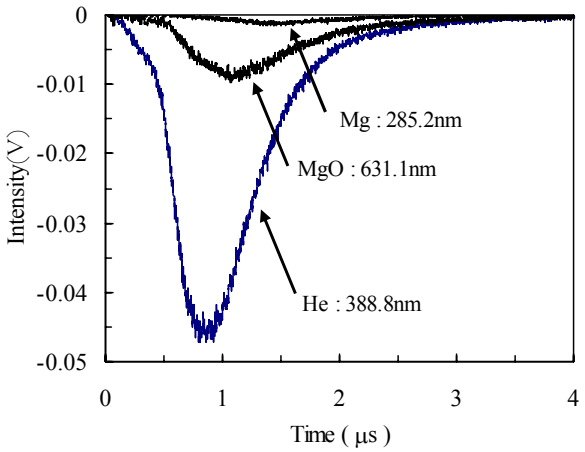

Fig. 7: Optical emissions due to He, MgO and Mg. The supply voltage to the photomultiplier was fixed.

5. Conclusions

Measurements of Mg atoms sputtered during the short-lived surface discharges were performed using a laser induced fluorescence technique. Based on the results, we evaluated the diffusion process of sputtered Mg atoms. It was found that some sputtered particles were immediately thermalized through collisions and diffused from the surface of MgO layer to measurement points. For the diffusion process, some Mg atoms were recombined with O atoms. Some MgO molecules produced by the recombination were dissociated by high energy electrons in the surface discharge, and then the dissociated Mg atoms were detected with ones diffused from the MgO layer.

References

[1] G. M. Turner, I. S. Falconer, B. W. James, and D. R. McKenzie, J. Appl. Phys. 65, (1989) 3671.

LIF measurement of neutral flow using a tunable diode laser

K. Ogiwara[1] , S. Etoh[1] , M. Aramaki[2] , S. Yoshimura[3] , M. Y. Tanaka[1]

[1] *Kyushu University, 6-1 Kasuga-koen, Kasugai, Fukuoka 816-8580, Japan*
[2] *Nagoya University, Furo-cho, Chikusa-ku, Nagoya, Aichi 464-8603, Japan*
[3] *National Institute for Fusion Science, 322-6 Oroshi-cho, Toki, Gifu 509-5292, Japan*

A vortical structure with anti-**E**×**B** flow has been observed in an argon plasma. It is considered that the anti-**E**×**B** flow is generated by interaction between the background neutral flow and the ion fluid. To confirm the new mechanism of vortex formation, we are developing the high resolution laser induced fluorescence (LIF) spectroscopy system for neutrals. Wavelength resolution of this LIF system is 14 fm, which corresponds to a velocity 6 m/sec. High performance in wavelength resolution is attained by using a tunable external cavity diode laser (ECDL), whose spectral width is typically 3 fm. Preliminary results on neutral flow velocity measurements using newly developed LIF system are presented.

1. Introduction

In understanding dynamical behavior of plasma, the effect of neutrals on the motion of ion fluid has been neglected (collisionless). Even it is considered, the contribution of neutrals is included as a small dissipation term, which slightly modifies the motion of ion fluid. In these circumstances, large-scale flow structure in a plasma is mainly determined by **E**×**B** drift.

However, it is experimentally found that there exists a class of vortices [1], which rotate to the opposite direction of **E**×**B** drift (referred to as anti-**E**×**B** vortex). One typical example is tripolar vortex, and is shown in Fig. 1. The result suggests that there is a force acting on ion fluid and it does exceed the electric field. The problem is then what produces this force.

As is shown in later section, anti-**E**×**B** vortices always accompany deep density depletion in the background neutrals, which strongly suggests that the interaction between neutrals and ions plays an essential role on generating the force exceeding the electrostatic force (see Fig. 2) [2]. To understand the effect of neutrals on the behavior of ion dynamics, visualization of neutral flow field is of primary importance. However, method for measuring neutral flow velocity has not been established yet. The reason is that neutral flow velocity is expected to be two-order slower than ion flow velocity, and consequently high resolution laser induced fluorescence (LIF) system is needed.

We have been developing a high precision LIF system using a tunable diode laser. It is capable of observing Doppler shift of about 9 MHz (14 fm), which corresponds to a velocity of about 6 m/sec. In this paper, a newly developed LIF system is described as well as the preliminary results on neutral flow velocity measurement.

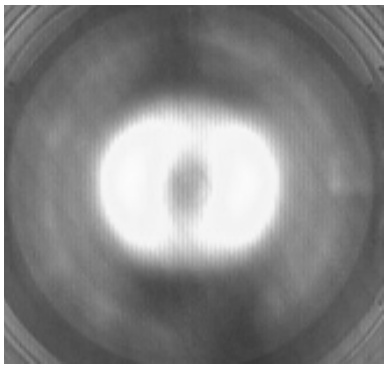

Fig. 1 : CCD image of tripolar vortex. Three vortices, center and two satellites, rotate to the anti-***E***×***B*** direction.

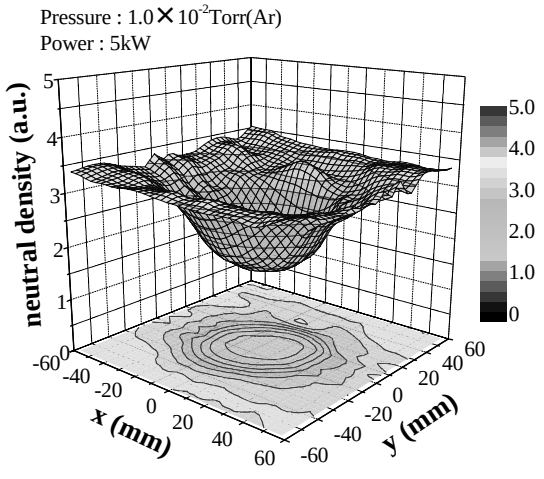

Fig. 2 : Density depletion of background neutrals

2. Measurement of neutral flow

The experiments have been performed in the high density plasma experiment (HYPER-I) device at National Institute for Fusion Science, (Fig. 3). The vacuum vessel is 0.3 m in diameter and 2 m in axial length. Plasmas are generated and sustained by electron cyclotron resonance (ECR) heating of argon with pressure of 1.0×10^{-2} Torr. The frequency of microwave is 2.45 GHz, and the input power (P_w) is changed from 40 W (low power operation) to 5 kW (high power operation).

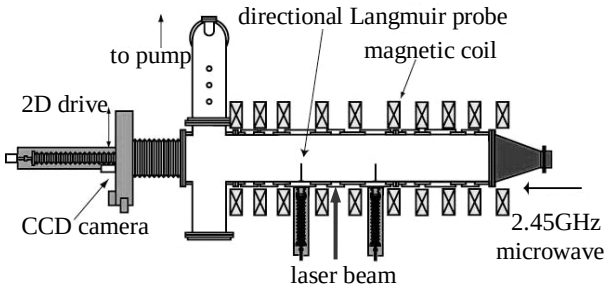

Fig. 3 : HYPER-I (High Density Plasma Experiment) device. A laser beam is introduced along *x* axis.

The LIF system (laser and collection optics) has been first developed with the plasma in low power operations, in which the LIF signal is easy to observe. The anti-**E**×**B** vortex appears in the high power operations.

The schematic diagram of LIF spectroscopy system is shown in Fig. 4. A tunable diode laser (external cavity diode laser), whose bandwidth is 2 MHz (3 fm) and output power is 15 mW, is tuned at a frequency 430281.8 GHz (696.7352 nm) and is introduced into the plasma. Metastable argon atoms are excited to an upper energy level ($3s^23p^5(^2P^o_{3/2})4s\rightarrow3s^23p^5(^2P^o_{1/2})4p$), and then deexcited by $3s^23p^5(^2P^o_{1/2})4p \rightarrow 3s^23p^5(^2P^o_{1/2})4s$ transition, emitting fluorescence photons of 362646.6 GHz (826.6794 nm). A photomultiplier tube (PMT) with collection optics is installed on the top viewing port of the vacuum vessel, and receives the fluorescence light collected by a lens. The laser beam is modulated by an optical chopper, and the PMT signal is detected by a lock-in amplifier to improve the signal to noise (S/N) ratio. The distance between the object point and the collecting lens is 250 mm, and the effective diameter of the lens is 45 mm. The solid angle of collection optics is 0.012 sr (the latest version of collection optics is 0.065 sr).

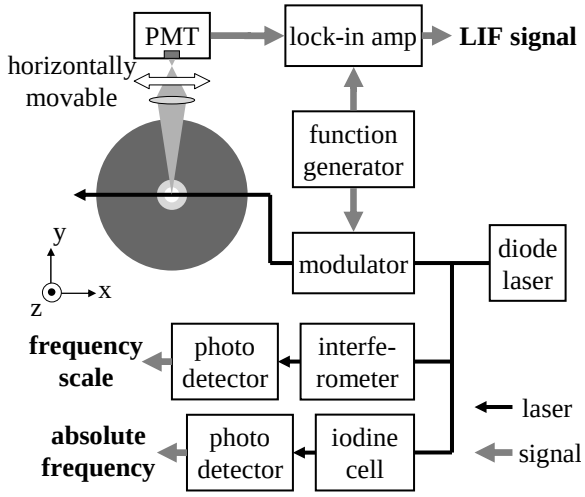

Fig. 4 : Schematic diagram of LIF spectroscopy system

The laser beam is split into two parts, and the sub beam is fed into two optional units; one consists of Fabry Perot interferometer, which gives a frequency scale, and the other consists of an iodine cell, which gives absolute wavelength reference. The free spectral range of the interferometer is 300 MHz, and the absorption lines of iodine located at 430277.1 GHz and 430282.7 GHz (696.7428 nm, 696.7337 nm, respectively) are used as the wavelength references.

Sweeping the laser frequency (15 GHz), we have obtained the LIF spectrum, which is proportional to the neutral distribution function. The velocity of neutrals is determined by the Doppler shift of distribution functions.

3. Experimental results

To confirm the existence of metastable atoms, we carried out absorption spectroscopy experiment. The maximum absorption was 34 % in the low power operation (P_w = 40 W), while 8 % in the high power operation (P_w = 5 kW). This result means that the number density of metastable atoms decreases in the high power operation due to collisional deexcitation process, and is anticipated a reduction in S/N ratio.

After confirming the presence of metastable atoms, we measured the LIF spectrum at P_w = 40 W, which is shown in Fig. 5. The observed spectrum is quite well fit by a Gaussian distribution, and the temperature is 0.034 eV. Measuring the LIF spectra and determining the Doppler shift at different points along the horizontal axis, we have obtained the radial flow velocity profile. Inward flow with a velocity 12 m/sec (maximum) has been observed.

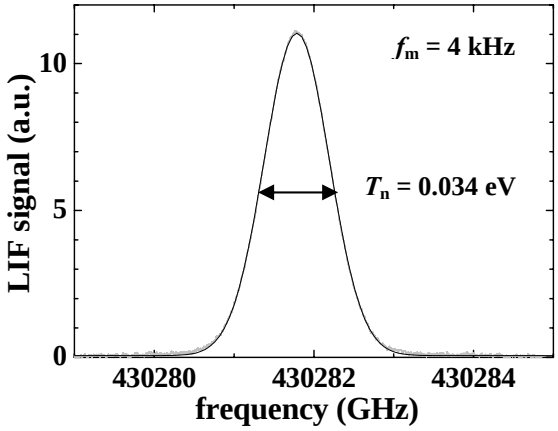

Fig. 5 : LIF spectrum for a low power case (P_w = 40W, f_m = 4 kHz). The neutral velocity distribution function is in well agreement with a Gaussian distribution.

In the high power operations, the level of background light increases by 20 times higher than the low power case (see Fig. 6), which causes further reduction in S/N ratio in addition to the decrease in metastable atoms. The LIF spectrum obtained with the same LIF system as in the low power case gives unphysical result as shown in Fig. 7. This means that S/N ratio is not sufficient for this case. The reasons for the result are already mentioned above, i.e., depletion of metastable atoms and increase of background light.

In order to overcome the reduction of S/N ratio, we have improved the collection optics so as to receive more LIF signal. The solid angle is increased to 0.065 sr, and the modulation frequency f_m is raised up to 100 kHz. As shown in Fig. 8, the output signal originates from the background light decreases with increasing the modulation frequency, and is minimum in a frequency range between f_m = 100 kHz and 600 kHz.

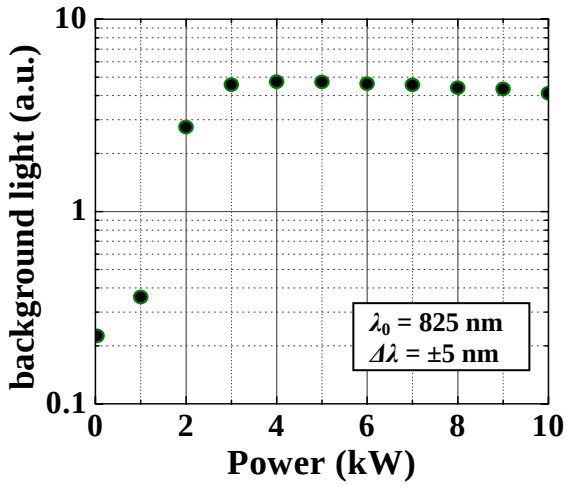

Fig. 6 : Background light as a function of input

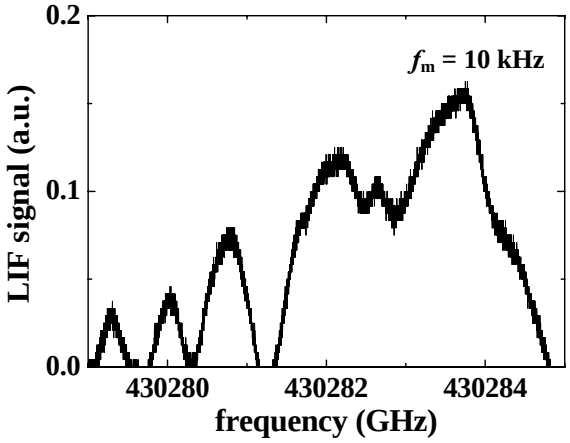

Fig. 7 : LIF spectrum at P_w = 5 kW, f_m = 10 kHz. The measurement doesn't work.

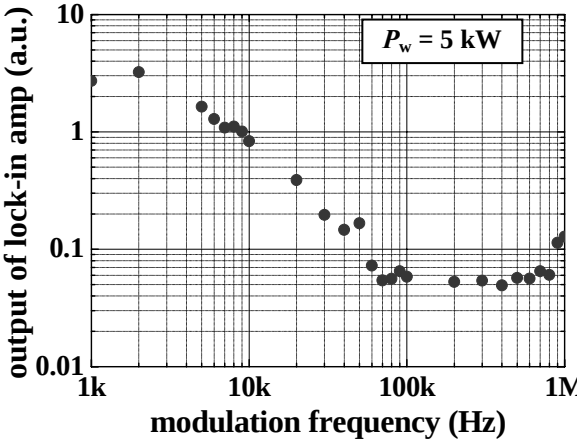

Fig. 8 : Plasma background light detected by a lock-in amplifier.

When the modulation frequency of lock-in amplifier is set at 100 kHz, several ten times of increase in S/N ratio is expected compared with that of 4 kHz modulation. Then, we have modified LIF spectroscopy system by introducing an electro-optical modulator, and carried out high frequency lock-in detection. The result is shown in Fig. 9. As seen in the figure, the expected LIF spectrum is clearly recovered. The temperature of neutrals in this case is 0.11 eV.

Radially measuring the distribution function of neutrals at different points, we have found that there is inward flow at a velocity 80 m/sec (maximum). In the present experiments, the spatial resolution (radial) of collection optics is suppressed down to 5 mm in order to receive much of LIF photons. Further improvement of S/N ratio with good spatial resolution is left for future work.

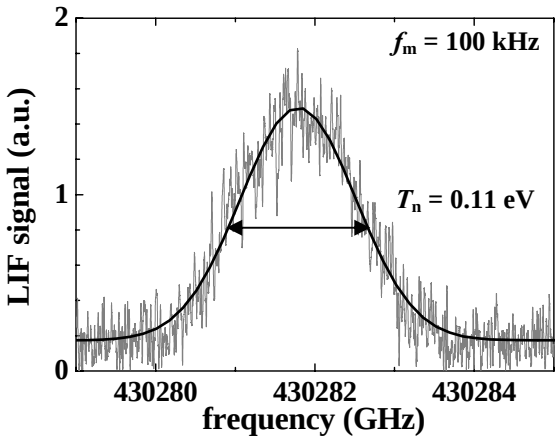

Fig. 9 : LIF spectrum for a high power case. (P_w = 5 kW, f_m = 100 kHz). By increasing modulation frequency f_m, LIF spectrum comes to be observable. A smooth solid line is a Gaussian fits to the experimental data.

4. Conclusion

A high resolution LIF spectroscopy system for neutral flow velocity measurements is described. The preliminary experiments show that this system is capable of measuring weak velocity field flowing at a velocity as low as 10m/sec. To extend this performance into the order of m/sec, there is still a few problems to be solved. Wavelength stabilization (long term and short term) is the most important. The present limit of wavelength resolution is close to the stability limit of the laser system (ECDL). Therefore, by introducing an additional external feedback circuit, the stability problem will be overcome.

The improvement of S/N ratio is still left for future work. It will be raised to a certain extent by increasing the laser power because the LIF signal does not saturate at the present power level (15 mW).

In addition to radial flow velocity, azimuthal flow velocity measurement is of interest from the viewpoint of ion-neutral interaction. The distribution function consists of neutrals from the wall and those from the ions through charge exchange collisions, the latter of which constitute fast rotating component. Therefore, measuring the azimuthal distribution will give us important information of the rate of ion-neutral interaction.

Our system can be applied to ion flow velocity measurements with choosing an appropriate ECDL, which is tuned to a certain energy level of ion. Comparison of the ion velocity distribution functions obtained by LIF spectroscopy and that with a directional Langmuir probe provides a systematic and *in-situ* calibration of probes (directional probe or Mach probe), which is still under discussion in case of supersonic regime.

References

[1] A. Okamoto, K. Hara, K. Nagaoka, S. Yoshimura, J. Vranješ, M. Kono, M. Y. Tanaka, Phys. Plasmas 10, (2003) 2211.

[2] A. Tomida, Master Thesis, Graduate School of Science, Nagoya University, 2006.

Diagnostics of high-density hydrogen plasmas by diode laser absorption spectroscopy: temperature and density of the *n*=2 state

K. Sasaki[1], Y. Okumura[2], M. Aramaki[2], M. Goto[3], S. Muto[3], and S. Morita[3]

[1] *Plasma Nanotechnology Research Center, Nagoya University, Furo-cho, Chikusa-ku, Nagoya 464-8603, Japan*
[2] *Department of Electrical Engineering and Computer Science, Nagoya University, Furo-cho, Chikusa-ku, Nagoya 464-8603, Japan*
[3] *National Institute for Fusion Science, 322-6 Oroshi-cho, Toki-shi, 509-5292, Japan*

Diode laser absorption spectroscopy at the Balmer-α line was applied to high-density hydrogen plasmas for detecting the *n*=2 state of atomic hydrogen. We evaluated the density and the temperature of the *n*=2 state from the broadening and the amplitude of the absorption line profile, respectively. We examined the temporal variation of the *n*=2 temperature after the ignition and the termination of the discharge. From the time constant of the temporal variation, we evaluated the power consumed for gas heating. We also compared the temperatures of hydrogen and deuterium. In addition, we examined the density ratio of hydrogen and deuterium at the *n*=2 state as a function of the mixing ratio of the feedstock H_2 and D_2. Based on this experiment, we propose diode laser absorption spectroscopy as a method for monitoring the D/T fuel ratio in nuclear fusion plasmas.

1. Introduction

The present work is driven by the following two motivations. The first motivation is related to plasma-aided material processing. The gas temperature in a low-pressure, nonequiribrium plasma has attracted much attention in the development of plasma-aided material processing. This is because the gas temperature has a direct influence on the absolute density and the distribution of neutral radicals in plasma reactors, kinetics and transport of radicals in the gas phase, and surface reactions. In addition, from the viewpoint of discharge physics, the gas temperature is important in considering the power balance of the discharge. Regarding the first motivation, we measured the temperature of atomic hydrogen at the *n*=2 state by diode laser absorption spectroscopy [1]. We evaluated the power for gas heating from the rise time of the *n*=2 temperature after the ignition of the discharge.

The second motivation is related to nuclear fusion research. An issue in the diagnostics of burning fusion plasmas is how to evaluate the D/T fuel ratio. A simple method is optical emission spectroscopy at the Balmer-α line, but spectrometer used in this method requires a very fine wavelength resolution since the wavelengths of the Dα and Tα lines are close. We propose diode laser absorption spectroscopy as a method for monitoring the D/T fuel ratio in nuclear fusion plasmas. The advantages of diode laser absorption spectroscopy are the fine wavelength resolution, the compact diagnostic system, and the maintenance-free operation of the laser source. Regarding the second motivation, we measured the density ratio of D(*n*=2) and H(*n*=2) as a function of the partial pressure ratio of feedstock D_2 and H_2.

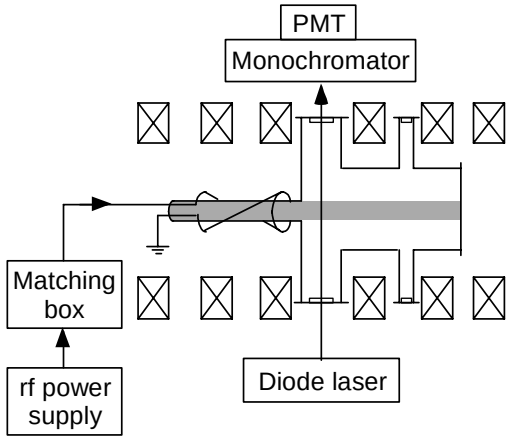

Fig. 1: Schematic of the experimental apparatus.

2. Experiment

The experimental apparatus is shown in Fig. 1. High-density hydrogen plasmas were produced by helicon-wave discharges in a linear machine

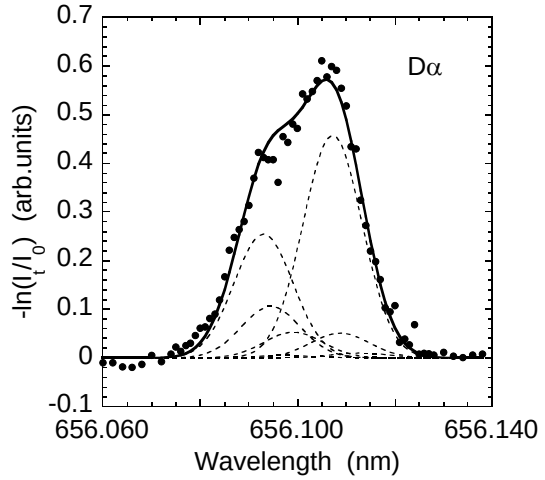

Fig. 2: An example of the absorption line profile of the Dα line.

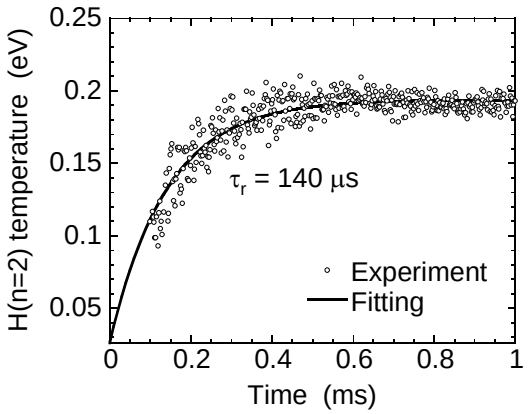

Fig. 3: Temporal evolution of the H(*n*=2) temperature after the initiation of the discharge.

with a uniform magnetic field, which radially confined a slender plasma column of 1.6 cm in diameter. The rf power at 13.56 MHz was pulse-modulated at 10 Hz with a duration of 4 ms. This plasma source was used as a divertor simulator [2], and was specialized for producing high-density hydrogen plasmas. The maximum electron density obtained in this plasma source with pure H_2 was $1x10^{13}$ cm^{-3} at an rf power of 3 kW. Pure H_2, pure D_2, and the mixture of H_2 and D_2 were used in the present experiment. The laser beam used for absorption spectroscopy was launched into the plasma from the radial direction. The laser beam passed through the plasma five or seven times to obtain sufficient absorption signal by elongating the absorption length. The temperatures of H(*n*=2) and D(*n*=2) were evaluated from the Doppler broadening of the absorption line profile of the Balmer-α line, while the densities of H(*n*=2) and D(*n*=2) were obtained from the absorption amplitude.

3. Results and discussion

3.1 Absorption line profile

Figure 2 shows an absorption spectrum of the Dα line. The vertical axis is $-\ln(I_t/I_0)$, which represents the profile function of the absorption line (I_0 and I_t denote the incident and transmitted laser intensities, respectively). The plasma was produced at an rf power of 3 kW in a mixture gas of H_2 and D_2. The partial pressure of both H_2 and D_2 were 20 mTorr.

The Balmer-α line of atomic hydrogen is composed of seven fine structure components. We fitted the absorption line profile with the superposition of the seven components having Gaussian profiles with the same widths. The amplitude ratio was assumed by considering the transition probabilities and the statistical weights of the relevant sublevels [3]. In Fig. 1, the dashed curves show the fine structure components, and the solid curve is the superposition of the dashed curves. The absorption line profile observed experimentally was fitted well by the superposition of the fine structure components, indicating the statistical distribution among all the D(*n*=2) sublevels. The temperatures of D(*n*=2) evaluated from the width of the absorption line profile was 0.16 eV.

3.2 Temporal variation of the H(*n*=2) temperature

Figure 3 shows the temporal variation of the H(*n*=2) temperature after the initiation of the discharge. The rf power was 3 kW, and the gas was pure H_2 at a pressure of 50 mTorr. The increase in the temperature was fitted by $T = T_0 + \Delta T\,(1-\exp(-t/\tau_r))$, where τ_r is the time constant for the increase in the temperature. The solid curve illustrated in Fig. 3 shows the result of data fitting, and the time constant for the increase in the gas temperature was evaluated to be τ_r =140 μs.

The temporal variation of the H(*n*=2) temperature after the termination of the rf power is shown in Fig. 4. The discharge conditions were the same as those in Fig. 3. The rf power was terminated at t=4 ms. It was found that the decay of the H(*n*=2) temperature had two

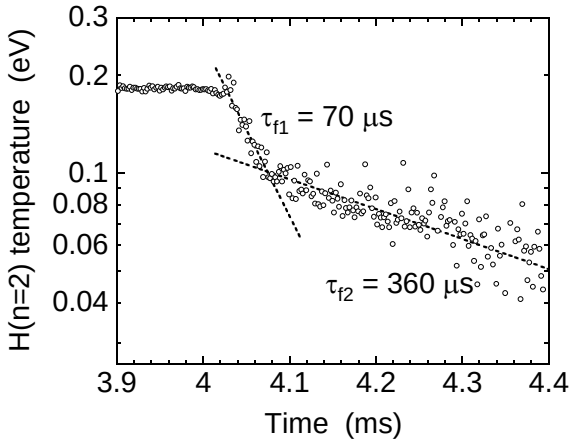

Fig. 4: Temporal decay of the H(*n*=2) temperature after the termination of the discharge.

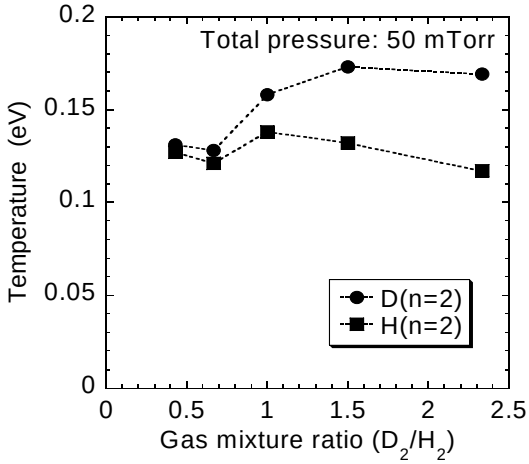

Fig. 5: H(*n*=2) and D(*n*=2) temperatures in H_2/D_2 mixture plasmas as a function of the gas mixing ratio.

components. The faster decay in the initial afterglow had a time constant of t_{f1}=70 μs. At 0.08 ms after the termination of the rf power, the decay of the gas temperature was switched to a slower one with a time constant of τ_{f2}=360 μs.

3.3 Estimation of the gas heating power

The steady-state gas temperature was achieved by the balance between heating and dissipation such that $W=Q/\tau_c$ with W, Q, and τ_c being the heating power, the energy stored in gas, and the confinement time of the stored energy, respectively. Under the assumption that the H(*n*=2) temperature is equal to the temperatures of H(*n*=1) and H_2, the stored energy Q is estimated from ΔT, the specific heats of H and H_2, the densities of H and H_2, and the volume of the plasma source. Under assumptions based on the experimental observations, we estimated Q=0.11 J at an rf power of 3 kW and a gas pressure of 50 mTorr. On the other hand, the time constant of the increase in the gas temperature τ_r may give a rough estimation of the confinement time τ_c. By assuming $\tau_c=\tau_r$, the heating power is estimated to be $W=Q/\tau_c$=0.8 kW. This means that approximately 30% of the input rf power is consumed for gas heating.

3.4 Comparison between the H(*n*=2) and D(*n*=2) temperatures

The H(*n*=2) and D(*n*=2) temperatures were measured in H_2/D_2 mixture plasmas with various gas mixing ratios. The rf power and the total gas pressure were fixed at 3 kW and 50 mTorr, respectively. As shown in Fig. 5, the D(*n*=2) temperature was higher than the H(*n*=2) temperature at all the gas mixture ratios. However, the difference between the H(*n*=2) and D(*n*=2) temperature was dependent on the gas mixture ratio. At a small amount of D_2 admixture into H_2, the temperatures of H(*n*=2) and D(*n*=2) were roughly the same. On the other hand, the D(*n*=2) temperature increased with the partial percentage of D_2, while the H(*n*=2) temperature decreased slightly, resulting in the large difference in the H(*n*=2) and D(*n*=2) temperatures.

3.5 Consideration for the difference in the H(*n*=2) and D(*n*=2) temperatures

It is pretty sure that the temperatures of H(*n*=2) and D(*n*=2) are the same as those of H(*n*=1) and D(*n*=1), respectively, since the interchanges between the *n*=1 and *n*=2 states are very frequent due to the radiation trapping of the resonance Lyman-α line [4]. Therefore, the difference between the H(*n*=2) and D(*n*=2) temperatures means the difference between the temperatures of H and D atoms.

According to the simple assumption that the steady-state gas temperature is determined by the balance between heating and dissipation, the candidates for inducing the temperature difference are the differences in the heating

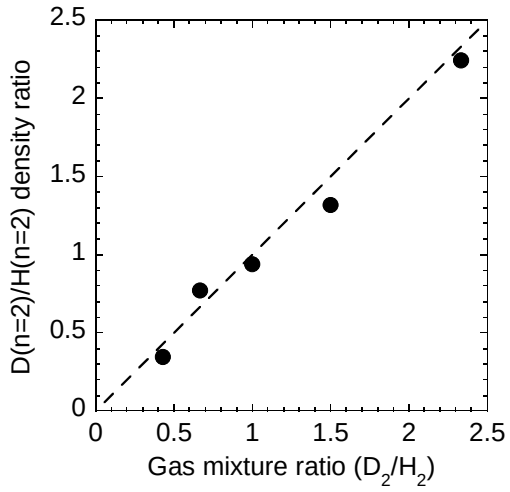

Fig. 6: The ratio of the D(*n*=2) to H(*n*=2) densities as a function of the gas mixture ratio.

power and the heat confinement time. We compared the temporal variations of the H(*n*=2) and D(*n*=2) temperatures after the ignition and the termination of the discharge. As a result, it was found that the rise and decay time constants of the H(*n*=2) and D(*n*=2) temperatures were completely the same. The same decay time constants of the H(*n*=2) and D(*n*=2) temperatures indicate that particle transport is not the dominant dissipation mechanism of the H(*n*=2) and D(*n*=2) temperatures.

The same rise and decay time constants suggest that the heating power is deposited into D atoms more efficiently than H atoms. This is rather puzzling, since in low-pressure plasmas, the electrical power is firstly transported to electrons and the heat transport from electrons to neutral species is more efficient when the mass of neutral species is closer to that of electron. Further investigation is necessary to obtain full understanding on the heating mechanism of neutral species in low-pressure glow discharges.

3.6 Comparison between H(*n*=2) and D(*n*=2) densities

Finally, we describe the comparison between the densities of H(*n*=2) and D(*n*=2). Figure 6 shows the ratio of the D(*n*=2) to H(*n*=2) densities as a function of the gas mixture ratio. As shown in the figure, the ratio of the D(*n*=2) to H(*n*=2) densities coincided with the gas mixture ratio. Since the production rates of H(*n*=2) and D(*n*=2) are determined by the densities of H and D atoms in the ground states, respectively, this result means that the ratio of the D to H densities also coincides with the gas mixture ratio, indicating both the production (dissociation of D_2 and H_2) and loss rates of H and D in the ground states are also the same. Based on the result shown in Fig. 6, we propose diode laser absorption spectroscopy at the Balmer-α line as a method for estimating the fuel ratio between D and T in fusion reactors. Since the wavelength difference between Dα and Tα is small, diode laser absorption spectroscopy with a fine resolution has an advantage in comparison with optical emission spectroscopy.

4. Summary

We measured the temperatures of H(*n*=2) and D(*n*=2) in helicon-wave H_2, D_2, and H_2/D_2 mixture plasmas by diode laser absorption spectroscopy. We examined the temporal variation of the H(*n*=2) temperature after the ignition and the termination of the discharge. From the time constants of the temporal variations, we evaluated the power consumed for gas heating. We also compared the temperatures of H(*n*=2) and D(*n*=2). It was found that the D(*n*=2) temperatures in H_2/D_2 mixture plasmas were higher than the H(*n*=2) temperatures. The difference in the H(*n*=2) and D(*n*=2) temperature was dependent on the gas mixture ratio. In addition, we examined the density ratio of hydrogen and deuterium at the *n*=2 state as a function of the mixing ratio of the feedstock H_2 and D_2. Based on this experiment, we propose diode laser absorption spectroscopy as a monitoring method of D/T fuel ratio in nuclear fusion plasmas.

References

[1] M. Aramaki, Y. Okumura, M. Goto, S. Muto, S. Morita, and K. Sasaki, Jpn. J. Appl. Phys. **44**, 6759 (2005).
[2] M. Aramaki, K. Kato, M. Goto, S. Muto, S. Morita and K. Sasaki, Jpn. J. Appl. Phys. **43**, 1164 (2004).
[3] NIST Atomic Spectra Database, http://physics.nist.gov/cgi-bin/AtData/main_asd.
[4] A. Rousseau, E. Teboul, and N. Sadeghi, Plasma Sources Sci. Technol. 13 , 166(2004).

Laser aided diagnostics of a neutral helium beam

A. Okamoto, S. Kitajima, M. Sasao

Quantum Science and Energy Engineering, Tohoku University, Aoba, Sendai 980-8579, Japan

Laser absorption spectroscopy applicable to measure a metastable population density in a helium neutral beam is developed. Density resolution of the measurement system, which is evaluated using a hollow cathode discharge plasma, is determined to be 5×10^{13} m^{-2}. Some improvements will enable us to measure the metastable density in the beam. Practical design of a multiple reflection cell using parallel plane mirrors, which is less affected by Doppler shift, is proposed.

1. Introduction

A diagnostic neutral beam using helium atom is proposed to measure the spatial and energy distributions of alpha particles in fusion plasmas[1,2]. If the neutral beam includes considerable amount of metastable atoms, it causes undesired beam attenuation. The neutral beam should be well controlled regarding the population of helium atoms in a metastable state.

The helium neutral beam is produced not directly from charge exchange of positive beam but from an autodetachment of a negative ion beam, where the negative ion beam is converted from a positive ion beam through an alkali vapor cell.[3,4] In this method almost all neutral helium is expected to be in ground state.[2] However there are few reports on experimental verification of metastable fraction after autodetachment. An experimental research has recently been started, where production of a helium neutral beam is performed using above-described method for proof of principle[5,6]. Current of the helium neutral beam produced in the proof of principle experiment is about 10 μA for 100 keV of the beam energy. Then the beam density is about 5×10^{11} m^{-3}. Thus a measurement system applicable to ultra-low density metastable atom is required. Density resolution in the system should be about one order less than the beam density.

We have proposed a measurement system using diode laser absorption spectroscopy[7], which is a popular method to measure atomic density in laboratory plasmas[8-10]. On the other hand, applying the method to beam diagnostics could be regarded as ambitious since the beam density is much lower than that of the plasmas. Evaluation of the density resolution is essential for development and improvement of the measurement system.

In order to assure sufficiently long absorption length, optical design of absorption region is also important. Some multiple reflection cells are used for absorption analyses of gases[11]; those cells achieve about a hundred meter of a absorption length. On the other hand, not only absorption length but also effect of Doppler shift in each laser pass will be affected for absorption spectroscopy applied to beam diagnostics.

In this paper, development of a measurement system using laser absorption spectroscopy is described, which is applicable to diagnostics of a helium neutral beam. In the following section, experimental apparatus of laser absorption spectroscopy and a metastable source using a hollow cathode plasma are described. Design concept on a multiple reflection cell is also given in section 2. Evaluation of density resolution is shown in section 3, where improvements of the density resolution are also discussed. Summary is given in section 4.

2. Apparatus

2.1. Laser absorption spectroscopy

A schematic of the measurement system using diode laser absorption spectroscopy is shown in Fig. 1(a). An external cavity-stabilized diode laser (DL100, Toptica photonics) was used for laser absorption in metastable (2^3S_1) helium atoms. The wavelength is tuned to 1082.9 nm, which corresponds to a 2^3S_1-2^3P_0 transition. When the wavelength is scanned using a piezo actuator placed in the external cavity, the wavelength and longitudinal modes are monitored by means of a multi-wavelength meter and an optical spectrum analyzer. When the scan-speed of the piezo-voltage is smaller than 4 V/s, a single mode laser beam without

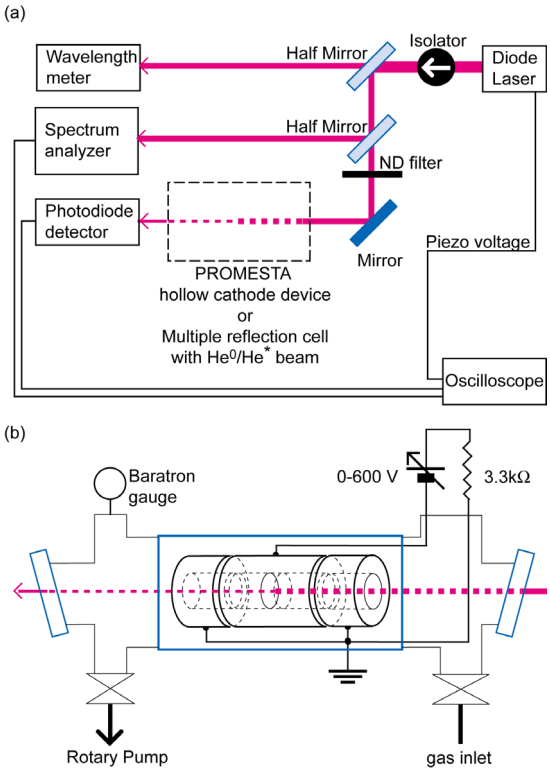

Fig. 1 : Schematics of experimental setup. (a) Absorption measurement system using a diode laser, (b) a hollow cathode device for production of metastable atoms (PROMESTA device).

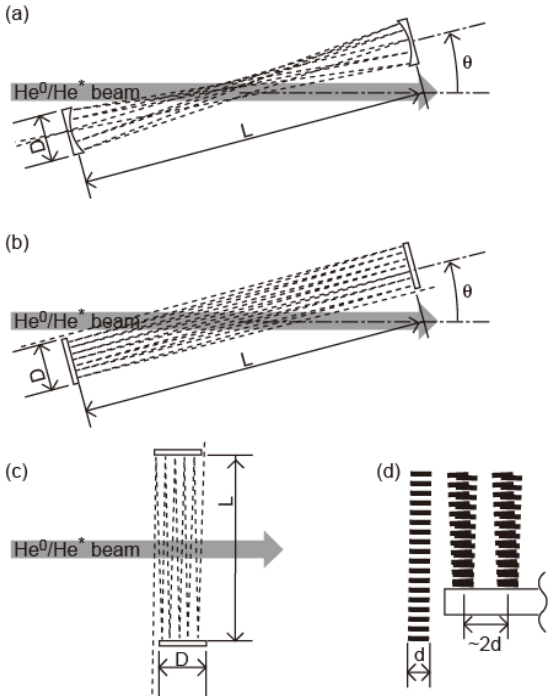

Fig. 2 : Schematics of laser absorption configurations. Dashed lines represent laser passes. (a) Multiple reflection cell with concave mirrors, (b) parallel plane mirrors with oblique beam trajectory, (c) the same as (b) but with the right angle beam injection, (d) detail of the laser pass near the edge of the mirror in (c) and (d).

mode hop is emitted. The scanning range of the single mode laser is about 5 GHz (0.02 nm), which is sufficiently wider than the Doppler broadening (1 GHz) at a room temperature. The signal detected by a photodiode was then averaged to reduce high frequency noise. The averaged data consist of about 20 samplings/GHz in the laser frequency scale. This is sufficient for Gaussian fitting based on the Doppler broadening.

2.2. PROMESTA device

The experiments were performed in a hollow cathode-discharge device for production of metastable atoms (PROMESTA device) in Tohoku University[12]. A schematic of the PROMESTA device is shown in Fig. 1(b). A cylindrical cathode made of aluminum and two cylindrical anodes positioned at both ends of the cathode are contained in a Pyrex glass tube. Inner diameter of the cathode is 10 mm and its length is 40 mm. The two anodes have the same inner diameter as the cathode. Both ends of the vacuum chamber contain a window to allow a laser beam to pass through the PROMESTA device.

2.3. Practical design of multiple reflection cell

Typical multiple reflection cells, such as White cell and Herriot cell, have concave mirrors. Thus an angle variation $\Delta\theta \sim D/L$ arises in a direction of each laser pass, where D is a mirror diameter and L is a distance between the opposed mirrors. Schematic of the optical layout is shown in Fig. 2(a). Then variation of Doppler shift is of the order of $\Delta\nu_D \sim \nu_b \sin\theta\,\Delta\theta$, where ν_b is the beam velocity, and θ is the angle between a beam trajectory and a laser pass. Due to limitation of mode-hop-free scanning range Δf_{MHF}, the variation of Doppler shift is limited to be $\Delta\nu_D/c << \Delta f_{MHF}/f$, where c and f are the light speed and laser frequency, respectively. Then maximum value of the ratio of the mirror radius to the mirror distance is determined as follows:

$D/L << (\Delta f_{MHF}/f)(c/\nu_b \sin\theta)$.

This relation means that the laser pass reflected near the edge of a large diameter mirror is not absorbed within the laser scanning range Δf_{MHF}. Even if nearly parallel ($\theta \sim 0$) configuration is

applied, finite minimum angle is determined by the size of the mirror itself, that is, $\theta \geq D/L$. Maximum mirror diameter is then determined $D/L << 5\times10^{-2}$ for $\Delta f_{MHF} \sim 5$ GHz and $v_b \sim 2\times10^6$ m/s (100 keV of beam energy).

To avoid the variation of Doppler shift, parallel plane-mirrors configurations [Fig. 2(b) and (c)] are candidates of our absorption cell. The order of the angle variation is then estimated by a size of laser spot d and mirror distance L: $\Delta\theta \sim d/L$. In this configuration limitation due to finite mode-hop-free range is expressed by

$d/L << (\Delta f_{MHF}/f)(c/ v_b \sin\theta)$,

which means sufficiently long mirror distance enables us Doppler shift free configuration. With almost parallel ($\theta \sim 0$) configuration, practical absorption length of about 1m is achieved. Typical layout of mirrors is shown in Fig. 2(b). The laser passes contributing to absorption are, for example, that from left to right, while the counter parts are not affected due to different Doppler shift. An effective absorption length 1.05 m with 12 reflections (0.15m for one pass) is achieved under the following conditions: θ = 4 degree, D = 50 mm, L = 0.8 m, d = 2.5 mm, and helium-beam diameter is 10 mm. In this configuration severe stability of the beam energy is required. On the other hand, with the right angle ($\theta = \pi/2$) configuration, robust measurement against unexpected variation of beam velocity is available. When mirrors with diameter of 50 mm are opposed with a distance 1 m and the beam trajectory passes through the center of the opposed mirrors with the right angle [Fig. 2(c)], absorption length of approximately 0.1 m will be achieved.

3. Results and discussion

3.1. Laser absorption spectroscopy applied to the PROMESTA device

The line density of the metastable helium atoms in the PROMESTA device was measured using the diode laser absorption spectroscopy. When the laser light is absorbed in a length l of a swarm of metastable atoms, the population density $n^* = n(2^3S_1)$ of metastable atoms is obtained by $n^* l\sigma(f) = -\ln(I(f)/I_0)$ [11], where f is the laser frequency, and $I(f)$ and I_0 are the laser power after and before the absorption, respectively. The absorption cross section $\sigma(f)$ is deduced from a Doppler-broadened spectrum.

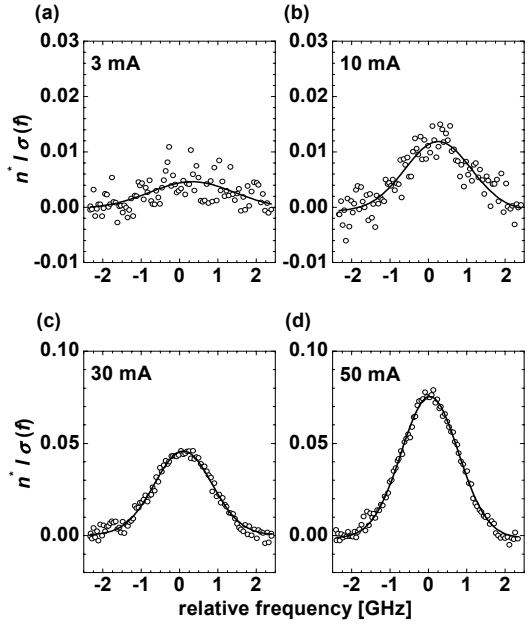

Fig. 3 : Laser absorption spectra obtained at various discharge current: (a) 3 mA, (b) 10 mA, (c) 30 mA, (d) 50 mA.

Absorption spectra obtained at some discharge current are shown in Fig. 3. To avoid a saturation of absorption, the laser power was attenuated to be less than 50 μW. The line density increases with the discharge current up to $9.03\pm0.19\times10^{14}$ m^{-2} [Fig. 3(d)], while in the case of the lowest discharge current a line density of $8.4\pm4.8\times10^{13}$ m^{-2} is obtained [Fig. 3(a)]. The temperature of the metastable helium atoms remains constant near room temperature. This result suggests that a line density more than 5×10^{13} m^{-2} is accurately measured by the present measurement system.

3.2. Improvement of density resolution

A density of the helium neutral beam produced for the proof of principle experiment[5,6] is 5×10^{11} m^{-3}. A less than 10% metastable fraction resolution is required for diagnostics of the helium neutral beam. Thus a density resolution of 5×10^{10} m^{-3} is required. When a 1 m absorption length is configured, the density resolution in the present measurement system is about 5×10^{13} m^{-3}. However, three orders discrepancy is overcome by the following improvements of the measurement system.

(i) Applying larger statistical weights of the upper state (g_j) results in much greater sensitivity. Applying laser absorption excitation

to the 2^3P_2 state leads to a level of sensitivity five times higher than the present excitation scheme using the 2^3P_0 state.

(ii) Using a more sensitive detector is required and planned for the diagnostics in the beam experiment. The sensitivity ~0.1 A/W at the wavelength 1083 nm is almost the upper limit of the sensitivity curve of the silicon photodiode. An InGaAs photodiode is more sensitive than silicon's one at 1083 nm; the typical sensitivity is about 0.7 A/W. Thus, an approximately seven-fold improvement is expected by changing the photodiode detector.

(iii) Noise reduction is also available. Because the detector emits white noise, applying lock-in detection is the most effective method. Commercial lock-in amplifiers, for example, have a -60 to -100 dB dynamic reserve, while data averaging applied to the present experiment equivalently has less than -20 dB. To reduce the noise caused by the fluctuation of laser power, another detector intended to obtain a reference signal will be added in the system. Then the noise produced by the fluctuations in laser power will be canceled by the absorption signal and the reference signal.

With these improvements in the detection system, the density resolution is expected to be three to five orders higher than that of the present system. Hence, the measurement of a metastable fraction of the helium neutral beam produced in the proof of principle experiment will be easily achieved.

4. Summary

Laser absorption spectroscopy is applied to measure a helium metastable population density. Density resolution of the measurement system, which is evaluated using a hollow cathode discharge plasma, is determined to be 5×10^{13} m^{-2}. Some improvements will enable us to measure the metastable density in the beam. Practical design of a multiple reflection cell using parallel plane mirrors is proposed. Combination of the improved measurement system and the cell will become a suitable method to measure the metastable population in a neutral helium beam.

Acknowledgments

This work was partly supported by the Ministry of Education, Culture, Sports, Science and Technology of Japan (MEXT) Grant-in-Aid for "*Priority area of Advanced Burning Plasma Diagnostics*," and was also supported by the MEXT Grant-in-Aid for Young Scientists (B), 17740362, 2006.

References

[1] D. E. Post, D. R. Mikkelsen, R. A. Hulse, L. D. Stewart, and J. C. Weisheit, J. Fusion Energy **1**, 129 (1981).

[2] M. Sasao and K. N. Sato, Fusion Technology **10**, 236 (1986).

[3] E. B. Hooper, Jr., P. A. Pincosy, P. Poulsen, C. F. Burrell, L. R. Grisham, and D. E. Post, Rev. Sci. Instrum. **51**, 1066 (1980).

[4] M. Sasao, A. Taniike, M. Nishiura, and M. Wada, Rev. Sci. Instrum. **69**, 1063 (1998).

[5] K. Shinto, H. Sugawara, S. Takeuchi, S. Kitajima, M. Takenaga, M. Sasao, M. Nishiura, O. Kaneko, S. Kiyama, and M. Wada, In *Proceedings of 2005 Particle Accelerator Conference, Knoxville, Tennessee* (2005) p. 2630.

[6] N. Tanaka, H. Sugawara, S. Takeuchi, S. Asakawa, A. Okamoto, K. Shinto, S. Kitajima, M. Sasao, and M. Wada, *to be appeared in* Plasma Fusion Res.

[7] A. Okamoto, K. Shinto, S. Kitajima, M. Sasao, *to be appeared in* Plasma Fusion Res.

[8] H. Scheibner, St. Franke, Samir Solyman, J. F. Behnke, and C. Wilke, and A. Dinklage, Rev. Sci. Instrum. **73**, 378 (2002).

[9] M. W. Millard, P. P. Yaney, B. N. Ganguly, and C. A. DeJoseph Jr., Plasma Sources Sci. Technol. **7**, 389 (1998).

[10] M. Aramaki, Y. Okumura, M. Goto, S. Muto, S. Morita, and K. Sasaki, Jpn. J. Appl. Phys. **44** 6759 (2005).

[11] W. Demtroder, *Laser Spectroscopy*, 3rd Ed., Ch. 6, Springer, (2003).

[12] A. Okamoto, T. Kobuchi, S. Kitajima, M. Sasao, Plasma Fusion Res. **2**, 029 (2007).

Local Diagnostics of Hydrogen Atom and Molecular Density Based on Laser Induced Ionization in FT-2 Tokamak

M.Yu.Kantor[1,2], L.A.Esipov[1], D.V.Kouprienko[1],
I.C.Nascimento[3], J.H.F.Severo[3], S.P.Yaroshevich[1]

[1]*Ioffe Institute RAS,194021, Saint-Petersburg, Russia*
[2]*temporarily at the FOM-Institute, Association EURATOM-FOM, 3430 BE Nieuwegein, The Netherlands*
[3]*Institute of physics of the University of Sao-Paulo, Brazil*

A local diagnostic for hydrogen atom and molecular densities based on quenching the line emission of excited hydrogen atoms by laser ionization has been developed at the FT-2 tokamak. A special multi-pass intracavity system has been proposed to provide a high diagnostic accuracy. Local densities of hydrogen atoms in the 3rd and 4th excited levels were measured by quenching the H_α and H_β line intensities. The ground state atom density has been derived assuming a radiative-collisional equilibrium. The local density of hydrogen molecules at the plasma edge has been calculated from excited atom densities as well.

1. Introduction

Local measurements of hydrogen atom density with Laser Induced Ionization (LII) [1] in confined plasma is based on laser ionization of excited atoms and quenching their line emission. The LII method takes important advantages over widely used Laser Induced Fluorescence [2] technique. It utilizes more simple laser and light detection system since the laser and emission wavelengths are well separated from each others.

The diagnostic utilizes lasers with photon energy exceeding the ionization energy from the atom level of interest and requires probing beam intensity in plasma ~10 MW/cm^2 for strong domination of laser ionization over recombination rate. These conditions should be combined with a large laser beam cross section and long pulse duration to get high quenching signals. The diagnostic sensitivity referred to the local density of excited atoms n_k at the level with principal number k at dominating photon counting noises is estimated as:

$$n_{k\min} = \sqrt{2\frac{n_{kL}}{D^2 S\Delta t}\frac{1}{A_{km}\Delta\Omega\eta}}\ .$$

where n_{kL} is the density of excited hydrogen atoms integrated along the line of sight, S is the cross section the observed radiated volume, D is the deepness of radiated volume along the line of sight, $\Delta\Omega$ is the solid angle of light collection, A_{km} is the probability of spontaneous radiation decay from k^{th} to m^{th} atomic level, Δt is the measurement time interval and η is the light detection efficiency including both the detector quantum efficiency and collection optic transmission.

The diagnostic sensitivity improves with probing cross section and pulse duration. A new multipass system has been developed for LII diagnostics to increase these values keeping high laser beam intensity in plasma. The system has been used in FT-2 tokamak with ruby laser which is capable to ionize hydrogen atoms starting from k=3 and to measure quenching both H_α and H_β line emissions.

2. Diagnostic system

General layout of the LII diagnostic system in the FT-2 is shown in Fig.1. A single ruby laser distanced from plasma by ~10 meters generates a beam (20 mm diameter, 1 mrad divergence) which is focused in the plasma center by a lens of F=3300 mm. The beam polarization is oriented so that to get minimal reflection from Brewster windows. The multipass system consists of two spherical mirrors 80 mm diameters, 2000 mm curvature radii and distanced by 2525 mm from each other. The beam comes in 16 cm diameter plasma through a 10 mm hole in the top spherical mirror, passes plasma 22 times and escapes the multipass system through the entrance hole in the direction of the ruby rod. Fig. 2 shows the beam path in the multipass system and the sequence of beam reflections denoted by numbers. Plasma light is collected along the beam fan in the vertical direction. The new multipass system combines a wide

radiation volume and long pulse duration which allow a high diagnostic sensitivity.

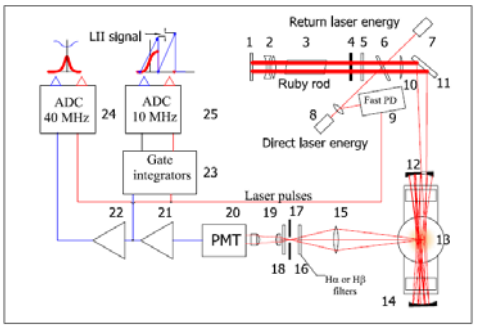

Fig.1: Diagnostic system layout
1. Rear flat mirror, 2. Laser objective, 3. Ruby rod, 4. Saturable absorber, 5,6. Flat glass plates 7,8. Laser energy meter heads, 9. Fast photodiode, 10. Focusing lens, 11. Flat steering mirror, 12,14. Spherical mirrors, 13.Plasma, 15. Collection objective, 16. Optical filters,17. entrance slit, 18. Notch filter, 19. Objective for PMT, 20 PMT, 21, 22. Amplifiers, 23. Gate integrators, 24. ADC 10 MHz, 25. ADC 40 MHz.

After amplification in the rod, the beam is reflected from rear mirror (1) back to plasma. So, the rear mirror and multipass system form a laser cavity of 75 m long and takes advantages of laser intracavity multipass probing [3] – multiple generation of laser pulses with the total probing energy as high as 750 J. (see Fig. 3).

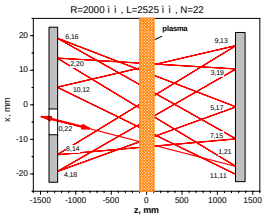

Fig.2: Beam path in the multipass system

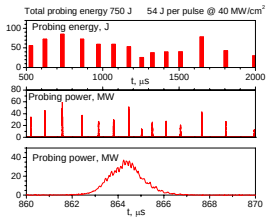

Fig. 3: Laser oscillation

The beam cross sections in the plasma center are shown in Fig.4. The upper section presents ray-tracing of laser beams emitted from the ruby rod face within 1 mrad divergence angle. The numbers indicate the pass numbers. The cross section of laser beam fan (4*25 mm) is much bigger than that of the multipass system for Thomson scattering in the FT-2 [3] shown in the figure as well.

The image of the laser fan cross section in the plasma center shown in Fig. 4b is well consistent with ray-tracing calculations. It was taken as reflections of even pass beams from Brewster window placed near the bottom mirror (14). High intensity of the 2-nd pass beam relates only to enhance reflection of small S-polarized portion of incident beam which completely reflected out after a few passes. Then, the reflected beams keep their intensity indicating low light losses in the multipass system (Fig. 4c).

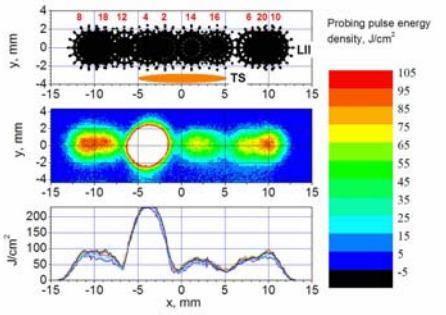

Fig. 4: Laser beam fan cross sections
a. ray tracing, b. beam image, c. central image slices.

Light was collected from 15 mm high radiated volume within 0.009 steradians solid angle by an objective (F=260 mm, f/2.5). H_α or H_β line were separated by ~2 nm pass band optical filters having 30% transmissions. Additional notch filter rejected the ruby laser wavelength out. The collected light was projected onto the photocathode of Hamamatsu R943-2 photomultiplier (15% QE).

PMT and laser signals were recorded by two 40 MHz 12 bit ADCs. A slower ADC couple of 10 MHz 12 bits stored these signals integrated during laser pulses and immediately afterwards.

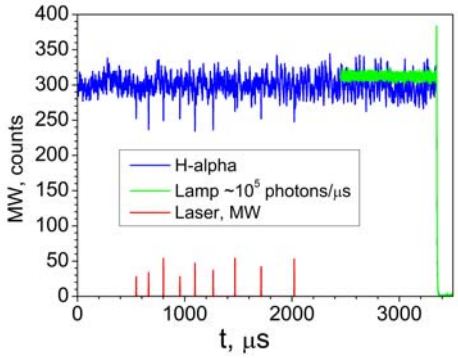

Fig. 5: Quenching Ha by laser probing pulses

Quenching H_α plasma emission at r=6 cm in steady state Ohmic discharge is shown in Fig. 5. The quenching signals are better seen in Fig. 6 in a lager time scale. There are nine time windows 30 μs wide each, corresponding to laser pulses. The 10th window contains noise signal measured at steady-state illumination level corresponding to plasma H_α

emission. Smoothed background H_α emission was polynomial fitted outside laser pulse within 30 μs time window and subtracted from the measured signals. The resulting LII signals together with laser pulses are presented in the same figure beneath. The integrated LII signals shown by circles demonstrate a high measurement accuracy.

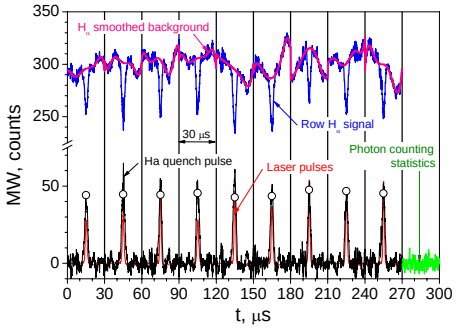

Fig. 6: LII signals and laser pulses in expanded time scale

3. Saturation of quenching

Analysis of saturation of LII signals should precede any measurements for correct LII data elaboration. The saturation of the 3rd energy level of

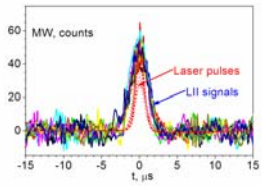

Fig. 7: Time broadening LII signals

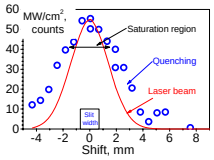

Fig. 8: Spatial broadening LII signal

hydrogen atoms is revealed as time and spatial broadening H_α LII signals in respect to laser probing pulse shape (Fig.7) and laser beam intensity profile (Fig. 8).

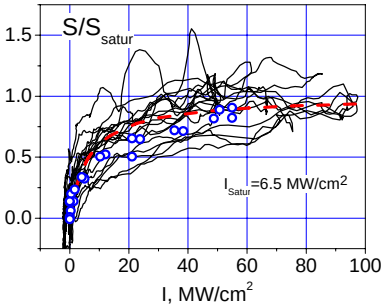

Fig. 9: Saturation of quenching

The saturation intensity I_{S3} of the 3rd energy level is found to be 6.5 MW/cm^2 from fitting these normalized LII data versus probing intensity I with saturation function $I/(I+I_{S3})$ (Fig. 9). The saturation intensity of the 4th energy level measured for Nd laser beam is 1 MW/cm^2 [1]. For ruby laser it gives I_{S4}~5 MW/cm^2 taking into account λ^{-3} scale of the photoionization cross section with laser wavelength [4].

Thus, to meet the saturation conditions, light was collected from 3 mm strip along the laser beam fan cross section and LII signals were elaborated for laser probing power higher than 10 MW only.

4. Measurements

Hydrogen atom and molecular densities were measured at steady state part of ohmic discharges. Main discharge parameters are: B_T=2.2 T, I_P=22 kA, $n_e(0)=3*10^{13}$ cm^{-3} and $T_e(0)$=400 eV. Fig. 10 and 11 show measurement data in terms of the number of photons collected for H_α and H_β spectral lines when the collection system scanned plasma. Two gas puffing pipes were located at the tokamak bottom in opposite poloidal cross sections distanced by 90^o angles from the diagnostic cross section.

Squares and circles refer to the number of photons collected correspondingly along the viewing plasma chord and quenched in the observed radiated plasma region of 1.125 cm^3. Dash curves present chord emission calculated from the measured local emission assuming axial symmetry of hydrogen atoms in plasma. The difference between the measured and reconstructed chord emissions reveals a significant asymmetry of hydrogen atom distribution both in the tokamak major

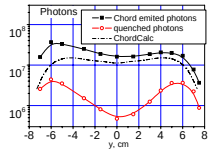

Fig.10: Chord and quenched H_α emission

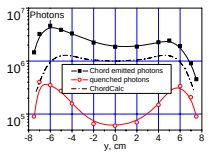

Fig.11: Chord and quenched H_β emission

radius and vertical direction.

The statistical error of measurements in a single laser pulse scales from ~3% at the edge to ~30% in the plasma center. Averaging all laser pulses in the train

improves the central error down to ~10%. The errors expected from the collected photon flux are ~1.5% at the plasma edge and 9% in the center. Poorer errors are accounted for preamplifier noises.

5. Analysis

Local densities of excited hydrogen atoms at the 3rd and 4th energy levels are calculated straightforward from the LII signals for H_α and H_β lines and shown in Fig. 12.

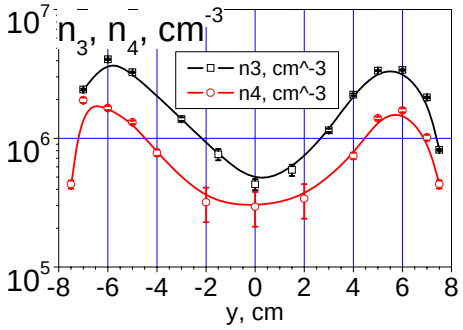

Fig. 12: Local density of excited hydrogen atoms

Local ground state atom densities (Fig.13) are derived from the excited atom densities assuming collisional-radiative equilibrium in plasma and using tabulated population coefficients [5]. Two profiles are obtained independently from H_α and H_β quenching are in a good agreement to each other.

Measured n_3 and n_4 profiles allow the calculation of molecular hydrogen density in plasma. According [6], the population of hydrogen atoms at

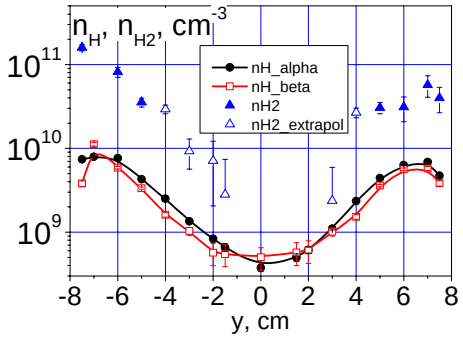

Fig. 13: Local densities of ground state hydrogen atoms and molecules.

the excited level with principal number k in the collisional-radiative model is given by

$$n_k = R_k^1 n_H n_e + R_k^2 n_{H_2} n_e$$

The molecular hydrogen density n_{H2} was found using this formula and tabulated population coefficients $R_k^{1,2}$ from two measured excited atom densities n_3 and n_4 and known electron density and temperature. The resulting local molecular density profile is shown in Fig. 13. Solid blue triangles were obtained from tabulated R values (T_e<100 eV), while opened triangles give estimation of the molecular density from R values extrapolated to T_e=350 eV. Error bars denote the statistical error of the measurements. But uncertainty of molecular density is most determined by irreproducibility of plasma because n_3 and n_4 values were measured in different discharges. A simultaneous measurement of latter densities improves significantly reliability of molecular hydrogen density profiles.

6. Conclusion

Local diagnostics of hydrogen atom density based on laser induced ionization and using new multipass intracavity probing system is capable to measure hydrogen ground state density as low as 10^8 cm^{-3} at 10% accuracy.

A good consistency of ground state hydrogen densities measured independently with quenching H_α and H_β emission lines has proved the collisional-radiative model for the FT-2 experimental conditions (ne=3*10^{12}-3*10^{13} cm^{-3} and Te=30-400 eV).

The molecular hydrogen density calculated from laser quenching H_α and H_β emissions is as high as 10 times higher than edge hydrogen atom density.

Acknowledgments

This work was partially supported by FAPESP – Foundation for the Support of the Research of the State of Sao Paulo, Brazil.

References

[1] V.Gladushchak, V.Gusev, M.Kantor et al. Nucl Fus. **35** (1995) 1385.
[2] G.Razdobarin et al. Nucl. Fus. **19** (1979) 1439.
[3] M.Kantor, D.Kouprienko. Rev. Sci. Instr. **70** (1999) 780.
[4] H.Kramers. Phil. Mag. **46** (1923) 836
[5] L.C.Johnson, E. Hinnov. J. Quan. Spectr. Rad. Trans. **13** (1973) 333.
[6] T.Fujimoto, K.Sawada, K.Takahata. J. Appl. Phys. **66** (1989) 2315.

Application of Laser Thomson Scattering to PDP Micro-discharges

Y. Sonoda, A. Akune, K. Tomita, S. Hassaballa, K. Uchino

Kyushu University, 6-1 Kasuga-kouen, Kasuga, Fukuoka 816-8580, Japan

In order to avoid laser perturbations for Xe containing discharges, the Laser Thomson scattering (LTS) system having an infrared laser at a wavelength of 1064 nm as a light source has been developed. It was found that linear LTS signals could be obtained if the power density of the infrared laser would be adjusted properly depending on the condition of discharges in the Ne/Xe gas mixture. The basic behaviour of electrons in the Ne/Xe discharges was investigated by using the infrared LTS system. Furthermore, it was demonstrated that the measurement of the electron energy distribution function was possible up to the electron energy corresponding to the excitation energy of the Xe atom.

1. Introduction

The plasma display panel (PDP) is leading the competition for the large-area flat panel display. One of the most important issues for PDP is improvement of its low luminous efficiency. In order to improve the efficiency, understanding of the PDP micro-discharges through direct measurements of the discharge parameters, such as the electron density (n_e) and the electron temperature (T_e) are necessary. For this purpose, we have applied laser Thomson scattering (LTS) to measure both n_e and T_e in PDP micro-discharges [1].

LTS is the non-intrusive method for measurements of plasma properties. In the incoherent regime, the scattered spectrum reflects the T_e, and the scattered intensity is proportional to n_e.

So far, using the visible LTS system, which has the frequency doubled Nd:YAG laser (λ=532 nm) as a light source, we have performed measurements of n_e and T_e of PDP micro-discharges produced in Ne/Ar gas mixtures [2, 3]. However, visible laser beams perturb Xe containing plasmas [4]. In order to overcome the situation, we have developed an infrared LTS system, which uses the fundamental output of the Nd:YAG laser (λ = 1064 nm). Using this system, we could measure n_e and T_e of the plasmas produced in Ne/Xe gas mixtures. Results of measurements for Ne/Xe plasmas are reported.

2. Summary of LTS measurements using a visible LTS system

For our first LTS system, we used the frequency doubled Nd:YAG laser as a light source. When we applied the LTS method to micro-discharge plasmas, there were two main difficulties, namely the small scattering volume and the high stray light level. The small size of micro-discharge plasmas implies a small scattering volume, which results in a very small Thomson scattering signal. This difficulty could be overcome by using the photon counting accompanied by data accumulation method.

The second difficulty is that the stray laser light is very strong because the wall of the discharge cell is very close to the discharge volume. In order to overcome this problem, we designed a special triple grating spectrometer (TGS). The stray light rejection factor of the TGS was measured to be 10^{-8} at $\Delta\lambda$ = 1 nm away from the laser wavelength. This high rejection allowed us to apply the LTS method to micro-discharge plasmas.

We achieved the spatial resolution to be below 50 μm for the LTS measurements. Then, we could perform LTS measurements at points as close as 60μm from the electrode surface for micro-discharges produced in a Ne/Ar gas mixture.

The structure of the PDP plasma was investigated by performing measurements of n_e and T_e distributions. We paid attention to the striation phenomenon which had been universally observed above the anode of ac-PDP [5, 6]. The mechanism of the striation phenomenon is not clear yet. The discharge was produced in the Ne/Ar (10%) gas mixture at a pressure of 200 Torr. Results of the LTS measurements showed modulations in both n_e and T_e profiles above the anode, and these modulations had a similar trend to striations appeared in the optical emission images. Also, it was found that the modulations

in n_e and T_e were out of phase [3, 7]. In order to examine the structures of n_e and T_e distributions more precisely, we performed LTS measurements for the discharge at a pressure of 100 Torr. In this condition, the pattern of the striation was large enough to be resolved by the LTS measurements. Figure 1 shows spatial distribution of n_e and T_e measured above the anode for the plasma produced in the Ne/Ar (10%) gas mixture at a pressure of 100 Torr. The modulations in n_e and T_e were clearly observed, and the phase difference was about 180 degree.

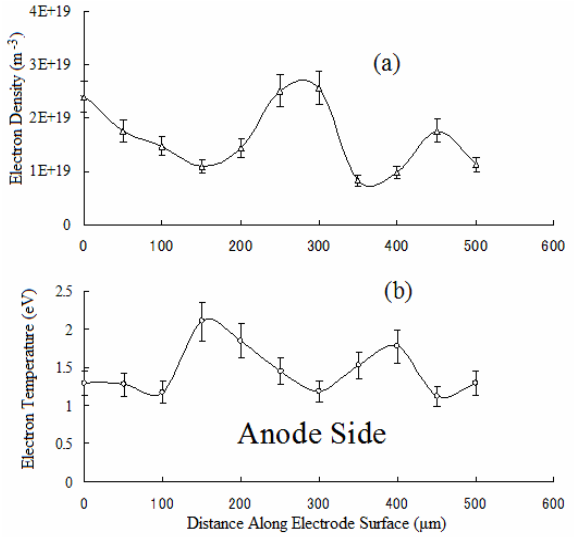

Fig. 1: Measured profiles of n_e and T_e for Ne/Ar (10%) at a pressure of 100 Torr.

3. Experiments using an infrared LTS system

3.1 Experimental setup

The configuration of the electrodes used in this study is shown in Fig. 2. The structure was similar to the sustaining electrodes of a coplanar ac-PDP. The electrodes were built on a glass substrate which has a width of 2 mm and a thickness of 3 mm. The electrodes had a discharge gap of 0.1mm. The electrodes were covered with a 15 μm glass layer, followed by a 0.5 μm MgO layer.

Figure 3 shows the schematic diagram of the experimental setup. The system was similar to the system using a visible light source. Differences were the laser light source having a wavelength of 1064 nm and the optical components, such as achromatic lenses and gratings used in the triple grating spectrometer (TGS), which were designed for 1064 nm. Also, the detector was for 1064 nm, namely an infrared photomultiplier tube (Hamamatsu, R5509) which had a quantum efficiency of ~5 % at 1064 nm and could be used for the photon counting mode.

The electrode substrate was housed in the chamber. After evacuating the dischage chamber, the Ne/Xe mixture was introduced. Alternating voltage pulses with a square waveform were applied between the electrodes at a frequency of 20 kHz and duty ratio of 0.4. The peak value of the applied pulse voltage was 270 V.

The performance of the LTS system was examined by conducting Raman scattering measurements from hydrogen gas. One of the rotational Raman scattering lines of the hydrogen gas was observed at about 41 nm away from the laser wavelength on the longer wavelength side. The observation wavelength of the system was tuned to this line by rotating the three gratings of the home-made infrared TGS, and we confirmed that rotation angles of these gratings were just as calculated, indicating that the optical components of TGS were properly arranged at designed positions. Also, we confirmed that the signal intensity was linear against the gas pressure. The absolute intensity of the observed Raman signal was 80 counts per 1000 laser shots when the laser energy was 20 mJ and hydrogen gas pressure was

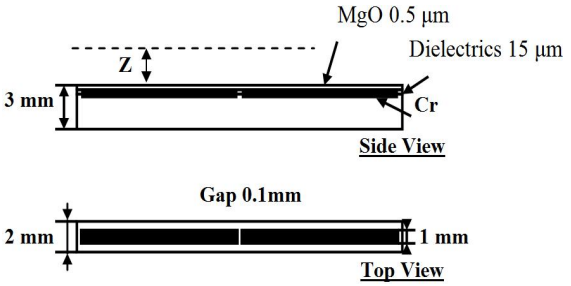

Fig. 2: Schematic diagram of the structure of the electrodes.

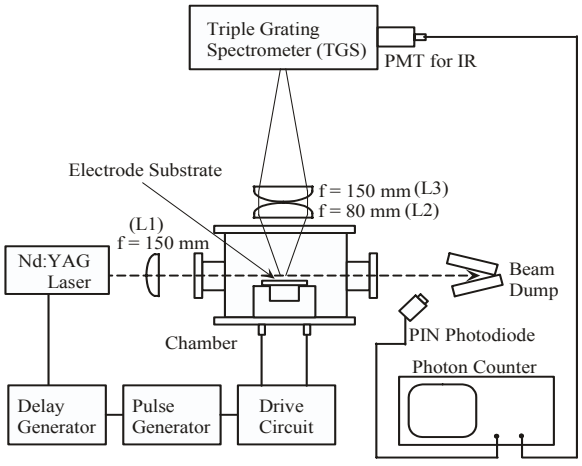

Fig. 3: Experimental setup.

100 Torr. This Raman signal corresponds to the Thomson scattering signal from the plasma having an electron density of 2×10^{18} m^{-3}. For the actual measurements, the Thomson scattering spectra should be analyzed by observing the scattering intensitiy at several differential wavelengths. Nevertheless, we can expect enough signal-to-noise ratios for Thomson signals when the electron density is more than 1×10^{19} m^{-3}. After confirming the performance of the infrared LTS system to be sufficient, we performed measurements of n_e and T_e distributions in plasmas produced in Ne/Xe gas mixtures.

3.2. Results and discussion

3.2.1 Laser Perturbations

In order to know the influence of the fundamental output of Nd:YAG laser on the plasmas in Ne/Xe gas mixtures, linearity of LTS signals against the laser pulse energy was examined. The variations in LTS signal intensity against the laser energy are shown in Fig. 4 for Xe percentages of 10 % (a), 20 % (b), and 30 % (c). In Fig. 4, the solid lines show the signal is linearly proportional to the laser energy and dotted lines show the signal is proportional to the 4th power of laser energy. Here, the laser energy of 4 mJ corresponds to the laser intensity of 10^{15} W/m^2. These measurements were carried out at the points where largest LTS signals were observed. Other conditions were fixed as follows. Gas pressure was 200 Torr, observation time was 270 ns from the start of the discharge, and the observed wavelength was at $\Delta\lambda$=2.6 nm from the laser wavelength (1064 nm).

It can be seen from Fig. 4 (a) that the LTS signal is linearly proportional to laser energy in the range < 20 mJ. While for laser energy > 20 mJ, the LTS signals deviate from the linearity and proportional to the 4th power of laser energy. This 4th power dependence can be due to the photo-ionization of meta-stable Xe atoms by 3 photon absorption. For higher Xe percentages, as shown in Fig. 4 (b) and (c), LTS signals deviate from the linearity at lower laser energy. This can be due to the increase of the excited Xe density with the increase of Xe percentage.

Obviously, LTS measurements must be done with the laser energy in the linear ranges of Fig. 4. Therefore, for new discharge conditions, signal linearity against laser energy must be checked before the full measurements of scattered spectra.

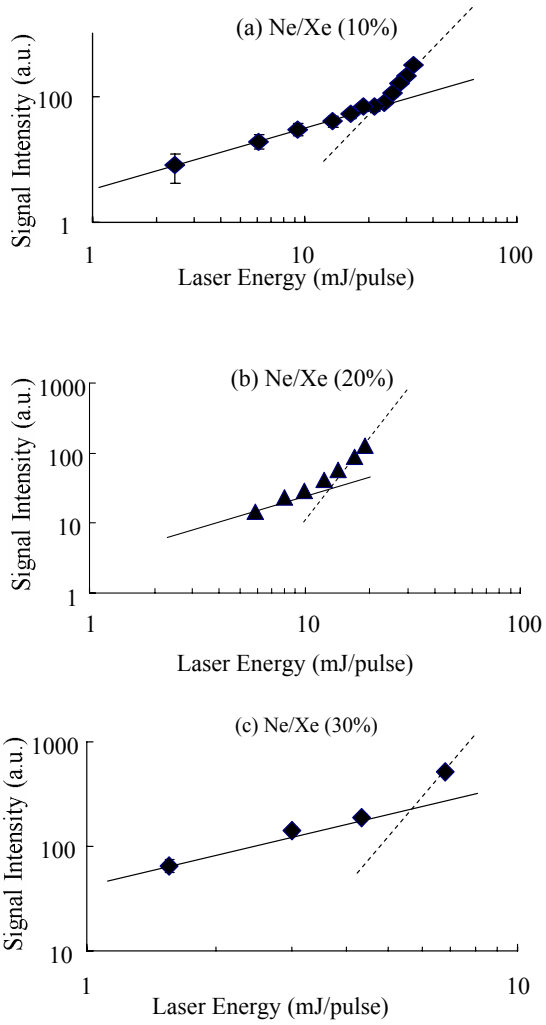

Fig. 4: LTS signal intensity against laser energy.

3.2.2 Results of LTS measurements

Figure 5 shows distributions of the LTS signals along the electrode surface for different Xe percentages of 5, 10, and 30 %. Measurements were performed at a fixed height of 100 μm above the electrode surface and at a fixed wavelength ($\Delta\lambda$=2.6 nm). The signal intensity at this wavelength is relatively insensitive against T_e in the range T_e =1.5 – 3 eV. Therefore, these distributions can be considered to indicate electron density distributions in the relative scale. It can be seen from Fig. 5 that the LTS signals increase with the increase of the Xe percentage.

In addition, height distributions of n_e and T_e above the electrode surface were measured at the

gap for different Xe percentages. Results showed that the positions of the density peaks were found to be inversely proportional to the Xe percentage, being closer to the electrode surface for the higher Xe percentage. This is because the effective mass of the discharge gas becomes heavier for the higher Xe percentage, and then, the diffusion of plasma particles are suppressed for the heavier effective mass of the gas.

The most remarkable characteristics of PDP micro-discharges are its unsteadiness and non-uniformity. Therefore, the electron energy distribution function (EEDF) of PDP micro-discharge plasmas would not be Maxwellian. If EEDF was non-Maxwellian, the measured T_e would not reflect the component of the high-energy electron. The excited energy level of Xe gas corresponding to 147 nm line lies at 8.3 eV above the ground level. The population of this level directly concerns with the luminous efficiency, and the excitation to this level are done by electrons having an energy > 8.3 eV. Therefore, measurements of electron components having energy > 8.3eV is very important.

Figure 6 shows a Thomson scattering spectrum measured for the discharge plasma produced in the Ne/Xe (20 %) gas mixture at a pressure of 100 Torr. The measurement was performed for the point at a height of 130 μm above the electrode surface, and at time of 270 ns from the start of the discharge pulse. In Fig. 6, Thomson scattering intensitiy are plotted in a logarithmic scale in the ordinate against the square of the differential wavelength from the laser wavelength $(\Delta\lambda)^2$, which is proportional to the electron energy, in the abscissa. From the straight line of the Thomson spectrum, we concluded that the EEDF was Maxwellian up to 8.5 eV, and from the slope of the spectrum, we obtained an electron temperature T_e of 2.5 (±0.6) eV. The Raman scattering calibration of the whole optical system gave the electron density n_e to be 5 (±2) × 10^{19} m^{-3}.

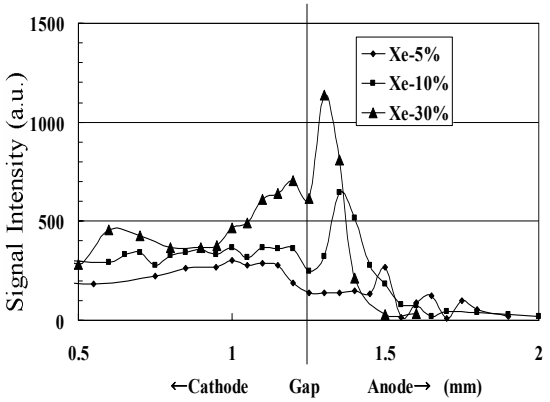

Fig. 5: Distributions of LTS sinals along the electrode surface.

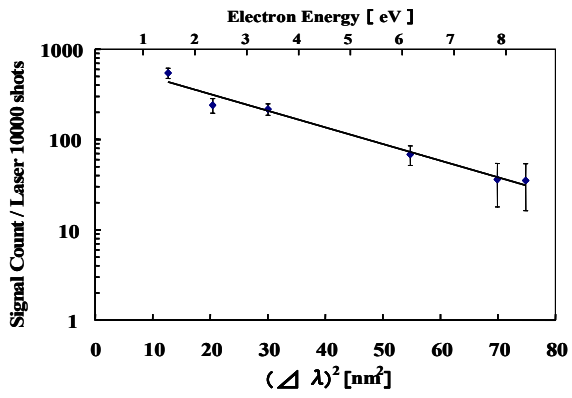

Fig. 6: Laser Thomson scattering spectrum.

4.Conclusion

We have developed an infrared LTS system. It was found that the system was very effective for measurements of n_e and T_e of PDP micro-discharge plasmas produced in the Ne/Xe gas mixtures. Also, we succeeded for the firsts time in collecting LTS signals from electron components having an energy more than the excitation energy of the Xe meta-stable atom.

References

[1] Y. Noguchi, T. Hondou, K. Uchino, K. Muraoka and N. Kosugi: IDW ’01 901.

[2] S. Hassaballa, M. Yakushiji, Y.K. Kim, K. Tomita, K. Uchino and K. Muraoka: IEEE Trans. Plasma Science **32** (2004) 127.

[3] S. Hassaballa, Y. Sonoda, K. Tomita, Y.K. Kim and K. Uchino: J. SID **13** (2005) 639.

[4] K. Tomita, Y.K. Kim, S. Hassaballa, M. Yakushiji, K. Uchino and M. Muraoka: IDW ’03 1049.

[5] G. Cho, E. H. Choi, Y. G. Kim, D. I. Kim, H. S. Uhm, Y. D. Joo, J. G. Han, M. C. Kim and J. D. Kim: J. Appl. Phys. **87** (2000) 4113.

[6] T. Yoshioka, A. Okigawa, L. Tessier and K. Toki: IDW’99 603.

[7] S. Hassaballa, K. Tomita, Y.K. Kim, K. Uchino, H. Hatanaka, Y.M. Kim, C. H. Park, K. Muraoka: Jpn. J. Appl. Phys. **44** (2005) L442

Development of a System for Measuring Flow Vector using Planar Laser Induced Fluorescence

E. Kawamori[1], S. Akanuma[2], C. Z. Cheng[1], Y. Ono[2]

[1] *Plasma and Space Science Center, National Cheng Kung University, Ta-Hsueh Road, Tainan 70101, Taiwan*
[2] *Graduate School of Frontier Sciences, University of Tokyo, Kashiwa-shi, Chiba 277-8568, Japan*

A novel method to measure two-dimensional (2-D) spatial profiles of flow velocity vector in Scrape-Off Layer (SOL) is proposed on the basis of Planar Laser Induced Fluorescence (PLIF) technique using RApid Frequency Scan (RAFS) Dye-Laser. This method will enable us to diagnose various flow structures in SOL of burning plasmas. At present status, the RAFS laser system and the measurement system of time dependent LIF signal that is used to obtain the poloidal components of flow velocity vector have been designed and are under construction.

1. Introduction

In recent years, significant progress has been made toward understanding the role and importance of plasma flow in scrape-off layer (SOL). Attempts to elucidate the mechanism of the flow generation and to control the flow by puff and pump or the divertor shape have been made intensively. Plasma flow toward divertors, which balances with the thermal force of impurity ions, is needed to confine impurities such as argon or neon seeded in order to reduce peak heat flux to plasma facing components and sputtered from the first wall in divertor region. Therefore, especially in burning plasmas, multipoint measurement of flow from SOL to diverter will be required for sustainment of high performance discharges.

The following two techniques have been mainly utilized for flow measurement in SOL so far: One is conventional Mach probe measurement with fast-scanning technique, which has been applied to JT-60U [1], Alcator C-Mod [2] and so on. This method led to reveal existence of "flow reversal" near separatrix in SOL in many Tokamaks. Another is tracer-gas injection technique which is developed in Alcator C-mod [3]. Gaseous impurities are injected from the tip of the probe inserted to the SOL plasma. CCD cameras view the toroidal and poloidal dispersion of the resultant visible-light emission plumes through selected optical interference filter. Although high spatial resolution and time resolution can be achieved by using fast scanning Mach probe method, it has some drawbacks such as being in-situ method, ambiguity of flow direction and absolute value of flow and so on. On the other hand, tracer-gas injection technique is a powerful tool which makes us to understand phenomena visibly. However this technique lacks quantitative accuracy. In this paper, a novel method to measure two-dimensional (2-D) spatial profiles of flow velocity vector in Scrape-Off Layer (SOL) is proposed on the basis of Planar Laser Induced Fluorescence (PLIF) technique using RApid Frequency Scan (RAFS) Dye-Laser. This method will enable us to diagnose various flow structures in burning plasmas.

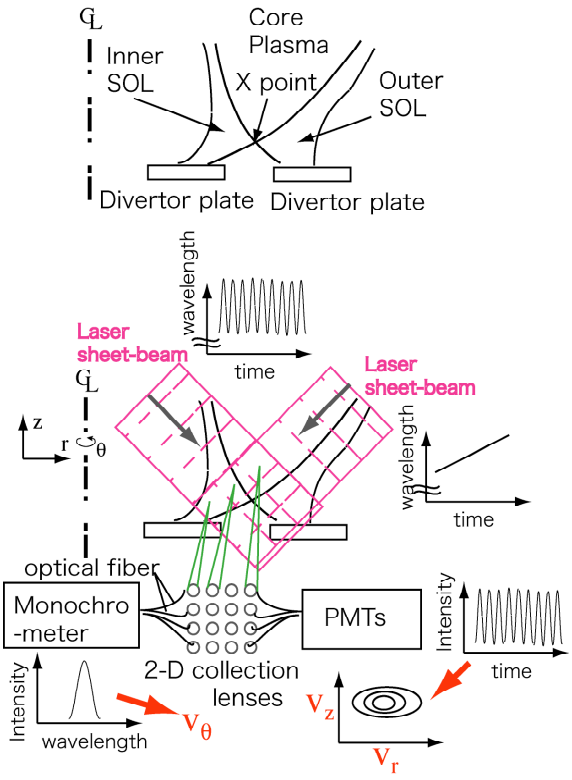

Fig. 1 : Schematic view of proposed method measuring flow vector on poloidal plane of SOL region.

2. Proposed method to measure two-dimensional spatial profile of flow vector

Figure 1 shows a schematic of proposed method to obtain two dimensional (2-D) spatial profile of flow vector on poloidal cross section in SOL region. Planar laser beam is injected into a measuring plane (poloidal plane) in order to induce fluorescence of the ions. Then spatially 2-D Doppler spectroscopy along viewing lines perpendicular to the poloidal plane provides toroidal components of flow velocities. This spectroscopy is done by a monochrometer. By employing two planar laser lights along different directions and scanning the frequencies of planar laser light with different scanning speed respectively, time evolution of fluorescence emission can be converted to ion distribution function in poloidal velocity space. The time trace of fluorescent light is acquired by photomultipliers (PMTs). In this method, however, time resolution is limited by repetition rate of the lasers. In near future, this drawback may be solved because recent progress of YAG laser is making its repetition rate reach a range of 1-5 kHz with its energy of 1-3 J [4].

3. Design of the system

The measurement system using the proposed idea has been now developed to install in the UTST (University of Tokyo Spherical Tokamak) device at University of Tokyo [5].

3.1. RAFS Nd-YAG/ Dye Laser

Scanning the frequencies of planar laser light is accomplished by using Rapid Frequency Scan (RAFS) Dye-laser [6]. We designed to employ PZT driven etaron as the frequency scanner of RAFS Dye-laser. The center wavelength of transmittance of the etaron is 611.492 nm because the excitation of $3d^2G_{9/4}$-$4p^2F_{7/2}$ (611.492nm) of ArII is considered. We utilize a dye laser (LAS, LDL Integra) with a pumping Nd-YAG laser (200 mJ at wavelength of 532 nm) as laser light source of the RAFS Dye-laser system.

Because LIF is a resonant process, the cross section for absorption of the laser photon is large, resulting in lower power requirements for the laser light. When the electron absorbs a photon and is excited into a higher energy level, it can decay back to the original state, or some other state, through a spontaneous or stimulated transition. For the spontaneous transition rate A_{ij}, is related to the lifetime in the excited state, independent of any external factors. The stimulated transition rate (the Einstein coefficient) B_{ij} is determined by the spectral flux intensity of the laser source. A laser having sufficient spectral flux intensity will cause the population of the upper level of the transition to reach saturation. This occurs when the ratio of the electron populations of the upper to lower levels equals their statistical weight factors. When the stimulated absorption rate is equal to the spontaneous transition rate, the required laser power I to obtain saturation is given by the equation below,

$$I = \frac{\sum_i A_{2i}}{A_{21}} \frac{g_1}{g_1 + g_2} \frac{8\pi hc^2}{\lambda^5} \Delta\lambda_{FWHM} \ [\mathrm{W \cdot m^{-2}}], \quad (1)$$

where $\Delta\lambda_{FWHM}$ is the linewidth of the laser or the homogeneously broadened absorption linewidth, whichever is greater. A_{2i} is the spontaneous transition rate from the upper level to all possible lower energy states, A_{2i} is the transition rate of

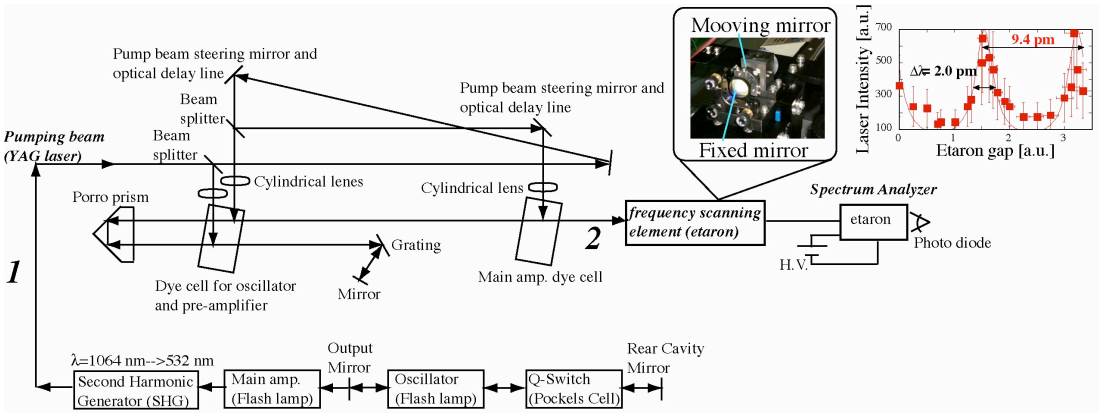

Fig. 2 : Schematic view of RAFS Nd-YAG/ Dye Laser system and the measurement of line width of the laser light by spectrum analyzer. The result is shown in top right.

the level that is excited by the laser, c is the speed of light, and h is Planck's constant. In the case of an atom or ion in a plasma, the situation is further complicated due to collisionally induced excitations.

At first we determine the finesse F of the PZT driven-etaron with air gap d. The maximum scanning range of laser light wavelength $\delta\lambda_{scan}$ is limited by the free spectral range FSR of etaron as shown below:

$$\delta\lambda_{scan} < \mathrm{FSR} \equiv \frac{\lambda^2}{2d},$$

$$\Delta\lambda_{FWHM} > \frac{\mathrm{FSR}}{F} = \frac{1}{F}\frac{\lambda^2}{2d}.$$

Line width $\Delta\lambda_{FWHM}$ of transmittance at λ=611.492 nm is expressed by FSR and F. Therefore, if the scanning range of the velocity and $\Delta\lambda_{FWHM}$ are assumed ±1/4 of the sound speed of argon with temperature of 100 eV and $\delta\lambda_{scan}$ /10 respectively, the air-gap should be limited as shown below,

$$\frac{1}{F}\frac{\lambda^2}{2\Delta\lambda_{FWHM}} < d < \frac{\lambda^2}{2n}\frac{1}{\delta\lambda_{scan}},$$

$$\frac{1}{F}\frac{(611.492\mathrm{nm})^2}{2(\delta\lambda_{scan}/10)} < d < \frac{(611.492\mathrm{nm})^2}{2}\frac{1}{\delta\lambda_{scan}}.$$

As a result, effective (total) finesse of the etaron F is required to be more than 10. The etaron constructed on the basis of the design is shown in the photo of fig. 2. Total transmittance T of the etaron is estimated at 40 %. $\Delta\lambda_{FWHM}$ is about 2 pm from the measurement as shown in the right plot of fig. 2.

Next we estimate the required laser energy W_{Dye} for our configuration of the laser system. Here, W_{Dye} corresponds to the laser energy at the location of 2 in fig. 2. Taking the transmittance of etaron T into account and using 100 times value of eq. (1), W_{Dye} can be calculated as

$$\frac{\sum_i A_{2i}}{A_{21}} = \frac{(2\times10^{-3}+6.1\times10^{-2}+7.89\times10^{-1}+8.0\times10^{-3}+3.7\times10^{-3})\times10^{8}}{7.89\times10^{-1}\times10^{8}}$$
$$= 1.37.$$
$$g_1 = 6, g_2 = 8.$$
$$\therefore\ W_{YAG} = \frac{\Delta\lambda_{before\ etaron}}{\Delta\lambda_{FWHM}}\frac{1}{T}\cdot I\cdot\Delta\tau\cdot A_{sheet}\times100$$
$$= 10\times\frac{1}{0.4}\times1.37\times\frac{6}{6+8}\times\frac{8\pi hc^2}{(611\times10^{-9})^5}\times(2\times10^{-12})\times(3\times10^{-3})\times100\cdot\Delta\tau$$
$$= 153000\cdot\Delta\tau\ [\mathrm{J}], \qquad (2)$$

where $\Delta\lambda_{\mathrm{before\ etaron}}$, A and $\Delta\tau$ are the line width of the laser light just before the frequency scanner etaron, area of cross section of the planar laser light and pulse width of the laser light, respectively. The relation between the required laser energy and pulse width is drawn by blue line in fig. 3 (b). Longer pulse width is better for our proposed scheme as long as the relation expressed by eq. (2) is satisfied because the pulse width should much larger than the life time of the spontaneous transition $4p^2F_{7/2}$-$3s^2D_{5/2}$. In fig. 3 (a), time traces of the laser light intensity of Nd-YAG laser used as pump of the Dye laser are shown. By changing the angle between the beam line and the Pockels cell of Q-switch, pulse width was expanded although the pek intensity and total energy of the laser light dropped markedly. Closed circle in fig. 3 (b) shows the energy and pulse width measured at the location of 2 in fig. 2. At present status, the pulse width could be expanded to 20 ns.

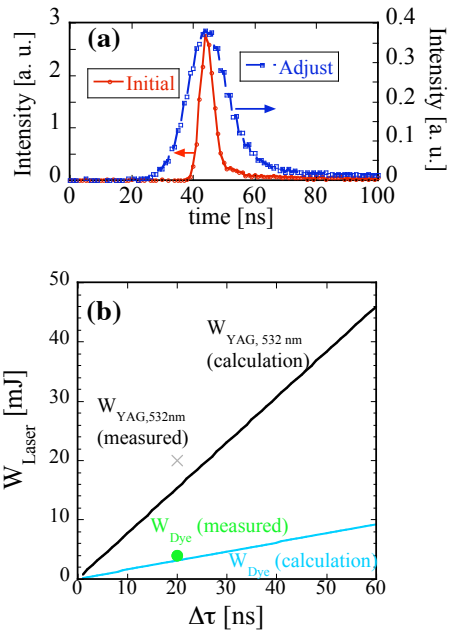

Fig. 3 : (a) Time traces of the laser light of Nd-YAG laser used to pump the Dye-laser. By changing the angle between the beam line and the Pockels cell of Q-switch, pulse width was expanded. (b) Calculated laser energies required for Nd-YAG laser which pumps the Dye laser. Measured energies of the laser system are shown together (cross: measured at the location 1, closed circle: location 2 in fig. 2).

3.2. Measurement system of time dependent LIF signal

Figure 4 shows the toroidal cross section of the configuration of the optical system in the

UTST device. Fluorescence emission induced by the planar laser light is collected by the lenses installed outside the window of the UTST vacuum chamber and transported and divided into a monochrometer and PMTs by two set of optical fiber bundles. Viewing region of each channel is also shown in fig. 4 (yellow and red lines). Optical system including lenses, band pass filters and fiber bundles was optimized by using a ray trace code in the design phase. Spatial resolution of the system is 40 mm both for radial (r) and axial (z) directions. The light transported to the monochrometer with a grating of 2400 grooves/mm (focal length is 50 cm, MC-50, Ritsu Kogaku) is analyzed to obtain the Doppler shift, which represents the toroidal component of the plasma flow.

Another light transported to the PMTs (R928, HAMAMATSU) is acquired temporally through the band pass filter and current-voltage converters by digital scopes. By employing two planar laser lights along different directions and scanning the frequencies of planar laser light with different speed respectively, time evolution of fluorescence emission can be converted to ion distribution function in poloidal velocity space. If we assume the electron density and temperature of argon plasma are 2.5×10^{19} m^{-3} and 20 eV, metastable fraction is about 0.4 % [7]. Then the power W_l collected by one lens and the current converted by the PMT are estimated as,

$$W_l = \frac{g_2}{g_1+g_2} A_{21} n_1(0) V \frac{hc}{\lambda} \frac{d\Omega}{4\pi} = 3.65\times10^{-3}\ [\mathrm{W}],$$

$$I_{PMT} = \eta_{lens}\eta_{filter}\eta_{fiber}\eta_{couple}\eta_{PMT} W_l \approx 0.1\,[\mathrm{mA}],$$

where, η_{lens}, η_{filter}, η_{fiber} η_{couple} and η_{PMT} are the efficiency of the lens-fiber coupling, transmittance of the band pass filter, the fiber transmittance, efficiency of coupling between fiber bundle and photocathode of the PMT and conversion efficiency of photon-current of the PMT, respectively. Here, η_{PMT}= 70 mA/W at λ =461 nm. Total system transmittance is estimated at 0.37. As a result, expected current converted by the PMTs is the order of 0.1 mA, which may achieve good signal-to-noise ratio.

4. Summary

A novel method to measure 2-D spatial profiles of flow velocity vector in SOL is proposed on the basis of PLIF technique using RAFS Dye-Laser. At present status, the RAFS laser system and the measurement system of time dependent LIF signal that is used to obtain the poloidal components of flow velocity vector have been designed and are now under construction to install in the UTST device.

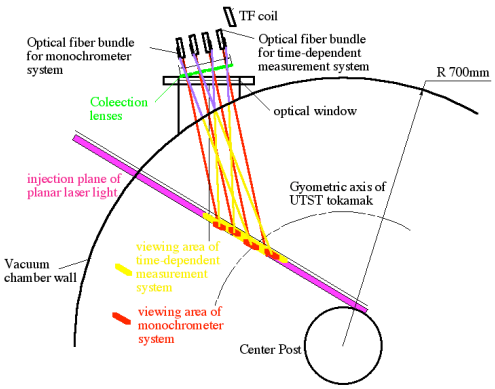

Fig. 4 : Toroidal cross section of the configuration of the optical system in the UTST device. Viewing region of each channel is also shown by yellow and red lines.

Acknowledgements

The authors are pleased to acknowledge TS group at University of Tokyo for their help at various stage of this work. The authors would like to thank T. Suzuki for technical support. This research was partially supported by the Japan Ministry of Education, Science, Sports and Culture, Grant-in-Aid for Scientific Research on Priority Areas “Advanced Diagnostics for Burning Plasmas”, 18035003, 2006-2007.

References

[1] N. Asakura et al., Nucl. Fusion Vol. 39, 1983 (1999).
[2] B. LaBombard et al., J. Nucl. Matter. Vol. 241-243, 149 (1997).
[3] B. LaBombard et al., J. Nucl. Matter. Vol. 266-269, 571 (1999).
[4] M. Nakatsuka, J. Plasma Fusion Res. Vol. 83, No. 6 (2007) 569-572.
[5] Y. Ono, et al., Fusion Energy 2006, EX/P7-12, (2007).
[6] C. Honda, et al., Rev. Sci. Instrum., Vol. 58, 758 (1987).
[7] F. M. Levinton, et. al., Rev. Sci. Instrum, Vol.72, 898 (2001).

Multipulse Thomson scattering on TEXTOR

M.Yu.Kantor[1,3], A.J.H.Donné[1], R.Jaspers[1], D.V.Kouprienko[3], H.J.van der Meiden[1], T.Oyevaar[1], A.Pospieszczyk[2], G.W.Spakman[1], S.K.Varshney[1], E.Uzgel[2] and TEXTOR Team

[1]*FOM-Institute for Plasma Physics Rijnhuizen, Association EURATOM-FOM, Trilateral Euregio Cluster, P.O. Box 1207, 3430 BE Nieuwegein, The Netherlands*
[2]*Institut für Plasmaphysik, Forschungszentrum Jülich, EURATOM Association, D-52425 Jülich, Germany*
[3]*Ioffe Institute, RAS, Saint Petersburg 194021, Russia*

The report discusses measurements of fast plasma events in TEXTOR plasmas with the multipulse TV Thomson scattering diagnostics. The diagnostic capabilities for fast dynamic measurements are analysed and illustrated by measurements of electron temperature and density profiles in magnetic islands, at ELM activity and during plasma disruption. Further upgrade of the diagnostics for faster and more accurate dynamic measurements are discussed.

1. Introduction

Fast dynamic measurements of electron temperature and density with Thomson scattering diagnostics are mostly limited by the capabilities of probing lasers to generate high energy pulses at a high repetition rate. The highest rate is achieved when many pulses are generated during a single flash tube discharge. For standard lasers, the average laser pulse energy decreases with the number of generated pulses and gets too low for Thomson scattering application.

In intracavity laser probing, the plasma is enclosed in the laser cavity giving a significant rise of the cavity quality. Such a system allows the generation of high energy laser pulses at a high repetition rate during a single flash tube discharge [1].

This approach is used in the multipulse TV Thomson scattering (MPTVTS) diagnostics [2] on TEXTOR tokamak (R=1.75, a=0.47 m). Below we analyze the capabilities of the MPTVTS diagnostics to study fast plasma dynamics, present new measurements of fast evolution of electron temperature and density profiles in magnetic islands, during ELMs and plasma disruption as well as discuss the coming upgrade of the diagnostic system for faster and more accurate measurements.

2. General capabilities of the MPTVTS diagnostics

The MPTVTS diagnostic system on TEXTOR utilizes a double pass intracavity system with a ruby laser [2]. After passing the plasma, the laser beam is reflected back to the laser body by a spherical mirror. This spherical mirror and rear mirror on the laser table form a laser cavity of 18 m long.

Scattered light is collected from the whole plasma diameter of 90 cm long by a Littrow grating spectrometer. Spectrally resolved images are detected by a fast Phantom V7.0 CMOS camera. The diagnostics routinely measures more than 15 electron density and temperature profiles at 5 kHz repetition frequency and 9 mm spatial resolution.

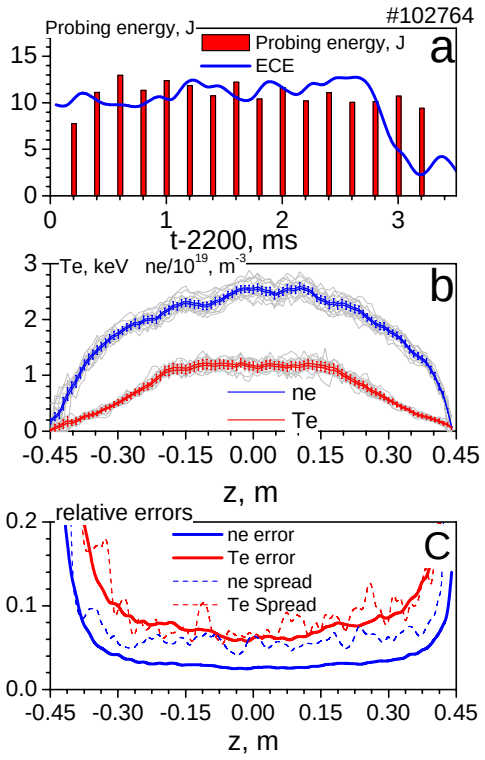

Fig. 1: a) Laser pulse train,
b) electron temperature and density profiles,
c) measurement errors and data spread.

Fig. 1 shows the electron temperature and density profiles measured in an ohmic plasma discharge. A typical 16-pulse laser oscillation with a total probing energy of 174 J is shown in Fig. 1a. ECE signal in Fig. 1a indicates the saw-tooth crash in plasma at the end of the laser train. All 16 measured electron temperature and density profiles are shown in Fig. 1b by grey curves.

Bars in this plot show the statistical measurement errors for a single pulse. The temperature and density errors are calculated from the statistical errors of each CMOS pixel. The latter errors were measured during calibration of the system and being rescaled for the measured scattered and plasma light signals. Relative errors for a single pulse amount to 6-10% for temperature and 3-5% for density in the plasma core at $n_e=2.5*10^{19}$ m^{-3}.

The errors relate to the number of collected photoelectrons from scattering light. The expected number of photoelectrons from a 12 J laser pulse in a single 9 mm spatial channel at $n_e=2.5*10^{19}$ m^{-3} is ~4500 and well corresponds to the measured number.

The averaged plasma light for this shot is ~ third of the scattered light. The most contribution from the H_α line emission was masked on the image plane by a paper strip. But H_α light still contributes a half of the collected plasma light because of its stray reflections in the spectrometer. This stray H_α light will be removed for better measurements of TS signals.

The relative statistical errors are shown in Fig. 1c by solid curves. Dash curves in the plot show TS data spreading for all pulses before the saw-tooth crash. The temperature spread well corresponds both to the calculated statistical errors and the 9% spread of the ECE signal before the crash. The spread of density is a bit higher than its statistical errors. This might be attributed to actual small plasma density variations indicated by the ECE signal or some measurement errors of individual laser

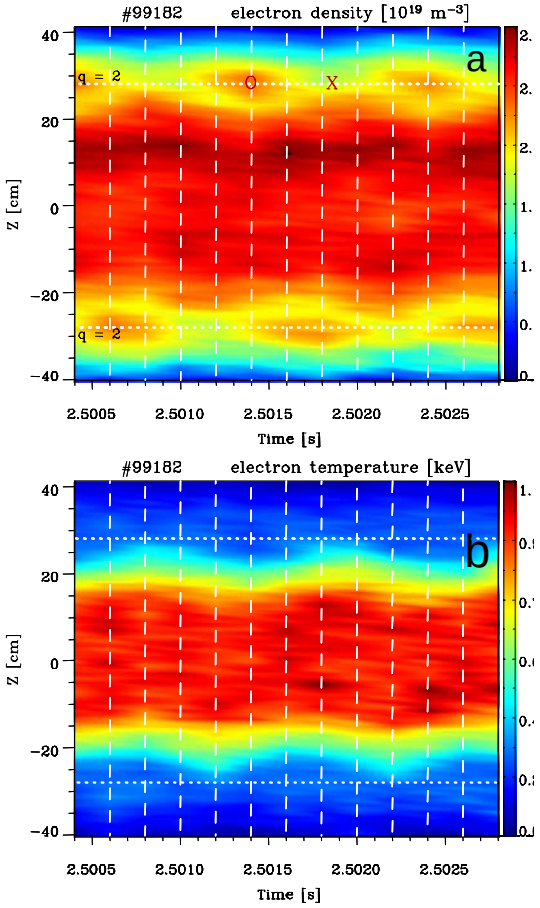

Fig. 2: Rotating island
a) electron density and b) temperature

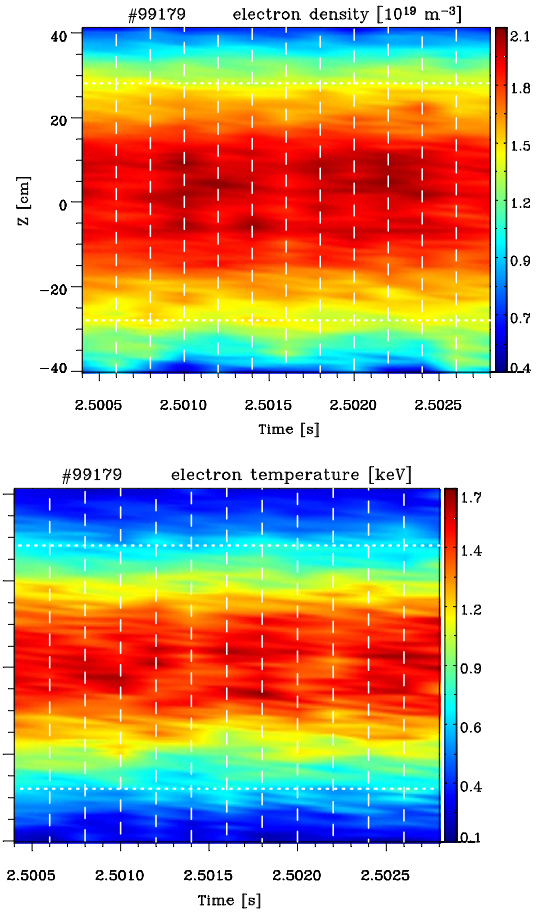

Fig. 3: Island suppressed by ECRH
a) electron density and b) temperature

pulse energies.

These low errors have been achieved in spite of a longer laser probing pulse duration (~1600 ns) than that in a standard laser probing system (~30 ns). The standard laser system would provide a twice better accuracy with a single 12 J probing pulse for the given TEXTOR discharge.

This looks as an advantage, but a standard probing laser has no possibilities for multipulse generation like shown in Fig. 1a and dynamic measurements presented below. Moreover, all measurements in the laser train can be averaged for steady state plasma conditions. The resulting fourfold reduced errors appear even better than those for TS diagnostics with a standard laser. The errors for the averaged measurements can be seen in Fig. 1b as the difference between two close curves within the error bars.

The actual resolution of the electron temperature and density variations is ~1.5 times worse than the measurement accuracy because of comparison of close noisy data. So, the MPTVTS diagnostics is capable to resolve ~10-20% temperature and ~5-10% density variations in the plasma core of 35 cm radius. It should be enough to observe general features of fast plasma dynamics in magnetic islands, during ELMs and disruptions.

3. Measurements of fast plasma dynamics

3.1. Rotating islands

A large m/n=2/1 island was created and locked to the rotating external perturbation magnetic field of the Dynamic Ergodic Divertor (DED) [3] in TEXTOR. Perturbations due to the rotating island are clearly observed in the time-space contour plots of electron temperature and density (Fig. 2). The 15 laser pulses generated at 5 kHz repetition rate cover 1.5 rotations of the island. Laser pulse times are shown in the figures by vertical dash lines. The measurement accuracy is high enough to distinguish 20% temperature oscillations and an island width of ~10 cm is well resolved.

At deposition of 800 kW of ECRH power inside the island, the island was suppressed and measurements with the MPTVTS system show the disappearance of the islands on the q=2 surface (see Fig. 3) [3].

3.2 ELM dynamics

Effect of ELMs on limiter H-mode and control of ELMs by DED DC current was studied in TEXTOR with MPTVTS [4]. Fast dynamics of electron temperature and density during ELM crash in H-mode is shown in Fig. 4. Black curve in the figure shows H_α emission burst during the ELM in arbitrary units. Saw-tooth crash happens simultaneously with the ELM which is indicated by ECE signal from R=1.6 m at the 3rd harmonic of the electron cyclotron frequency. The smoothed ECE signal in arbitrary units is shown by white curve. Red bars indicate times and energies of laser pulses. The horizontal red line marks 10 J level for these pulses.

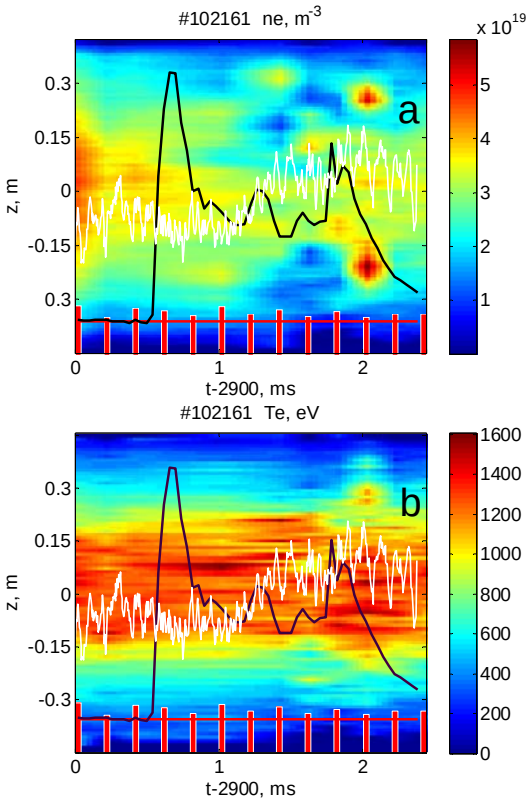

Fig. 4: ELM and saw-tooth crash
a) electron density and b) temperature

The density perturbations are quite high and fast - more than ±50% during 1 ms of the ELM and saw-tooth crashes. Noticeable temperature variations occur only at the end of the ELM burst and saw-tooth crash when two symmetrical ‘bat ears’ appear in the density plot. They indicate the plasma column with hollow density arising for a short time. Note, that both density and temperature variations

are quite symmetrical in z-direction indicating strong perturbations of the plasma as a whole.

Strong ELMs were suppressed by a perturbation of magnetic structure at the plasma edge by DC current in DED coils [4] resulting in fourfold less H_α burst shown in Fig. 5 by black curves in the same scale as before. The density variations are less than half of those in the previous case and temperature variations are even hardly detectable.

Plasma perturbation structure in the saturated ELM is completely different from that in the crash ELM. There are three symmetrical local density hollows of ~5 cm size and ~30% deep located at z~±0.1 m. They are well synchronized with the loop voltage variations shown in arbitrary units by white curves. The temperature variations are nearly undetectable. Nevertheless, in the density hollows, electron temperature is ~ 8% below than in the surrounding regions. Fig. 5 could indicate a rotating helical structure with hollow electron pressure in the TEXTOR plasma. Taking into account the Shafranov shift and probing beam position, the helical structure might be located at the radius of ~0.15 m.

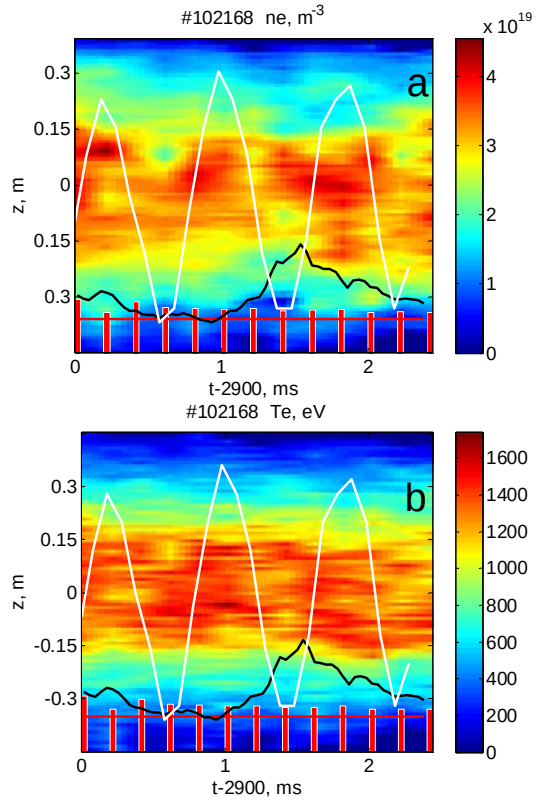

Fig. 5: Suppressed ELM
a) electron density and b) temperature

3.3 Plasma disruption

MPTVTS diagnostics was used also to study the mitigation of plasma disruption in TEXTOR. Plasma discharge was disrupted by a fast injection of Ar gas [5]. The dynamic of electron temperature and density is shown in Fig. 6. The start of the injection precedes the first 1aser pulse by 1 ms. While gas flows in a vacuum duct, the temperature and density are unchanged. They start changing simultaneously with the H_α emission rise shown in the figure by the black curve. During a short time (~200 μs), plasma decays and the discharge comes to a complete thermal quench with formation of a hollow plasma which is very dense at the edge. Both TS and HCN interferometer data show double line average density of the hollow plasma in comparison with that before the disruption.

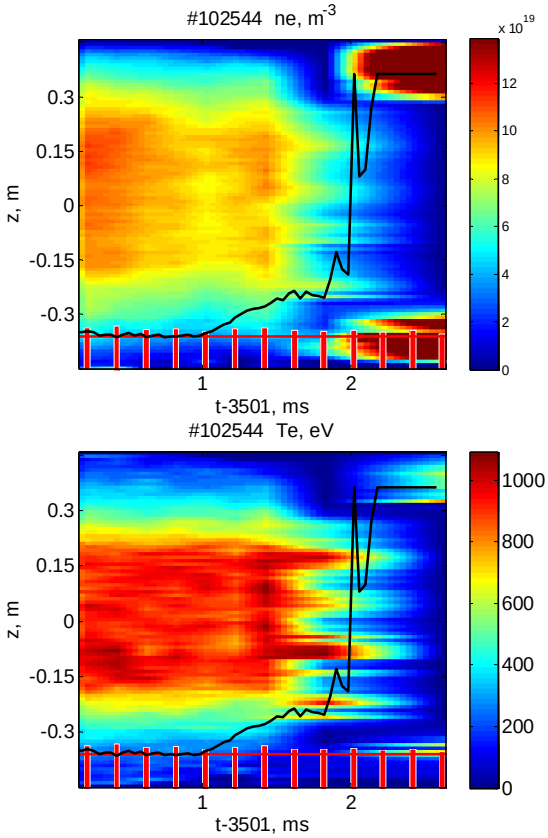

Fig. 6: Plasma disruption
a) electron density and b) temperature

4. Upgrade of the MPTVTS

From the presented results one can conclude that the MPTVTS diagnostics on TEXTOR is capable to measure fast dynamics of electron temperature and density in the plasma core at 9

mm spatial resolution, at 5 kHz repetition rate during ~3 ms time interval and to resolve ~10-20% temperature and ~5-10% density variations in the plasma core.

More detailed study of fast plasma dynamics in TEXTOR with Thomson scattering requires to

1) elongate the measurement interval,
2) increase the measurement frequency and
3) improve the measurement accuracy.

These new challenges can be replied by multipass intracavity laser probing [1]. The multipass system utilizes a second spherical mirror located between the laser and tokamak vessel. The beam from the ruby rod is directed in plasma and focused in the plasma center by a lens. After several passes between the spherical mirrors, it is reflected back to the laser. So, now two spherical mirrors and rear mirror form the laser cavity.

An application of multipass intracavity probing for TEXTOR was studied in [6]. The mock up experiment showed that laser can pass plasma up to 14 passes in the TEXTOR geometry. Correctly designed and tuned multipass system provides low light losses (<1% per pass) and significant increase of probing energy in comparison with the double pass system.

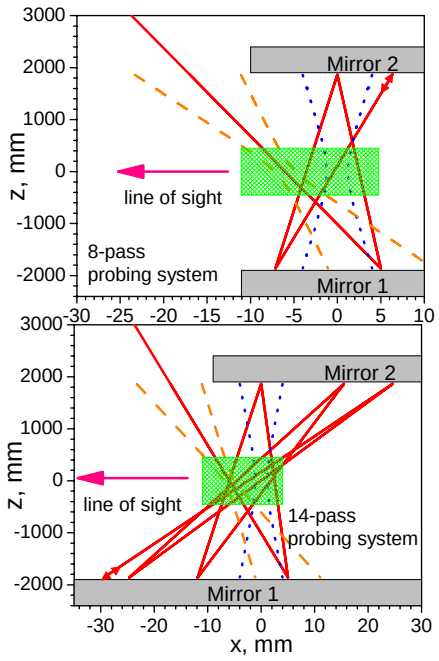

Fig. 7: Beam path in 8 and 14 pass systems

Such a system was recently designed and some of its parts are already installed on TEXTOR. The multipass system on TEXTOR consists of two spherical mirrors of 1900 mm curvature radii and 76 mm diameter each. They are located ~ by 1900 mm from the plasma center. The entrance laser beam is focused in plasma by a lens of 2500 mm focus length.

The layouts of 8- and 14-pass systems are presented in Fig. 7. The laser beam paths in the systems are shown by straight red lines. The beam enters the plasma from the upper left corner and turns back from reflection points marked by two small opposite directed arrows. The caustic edges of the input beam are illustrated by dash orange curves. The beam caustic of the double pass system is shown by the dot blue curves for comparison.

When tuned correctly, the system keeps the caustic and beam waist from pass to pass in the compact plasma region shown in Fig. 7 by hatched green rectangles. The dimensions of the region are 900 mm high and 15 mm width. The deepness of the region changes from <2 mm in the center to 4 mm at the edge according to the beam caustic size.

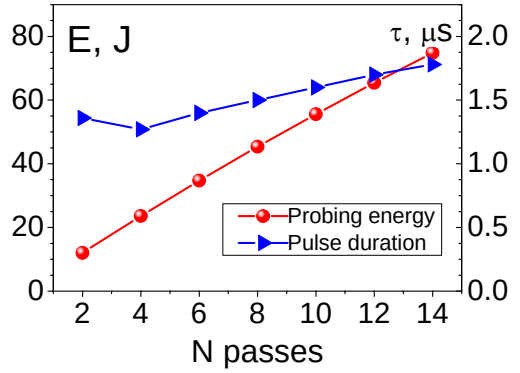

Fig. 8: Laser probing energy and pulse duration versus the number of passes

Scattered light is collected from this region along the line of sight shown in the figure. The horizontal expansion of the laser beam fan results in some deterioration of the spatial resolution of the diagnostics. It does not depend much on the number of passes and takes place mostly at the plasma edges, expanding from 9 to 15 mm. But the 9 mm spatial resolution is not achievable for the present double pass system because of low scattering signals at the edge (see Fig. 1). In

practice, several spatial channels have to be binned together to get acceptable measurement errors at the edge. So, the multipass system is expected to keep and even to improve the spatial resolution of MPTVTS diagnostics on TEXTOR.

An important point to discuss is an elongation of the laser pulses because of a longer traveling time in the multipass laser cavity. The expected elongation of laser pulses as well as the probing energy increase with the number of passes is shown in Fig. 8. The data were calculated assuming 1.6% light losses per pass.

For the present double pass system, average probing energy is 12 J, and pulse duration at FWHM is 1.35 μs. For four pass system on TEXTOR the pulse is shorter because the first spherical mirror was moved closer to the vessel by 2 m during the upgrade reconstruction. Thus, up to 8 passes the probing laser system on TEXTOR is expected to generate pulses of the same duration as the double pass does, but with the probing energy up to 3.5 times higher. The system with a more than 8 passes delivers more probing energy with a little bit longer pulse duration and looks also attractive.

The system can be easily switched between multipass and double pass by tuning the spherical mirror 1.

The statistical errors for 10 pass probing system are expected to be ~3-5% for core temperature and 1-3% for core density at $n_e=2.5*10^{19}$ m^{-3} and at the same level of pumping the laser. This certainly would allow more detailed study of fast plasma dynamics.

The multipass probing expands also the capabilities of the MPTVTS diagnostics to measure dynamics for a longer time interval at a higher repetition rate. The maximum laser train duration was designed to be 9 ms. The maximum pulse repetition rate is 10 kHz and restricted by the frame rate of the CMOS cameras used.

The laser operation at these maximal parameters with the double pass intracavity system is possible only at a lower pumping level in order to reduce the thermal shock in the laser active media. But, lower laser pulse energy results in an unacceptable decrease of the diagnostic sensitivity.

The upgraded system will allow laser operation at a reduced pumping because of the gain of the scattered energy in the multipass system. One could expect the operation of the MPTVTS diagnostics with the laser multipass intracavity system at the designed maximum capabilities.

5. Conclusion

The MPTVTS diagnostics on TEXTOR based on the double pulse intracavity laser probing system is capable to measure fast evolution of electron temperature and density at 5 kHz repetition rate during ~3 ms time interval and ~10% accuracy.

The diagnostics has proved this capability in a number of experiments with fast plasma dynamics like rotating islands, ELMs and plasma disruption.

The coming diagnostics upgrade with multipass intracavity laser probing system is expected to increase the diagnostic accuracy by a factor of 2. The upgrade also extends the diagnostic capabilities to a higher repetition rate and time interval of the measurements.

Acknowledgments

This work, supported by the European Communities under the Contract of Association between EURATOM-FOM, was carried out within the framework of the European Fusion Programme. The views and opinions expressed herein do not necessarily reflect those of the European Commission.

References

[1] M.Yu.Kantor and D.V Kouprienko. Rev. Scien. Instr, 70 (1999) 780

[2] H. J. van der Meiden et al. Rev. Sci. Instrum. **75** (2004) 3849

[3] H. J. van der Meiden et al. Rev. Sci. Instrum. **77** (2006) 10E512

[4] B.Unterberg et al. to be published in the Proceedings of 34th European Physical Society Conference on Plasma Physics.

[5] S.A Bozhenkov et al. to be published in the Proceedings of 34th European Physical Society Conference on Plasma Physics.

[6] M.Yu.Kantor et al. Proceedings of 27th European Physical Society Conference on Plasma Physics, Budapest (2000) P1.113.

ITER Core LIDAR Thomson Scattering

M.J.Walsh

EURATOM/UKAEA Fusion Association, Culham Science Centre, Abingdon, Oxfordshire, OX14 3DB, United Kingdom

The design of the core LIDAR system for ITER where temperatures up to 40keV are expected provides several challenges. These are related to issues such as neutron control, mirror degradation due to long pulse lengths, high temperatures giving broad scattered spectra, required reliability and optics accessibility. These interacting challenges are being addressed in an integrated way. Where possible, redundancy is being employed as a way of minimising or mitigating risk in the system design. These factors demand several iterations of the design to find a solution that can be deployed to ITER and will work reliably. A study of some of the key components of the system is presented below.

1 Outline Core LIDAR scheme

The basic design of the core LIDAR system is described in [1,2,3,4,5]. An outline scheme for the collection optics is shown in Figure 1. In the case shown, the laser beam is injected through a hole in the first light collection mirror. This has the key advantage of separating the requirements for high power handling of the laser mirror from wide spectral bandwidth for the collection mirror, at the expense of a small hole in the collection mirror. The scattered light is relayed through a labyrinth to the vacuum window at the rear of the port plug. The etendue of the system will reduce with distance across the tokamak, with the minimum light being collected at the inner wall. The system indicated in Figure 1 has a variation of f-numbers from ~f/6 at the outboard side to ~f/17 at the inner wall. This is compatible with collecting the light scattered from the whole cross-section of the laser beam onto a single detector of diameter typical of available detectors (around 18mm diameter at f/0.7) although a twin detector approach (approximately 11-14 mm diameter each) for each spectral channel may be useful to reduce background light and allow the use of higher speed detectors. First and second harmonic NdYAG are presently considered as the main candidates for the lasers, although TiS is also being analysed.

2 Performance analysis and relation to detector requirements

The expected performance of the LIDAR system is shown in Figure 2 for a range of different potential laser options. In this case, the electron density is $3x10^{19}m^{-3}$, $Z_{eff}=2$ with background enhancement over bremsstrahlung assumed to be a factor two. The cut-off wavelength for the collection system is taken as 380nm except where shown. The transmission of the laser to the target is estimated at 50% and the collection of the light from the target 11%. The efficiency of the detectors is set at a constant value of 3% at wavelengths below 550nm and a constant value of 4% above this value. An 18mm detector area is assumed and the collection f-number is 0.7 at this point. The scattering volume is taken to be a cylinder ~7cm long and the radius is set by the optics (i.e. the detailed de-convolution of the laser and detector pulse shapes is not included in this simulation). The energy for the 532nm laser was set at 50% of the 1064nm laser, in line with easily achievable second harmonic conversion efficiencies. The fractional error represents 1 standard deviation based on photon statistics (scattered + background). To simulate the effect of extending the wavelength region, one TiS case has an extended collection wavelength, down to 300nm[6].

A multi-laser system to measure the core temperatures to better than 10% appears feasible with present technology assuming the laser specification can be met.

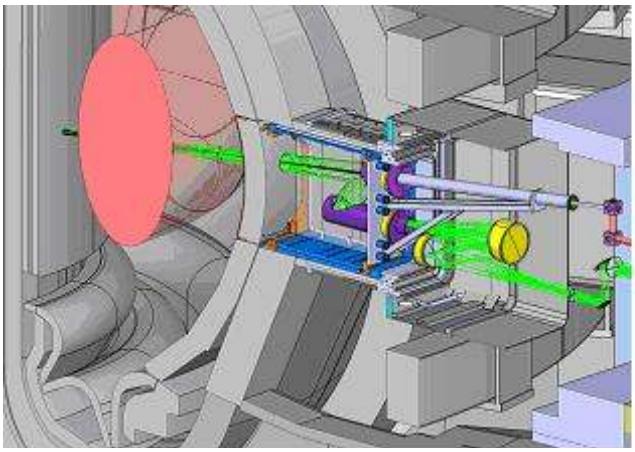

Figure 1: Outline schematic of the port plug area LIDAR design for ITER.

3 Lasers

The measurement requirements for the system and studies as in the earlier section (which include assumptions about the detector quantum efficiency and optical throughput etc) lead to the following approximate specification/performance goals for the laser(s):

Energy	~5J
Pulse length	~250ps (compromise between power density and spatial resolution). It is important that there are no leading edges on the laser pulse entering the ITER port plug (i.e. regions seen by the collection optics) before the main pulse.
Rep rate	100Hz for the complete system (could and probably should be more than one laser) – lasers above ~15Hz are therefore relevant.
Spectral width	The relative power should drop by ~10^{7}-10^{8} by ~1nm from the line centre if Raman scattering in N_2 gas is to be used for calibration. For the LIDAR measurement itself, the relative power should be down to about 10^{-8} @5nm from the line centre. These numbers depend on achievable stray light levels.
Wavelength	800nm or higher to allow the highest temperatures to be measurable (using strongly blue-shifted backscattered light). Two wavelengths might be needed which could be ~500-850nm and ~800 - 1060nm.
Other requirements	There will be control and instrumentation standards to meet and other interfaces. Pointing stability (25-50microrad) and other beam properties are not expected to be major challenges.
Operational duty cycle	Periods of ~1hr, several times/day, 7 days a week for months at a time (this could evolve depending on ITER operating regime). Overall lifetime of ITER is presently ~4600 hours of operation.

The options for realisable lasers with high energy and short pulse (<300ps) are relatively limited. Achieving all the specifications of energy, pulse width and pulse repetition rate simultaneously is not possible with currently available technology. Repetition rates in the 10 to 20 Hz region are feasible and the ITER specification may be achieved by utilising multiple lasers. Three laser media have been considered in some detail: NdYAG, TiS and ruby. A brief examination of a diode pumped NdYLF system has also been carried out. Other materials do not at present seem attractive – e.g. NdGlass is not suited to high repetition rate due to poor thermal conductivity.

The flash-lamp replacement time can be estimated as follows. Assuming a lifetime of around 20million flashes, a 20Hz laser would need replacing every ~300hours. In principle, changing the flashlamps is a relatively straightforward job in most modern lasers. No re-alignment is usually necessary, and use of multiple lasers makes such maintenance much easier.

An issue that will be of great importance for ITER is laser source redundancy and this is critical in any complex laser system. Generally, it is expected that more than one laser of each colour will be used to reduce the chances of losing all data during an ITER pulse. To achieve the ITER specification, several lasers would need to be used [1] along the lines demonstrated on existing tokamaks in [7,8,9,10].

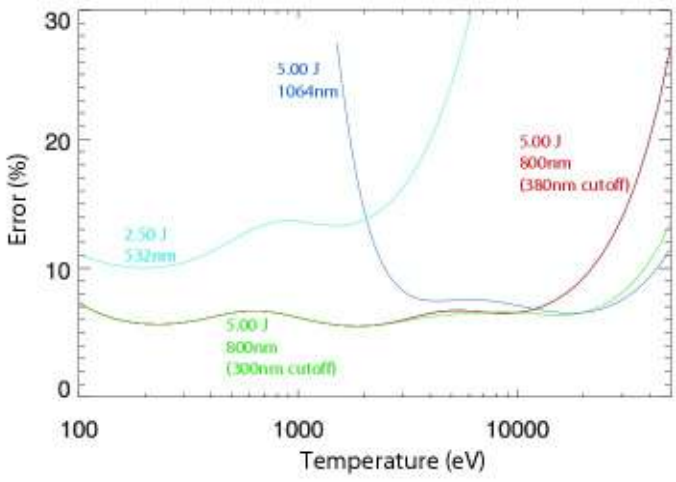

Figure 2: Typical error estimates expected for core (centre) measurements. The blue 1064nm curve omits detectors above 850nm, unlike the green 1064nm curve.

4 Detectors

Based on the analysis of the specification of the system and work carried out previously, an indicative detector performance specification is given below.

Time response	~200-250ps response or less, to allow accurate unfolding of a LIDAR pulse ~15ns long. Adjacent laser pulses could be ~1μs apart. The units should be gateable in ~2-5ns (on and off) – "off" means gain drops by say 10^6 to block the flash from the back wall of the torus
Spectral response	Overall ~250nm - ~1060 nm (depending on laser) using several detectors. Bandwidth can be modest (should be ~100nm to allow enough photons in each band of the filter-based spectrometer, but some flexibility). At present the 850-1060nm region is challenging.
Physical dimensions	~20mm diameter for single detector/spectral channel, or ~11-14mm diameter if split image field.
Quantum efficiency	EQE of 6-10% is the present target (EQE=QE*fraction of used photoelectrons or EQE=QE/NF^2) where NF is Noise Factor
Linearity	A key specification – non-linearity needs to be small and known.
Stability/drift	Negligible drift during an ITER pulse, with high stability of EQE
Lifetime	Several years in operation
Other issues	Radiation tolerance is not expected to be an issue as detectors will be remote.

The detectors used in the present LIDAR system on JET[11,12] are based on the micro-channel plate photomultiplier. The main detection is done by a photocathode and the subsequent electrons generated are accelerated through micro-channel pores and the amplified signal is collected at the output anode. Present relevant photocathodes are S20 (multi-alkali), gallium-arsenide and gallium-arsenide-phosphate. The response of the complete system is set by a combination of the type of photo-cathode, the size of the detector, the detailed structure of the MCP-anode unit and the electrical coupling. These three photocathodes cover the wavelength range from ~300nm to ~850nm. The S20 efficiently covers the range up to 480nm. The GaAsP covers the next range up to approximately 750nm with relatively good sensitivity and the GaAs covers the range from 500nm to around 850nm but with slightly less sensitivity than the GaAsP.

To be able to use a Nd:YAG laser as the main laser for ITER core LIDAR would require a detector with good sensitivity in the range 850nm to over 1060nm. There are detectors in this area but as a general rule they are not fast or sensitive enough. Reports of detectors with reasonable sensitivity in this area can be found [1]. "Reasonable sensitivity" means that it is within a factor of approximately 2 to 3 of the performance at lower wavelengths. More work is being undertaken in this area to determine what improvements are feasible. Detectors other than MCP-PMTs are also being considered.

It is possible right now to get a detector with full width half maximum multi-photon response times below 200ps which is manufactured using the S20 photocathodes [13]. (Multi-photon response times are important because transit-time-spread (TTS) can significantly increase the response time of the system). These times should be compared to the times of approximately 250ps required for the ITER core LIDAR laser. Suppliers of the compound

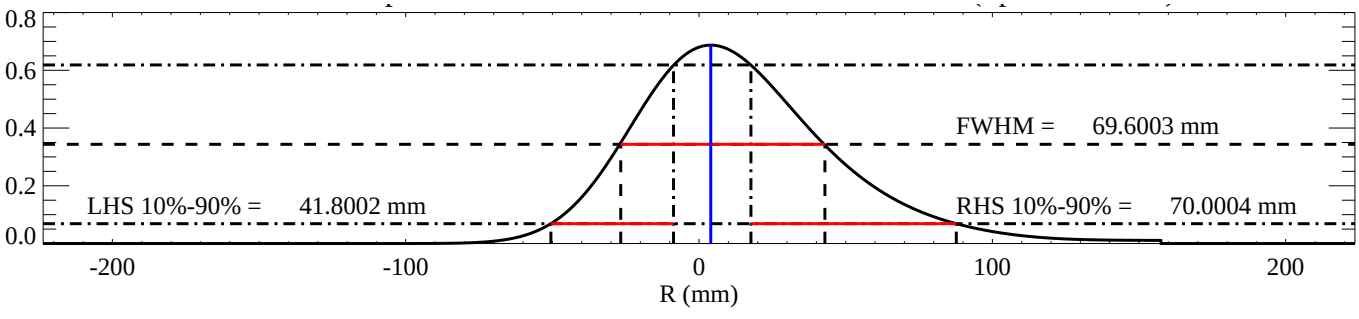

Figure 3: Response of an 11mm (gridless) detector convolved with laser response time of FWHM of 300ps.

semiconductors are presently quoting Full-Width-Half-Maximum (FWHM) response times in the region of ~300ps for GaAsP (see Figure 3 which shows an example of a detector that shows a combined response FWHM equivalent to ~70mm) and ~350ps for GaAs. It is not clear how much these response times are governed by the photocathodes and how much by the overall design of the system. Improvements in speed and efficiency of the 250-800nm detectors are quite slow. As noted above, the development of a high efficiency detector in the 800-1050nm region would be a great benefit. One concern is that at these wavelengths, the detection layer may be thicker and hence slow.

5 Conclusions

The maximum temperature expected in ITER is in the region of 40 keV and the minimum average density of approximately 3×10^{19} m^{-3}. The proven reliability of the LIDAR concept in large tokamaks has been successfully demonstrated. Key items in the design of the core LIDAR system have been outlined. Transfer of the technology to the next step device, ITER brings new challenges, as it does for most diagnostics being prepared for this device. This paper has addressed some of the key topics in this area. In particular, an investigation of the laser and detector options has been undertaken.

Acknowledgments

This work was funded jointly by the United Kingdom Engineering and Physical Sciences Research Council and by the European Communities under the contract of Association between EURATOM and UKAEA. The views and opinions expressed herein do not necessarily reflect those of the European Commission. This work was carried out within the framework of the European Fusion Development Agreement and is largely based on a collaborative programme with the Russian Federation. The fruitfulness of the collaboration with the Ioffe Institute, St. Petersburg is gratefully acknowledged in particular G. T. Razdobarin, and E.E.Mukhin.

Many other people have contributed to this work, which is now being continued in the framework of a European cluster, and the following have played a major role A. Darke, N.H. Balshaw, M. N. A. Beurskens, M. Kempenaars, K. Hawkins, R. B. Huxford, L. McMenemy, A.W.Morris, P. Parsons, G. Phillips R. Scannell.

References:

1. M. J. Walsh et al, Review of Scientific Instruments, No. 10, Vol.77, Part II, October 2006, p.10E524-1:10E525-4.
2. A. E. Costley, 'Laser Based diagnostics for ITER and beyond', Proc. 12th Int. Symp. On Laser-Aided Plasma Diagnostics, Snowbird (2005), paper I-A.1.
3. G. Razdobarin, M. Walsh et al, IAEA 2006, to be published
4. L de Kock, Design description document; Thomson scattering (core) LIDAR. ITER Document G 55 DDD 3 97-12-05 W 0.5 (1998).
5. P. Neilsen, 'Update to Core Lidar system for ITER-FEAT', EFDA Contract no 00/557, May 2001
6. P. Martin, A. Morono and E. R. Hodgson, J. Nucl. Mater. 283-287 (2000) 894-897, "Radiation effects on laser damage in KU1 quartz glass.
7. M. J. Walsh et al**,** RSI, No. 3, Vol.74, Part 11, March 2003, p.1663-1666.
8. M. J. Walsh et al**,** RSI, No. 10, Vol.75, Part II, October 2004, p.3909-3911.
9. T. N. Carlstrom et al, RSI, No. 10, Vol.63, October 1992, p.4901-4906.
10. B. Kurzan et al, Plasma Physics and Controlled Fusion, Vol. 46, No 1, January 2004, p.299-317.
11. H. Salzmann et al, Nuclear Fusion vol.27 no.11 November 1987 pp.1925-1928.
12. M. Kempenaars et al, Review of Scientific Instruments, No. 10, Vol.75, Part II, October 2004, p.3891-3894
13. J. Milnes and J. Howorth, Picosecond time response characteristics of Micro-channel plate PMT detectors, Proc. SPIEE vol 5580 (2005),p.730

Progress in development of collective Thomson scattering diagnostic with high power CO_2 laser

T. Kondoh, Y. Kawano, T. Hatae, T. Sugie, T. Hayashi, Y. Kusama

Japan Atomic Energy Agency, Naka, Ibaraki, 311-0193, Japan

High power and high repetition CO_2 laser has been developed for collective Thomson scattering (CTS) diagnostic to establish a diagnostic method of confined a-particles in burning plasmas. Pulse energy of 17 J at a repetition rate of 15 Hz has been achieved in a single-mode operation. This result gives a prospect for the CTS diagnostic on International Thermonuclear Experimental Reactor (ITER), which requires energy of 20 J with repetition rate of 40 Hz. The laser injection test into the vacuum vessel of the JT-60U tokamak has been carried out to check the electric noise and stray signals of the receiver system using the new CO_2 laser without plasma. As a result, electrical noise has been decreased, however, stray signal due to multimode oscillation has been observed in about 30% of the pulses and a further improvement of the laser is needed.

1. Introduction

A diagnostic of confined fusion-generated α-particles is a one of the key issues of burning plasma diagnostics to understand their contribution to plasma heating and influence on plasma instabilities. However, an effective and reliable measurement method has not yet been established. In International Thermonuclear Experimental Reactor (ITER), measurement of velocity and spatial distributions of confined α-particles requires temporal resolution of 0.1 s and spatial resolution of 10 % of the plasma minor radius.

A collective Thomson scattering (CTS) diagnostic is a very attractive method to measure α-particles in burning plasmas. The CTS diagnostic for the measurement of α-particles is being developed using and carbon dioxide (CO_2) lasers [1-7] and gyrotrons[8-9]. The CTS diagnostic based on the CO_2 laser (wavelength 10.6μm) has an advantage of negligible plasma refraction, which enables to simplify the tracking of the scattered radiation.

Key issue of the CO_2 laser CTS diagnostic is the development of high-power and high-repetition laser. Laser energy of 20 J with 40 Hz is needed, which has been estimated from expected scattered spectra of the CTS diagnostic on ITER to obtain a signal-to-noise ratio (S/N) larger than 10 with a time resolution of 0.1 s. The estimation assumes that fusion alpha density is $1x10^{18}m^{-3}$ and α-particles have a classical slowing down distribution.

The target of energy per pulse and repetition rate of the CO_2 laser is indicated in Fig. 1. Repetitive CO_2 lasers available for industries or laboratories are plotted in the figure. Previous CO_2 laser system (15 J, 0.5 Hz) [3-5] developed by Oak Ridge National Laboratory (ORNL) for JT-60U is also plotted in the figure. For the CO_2 laser CTS diagnostic, laser light of single-transverse-mode and single-longitudinal mode is needed to measure Doppler broadened spectra of laser light scattered by plasmas.

Since there is no laser available which meets requirement for CTS diagnostic on ITER at present, a high-energy and high-repetition laser has been developed. The new laser was designed based on an industrial Transversely Excited Atmospheric (TEA) CO_2 laser.

The target values of the TEA CO_2 laser are output energy of 20 J and repetition rate of 20Hz with single- transverse and single-longitudinal- mode. Combination of two lasers will generate energy of 20 J with 40 Hz and is expected to provide a good S/N ratio for the CTS diagnostic on ITER.

This article gives a description of the development of the new TEA CO_2 laser for the CTS diagnostic.

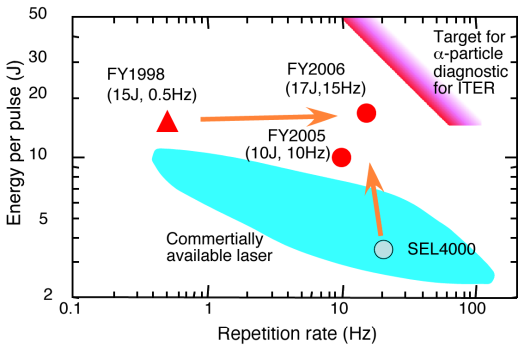

Fig. 1:Progress of the energy and the repetition rate of CO_2 laser for α-particle diagnostic. Output energy of 17J at a repetition rate of 15 Hz has been obtained. The new laser was designed based on the industrial laser SEL4000.

2. Pulsed CO_2 laser

2.1 Development of the laser

The new laser has been designed and fabricated based on the industrial TEA CO_2 laser, SEL4000 (SHIBUYA KOGYO CO., LTD. [10]) which has the output energy of 3.5 J at the repetition rate of 20 Hz. The output beam shape is 27-mm wide × 24-mm height. The discharge unit of the laser consists of a pair of discharge electrodes, pre-ionization electrodes, and a heat exchanger. In order to increase the output energy, six discharge units were combined in series to a cavity of the new laser as shown in Fig. 2(a). Three high-voltage power sources were used in the laser. A power source supplies to two discharge units as shown in Fig. 2(b). The discharge voltage for excitation of the laser gas

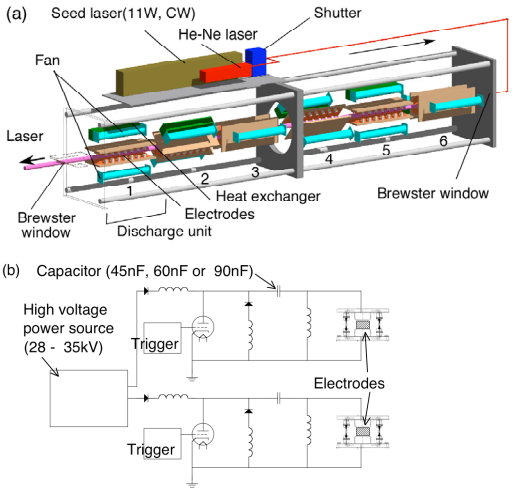

Fig. 2: (a) Schematic view of the CO_2 laser. Six discharge units are combined in series to obtain high energy. (b)Electric circuit of the power supply of the laser.

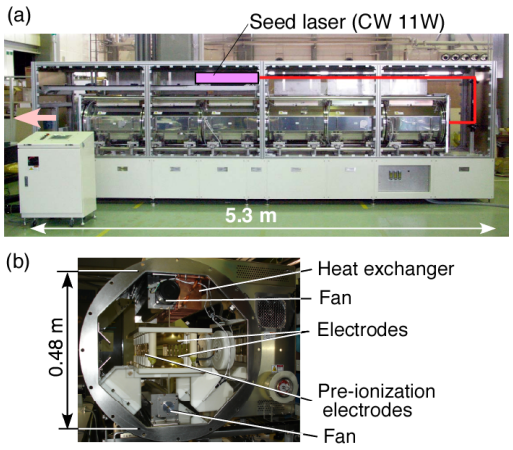

Fig. 3: (a) Photograph of the high-repetition TEA CO_2 laser developed for collective Thomson scattering diagnostic. (b) Inside of the discharge tube.

was increased from 30 kV to 35 kV to increase electric stored energy from the original laser. Electric insulating of the power supply and electrodes was reinforced to increase the voltage. Photograph of the newly developed CO_2 laser is shown in Fig. 3. The size of the casing is 5.3-m length × 1.9-m height × 1.1-m wide and the cavity length is 4.35 m. The beam size was changed to a circular with the diameter of 4 cm in order to enlarge the excitation volume. Adjacent electrodes are rotated 45 deg. to make circular beam.

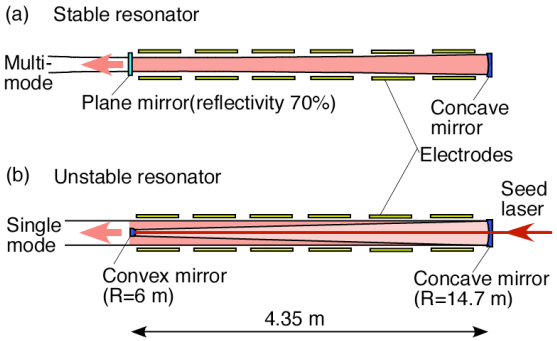

Fig. 4: Schematic view of (a) stable resonator and (b) unstable resonator of the TEA CO_2 laser.

In a high-repetition TEA CO_2 laser, the O_2 formation in the mixture gas induces an arc discharge. High repetitive discharge is stabilized by adding CO and H_2 gases. Then the constituents of the mixture laser gas are CO_2 (8 %), N_2 (8 %), CO (4 %), H_2 (0.3 %), and He (balance). The laser gas heated by discharges is cooled by the heat exchangers in the chamber. The gas pressure in the chamber is 3 % higher than the atmospheric pressure and the gas input rate to the chamber is about 10 liters per hour to avoid arc discharges at the electrodes.

2.2. Stable resonator (multimode operation)

The laser was initially operated with stable resonator as shown in Fig. 4 (a) to test the performance of gas cooling, power supply, deterioration of laser gas, and high voltage insulation. The stable resonator consists of a zinc selenide (ZnSe) flat window with reflectivity of 70 % and a concave copper rear mirror. The energy of the laser was measured by a thermopile sensor or a pyro electric sensor. The laser energy is measured after reflection to a ZnSe beam splitter calibrated using a low power CO_2.

In the multimode operation, the energy storage capacitors of 90 nF or 45 nF were used in the discharge circuit shown in Fig. 2(b).

Maximum energy of 36 J was obtained in single shot operation with the capacitor of 90 nF. An arc discharge was induced around the electrodes with repetition rate of 10 Hz when the capacitor of 90 nF was used. Therefore, tests were carried out with 45 nF not to damage the electrodes and power supplies. Output energy of 18 J at repetition rate of 10 Hz has been achieved with the capacitor of 45 nF. Conversion efficiency defined by a ratio of the output laser energy to the stored energy in the capacitor is 11 %.

2.3 Unstable resonator (single mode operation)

After the test on the stable resonator, the laser was modified to an unstable resonator as shown in Fig. 4 (b) to obtain a single-transverse mode. Continuous wave (cw) CO_2 laser power of 11 W is injected into the TEA laser cavity through a 3 mm hole concave mirror with 14.7 m radius of curvature to obtain single longitudinal mode. A front mirror is a convex mirror of 16 mm diameter with 6 m radius of curvature

Figure 5 shows waveforms of the output power of the TEA laser measured with Ge photon drag detector. The waveforms are shown for the case with and without the seed laser. Without seed laser injection, multiple-longitudinal modes are observed. The oscillation frequency of 34 MHz corresponds to the longitudinal mode frequency $f = c/(2\ L_{cacity})$, where c is light speed and L_{cacity} is cavity length. If the seed laser was injected, lasing occurred faster than without injection and multiple-longitudinal mode was drastically reduced.

Output energy of 17 J at the repetition rate of 15 Hz with single-mode output has been achieved with the capacitor of 60 nF. The electrodes and the heat exchangers were designed to have a capability of 30-Hz operation. At the present, the laser is operated at a repetition rate of 15 Hz since one power source supply to two discharge units as shown in Fig. 2(b)

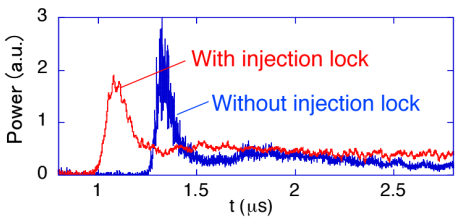

Fig. 5: Waveform of the laser power with and without seed laser injection.

3. Application of the CO_2 laser to JT-60U CTS diagnostic

3.1 CTS System in JT-60U

In order to demonstrate the feasibility of CTS technique, the CTS diagnostic system has been installed in the JT-60U tokamak. A schematic diagram of the CTS diagnostic system is shown in Fig. 6. Scattering angle must be small (θ = 0.5 deg.) in order to obtain larger contribution from ions than electrons. An absorption cell with hot CO_2 gas is used as a stray light notch filter. The bandwidth of the absorption is less than 500 MHz, and the attenuation is larger than 10^{-6} at a wavelength of 10.6μm. Scattered laser power is detected by a heterodyne receiver with a CW CO_2 laser as a local oscillator. Frequency spectrum of output signal from quantum-well infrared photodetector (QWIP) is analyzed by a filter bank (0.4 - 4.5 GHz) with six channels.

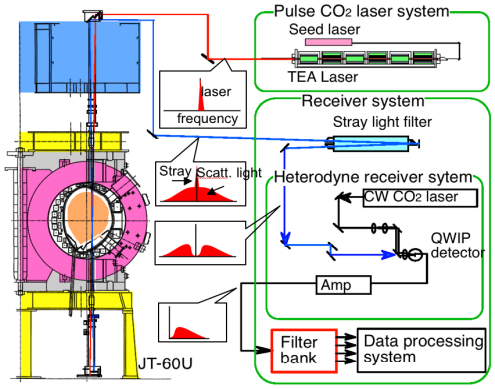

Fig. 6: The collective Thomson scattering diagnostic system on JT-60U.

3.2 Data processing system

In the previous system [3, 5], the output signals were digitized by a CAMAC system in every 2 s. Since the repetition rate of the CO_2 laser increased to 15 Hz from 0.5 Hz, a new fast data processing system has been developed using a Windows XP based digital oscilloscope, LeCroy WaveRunner 44Xi (WR44Xi). Specification of the WaveRunner 44Xi is as follows: bandwidth 400 MHz, sampling time 5 GS/s, number of channels 4, vertical resolution 8 bit, memory 12M words/ch, sequential data acquisition 1.25M waveforms/s in each channels.

Data acquisition, analysis, and storage of the CTS system are carried out using the two oscilloscopes as shown in Fig. 7. The memory is divided into 1000, and waveforms are collected at 15 Hz into the divided memory during 60 s. Data is analyzed and then stored in the hard disk on the oscilloscope temporally. Raw data and analyzed data can be shown in the display. Then

the data is transferred to the hard disk via Ethernet and detailed analysis is performed with a computer.

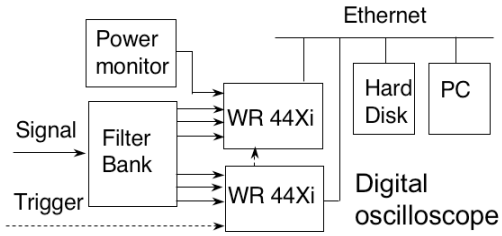

Fig. 7: Data processing system using the digital oscilloscope WaveRunner 44Xi.

3.3 Test injection of the laser into the JT-60U tokamak

The laser injection test into the vacuum vessel of the JT-60U tokamak has been carried out to check the electric noise and stray signals of the receiver system using the new CO_2 laser without plasma. Figure 8 shows an example of the waveforms of the laser power monitor and output of the filter bank. Electrical noise originated from discharges of the TEA laser was a serious problem in the previous laser system[5]. The pulse laser discharge fired about 1μs before the lasing occurs for excitation of the laser gas. Large electric noise was generated from the initiation of the discharge in the previous system. Laser tube of the previous system was made of glass and the electric noise was emitted through the tube. In the new laser system, laser tube is made of stainless steel and the casing of the laser is also carefully shielded to prevent electric noise radiation. Electrical noise in the output of the filter-bank has been clearly reduced.

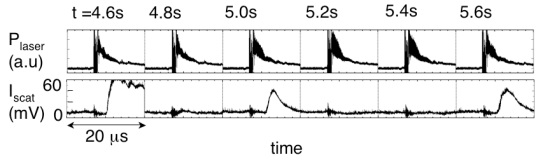

Fig. 8: Waveform of CO_2 laser power monitor, P_{laser}, and output of the filter-bank (1ch 0.4 -0.7 GHz), I_{scat}.

In the figure of t = 4.6, 5.0 and 5.6 s, a stray signal was observed. The stray signal was generated by degenerated components of the laser frequency. The stray signal could not be attenuated by the stray light filter (bandwidth~500MHz). At present, about 30 % of the laser pulses cause stray signals and about 70% of the laser pulses do not generate the stray signal. It is necessary to improve the percentage of the laser pulses without stray signal. To improve purity of the spectrum, Faraday isolator will be installed between the seed laser and the TEA laser.

4. Summary

High-repetition and high-power CO_2 TEA laser has been developed for the α-particle diagnostic in burning plasmas. Output energy of 17 J at the repetition rate of 15 Hz with single-mode output has been achieved for the CTS diagnostic. This result gives a prospect for the CTS diagnostic on ITER.

Scattered signal from the JT-60U plasma has not been identified during two weeks experiment in 2006 using the new laser. To improve purity of the spectrum of the laser, Faraday isolator will be installed between the seed laser and the TEA laser. Experiment in JT-60U will be carried out after the modification of the laser system.

Acknowledgment

The authors would like to thank to the JT-60 team for their cooperation and support of the experiments. This work was partially supported by Grant-in-Aid for Scientific Research on Priority Areas "Advanced Diagnostics for Burning Plasmas" (16082210) and Grand-in-Aid for Scientific Research (C) (19540530).

References

[1] D. P. Hutchinson, et al., Rev. Sci. Instrum. **58**, (1985) 1075.
[2] R. K. Richards, et al., Appl. Phys. Lett., **62**, (1993) 28.
[3] T. Kondoh, et al., Rev. Sci. Instrum., **72**, (2001) 1143.
[4] S. Lee, T. Kondoh, et al., Rev. Sci. Instrum., **71**, (2000) 4445.
[5] T. Kondoh, et al., Rev. Sci. Instrum., **74**, (2003) 1642.
[6] T. Kondoh, et al., Trans. of Fusion Sci. Tech, **51**, (2007) 62.
[7] T. Kondoh, et al to be published in Plasma and Fusion Research, (2007)
[8] H. Bindslev, et al., Phys. Rev. Lett., **83**, (1999) 3206.
[9] H. Bindslev, et al., Phys. Rev. Lett., **97**, (2006) 205005.
[10] http://www.shibuya.co.jp/english/sby/

Development of New High Resolution Thomson Scattering system for the COMPASS tokamak

J. Brotankova[1], P. Belsky[1], R. Barth[2], H. van der Meiden[2], V. Weinzettl[1], P. Bohm[1]
[1] *Institute of Plasma Physics AS CR,v.v.i., Association EURATOM / IPP.CR, Czech Republic*
[2] *Institute for Plasma Physics Rijnhuizen, Associacione EURATOM / FOM, Netherlands*

The COMPASS tokamak is being re-installed to IPP Prague from Culham in U.K. Within an innovation, new diagnostics will be constructed, including a High Resolution Thomson Scattering System measuring both electron temperature (T_e) and electron density (n_e) profiles. A scientific programme of the COMPASS tokamak is focused on pedestal studies, thus the main stress will be laid on the edge part of the system.

1. Introduction

Thomson scattering (TS) is a powerful diagnostic measuring both electron temperature (T_e) and electron density (n_e) profiles. A disadvantage of the TS diagnostic is its construction demandingness due to a low scattering cross-section thus the most powerful lasers and extremely sensitive detectors must be used. A new TS system is being built for the COMPASS tokamak, which is being re-installed to IPP Prague from Culham in Great Britain.

The COMPASS tokamak [1] (COMPact ASSembly) is a divertor tokamak with a clear H-mode and ITER- relevant geometry (R=0.56 m, a=0.23 x 0.38 m, I_p=200-400 kA, B_{tor}=1.2-2.1 T and pulse length up to 1 s). COMPASS is equipped with a unique set of copper saddle coils for resonant perturbation techniques. ITER-relevant plasma conditions will be achieved by an installation of two neutral beam injection (NBI) systems with total power of 2 x 300 kW, and a re-deployment of the lower hybrid heating (LHH) system with total power of 400 kW. For diagnostics, 60 ports are available.

The scientific programme proposed for the COMPASS tokamak will benefit from these unique features and it consists of two main scientific projects, both highly relevant to ITER: Edge plasma physics (H-mode studies, Plasma-wall interaction) and Wave-plasma interaction studies (e.g., Parasitic lower hybrid wave absorption in front of the antenna, Lower hybrid wave coupling in detached plasmas) [1].

A new HRTS system is supposed to contribute to this scientific programme by detailed measurements of both electron temperature and density radial profiles.

2. Thomson Scattering Systems

Thomson scattering [2] is a scattering of light on electrons in plasma. A coherent light from a monochromatic laser beam is led through the plasma and is scattered by free electrons. Because of the thermal motion, the scattered light is Doppler-shifted. If the electron velocity distribution is Maxwellian, the scattered spectrum has a Gaussian profile. From its width, the electron temperature can be determined. From the total intensity of the measured light, the electron density can be determined.

Due to a very low cross-section of Thomson scattering, a high-power laser and an extremely sensitive detection system is required. Also, stray light and light emitted by plasma itself as well as the noise of the detector is of the essential problems of this diagnostics. To minimize these effects, pulse lasers are used with the pulse length around 10-20 ns and the detection system is open just for this short time.

As a source of the primary light, two kinds of laser systems are commonly used: ruby laser and Nd-YAG laser. Ruby laser (λ=694.3 nm) has a sufficient energy, however it does not enable a sufficient repetition rate. Nd-YAG (or Nd-glass) lasers enable the repetition rate giving enough energy, and can be run either at the first harmonic in the near infra-red (NIR) region (λ=1064 nm) or at the second harmonic, green (λ=532 nm). For our new system, we are considering these two frequencies.

The scattered light from each observed spatial element must be collected and separated into different wavelength bands. This is realized by two basic types of the detection systems [1]: a spectrometer with a 2-D CCD/CMOS camera or a cascade of spectral filters with avalanched

photodiodes (APD). Usage of these systems depends mainly on the wavelength of the detected light.

2. HRTS for the COMPASS tokamak

T_e and n_e profiles will be measured along a vertical chord as shown in Fig. 1. The whole

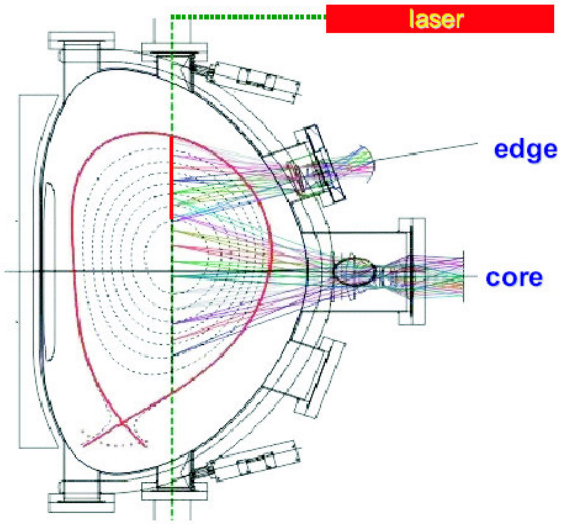

Fig. 1 : Layout of the TS system for the COMPASS tokamak.

chord is too long to be seen by only one collecting optics, i.e. a solid angle is too big. Thus, two detection systems will be built: one for the core and another one for the edge plasma. A spatial resolution of 3 mm at the pedestal region of 18 cm width, derived from the scientific programme demands, gives 60 spatial channels of the edge system. For the core, only 10 mm of spatial resolution is required along 400 mm, which gives 40 spatial channels. The time resolution (repetition rate of the laser pulses) will be 20-30 Hz.

Since the scientific programme is focused on the studies of pedestal plasma, first the edge detection system will be built, contrary to a typical situation, when an experience with a core TS helps much to estimate needed parameters of an edge system. Expected plasma parameters are 10×10^{19} m^{-3} to 1×10^{19} m^{-3} for the n_e, and 1 keV to 20-40 eV for the T_e in the central and edge parts of this system, respectively.

The challenging parameters required for HRTS on the COMPASS tokamak make us to touch possibilities of today's technology of both laser and detection systems. High spatial resolution implies small scattering volumes and consequently a small number of detected photons. Especially in the wavelength channels far from the laser wavelength, the number of detected photons may be comparable with the noise. Further, due to steep gradients of T_e and n_e in the pedestal region (see Fig. 2), a high dynamic range of the detection system is required.

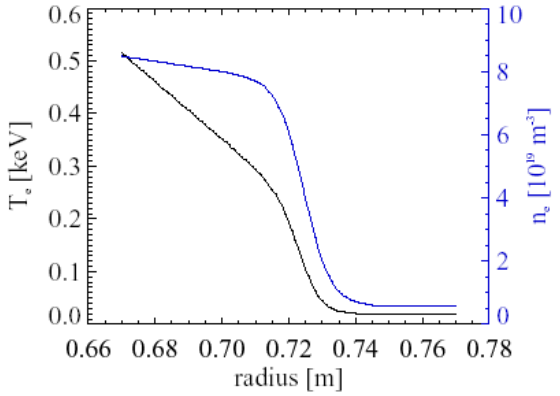

Fig. 2 : Expected profiles of electron temperature and density. Data originate in previous measurements at Culham.

3. Possibilities for COMPASS

To estimate sufficient laser energy and to choose a suitable kind of detection system, the ratio of the scattered photons to the plasma background photons (R) was calculated. For the same energy of the laser pulse, R is about eight times lower for the second harmonic frequency. This is caused by: (i) efficiency of the conversion to the second harmonic frequency (about 50%), (ii) twice lower background (from bremsstrahlung) and (iii) the fact that since the photons have a half of the energy, the number of them is double. Moreover, there are strong spectral lines emitted by the plasma and impurities in the visible region.

Due to these reasons, it seems to be better to choose the first harmonic frequency. In order to estimate a real difference between the systems, the efficiency of the detectors must be included. Main factors spoiling the ratio R are: quantum efficiency of the detectors and the time duration for which the detector is open.

Above mentioned considerations are charted in Fig. 3. A laser with a power of 10 J at the first harmonic frequency or 5 J at the second one and the pulse length of 15 ns was taken as a "reference" laser system. Value R=50 for the

second harmonic was obtained from real experimental data from the T-10 tokamak at the Kurchatov Institute in Moscow, recalculated for the conditions of tokamak COMPASS. For all the possible detection systems, the ratio *R* was evaluated.

Standard TS systems work with detection options A and D (Fig. 3): APDs in NIR region or ICCD in green visible region. However, the parameters required for the COMPASS edge detection system are challenging and touch the limits of possibilities of these systems. In order to improve the parameters, we have carried out a

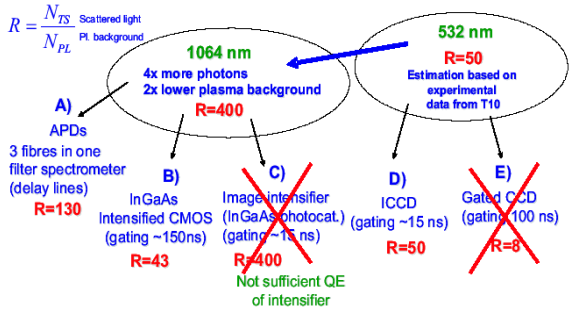

Fig. 3 : Schema of possible detection systems with calculated ratio R.

large trade survey, looking for new technologies.

For the second harmonic frequency, we have found a CCD camera [3], which can be gated for 100 ns (item E in Fig. 3). Due to a high noise coming from plasma, this time interval is still too long and the ratio *R* is consequently only 8. In this region, a standard system using an intensifier for gating is more suitable. This ICCD (item D in Fig. 3) can be gated for 15 ns, giving *R*=50.

For the first harmonic frequency, the situation is much more interesting. Until now, only APD systems were constructed due to missing fast cameras with a reasonable quantum efficiency in the NIR region. Now, an intensified CMOS camera equipped with an InGaAs photocathode [4] appeared on the market, which enables gating of 150 ns (item B in Fig. 3). This system would give the ratio *R*=43. Another possibility is, as in the case of the second harmonic, using a NIR camera and an intensifier (item C in Fig. 3) with gating 15 ns. For this system, the ratio *R* would be 400, which is the highest possible value. Unfortunately, the most advanced intensifiers available now have such poor quantum efficiency, that they would completely spoil the signal. The standard APD-based system gives the ratio *R*=130 (item A in Fig. 3).

If we exclude systems C and E, we have a choice of using the green laser combined with an ICCD, or the NIR laser combined with APDs or a CMOS camera. What are their characteristics?

The ICCD system in the green region is a standard compact system but for the edge plasma, the calculations show possible problems with noise. Pushing up the power of the laser can solve it but it significantly increases a price of the laser and approaches its power limit. This kind of system can be used for both edge and core plasmas.

The APD system in NIR region is also standard, however very complex. The dynamic range is poor and the number of spectral filters is limited. In order to reduce the number of detectors, three optical fibres from three spatial points can be joined using delay lines [5]. The time duration of the detection opening is thus larger; on the other hand, this system enables a very efficient subtraction of the background since the photodiodes work in a continuous regime. This system can also be used for both edge and core plasmas.

The CMOS camera in the NIR region is a tempting option. It has the advantages of both previous systems: it is compact, it has a high dynamic range and the plasma background is low. However, the camera has a disadvantage: the detection chip is too small (6 mm x 7 mm) to project the chord without losses of light. If we accept the cutting off the part of the collected light, the efficiency drops at least by a factor of two. Because of this reason, the detector is not suitable for the edge system, but can be successfully used for the core, where the density is higher.

The power of the laser can be effectively increased using a multi-pass system. The laser beam is injected into the tokamak chamber, where is reflected back and forth by several mirrors. The detector is opened for a slightly longer period; during this time, the laser beam crosses the chamber several times. This settlement can increase the TS signal but in the simplest configuration with non-gated reflection elements, it spoils either the spatial resolution or focalisation of the detected light. The mirrors are exposed to plasma and sputtered.

4. Conclusions

For TS experiments on the COMPASS tokamak, several different systems are considered and relevant parameters were calculated for both edge as well as core plasma. Possibilities of the edge detection system realization were found dues to a large trade survey looking for new technologies.

With regards to the required measured range of electron temperature (1 keV to 20-40 eV in the central and edge parts, respectively) and density (10×10^{19} m^{-3} to 1×10^{19} m^{-3}), two possibilities were chosen as the most suitable: a use of the Nd-YAG laser at the second harmonic frequency and the Littrow spectrometer with the ICCD camera, or a use of this laser at the first harmonic frequency and the Littrow spectrometer with the CMOS camera for the core, and the spectral filters with APDs for the edge. A multi-pass system can be taken into account in order to increase the laser power effectively.

These two possibilities are now being investigated, all available information is being collected and detailed parameters are being calculated in order to choose the proper TS system.

Acknowledgments: This research has been supported by the Doctoral grant project GACR 202/03H162.

References

[1] Panek R., et al., Czech. J. Phys. **56** [suppl. B] (2006) B125-B137.
[2] R. Barth, Third Carolus Magnus Summer School on Plasma Physics (George H. Miley), Spa, Belgium, 1998, p. 305-312.
[3] Fast CCD camera CoolSnap.
[4] Fast NIR camera LIVAR 400.
[5] R. Pasqualotto et al., Review of Sci. Instr., Vol. **72**, No. 1, January 2001.

Development of short wavelength FIR lasers for two color interferometer

K. Nakayama[1], M. Tomimoto[1], S. Okajima[1], K. Kawahata[2], K. Tanaka[2], T. Tokuzawa[2], T. Akiyama[2]

[1] *Chubu University, 1200 Matsumoto-cho, Kasugai-shi, Aichi 487-8501, Japan*
[2] *National Institute for Fusion Science, 322-6 Oroshi-cho, Toki-shi, 509-5292, Japan*

Simultaneously oscillated multi-line FIR lasers from a single FIR laser cavity pumped by two wavelength CO_2 lasers have been developed as optical sources of a two color interferometer for plasma diagnostics. Using two pump cw CO_2 lasers, we have obtained simultaneous oscillations as following : (i) 62- and 119-μm CH_3OH lasers from pumping by 9R(18) CO_2 laser and 9P(36) CO2 laser, (ii) 71- and 119-μm CH_3OH lasers from pumping by 9P(34) CO_2 laser and 9P(36) CO_2 laser, and (iii) 57-μm CH_3OD and 119-μm CH_3OH lasers from pumping by 9R(8) CO_2 laser and 9P(36) CO_2 laser.

1. Introduction

Far-infrared (FIR) lasers have been utilized as optical sources for various measurements. In the Large Helical Device (LHD) at National Institute for Fusion Science (NIFS), the electron density profile has been measured by a 13-channel Michelson interferometer using a cw 119-μm CH_3OH laser, routinely [1]. For high density operation of the LHD and for future plasma device such as the International Thermonuclear Experimental Reactor (ITER), powerful and stable FIR lasers with different wavelength at 40 μm to 100 μm are required to measure the vibration compensated electron density profiles. So we have been developing a two color interferometer using 48-μm and 57-μm CH_3OD lasers pumped 9R(8) CO_2 laser [2]. These multi-line lasers can be oscillated simultaneously [3]. To date many FIR laser lines have been reported from many kinds of molecules [4]. In view of the output power and the pressure dependence, simultaneously oscillated multi-line FIR laser is few except for the 48-μm and 57-μm lasers. A conventional FIR laser system consists of a single pump CO_2 laser and a single FIR laser. We propose multi-line FIR lasers from a single FIR laser cavity pumped by two CO_2 lasers. In our FIR laser system, 78 FIR laser lines have been obtained from CH_3OH, the isotopes, and other molecules in the wavelength region from 40 μm to 500 μm. A 119-μm laser is useful FIR laser line for plasma diagnostics and other applications [5]. Therefore we have investigated FIR laser lines which can be oscillated simultaneously with the119 μm laser. In this paper, the characteristics of simultaneously oscillated multi-line FIR lasers will be reported.

2. Experimental

A block diagram of the experimental setup is shown in Fig. 1. This system is set up on vibration isolating optical benches. The laser cavity of the CO_2 laser is formed by a ZnSe output coupler (55 % reflectivity, 20 m radius of curvature) attached to a piezoelectric transducer (PZT) and a grating (150 g/mm groove spacing). The cavity length is a 2.5-m-long for the CO_2 laser 1 and a 4.0-m-long for the CO_2 laser 2. In this experiment, both lasers were operated at powers between 25 W and 50 W. The pump CO_2 lasers are coupled into the FIR laser via concave mirrors (MR) with a 1.5 m radius of curvature. The input coupler of the FIR laser is a flat mirror with two off-axis holes, and the output coupler is silicon hybrid mirror with a 6-mm-diameter or

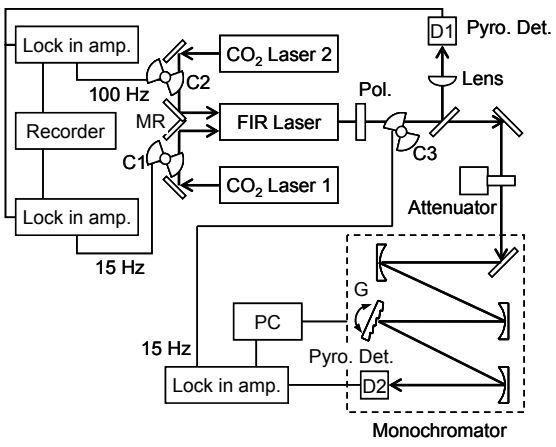

Fig. 1 : A block diagram of the experimental setup.

10-mm-diameter clear aperture at the center. The output mirror is movable by a stepping motor in order to tune the cavity length. The FIR laser tube is a 4.0-m-long, 25-mm-inner-diameter glass tube. The output window is used a CVD diamond because of a good transmission in the FIR region. The laser gases (CH_3OH and CH_3OD) are slowly flowing in order to keep the purity using mass flow controllers. The output radiation of FIR laser is passed through a polarizer, and it is divided by a beam splitter. The reflected light is detected by a pyro-electric detector (D1) for measurements of detuning curve and pressure dependence. The transmitted light is coupled into a Czerny-Turner type monochromator. A diffraction grating (G) in the monochromator is a 220 μm groove spacing and 26 ° blaze angle. The grating set on a motorized stage is rotated at incident angle from 0 ° to 60 °. The diffracted light is detected by a pyro-electric detector (D2).

In this experiment, simultaneously oscillated FIR lasers from CH_3OH and a gas mixture of CH_3OHa and CH_3OD have been investigated by using two wavelength cw CO_2 lasers.

3. Results and Discussion

Table I shows the characteristics of FIR laser lines for the experiment. The polarizations of these lasers are perpendicular to the pump CO_2 laser. The polarization of the pump CO_2 laser 1 and 2 are the same. Each FIR laser power has been obtained by FIR laser system of different conditions (laser tube, output mirror, output window, etc.). The 119-μm laser and the 71-μm laser are known to have different laser transitions [6]. An assignment of energy levels for the 62-μm laser and the 57-μm laser is unknown.

Table I : Characteristics of FIR lasers for the experiment.

λ (μm)	Pump	Assignment[a)]	Molecule	Pol.[b)]	P[c)] (mW
118.834	9P(36)	E,gr,0,8;16 →co,0,8;16 →co,0,7;15	CH_3OH	⊥	680 (148 W)
70.5116	9P(34)	A,gr,1,5;9 →co,1,5;9 →co,0,6;10	CH_3OH	⊥	65 (75 W)
61.6133	9R(18)	—	CH_3OH	⊥	9.5 (129 W)
57.1511	9R(8)	—	CH_3OD	⊥	1.6 W (138 W)

a) $|\sigma, v, n, K; J\rangle \rightarrow |v, n, K; J\rangle \rightarrow |v, n, K; J\rangle$, [6]
b) Polarization relative to polarization of pump CO_2 laser.
c) FIR laser power and pump CO_2 laser power.

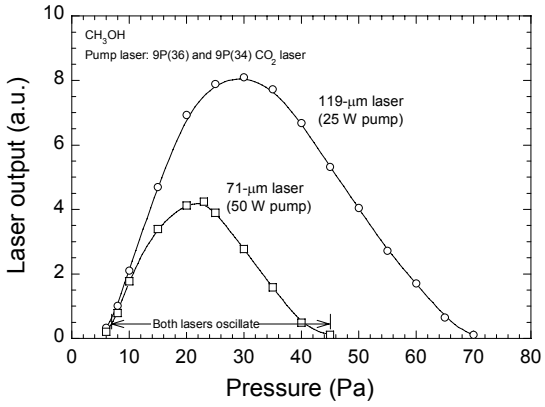

Fig. 2 : FIR laser output as a function of pressure for the 119-μm CH_3OH laser and the 71-μm CH_3OH laser.

Shown in Fig. 2 are the data from pressure dependence measurements for the 119-μm laser and the 71-μm laser. Both lasers oscillate in the pressure range from 6 Pa to 45 Pa. Therefore the pressure was set at 25 Pa. A resonance condition given by the following equation

$$m \times \lambda = 2L, \qquad (1)$$

where m is an integer, λ is the wavelength, and L is the cavity length. There is a cavity length (for example 118.834/2 μm×19=1128.9 μm and 70.51163/2 μm×32=1128.2 μm) which satisfies the resonance condition for the two wavelengths. Figure 3 shows the detuning curves of the 119-μm laser and the 71-μm laser by two CO_2 laser pumping. The CO_2 lasers were chopped by two optical choppers (C1 and C2) with a different frequency. The cavity length at which both lasers oscillate can be decided from the detuning curves.

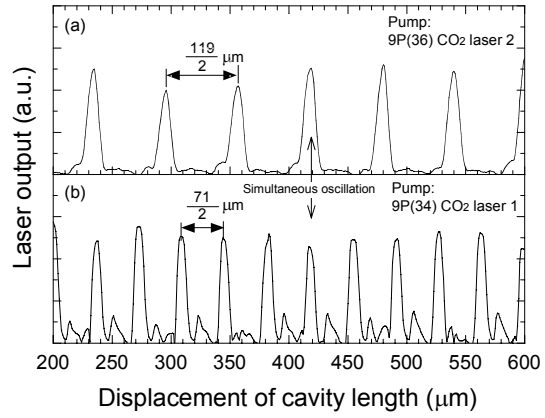

Fig. 3 : Detuning curves of (a) the119-μm CH_3OH laser and (b) the 71-μm CH_3OH laser by two CO_2 laser pumping.

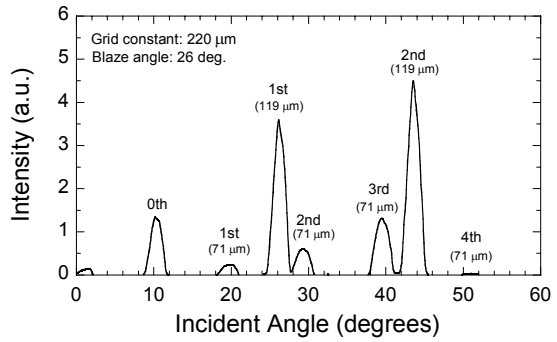

Fig. 4 : Spectrogram of the simultaneity oscillated 119-μm and 71-μm CH_3OH lasers by two CO_2 laser pumping.

The cavity length is fixed at the position, and the output radiations of FIR lasers were analyzed by the monochromator. The FIR lasers were chopped by optical chopper (C3) then. Figure 4 shows the diffraction patterns of the 119-μm and 71-μm lasers as a function of the incident angle. It is clear that these lasers can be oscillated simultaneously. The difference in power between the 119-μm laser and the 71-μm laser can be adjusted by changing the input power of the CO_2 lasers and the coupling mirrors (MR). We have also realized a simultaneous oscillation of the 119-μm and 62-μm lasers by this way.

Figure 5 shows are the pressure dependence of output power for the 119-μm CH_3OH laser and the 57-μm CH_3OD laser. Both lasers oscillate in the pressure range from 6 Pa to 65 Pa. Theses lasers are a similar pressure dependence. The optimum pressure is about 30 Pa. To test the simultaneous oscillation of these lasers, the pressure is set at 30 Pa. A gas mixture of 2 cc/min CH_3OH and 2 cc/min CH_3OD were

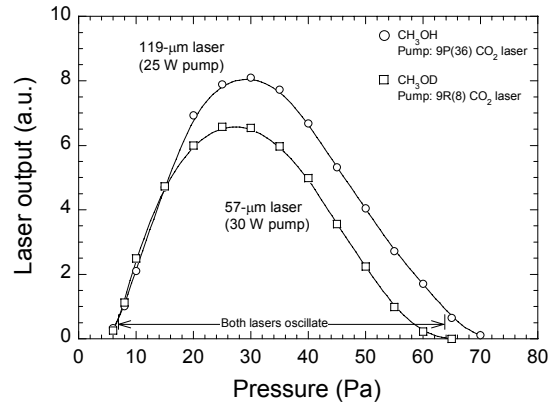

Fig. 5 : FIR laser output as a function of pressure for the 119-μm CH_3OH laser and the 57-μm CH_3OD laser.

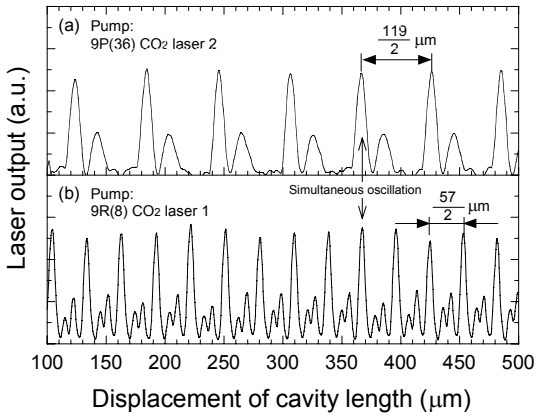

Fig. 6 : Detuning curves of (a) the119-μm laser and (b) the 57-μm laser from CH_3OH and CH_3OD mixed gases by two CO_2 laser pumping.

supplied by mass flow controllers. There is a cavity length (for example 118.834/2 μm×13=772.4 μm and 57.1511/2 μm×27=771.5 μm) which satisfies the resonance condition for these lasers. The data shown in Fig. 6 are the detuning curves from CH_3OH and CH_3OD mixed gases by two pump CO_2 lasers. Figure 7 shows the spectrogram of the simultaneously oscillated the 119-μm CH_3OH and 57-μm CH_3OD lasers as a function of the incident angle. In this experiment, the output power was decreased about 25 % compared with a single gas operation. The decrease in power is believed to be due to absorption of each gas and a decrease in quantity of gas in the laser cavity.

We have obtained simultaneously oscillated the 119-μm and 71-μm CH_3OH lasers, the 119-μm and 62-μm CH_3OH lasers, and the 119-μm CH_3OH and 57-μm CH_3OD lasers by using two pump CO_2 lasers. This excitation

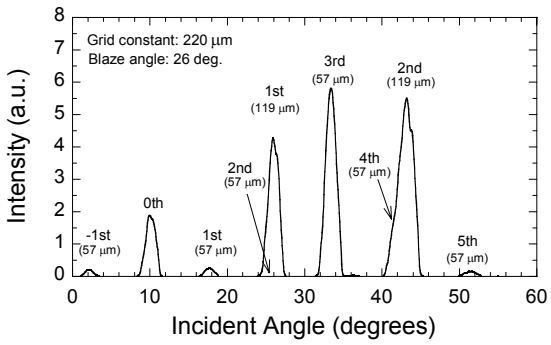

Fig. 7 : Spectrogram of the simultaneously oscillated 119- μm and 57-μm lasers from CH_3OH and CH_3OD mixed gases by two CO_2 laser pumping.

method can obtain optional multi-line FIR lasers easily, in comparison with a conventional method by single CO_2 laser pumping. These lasers are expected as optical sources of the two color FIR laser interferometer. We intend to survey other simultaneously oscillated multi-line FIR lasers from other molecules, also.

Acknowledgments

This work was supported in part by a grant from the High-Tech Research Center Establishment Project of a Grant-in-Aid for Scientific Research from Ministry of Education, Culture, Sports, Science and Technology.

References

[1] K. Kawahata *et al*., Rev. Sci. Instrum., **70,** (1999) 707.
[2] K. Kawahata *et al*., Rev. Sci. Instrum., **77,** (2006) 10F132 1-4.
[3] K. Nakayama *et al*., Rev. Sci. Instrum., **75,** (2004) 329.
[4] N. G. Douglas, Millimetre and submillimetre wavelength lasers. Springer-Verlag, (1989) part II.
[5] H. Ohkuma *et al*., Prof. 10th biennial European Particle Accelerator Conference, Edinburgh**,** (2006) TUOAFI03.
[6] G. Moruzzi *et al*., Microwave, infrared and laser transitions of methanol. CRC Press**,** (1995) Chapter 6.

Analysis of the noise of the Tore Supra Thomson Scattering measurements

L. Manenc, J. Lasalle

Association Euratom-CEA, Département de Recherche sur la fusion Contrôlée,
CEA/Cadarache F-13108 Saint Paul Lez Durance, France E-mail : laurent.manenc@cea.fr

On the Thomson scattering of Tore Supra a systematic study of the noise was carried out in order to take measures to upgrade the system and to give a polychromator prototype benefit from that.
In this paper, we discuss:

- a description of the various noises observed in particular using a controllable fast oscilloscope remotely by network Intranet,
- the conclusions that we have derived for the prototype, acquisition and processing associated. The installation of fast acquistion and processing based on correlator should improve the signal to noise ratio of about 6 to 10 dB during plasma with strong additional heating and make disappear aberrant points.

1. Introduction

On Tore Supra the Thomson scattering provides the Temperature and the Electron Density at 12 points of plasma. This, thanks to rigorous procedures of calibration, in particular the Rayleigh calibration and the permanent monitoring of the thermal drift of the detectors. Very interesting because of the localization of its measurement, this diagnostic nevertheless suffers from a low signal to noise ratio. We have, using a numerical oscilloscope, identified and quantified the various sources of noises which is the first step for improving the diagnostic.
These findings will also be used to design a new prototype polychromator who will be equipped with an optimized acquisition system.

2. Description of the diagnostic

2.1 general

The diagnostic consists of three synchronized lasers which send at the frequency of 27 Hz, pulses (~30ns) in the plasma. This beam is observed by 12 polychromators who are blind at the laser wavelength and collect the Thomson signal in 3 windows of the spectrum. They are also sensitive to the radiation emitted by plasma in this field of wavelength. In order to eliminate this continuous component, the link towards acquisition is made via a capacitive coupling. Then the signal is amplified then integrated during a gate triggered by the laser with an adapted delay. Then it is digitized and memorized to be used by a processing which is launched only at the end of the shot. Whatever its origin, the noise seems only to be a fluctuation of a signal at 27Hz.

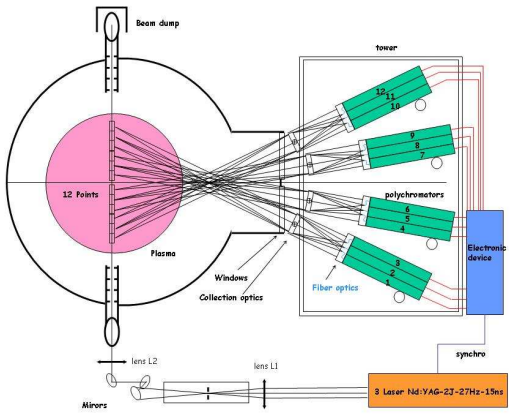

Fig. 1: Diagnostic overview

Only an analysis high frequency on the signal before integration made it possible to identify the origins of the noises, and to evaluate their relative importance.

2.2. Polychromator

The polychromator breaks up the incident light in three bands via filters.Luminous flow leads on a APD (Avalanche Photodiode) which widens a little the pulse because of the limitation of its bandwidth (20MHz). Considering current acquisition this limitation of the bandwidth is not detrimental because it corresponds to the minimal duration of the integration gate (60ns).

2.3. Processing

The processing is based on the calculation of the ratios of the channels of a given polychromator. Knowing the theoretical spectrum of the

Thomson scattering, the value of this ratio between channels is characteristic of a particular value of the electron Temperature T_e. The latter being determined, owing to the fact that we have an absolute calibration of the diagnostic via the Rayleigh scattering, we can then calculate the electron density n_e.We can connect the signal to noise ratio of T_e and n_e to that of the channels being used to determine it.

2.4. Signal

The raw signal varies between 0-10V and is coded on 12 bits. In the case shown in fig 2 and 3 (ohmic shot), the quality of measurements is correct and allows SN (Power signal to noise ratio) about a 30dB.

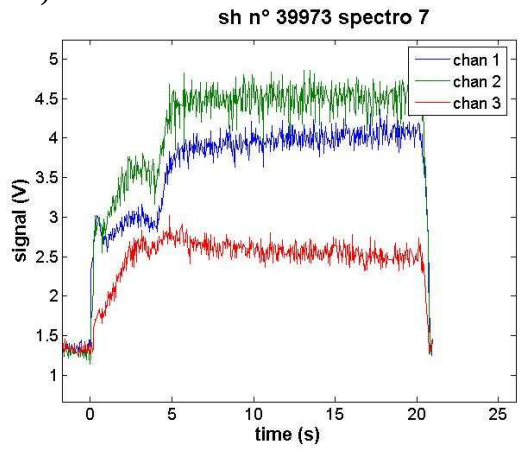

Fig. 2: 3 polychromator's channels shot 39973

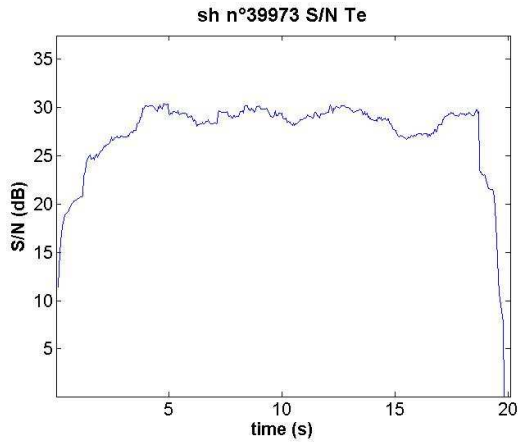

Fig. 3: signal to noise ratio shot 39973

3. Noise in the present configuration

3.1. Measurement configuration

We had the constraint not to obstruct the exploitation of Tore Supra which means keeping the diagnostic operational. This aspect has strongly constrained our experimentation by limiting the number of channels instrumented as well as the access to the diagnostic.

We positioned the oscillocope in two points of the acquisition system :

- At the exit of the APD,
- After the amplifier before the integrator.

We checked the coherence between two measurements like after numerical integration with the noise observed by standard acquisition.

On the level of the polychromator we made measurements with and without masking of fibre.

We carried out acquisition in the situations:

- Without plasma
- With ohmic plasma
- With plasma and additional heating

To illustrate the interest to have sampled signal, one accounted for 3 distinct frames acquired with the oscilloscope (2500 pts Fe = 2.5Ghz) during shot, we can see the laser pulse drowned in noise (fig 4).

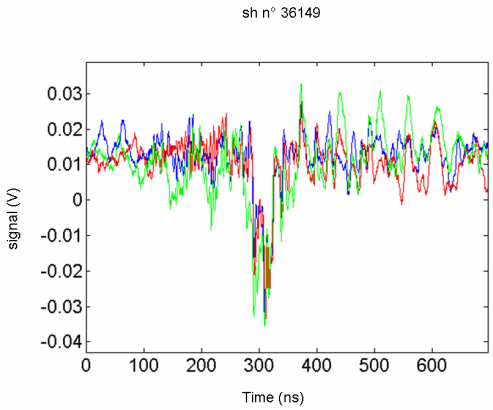

Fig. 4: 3 frames with laser pulse in the noise

2.2. Inventory

The principal noises which could be quantified are listed below:

Detector noise

The signal from the detector was measured in the absence of any light. After filtering by LB filter of 20Mhz we find

$\sigma = 170\mu V$

Which corresponds to the data of the manufacturers: there isn't ageing of the detectors after "20 years" of usage, eventhough the detectors are in direct sight of plasma.

After amplification (gain = 10) we obtain a noise of the order $\sigma = 1.88mV$ which confirms that the amplifier does not degrade the signal significantly. By simulating the effect of the

integrator on this signal we obtain a noise with σ=50mV which corresponds well to what we observe on standard acquisition.

Laser Parasitic signal

With each laser shooting, we note the presence of a parasitic signal (duration ~1µs). It is relatively stable and its contribution after integration is weak, thus, it appears as one light offset which is easily corrected. There remains however a residual noise related to the fluctuations of this parasitic signal and to the jitter. Although it is significantly different for each channel it is possible to evaluate the typical level of noise after integration around $\sigma = 25mV$

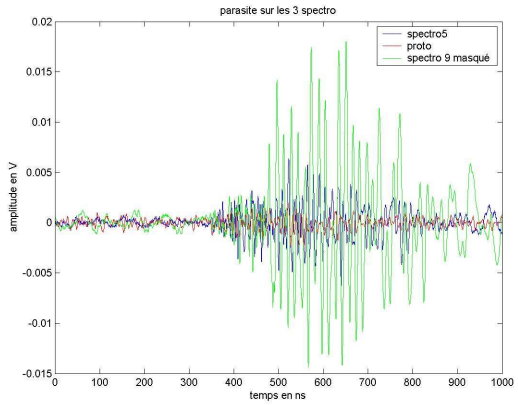

Fig. 5: examples of parasitic laser signal

Jitter

We could highlight a jitter approximately 1 ns on integrator's trigger. In order that this effect remains negligible, we must have a good positioning of laser pulse in the integration gate.

This jitter contributes nevertheless to the noise of offset correction, the laser parasitic signal being much wider than the integration gate.

Other parasitic noises

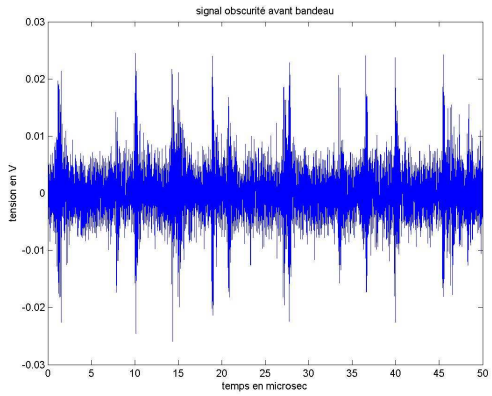

Fig. 6: 3 pulses modulated

Certain channels, sometimes, without explanation, present parasitic signal in the form of modulated pulses.

When they coincide with the laser pulse, they have a strong effect on the current processing by varying the pedestal. They are the cause of the aberrant points which appear occasionally.

LF Noise

During the plasma there is LF- noise below the coupling frequency. This remains negligible up to now.

Photonic noise

In the situations without heating it appears that the noise increases with the signal. Several approaches permit to analyze this effect:

- The noise calculation during shot,
- The noise calculation during Rayleigh calibration,
- The noise calculation starting from the energy balance of the number of incidental photons on the detector (order of magnitude 10^4)

The three approaches give coherent results. Although depending on the channel, this noise seems Poissonian and to verify:

$\sigma^2 = \alpha S$ with $\alpha \approx 2mV$

S ,σ the average and the standard deviation of the signal in mV

Plasma noise

In the absence of heating:

The noise could be determined by observation of the signal outside of pulses, it remains appreciably lower than the detection noise.

In the presence of heating:

It is advisable to distinguish two kind of noises:

- a noise of electromagnetic origin (heating ICRH) which appears even when the fibre is hidden (line~50MHz spectro 9 fig 7), It isn't harmful since it is above the integrators's bandwith.
- a noise which goes through the APD and whose spectral density corresponds to the transfer function of the system(cf fig7 spectro 5 and proto). This noise becomes dominating quickly. It probably correspond to the fluctuation of the radiation emitted by plasma.

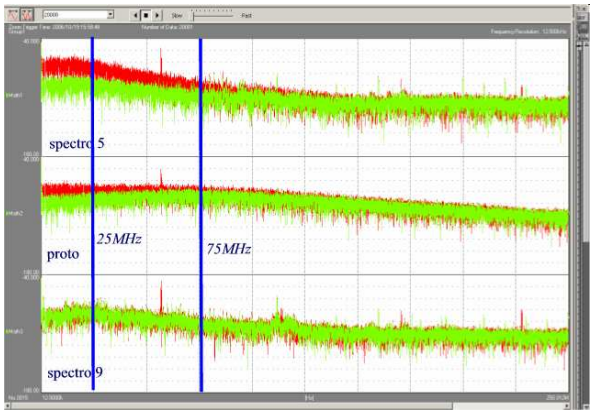

Fig. 7: noise spectral density on 3 polychromator, g :without heating, r : with ICRH heating

3.2. Current limitations

In the absence of additional heating the noise is dominated by the photonic noise except in two cases:

- The low levels in particular for the polychromators viewving the plasma edge where the noise of the detectors remains significant,
- The aberrant points on certain channels caused by the variation of the pedestal due to a parasitic signal.

When there is a significant heating (> 4MW) it is the noise related to the fluctuating light plasma which becomes dominating.

4. Prototype and matched processing

4.1. Upgrade

An improvement of the space resolution and quality of measurement are required. For that purpose, these modifications were brought:

- Doubling the number of the detectors, 2 space channels by polychromator,
- Improvement of the optical coupling,
- Photodiode more powerful: better bandwith, temperature stabilization.

In addition:

- A laser monitor was installed,
- A completely different acquisition is under development. A sampler is substituted for the integrator.

4.2. Improvements expected

The loss of energy due to the increase in the spatial resolution was compensated by an improvement of the optical coupling. In the end the incident energy on the detector remains unchanged. Thermal stabilization makes it possible to avoid the optoelectronics calibration which is currently carried out before each shoot.
In addition, the increase in the bandwidth associated to the fast acquisition at the same time makes possible to reduce the duration of laser pulse at exit of diode and to adapt detection, reducing by that the noise coming from the light emitted by plasma. To this new acquisition will be associated processing based on a correlator and algorithms for elimination of the pedestal .

4.2. Experimental data

A first series of tests could be carried out with a monochannel prototype version and by using the numerical oscilloscope in own way of acquisition. Thus we made a first evaluation of the profit brought: during the phases of heating the signal to noise ratio can be improved about 6dB(fig 8).

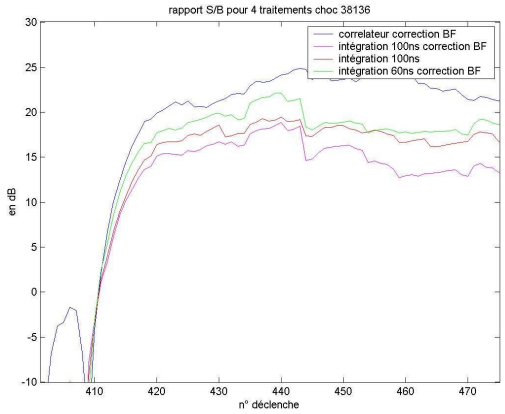

Fig. 8: signal to noise ratio with various processing

In addition, the monitor allowed to improve the laser synchronization and thus to shorten the pulse duration, which could be fully exploited latter at the time of the prototype installation with its final acquisition.

5. Conclusion

In general, besides some erratic parasitic noises, current acquisition does not degrade in a significant way the signal but runs up against the physical limits which are the number of photons collected as well as the fluctuation of the radiation emitted by plasma. The experiments carried out let foresee that the prototype and the associated treatment should improve appreciably (6 to 10dB) the signal to noise ratio, in particular in the cases of aberrant points and that of plasma with strong additional heating.

First operation of Polaization Interferometer for Thomson Scattering Diagnostics

T. Hatae[1], J. Howard[2], Y. Hirano[3], H. Koguchi[3], S. Kitamura[1], O. Naito[1], S. Kajita[1]

[1] *Fusion Research and Development Directorate, Japan Atomic Energy Agency, Naka, Ibaraki 311-0193, Japan*
[2] *Plasma Research Laboratory, The Australian National University, Canberra ACT 0200 Australia*
[3] *National Institute of Advanced Industrial Science and Technology, Tsukuba, Ibaraki 305-8568, Japan*

A polarization interferometer based on the Fourier transform spectroscopy for the Thomson scattering diagnostics was developed to demonstrate the proof-of-principle for the first time. Target T_e and n_e ranges for the polarization interferometer are < 1 keV and > 5×10^{18} m^{-3}, respectively. The electron temperature was successfully measured by the polarization interferometer in TPE-RX reversed field pinch machine. The temperature of the polarization interferometer nearly agrees with that of the filter polychromator.

1. Introduction

Incoherent Thomson scattering [1] that can measure electron temperature T_e and density n_e profiles simultaneously is a standard diagnostic in magnetic confinement experiments. Usually grating spectrometers or interference filter polychromators have been used to analyze the scattered spectrum. Though these are established methods, the throughput decreases when there are many wavelength channels, while the relative calibration between wavelength channels is necessary.

It is well known that Fourier transform spectrometers [2] offer some potential advantages over dispersive systems. Fourier transform spectroscopy is a measurement technique whereby spectra are collected based on measurements of the temporal coherence of a radiative source, using time-domain measurements of the electromagnetic radiation. In general, the main advantages of the Fourier spectroscopy are as follows. (1) The Fourier transform spectrometer (i.e. interferometer to measure the temporal coherence) can use the optical system of the high throughput (Jacquinot advantage), (2) Since the Fourier transform spectrometer observe the whole wavelength area at the same time, the S/N ratio is improved (Fellgett advantage). More importantly, for this application, the method can be implemented in a simple and compact, high-throughput system. Optical coherence techniques have been applied successfully for plasma spectroscopy. In particular, high-throughput, wide field-of view polarization interferometers have been used for Doppler imaging of ion temperature in the H-1 heliac [3-5]. These modulated or static coherence imaging systems monitor the complex coherence (fringe visibility and phase) of an isolated spectral line at one or more optical delays. A method based on measurement of the optical coherence of scattered radiation at a fixed optical delay has also been proposed for incoherent Thomson scattering [6]. However, this method has not been demonstrated to date.

To demonstrate this method, we are developing a Fourier filter for Thomson scattering based on a fixed delay polarization interferometer. Proof-of-principle tests have been carried out in TPE-RX reversed-field pinch (RFP) machine (Major radius 1.72m, Minor radius 0.45m, Plasma current 0.5MA, T_e (0)~1keV, pulse duration 100ms) [7], using the existing single-channel YAG laser Thomson scattering system.

2. Polarization interferometer based on Fourier transform spectroscopy

The polarization interferometer is composed of a birefringent plate of fixed optical delay sandwiched between polarizers [6]. When the light is observed through this interferometer, interference fringes appear at infinity due to Fresnel-Arago law. Thomson scattered radiation that traverses the first polarizer is incident on a birefringent plate whose fast axis is oriented at 45° to the polarization direction. The plate splits the incident scattered scalar wave component, relatively delaying nominally equal amplitude components by time τ before they recombine at a final polarizer and are focused on to a detector. The orthogonally polarized outputs at the final

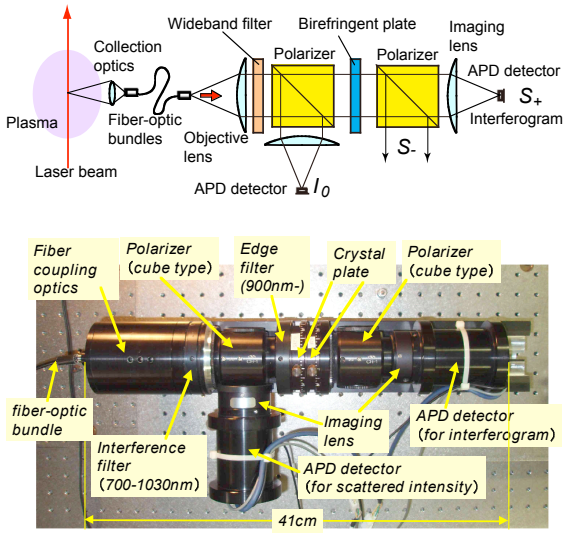

Fig. 1 : Upper: Schematic of a polarization interferometer for Thomson scattering diagnostics. Lower: Picture of the prototype polarization interferometer.

polarizing splitter form complementary, or antiphase interferometric images of the input radiation. By suitably choosing the optical delay, these independent outputs provide sufficient information to determine both the electron temperature and density.

A schematic of the prototype polarization interferometer for Thomson scattering diagnostics is illustrated in Fig. 1. Scattered light is collected and introduced to the polarization interferometer through a fiber-optic bundle. This polarization interferometer consists an objective lens as the fiber coupling optics, a band pass filter, polarizers, a birefringent plate which gives optical path delay, an imaging optics to detector, and dual detectors.

For radiation of centre frequency ν_0, the interferometer signal at either of the final polarizer ports is given by

$$S_{\pm} = \frac{I_0}{2}(1 \pm \zeta \cos\phi_0) \qquad (1)$$

where $\phi_0 = 2\pi\nu_0\tau_0 = 2\pi N$ is monochromatic birefringent phase delay, and τ_0, N are the center-frequency time delay and the order of interference, respectively [6]. The fringe visibility (fringe amplitude normalized to mean intensity) $\zeta = \zeta_I\zeta_T$ includes an instrumental component ζ_I due to the average of the birefringent plate delay over the angular extent of the source (analogous to familiar slit function for grating spectrometers) as well as the degradation ζ_T due to the finite source spectral width.

For a thermal distribution of T_e < 1keV, the fringe visibility associated with the Thomson scattered light takes the simple from

$$\zeta_T(\phi_0) = \exp[-\hat{\phi}_0^2 sin^2(\theta/2)v_{th}^2] = \exp(-T_e/T_C) \qquad (2)$$

where $\hat{\phi}_0, \theta$ are the group phase delay and the angle between the incident and scattered wavevectors, respectively. T_C is a 'characteristic temperature' set by the waveplate delay and the scattering angle

$$kT_C = \frac{1}{2}m_e c^2 \Big/ [\hat{\phi}_0 sin(\theta/2)]^2 . \qquad (3)$$

Optimum sensitivity to temperature variation is obtained when the optical delay is chosen such that $T_e \sim T_C$, or $\Delta\nu/\nu_0 \sim 1/N$, where $\Delta\nu/\nu_0$ is the Thomson spectral bandwidth [4].

For low temperatures, the variation of fringe visibility with temperature is best measured by setting $\phi_0/2\pi = M/2$ where M represents an integer number of half waves. A quartz waveplate will be used as the birefringent plate in this design. The interferogram calculations take into account the wavelength-dependence of quartz birefringence and, for now, assume the spectrum to be ideally passed by the wideband filter. At a zero crossing, the scattered signals at the complementary output ports are

$$S_{\pm} = \frac{I_0}{2}\left[1 \pm \zeta_T(\phi_0)\right], \qquad (4)$$

where $\zeta_T(\phi_0)$ is the Thomson spectrum fringe visibility at delay $\phi_0 = M\pi$.

Since proof-of-principle tests is carried out in TPE-RX using the existing YAG laser Thomson scattering system [7], parameters for design of a prototype polarization interferometer are fixed as follows: $T_e \leq 1$ keV, $n_e \geq 5 \times 10^{19}$m^{-3}, scattering angle 90°, YAG laser wavelength 1064nm. Thomson spectra and their associated interferograms for T_e = 0.2, 0.4, 0.6, 0.8, 1.0 keV are shown in Fig. 2. To reject stray light by the YAG laser and reduce plasma background light, the wideband filter is placed at the entrance of the polarization interferometer. Variations of fringe visibility ζ_T with electron temperature for the quartz plate thickness = 0.545, 0.550, 0.555 mm are shown in Fig. 2. Based on these calculations, a thickness of 0.555mm will deliver a sensitive variation of fringe visibility with electron temperature as illustrated in Fig.2.

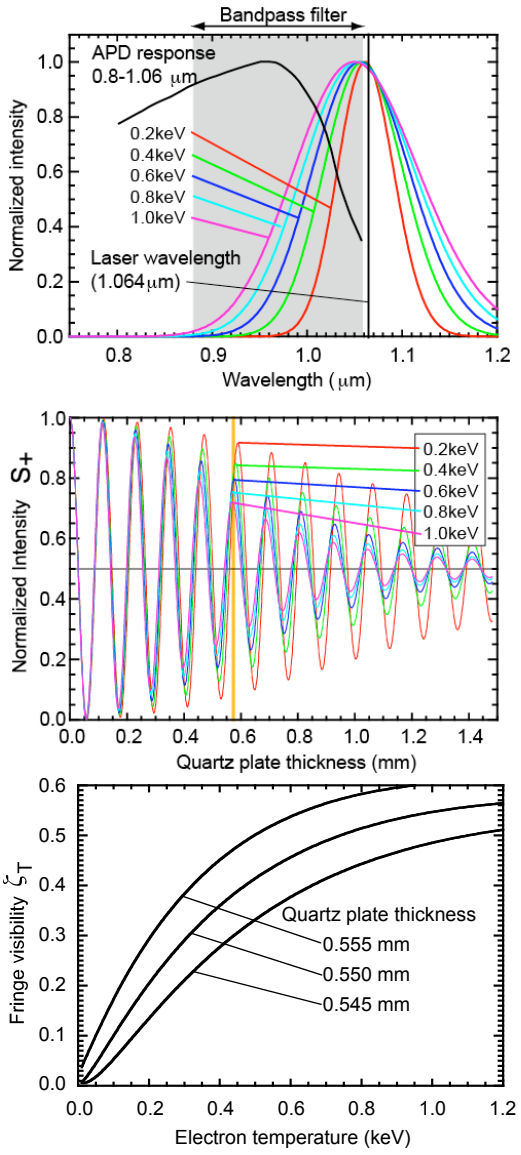

Fig. 2: Upper: Thomson scattered spectra for temperatures in the range of 0.2-1.0keV. Middle: The calculated interferograms S_+. Lower: Variations of fringe visibility ζ_T with temperature for three quartz plate thicknesses (0.545, 0.550, 0.555mm).

3. Initial test using a blackbody radiation source

When the temperature of the blackbody is changed from 1273K to 1773K (1000-1500 °C), the spectrum changes as shown in Fig. 3. LAND R1500T as the blackbody radiation source is used for this test. The fringe visibility for the blackbody temperatures in this range, and in the bandpass 750nm-1000nm, is calculated and plotted in Fig.6 (solid line). To obtain a sensitive variation with temperature we used two crossed quartz waveplates having a measured effective thickness

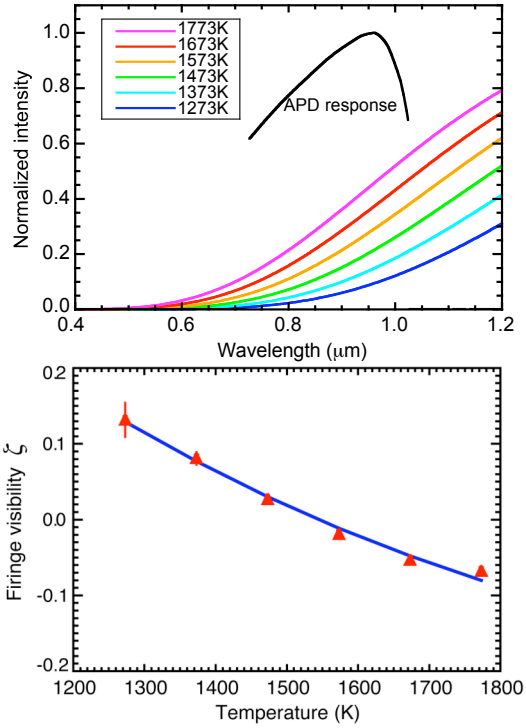

Fig.3: Upper: Spectra of blackbody radiation source for temperatures in the range 1273-1773K. Lower: Variations of fringe visibility ζ with temperature for a quartz plate thickness (0.1293mm). The calculated fringe visibility (solid curve) is compared to experimental values (triangle).

of 0.1293 mm. Fringe visibilities for blackbody temperature in the range 1273-1773 K produced by the polarization interferometer are measured using two APD detectors, and the ideal value of ζ is calculated numerically. The error bars are calculated taking into account the estimated 1mV uncertainty on the voltage levels. To fit ideal curve with experimental values, an arbitrary offset of value 0.11 in the visibility is required to be added to experimental values as shown in Fig.3. The effective centre wavelength has to shift to the blue to account for this additional offset. Because most of the power from the blackbody radiation source is in the near infrared, the effective wavelength of the light in the APD passband is sensitive to the details of the APD responsivity. Moreover, the interferometer instrumental fringe visibility degrades near 1000 nm due to the inefficiency of the first film polarizer. This will give rise to a blue bias, though we have not attempted to account for this numerically. The important point is that the magnitude of the change in fringe visibility agrees with the numerical calculation. This result

confirms that, following suitable calibration, we will be able to sense visibility changes due to changes in the electron temperature.

4. First measurements of electron temperature using polarization interferometer

Proof-of-principle test of the polarization interferometer were carried out in TPE-RX reverse field pinch machine. The picture of the polarization interferometer is shown in Fig.1. The pulsed poloidal current drive (PPCD) operation was applied to produce high T_e, n_e (T_e ~1keV, n_e ~1×10^{19}m^{-3}) plasmas. A YAG laser Thomson scattering system has been installed in TPE-RX, and this system has a conventional filter polychromator (4 spectral channels). The existing Thomson scattering system is utilized for this test. The electron temperature of one spatial point at the plasma center was measured employing the filter polychromator and the polarization interferometer alternately. Similar T_e values within data variation and error bar ranges were measured by both spectrometer. Data range of the polychromator is 799-1019eV, measured values of the polarization interferometer are 1110±145eV, 1140±280eV. Typical waveform of polarization interferometer is shown in Fig.4.

The data variation of the polychromator is caused by reproducibility of the PPCD discharge. The relatively large error of the polarization interferometer data proceeds from (1) entry of external noise to preamplifier circuit, (2) increasing of photon noise caused by increasing of intensity of background light (plasma light) due to Jacquinot and Fellgett advantages. To reduce the external noise, further shielding is necessary. To reduce the photon noise, it seems that appropriate filtering using bandpass filter is effective.

5. Conclusion

A polarization interferometer based on the Fourier transform spectroscopy for the Thomson scattering diagnostics was developed to demonstrate the proof-of-principle for the first time. The electron temperature was successfully measured by the polarization interferometer in TPE-RX. The temperature of the polarization interferometer nearly agrees with that of the filter polychromator.

For the next step, improved polarization interferometer having the wider T_e range (T_e <40keV) is considering for JT-60U.

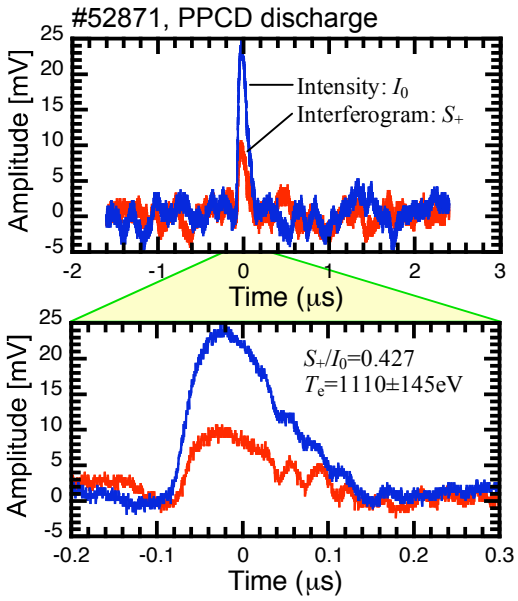

Fig.4: Thomson scattering signal by the polarization interferometer

Acknowledgments

The authors wish to thank Drs. M. Kiyama, H. Sakakida, K. Yamabe for their useful discussions at TPE-RX. One of the authors (TH) is grateful to M. Gwynneth for his technical assistance in initial test at ANU. This work is supported in part by Grant-in-Aid for Scientific Researches on Priority Area "Advanced diagnostics for burning plasma" from Ministry of Education, Culture, Sports, Science and Technology (No. 18035016).

References

[1] J. Sheffield, *Plasma Scattering of Electromagnetic Radiation* (Academic press, New York, 1975), p.191.

[2] K.D. Möller, *Optics* (University Science Books, Mill Valley, 1988), p.311.

[3] J. Howard, C. Michael, F. Glass, and A. Cheetham, Rev. Sci. Instrum. **72**, (2001) 888.

[4] J. Howard, Appl. Otp. **41**, (2002) 197.

[5] J. Howard, C. Michael, F. Glass, and A. Danielsson, Plasma Phys. Control Fusion **45**, (2003) 1143.

[6] J. Howard, Plasma Phys. Control Fusion **48**, (2006) 777.

[7] H. Koguchi, Y. Hirano, H. Sakakita, et al., preprint of 21st IAEA Fusion Energy Conference, IAEA-CN-149/EX/P3-8 (2006).

THz gyrotron FU CW Series for application to high power THz technologies

T. Idehara, La Agusu, H. Mori, S. Kobayashi, T. Saito, I. Ogawa and S. Mitsudo
Research Center for Development of Far Infrared Region, University of Fukui (FIR FU)

Abstract
For application of high frequency gyrotrons to high power THz technologies, we are developing THz CW gyrotron, FU CW Series. Gyrotrons FU CW I, II and III are being developed. The present status of the gyrotron series is presented.

1 Introduction

The development of high frequency gyrotrons with high field superconducting magnets is rather a minor way of the gyrotron development. It was carried out in several research institutes, that is, IAP RAS, MIT, the University of Sydney and the University of Fukui (FIR FU). The frequency range of submillimeter waves is achieved in 1980s and 1990s by several gyrotrons in these institutions.

In FIR FU, we have developed high frequency Gyrotron FU Series which consists of nine gyrotrons. In 1996, Gyrotron FU IVA achieved the frequency of 889 GHz with the output power of around 100 W. The frequency corresponds to the wavelength of 377 μm. This frequency was the long-term world record for high frequency operation of gyrotron untill 2006. Recently, our pulsed gyrotron with a high field pulse magnet achieved the breakthrough of 1 THz by the second harmonic operation at the field intensity of 19.1 T.

Now, we are developing the THz Gyrotron FU CW Series, which will cover sub-THz to THz range and operate in a complete CW mode. In this paper, we will present about three gyrotrons Gyrotron FU CW I, II and III in detail and some applications of these gyrotrons.

2. Gyrotron FU CW I

The first gyrotron of the FU CW Series, Gyrotron FU CW I was developed in FIR FU under collaboration with Institute of Applied Physics, Russian Academy of Science (IAP RAS). The main parameters are summarized in Table 1. Designed cavity mode is $TE_{22,8,}$ the corresponding frequency 300 GHz and maximum output power 3.5 kW. Measured parameters are also shown in the table. The frequency is exactly same as the designed value. The output power has been increased up to the just half value of the designed. Now, we are trying to increase the output power by adjusting the operation parameters precisely and the alignment. We have gegun to apply the gyrotron for material processing, for example, ceramics sintering.

Table 1 Specification of Gyrotron FU CW I

	Designed	Measured
Frequency	300±2 GHz	300.1±1.1 GHz
Output power	0.5 - 3.5 kW	0.1 - 1.75 kW
Acceleration voltage	16±1 kV max	15 kV
Beam current	1.1±0.1 A	1.0 A
Radius of beam electron	3.71 mm	−
Pitch factor	1.2 – 1.3	−
Diameter of window	80 mm	−
Material of window	BN	−
Output mode	Wave beam	close to Gaussian beam
Radius of cavity	8.39 mm	−
Q value of cavity	6000	−
Electron gun	quasi-diode	−
Emitter	LaB_6	−
Operation mode	$TE_{22,8}$	

3. Gyrotron FU CW II

Fig. 1 shows a typical experimental results of the gyrotron. Many radiation peaks appear at both fundamental and the second harmonics, when a magnetic field is varied

A single mode operation of TE06 cavity mode at the second harmonic (corresponding magnetic field intensity is 7.14 T) has achieved the frequency of 394.3 GHz and the output power of 32 W. These parameters satisfy the condition of radiation source for DNP/proton-NMR at the frequency of 600 MHz

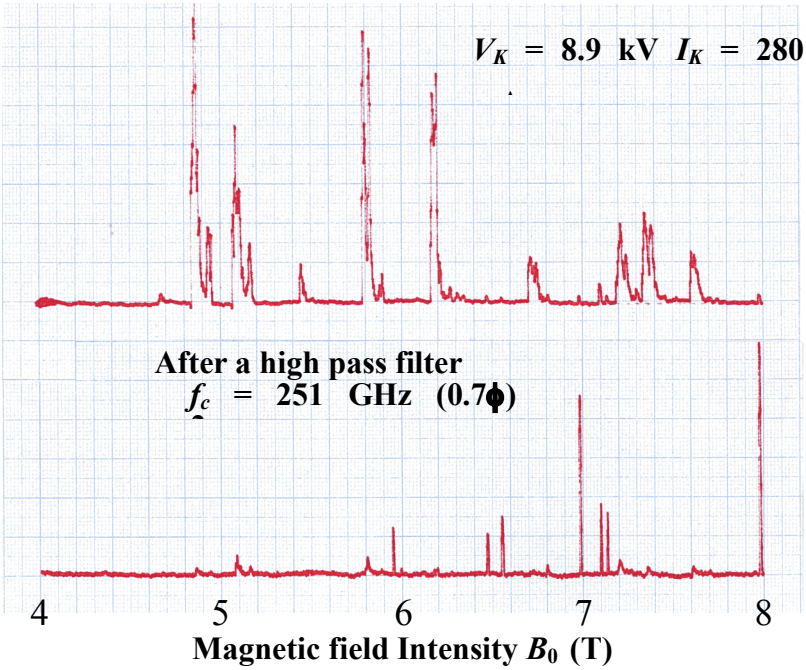

Fig. 1 Radiation power from the gyrotron FU CW II as functions of magnetic field intensity. Upper trace: Radiation power measured just after the output window. Lower trace: Radiation power coming out through the high pass-filter with a thin circular waveguide whose diameter is 0.7 mm. (The corresponding cutoff frequency is 251 GHz.)

4. Gyrotron FU CW III

The third gyrotron, Gyrotron FU CW III with a 20 T superconducting magnet has already been constructed and will be operated soon. In Table 2, main parameters of the gyrotron are shown.

The gyrotron is optimized for the second harmonic operation of $TE_{4,12}$ at the frequency of 1013.7 GHz. The operation mode is complete CW. This gyrotron will achieve the breakthrough of 1 THz in CW operation. In addition, it is expected that many other cavity modes will be excited by adjusting the field intensity at the optimum value for each cavity mode. As the results, it will achieved frequency step tenability in wide range covering sub-THz to THs frequency region.

Table 2 Specification of Gyrotron FU CW III

Total height from electron gun to the window: 2.4 m
Superconducting magnet : Maximum magnetic field : 20 T, Inner bore : 50 mm
Cavity :Radius: 1.95 mm, Length : 10 mm, Frequency : 1013.7 GHz at the second harmonic, Operating mode : $TE_{4,12}$, Q-factor : 23720
Operation mode: Complete CW
Operating magnetic field : 19.1 T for : $TE_{4,12}$
Triode-type electron gun : Cathode radius : 4.5 mm, Maximum cathode current: 1 A, Cathode voltage: 30 kV
Gun coil: Maximum input current: 300 A, Maximum magnetic field : 0.183 T
Water cooling jackets are installed at a Cavity and a Collector regions.

5. Summary

Three CW gyrotrons, Gyrotron FU CW I, II and III operating in sub-THz to THz region are being developed. Operation test of FU CW I and II have already carried out. Gyrotron FU CW I is being used for material processing. Gyrotron FU CW II has benninstalled on a 600 MHz proton-NMR device for sensitivity enhancement of NMR spectroscopy by using Dynamic Nuclear Polarization (DNP). Gyrotron FU CW III will be used for development of high power THz technologies in future, after operation test is completed.

Plasma Scattering Measurement using a Gyrotron as a Radiation Source

I.Ogawa[1], T.Idehara[1], T.Saito[1], H.Park[2], E.Mazzucato[2]

[1] *Research Center for Development of Far Infrared Region,University of Fukui, Bunkyo 3-9-1, Fukui 910-8507, Japan*
[2]*Princeton Plasma Physics Laboratory*

Application of high intensity, well-collimated submillimeter probe beam is effective in improving the S/N ratio and the spatial resolution of plasma scattering measurement. High quality operation of the gyrotron and production of well-collimated Gaussian-like beam are required to improve the performance of the measurement. The high quality operation can be achieved by decreasing the fluctuations of the cathode voltage. Gyrotron output is converted into Gaussian-like beam by quasi-optical system consisting of a quasi-optical antenna and focusing mirrors.

1. Introduction

The density fluctuations are theoretically expected to enhance the energy loss of the confined plasma across the magnetic field. It is important to measure these physical quantities as a port of the basic study of plasma confinement. The scattering method with electromagnetic wave makes it possible to observe both the frequency and the wavenumber of the fluctuations directly with a high spatial resolution.

If we employ a low frequency wave (millimeter wave) as a probe beam, it is difficult to focus the probe beam. A non-collimated probe beam degrades the spatial resolution of the measurement. On the other hand, the use of a high frequency probe beam makes the scattering angle small. Such a condition brings poor spatial and wavenumber resolutions. There is an optimum wavelength of the probe beam in consideration of the spatial and wavenumber resolutions. The range of the available wavelengths is in submillimeter region, which allows refractive effects to be sufficiently small while still permitting large scattering angle.

Application of high frequency gyrotron is effective in improving the S/N ratio of the measurement because of its capacity to deliver high powers [1, 2]. A final goal is to produce an optimal probe beam (high quality, intense submillimeter wave beam) and to apply it to plasma scattering measurements with the aim of optimal performance of the measurement.

2. Scattering measurement in NSTX tokamak

In order to investigate ETG driven turbulence for the transport of electron energy in NSTX plasmas, high sensitivity and spatial resolution are necessary to the measurement. We are planning to apply the submillimeter wave gyrotron (Gyrotron FU II) as a radiation source to the scattering measurement in NSTX tokamak at Princeton University.

The Gyrotron FU II [3] is one of high frequency, medium power gyrotrons included in Gyrotron FU Series developed in University of Fukui. In the gyrotron, as well as other gyrotrons included in the series, a narrow resonant cavity with high Q value is installed for achieving high separation between the cavity modes. Such a situation is important for high harmonic operation of high frequency gyrotrons. Because of this narrow cavity, our gyrotrons could be operated in many single modes at the fundamental, the second and third harmonics of electron cyclotron resonance. The value of high Q value confirms reductions in the starting current for operation and the linewidth of the radiation. The lower starting current is suitable for avoiding overheating the gyrotron in case of a long pulse operation (τ ~2s).

The Gyrotrn FU II consists of an 8T superconducting magnet, water-cooled gun coils and sealed-off gyrotron tube (Fig.1). The electromagnetic wave generated in the cavity transmits in a circular waveguide and emitted from the vacuum window. The TE_{161} mode output (P=80W, f=354GHz) at the second harmonic (n=2) resonance is used for plasma scattering measurement.

3. Mode conversion into Gaussian-like beam and coupling with corrugated waveguides

Unlike a molecular laser, the gyrotron generates spreading radiation with TEmn mode structure. It is therefore necessary to convert the output radiation into a Gaussian beam (TEM_{00}

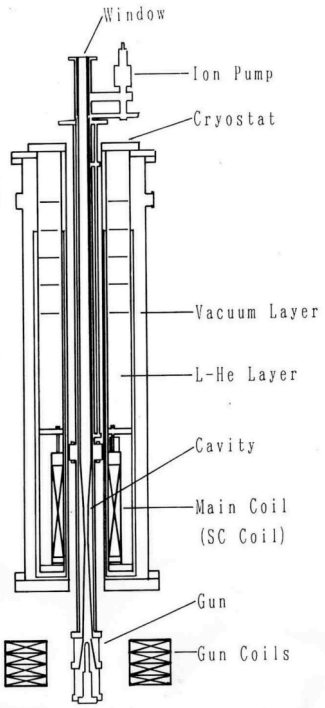

Fig. 1. Schematic drawing of Gyrotron FU II.

mode). In this scattering measurement, gyrotron output will be transmitted by corrugated waveguides and incidence on plasma as a probe beam. To improve the sensitivity of the measurement, it is essentially important to realize the high coupling efficiency to the corrugated waveguide.

The gyrotron output produced as the structure of a circular waveguide TE_{15} mode is converted into a linearly-polarized beam by using a quasi-optical antenna [4, 5](Fig.2). The far-field pattern of the linearly-polarized beam consists of a main beam and side lobes. The main beam is similar to a Gaussian beam. The far-field pattern will appear by using phase shift effect due to a focusing mirror. The radiation pattern thus obtained (Fig.3(a)) is incident on corrugated waveguides. The radiation pattern from the end of the corrugated waveguide is shown in Fig.3(b). The radiated power measured by using power meter is 8W. This power level is intense enough to improve the S/N ratio of the measurement.

4. Compact arrangement of gyrotron system for installation

The space for installation of Gyrotron system including the quasi-optical system is restricted to 1.8m high, 2.0m long, and 4.0m wide. The height of the present gyrotron FU II device is close to that of the installation space. The corrugated

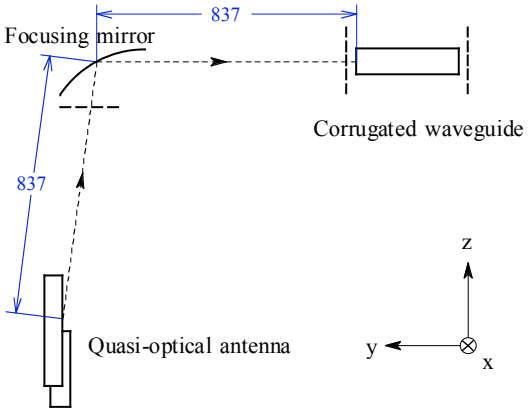

Fig. 2. Quasi-optical system to convert gyrotron output into Gaussian beam.

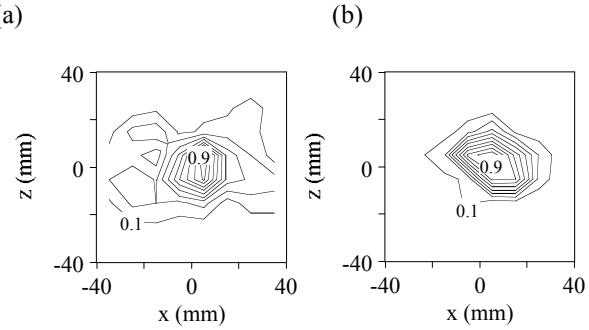

Fig.3. Intensity profiles of (a) Gaussian-like beam converted from gyrotron output and (b) radiated beam from the end of corrugated waveguide.

waveguide for transmitting the gyrotron output radiation and incidence on plasma as a probe beam are installed at 1.7m high of this space.

In order to meet the requirements of present gyrotrn system imposed by the mentioned space limitations, the height of the system should be reduced. The compact arrangement of the adopted system is shown in Fig. 4. In this system, gyrotrn output is converted into a linearly polarized beam by a quasi-optical antenna. The beam is directed downward by the flat mirror and hits the focusing mirror. The beam is oriented the horizontal direction by the final flat mirror and is coupled to the aperture of the corrugated waveguide.

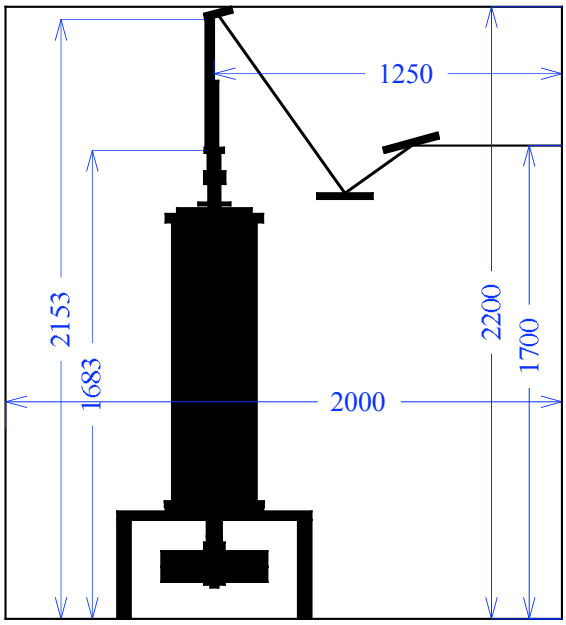

Fig. 4. The compact arrangement of gyrotron device.

References

[1] T.Idehara et al., Proc. of 3rd Int. Conf. on Strong Microwave in Plasmas, Moscow, Russia, **2**, (1997) 634.

[2] K.D.Hong et al., J. Appl. Phys., **74**, (1993) 5250.

[3] T.Idehara et al., Phys. Fluids, **B4** (1), (1992) 267.

[4] S.N.Vlasov et al., Radiofizika, **17**, (1974) 115.

[5] O.Wada et al., Space Power, **6**, (1986) 213.

Electron temperature and density measurements on TST-2

S. Kainaga[1], A. Ejiri[2], Y. Takase[2], O. Watanabe[3], Y. Adachi[2], T. Osako[2], M. Sasaki[1], H. Tojo[2], T. Masuda[2], and J. Sugiyama[2]

[1] *Graduate School of Science, University of Tokyo, Bunkyo 113-0033, Japan*
[2] *Graduate School of Frontier Sciences, University of Tokyo, Kashiwa 277-8561, Japan*
[3] *High Temperature Plasma Center, University of Tokyo, Kashiwa 277-8561, Japan*

A compact Thomson scattering (TS) system was designed and constructed for the TST-2 spherical tokamak. This TS system uses a 10 Hz Nd:YAG laser with an energy per pulse of 0.45 J and a pulse width of 5 ns, operated at the fundamental wavelength of 1064 nm. For light collection optics, a Newtonian mirror system is used because of its compactness and high throughput. The light collection optics was optimized with the help of ray tracing calculation. According to the calculation, a solid angle of 50 millisteradian can be realized when the center of the plasma is measured. The collected light is resolved in wavelength by an interference filter polychromator and detected by avalanche photodiodes. Outputs of the avalanche photodiodes are recorded by a high speed oscilloscope with a bandwidth of 500 MHz. In order to calibrate the TS system, the TST-2 vacuum vessel was filled with nitrogen gas and the Rayleigh scattering signal and the rotational Raman scattering signal were measured. For a typical plasma discharge, the measured electron temperature and density were 190 eV and 1×10^{19} m^{-3}, respectively. When the plasma is heated by the high harmonic fast wave (21 MHz/240 kW), the electron temperature increased to 290 eV.

1. Introduction

Thomson scattering (TS) is the most reliable diagnostic to measure the electron temperature T_e. It has been widely used as a basic diagnostic tool in plasma experiments for about 40 years. On the TST-2 spherical tokamak [1] at the University of Tokyo, RF heating experiments using the high harmonic fast wave (HHFW) at a frequency of 21 MHz is in progress [2]. HHFW is the fast wave in the frequency range of several times the ion cyclotron frequency. Because of its good accessibility to plasmas with high dielectric constants ($\varepsilon \equiv \omega_{pe}/\Omega_e$) and strong absorption by electrons [3], HHFW is considered to be an attractive wave for electron heating and current drive in spherical tokamaks.

Up to now, electron heating by HHFW in TST-2 has been inferred from increased soft X-ray emission. By such an indirect method, however, RF power absorption by electrons cannot be determined quantitatively. In order to evaluate the electron heating efficiency quantitatively, and to elucidate the physics of HHFW heating, a TS system was installed in TST-2. This paper describes the TST-2 TS system and presents experimental data.

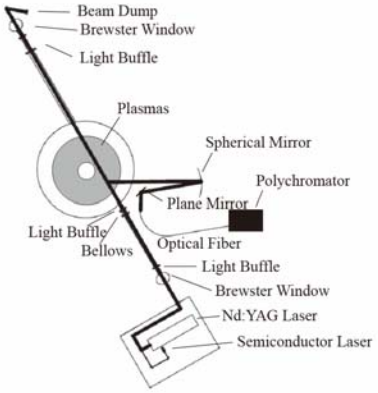

Fig. 1: Schematic diagram of the TST-2 TS system.

2. Components

TST-2 is a compact spherical tokamak with major radius R = 38 cm, minor radius a = 25 cm, and toroidal magnetic field at the plasma center $B_T \leqq 0.3$ T. The TST-2 TS system is composed of laser and injection optics, light collection optics, signal detection electronics, and recording system. The schematic diagram of the TST-2 TS system is shown in Fig. 1.

2.1. Laser and injection optics

A schematic layout of the TST-2 TS injection optics is described in Fig. 2. We use a 10 Hz Nd:YAG laser (Continuum Surelite 1-10) with an

energy per pulse of 0.45 J and a pulse width of 5 ns, operated at the fundamental wavelength of 1064 nm. The laser is injected along a horizontal line on the midplane of the plasma. The angular distribution of the differential cross section of the Thomson scattering light is given by

$$\frac{dI_T}{d\Omega} = \frac{3}{8\pi}\sin^2\beta, \qquad (1)$$

where β is the angle between the polarization direction of the incident laser light and the observation direction. As shown in Fig. 1 and Eq. (1), in order to maximize the signal intensity the incident laser should have linear vertical polarization. However, as can be seen in Fig. 2, the laser initially has a linear horizontal polarization. By using two mirrors M1 and M2, it is changed to linear vertical polarization.

A semiconductor laser is made collinear with the Nd:YAG laser and is used for alignment of the optical axis. The laser energy of the Nd:YAG laser is monitored by a photodiode placed behind M3. The transmission loss from the laser entrance to the center of the plasma is about 5%. Long entrance and exit tubes containing a series of light baffles are used to suppress the stray light (Fig. 1). In order to keep the beam dump away from the field of view, the laser beams are reflected downwards at the end of the exit tube.

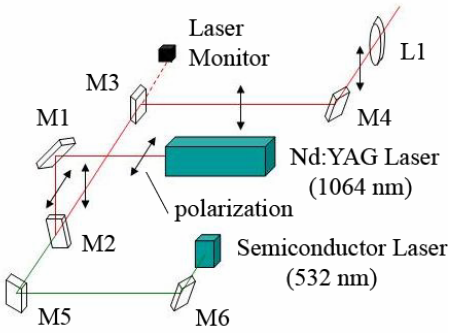

Fig. 2 : Schematic diagram of the laser and injection optics.

2.2. Light collection optics

In order to make a compact TS system, compact and efficient collection optics is required. For light collection optics, a Newtonian mirror system is employed. The Newtonian mirror system consists of a primary spherical mirror and a secondary flat mirror. The scattered light is collected by the spherical mirror, reflected downward by the plane mirror, and reaches the optical fiber with a diameter of 1 mm and a numerical aperture of 0.37. An advantage of the Newtonian mirror system is that we save the space needed to bend the optical fiber. Thus, it enables us to bring the spherical mirror closer to the vacuum vessel. As a result, we can use a rather small spherical mirror with a diameter of 25.4 cm. According to the calculation described below, without the Newtonian mirror system, a spherical mirror with a diameter or 45 cm is required to obtain the same efficiency.

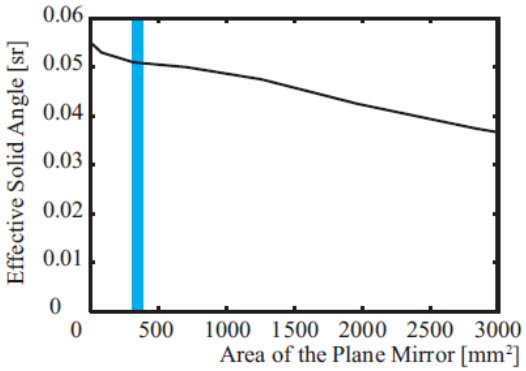

Fig. 3 : Results of the ray tracing calculation. The values of effective solid angle are calculated when the center of the plasma is measured. The thick vertical line shows the experimental condition.

However, there is a disadvantage in the Newtonian mirror system. The plane mirror becomes an optical mask for the scattered light. In order to estimate this effect and maximize the efficiency of the collection optics, a computer simulation based on a ray tracing calculation was performed. The efficiency which we call an effective solid angle is estimated by the ratio of the light that arrived at the fiber to the total scattered light when the scattered light is distributed with spherical symmetry. The relationship between the effective solid angle and the area of the plane mirror is shown in Fig. 3. The area is defined by a projection along the optical axis. The effective solid angle decreases linearly with of the area of the plane mirror. The thick vertical line shows our experimental condition. Despite the loss of about 10%, an effective solid angle of 50 millisteradian can be realized when the center of the plasma is measured. This value is rather large compared with the value obtained with other devices typically about 10 millisteradian.

2.3. Polychromator

A conventional filter polychromator, which is on loan from National Institute for Fusion Science (NIFS), is used. Three channels with interference filters are used for obtaining the TS spectrum and one channel without an interference filter is used for absolute calibration by Rayleigh scattering. The normal incidence transmission curves for three interference filters together with the Thomson spectrum for T_e = 100 eV and 500 eV are shown in Fig. 4. The spectral responsivities for three filters were measured by use of a standard lamp and a monochromator.

Avalanche photodiodes (APDs) C30950E (EG&G Canada) with an internal preamplifier are used for detection because of their high quantum efficiency and high internal gain. These APD units are also on loan from NIFS. Their quantum efficiency is 40% at 1060 nm and the bandwidth is 50 MHz.

Since the collected light is incident on the fiber surface at various angles, angular dependencies of transmission efficiency of the fiber and the polychromator are important. Measured angular dependencies of transmission efficiency of the fiber and each polychromator channel are shown in Fig. 5. When the transmission efficiency of the polychromator was calculated, responsivity of the APDs measured beforehand was used. Measured angular distribution of the fiber transmission is nearly equal to the nominal value, however, the transmission efficiency of each polychromator channel is worse than that of the fiber. Measured angular spread for each polychromator channel corresponds to a numerical aperture of 0.30.

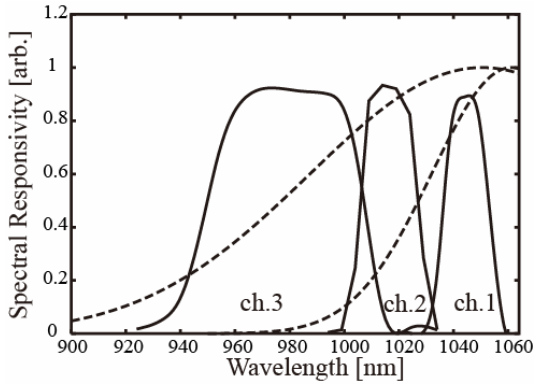

Fig. 4 : Measured transmission curves for three interference filters of the polychromator (solid curves) and the Thomson spectrum for T_e = 100 eV, 500 eV (dashed curves).

2.4. Data recording system

The most common approach to record the TS signal is to digitize the integrated charge over a gate period slightly larger than the laser pulse. Another scheme is to use transient recorders. Transient recorders can digitize the time evolution of the detector signal. It enables us to determine the scattering signal even in a noisy environment. We use a 4-channel digital oscilloscope (DL7440, YOKOGAWA) with a sampling rate of 500 MS/s and a bandwidth of 500 MHz. The oscilloscope is connected through Ethernet to a PC.

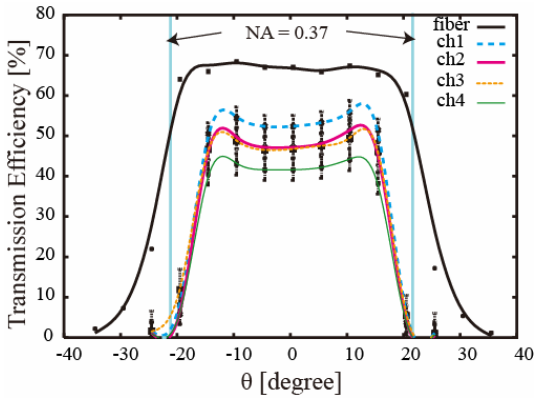

Fig. 5 : Angular dependencies of transmission efficiency.

3. Calibration

For electron density measurement, the TS system must be absolutely calibrated. Rayleigh scattering and rotational Raman scattering by nitrogen gas were used to calibrate the TS system. The Rayleigh signal was measured with channel 4 of the polychromator, whose filter is removed, and the rotational Raman signal was measured with channel 1. The pressure dependence of the measured signals is shown in Fig. 6. The calculated result using the measured transmission efficiency of the injection optics, detection electronics, and the calculated efficiency of the collection optics is also shown for comparison. The measured Rayleigh and Raman signals were proportional to the nitrogen pressure as expected. In Fig. 6(a) the stray light signal is observed at zero pressure. The stray light intensity corresponds to the Rayleigh scattering signal at 260 Torr. Although the rejection of the filters at the incident laser wavelength is larger than 10^5, the stray light signal is also observed in Fig. 6(b). Since the angular dependence of Raman scattering is different from that of TS, Rayleigh

scattering data are used for the absolute calibration.

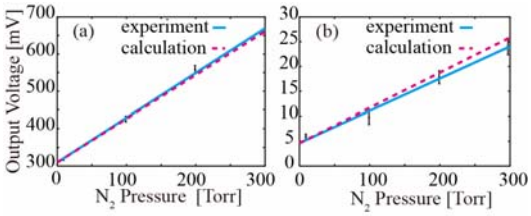

Fig. 6 : Pressure dependences of measured and calculated (a) Rayleigh scattering signal and (b) rotational Raman scattering signal. Raman scattering signal is increased by a factor of 8.1 with an amplifier.

4. Experimental results and discussion

With the calibrated TS system, we measured electron temperature and density of TST-2 plasmas. Plasma current and line-integrated electron density are shown in Fig. 7(a) for a typical discharge. The thick vertical line shows the Nd:YAG laser injection timing at t = 20.87 ms. The signal of the photodiode monitoring the Nd:YAG laser is shown in Fig. 7(c). Signals of channels 1 and 2 of the polychromator are shown in Fig. 7(b). Peaks in channels 1 and 2 occur about 30 ns after the peak of the photodiode signal. This delay is consistent with the sum of the lengths of the laser path and that of the cable (about 8 m). The pulse width of the polychromator signal is broadened due to the insufficient bandwidth of the APD units. Up to now, the signal-to-noise ratio is small, so averaging of several discharges is necessary to obtain a clear signal. From this result, electron temperature and density are calculated to be 190 $\pm$ 20 eV and (1.0 $\pm$ 0.2) $\times$ 10^{19} m^{-3}, respectively. Errors are estimated from the polychromator signals during the period just before laser injection.

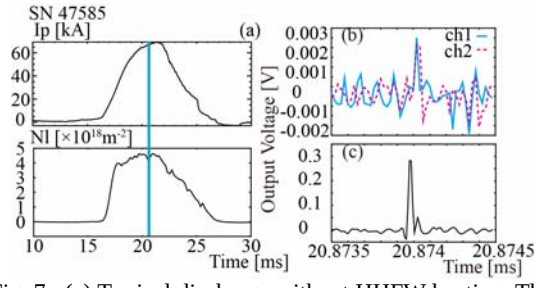

Fig. 7 : (a) Typical discharge without HHFW heating. The thick vertical line shows the laser injection timing. (b) Output voltages of the channels 1 and 2 of the polychromator. Due to insufficient signal-to-noise ratio, 14 discharges are averaged. (c) Output voltage of the photodiode monitoring the laser power.

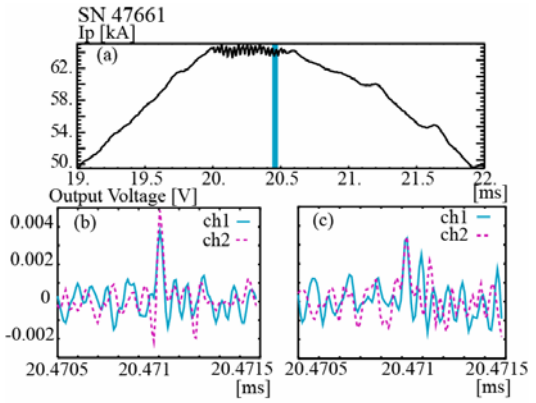

Fig. 8 : (a) Typical discharge with HHFW heating. The thick vertical line shows the laser injection timing. Output voltages of the channels 1 and 2 of the polychromator (b) with HHFW (13 shot averaging) and (c) without HHFW (4 shot averaging).

4.1. HHFW Injection

We injected RF power from t = 20 ms to t = 20.5 ms and measured electron temperature and density at t = 20.47 ms. The average RF power was 240 kW. The signals of channels 1 and 2 of the polychromator with and without HHFW are shown in Figs. 8(b) and (c), respectively. During RF injection, the ratio of the peak value of channel 2 to that of channel 1 increased significantly, implying electron heating. The measured electron temperature was 290 $\pm$ 70 eV with HHFW and 170 $\pm$ 40 eV without HHFW, respectively.

5. Summary

In summary, a Thomson scattering system was designed, constructed and applied to TST-2 in order to measure electron temperature and density. For collection optics, a compact Newtonian mirror system was employed and high efficiency was achieved. The arrangement of the collection optics was optimized using a ray tracing calculation. Absolute calibration of the TS system was performed by Rayleigh scattering measurements. Using this TS system electron heating by HHFW was clearly observed.

References

[1] Y.Takase *et al.*, Nuclear Fusion **41**, (2001) 1543.
[2] Y.Takase *et al.*, Nuclear Fusion **46**, (2006) S598.
[3] M.Ono, Phys.Plasmas **2**, (1995) 4075.

Design status of the KSTAR Thomson scattering

Jongha Lee

National Fusion Research Center, 52 Eoeun-dong, Yuseong-gu, Daejeon, 305-806, Korea

The engineering design of Laser input port system, laser beam guiding system and laser shutter system for KSTAR (Korean Superconducting Tokamak Advanced Research) Thomson scattering is designed. The laser beam guiding system is located at the *Lm*-Port and this system consists of gate valve, vacuum system, baffle and window. The laser beam guiding system has beam collimate system with vacuum. The laser safety shutter system consists of mirrors, linear motion stage and beam dump. And this shutter is remotely controlled at the Thomson diagnostics room and KSTAR main control room.

1. Introduction

Thomson scattering has became an important diagnostic for measuring electron temperature and density profiles in most world-class tokamaks.[1][2][3] The Korea Superconducting Tokamak Advanced Research (KSTAR) tokamak[4], which is under construction at the National Fusion Research Center (Daejeon, Korea), is aiming at the successful performance of steady-state tokamak plasmas by utilizing fully superconducting magnets and a state-of-the-art plasma control system. The goal of the Thomson scattering diagnostic on KSTAR is to provide reliable electron temperature and density profiles in both core and edge region during long-pulse tokamak plasma discharges. To meet this goal, we have conducted design activities for the KSTAR Thomson scattering diagnostic with reference to state-of-the-art technology, which was developed in the currently operation fusion research devices such as DIII-D[3], LHD[5], NSTX[6], JT-60U[7], etc. In this proceeding we describe a engineering design of Laser input port, Laser beam guiding duct and laser shutter systems.

2. General Layout and Optical System

The Thomson scattering system on KSTAR is designed to configure 90° scattering optics, including a single tangential beam of multiple 100-Hz Nd:YAG lasers(supported from JAEA)[8] and horizontal core and edge collection systems, as illustrated in Fig. 1. The laser beam, transported for a distance about 40 m and focused by a 5.5 m focal length lens, is directed into the vacuum vessel through the midplane port of Bay *L*. in Fig. 2. The focal lens and steering mirror are mounted on an optical bench, which is located in the tokamak machine hall. On the other hand, lasers, polychromators, and detectors are located in a diagnostics room outside the radiation shield, allowing personal access during machine operation.[6] The scattered light is imaged onto the optical fibers bundle arrays at the midplane port of bay *N*, transmitted to polychromators with five wavelength filter channels, and detected by avalanche photodiode (APDs). The beam-dump is mounted on the vacuum-duct plate, which is located at the midplane port of Bay *B*. The design requirements for parameters to be measured are as follows; time resolution: 10 ms (100Hz), spatial resolution: 3 ㎝ at core and 5 mm at edge, temperature range: 0.5 keV < T_e < 20keV at core and 10 eV < T_e < 1.5 keV at edge, density range: $3 \times 10^{12} < n_e < 2 \times 10^{12}$[9]

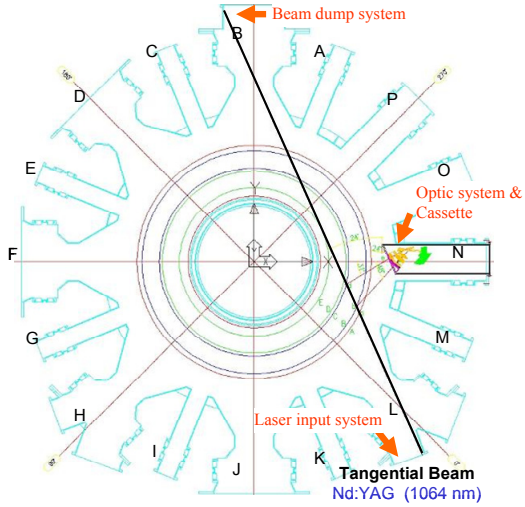

Fig 1. Port allocation of KSTAR Thomson scattering system

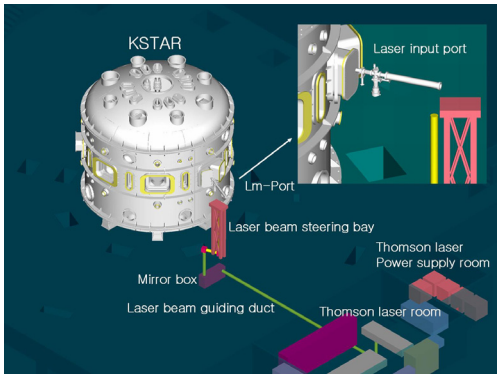

Fig 2. 3D view of KSTAR Thomson system

3. Laser Input Port (Lm-port) Design

The laser input port of KSTAR Thomson is located at the midplane port *N (Nm)*. The Thomson laser input system has to share space in the *Lm*-port (midplane port *L*). with the Bolometer system. This laser input system consists of four parts. First part is a motorized gate valve, second part is vacuum pumping system, which is pumped about 10^{-7} Torr using turbo vacuum pump. Next structure is laser baffle system, which has 42 blades, made by anodized Al and total length is about 1.4 m. A Last part is 8″ A.R. coated quartz glass window shown in Fig. 3.

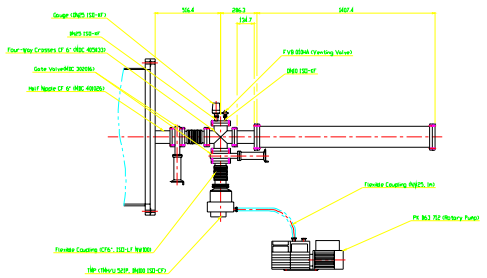
(a) Side view of laser input system

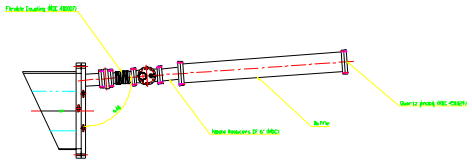
(b) Top view of laser input system

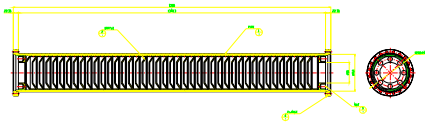
(c) Baffle system

Fig 3. Laser input system design (a) Side view of laser input system, (b) Top view of laser input system, (c) Baffle system

4. Laser Beam Guiding Duct Design

Considering the divergence of laser beam, we designed laser beam guiding duct. This laser beam guiding duct has beam collimate system, which has two plano-convex lens with equal focal length F.L. ~ 6m and pumped by rotary pump about 10^{-3} Torr. And the first lens is different from the second lens is that the first lens position is adjustable but the second lens is fixed. So, in order to achieve the required beam collimate performance, we adjust the first lens. This system will be attached at the ceiling of basement level 1. The total length of this laser beam guiding duct is 12m and the diameter of vacuum duct is 16 ㎝ in Fig. 4.

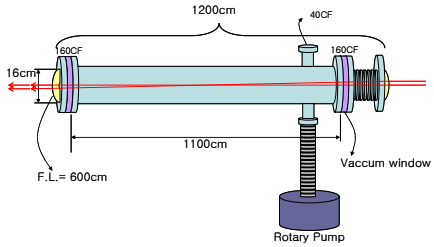

Fig 4.Laser beam guiding duct design

5. Laser Shutter System Design

The laser shutter system is very important system because when the sudden uncommon state is occurrence, the laser shutter automatically changes the laser beam path for safety. The KSTAR Thomson laser shutter system has three refraction mirrors. The first mirror refract the laser beam into the laser beam guiding duct and the second mirror is on the motorized linear rail system, which is controlled at the Thomson control room and is interlocked KSTAR main control room. The last mirror is placed in the beam dump shows in Fig. 5. This shutter system is located at the basement level 1, which is under the KSTAR diagnostics room. This system is made by SUS 304 and the dimension is 70 ㎝ (width) × 70 ㎝ (length) × 130 ㎝(height).

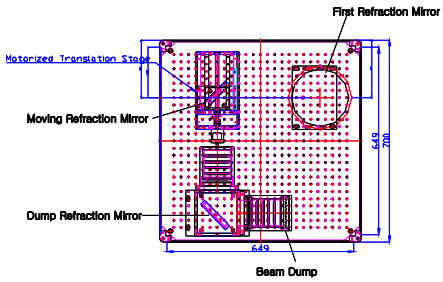

(a) Top View of laser shutter system

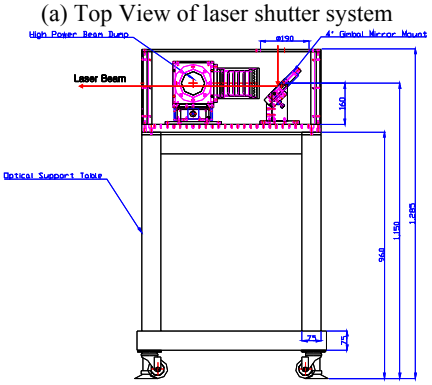

(b) Side view of laser shutter system

Fig. 5. Laser shutter system design (a) Top view of laser shutter system, (b) Side view of laser shutter system

6. Future Work

The engineering design of Laser input port, Laser beam guiding system and laser shutter systems are complete. We will continue the KSTAR Thomson system design and upgrade it until fabrication and installation.

References

[1] N. J. Peacock *et al*., Nature (London) **224**, (1969) 488.

[2] H. Murmann *et al*., Rev. Sci. Instrum. **63**, (1992) 4941.

[3] T. N. Carlstrom *et al*., Rev. Sci. Instrum. **63**, (1992) 4901.

[4] G. S. Lee *et al*., Nucl. Fusion **40**, (2000) 575.

[5] K. Narihara *et al*., Rev. Sci. Inastum. **72**, (2001) 1122.

[6] D. Johnson *et al*., Rev. Sci. Instrum. **70**, (1999) 776

[7] H. Yoshida *et al*., Rev. Sci. Instrum. **70**, (1999) 751.

[8] Hatae Takaki *et al*., J. Plasma Fusion Res. **80**, (2004) 870.

[9] H. G. Lee *et al*., Rev. Sci. Instrum. **75**, (2004) 3903.

Conceptual Design of FIR Interferometer/Polarimeter System for KSTAR

Y. U. Nam[1], M. S. Cheon[2]

[1] *National Fusion Research Center, Daejeon, Korea*
[2] *Seoul National Univ., Seoul, Korea*

A FIR Interferometer/Polarimeter system will be constructed on the KSTAR (Korea Superconducting Tokamak Advanced Research) for an electron density profile measurement. This system consists of a single-channel vertical line for a density feedback control and multi-channel tangential lines for a radial density profile measurement. Beam sources are three 118.8 μm CH_3OH lasers optically pumped by 9.7 μm CO_2 laser. An interferometry and a polarimetry are performed simultaneously in one beam line with three CH_3OH laser system includes a Stark-tuned laser. Due to complex inner-wall geometry and long diagnostics port, specially designed in-vessel optic system is necessary to ensure sufficient beam lines for an inversion of density profile. A numerical profile inversion code has been developed for a determination of density profile shape with limited number of beam lines. The FIR interferometry is robuster than CO2 interferometry in mechanical vibration but a fringe-jump effect can be a problem due to large phase variation. A multi-fringe counting circuit will be adopted for this purpose.

1. Introduction

An interferometry is a typical diagnostics system for a plasma electron density measurement in tokamak device. In KSTAR (Korea Superconducting Tokamak Advanced Research), three types of interferometry systems will be installed. First one is a single-channel millimetre-wave interferometry system, which uses two 280GHz Gunn Diodes as frequency sources.[1] This system has been installed on horizontal line for a rough measurement of the line integrated electron density. Next one is a single-channel vertical FIR interferometry system for a density feedback control. Finally, a multi-channel tangential interferometry /polarimetry system will be installed for a radial density profile measurement.

The installation of FIR interferometry/ polarimetry system is scheduled on 2009~2010. Conceptual design of the system has been performed such as selection of laser sources, in-vessel beam-line design, phase measurement circuit design, and profile inversion scheme. These results are described in this paper, and technical problems should be solved are mentioned.

2. System configuration

2.1. Laser system

Three 118.8 μm CH3OH lasers pumped by 9.7 μm CO2 laser will be used for simultaneous measurement of interferometry and polarimetry in one beam line. A probing beam is circularly rotating linear polarized wave. The interferometry is performed by measuring a phase variation of linear polarized wave, and the polarimetry is performed by measuring a variation of rotating phase. The probing beam is composed by two circular polarized FIR laser beams. Other laser generates reference beam. A frequency of the reference laser will be shifted by Stark-effect for a better temporal resolution. Optical schematic of the triple-laser system is presented in Fig. 1.[2]

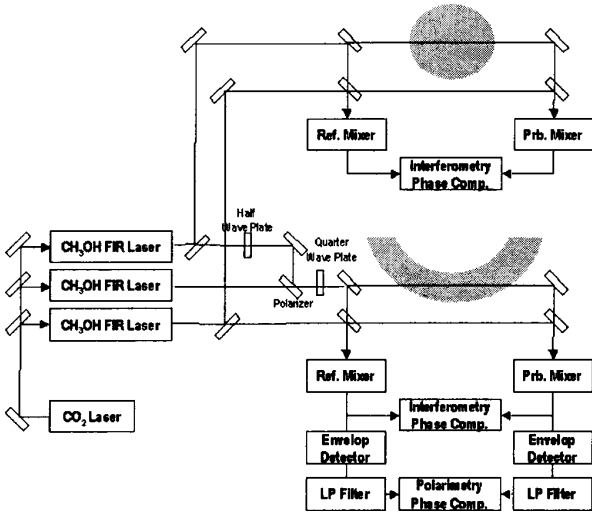

Fig. 1 : Optical schematic of the triple-laser system for the KSTAR tokamak.

2.2. Beam line design

Since KSTAR is a superconducting tokamak that needs large cryostat on the outside of vacuum vessel, diagnostics devices should be installed via long narrow ports. This feature requires a complex optics system to ensure sufficient beam lines for an inversion of density profile. An optimum number of the beam lines is determined by a computer simulation using profile inversion code developed for this purpose. At least seven channels are required for an estimation of the density profile shape. Detailed processes will be described later on this paper.

Each beam lines should be positioned on a tangential plain with different radial distant. The beam-lines are split on a beam splitting module placed on the outside of cryostat, and are entered into plasma through etalon windows. A specially designed alignment optics module consists of several reflecting mirrors with aligning knob will be installed for aligning beam-lines to assigned radial positions. Beams entered into plasma will be reflected at the corner-cube reflectors mounted on the inner-wall of vacuum vessel. The size of beam radius inside plasma is less than 30mm. The interferometry is very sensitive to a mechanical vibration. Hence, the inner alignment optics module and corner-cube reflectors should be mounted on the vessel wall using vibration compensating mounts. All components consist of the mounts should be selected considering the vacuum environment. They also can stand against high magnetic field, high heat flux and high radiation. Development of vibration compensating schemes using spring with non-magnetic materials such as beryllium-copper are planned and will be tested. Conceptual lay-out of beam-lines is presented in Fig. 2.

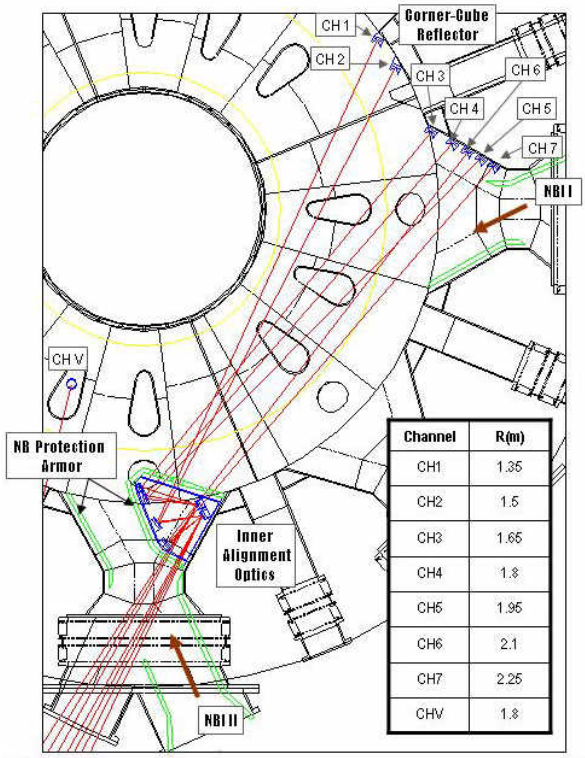

Fig. 2 : Conceptual beam-lines lay-out of tangential interferometer/polarimeter system

2.3. Phase comparison circuit

As mentioned above, interferometry and polarimetry are performed simultaneously in one beam-line. Two probing laser with slightly different frequency (ω_1 and ω_2) makes a circularly rotating linear polarized wave, and one reference laser makes a frequency-shifted (ω_{LO}) wave using Stark-tuned effect. The interferometry signal comes from $|\omega_1 - \omega_{LO}|$ or $|\omega_2 - \omega_{LO}|$, and the polarimetry signal from $|\omega_1 - \omega_2|$. Since frequency of the later is larger than that of the former, theses signal can be separated from each other on the comparison circuit.

A phase shift of polarimeter will be lesser than one fringe (6.28 radian), and it can be traced with typical comparison circuit. But a fringe-counting capability is necessary for the interferometry, since the phase shift of interferometer will be varied over several fringes. A multi-fringe counting circuit using counter-chip has been developed and installed for the millimetre-wave interferometry system for KSTAR. This circuit will be tested and applied for the FIR interferometry system with adding a signal separation module.

2.4. Profile inversion code

A shape of density profile can be determined using shifted phase data of each tangential beam-line. Abel inversion is well established technique for a cylindrical symmetric geometry, and various inversion techniques such as a slice-and-stack method have been developed for a cylindrical asymmetric geometry. For an estimation of radial density profile using tangential interferometric measurement in KSTAR, an improved Abel inversion method has been developed.[3] This technique is similar to the slice-and-stack method, but it assumes density of the sliced region as a double-line instead of as a flat line. Hence, it can estimate

shape of density profile more close to the real shape.

An optimum number of beam lines have been determined by this technique. Fig. 3. is RMS density errors for various shape of density profiles as a function of the interferometer channel number. The peak density of these profiles is 10^{20} m^{-3}. RMS errors of estimated profile can be suppressed less than 5% of peak density when the interferometric channel number is larger than 7.

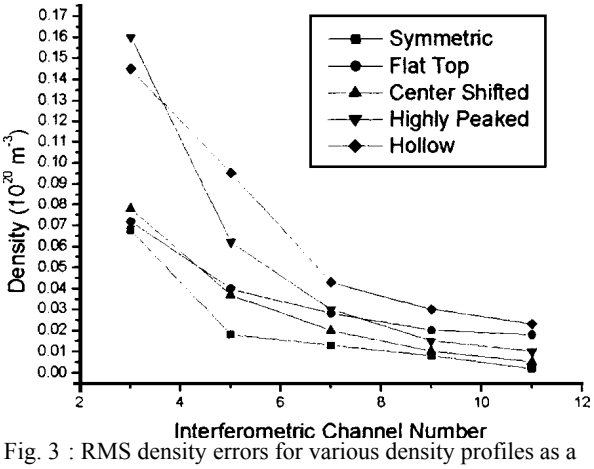

Fig. 3 : RMS density errors for various density profiles as a function of the interferometer channel number

3. Conclusion

Conceptual design of FIR interferometer/ polarimeter system for KSTAR has been performed and these results were described. The laser system is triple-FIR laser pumped by CO_2 laser. Total 7 beam-lines will be positioned on tangential plane with different radial distant. For the positioning and aligning of these lines, specially designed inner-alignment optic module and corner-cube reflectors with non-magnetic vibration- compensating mount for vacuum interface have been designed. The phase variation of beam lines are measured by the multi-fringe counting circuit, and the shape of density profile will be determined by the newly developed profile inversion code using measured signals.

References

[1] Y. U. Nam, M. S. Cheon, M. Kwon and Y. S. Hwang, Rev. Sci. Instrum., **74,** (2003) 1613.
[2] M. S. Cheon, Y. U. Nam, J. H. Ha, and Y. S. Hwang, Rev. Sci. Instrum., **75,** (2004) 3402.
[3] J. H. Ha, Y. U. Nam, M. S. Cheon, and Y. S. Hwang, Rev. Sci. Instrum., **75,** (2004) 3408.

A simple analytical expression for electron temperature in an ac plasma display discharge

K. Muraoka[1], K. Suzuki[2], M. Azumi[3], Y. Yamagata[4], M. Yagi[5]

[1] *School of Engineering, Chubu University, Kasugai, Aichi 487-8501, Japan*
[2] *Hitachi Research Laboratory, c/o Central Research Laboratory, Hitachi Ltd., Kokubunji, Tokyo 185-8601, Japan*
[3] *Center for Promotion of Computational Science and Engineering, Japan Atomic Energy Research Agency, Daito, Tokyo 110-0015, Japan (now retired)*
[4] *Interdisciplinary Graduate School of Engineering Sciences, Kyushu University, Kasuga, Fukuoka 816-8580, Japan*
[5] *Research Institute for Applied Mechanics, Kyushu University, Kasuga, Fukuoka 816-8580, Japan*

A simple analytical expression was derived for electron temperature T_e in discharge conditions typical for an ac-PDP (alternating current plasma display panel) discharge for the first time, in which the least possible number of parameters was introduced so as to provide good physical insight into the mechanisms of determining T_e under various discharge conditions. From this derivation, an explicit dependence of T_e on discharge parameters (gas composition and pressure, and the strength of electric field E) has been derived. It was tested for a discharge condition studied in our previous article on the discharge-radiation dynamics (DRD), yielding reasonable values for a cathode fall and a positive column. Also, the values of T_e obtained experimentally using laser Thomson scattering in a positive column are well predicted from this analysis.

1. Introduction

One of the authors (KS) showed that electron temperature in an ac-PDP (alternating current plasma display panel) discharge dictates the efficiency of the electrical power input into VUV radiation.[1] Thus, it is important to know how electron temperature behaves under different discharge conditions. In order to provide insight into the problem, the DRD (discharge radiation dynamics) analysis[2] has been developed for ac-PDPs. In this DRD analysis, discharge voltage and current waveforms in the discharge volume of a cell were calculated from the measured panel voltage and current waveforms using given geometrical configurations and electric circuit calculations. Then, discharge processes were analyzed so as to satisfy the latter waveforms using plausible assumptions from the discharge physics point of view and known constants for elementary processes, yielding, among other parameters, electron density and electron temperature. The results thus obtained were then discussed in terms of the plasma radiations with those experimentally measured for the same discharge conditions. The comparison of the DRD analysis and the measurements indicated a fair agreement, thus showing the validity of the DRD analysis. In addition, the striation structure was well represented[3] using the values of electric fields in the cathode fall and the positive column, which were obtained using the DRD analysis, yielding further confidence in this DRD analysis.

Because the processes involved in the electron temperature determination in the above DRD analysis (and also in other numerical simulations[4]) are complex, it is difficult to identify which discharge parameters affect the final electron temperature. It is the purpose of this paper to derive a simple analytical expression, which shows parametric dependences of electron temperature on various discharge physics parameters. For this purpose, the least possible number of parameters and geometry were introduced in the analysis, while taking into account the most important ones. Then, the result of the analysis is discussed by testing it with the discharge condition used for the above DRD analysis. The results were also discussed by comparing it with experimental data obtained using laser Thomson scattering.[5,6]

2. Formulation

In the DRD analysis,[2] a one-dimensional approximation was made, together with the two-region model consisting of a cathode fall

(c.f.) and a positive column (p.c.). Electron temperature was assumed constant in each of the two regions, which was, however, treated as variable in time so as to satisfy the measured voltage and current waveforms. The present derivation of an analytic expression for electron temperature follows these lines of thinking. In addition, a steady state was assumed, so as to make the analysis tractable. Implications of these and subsequent assumptions are discussed at the end of this paper.

We consider energy balance for a one-dimensional control volume in the x-direction, being separated by (x_l, x_r), as follows;

(i) Electric energy input

The energy E_j obtained by electrons from an applied electric field E is written as

$$\Delta^2 E_j = eEv_{dre}n_e\Delta x\Delta t \quad [\mathrm{J/m^2}] \quad (1)$$

where $n_e\Delta x$ is the number of electrons in a unit cross sectional area in the y-z plane with a length of Δx in the x direction, and $v_{dre}\Delta t$ is the distance of electron (directional) motion during a time interval Δt.

(ii) Electron energy loss due to elastic collisions with neutral particles

The energy loss by a group of electrons $n_e\Delta x$ at a temperature T_e through elastic collisions during a time interval Δt is written as

$$\Delta^2 E_{el} = (n_e Q/\lambda_{en})(3\kappa T_e/m_e)^{1/2}\Delta t\Delta x \quad [\mathrm{J/m^2}] \quad (2)$$

where Q is the energy loss for one elastic collision of an electron having a mass of m_e against a neutral particle having a mass of m_n and is written as

$$Q = 4(\frac{m_e}{m_n})\kappa T_e \quad [\mathrm{J/m^2}] \quad (3)$$

Here, κ is the Boltzmann's constant and λ_{en} is the mean free path length of electrons determined by elastic collisions with neutral particles.

(iii) Electron energy loss due to inelastic collisions with neutral particles

Electrons are separated into two groups, with the first group having energies $\frac{1}{2}m_e v_e^2 < E_{exmin}$ (where E_{exmin} is the minimum value among excitation energies of neutral particles), and the second group $\frac{1}{2}m_e v_e^2 > E_{exmin}$. The first group, constituting the bulk of the electrons, obtains energy from an electric field E and loses it through elastic collisions with neutral particles, together with thermalization by electron-electron collisions. The second group is the high-energy tail borne through acceleration by the electric field E. This second group loses energy in a time τ^*=inverse of an excitation collision frequency with neutral particles. Because $\tau^* = 1/(\sigma_{en}^* n_{Xe} v_{the})$ (here, σ_{en}^* is the excitation cross section of Xe, n_{Xe} is the neutral Xe density and v_{the} is the thermal velocity of electrons) with $\sigma_{en}^* \sim 1\times10^{-21}$ m^2, $n_{Xe} \sim 1\times10^{23}$ m^{-3} (partial pressure of Xe being about 3 Torr) and $v_{the} \sim 1\times10^6$ m/s for v_e at $\frac{1}{2}m_e v_e^2 > E_{exmi}$, one obtains $\tau^* \sim 1\times10^{-9}$ s. This time interval is sufficiently short in a positive column for the second group of electrons to travel only a few μm before getting into the first group. On the other hand, in a cathode fall, whose length is short (a few tens of μm) and where the electric field is very strong, the second group of electrons do not have sufficient time to get back into the first group.

An average collision frequency of an electron undergoing inelastic collisions with neutral particles, g', is written as

$$g' = n_n < \sigma_i v_e > \quad (4)$$

where n_n is a neutral particle density, σ_i is the inelastic collision cross section with neutral particles, the average of which over the electron velocity distribution function is σ_{en}^*, and $<>$ designates an average over the velocity distribution function of an electron.

Assuming that all kinetic energy $\frac{1}{2}m_e v_e^2$ is lost upon every inelastic collision g', one obtains the expression of inelastic energy loss $\Delta^2 E_{inel}'$ for electrons $n_e\Delta x$ during a time interval Δt as

$$\Delta^2 E_{inel}' = \tfrac{1}{2}m_e n_e n_n < \sigma_i v_e^3 > \Delta t\Delta x \quad [\mathrm{J/m^2}] \quad (5)$$

If we approximate σ_i as $\sigma_i(E) = a(E-E_{min})\exp(-E/b)$ where a, b and E_{min} are constant, and the velocity distribution function of electrons as Maxwellian, the integration of Eq. (5) can be carried out, yielding

$\Delta^2 E_{inel}'$

$$= \alpha n_e n_n \left(\frac{8}{\pi m_e}\right)^{1/2} (\kappa T_e)^{-3/2} \xi^2 \left\{E_{exmin}^2 + 4\xi E_{exmin} + 6\xi^2\right\} e^{-E_{exmin}/\xi} \Delta t \Delta x \quad (6)$$

where $1/\xi = (1/b) + (1/\kappa T_e)$, and the shift of the velocity distribution function in the x direction due to the current was neglected because it is about 1 eV and small compared with E_{exmin}.

(iv) Electron energies coming in and flowing out from both ends of the control volume

The electron energy coming in from x_l, the left-hand side of the control volume, E_{in}, and that flowing out from x_r, the right-hand side, E_{out}, are written as

$$\Delta E_{in} = n_e \left\{\frac{3}{2}(\kappa T_e)_{in}(V_{dre})_{in}\right\} \Delta t \quad [\mathrm{J/m^2}] \quad (7)$$

$$\Delta E_{out} = n_e \left\{\frac{3}{2}(\kappa T_e)_{out}(V_{dre})_{out}\right\} \Delta t \quad [\mathrm{J/m^2}] \quad (8)$$

where $v_{dre} = E\mu_e$, $\mu_e = eD_e/(\kappa T_e)$, $D_e = \lambda_{en} V_{the}/3$, $v_{the} = (3\kappa T_e/m_e)^{1/2}$, and $(\kappa T_e)_{in}$ and $(v_{dre})_{in}$ represent values coming into the control volume, and $(\kappa T_e)_{out}$ and $(v_{dre})_{out}$ are those flowing out.

After Eqs. (1), (2), (7) and (8) are rearranged, by integrating Eqs. (1), (2) and (6) between (x_l, x_r), and taking into account the electron energies coming into and flowing out of the control volume expressed by Eqs. (7) and (8), one gets

$$\kappa T_e = \frac{(eE\lambda_{en})^2}{3Q + 3\alpha + \frac{3}{2}\{e\lambda_{en}E\}\beta} \quad (9)$$

where

$$\alpha = \left(\frac{24}{\pi}\right)^{1/2} (\kappa T_e)^{-2} \xi^2 \frac{a\left\{E_{exmin}^2 + 4\xi E_{exmin} + 6\xi^2\right\}}{\sigma_{en}} e^{-E_{exmin}/\xi}$$

$$\beta \equiv \lambda_{en}(\gamma_r - \gamma_l \eta \zeta^{1/2}),$$

$$\gamma_r \equiv [n_e]_{x_r} / \int_{x_l}^{x_r} n_e dx, \quad \gamma_l \equiv [n_e]_{x_l} / \int_{x_l}^{x_r} n_e dx$$

and η and ζ are the ratios of electric field and electron temperature across the left-hand boundary of the control volume.

One sees that the numerator of the right-hand side of Eq. (9) represents the square of the energy input into electrons from the electric field E, and the denominator represents various electron energy loss processes, with the first term due to elastic collisions, the second term due to inelastic collisions, and the third term due to energies coming in and flowing out at both boundaries of the control volume. It is noted that β is positive for cathode fall and negative for positive column.

3. Results and discussion

The foregoing results were used to evaluate electron temperatures for various values of the electric field E. For this calculation, consistent with the case used in the DRD analysis,[2] the total pressure was fixed at 500 Torr with a neon based mixture having a small content of xenon, yielding $\lambda_{en} = 7.6\times10^{-7}$ m and $\sigma_{en} = 8.2\times10^{-20}$ m^2, together with $a = 1.1\times10^{-21}$ m^2/eV, $E_{exmin} = 8.3$ eV and $b = 16.7$ eV, the latter three being decided as values for Xe, and $m_e = 9.1\times10^{-31}$ kg and $m_n = 3.4\times10^{-26}$ kg (for Ne).

The calculated results are shown in Fig. 1. Here, the straight line shows the case of electrons experiencing elastic collisions only and indicates, from Eq. (9) together with the above values,

$$\kappa T_e = 4.2\times10^{-5} E \quad (10)$$

where κT_e is in [eV] and E is in [V/m].

On the other hand, the chain line (β=0) is obtained iteratively, together with the above values, from the following equation;

$$\kappa T_e = \frac{6.1\times10^{-13} E^2}{3Q + 3\alpha} \quad (11)$$

The third group of data are for the case when all three terms of Eq. (9) were retained. The parameter β in Eq. (9) is usually small, of the order of $\lambda_{en}/(x_r - x_l)(1-\eta\zeta^{1/2})$, which is typically +0.01 for a cathode fall and -0.1 for a positive column. Thus, the cases of β at +0.1 and -0.1 are shown in Fig. 1 as the two extreme values.

As seen in Fig. 1, the case when only elastic collisions were taken into account is the limiting case when the electric field is relatively weak so that the electron temperature is below 1 eV. For this case, the energy input from the electric field is balanced by the energy transfer into gas atoms, which are implicitly assumed to have an infinite energy sink. The cases when inelastic collisions and energy flows across the boundaries asymptotically approach this limiting case when the electric field is weak.

From the DRD analysis,[2] the intensities of the electric fields at the cathode fall and the positive column are found to be 9×10^6 V/m and 1×10^5 V/m, respectively, for the present

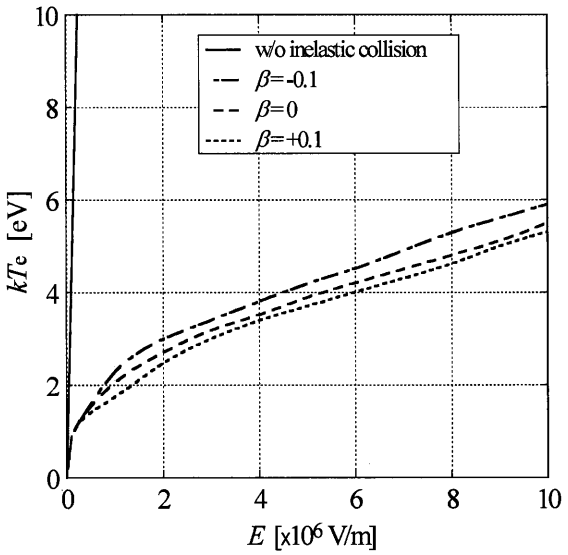

Fig. 1 Electron temperature T_e as a function of electric field E. The straight line is for the case when only elastic collisions of electrons with atoms are present, while three curves are for the case in which elastic and inelastic collisions are present, with for β=0 (chain line) being for the case when there are no energy flows through boundaries, i.e., having an infinite extent. β=+0.1 (dotted line) and -0.1 (long dotted line) are shown as the cases of two extreme values for a cathode fall and a positive column, respectively. The calculations were carried out for the neon-based mixture gas having a small content of xenon at a total pressure of 500 Torr.

discharge condition having a discharge gap of 0.24 mm at a voltage between the electrodes of 170 V. From Fig. 1, one gets the values of electron temperature T_e of 5.1 eV and 1.1 eV, respectively. These values are in good agreement with those obtained in the DRD analysis[2] of 4 ~ 7 eV and about 0.1 ~ 1 eV, respectively.

On the other hand, experimental values of T_e are very scarce, and the only reliable values are those by the group of one of the authors (KM),[5,6] which were obtained using laser Thomson scattering in positive columns in an Ar(10 %)/Ne(90 %) mixture at 200 Torr, yielding T_e of around 1.5 – 3 eV. Equation (9) for these conditions, together with an assumption of the same electric field of $E \sim 10^5$ V/m for a positive column as that for the DRD analysis,[2] yield the value of T_e around the above measured values. This fact shows further confidence in the result of Eq. (9).

It is to be noted that a discharge condition is self-consistently realized so that spatial distributions of the electric field, and densities and temperatures of both ions and electrons are simultaneously determined. The main outcome of the present calculation is that T_e is not explicitly dependent on densities of ions and electrons under the present simplification, although implicitly dependent on them through E via the Poisson's equation. Thus, it is possible to obtain the value of E from Eq. (9), if one knows T_e by some means, such as from laser Thomson scattering, and vice versa, for a given gas composition and pressure.

As mentioned at the beginning of this paper, it is the authors' belief[1] that the lowering of T_e enhances the conversion efficiency of electrical input into VUV radiation. From the foregoing arguments, one sees from Eq. (9) that either decrease of λ_{ei} and/or increase of α reduce T_e. As are well known from experiences in the PDP community, increases in the filling gas pressures and/or in the partial pressure of Xe enhance the conversion efficiency, and these observations can be understood from the above arguments of decrease of λ_{ei} and/or increase of α, while giving an explicit dependence on these parameters for the first time.

The main point of the present work is to formulate the derivation of electron temperature in the simplest possible way, at the same time, taking into account the most important factors. Thus, a steady one-dimensional treatment and the fluid approximation were made, together with energy flows at both boundaries. These simplifications have enabled us to obtain an explicit expression of electron temperature as functions of collision parameters and an electric field for the first time, as shown in Eq. (9). The applicability of the assumptions of fluid approximation and one-dimensional approximation are being checked using a Monte Carlo simulation and numerical solutions of the Boltzmann equation, and will be published soon. It is to be noted, however, that the one-dimensional approximation was marginally valid for the present case. The assumption of a Maxwellian energy distribution function for the electrons is obviously an oversimplification in the cathode fall region, where the electric field is very strong. Thus, the derived "electron temperature" must be interpreted as representing some average in energy space.

Regarding the steady state assumption, the fluid[7] and kinetic[4] simulations and the DRD analysis[2] indicate that steady states are quickly approached after applications of ac PDP discharge pulses. Thus, the present analysis, made under the steady state assumption, is applicable to these steady states, which typically last 0.1-0.2 μs in a discharge pulse.

4. Summary

A simple analytic expression was derived for electron temperature T_e for discharge conditions typical for an ac PDP discharge, where a very limited parameters for inelastic collisions (a, b, and E_{exmin}) together with gas pressure (through λ_{en}) and electric field E were involved. The result also indicates that once the electron temperature is obtained experimentally or by some other means, one can estimate the strength of electric field from Eq. (9). It is hoped that this information is useful for determining electron temperature which dictates the VUV emission efficiency for various ac-PDP discharges.[1]

The work of one of the authors (KM) is supported by a grant from the High-Tech Research Center Establishment Project from the Japanese Ministry of Education, Culture, Sports, Science and Technology. The authors wish to thank Professor N. C. Luhmann, Jr. for improving English expressions of this paper.

Note added at the last moment:

The contents of this article have just been published in a Journal.[8]

References

[1] K. Suzuki, Y. Kawanami, S. Ho, N. Uemura, Y. Yajima, N. Kouchi, and Y. Hatano, J. Appl. Phys. **88**, 5605 (2000).

[2] K. Suzuki, K. Yamamoto, H. Kajiyama, S. Ho, N. Uemura, and K. Muraoka, J. Appl. Phys. **96**, 6082 (2004).

[3] K. Muraoka, M. Azumi, K. Suzuki, Y. Yamagata, and M. Yagi, J. Phys. D: Appl. Phys. **39**, 2135 (2006).

[4] H. C. Kim, F. Iza, S. S. Yang, M. Radmilovic, and J. K. Lee, J. Phys. D: Appl. Phys. **38**, R283 (2005).

[5] Y. Noguchi, A. Matsuoka, M. D. Bowden, K. Uchino, and K. Muraoka, Jpn. J. Appl. Phys. **40**, 326 (2001).

[6] Y. Noguchi, A. Matsuoka, K. Uchino, and K. Muraoka, J. Appl. Phys. **91**, 613 (2002).

[7] C. Shon and J. K. Lee, Phys. Plasmas **8**, 1070 (2001).

[8] K. Muraoka, K. Suzuki, M. Azumi, Y. Yamagata, and M. Yagi, J. Appl. Phys. **102**, 043301 (2007).

LIF measurement for metastable state argon atom in igniting stage of fluorescent lamp under light irradiation

M. Hamamoto, S. Kai, T. Haizaki and M. Ishibashi

Department of Mechanical and Energy Systems Engineering, Faculty of Engineering, Oita University, 700 Dan-noharu, Oita 870-1192, Japan

As a spectroscopic approach to investigate ignition property of fluorescent lamp under light irradiation, LIF measurement was carried out for metastable state argon atom in fluorescent lamp. Just after a breakdown, large LIF signal was observed to show higher generation of metastable argon atom with increase of lamp current. But in pre-breakdown period, LIF signal was too small to confirm the effect of light irradiation on increase in ignition voltage of fluorescent lamp through decrease of Penning ionization.

1. Introduction

The phenomenon that the ignition voltage of a fluorescent lamp in the illuminated environment increases is known empirically, but its mechanism is not yet clarified. The breakdown process for a uniform electric field, a small electrode gap and low pressure is well explained by the Townsend theory. But, for the case of a non-uniform electric field, a large electrode gap and dielectric of glass in close vicinity, as in normal fluorescent lamps, the breakdown process is complicated and not well understood. Recently, transitional movement in the gas phase between electrodes has been observed to investigate this process [1-3]. In addition the effect of irradiated position[4] and wavelength[5] of locally irradiated light and the effect of applied voltage property (polarity and increase rate)[6] have been examined, in order to investigate the mechanism for the increase in ignition voltage of fluorescent lamp.

In this paper, as a spectroscopic approach to investigate ignition property of fluorescent lamp under light irradiation, laser-induced fluorescence (hereafter LIF) measurement was carried out for metastable state argon atom in fluorescent lamp.

2. Experimental

The fluorescent lamp and its electric circuit are shown in Fig. 1 (a). And typical voltage and current waveforms are shown in Figs. 1 (b) and (c). Applied voltage V to the lamp varies with time t as $V=V_0(1-\exp(-t/\tau))$, where V_0 is dc power supply voltage and τ is time constant determined by the circuit elements, and this operation repeats with a rate of 10 Hz.

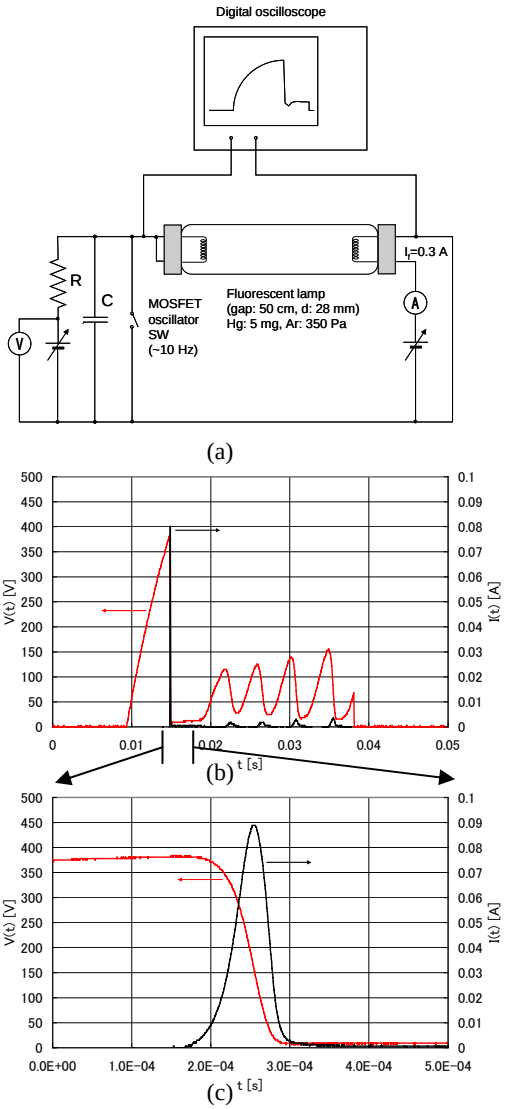

Fig. 1 : (a) Fluorescent lamp with no fluorescent material and its electric ignition circuit used for experiment. (b) Typical voltage and current waveforms. (c) Expansion of (b) around breakdown.

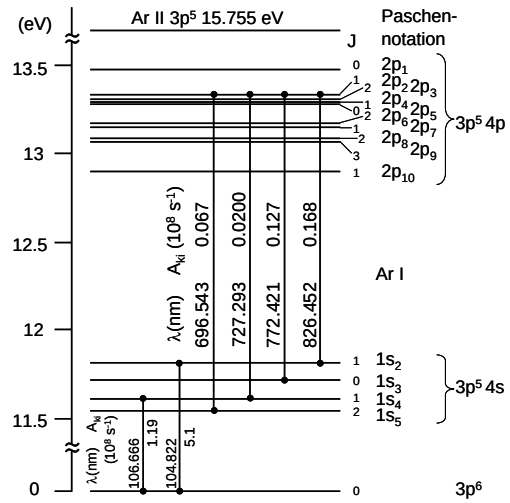

Fig. 2 : Partial Grotorian diagram for argon atom.

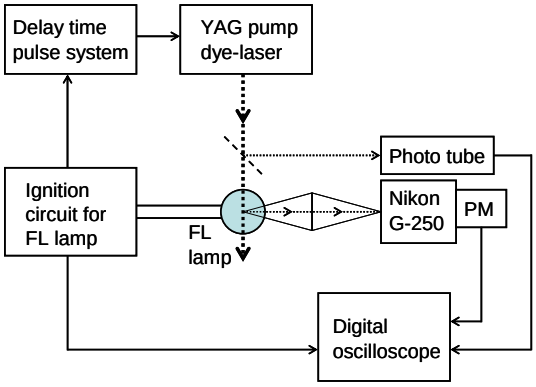

Fig. 3 : Experimental arrangement for LIF measurements.

Partial Grotorian diagram for argon atom is shown in Fig. 2. For LIF method, 696.543nm is used for laser excitation from a metastable state ($1s_5$[Paschen-notation, alike hereafter], $4s[3/2]^o_2$) to a excited state ($2p_2$, $4p'[1/2]_1$), and emission of 772.421nm corresponding to a transition from the excited state to another metastable state ($1s_3$, $4s'[1/2]^o_0$) is used for fluorescence observation.

Schematic experimental arrangement for LIF measurements is shown in Fig. 3. The timing of lasing pulse of YAG pumped dye-laser (Spectra-Physics GCR-12&PDL-3, LDS698 dye) can be changed with respect to onset of voltage application to the FL lamp by using a delay time pulse system. Laser pulse is monitored by a bi-planar photo tube (Hamamatsu R1193U-02), and fluorescence is observed by combination of a monochromator (Nikon G-250) and a photomultiplier (Hamamatsu R1464).

3. Results and discussions

3.1. Optical emission spectra

For dc discharge (current ~1mA), only several line spectra of mercury atom were observed at middle of the FL lamp, as shown in Fig. 4 (a), and line spectra of argon atom were observed only near cathode, where large potential gradient is expected, as shown in Fig. 4 (b).

For pulse discharge, large emission was observed just after breakdown corresponding to large peak of lamp current shown in Fig. 1 (c). Spatial distribution of peak emission of argon spectral line (772.421nm) is shown in Fig. 5, for both dark and irradiated circumstances. Striated structure of the distributions coincides with appearance seen with human eye. Difference between both distributions for dark and irradiated conditions may come from difference of ignition voltages and of resultant currents.

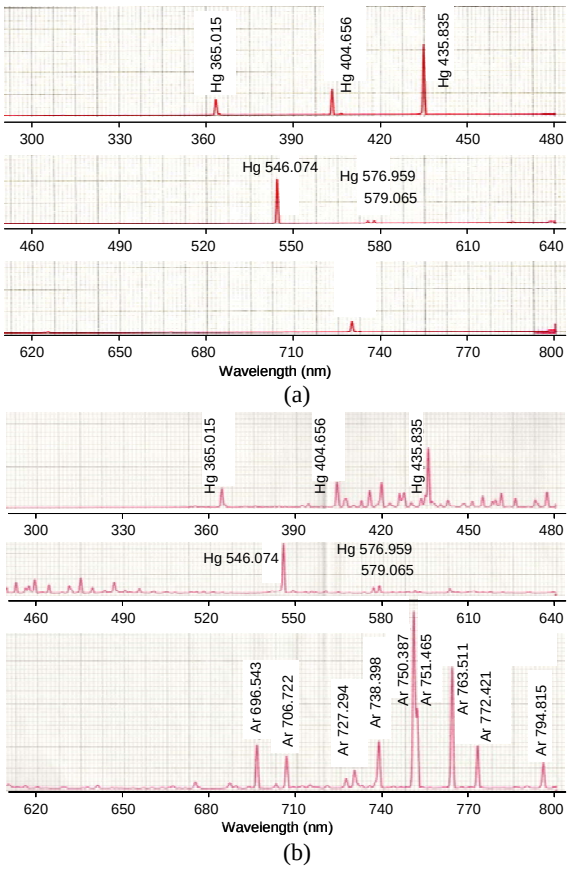

Fig. 4 : Emission spectra for dc discharge observed (a) at middle of lamp and (b) near cathode (z = -5 mm).

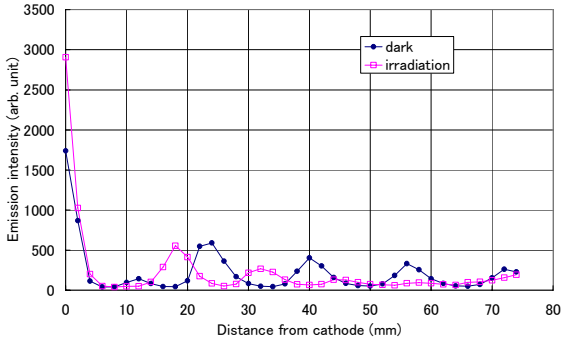

Fig. 5 : Spatial distribution of peak emission (772.421nm) for pulse discharge.

3.2. LIF measurement with hollow cathode lamp

Adjustments of LIF system was done with using hollow cathode lamp (Hamamatsu L223-11NB (W), hereafter HCL), as a stable source of metastable state argon atom, instead of FL lamp.

Tuning curve and saturation characteristics of LIF signal were confirmed as shown in Fig. 6 and Fig. 7, respectively.

LIF signal as a function of lamp current is shown in Fig. 8. Increase in lamp current does not increase but rather decrease LIF signal, that is, density of metastable argon atom. Increase in lamp current may cause that deconstruction of metastable by electron-collision excitation and de-excitation surpasses generation of metastable by electron-collision excitation, although configuration of hollow cathode and ring-like anode and current density should be considered.

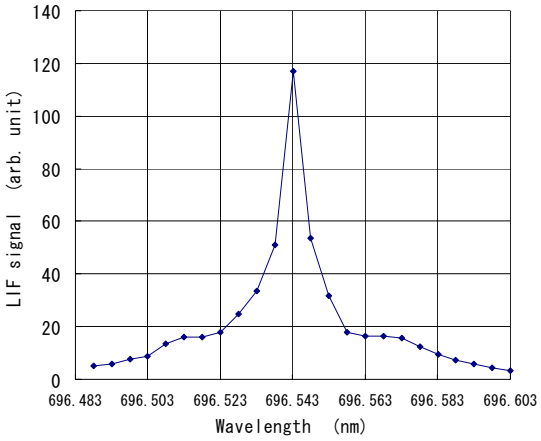

Fig. 6 : Tuning curve for metastable state of argon atom.

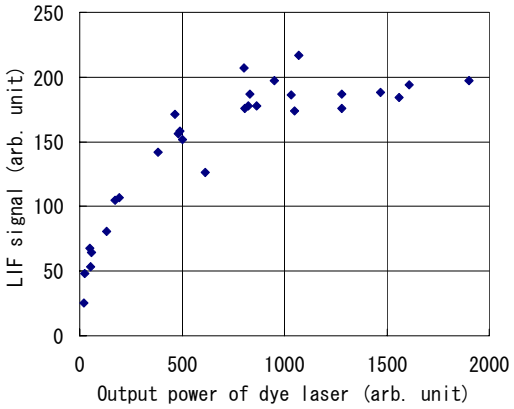

Fig. 7 : Saturation characteristics of LIF (shot by shot).

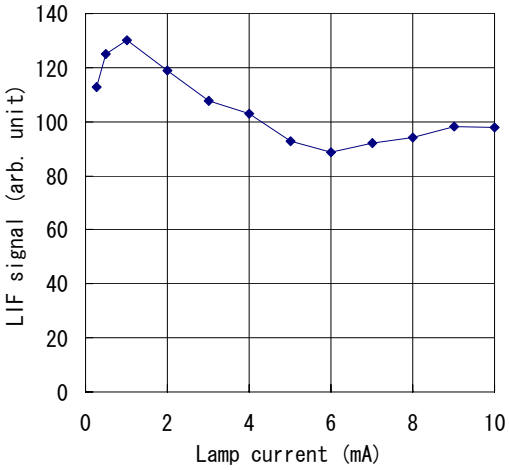

Fig. 8 : LIF signal for HCL as a function of current.

3.3. LIF measurement with fluorescent lamp

For dc discharge (current ~1mA), LIF signal as shown in Fig. 9 was observed only near cathode, which was same as the results of emission shown in Fig. 4.

For pulse discharge, because the jitter of timing when breakdown occurs is large in order of ms, it was difficult for measurement to be carried out in the same igniting condition. By changing the timing of laser pulse, LIF signal was observed and arranged afterwards either by time from onset of breakdown, that is start of decrease of voltage between electrodes, or by time from peak of emission. For detecting circuit, 32kΩ resistance was used instead of 50Ω, in order to produce wide width signal of ~10μs to be observed simultaneously with voltage or emission, which change in time of ~100μs as shown in Fig.1.

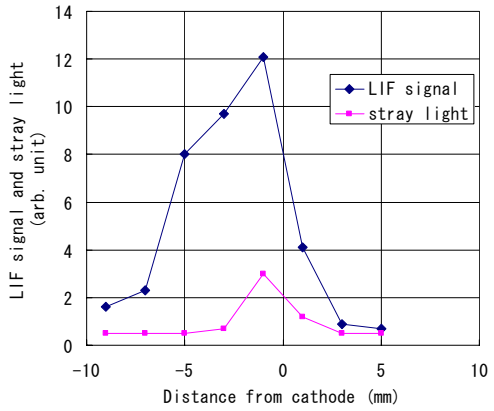

Fig. 9 : LIF signal and stray light near chathode for dc discharge (~1mA).

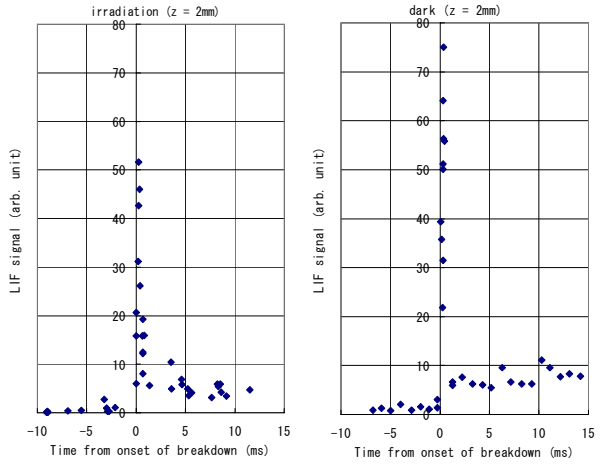

(a) irradiation (b) dark

Fig. 10 : Time variation of LIF signal for pulse discharge (z = 2mm).

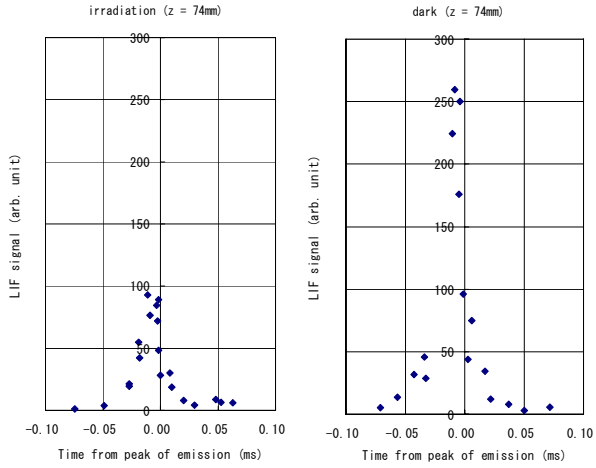

(a) irradiation (b) dark

Fig. 11 : Time variation of LIF signal for pulse discharge (z = 74mm).

LIF signals observed at 2mm from cathode as a function of time from onset of breakdown are shown in Fig. 10 (a) for condition of irradiation by another fluorescent lamps and in Fig.10 (b) for dark condition. Steep LIF signals, observed just after breakdown, are followed by small signals. LIF signals observed at 74mm from cathode as a function of time from peak emission are shown in Fig. 11 for (a) irradiation and (b) dark conditions. About ~10μs before peak of emission, LIF signals have their maxima. This indicates that higher current or higher emission do not necessarily mean higher density of metastable. And considering that breakdown voltage in dark is smaller about 100V than that in irradiation, magnitude of LIF signals in both cases is in reverse. In any case, in pre-breakdown period, LIF signals were too small to detect.

4. Conclusion

As a spectroscopic approach to investigate ignition property of fluorescent lamp under light irradiation, LIF measurement was carried out for metastable state argon atom in fluorescent lamp. Just after a breakdown, large LIF signal was observed to show higher generation of metastable argon atom with increase of lamp current. But in pre-breakdown period, LIF signal was too small to confirm the effect of light irradiation on increase in ignition voltage of fluorescent lamp through decrease of Penning ionization.

Acknowledgements

The authors would like to thank Messrs. E. Kawano, Y. Uryuda and M. Ohtawara for their technical help.

References

[1] M. F. Gendre, *et al.*, Proc. 26th Int. Conf. Phenomena in Ionized Gases, Greifswald, Germany, (2003) Abstr. 03-6.
[2] W. J. M. Brok, *et al.*, J. Phys. D **36** (2003) 1967.
[3] M. F. Gendre, *et al.*, Proc. 27th Int. Conf. Phenomena in Ionized Gases, Eindhoven, The Netherlands, (2005) Abstr. 13-345.
[4] M. Hamamoto, Jpn. J. Appl. Phys. **45** (2006) L172.
[5] M. Hamamoto, Jpn. J. Appl. Phys. **45** (2006) L175.
[6] M. Hamamoto, *et al.*, Proc. 28th Int. Conf. Phenomena in Ionized Gases, Prague, Czech Republic, (2007) 1973.

Measurements of localized electrostatic potential well profiles in a He discharge plasma by LIF polarization spectroscopy

S. Furukawa, Y. Kuramoto, S. Namba and K. Takiyama

Graduate School of Engineering, Hiroshima University,1-4-1 Kagamiyama, Higashi-Hiroshima, Hiroshima 739-8527, Japan

We have developed a high-sensitive method for electric field measurement in plasmas using the interference between atomic transition amplitudes, which relies on circular polarization of laser-induced fluorescence of He atoms. This method has a detectability of polarity of electric field, which makes it possible to identify the position of potential extrema. In this work, to demonstrate the precise potential profile measurement by our method, the potential in cylindrical inertial electrostatic confinement He plasma was measured. The potential profile known as single-well potential was obtained. The minimum electric field strength of 8 V/cm was measured and the potential peak position was detected with a spatial resolution of 0.5 mm.

1. Introduction

The inertial electrostatic confinement (IEC) fusion device has attracted much attention for application as a compact neutron/proton source [1], in which fusion reactions are obtained from the collisions of high-energy ions accelerated and focused locally onto the center region of the device. Complicated potential profiles (single-well, double-well potentials) are formed in the IEC plasmas since the space charge associated with focused ions attracts electrons [2]. It is important to measure the potential profile in plasmas because the potential plays a key role in neutron /proton generation rate.

We have developed a high sensitive method to directly measure the electric field E in plasmas by laser-induced fluorescence (LIF) polarization spectroscopy utilizing the Stark-mixing of helium atoms [3, 4]. In this technique, the electric field can be determined from the liner polarization degree P_L of LIF (He I: $n^1\mathrm{D}\rightarrow 2^1\mathrm{P}$, n = 3, 4) involving excitation of forbidden transitions (He I: $2^1\mathrm{S}\rightarrow n^1\mathrm{D}$, n = 3, 4) caused by electric quadrupole (QDP) moment and Stark induced electric dipole moment in the electric fields (linear polarization method), as shown in Fig. 1. Yoshikawa *et al.* have applied this method to the spherical IEC He plasma, and succeeded in direct measurement of the potential well [5]. More precise measurement method is, however,

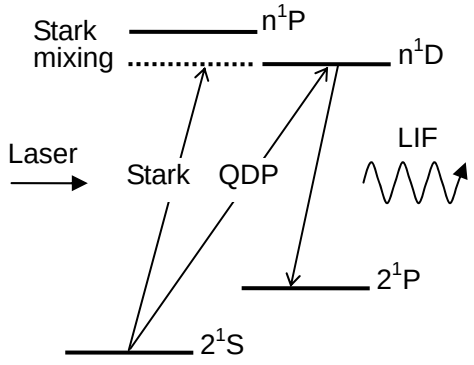

Fig. 1. Energy level diagram of He I for the electric field measurement. Stark and QDP represent the Stark- induced and the electric QDP transition, respectively. Level mixing occurs between the levels of n^1P and n^1D. The electric field is determined by linear polarization degree P_L of LIF.

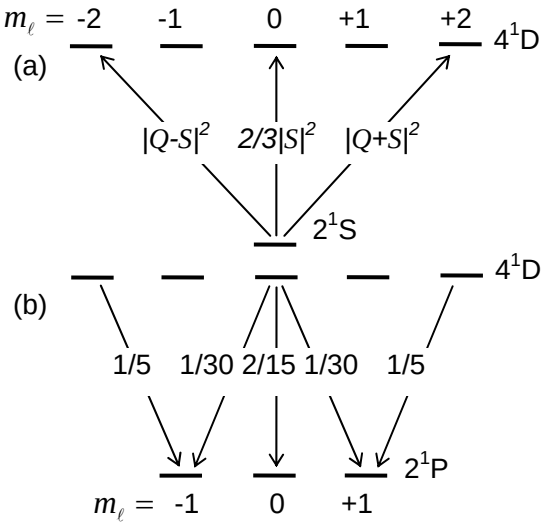

Fig. 2. The Kastler diagrams in **E** × **B** geometry, (a) for the forbidden excitation (He I: $2^1\mathrm{S}\rightarrow 4^1\mathrm{D}$, 397.2 nm) with the linearly polarized light and (b) for the transition (He I: $4^1\mathrm{D}\rightarrow 2^1\mathrm{P}$, 492.2 nm) showing the fluorescence process. Relative excitation and transition probabilities are shown. S and Q represent Stark and QDP amplitudes, $|Q\text{-}S|^2$ and $|Q\text{+}S|^2$ are interference terms.

essential to study the influence of plasma conditions on the formation of potential well,which requires the improvement in spatial resolution and sensitivity, and the detectability of position of potential extremum.

Recently, in **E** × **B** geometry, a higher-sensitive electric field measurement method has been developed [6] using the interference between the Stark-induced electric dipole and the electric QDP transition amplitudes [7], as shown in Fig. 2. The laser excitation generates the anisotropic populations, known as orientation, among magnetic sublevels with opposite sign, *e.g.* m_l = +2 and -2. The anisotropy caused by electric field can be observed as the circular dichroism of LIF (circular polarization P_C) along the magnetic field. The relationship between P_C and E is shown in Fig. 3. This circular polarization method is an order of magnitude higher than the liner polarization method in sensitivity (cf. P_L in Fig. 3). Additionally, the polarity of electric field can also be determined from the sign of P_C [6]. Detectability of the polarity makes it possible to determine the position of potential extremum and whether the extremum is a peak or a bottom.

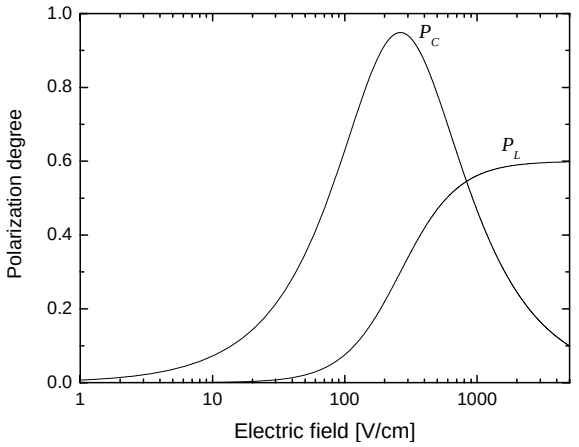

Fig. 3. Relationship between P_L/P_C and the electric field. Electric field dependence of P_C is very large up to about 10 V/cm, in contrast, that of P_L is small below 100 V/cm.

In this study, to demonstrate the precise potential profile measurement by the circular polarization method, we apply our method to a cylindrical IEC He plasma, in which the radial electric field is induced. The weak magnetic field is applied along cylindrical axis to measure the potential profile. Based on the result, we briefly discuss the performance of potential measurement by our method.

2. Experiment

The experimental apparatus is shown in Fig. 4, consisting of a vacuum chamber as an anode and a cylindrical hollow cathode which has a structure of arraying 12 annular electrodes (inner diameter of 30 mm, outer diameter of 40 mm, and 0.5 mm thickness) at intervals of 5 mm. The weak magnetic field was applied in the *z*-direction by a Helmholtz coil, which has little influence on plasma. The IEC He plasma was produced in a cylindrical hollow cathode with a discharge current of 24 mA, discharge voltage of 4 kV, He gas pressure of 25 mTorr and magnetic field strength of 15 G.

The metastable helium atoms (2^1S) produced in plasma were excited to the 4^1D level by a YAG-laser pumped dye laser (He I: 2^1S→4^1D, 397.2 nm). The laser light with a polarization vector $\mathbf{e_L}$ parallel to the *x*-axis ($\mathbf{e_L}$ // *x*) was injected into the cathode along the *y*-axis. The circular polarization of LIF (He I: 4^1D→2^1P,

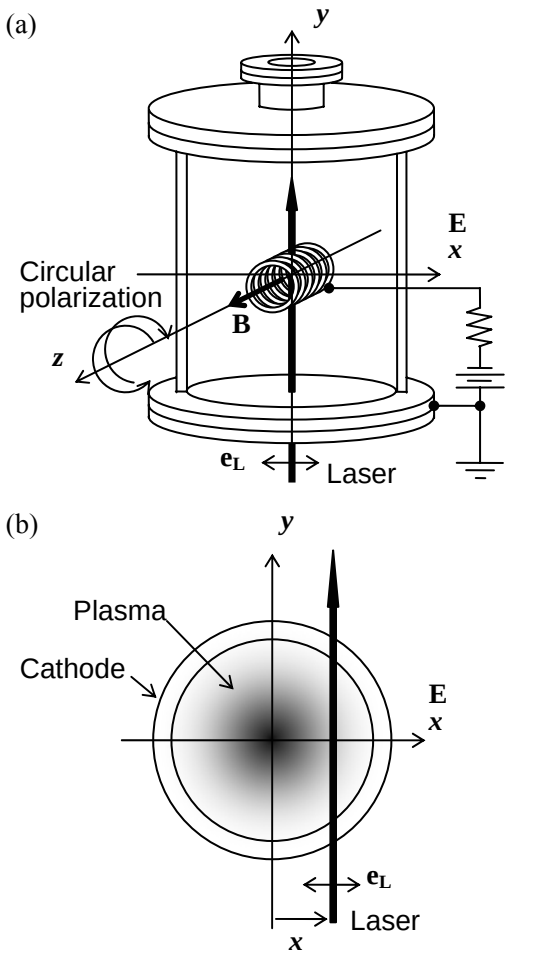

Fig. 4. (a) Experimental arrangement. (b) Cross section of the cathode.

492.2 nm) was observed in the *z*-direction. Spatial distribution of LIF was measured as a function of the distance *x* from the center of the cathode with a spatial resolution of 0.5 mm. The right hand I_R and left hand I_L circular polarization components were separated by a quarter-wave plate and a Glan-Thompson polarizing beam splitter. The circular polarization degree P_C is defined by $P_C = (I_L - I_R)/(I_L + I_R)$. The relationship between the sign of P_C and the polarity of *E* was investigated in hollow cathode discharge plasma. The positive sign of P_C corresponds to the negative electric field and vice versa.

3. Results and Discussion

Figure 5 shows typical waveforms of the circularly polarized LIF components I_R (closed circles), I_L (open circles) and P_C observed at (a) *x* = -7.5 and (b) *x* = +2 mm. Each experimental data is fitted by solid lines by using the rate equation procedure [8]. The origin in the abscissa corresponds to the beginning of irradiation by the incident laser. The values of P_C decay gradually with time due to the depolarization caused by collisions of the excited atoms with the plasma particles. For the determination of P_C, therefore, the reliable value is only obtained immediately after the onset of LIF pulse. In cases (a) and (b), the values of P_C were obtained to be +0.8 and -0.5, respectively. Using the theoretically calculated P_C-*E* relationship (Fig. 3), the values of electric field were determined to be -145 and +75 V/cm, respectively considering the relationship described in Section 2.

Measured spatial distributions of P_C and *E* along the *x*-axis are depicted in Fig. 6 (a) and (b), respectively. The axisymmetric electric field distribution was obtained and its direction was from the central region toward the peripheral plasma region. The reversing position of sign of P_C existed between *x* = -0.5 and +0.5 mm. From the reference [5], the potential structure known as double-well is considered to have three extrema at interval of about 5 mm, thus it is possible to determine their positions precisely. The minimum electric field strength measured in this study was about 8 V/cm which is consistent with theoretical detection limit (~10 V/cm).

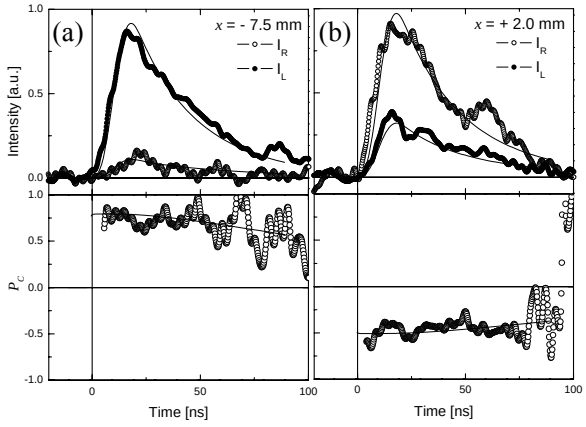

Fig. 5. Typical waveforms of the circularly polarized LIF components I_R (closed circles), I_L (open circles) and P_C, at (a) *x* = -7.5 and (b) *x* = + 2 mm. The solid lines are results of waveform fitting by using the rate equation procedure.

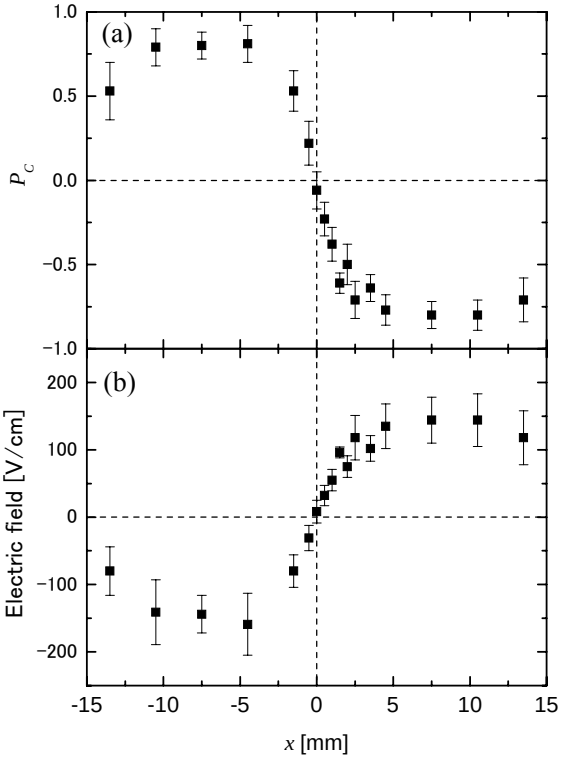

Fig. 6. Spatial distributions of (a) P_C and (b) electric field along *x* axis. The center of cathode is located at *x* = 0 mm, and *x* = ±15 mm is the position of cathode inner surface.

The potential profile is obtained from the spatial integration of electric field distribution. Figure 7 shows potential profiles obtained at (a) discharge voltage of 4 kV and He gas pressure of 25 mTorr, and (b) 2 kV and 60 mTorr. The profile had a peak due to the space charge associated with ions focused onto the center of cathode, which is known as the single-well potential [2]. The potential difference between the central and the peripheral region in plasma was estimated to be (a) 165 V and (b) 120 V. More effective ion focusing occurs in (a) due to higher applied

voltage. The variation in profile was successfully detected by changing the plasma conditions.

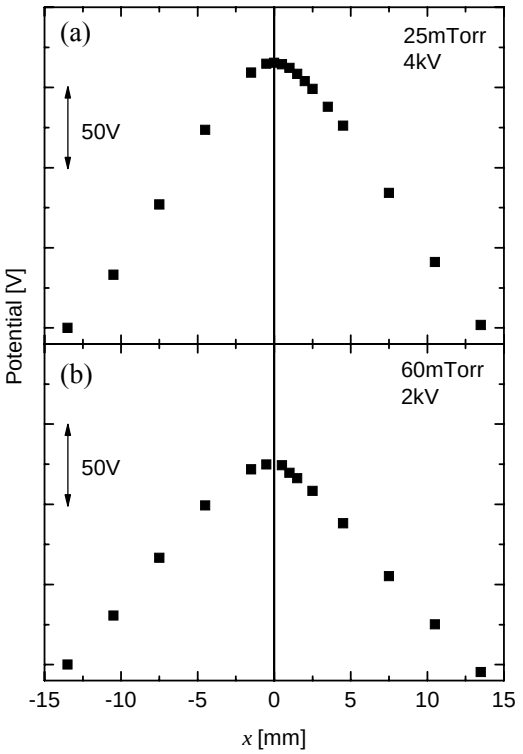

Fig. 7. Potential profile in cylindrical IEC plasma known as single-well potential, obtained at (a) discharge voltage of 4 kV and He gas pressure of 25 mTorr, and (b) 2 kV and 60 mTorr.

4. Summary

We have developed a high-sensitive method for electric field measurement in plasmas using the interference between atomic transition amplitudes, which relies on circular polarization of LIF. This circular polarization method was applied to the cylindrical IEC He plasma for the demonstration of precise potential profile measurement. The profile known as single-well potential was obtained. The minimum electric field strength measured in this study was about 8 V/cm and the potential peak position was identified with spatial resolution of 0.5 mm. Our method has a high potentiality to precisely measure the complicated and localized potential profiles, such as double-well potential structure.

Acknowledgments

This work was partially supported by a Grant-in-Aid for Scientific Research from the Japanese Ministry of Education, Culture, Sports, Science, and Technology.

References

[1] T. Takamatsu, K. Masuda, T. Kyunai, H. Toku and K. Yoshikawa, Nucl. Fusion **46**, (2006) 142.

[2] M. Ohnishi, K. Sato, Y. Yamamoto and K. Yoshikawa, Nucl. Fusion **37**, (1997) 611.

[3] K. Takiyama, T. Usui, Y. Kamiura, T. Fujita, T. Oda and K. Kawasaki, Jpn. J. Appl. Phys. **25**, (1986) L455.

[4] M. Watanabe, K. Takiyama, and T. Oda, Jpn. J. Appl. Phys. **39**, (2000) L116.

[5] K. Yoshikawa, K. Takiyama, T. Koyama, K. Taruya, K. Masuda, Y. Yamamoto, T. Toku, T. Kii, H. Hashimoto, N. Inoue, M. Ohnishi and H. Horiike, Nucl. Fusion **41**, (2001) 717.

[6] K. Takiyama, S. Namba, S. Furukawa, T. Oda, B. W. James, D. Andruczyk, Proc. 4th Int. Sympo. Plasma Polarization Spectroscopy, Kyoto, Japan, Feb. 4-6, 2004.

[7] L. R. Hunter, W. A. Walker and D. S. Weiss, Phys. Rev. Lett. **56**, (1986) 823.

[8] K. Takiyama, M. Watanabe and T. Oda, Proc. Japan-US workshop on Plasma Polarization Spectroscopy and the Int. Seminar on Plasma Polarization Spectroscopy (Kyoto, Japan, 1998), edited by T. Fujimoto and P. Beiersdorfer, NIFS-PROC-37, pp. 236-242

Study of Emitter Material Dynamics in a Low-Pressure Fluorescent Lamp by Laser-Induced Fluorescence

T. Ueda[1] , Y. Egashira[2] , M. Naka[2] , A. Samir[2] , Y. Manabe[1] , Y. Yamagata[2] , K. Uchino[2]

[1] *Lighting Company, Matsushita Electric Industrial Co., Ltd., 1-1 Saiwai, Takatsuki, Osaka 569-1193, Japan*
[2] *Kyushu University, 6-1 Kasugakoen, Kasuga, Fukuoka 816-8580, Japan*

The loss of Ba atom from the electrode of a fluorescent lamp was measured while the lamp was operated under both the glow and the arc discharges. A laser-induced fluorescence method was applied to the measurements of the temporal and spatial distributions of Ba atoms in the vicinity of the electrode. The temporal and spatial distributions of Ba atoms were found to be completely different in these discharges. At the arc mode, Ba atoms were mainly emitted in the anode half-cycle by thermal evaporation. At the glow mode, on the other hand, Ba atoms were emitted in the cathode half-cycle by sputtering, and the amount was 2 orders larger than that at arc discharge mode. The mechanism of Ba atom loss in both modes was discussed.

1. Introduction

Barium oxide as an emitter material is usually coated onto electrodes of low-pressure fluorescent lamp (FL) to emit thermal electrons at low temperature. Because existence of Ba atoms in the electrode surface substantially lowers the work function of bare tungsten of about 4 eV to about 1.38 eV [1], a low discharge voltage (sheath potential) resulting high efficiency operation of the FL can be achieved. Although Ba atoms are evaporated and sputtered from the electrodes during lamp operation, which shortens the life time, there have been only a few studies describing the features of Ba atom loss from the electrode [2-4].

At a low discharge current, the FL is sustained by glow discharge with a cathode sheath potential higher than 100 V, because it is not sufficient to increase the electrode temperature. As for the arc discharge mode, the cathode sheath potential is much lower than that for the glow mode. Because the cathode sheath region does not contribute to fluorescent luminescence and electric power consumption is large in the region, the domination of the hot cathode is clear from the viewpoint of luminescence efficiency. For these reasons, in a dimming operation mode of a high-frequency operating FL, an auxiliary current is usually applied to the filament in addition to the discharge current. Although the transition from glow discharge to arc discharge affects the different discharge parameters and it is important to study the effect of the glow-to-arc transition on the loss of Ba atom, there are as yet no such investigations, particularly for understanding the mechanism of emitter material loss.

In this study, we have investigated the emitter material dynamics in FL using a laser-induced fluorescence (LIF) method [5-7]. The temporal and special distributions of Ba atom density near the electrode surface were measured in both the glow and arc discharges. The mechanism of Ba atom loss from the electrode is described in both the glow and arc discharge modes.

2. Experimental Procedure

The experimental arrangement is schematically shown in Fig. 1 (a). The studied FL was a commercially based fluorescent lamp of 26 mm diameter and 600 mm length and filled at 350 Pa by Ar and a small amount of Hg, which was constructed with a clear glass tube to ensure UV laser beam passage. Ba atoms in ground-state (6^1S_0) were excited to a 5^1P_1 level by a SHG beam (350.1 nm) of a dye laser, and the subsequent fluorescence ($5^1P_1 - 5^1D_2$, 582.6 nm) was detected through a collection lens by a photomultiplier tube equipped with a monochromator. These transition states have been chosen because they have the strongest fluorescence intensity, where the radiative decay is much faster than the quenching by collisions in such a pressure of 350 Pa, and the time constant of the excitation from the ground-state is lower than the laser pulse duration time [3-7]. The laser pulse (7 ns duration and 10 mJ/ pulse) with a repetition rate of 10 Hz was synchronized and varied with respect to the discharge current (I_d)

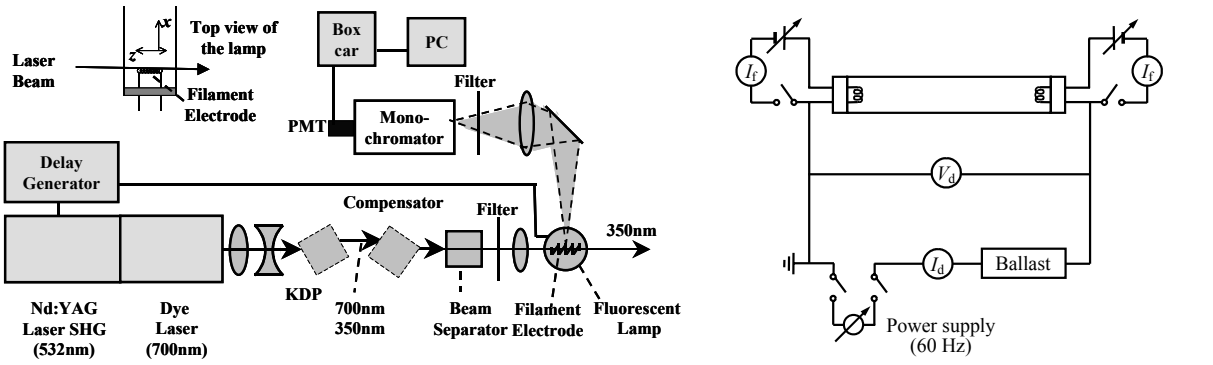

(a) LIF measurement system (b) Electric circuit of FL

Fig. 1. Experimental setup for LIF measurements of FL.

using a delay generator. In order to increase the signal to noise ratio, the LIF signal was averaged over 600 laser pulses by a boxcar integrator and recorded by a computer based data acquisition system. The FL was operated by an AC (60 Hz) power supply with a ballast, and DC auxiliary current (I_f) was used to change the electrode temperature apart from I_d as shown in Fig. 1 (b).

3. Results and Discussion

Figure 2 shows the temporal distribution of the measured LIF intensity at different values of the discharge current (I_d) without the auxiliary current (I_f) and both voltage and current waveforms at I_d = 0.35 A. The temporal distribution of Ba atoms was measured near the surface of the electrode (x=0) with the spatial resolution of 50 μm × 16 mm, which covered the whole length of the electrode. As can be observed in Fig, 2, there is no apparent change in the temporal profile of two or more different I_d.

Figure 3 shows the temporal distribution of the LIF intensity in the following three cases: (1) at I_d = 5 mA without I_f, (2) at I_d = 5 mA with I_f = 0.27 A, and (3) at I_d = 0.29 A without I_f. Note that the temporal distribution of Ba atoms emitted from the electrode in the three cases is completely different. In case (1), Ba atoms are mainly emitted during the cathode half-cycle with a very high rate. At such low I_d, the electrode is cold and the discharge is sustained on the glow discharge mode. In the glow discharge, the positive ions bombard the cathode, which are accelerated by the large cathode sheath potential. As a result, large amounts of Ba atoms are sputtered from the electrode during a cathode half-cycle with a high rate. On the other hand, in the anode half-cycle, only a few Ba atoms are

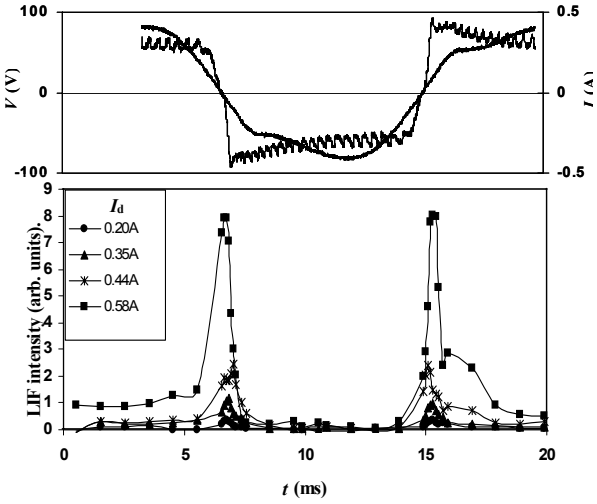

Fig. 2. Voltage and current waveforms and temporal distribution of LIF signal intensities with respect to discharge current.

evaporated due to a low electrode temperature. In case (2), the electrode temperature is increased by I_f. This increase causes a marked decrease in the loss of Ba atom due to the decrease in the energy of the bombarding ion, as will be discussed later. At this high temperature, the thermionic electrons are emitted from the cathode, and a mode transition occurs from glow discharge to arc discharge. In case (3), the FL is operated by arc discharge but this time the cathode is heated only by the alternating I_d. The observed differences between cases (2) and (3) in the cathode and anode half-cycles can be inferred from the finding that in the anode half-cycle, the electrode temperature is increased by electron collection and then more thermal evaporation and Ba atom loss occur. On the contrary, in the cathode half-cycle, there is some cooling of the electrode due to thermionic cooling, which is

mainly electron cooling caused by thermal electron emission with an energy of $e\varphi$ (φ: work function) from the cathode electrode [8]. Using black-body radiation measurement, it was clarified that the electrode temperature increases during the anode half-cycle and decreases during the cathode half-cycle as a FL is operated at 6 Hz [9]. As the operating frequency becomes higher than 60 Hz, there is no obvious temperature change in time because of its large thermal capacity. However, because the electron collection/emission, ion bombardment, and the Ba atom loss take place on the surface of the electrode, it seems that the temperature change of the thin surface layer of the electrode is large [5, 6]. In case (3), the electrode temperature is dominated only by I_d (AC). It is conjectured that the electrode temperature of the thin surface layer during the anode half-cycle is higher than that during the cathode half-cycle. In case (2), on the contrary, the electrode temperature is dominated by I_f (DC) and maintained constant, because the fluctuation due to the heating/cooling by I_d (AC) is negligibly small. This is suggested by the finding that during the anode half-cycle, the LIF intensity for case (3) is larger than that for case (2), whereas it is smaller during the cathode half-cycle, as can be observed in Fig. 3. It is concluded that in arc discharge, heat evaporation is the dominant factor for Ba atom loss from the electrode but not sputtering by ion bombardment. This is consistent with our previous considerations [5-7].

Electrode temperature causing discharge mode transition plays an important role in the loss process in both the glow and arc discharge modes. The electrode temperature in this study was changed using $I_f = 0 – 0.3$ A. Figure 4 shows the rms values of the discharge voltage V_d as functions of I_f at a low I_d of 5 mA. It is clearly shown that V_d was found to decrease with increasing I_f. As the electrode temperature is increased by I_f, the rate of electron emission from the cathode increases, and the cathode sheath potential decreases consequently, which appears as a decrease in the V_d. Under the same conditions, the LIF signal was measured and integrated over the entire period of one cycle of discharge. The integrated values of LIF are also shown in Fig. 4. Note that as I_f increases to 0.2 A the loss rate of Ba atoms decreases to about 6 % of its value at I_f = 0. This behavior can be

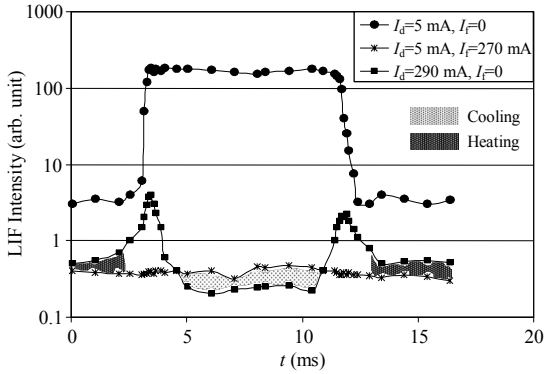

Fig. 3. Temporal distribution of LIF signal intensity in glow and arc discharges.

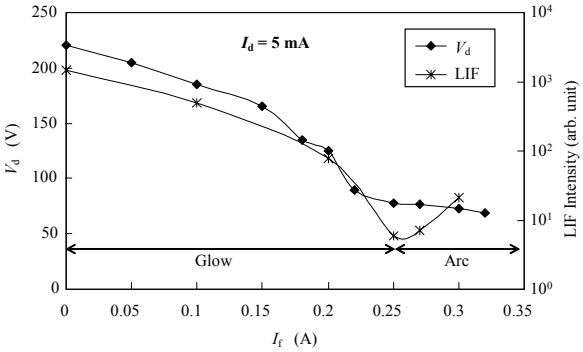

Fig. 4. Integrated LIF intensity and rms values of V_d as functions of filament current I_f at I_d = 5 mA

inferred from the finding that as the cathode temperature is increased, the cathode sheath potential decreases due to the emission of thermionic electrons from the cathode. This decrease causes a decrease in the energy of the bombarding ions and hence reduces the sputtering yield of Ba atoms. As I_f reaches 0.25 A, the loss of Ba atom becomes very low (2 orders of magnitude less than for I_f = 0). Further increase in I_f (0.3 A) causes an increase in the Ba atom loss due to thermal evaporation. This change in the effect of I_f on the loss rate can be inferred to the discharge mode transition from glow to arc, where it was found that at $I_f = 0.25$ A, the electrode temperature is sufficiently high to induce thermionic emission [6]. These opposite effects of the electrode temperature on Ba atom loss in glow and arc discharges play an important role in the improvement of the FL lifetime. If the FL is operated by glow discharge (*ex.* dimming mode operation), it is better to increase its temperature using an auxiliary current.

Figure 5 shows the spatial distribution of Ba atoms in front of the electrode in the glow and arc discharge modes. The spatial distribution was measured in glow discharge in the cathode half-cycle and in arc discharge at the first peak observed in case (3) in Fig. 3. The spatial resolution of these types of measurement was chosen to be 50 μm × 2 mm. As can be observed in Fig. 5, the transition from glow discharge to arc discharge affects the distribution of Ba atoms in front of the electrode. In glow discharge, the Ba atoms are emitted homogeneously from all parts of the electrode and diffuse symmetrically. In glow discharge, the Ba atoms are sputtered due to the bombardment of ions that are accelerated in the high electric field of the cathode sheath. In arc discharge, the Ba atoms are mainly emitted from the hot spot of the electrode. The hot spot is the nearest point of the electrode to the discharge circuit, because of electrode resistance, this point carries most discharge current, and hence, it has the maximum temperature. The high temperature of the hot spot results in a maximum evaporation rate of Ba atoms from it. Therefore the hot spot is the main source of Ba atom loss in arc discharge. The emitted Ba atoms diffuse randomly, so that the density of Ba atoms decreases with x, as shown in Fig. 5. The shapes of spatial distribution in both discharge modes confirm the change in the mechanism of Ba atom loss due to the glow-to-arc transition.

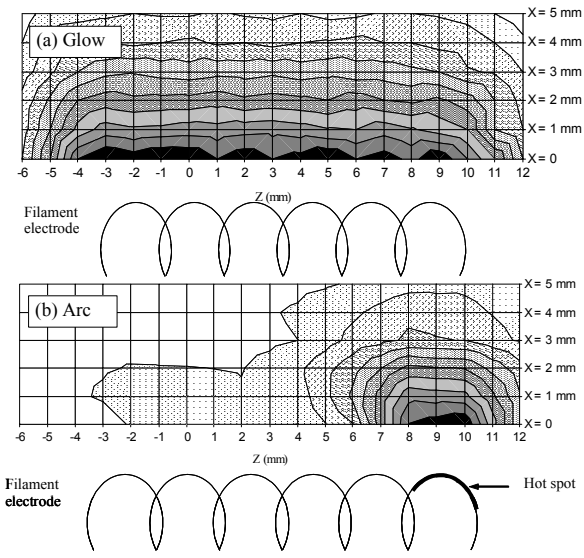

Fig. 5. Spatial distribution of Ba atoms in front of the electrode in (a) glow and (b) arc discharge modes.

4. Conclusion

The LIF technique has been applied to study the emitter material dynamics in a low-pressure fluorescent lamp, and shown to be a powerful tool for discussing the loss mechanism. The present measurements show that in the glow discharge the Ba atoms are mainly emitted in the cathode half-cycle, while in the arc discharge an amount of Ba atoms emitted in the anode half-cycle is larger than that in the cathode half-cycle. The electrode temperature has been found to play an important role in the control of the loss rate of Ba atom, and hence the lifetime of the lamp. It is shown that the Ba atom loss can be reduced effectively as the electrode temperature is raised in the glow discharge. In glow discharge the Ba atom loss is mainly caused by the sputtering, while in arc discharge by the thermal evaporation. As the electrode temperature is raised to a high value, the discharge mode transition occurs from glow to arc even at low discharge current, also this transition causes a change in the loss mechanism.

References

[1] K. C. Mishra, R. Garner, P. C. Schmidt, J. Appl. Phys. **95,** (2004) 3069.
[2] G. Ladatos, J. Bito, Br. J. Appl. Phys. **15,** (1964) 189.
[3] A. K. Bhattacharya, J. Appl. Phys. **65** (1989) 4595.
[4] S Hadrath, M Beck, R C Garner, G Lieder, J Ehlbeck, J. Phys. D: Appl. Phys. **40**, (2007) 163.
[5] A. Samir, G. Yamashita, Y. Yamagata, K. Uchino, T. Ueda, Y. Manabe, Jpn. J. Appl. Phys. **45,** (2005) 8109.
[6] A. Samir, G. Yamashita, Y. Egashira, S. Shimada Y. Yamagata, K. Uchino, T. Ueda, Y. Manabe, IEEJ Trans. A *(in print)*.
[7] T. Ueda, A. Samir, Y. Egashira, G. Yamashita, S. Shimada Y. Yamagata, K. Uchino, Y. Manabe, Jpn. J. Appl. Phys. *(in print)*.
[8] J. Waymouth, *Electric Discharge Lamps* (MIT Press, Cambridge, MA, 1971).
[9] K. Misono, M. Kando, J. T. Verdeyen, J. Illum. Engng. Inst. Jpn. **83,** (1999) 819 *(in Japanese)*.

Behaviors of Ground and Excited O Atoms in O_2 and Rare Gases Mixture Surface Wave Plasmas Measured by Vacuum Ultraviolet Laser Absorption Spectroscopy

K. Takeda, S. Takashima, M. Hori

Graduate School of Engineering, Nagoya University, Furo-cho, Chikusa-ku, Nagoya 464-8603, Japan

Measurement of absolute densities of O atoms in surface wave plasmas (SWP) with oxygen and rare gases mixture was carried out by using vacuum ultraviolet (VUV) absorption spectroscopy with tunable VUV laser system (VUVLAS). Absolute densities of O atoms in the ground ($^3P_2$) and excited state ($^1D_2$) were measured as functions of input power density of microwave. From these results, the absolute density of O ($^3P_2$) atom slightly increased with increasing the microwave power density. On the other hand, that of O ($^1D_2$) atom was larger than that of O ($^3P_2$) atom in the condition of high microwave power density. Moreover, we confirmed that the Ar and O_2 mixture SWP was able to realize the high density condition of O ($^1D_2$) atom compared with Kr and O_2 mixture SWP.

1. Introduction

In the nano fabrication technologies, high speed operations to process at lower temperature are strongly required to realize the ultra-high integration devices with precise doping profile control, flexible devices with organic films, etc. Plasma nanotechnology is most likely candidate for realizing such processes. However, reactive plasma processes are typically complication, because of surface and gas-phase reactions due to various species in the plasmas. Therefore, in order to achieve the fabrication of high precise plasma processes, it is important to get an insight into the behaviors of those reactive species in the process plasmas.

In oxygen (O_2) based plasmas, oxygen (O) atoms have attracted very much because of their high reactivity compared with other species. Therefore, the behaviors of the O atoms in the plasmas must be controlled for realizing the high performance on several applications, such as resist ashing, surface cleaning, material oxidizing, etc. [1, 2] Nowadays, a quantitative study on the behaviors of O atoms in O_2 based plasmas with a high rare gas dilution is strongly required from the viewpoint of developing high precise oxygen based plasma processes used on several processes. It was reported that O_2 based plasma with high krypton (Kr) gas dilution had a great potential to realize the high speed plasma Si oxidation process at low temperature because excited O atoms which has high reactivity were efficiently generated by the collisional dissociation between metastable Kr atom and O_2.[3] We have focused on the measurement of the absolute density of O atoms in the ground (^3P_j) and excited state ($^1D_2$) in a surface wave plasma (SWP) with Kr and O_2 gas mixture. Moreover, the production processes of O atoms were discussed. From these results, we confirmed electron impacts were dominant processes to generate the O (^3P_j) and ($^1D_2$) atoms in the Kr/O_2 SWP.[4] However, the Ar/O_2 SWP has been frequently used for synthesizing the Si oxidation films in the industry. In order to investigate the optimum condition of the plasma oxidation process, the quantitative information of the behaviors of O atoms in the Ar/O_2 SWP is of extreme importance. In this study, the measurements of absolute density of O (^3P_j) and ($^1D_2$) atoms in an Ar/O_2 SWP were carried out by using vacuum ultraviolet laser absorption spectroscopy (VUVLAS).

2. Experimental setup

Figure 1 shows a schematic diagram of experimental setup for measuring the absolute densities of O ($^3P_2$) and O ($^1D_2$) atoms in the rare gas and O_2 mixture SWP. The plasma chamber is 60 cm in diameter and 70 cm in height, which is a production level apparatus for 200 mm Si wafer. Microwave of 2.45 GHz was supplied to the flat top quartz window to produce the SWP. In this study, the rare gas and O_2 mixture SWP was generated at the condition of an total pressure of 133.3 P and the O_2/(Ar+O_2) flow rate ratio of 1 %. The input power density of microwave was changed from 0.8 to 2.2 W/cm^2. The measurements of O atoms in the rare gas and O_2 mixture SWP were carried out at the point of 7.3 cm below the quartz window.

The absolute densities of O ($^3P_2$) and O ($^1D_2$) atoms were measured by a vacuum ultraviolet

laser absorption spectroscopy (VUVLAS). In the measurement of O ($^3P_2$), we used the VUV laser radiations around 130nm generated by the two photon resonance four wave sum frequency mixing. The O ($^3P_2$) has a transition line of 3s $^3S^0$-2p^4 $^3P_2$ at 130.217 nm. VUV laser light at around 130.2 nm was passed through the SWP and then was focused on the slit of a VUV monochromator with a MgF_2 lens and detected by a solar blind type photomultiplier tube.

The absolute density of the O ($^1D_2$) atom was also measured by VUVLAS on the 3s $^1D^o$-2p $^1D_2$ transition at 115.22nm. The VUV laser radiations around 115nm were generated by phase-matched frequency tripling in the rare gas mixture. The VUV light generated in the rare gas mixture gas cell was passed though the LiF window and was introduced into the SWP reactor. The VUV light going through the SWP was detected by the photo-ionization current of NO gas.

In this experimental setup, two stainless-steel pipes of 34 mm in diameter and 15 cm in length were introduced into the chamber in order to avoid the saturation of the absorption intensity. Thus, the absorption path length of the VUV laser light was adjusted to be around 30 cm.

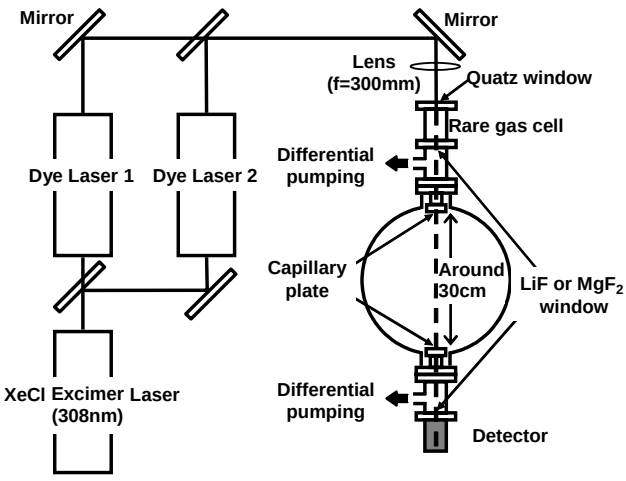

Fig. 1 Experimental setup for measuring the absolute densities of O ($^3P_2$) and O ($^1D_2$) atoms in rare gas and O_2 SWP.

3. Profiles of VUV laser radiations

In this study, the profiles of the VUV laser radiations were estimated from the VUVLAS measurement results of absorption profile of molecular and rare gases without discharge.[5]

The profile information of the VUV laser radiation generated by two photon resonance four wave sum mixing in Kr gas was obtained by measuring the absorption intensity profile of Xenon (Xe) on the condition of a pressure of 4 × 10^{-2} Pa and without discharge (300K). In order to measure the absorption intensity profile of the Xe, we used the transition of Xe at 129.559 nm [$^1S_0$-$^1P_1$]. From this result, the hull width at half maximum (FWHM) of Xe absorption intensity profile was 0.43 cm^{-1}. The absorption profile of Xe atom was a Doppler profile and had the FWHM of 0.083 cm^{-1} at a room temperature. Considering the profile of the VUV laser radiation, the profile of the VUV laser radiation had the FWHM of 0.4 cm^{-1} and a Gaussian type profile.

As described above, in order to observe the behaviors of O ($^1D_2$) atom, the technique of phase-matched frequency tripling in the Xe and Ar gas mixture to generate the VUV laser radiations around 115.22 nm. Therefore, the profile of the VUV laser radiations around 115.22 nm should be also estimated from the measurement of absolute density of O ($^1D_2$) atom. In this estimation, CO molecule was used for the profile of the VUV laser radiation to be determined. The measurement of absorption intensity profile was carried out at a pressure of 0.13 Pa without the discharge (300 K). Under the condition, the absorption profile of CO molecule can be assumed as a Doppler and that FWHM was 0.17 cm^{-1}. The FWHM of the absorption intensity profile of CO molecule was 0.45 cm^{-1}. Therefore, the profile of the VUV laser radiation generated by the phase-matched frequency tripling was the Gaussian type and the FWHM was 0.44 cm^{-1}.

4. Results and discussions

Figure 2 shows the absolute densities of O ($^3P_2$) and O ($^1D_2$) atoms in the Ar and O_2 mixture SWP as a function of input power density of microwave. The plasma was discharged at a pressure of 133.3 Pa, O_2 flow rate ratio (O_2/(Ar+O_2)) of 1 %. Microwave power density was changed from 0.8 to 2.2 W/cm^2. The absolute density of O ($^1D_2$) atom in the Ar and O_2 mixture SWP increased markedly up to the microwave power density of 1.2 W/cm^2. Above 1.2 W/cm^2, the absolute density of O ($^1D_2$) atom increased slightly with the microwave power density. The absolute density of O ($^1D_2$) atom was estimated to be 1.1 ~ 2.8 × 10^{12} cm^{-3}. On the other hand, the

absolute density of O ($^3P_2$) atom increased slightly from 1.6 to 2.5 × 10^{12} cm^{-3} with increasing the microwave power density. In the condition below the microwave power density of 1.2 W/cm^2, absolute density of O ($^3P_2$) atom was higher than that of O ($^1D_2$) atom. However, above the 1.2 W/cm^2, the high density condition of O ($^1D_2$) atom was realized by using this SWP reactor. From the measurement results of electron density and temperature using Langmuir single probe, the electron density in the SWP increased drastically from 10^{10} to 10^{11} cm^{-3} with increasing the microwave power density up to 1.2 W/cm^2. However, the electron temperatures were almost constant around 1 eV. From these results, it is supposed that the O ($^1D_2$) atom was generated efficiently by the electron impact dissociation of O_2 because of increasing the density of electron with high energy which cannot be measured by using Langmuir single probe.

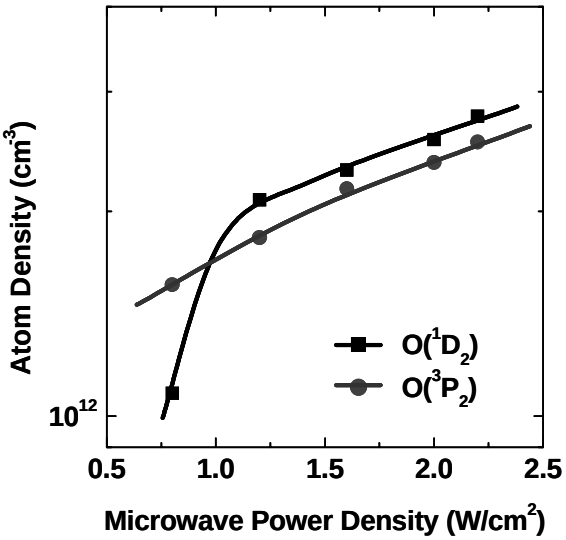

Fig. 2 Absolute densities of O atoms in the ground and excited states as a function of the input power density of microwave.

Next, the comparison between the Ar/O_2 SWP and Kr/O_2 SWP was carried out from viewpoints of absolute density of O ($^1D_2$) atom in each SWP. As shown in Fig. 3, the absolute density of the O ($^1D_2$) atom in the Kr or Ar diluted O_2 SWP was measured as a function of the microwave power density. The plasma was discharged at a pressure of 133.3 Pa, and an O_2 flow rate ratio (O_2/(O_2+Rg)) [Rg: rare gas] of 1 %. Microwave power densities were changed from 0.8 to 2.2 W/cm^2. The absolute density of O ($^1D_2$) atom in the Ar and O_2 mixture SWP markedly increased from 1.1 to 2.1×10^{12} cm^{-3} up to the microwave power density of 1.2 W/cm^2. Above this value, the absolute density of O ($^1D_2$) atom slightly increased from 2.1 to 2.8×10^{12} cm^{-3} with an increase in the microwave power density. On the other hand, the behavior of the absolute density of the O ($^1D_2$) atom in the Kr and O_2 mixture SWP was similar to that in the Ar and O_2 mixture SWP. However, the absolute density of O ($^1D_2$) atom in the Kr diluted O_2 SWP was lower than that in Ar diluted O_2 SWP in all microwave power densities. The absolute density of O ($^1D_2$) atom in the Kr diluted O_2 SWP increased from 6.7×10^{11} to 1.6×10^{12} cm^{-3} with the microwave power density. These results also suggest that the generations of O ($^1D_2$) atom due to the electron impact dissociation of O_2 and excitation from O (^3P_j) atom were dominant under our measurement conditions.

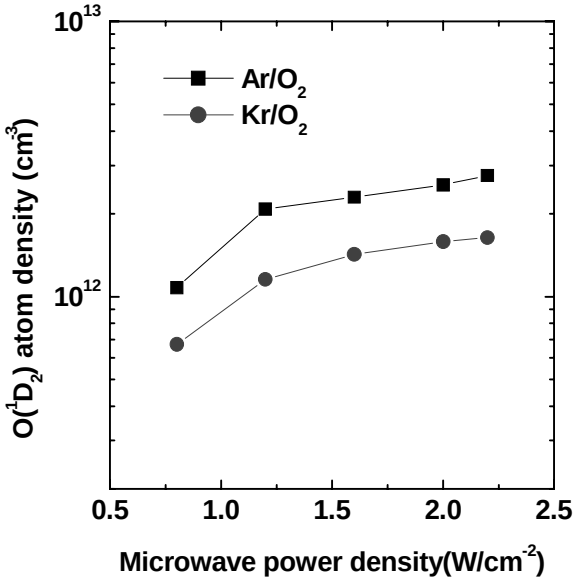

Fig. 3 Absolute densities of the O atom in the excited state in the Kr or Ar and O_2 mixture SWP as a function of the microwave power density.

5. Conclusions

Absolute densities of O atoms in the ground ($^3P_2$) and excited state ($^1D_2$) in the rare gas and O_2 mixture surface wave plasma (SWP) were measured by using vacuum ultraviolet laser absorption spectroscopy (VUVLAS). The absolute density of O ($^1D_2$) atom in the Ar and O_2 mixture SWP increased markedly up to the microwave power density of 1.2 W/cm^2. The

absolute density of O ($^1D_2$) atom increased slightly with the microwave power density. The absolute density of O ($^1D_2$) atom was estimated to be 1.1 ~ 2.8 × 10^{12} cm^{-3}. On the other hand, the absolute density of O ($^3P_2$) atom increased slightly from 1.6 to 2.5 × 10^{12} cm^{-3} with increasing the microwave power density. From these results, it was found that the high density condition of O ($^1D_2$) atom was realized in the condition above the 1.2 W/cm^2 by using our SWP reactor. Moreover, the absolute O ($^1D_2$) atom density in the Ar and O_2 SWP were compared with that in Kr and O_2 mixture SWP from results measured by VUVLAS. From this result, the Ar dilution plasma had a potential to realize the higher density condition of O ($^1D_2$) atom compared with the Kr dilution plasma. These results also suggest that the generations of O ($^1D_2$) atom due to the electron impact dissociation of O_2 and excitation from O (^3P_j) atom were dominant under our measurement conditions.

Reference

[1] M. Hori, K. Takeda, K. Kubota, M. Sugiura, Y. Matsumi, S. Takashima, and K. Kubota, Proceeding of 5th International Symposium on Dry Process, 29 (2005).

[2] M. Iwasaki, K. Takeda, M. Ito, T. Yara, T. Uehara, and M. Hori, Jpn J. Appl. Phys., **46**, (2007) L540.

[3] K. Sekine Y. Saito, M. Hirayama, and T. Ohmi, IEEE Tran. Electron Devices, **48** (2001)1550.

[4] K. Takeda, Y. Kubota, S. Takashima, M. Hori, A. Serdyuchenko, M. Ito, and Y. Matsumi, J. Appl. Phys., **102** (2007) 013302.

[5] P. M. Griffin and J. W. Hutcherson, J. Opt. Soc. Am. **59** (1969) 1607.

Sensitive Drift Measurements by Thomson scattering in a Low-Temperature plasma

D.L. Crintea[1], D. Luggenhölscher[1], T. Gans[2], D. O'Connell[3], U. Czarnetzki[1]

[1] *Ruhr University Bochum, Insitute for Experimental Physics V, NB 05/692, D-44780, Bochum, Germany*
[2] *Center for Plasma Physics, Queens's University Belfast, Northern Ireland*
[3] *Ruhr University Bochum, Faculty for Electrical Engineering, IC/051, Bochum, Germany*

In a low-temperature magnetized plasma, a neutral loop discharge, a collective drift of electrons has been identified for the first time by Thomson scattering. These observations are confirmed by a novel emission spectroscopic technique based on the modulation of the electron energy distribution function by an induced radio-frequency electric field. The drift is identified as the diamagnetic drift. The resulting velocity depends on the gas pressure. Between about 1 Pa and 10 Pa the drift decreases from about 100 km/s towards zero due to collisions and from 1 Pa to about 0.01 Pa the drift increases by the increase of the electron temperature to a maximum value of 200 km/s. The sensitivity of our system is about 10 km/s.

1. General

In the early 90s a new type of plasma discharge was introduced by Uchida et all [1], the so called Neutral Loop Discharge (NLD). The development in the etching and deposition processes in the semiconductor industry requires plasma discharges to be operational at very low pressures, bellow 0.1 Pa with high electron and ion densities. At these conditions anisotropic etching over large areas can be achieved. The Neutral Loop Discharge proved to be very efficient and it has been successfully applied in the industry for large area processing [2]. An NLD reactor was designed and built [3] in order to allow diagnostic access both to the main plasma region as well as to a downstream region, where a substrate for processing can be located. The inhomogeneous magnetic field is generated by three coaxial coils, and in essence is a magnetic quadrupole bent into a torus. This leads both to a chaotization of the electron trajectories and to a confinement of the electrons in the Neutral Loop (NL) region. Knowledge of the electron properties of the discharge is of outmost importance since the deposited power is absorbed initially by these light particles and transferred afterwards by elastic or inelastic collisions.

In this abstract application of the Thomson scattering and first identification of a rotational plasma drift identified as a diamagnetic drift in the Neutral Loop Discharge is presented together with the description of our laser scattering setup and detection system.

2. Experimental setup

A sketch of the experimental setup for the plasma production is given in Figure 1. This novel design follows the industrial one with the distinction that the Neutral Loop (NL) plane is shifted from the middle coil plane, allowing diagnostic access on the NL region through several view ports.

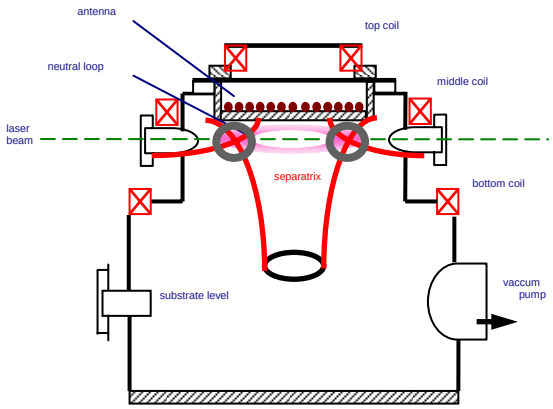

Figure 1. Neutral Loop Discharge experimental setup

The experimental setup together with the magnetic field structure is described elsewhere [3]. Figure 2 shows the simulated magnetic field together with the region probed by Thomson scattering. The plasma is generated by inducing an oscillating radio-frequency field along the Neutral Loop through a planar 4-fold, 2 ½ turn ICP antenna operated at 13.56 MHz. This novel antenna design significantly reduces the non-uniformities in the induced electric field. The

setup allows a versatile operation both in the NLD and in the ICP mode with the magnetic field turned off.

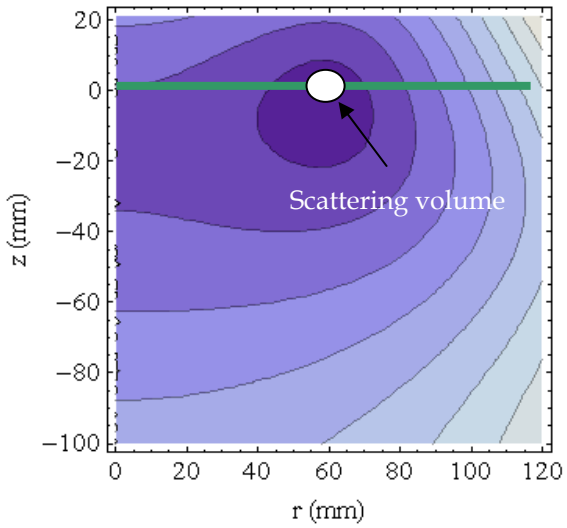

Figure 2. Simulation of the NL and the position of the scattering volume. The lines and shadings represents regions of constant absolute magnetic field strength in steps of 2 mT.

3. Thomson scattering

The classical theory of the light scattering [5] discriminates, based on the parameter α, between the incoherent regime ($\alpha << 1$) and the coherent regime ($\alpha > 1$). In general scattering takes place on electron density fluctuations. In the incoherent case the density fluctuations are random on a Debye shielding length and electrons do not bear any phase relation between them, consequently they can be seen as "free electrons".

As a plasma diagnostic technique, laser scattering can provide a substantial amount of information on the plasma parameters, electron temperature and density [5], as well as on the electron energy distribution function [6, 7], which is a key parameter in understanding the ionization and dissociation processes.

If the electron energy distribution function is assumed to be Maxwellian, the scattered spectrum has a Gaussian shape reflecting the velocity distribution function. As a result Thomson scattering gives a straightforward and non-intrusive method to obtain the Electron Velocity Distribution Function (EVDF) with high spatial and temporal resolution.

Therefore if an additional velocity will be superimposed in the direction of the scattering vector, this will result in a shifted spectral distribution.

Because of a small scattering cross section Thomson scattering experiments are requiring a high power light source and a sensitive detection system. In addition stray light can cause severe problems.

3.1 Experimental setup for Thomson scattering

In Figure 3 is shown the experimental setup for Thomson scattering measurements.

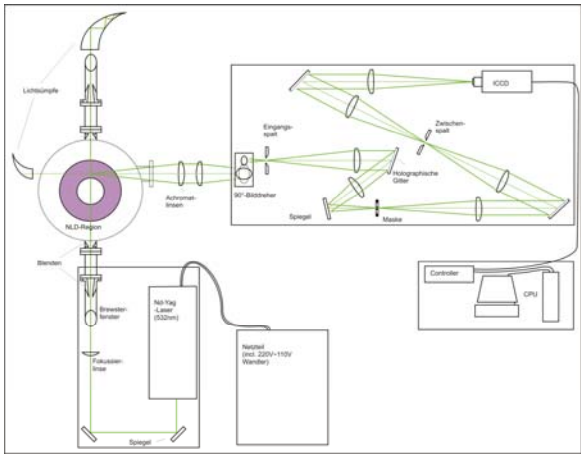

Figure 3. Thomson scattering experimental setup

The laser used is a frequency doubled Nd:YAG laser (Continuum 9050) with a wavelength of 532 nm, pulse length of 7 ns, pulse energy of 600 mJ and a repetition rate of 50 Hz. The laser beam was guided through a baffles system for stray light reduction by a pair of dichroic mirrors and focused into the scattering volume by a plano-convex AR coated lens with a focal length of one metre. The cross section of the laser beam in the focus point of the lens can be approximated with a Gaussian with a 1/e width of 250 μm. The scattered photons are detected at an angle of 90°. Figure 4 shows the scattering geometry used in this experiment.

The scattered light is collected with a system of two achromatic doublet lenses which creates a 1:1 image of the scattering volume onto the entrance slit of a Triple Grating Spectrograph (TGS). The design of the TGS is based on previous versions [7, 8] and is shown in Figure 3.

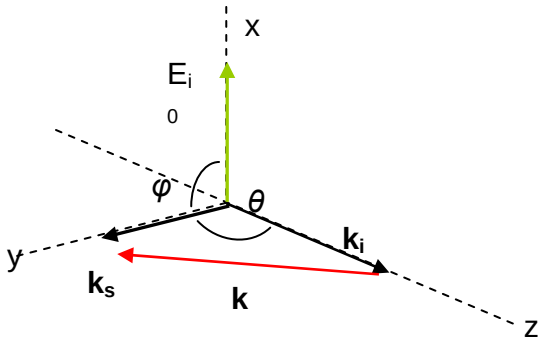

Figure 4. Thomson scattering geometry

The three holographic gratings have 1800 grooves/mm and are used in the first diffraction order. To reduce optical aberrations doublet-achromat AR coated @ 532 nm lenses are used, with a focal length of 500 mm and a diameter of 100 mm.

The obtained scattered spectrum is recorded on an intensified CCD camera (Roper Scientific PI:MAX II) over 90000 laser shots using a normal accumulation technique. The efficient usage of a Triple Grating Spectrograph together with an ICCD camera was previously demonstrated [7] in Thomson scattering measurements by using a photon counting technique.In order to separate the Thomson signal from the stray light and the Rayleigh contribution which affects the centre part of the spectrum together with the continuous plasma signal and the dark current of the detector which affects the low intensity part of the spectrum several subtraction methods are applied. The TGS allows by design a stray light rejection factor of 10^{-6} and a lower detection limit down to 10^{15} m^{-3}.

Typical EEDFs obtained with the TGS for an NLD discharge at 0.05 Pa and 5 Pa is shown in figure 5.

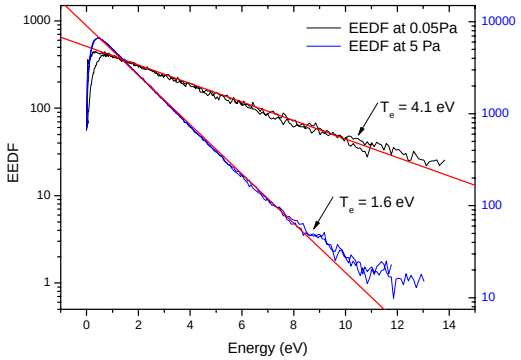

Figure 5. EEDF – Thomson scattering for NLD at 1000 Watt in Argon at 0.05Pa and 5 Pa

A dynamic range up to 3 orders of magnitude in the EEDF can be achieved over 12 eV in the energy scale. The determined electron temperature as a function of pressure at two input powers and a power variation at two operating pressures in the NLD are shown in figures 6 and 7 for a given set of coil currents.

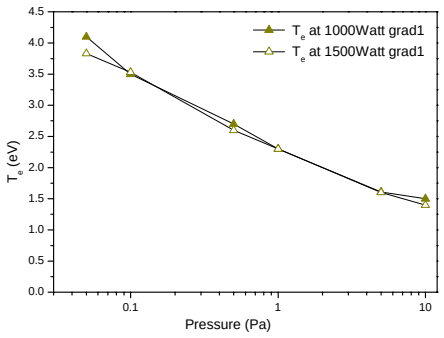

Figure 6. Electron temperature as a function of pressure for two input powers in the NLD

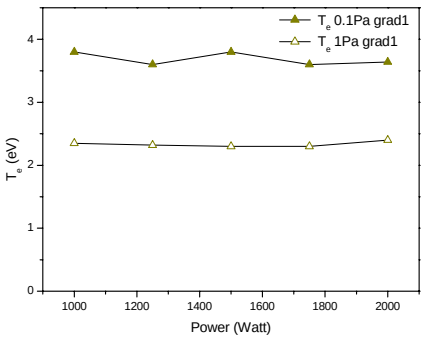

Figure 7. Electron temperature as a function of power for two operating pressures in the NLD

Since a mask is used in the TGS to block the Rayleigh signal at the centre wavelength of the laser, for inferring the absolute values of the electron density we are using Raman calibration on nitrogen at room temperature and atmospheric pressure. At the time of these measurements the TGS was newly realigned and the calibration was not performed.

The high performance of the TGS allowed identification of a drift rotation of the plasma both in the ICP and in the NLD mode and therefore to deduce and quantify a drift velocity. Since the diamagnetic drift has a velocity component superimposed on our scattering vector, see Figure 4 and we probe by Thomson scattering the velocity distribution function, this will result in a shifted velocity distribution.

Figure 8 shows a clear shift in the distribution function for the case of ICP and NLD.

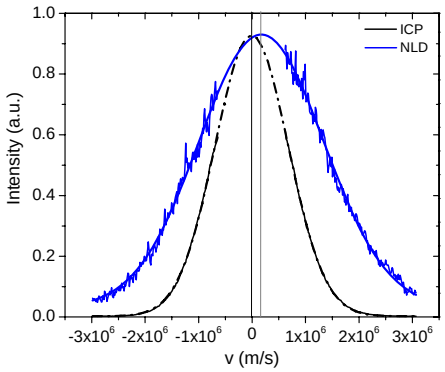

Figure 8. Isotropic and anisotropic velocity distribution function for the ICP and NLD respectively

Figure 9 shows the measured drift velocity as a function of pressure in an Argon NLD discharge at 1000 Watt both in normal and reverse magnetic field. The sign of the drift can be changed by changing the direction of which the current flows in the three coils. The drift is believed to be caused by a diamagnetic drift effect. The drift is strongly dependent on the magnetic field gradients.

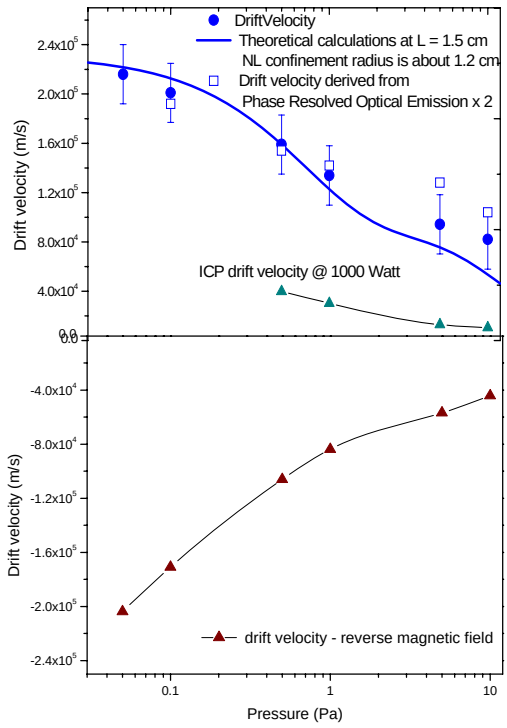

Figure 9. Drift velocity as function of pressure / magnetic field

The calculated values are shown with a continuous line, and are in good agreement with the measured data both from Thomson and Phase Resolved Optical Emission Spectroscopy. The fitting parameter used was only L – electron pressure gradient length. In this particular case the motion of the electrons and ions in the magnetic field can be uncoupled. Therefore the equations describing the drift can be written as:

$$u_\varphi = \frac{1}{1+\left(\frac{\nu_e}{\omega_c}\right)^2} \frac{\nabla p_e}{B \cdot en}$$

where the u_φ is the drift velocity probed by Thomson scattering.

The drift velocity increases at pressures bellow 1Pa and is on the order of 10^5 m/s and goes close to zero at pressures close to 10 Pa. This can be explained in the low pressure regime by an increase in the electron temperature. With pressure increase the drift is damped by collisions.

Summary

For the first time a diamagnetic drift in the Neutral Loop has been observed experimentally and quantified. The high sensitivity of the detection system allowed detection of drift velocities down to 10 km/s.

References

[1] Uchida et all, Jap. J. Appl. Phys. **34,** (1995) 2476.

[2] Chen W et all, J. Vac. Sci. Technol. **A 17,** (1999) 2546

[3] T. Gans, D.L. Crintea,, D. O'Connell, U. Czarnetzki, J.Phys. D. **40**, (2007)

[4] J. Sheffield, Plasma scattering of electromagnetic radiation, Academic Press (1975)

[5] K. Muraoka, K Uchino, M.D. Bowden, Plasma Phys. Control. Fusion **40**, (1998) 1221

[6] T.Hori, M. Kogano, M.D. Bowden, K. Uchino, K. Muraoka, J Apply. Phys. **83**, (1995) 1909

[7] A. Kono, K. Nakatani, Rev. Sci. Instrum. **71**, (2000) 2716

[8] Marco Van de Sande, PhD. Thesis TUE, 2002

Acknowledgments

The financial support from DFG, SFB 591, GRK 1051, MIWFT is greatly acknowledged.

Laser Observation of Charged Dust Particles in RF Plasma under the Irradiation of Ultraviolet Light

Tatsuya Misawa [1], Yasunori Ohtsu [1], Hiroharu Fujita [1]

[1] *Department of Electrical and Electronic Engineering, Faculty of science and Engineering, Saga University, 1, Honjo-machi, Saga-shi, 840-8502, Japan.*

Influence of ultraviolet light on the Coulomb coupling between dust particles was experimentally investigated in Radio-Frequency plasma. Flask-shape and the filamentary-shape dust cloud were observed in the RF plasma generated by ring antenna. The ultraviolet radiation seemed to be not easy to pick up the polarization of the dust particles in the laboratory.

1.Introduction

It has been investigated that surfaces of artificial satellite become positively or negatively was charged in space by the strong ultraviolet light from the sun [1]. Since under the irradiation environment of the strong ultraviolet ray from the sun, photoelectrons can be emitted from the object surface, a part of irradiated surface would be possible to be charged positively.

Then, the surface charge distribution and spatial potential around the object should depend on the object characteristics such as conductor or insulator. In particular, UV irradiated surface of insulator object take a positive charge because electron emission current causes by the photoemission increases further than electron current from space plasma, while non-irradiated side becomes negative. As the result, the polarity of the charge and spatial potential around the object is reversed in the irradiated side and non-irradiated side of the object [1].

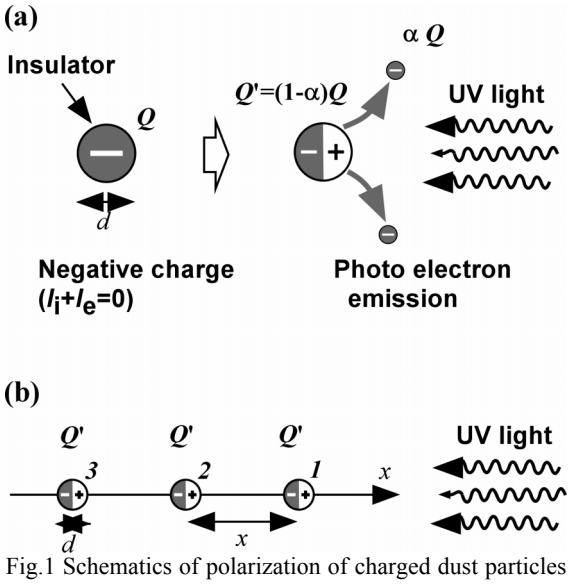

Fig.1 Schematics of polarization of charged dust particles by the irradiation of ultraviolet light.

It should be possible to produce the dusty plasma with the property of electric dipole by UV light irradiation to the insulator dust particles in the laboratory plasma (Fig.1(a)). It is anticipated that Coulomb interaction and the interaction between dust and ion flow of are different from the interaction which assumes that dust particle is point charge.

The potential of polarized charged dust particles in the supersonic ion flow has been reported [2]. And recently, it is consider that the interaction between charge distribution on the dust particle and electric field which has caught dust particle become the driving force of rotary motion of fine particle [3].

When the dust particle in the horizontal line is irradiated with ultraviolet light (Fig. 1(b)), the Coulomb interaction between the dust particles can be modified as the Coulomb potential $\phi(x)$,

$$\phi(x) = \frac{Q}{4\pi\varepsilon_0 x}(1-\alpha) + \frac{Q}{4\pi\varepsilon_0 x}\left(\frac{\alpha d}{2x}\right), \quad (1)$$

x: inter-particle distance, d : dust radius, Q : dust charge in the case of non-irradiation condition and α : relative value of photoelectron charge to the total charges. (Condition of α=0 corresponds to the absence of photoelectron.) First and second term in eq.(1) are the potential formed by non-irradiated and irradiated dusts, respectively. Then, for α > 0.5, the dust can be positively charged. Assuming α = 0.5, x = 50 - 100 μm and d = 10 μm in diameter of dust particles, the dipole potential must amount about 5 - 10% of first term of eq.(1), and it may be able to observe the phenomena induced by the ultraviolet irradiation.

With increasing in the photoelectron emission from the ultraviolet light, the magnitude of

positively charge on the dusts should increase resulting in the decrease in total dust negative charges with keeping the total dust charge negatively. This fact should provide levitated dusts begin to move toward down-side, and finally all of dusts should fall down on the bottom. Using the electrostatic field required using Bohm sheath criterion and dust charge considering the orbit-limited-motion (OLM) theory, the levitation height of the dust particle from the disk electrode with the photoemission was evaluated (Fig.2)[4]. The parameter used the typical value of the experiment. This figure shows that dust particles which the experiment used are possible to levitate even in the photoemission like $\alpha > 0.5$.

By using the ultraviolet light, it seems to be possible to independently control the direction of the ion flow and the polarization. In this work, we tried generation of the dusty plasma to be an aggregate of electric dipole by irradiation of ultra violet light and observation of the dynamics of polarized dust particles.

2. Experimental setup

The experimental setup is shown in Fig.3(A). One-turn and two-turn RF internal copper antenna with a diameter of 18 cm and 16 cm, covered by glass tubes, is located the center of the stainless chamber. RF antenna was coupled to an RF power supply at 13.56 MHz with the matching network. Typical plasma parameter measured with a Langmuir probe for RF power of 40W and Ar gas at 5 - 8 Pa were $n_e \sim 10^{13} - 10^{14}$ m^{-3}, $T_e \sim 3$ - 5 eV. The negative biased electrode was composed of the disk electrode (V_{disk}= -60 - 0V) of 90 mm in diameter and ring electrode (V_{ring}= -90 - 0 V) of 90 mm in diameter for levitation control (Fig.3(B)). Distance between the ring and disk electrode was ~ 10 mm.

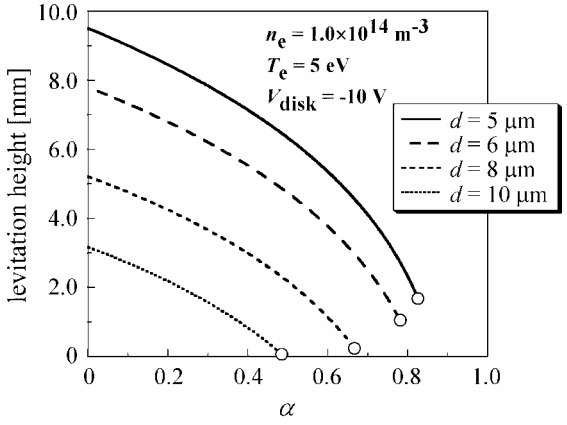

Fig.2 The dependence of the levitating position and falling condition of the dust particle in the ion sheath on the relative value α. (d: diameter of dust particle; open circles: falling condition.)

Ultraviolet light emitted by the deuterium DC discharge lamp (λ = 115 - 400 nm), and is irradiated from the horizontal and downward direction of levitating dust particles. In the case of irradiation from horizontal direction, ultraviolet light is converged by the fused quartz lens (f = 74 mm in λ = 200 nm) which was installed in the vacuum. The optical system was designed so that the condensing point may consist near the trapping region of dust particles. The observation of dust particles was carried out using the charge coupled device (CCD) camera with the microscopic lens, imaging the scattered light from the dust particles by the vertically expanded semiconductor laser.

We used two type dust particles in the experiment, acrylic resin particles and MgO particles. Acrylic resin dust particle is 10 μm in

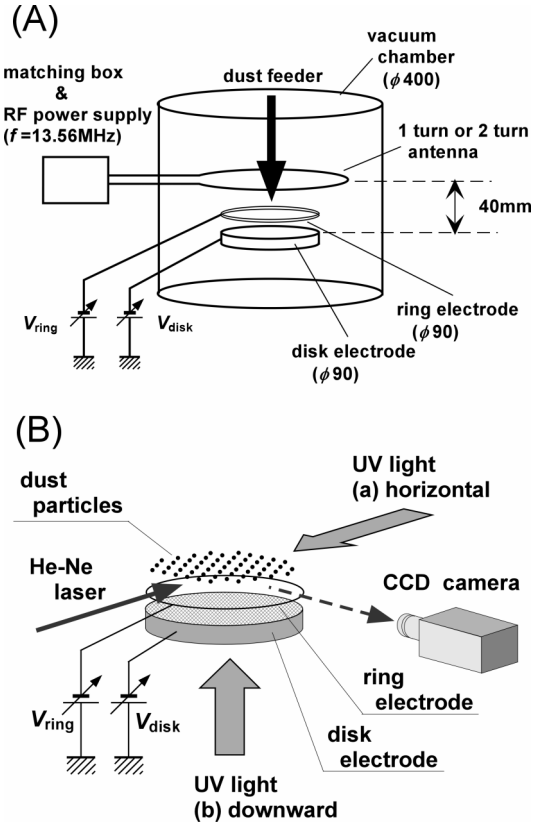

Fig.3 Experimental setup
(A): schematics of experimental device.
(B): extended view of negative biased electrode.

diameter, and dispersion of diameter is relatively small. MgO particles have three kinds of diameters, 0.05 μm, 0.2 μm, 10 μm, and has large dispersion of diameter. Dust particles were dropped from a dust feeder located at 30 mm up from the RF antenna, and levitate in the RF ion sheath around the disk electrode.

3. Experimental result

3.1. Shape and structure of dust cloud

In case of the experiment using the one turn antenna, the spatial structure of levitated dust particles was found to be flask shape (Fig. 4(a)). The dust particles were distributed above the disk electrode through the ring electrode with the vertical length of about 20 - 30 mm and the horizontal width of about 20 - 40 mm, and typical inter-particle distance is about 0.5 - 1.0 mm in upper part. In addition, it should be also noted that the dust particles were vertically oscillating near the bottom face of dust cloud, and it seems that coupling between dust particles is weak. In case of the experiment using the two turn antenna, the filamentary structure of dust particles was found in the trapped dust cloud. The vertical arrangement of the fine particle was observed in the upper part (Fig. 4(b)), and the dust particles have irregularly lined up in the lower part.

Inter-particle distance is 0.7 - 1.0 mm in vertical direction, and 1.0 - 1.5 mm in horizontal direction, and it is a half order of typical Debye length (λ_d ~ 2 - 2.5 mm). This shows that main interactions between vertical aligned particles are electrostatic force or wake potential further than the coulomb interaction. The length of dust particles column is about 10 mm. Particles in vertical neighbourhood move with the correlation, and it is indicated that dust particles are strongly coupled to vertical direction.

3.2. Under the ultraviolet irradiation condition

With the irradiation of the UV light to the dust particles, it is expected that the decrease in floating position by the photoemission and the change of the cloud structure and behaviour by polarization of dust particles. The change of the dust chain with the ultraviolet light irradiation is shown in Fig. 5(b). The direction of dust

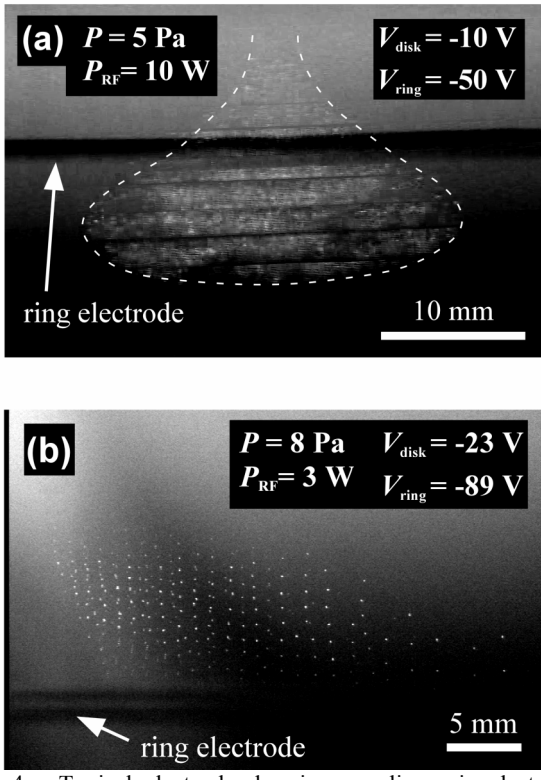

Fig.4 Typical dust cloud using acrylic resin dust particles, diameters is 10 μm.
(a): One turn antenna experiment.
(Broken line is the envelope of dust cloud.)
(b): Two turn antenna experiment.

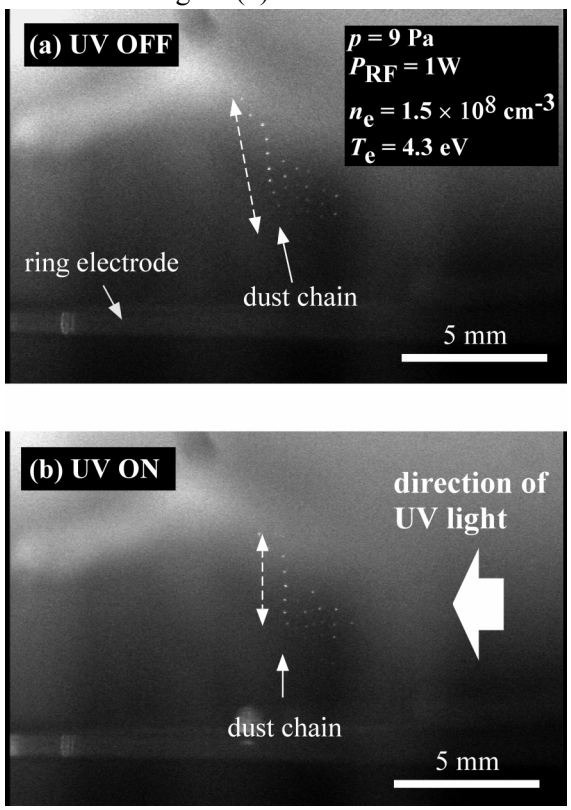

Fig.5 The alignment direction of the dust particles in irradiating the ultraviolet light.(Broken line indicates the direction of alignment.)
(a): Without ultraviolet light.
(b): With ultraviolet light.

arrangement vertically changed very small by the incidence of the ultraviolet light, and it is not cleared that the mechanism of this phenomena. It seems that the strength of irradiated UV light is insufficient to polarize the dust particles. Experiments using the stronger ultraviolet radiation and the more precise observation are necessary in order to clarify the effect of the ultraviolet ray irradiated from the uni-direction.

3.3. Experiment using MgO dust particles

In order to observe clearly the effect of ultraviolet irradiation on the charged dust particles, MgO dust particles were used in the experiment. Work function of MgO is relatively low (W_f = 4 - 5 eV; λ = 249 - 311 nm), it is anticipated that photoemission of MgO particles is more remarkable than the acrylic particles. If non-charged dust particle was irradiated in ultraviolet light, rough estimation of the maximum charge of MgO particle is as follows.

$$h\nu > eW_f + e\frac{Q_{pe}}{4\pi\varepsilon_0 r_d} \tag{2}$$

$$\therefore Q_{pe} < 4\pi\varepsilon_0 r_d\left(\frac{h\nu}{e} - W_f\right) \tag{3}$$

When r_d = 5 μm (10 μm in diameter) and λ = 150 nm, maximum charge by photoemission Q_{pe} = 10000e - 14000e, and it is comparable to the negative charge of the dust particle by plasma current (Q_d = 15000e – 30000e).

Typical image of trapped MgO dust particles in RF plasmas with the non-irradiation condition is shown in Fig.6. In spite of these particles have difference and large dispersion of the diameter, large change of levitating position and structure of dust cloud were not observed. Inter-particle distance of vertical alignment short expands for the increase in the diameter of the fine particle. And when the ultraviolet ray was irradiated, it was not possible to clearly observe the change of the levitating position and structure.

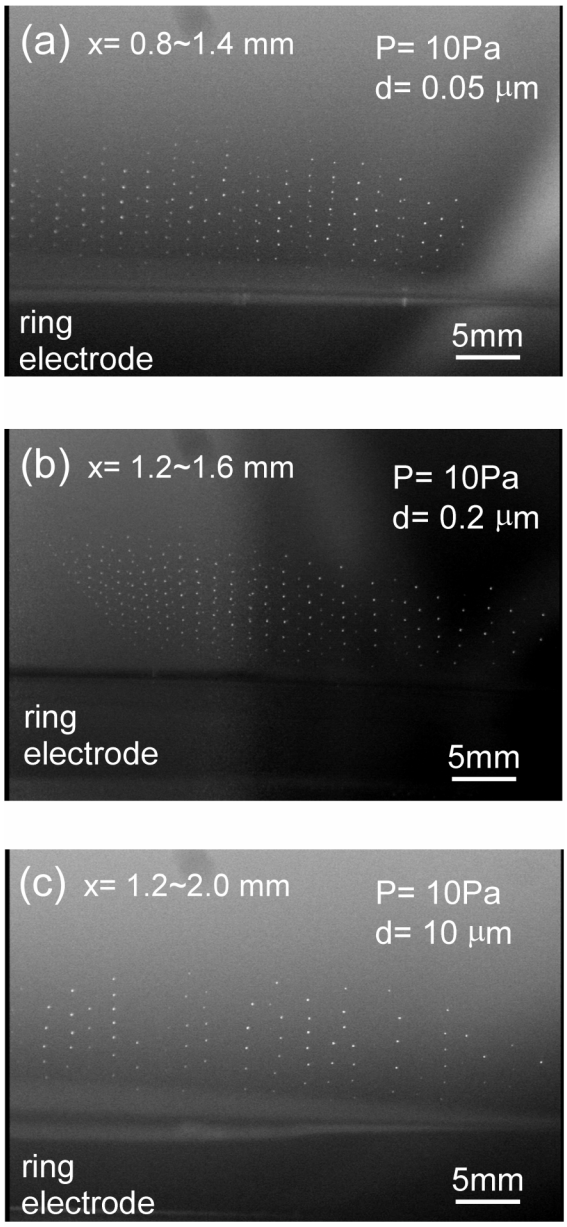

Fig.6 Typical dust cloud using MgO particles. (a): diameter of MgO dust d = 0.05 μm; (b): d = 0.2 μm; (c): d = 10 μm.

References

[1] R. Grard, K. Knott and Pedersen, Space Science Review **34**, (1983) pp. 289-304.

[2] A. V. Ivlev, G. Morfill and V. E. Fortov, Phys. Plasmas **6**, (1999) pp. 1415 – 1420.

[3] I. H. Hutchinson, New Journal of Physics **6**, 2004, p. 43.

[4] S. Takamura, T. Misawa, N. Ohno, S. Nunomura, M. Sawai, K. Asano and P. K. Kaw, Phys. Plasmas **8** (2001), pp. 1886-1892.

VUV-LIF Spectroscopy of Ro-vibrationally Excited HD Molecules Produced in Hydrogen-Deuterium Plasmas

W.M. Soliman[1], O. Gabriel[2], J.J.A v.d.Dungen[2], D.C Schram[2] and R. Engeln[2]

[1] *Department of Laser Sciences and Interactions, National Institute of Enhanced Laser Science, Cairo University, Egypt.*
[2] *Department of Applied Physics, Plasma and Materials Processing, Eindhoven University of Technology, PO Box 513,5600 MB Eindhoven, The Netherlands*

Spectra of H_2/HD/D_2 are recorded by means of VUV-LIF spectroscopy in the range from 63500 cm^{-1} to 79000 cm^{-1}, where we identified transitions from rovibrationally excited HD molecules up to v=12, J=4. To the best of our knowledge, these are the highest excited energy states of HD molecules that have been measured up to now. Since the HD molecules are produced from the mixture of H_2 and D_2, the VUV-LIF spectra of H_2 and D_2 are recorded at the same time with the HD spectrum. The axial and the radial distribution of HD excited molecules will be reported. We will use these data to study the role of surface processes in the formation of HD molecules in discharges of H_2 and D_2.

1. Introduction

Molecular hydrogen and its isotopologues HD and D_2 are of great importance in astronomy. Pure rotational lines of HD molecules have been detected in the infrared in planetary atmospheres and in interstellar clouds with the help of the ISO satellite. Such transitions are also thought to play an important role in the cooling processes in pre-galactic clouds [1-3].

Furthermore, HD molecules play a vital role in experimental plasma fusion reactors. Here, hydrogen molecules are formed close to the surfaces such as the wall, divertor or limiter plates. In hydrogen-deuterium plasmas, the flux of re-emitted particles includes the possible re-emission of HD molecules [4].

We report on densities of rovibrationally excited HD molecules produced in a hydrogen-deuterium plasma expansion by vacuum-ultraviolet laser induced fluorescence (VUV-LIF) spectroscopy. The VUV radiation is produced using the stimulated Anti-Stokes Raman Scattering (SARS) process. VUV generation by SARS covers almost the entire range in the VUV region [5,6].

2. Experimental setup

The measurements were performed in the PLEXIS setup (plasma expansion in interaction with surfaces). As shown in fig. 1, the plasma is created in a high current, sub-atmospheric cascaded arc, with an arc channel of 4 mm diameter The ionization degree of the plasma is 10 % or even much less. The plasma expansion is then almost like a hot gas: while the plasma expands from the source, it accelerates and both the temperature and density decrease (forming a so called zone of silence region). When the jet total pressure approaches the background pressure, the flow goes through the stationary shock, after which the plasma expands sub-sonically [7,8]

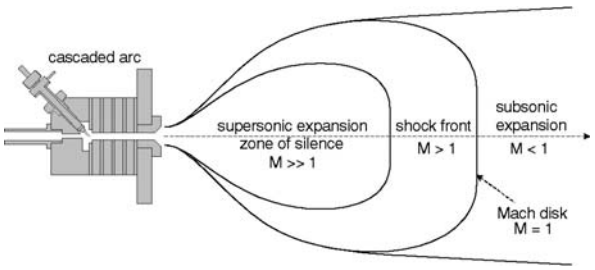

Fig. 1: Schematic diagram of the plasma source and the expansion.

The measurements are performed with flows of H_2 of 1500 sccm and D_2 of 1500 sccm, an arc current of 40 A, and vacuum vessel pressure 100 Pa. The fluorescence generated in the LIF process is detected at 8 mm in front of the nozzle.

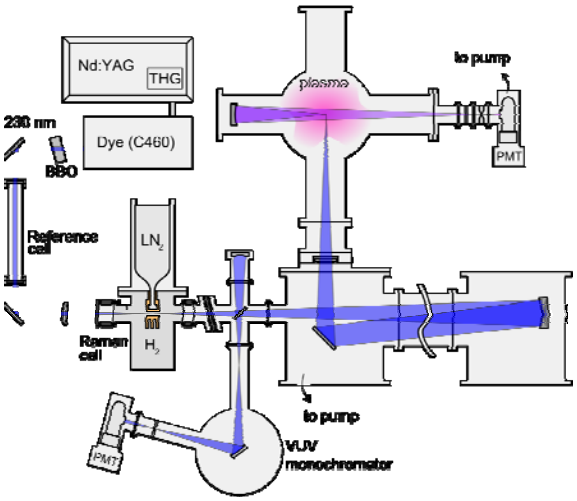

Fig. 2: Schematic diagram of the experimental arrangement

The scheme of the experimental arrangement is shown in fig. 2. After passing a frequency doubling BBO crystal, the second harmonic (SH) laser beam is focused into a Raman cell filled with 2 bar of hydrogen at 77 K. In the cell the SARS process takes place, and up to 10 anti-Stokes (AS) beams are produced while each beam is subsequently shifted in frequency by 4155.19 cm^{-1}. With scanning the SH beams from 42800 to 45700 cm^{-1}, all AS beams are scanned simultaneously covering a large frequency range in the VUV region (63500 cm^{-3} to 79000 cm^{-3}, resp. 157.3 nm to 126.7 nm).

The anti-Stokes beams are focused by a concave mirror and are directed into the vacuum chamber using a flat VUV mirror, where the detection focus in the center of the chamber is around 0.5 mm in diameter. Here, HD molecules are excited by the radiation from ro-vibrational levels in the electronic ground state $X^1\Sigma_g^+$ to levels in the first electronic state $B^1\Sigma_u^+$ (Lyman transitions). This state radiatively decays back to the ground state. The fluorescence generated in this LIF process is detected perpendicular to the laser beam by focusing it into a photomultiplier tube (PMT).

To identify the peaks in the spectra, the wavelength scale has to be known accurately. This is achieved by detecting parts of the remnant dye laser fundamental beam, which is led through a Fabry-Perot etalon. The resulting pattern of fringes is used to linearize the wavelength scale.

3. Results and discussion

The aim of this work is measuring high rovibrational excited states of HD molecules. There are three possible excitation mechanisms that could lead to ro-vibrationally excited HD molecules: 1. radiative pumping, 2. collisions and 3. chemical formation of HD molecules. The radiative pumping involves absorption by Lyman transitions. The excited B-state decays towards rovibrational levels of the ground state, which can decay further via faint electric dipole transitions as calculated by Abgrall et. al. [3,9]. The collisional excitations occur with most abundant species and electrons in the plasma expansion region. Finally, the chemical formation process of HD proceeds as follows[10]:

$$H + D_2 \rightarrow HD + D$$
$$D + H_2 \rightarrow HD + H$$
$$H_2 + D^+ \rightarrow HD + H^+$$

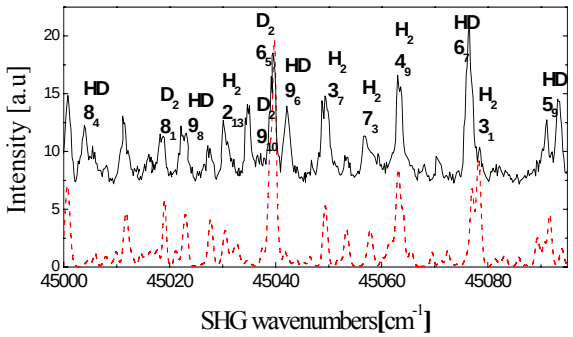

Fig. 3: Part of the LIF spectra of H_2, HD and D_2 : dashed line represents the calculated spectrum and solid line represents the measured spectrum. The lines are identified by the molecule (HD, D_2 or H_2) and the energy state v_J.

Since the HD molecules are produced from the mixture of H_2 and D_2, the VUV-LIF spectra of H_2 and D_2 are recorded at the same time with the HD spectrum. In fig. 3 are presented parts of measured SARS spectra of H_2, HD and D_2. The fluorescence is plotted as a function of the SH wavelength of the dye laser. Line identification is performed by using spectroscopic data from Abgrall et. al. [3]. Fig. 3 shows clearly the matching between measured and calculated spectra, which contain HD lines from v = 2 to v = 9 with different J levels and additionally lines from H_2 and D_2. From our observations, there is a shift in the whole spectra to the visible range for heavier molecules with compatible energy levels. As it turned out that lines from higher excited levels were present in our spectra, table 1 presents the parameters of the identified lines of

HD molecules in the Lyman band from v = 2 to v = 12 with lowest and highest detected rotational levels for each detected vibrational level.

Table 1: The parameters of the identified lines of HD molecules.

v_1	J_1	v_2	J_2	Freq. (cm^{-1})	SH Freq. (cm^{-1})
2	7	0	6	81,700.51	44,303.53
	10	0	9	80,344.65	42,947.67
3	5	1	4	80,309.13	42,912.15
	10	1	9	78,358.00	45,116.24
4	0	0	1	76,952.64	43,710.88
	8	1	7	76,271.77	43,030.01
5	0	0	8	74,013.34	44,926.80
	9	0	8	71,989.52	42,902.98
6	2	2	3	73,442.44	44,355.90
	10	0	9	69,031.59	44,100.27
7	0	0	1	68,646.07	43,714.75
	9	1	8	68,054.70	43,123.38
8	2	0	1	66,044.40	45,268.30
	10	1	9	65,512.44	44,736.34
9	1	0	2	63,978.97	43,202.87
	7	1	8	64,576.55	43,800.45
10	2	2	3	64,159.92	43,383.82
	3	2	2	63,928.16	43,152.06
11	4	1	5	61,120.05	44,499.17
12	4	6	5	64,779.19	44,003.09

The development of the rovibrational distribution of HD molecules in the plasma expansion is shown in fig 4. The axial distribution of HD at v = 5 and J up to 5 is measured at distances 20 mm, 50 mm and 100 from the nozzle along the axis of the plasma expansion.

The axial distribution can almost be described by a Boltzmann distribution, corresponding to a rotational temperature of around T_{rot} = 400K. By comparing the population density measurements of HD molecules with the population density of H_2 molecules, which have been performed in the past (see fig. 5), it is found that the populations of HD molecules decay faster with z than that of H_2. This indicates a different relaxation mechanism for HD compared to those for H_2. As known form astrophysics, HD has a better cooling efficiency than H_2 because its permanent dipole moment. Another factor are the smaller rotational level spacings in HD [11].

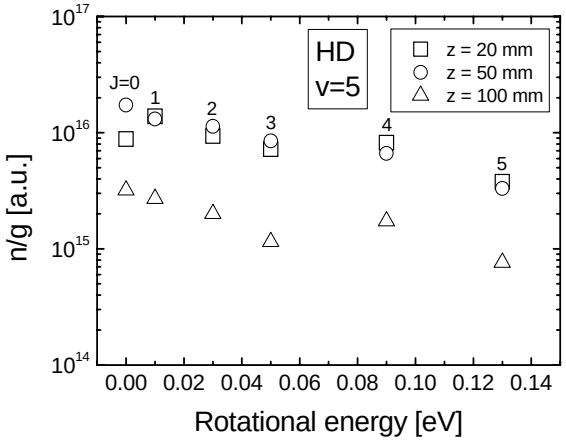

Fig. 4: The axial distribution of HD molecules for v = 5 and J from 0 to 5.

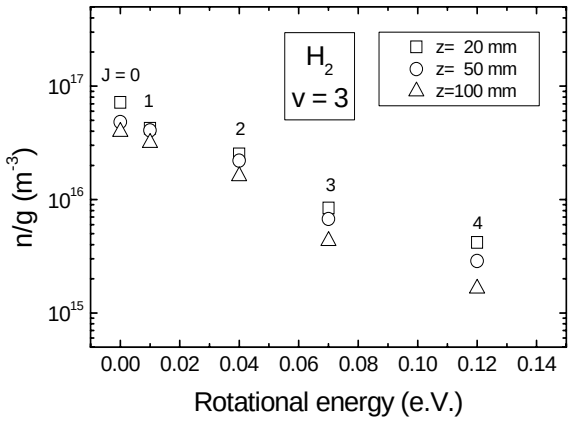

Fig. 5: The axial distribution of H_2 molecules for v = 5 and J from 0 to 5 (taken from [7]).

4. Conclusion

LIF spectra of H_2, HD and D_2 molecules are recorded through the Lyman emission after VUV excitation from the electronic ground state $X^1\Sigma_g^+$ to the first electronic state $B^1\Sigma_u^+$. The measured LIF spectra include the spectra of H_2, HD and D_2 with a good agreement with calculated data. The vibrational states from v = 2 to v = 12 with different rotational states are detected. The axial distribution of HD molecules corresponds to a Boltzmann distribution, in contrast to what we have recorded previously for H_2 molecules. The decay behaviour of HD molecules is faster than

that of H_2 molecules due to the higher radiative transition probabilities of HD molecules. The results reported here will be used to investigate the role of surfaces in the formation of HD molecules.

Acknowledgment

One of the authors, W.M.S., would like to acknowledge the financial support from the PMP-group of Eindhoven University of Technology (TU/e) during her stay in the Netherlands. This work has been performed in the PMP-group, Department of Applied Physics, Eindhoven University of Technology.

References:

[1] E. Roueff and C.J. Zeippen, Astron. Astrophys. **343**, (1999), 1005-1008.
[2] D. A. Varshalovich, A.V. Ivanchik, P.Petitjean, R.Srianand, and C.Ledoux, Astron. Lett. **27, No.11**, (2001), 683-685.
[3] H. Abgrall and E. Roueff A&A **445**, (2006), 361-372.
[4] S. Brezinsek, P.T. Greenland, Ph. Mertenes, A. Pospieszczyk, U. Samm, B. Schweer and G.Sergienko, Physica Scripta.**T103**, (2003), 63-67.
[5] H.F Döbele, Plasma Sources Sci. Tech. **4**, (1995), 224.
[6] P. Vankan, S.B.S. Heil, S.Mazouffre, R. Engeln, D.C. Schram and H.F. Dobele, Rev. Sci. Instrum. **75**, (2004), 996.
[7] P. Vankan, Ph.D. thesis, TU/e (2005).
[8] S. Mazouffre, P. Vankan, W.M.M. Kessels, R. Engeln, M.C.M. van de Sanden and D.C. Schram, IEEE Trans. Plasma Sci. **30, No. 1**, (2002), 146.
[9] H. Abgrall, E. Roueff, and Y. Viala, Astron. Astrophys. Suppl. Ser. **50**, (1982), 505-522
[10] F.Le Petit, E. Roueff, and J. Le Berlet, A&A **390**, (2002), 396-381
[11] V. Bromm and R.B. Larson, Annu. Rev. Astron. Astrophys., **42** (2004) 79

Estimations of electron temperature and electron density in plasmas based on diode laser absorption spectroscopy

R. Asaoka[1], N. Nafarizal[1], and K. Sasaki[2]

[1]*Department of Electrical Engineering and Computer Science, Nagoya University, Furo-cho, Chikusa-ku, Nagoya 464-8603, Japan*
[2]*Plasma Nanotechnology Research Center, Nagoya University, Furo-cho, Chikusa-ku, Nagoya 464-8603, Japan*

We propose a method for estimating electron temperature and electron density in plasmas. This method is based on the density measurements and the population-kinetics modeling of argon metastable states. Diode laser absorption spectroscopy is employed for measuring the metastable densities. We believe that this method is applicable to *in-situ* monitoring of plasma processing tools in factories because of the low cost, the small footprint, and the maintenance-free operation of a diode laser. We demonstrated this method in a magnetron sputtering plasma and an inductively-coupled N_2/Ar mixture plasma.

1. Introduction

Recently, a metrological method which is suitable for monitoring plasma processing tools in factories is significantly required from the industrial point of view. This is because the production cost of devices is mainly determined by the rate of fine operations of plasma processing tools in factories. Although many methods for precise plasma diagnostics have been developed for the last decade, almost all the methods are designed for laboratory experiments, and are not applicable to industrial plasma monitoring because of the complexity, the high cost, and the big footprint. An industrial plasma monitoring tool should be cheap, robust, and small. In addition, a non-contact method with negligible disturbance to processing plasmas is preferable.

In this work, we propose a method for estimating electron temperature and the electron density in plasmas based on diode laser absorption spectroscopy. Diode lasers have merits in the low cost, the small footprint, and the maintenance-free operation. Because of the merits of diode lasers, we believe that the proposed method can be used as a minitoring technique for plasma processing tools in factories.

2. Principle

The proposed method works in argon plasmas or argon-containing processing plasmas. Since argon is inert, the admixture of a small amount of argon into process gas for the diagnostic purpose is arrowed in practical plasma processing.

Argon has two metastable states, $4s[3/2]^o_2$ and $4s'[1/2]^o_0$. The priciple of this method is the comparison of the metastable densities measured experimentally with those calculated by a model for their population kinetics. In low-temperature processing plasmas, the dominant production process of the argon metastable states is electron impact excitation from the ground state. On the other hand, the loss of the metastable states is composed of electron impact quenching, electron impact ionization, quenching by collison with argon, quenching by collision with process gas, and diffusion. Based on the above assumption on the production and loss processes, the densities of the metastable states are determined by the following rate equations,

$$\frac{\mathrm{d}n(4s[3/2]^o_2)}{\mathrm{d}t} = k_{ex}(4s[3/2]^o_2)n_{Ar}n_e - k^e_{dex}(4s[3/2]^o_2)n(4s[3/2]^o_2)n_e - k_i(4s[3/2]^o_2)n(4s[3/2]^o_2)n_e - k^{Ar}_{dex}(4s[3/2]^o_2)n(4s[3/2]^o_2)n_{Ar} - k^g_{dex}(4s[3/2]^o_2)n(4s[3/2]^o_2)n_g - \frac{n(4s[3/2]^o_2)}{\tau_D} = 0, \quad (1)$$

$$\frac{\mathrm{d}n(4s'[1/2]^o_0)}{\mathrm{d}t} = k_{ex}(4s'[1/2]^o_0)n_{Ar}n_e - k^e_{dex}(4s'[1/2]^o_0)n(4s'[1/2]^o_0)n_e - k_i(4s'[1/2]^o_0)n(4s'[1/2]^o_0)n_e - k^{Ar}_{dex}(4s'[1/2]^o_0)n(4s'[1/2]^o_0)n_{Ar} - k^g_{dex}(4s'[1/2]^o_0)n(4s'[1/2]^o_0)n_g - \frac{n(4s'[1/2]^o_0)}{\tau_D} = 0, \quad (2)$$

where $n(4s[3/2]^o_2)$, $n(4s'[1/2]^o_0)$, and n_{Ar} stand for the densities of the $4s[3/2]^o_2$, $4s'[1/2]^o_0$, and ground states of argon, respectively, and n_e and n_g are the densities of electron and process gas, respectively. The rate coefficients for electron impact excitation, electron impact quenching, electron impact

Table I: Quenching rate coefficients of argon metastable states [1-4].

Quencher	$4s[3/2]^o_2$ (cm^3/s)	$4s'[1/2]^o_0$ (cm^3/s)
electron	2×10^{-7}	3.5×10^{-8}
Ar	3×10^{-15}	5.3×10^{-15}
H_2	6.6×10^{-11}	7.8×10^{-11}
N_2	3.6×10^{-11}	1.6×10^{-11}
O_2	2.1×10^{-10}	2.4×10^{-10}
SF_6	1.6×10^{-10}	1.7×10^{-10}
CF_4	4×10^{-11}	4×10^{-11}
CH_4	3.3×10^{-10}	5.5×10^{-10}

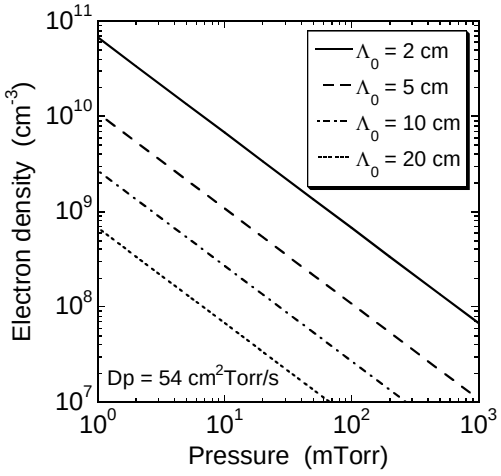

Fig. 1: Curves showing the relationship $1/\tau_D = k_{dex}^{e}(4s[3/2]^o_2)n_e$ for various diffusion lengths.

ionization quenching by collison with argon, and quenching by collision with process gas are denoted by $k_{ex}(i)$, $k_{dex}^{e}(i)$, $k_i(i)$, $k_{dex}^{Ar}(i)$, and $k_{dex}^{g}(i)$, respectively, with i representing the metastable state. The diffusion time constant is denoted by τ_D.

The rate coefficients $k_{dex}^{e}(i)$, $k_{dex}^{Ar}(i)$, and $k_{dex}^{g}(i)$ (for various process gases) are listed in Table I by referring to literature [1-4]. The values of n_{Ar} and n_g are roughly known from the partial pressures of argon and process gas, respectively, before igniting the discharge. The rate coefficients $k_{ex}(i)$ and $k_i(i)$ are calculated by using the cross section data in literature for electron impact excitation [5-7] and ionization [8,9], respectively, when we assume a Maxwellian electron energy distribution function corresponding to an electron temperature T_e. Accordingly, eqs. (1) and (2) are coupled equations with unknown values T_e and n_e. Therefore, we can basically obtain T_e and n_e by solving eqs. (1) and (2), with the values of $n(4s[3/2]^o_2)$ and $n(4s'[1/2]^o_0)$ measured by diode laser absorption spectroscopy.

Figure 1 shows the relationship $1/\tau_D = k_{dex}^{e}(4s[3/2]^o_2)n_e$, where τ_D is calculated by

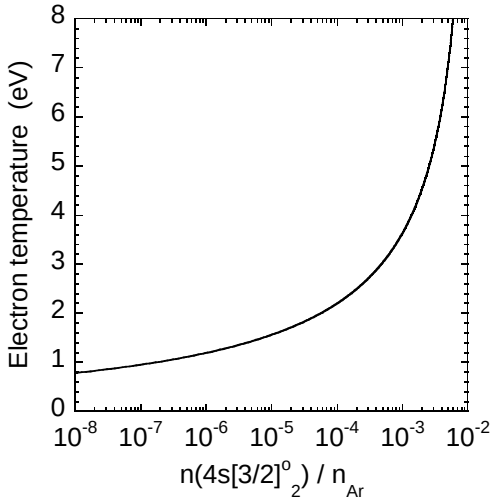

Fig. 2: Relationship between T_e and $n(4s[3/2]^o_2)/n_{Ar}$ in the case of pure argon plasma.

$\tau_D=\Lambda_0^2/D$ with Λ_0 and D being the diffusion length and the diffusion coeffieicnt, respectively. In calculating Fig. 1, we used D=54 cm^2/s at 1 Torr [10]. It is known from Fig. 1 that $k_{dex}^{e}(i)n_e >> 1/\tau_D$ is satisfied in plasma sources used for material processing. In the following, we neglect diffusion in the loss processes of the metastable states.

3. Evaluation of electron temperature in pure argon plasmas

A simple case is pure argon plasma with $n_g=0$. As shown in Table I, $k_{dex}^{e}(4s[3/2]^o_2)$ is eight orders of magnitude greater than $k_{dex}^{Ar}(4s[3/2]^o_2)$. Therefore, if the degree of ionization of the plasma is greater than 10^{-7}, $k_{dex}^{e}(4s[3/2]^o_2)n_e >> k_{dex}^{Ar}(4s[3/2]^o_2)n_{Ar}$ is satisfied. Accordingly, in usual pure argon plasmas, quenching of the $4s[3/2]^o_2$ state by collision with argon is negligible in comparison with that by electron impact. In this case, $n(4s[3/2]^o_2)$ is independent of the electron density and is given by

$$n(4s[3/2]^o_2) = \frac{k_{ex}(4s[3/2]^o_2)}{k_{dex}^{e}(4s[3/2]^o_2) + k_i(4s[3/2]^o_2)} n_{Ar}. \quad (3)$$

Figure 2 shows the relationship between T_e and $n(4s[3/2]^o_2)/n_{Ar}$ calculated by Eq. (3). We can estimate T_e from the measurement of $n(4s[3/2]^o_2)$ and the relationship shown in Fig. 2.

The estimation of T_e was demonstrated in a magnetron sputtering plasma source employing a Ti target, argon gas, and a dc power supply. A diode laser beam was launched into the plasma from a radial observation port, and $n(4s[3/2]^o_2)$ was evaluated from the absorption strength. The distance between the target surface and the laser

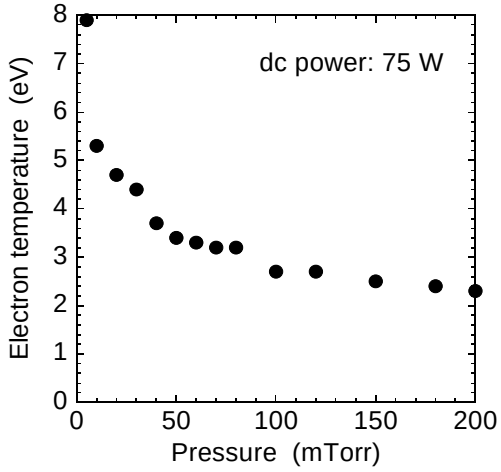

Fig. 3: Electron temperature of magnetron sputtering plasmas evaluated by the proposed method.

beam was 3 cm. The value of $n(4s[3/2]^o_2)$ thus evaluated was line-averaged one along the path of the laser beam. Figure 3 shows T_e evaluated from $n(4s[3/2]^o_2)$ as a function of the gas pressure. The dc discharge power was 75 W. The decrease in T_e with the gas pressure is fairly realistic as the pressure dependence in a dc discharge.

4. Evaluation of electron temperature and electron density in argon-containing processing plasmas

In argon-containing processing plasmas, quenching by collision with argon is negligible in comparison with that by collision with process gas since $k_{dex}^{g}(i) >> k_{dex}^{e}(i)$ as shown in Table I. In relation to the proposed method, processing plasmas are divided into two cases. The first one is the high-density case such that $k_{dex}^{e}(i)n_e >> k_{dex}^{g}(i)n_g$. This case is equivarent to the case of the pure argon plasma, and only T_e can be evaluated from the the measurement of $n(4s[3/2]^o_2)$. The second one is the low density case. In this case, $n(4s[3/2]^o_2)$ and $n(4s'[1/2]^o_0)$ are dependent on both T_e and n_e since $k_{dex}^{g}(i)n_g$ and $k_{dex}^{e}(i)n_e$ are comparable. Both T_e and n_e can be evaluated by solving the coupled equations (1) and (2) with the measurements of $n(4s[3/2]^o_2)$ and $n(4s'[1/2]^o_0)$.

Figure 4 shows an example of solving the coupled equations (1) and (2). In this calculation, an Ar/N_2 mixture plasma with the partial pressures of Ar and N_2 being 20 and 2 mTorr, respectively, is assumed. The densities of the metastable states are assumed to be $n(4s[3/2]^o_2)=7.5\times10^9$ cm^{-3} and $n(4s'[1/2]^o_0)= 5.3\times10^9$ cm^{-3}. The two curves in Fig. 4 show the relationships between T_e and n_e given by eqs. (1) and (2) with assumed $n(4s[3/2]^o_2)$ and

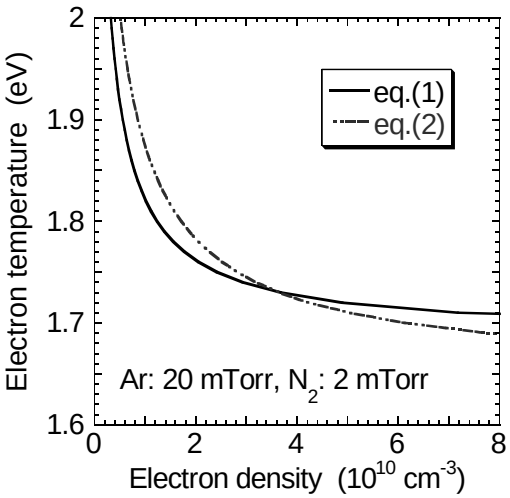

Fig. 4: Two curves corresponding to the coupled equations (1) and (2) with $n(4s[3/2]^o_2)=7.5\times10^9$ cm^{-3} and $n(4s'[1/2]^o_0)= 5.3\times10^9$ cm^{-3}. The solution is obtained as the cross point of the two curves.

$n(4s'[1/2]^o_0)$. As shown in Fig. 4, the cross point between the two curves is well-identified, and T_e and n_e are evaluated to be 1.73 eV and 3.5×10^{10} cm^{-3}, respectively.

Whether the cross point of the two curves is well-identified or not is dependent on plasma parameters. For a set of plasma parameters, the two curves become almost the same near the cross point. In this case, the solutions of eqs. (1) and (2) become ambiguous. We examined the two curves for many sets of plasma parameters, and evaluated the conditions in which the cross points of the coupled equations are well-identified. Figure 5 is a map showing the conditions where the cross point of the

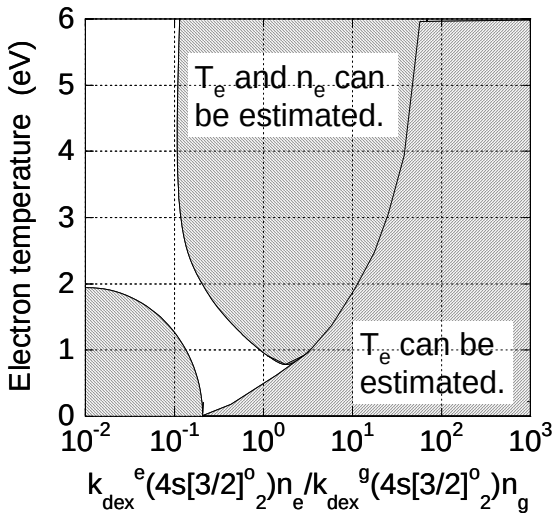

Fig. 5: Map of plasma parameters where the proposed method is applicable.

two curves is well-identified. The horizontal axis of this figure is the ratio of the electron impact quenching frequency to the quenching frequency by collision with process gas. By referring to Table I and Fig. 5, it is known that the estimation of both T_e and n_e is possible for processing plasmas with usual pressures, electron temperatures, and electron densities. As has been described, the estimation of only T_e is possible in high-density plasmas ($k_{dex}^{e}(i)n_e >> k_{dex}^{g}(i)n_g$).

The estimation of both T_e and n_e is demonstrated in inductively-coupled Ar/N_2 mixture plasmas. In this experiment, the partial pressure of N_2 was fixed at 2 mTorr and the partial pressure of argon was varied from 10 to 50 mTorr. The rf power was 300 W. Figure 6 shows T_e and n_e evaluated by the proposed method, together with those measured using a Langmuir probe. As shown in Fig. 6(b), the electron density evaluated by the proposed method roughly agreed with that measured using a Langmuir probe. On the other hand, it was found that the electron temperature evaluated by the proposed method is slightly lower than that measured using a Langmuir probe. The reason for the discrepancy has not been understood yet. A possible explanation may be the inaccuracy in the cross section and rate coefficient data. Another possibility is the change in n_{Ar} from the value evaluated from the partial pressure of argon before igniting the discharge. There is a possibility that n_{Ar} in the discharge is lower than that before the ignition because of the increase in the gas temperature. Except for the slight difference in T_e, it has been shown that both T_e and n_e can roughly be evaluated by the proposed method.

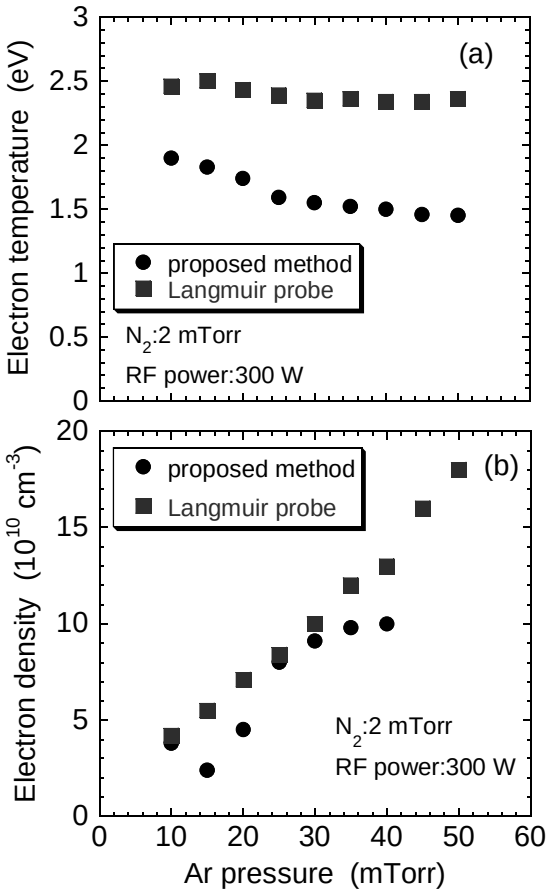

Fig. 6: (a) Electron temperature and (b) electron density obtained using the proposed method and a Langmuir probe. The experiment was carried out in inductively-coupled Ar/N_2 mixture plasmas.

5. Summary

We have proposed a method for estimating electron temperature and electron density in plasmas. This method utilizes diode laser absorption spectroscopy, and is non-contact to the plasma. We have shown the rough agreement between the proposed method and a Langmuir probe measurement for evaluating T_e and n_e in inductively-coupled Ar/N_2 mixture plasmas. Since diode lasers are compact, cheap, and easy to use, the proposed method can be used as a plasma monitoring tool in factories.

References

[1] M. W. Kiehlbauch and D. Graves, J. Appl. Phys. 91, 3539 (2002).

[2] L. G. Piper, J. E. Velazco, and D. W. Setser, J. Chem. Phys. 59, 3323 (1973).

[3] J. H. Kolts and D. W. Setser, J. Chem. Phys. 68, 4848 (1978).

[4] C. M. Ferreira, J. Loureiro, and A. Ricard, J. Appl. Phys. 57, 82 (1984).

[5] S. Tsurubuchi, T. Miyazaki and K. Motohashi, J. Phys. B: At. Mol. Opt. Phys. 29., 1785 (1996).

[6] A. Dasgupta, M. Blaha, and J. L. Giuliani, Phys. Rev. A 61, 012703 (1999).

[7] C.M.Ferreira, J.Loureiro and A.Ricard, J. Appl. Phys. 57. 1. 82-90, Jan. 1985

[8] H. Deutsch, K. Becker, A. N. Grum-Grzhimailo, K. Bartschat, H. Summers, M. Probst, S. Matt-Leubner, and T. D. Mark, Int. J. Mass Spec. 233, 39 (2004).

[9] H. Deutsch, K. Becker, S. Matt-Leubner, and T. D. Mark, J. Phys. B: At. Mol. Opt. Phys. 32, 4249 (1999).

[10] A. V. Phelps and J. P. Molnar, Phys. Rev. 89, 1202 (1953).

Generation of energetic neutral lithium by Laser-Blow-Off technique

Ajai Kumar, R. K. Singh and V. Prahlad

Institute for Plasma Research, Bhat Ghandhinagar-382428, INDIA

Interaction of laser with metal film-glass interface generates short bursts of high intensity atomic beam with energy 1-10 eV. A super-thermal atomic beam generated by laser-blow-off (LBO) technique is extensively used to measure the parameters of high temperature tokamak plasma. We have characterized the Li plasma generated by laser blow off of a multilayer LIF-C film using fast optical emission spectroscopy. The temporal evolution of the spectra lines Li II (at 478.8 nm, $3p^1P_1 \leftarrow 4d^1D_2$) and Li II (548.4 nm, $3p^1S_1 \leftarrow 4d^3P_{2,1,0}$) were studied for distances 4-12 mm away from the target. It was found that emission intensity from the upper state is greater than those from the lower state. Under the assumption of local thermodynamic equilibrium (LTE), the intensities of these two ionic lines were used to estimate the electron temperature. Our result shows that the electron temperature is always grater than 8 eV. No significant reduction in temperature was observed with an increase in distance from target. Using the above technique, we explore the possibility for production of energetic lithium beam (> 100 eV) for potential application as a beam diagnostic for tokamak plasmas.

1. Introduction

Diagnostic of edge plasma parameters are important as they play key role to determine the global plasma confinement. Understanding and controlling the edge plasmas parameters are important for the divertor design in fusion reactors. A lithium beam probe is proved to be the best technique for the measurement of the edge plasma density profile. This method is utilizing the emission of Li I resonance line ($^2S_{1/2}$ – $^2P^0_{1/2}$ transition) from the injected neutral lithium atom by electron impact excitation [1,2].

The injection of atomic lithium beam, generated by Laser-blow-off (LBO) technique, has been used to determine the electron density profiles from SOL and edge plasma region. The velocity of the injected atoms and the equilibration time constant of the involved atomic processes determine the spatial resolution of this diagnostics. Presently we have Li probe beams in the energy range thermal to super-thermal (1-10 eV), or in few KeV range. Therefore the gap is exist in the intermediate energy range. There is need to have these probe beam in the intermediate energy range to determine the electron density profile in SOL, edge and some part of the core plasma with the spatial resolution in the direction of propagation ~2-2.5 mm. This energy range combines both the advantages, namely, the higher spatial resolution of super-thermal beam and the longer penetration depth of the KeV range.

In view of above, we explored the possibility of generation of a Li beam in the energy range 100 – 500 eV. We were motivated by the observation of fast neutrals in our laboratory experiments of interaction of laser radiation with metallic films. We therefore undertook the study of evolution features of the ionic and neutral species produced by Laser-blow-off LiF thin film. In this report, a direct comparison between the conventional solid ablation (LPP) and laser blow off (BBO) of thin film are presented. The objective of the present experiment was to produce high quality ionic and neutral beams for a potential application as a tokamak plasma diagnostic.

2. Experimental setup

A detailed description of the experimental setup was reported previously [3,4]. Only the main features are summarized here.

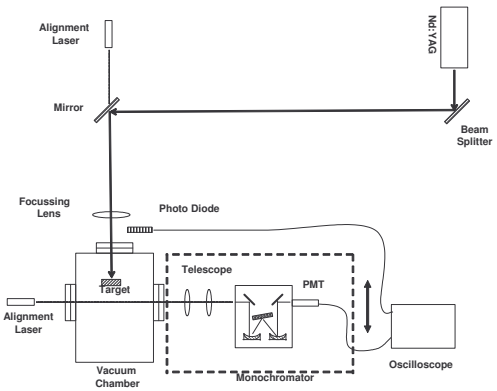

Figure 1: schematic of the experimental set up.

The plasma plume was generated inside a stainless steel chamber, which was evacuated to a base pressure better than $5x10^{-6}$ mbar. In LBO

experiment, the target was composed of uniform layers of 0.5 μm thick carbon film and 0.05 μm of LiF film on a thick quartz substrate. A Nd:YAG laser (λ = 1.064 μm) having a pulse width of 8 ns was used to generate the plasma plume. The plasma plume was viewed normal to the direction of expansion and was imaged onto the entrance slit of a monochromator (Δλ= 12.5 Å). The imaging system and monochromator were mounted on a single-stage translator system, which enabled space-resolved scan of the plume along its expansion axis. We used the photo multiplier tube (BURLE C31034), having a flat spectral response for the wave length range 470 – 680 nm. The output of the PMT was directly fed to a 1 GHz digital oscilloscope. The time resolution in the present experiment was about 4 ns. A small fraction of light reflected from the laser focusing lens was detected by a photodiode and was used as time- reference.

For the LPP experiment, thin film target was replaced by the 12 mm diameter solid lithium rod. Rest of the set up was same as described above.

3. Results and discussion

We have observed the emission spectra of the laser produced lithium plasma generated by two different schemes; conventional laser ablation of solid lithium (LPP) and laser-blow-off of thin film (LBO). Temporal evolution for the spectral lines Li II (at 478.8 nm, $3p^1P_1 \leftarrow 4d^1D_2$) and Li II (548.4 nm, $3p^1S_1 \leftarrow 4d^3P_{2,1,0}$) are as shown in figure 2. The profiles were recorded in vacuum and at z = 6 mm form the target. Figure 2 clearly indicates that velocity of the lithium ions generated by the LBO scheme is higher than those of ions produced by LPP. The peak velocity of ions produced by LBO and LPP are 9.4×10^6 and 3.5×10^6 cm/sec respectively for laser fluence 40 J/cm^2. Also, the LBO profile was more confined than LPP profile. These observations prove that LBO scheme is better suited for the production of energetic ionic beam with minimum energy spread.

Another remarkable difference was observed in the relative intensities of these two ionic lines. In LBO, the relative intensity for transitions from the upper state (for 478.8 nm) is greater than the transitions from lower state (for 548.4 nm). A different scenario was observed in the case of LPP, where the intensity of the

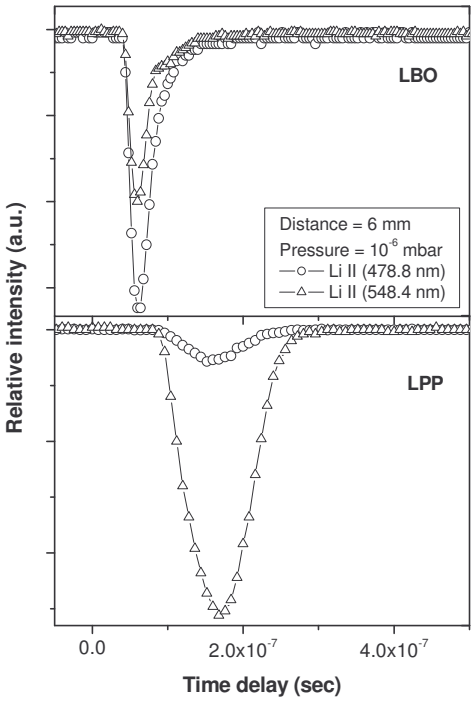

Figure 2: Temporal profile of Li II at 478.8 and 548.4 nm observed by LBO and LPP scheme. The profiles were recorded in vacuum and at z = 6mm.

spectral line 548.4 nm, dominated over that of 478.8 nm lines. We expected that electron temperature play an important role for the reversal in the intensity of these two ionic lines observed with two schemes.

To support the above argument, we have estimated the electron temperature by the method given in the literature [5]. The relative efficiency of the grating and the spectral response of the detector are independent in the considered wave length range. Also, there are no self absorption for these spectral lines, as their transitions do not terminate to the ground state. Therefore the electron temperature estimated by using the ratio of these two ionic lines as follows-

$$\frac{I^1}{I^2} = \frac{g_k^1 A_{ki}^1 \lambda_{ki}^2}{g_k^2 A_{ki}^2 \lambda_{ki}^1} \exp\left(\frac{E^2 - E^1}{kT}\right)$$

where, A_{ki} is the transition probability, g_k is the statistical weight of the upper level, E is the energy of the upper level of the transition. All the required atomic data were taken from the NIST's Atomic Spectra Database [6]. The intensity of the spectral line was obtained by integrating the area under the temporal profile. The estimated

electron temperature was ~8 eV and ~2 eV respectively for the LBO and LPP generated plasma. Based on the above estimates, we could say that a portion of LBO plume was super heated by the incident laser beam produced an electron temperature four times higher than that of conventional laser plasma under the same experimental conditions. Also, this interpretation explains why the LBO generated ionic species are found to be more energetic than that of ions generated by conventional solid ablation.

We did not find any significant reduction in electron temperature with the distance form the target for LBO generated plume. The electron temperature almost remained constant (within the 10% of the statistical error) for the distance z = 4mm to 12 mm. This observation is in contradiction with the several results reported in the past for the solid ablation, where a decrease of electron temperature was observed with distance.

The time distribution for the arrival of the neutral species produced by LBO as well as LPP scheme are shown in figure 3. In conventional solid ablation, neutral profile was appeared as a single peak structure. In contrast to the LPP result, a double peak structure, designated as 'fast neutral' and 'slow neutral' was observed in LBO scheme. The kinetic energy of the fast and slow neutrals at z = 6 mm are 318 eV and 6 eV respectively. This observation clearly demonstrates that the LBO plume consists of two species having different temperatures. A portion of target film is superheated by the laser beam and produces the energetic ions. These energetic ions form the leading edge of the plasma. On the other hand, majority of the materials propels from the substrate in the form of neutral vapor, moving with much low velocity as compared to its faster counterpart.

As we earlier stated that leading edge of the plasma plume contains mostly of energetic ions, therefore a question arises about what is the source of fast neutral. For better understanding of the production mechanism of the neutral, we overlapped the ionic and neutral profile as shown in inset of figure 2a. As seen from the figure, the peak velocities of the fast neutrals are exactly coincide with the velocity of ions. This implies that fast neutrals are formed by a neutralization of energetic ions. Neutralization of ions occur

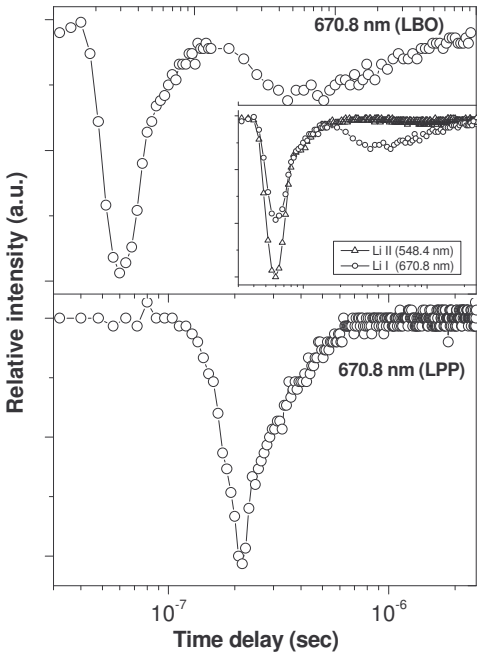

Figure 3: Arrival time distributions of Li I at 670.8 nm produced by LBO and LPP. Inset of the figure shows the temporal profiles of Li I and Li II formed by LBO.

either by recombination or charge exchange processes. Due to the high electron temperature, the recombination process is safely ruled out in the present experiment. Therefore we proposed the charge exchange between the fast ions and slow neutrals is the causative mechanism for the formation of fast neutrals.

Further, it was observed that the relative intensity as well as the translational velocity of the ionic species was increase with laser fluence. Since the energetic neutrals are formed by the neutralization of energetic ions. Consequently the number density and kinetic energy of the fast neutral could be controlled by adjusting the laser fluence.

The formation of fast neutrals by the charge exchange process is the important finding of the present experiment. This may be used to enhance the energetic neutrals beam for plasma diagnostic. We plan to conduct an experiment for this purpose. In the proposed experiment, thermal neutral beam interact with LBO plume in a cross-beam geometry. Naturally, we expect that charge exchange between the energetic ions and thermal atoms should increase production of the energetic neutrals.

Conclusion

We have demonstrated that the LBO technique can be used for the production energetic ionic and neutral beams (> 100 eV) .

References

1. A. Hubber, U. Samm, B. Schweer and Ph. Mertens, *Plasma Phys. Controlled Fusion* **47**, 409 (2005)
2. K. Nakamura et al, *Rev. Sci. Instr*. **76**, o13504 (2005)
3. Ajai Kumar, R.K. Singh, K.P. Subramanian, B.G. Patel, S. Sunil and I.A. Prajapati, J. Phys. D: Appl. Phys. **39**, 4860 (2006).
4. R.K. Singh, Ajai Kumar and K.P. Subramanian, *J. Appl. Phys*.**101**, 103301 (2007).
5. H. Griem, *Plasma Spectroscopy* (New York: McGraw-Hill, 1964)
6. NIST database, http:// physics.nist.gov/PhysRefData/

Determining absolute oxygen densities by TALIF in (the effluent of) a micro atmospheric pressure plasma jet

V. Schulz-von der Gathen, N. Knake, K. Niemi, St. Reuter, J. Winter

Center for Plasma Science and Technology, Ruhr-University Bochum, 44780 Bochum, Germany

A micro atmospheric pressure plasma jet (μ-APPJ) has been designed providing excellent access for optical diagnostics and a simple geometry ideally suited for modeling and simulation. The plasma jet is a homogeneous non-equilibrium discharge at ambient pressure. It operates with a noble base gas and a volume-percentage admixture of a molecular gas. Laser spectroscopy and optical emission spectroscopy can be applied in the discharge volume and the effluent region. Applications of the discharge are mainly based on reactive species in the effluent. The effluent region of the discharge operated in helium with an oxygen admixture has been investigated. Highly reactive ground state atomic oxygen as measured by absolutely calibrated two-photon laser induced fluorescence spectroscopy (TALIF) is observed up to several centimeters away from the nozzle in the effluent. Detailed understanding of the underlying transport mechanisms requires investigations of both the discharge volume and the effluent region.

1. Introduction

There is rapidly growing interest in non-thermal atmospheric pressure plasmas, especially diffuse homogeneous glow discharges [1,2]. These non-equilibrium discharges have drawn considerable attention due to their enormous potential for technological applications. High concentrations of radicals, suitable for many applications preferably in surface modifications, can be provided without the requirement of complicated and expensive vacuum systems. The absence of streamer-like micro-discharges and a low gas temperature allow application to sensitive surfaces. Many of these discharges operate in a mixture of a noble gas, preferably helium, and a small molecular component - depending on the application envisaged.

The discharge concept adopted here is the Atmospheric Pressure Plasma Jet (APPJ) introduced by Selwyn, Hicks and co-workers [3] in 1998. This technically relatively simple capacitively coupled device (figure 1) is typically operated at 13.56 MHz excitation frequency and an electrode spacing of about 1 mm. The length and width dimensions are a few centimetres. The gas mixture is flushed through the discharge area at a high flow rate in the order of m^3h^{-1}. The effluent can easily be applied for treatments of various substrates as demonstrated by Selwyn and co-workers: deposition and removal of silicon oxide layers, removal of tungsten layers, and cleaning of surfaces from biological contamination [4-6].

At low powers the discharge is characterised as a typical α-mode discharge, while at higher powers it turns into γ-mode [7,8]. The discharge then becomes inhomogeneous showing bright constricted discharge columns. It has recently been demonstrated that the homogeneous operation is also possible with argon as a base gas [9]. In this case the power operation range is significantly narrower than with helium. The discharge ignites at higher power with hotter effluent and switches earlier into the inhomogeneous γ-mode. The distinction between both modes is not precise in literature.

Parameters determining the onset of the transition into the inhomogeneous mode are manifold. Apart from the rf power and frequency the electrode spacing, the gas flow, and the admixture of the molecular component influence the mode transition. A typical limit of the molecular admixture is of the order of 1%.

The experiments mentioned above revealed that in order to understand the complex energy transport mechanisms in the APPJ, the connection between the effluent and the discharge region is crucial. Investigations of the discharge dynamics and transport processes within the discharge volume are, therefore, essential. The plasma chemistry inside the discharge volume determining the effluent is strongly influenced by the dynamics of the plasma boundary sheaths and corresponding surface processes.

In the following measurements of excited species and ground state atomic oxygen in the effluent region are presented. Atomic oxygen is regarded as the key constituent for surface

modification processes due to its high reactivity.

In particular, absolutely calibrated measurements of atomic oxygen using two-photon absorption laser induced fluorescence (TALIF) under atmospheric pressure conditions are discussed. The design of a new micro-APPJ (µ-APPJ) allows excellent optical access to the discharge volume as well as to the transition region and the effluent.

2. Microplasma jet

The standard APPJ consists of a collinear electrode configuration geometry that does not allow direct optical access to the discharge core volume. Our specifically modified version of the APPJ with reduced discharge volume (µ-APPJ) provides excellent access for optical techniques. Figure 1 shows a photograph of the µ-APPJ and a sketch of an optical diagnostics inside the discharge volume. Even diagnostics requiring a large observation angle, such as various laser diagnostics, can be applied to the µ-APPJ.

This allows detailed investigations of the discharge mechanisms in the core region as well as energy and particle transport mechanisms to the effluent region. The µ-APPJ consists of 1 x 10 x 30 mm^3 housing made out of 1 mm thick glass or quartz windows. One end of the 30 mm long housing merges into a tube for feed gas supply. Two laser-cut stainless steel electrode blades with rounded edges are positioned inside the housing resulting in a rectangular discharge volume of about 1 x 1 x 25 mm^3 between the electrodes and the glass windows.

3. TALIF

The effluent leaving the jet is primarily composed of helium, atomic and molecular oxygen and ozone. Excited oxygen atoms can be observed in this effluent up to a distance of 10 cm from the nozzle. This distance is by far to large to be explained by the gas velocities of about 30 m/s and the lifetime of excited atomic oxygen of about 30 ns [9]. It is therefore desirable to investigate the atomic oxygen ground state concentration outside te jet.

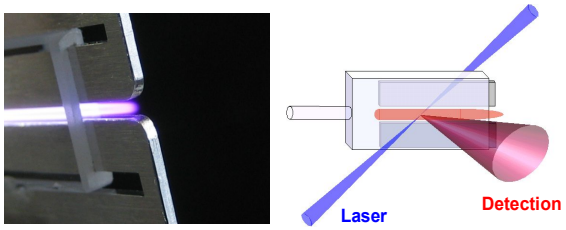

Figure 1: Photograph of the µ-APPJ operated in pure helium at ambient pressure and schematics of optical diagnostics inside the discharge volume.

For this purpose we applied quantitative, spatially resolved two-photon absorption laser-induced fluorescence (TALIF) measurements of atomic oxygen ground state densities in the effluent of the µ-APPJ operated with about 1 vol-% O_2 in helium, as described in the following. The discharge is operated at 13.56 MHz at generator powers of about 5 to 20 watts. For higher admixtures of oxygen higher powers are required. Figure 2 sketches the experimental setup. The vessel warrants the absolute calibration of the system at a defined xenon filling.

The results presented here are based on a TALIF calibration scheme with xenon as described extensively in [10, 11]. The method is based on comparative TALIF measurements using xenon as a reference with a two-photon resonance spectrally close to that of the atomic oxygen at λ= 226 nm to be quantified. Figure 3 shows the respective states and transitions. The radiation is provided by a frequency tripled

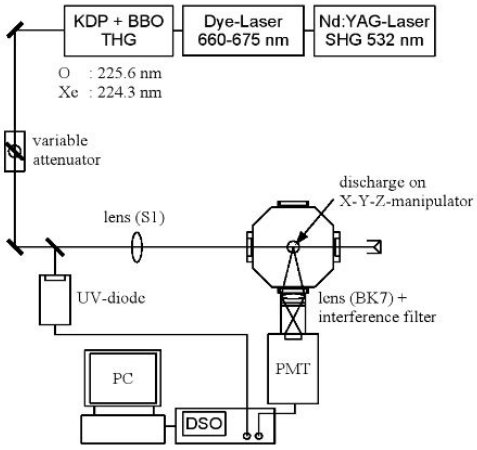

Figure 2: Experimental setup

Nd:Yag pumped dye-laser system. Since TALIF has already been described in greater detail elsewhere [12, 13] we will restrict here on the most critical features particularly considering atmospheric pressure.

Several rules have to be observed:

- the conditions of excitation and detection should be as similar as possible for both two-photon transitions; this includes the properties of the laser output and the optical set-up.
- Only the unsaturated quadratic signal response allows a quantitative comparison.

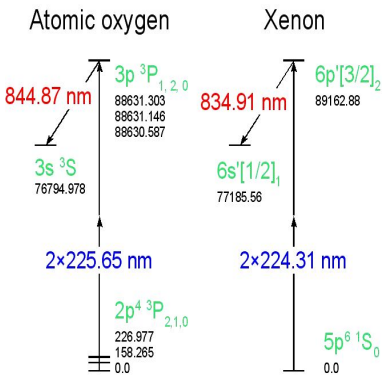

Figure 3: Two-photon excitation schemes of atomic ocygen and xenon.

Various saturation effects as ground state depletion exhibit rather complex intensity dependencies with individual thresholds.

- Artificial particle generation, e.g. by photo-dissociation has to be mentioned here explicitly due to its particular importance for mixtures with molecular components. In conclusion the laser intensity has to be kept as low as possible.

The unknown atomic ground state density n_O is then related to the reference gas density n_{Xe} by

$$\frac{S_O}{S_{Xe}} = \frac{n_O}{n_{Xe}} \frac{\sigma_O^{(2)}}{\sigma_{Xe}^{(2)}} \frac{T_O \eta_O}{T_{Xe} \eta_{Xe}} \frac{a_O}{a_{Xe}} \quad ,$$

with the fluorescence signal S (integrated over fluorescence wavelength, excitation wavelength and interaction time), the effective branching ratio a of the observed fluorescence transition, the transmission T of the detection optics and the detector's quantum efficiency η for the fluorescence wavelength, and the two-photon excitation cross section $\sigma^{(2)}$.

At atmospheric pressure collisional quenching generally dominates over the spontaneous emission. Thus the effective branching ratio a of the spontaneous transition i → k is reduced by

$$a = \frac{A_{ik}}{A_i}$$

where A_i denotes the effective decay rate including quenching:

$$A_i = \sum_k A_{ik} + \sum_q k_q n_q$$

Here, it becomes obvious that knowing the relevant quenching coefficients k_q and the densities of the corresponding quenching partners n_q is essential. The majority species in the jet effluent are the feed gases helium and molecular oxygen. Under the conditions investigated molecular oxygen is the dominant quenching partner [13].

Accordingly the local effective quenching rate can be calculated on the basis of the measured room temperature quenching coefficients and the measured gas temperature field shown in figure 4 (a) as measured here by a thermocouple. The density distributions of both colliders are simply related to the gas temperature according to Dalton's law assuming a constant ratio of molecular oxygen to helium throughout the jet's effluent.

The determination of the absolute atomic density is performed in two steps. Primarily, a two-dimensional on-resonance fluorescence map of the jet effluent is recorded. Then, the calibration measurement is performed at one spatial position. The analogous procedure is repeated for the case of xenon filling at the close-by Xe resonance. Finally the fluorescence map data are converted into spectrally integrated data accounting for the measured temperature distribution. The resulting map of the absolute atomic oxygen density for 1.4 slm helium flux, 1% O_2 admixture and 15 W of launched RF power is shown in figure 4 (b). The effective radial resolution is of the order of 2 mm.

The atomic oxygen density as well as the gas temperature are highest close to the nozzle: 8 x 10^{13} cm^{-3} and 35°C, respectively. The atomic density decreases by roughly a factor five over a distance of 4 centimeters. The axial behavior is close to that of the standard APPJ as measured by Niemi et al. [13]. Deviations can be attributed to differences in the setup and possibly to enhanced recombination at the quartz walls of the µ-APPJ that are much closer to the discharge center compared to the standard APPJ. In conclusion we

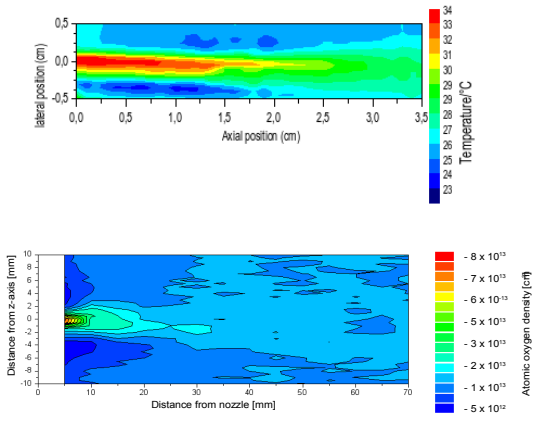

Figure 4: Gas temperature field (a) and map of absolute atomic oxygen density (b) in the APPJ effluent.

assume that the O atom production of the µ-APPJ is comparable to that of the APPJ as expected by the down scaled operational parameters.

An important finding is that the atomic density in this helium atmosphere remains sharply concentrated to the beam axis showing only a slightly larger beam divergence than the temperature. The observed distribution map of ground state O atom correlates reasonably well with the observation that fluorescence of excited

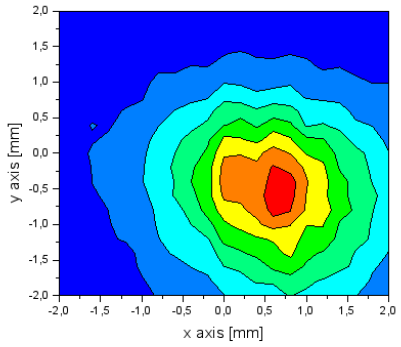

Figure 5: Cross section of the emerging effluent at 6 mm distance from the nozzle.

atomic oxygen extends several centimeters outside the jet. Radiation in the UV and VUV wavelength ranges has then to be taken into account as a second energy transport mechanism for the production and excitation of atomic oxygen outside the discharge.

Figure 5 shows a cross section through the effluent at a distance of about 6 mm from the nozzle. This measurement is done by displacing the jet with a translational stage in a plane perpendicular to the effluent. It is obvious that at this distance the square shape defined by the electrode and windows is already transformed by diffusion into a circular one.

The observed distribution map of ground state atomic oxygen correlates well with the mentioned fluorescence range of excited atomic oxygen. The energy transfer processes providing excited atomic oxygen relatively far (10 cm) outside the discharge are still being discussed. Possible explanations such as excitation by helium metastables are not convincing. Radiation in the UV and VUV wavelength ranges, however, has to be taken into account as a second energy transport mechanism for the excitation or production of excited atomic oxygen outside the discharge

4. Conclusions

We presented measurements of absolute oxygen density maps within the effluent of a micro jet discharge. The results can be correlated to measurements of excited oxygen and ozone concentrations. Measurements of the oxygen concentration within the discharge core are actually prepared.

Acknowledgements

Support by the ministry of commerce and research of North Rhine-Westphalia in the frame of the project ”Atmospheric pressure discharges for modification of surfaces with bio-technical and medical relevance”, by the SFB591 and the GRK1051 is gratefully acknowledged. The authors would especially like to thank Prof. H.F. Döbele for an enduring support of the project.

References

[1] K.H. Becker, J.G. Eden, and K.H. Schoenbach (Guest Editors), J. Phys. D: Appl. Phys. 38 (2005)

[2] J.G. Eden et al., J. Phys. D: Appl. Phys. 23, 2869 (2003)

[3] A. Schütze, J.Y. Jeong, et al., IEEE Trans. Plasma Sci. 26, 1685 (1998)

[4] G.S. Selwyn, H.W. Herrmann, et al., Contrib. Plasm Phys. 10, 573 (2001)

[5] S.E. Babayan, et al., Plasma Sources Sci. Technol. 10, 573 (2001)

[6] J Y Jeong, S E Babayan, et al., Plasma Sources Sci. Technol. 7, 282–285 (1998)

[7] J. Park et al., J. Appl. Phys. 89, 15 (2001)

[8] X. Yang, et al., Plasma Sources Sci. Technol. 14, 314 (2005)

[9] S. Wang, V. Schulz-von der Gathen, H.F. Döbele, Appl. Phys. Lett. 83, 3272 (2003)

[10] H.F. Döbele, T. Mosbach, et al., Plasma Sources Sci. Technol., 14, S31 (2005)

[11] A. Goehlich, T. Kawetzki, H.F. Döbele, J. Chem. Phys. 108, 9362 (1998)

[12] K. Niemi, V. Schulz-von der Gathen, H.F. Döbele, J. Phys. D: Applied Physics, 34, 2330 (2001)

[13] K. Niemi, V. Schulz-von der Gathen, H.F. Döbele, Plasma Sources Sci. Technol. 14, 375 (2005)

Laser-aided diagnosis of the gas phase chemistry in microwave activated plasmas used for depositing diamond thin films.

Jie Ma[1], A. Cheesman[1], J.C. Richley, M.N.R. Ashfold[1],
S. Wright[2], G. Duxbury[2] and Yu.A. Mankelevich[3]
[1] *School of Chemistry, University of Bristol, Bristol BS8 1TS, U.K.*
[2] *Department of Physics, University of Strathclyde, 107 Rottenrow, Glasgow G4 0NG, U.K.*
[3] *Nuclear Physics Institute, Moscow State University, 119992 Moscow, Russia*

Absolute column densities of a number of stable (CH_4, C_2H_2) and transient species (C_2 and CH radicals and H(n = 2) atoms) have been measured by direct infrared absorption (using a quantum cascade laser) and by cavity ring down spectroscopy (using a pulsed dye laser) in microwave activated $CH_4/Ar/H_2$ and $C_2H_2/Ar/H_2$ plasmas, as functions of process conditions and height above the substrate. Gas phase $CH_4 \leftrightarrow C_2H_2$ inter-conversion is clearly observed, serving to reinforce and to refine reaction schemes proposed by Ashfold *et al*. (*Phys. Chem. Chem. Phys.* **3**, (2001) 3471).

1. Introduction

Hydrocarbon/H_2 gas mixtures, with or without added Ar, are commonly used as the feedstock gas for diamond chemical vapour deposition (CVD). The complex plasma induced chemical processes occurring during CVD provide many questions and challenging opportunities – both experimentally and of our theoretical knowledge. One such question is the inter-conversion mechanism between C_1H_x ($x \leq 4$, *e.g.* CH_4, CH_3, *etc*) and C_2H_y species (C_2H_2, C_2, *etc*), and its variation with process conditions and spatially within the reactor.

The crucial role of H atoms in initiating gas phase and gas-surface reactions is widely recognised [1]. The traditional reaction scheme, with CH_4 as the source hydrocarbon, involves a series of H-atom abstraction or 'H-shifting' reactions resulting in formation of CH_x radicals (CH_3, CH_2, CH) and C atoms as shown by the solid arrows on the left hand side of fig. 1. Self-reactions between CH_x radicals can result in formation of C_2H_y species ($y \leq 6$), which can also undergo H atom abstractions yielding species like C_2H_4, C_2H_2, C_2H and C_2 *etc* – as shown in fig. 1 (solid arrows, right hand side). This scheme paves the way for efficient conversion of input CH_4 to C_2H_2. Using C_2H_2 as the source gas, however, the complementary gas-phase processes that lead to creation of C_1H_x species are less well established. Nonetheless, both CH_4 and C_2H_2 have been identified (*e.g.* by mass spectrometry [2]) in diamond growing plasmas, irrespective of which is used as the carbon source gas. An efficient mechanism for converting acetylene to methane must therefore exist.

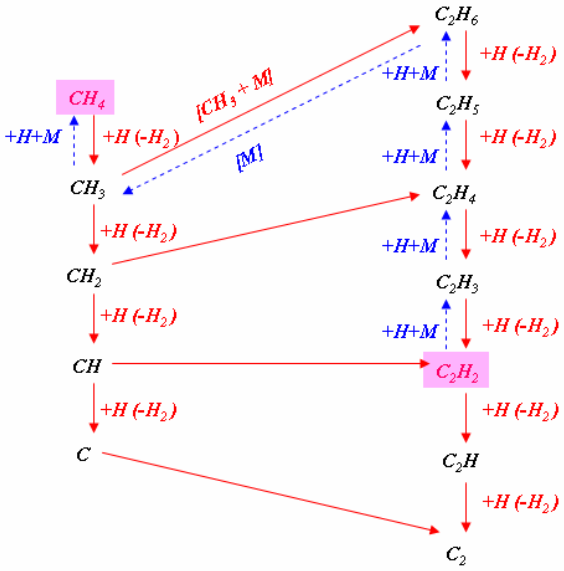

Figure 1 Illustration of many of the possible steps involved in the inter-conversion between gas phase C_1H_x and C_2H_y species in hydrocarbon/H_2 plasmas used for diamond CVD.

Heterogeneous chemistry, on the reactor walls or the growing diamond surface, has been proposed as one possible conversion path. C_2H_2 is assumed to pyrolyse on such surfaces, and the resulting graphitic carbon layer then to be etched, by H atoms, yielding gas phase species like CH_3 [1,3]. An alternative mechanism, proposed [4] following laser (resonance enhanced multiphoton ionisation, REMPI) probing of CH_3 radicals in hot filament activated CH_4/H_2 and C_2H_2/H_2 gas mixtures used for diamond CVD [5], invokes a sequence of H-atom additions to C_2H_2, followed by dissociation of C_2H_y to C_1H_x species (as illustrated by the dashed arrows in fig. 1). Such three-body stabilised H-atom addition reactions are unlikely at high gas temperatures, T_{gas}, but

become favourable at lower T_{gas} given suitably high H atom (and total) number densities.

Provided the $C_1H_x \leftrightarrow C_2H_y$ inter-conversion rate is sufficiently fast, one might anticipate that the equilibrium gas mixture and the eventual plasma should be relatively insensitive to the choice of hydrocarbon feedstock gas. This assumption is tested further in the present work, wherein we determine spatially resolved, absolute column densities of a number of species (CH_4 and C_2H_2, CH and C_2 radicals, and H(n = 2) atoms) in microwave activated plasmas operating with a range of hydrocarbon feedstock gas mixtures.

2. Experimental

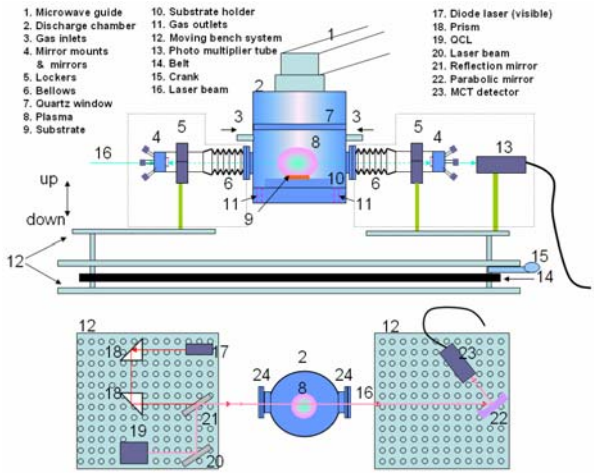

Figure 2 Schematic of the QCL and CRDS experimental set-ups. The reactor side arms are for CRDS measurements only and are substituted by two diamond windows (as shown in the lower panel) for the QCL experiments.

A schematic illustration of the experimental apparatus is shown in fig. 2. The microwave power is delivered along the rectangular waveguide (*1*) and coupled into the cylindrical chamber (*2*). The chamber is partitioned into two parts by a centrally mounted quartz window (*7*). The lower section is vacuum-sealed, and the plasma is formed in this chamber. The pre-mixed hydrocarbon/Ar/H_2 source gas mixture is fed through two opposed inlets (*3*) located near the top of the lower chamber and exhausted through outlets (*11*) at the base of this chamber. The microwave radiation partially ionizes and dissociates the gas mixture, 'active' species are produced, some of which diffuse to the substrate (*9*), are accommodated and/or react at its surface, and result in diamond growth on the substrate.

Two sets of plasma diagnoses are described. The first uses a quantum cascade laser (QCL) to make single-pass line-of-sight absorption measurements of species that are stable at low T_{gas} (CH_4 and C_2H_2). Preliminary experiments of this type have been reported previously [6], but more extensive, spatially resolved studies are reported here. The second uses a tuneable, pulsed dye laser and the cavity ring-down spectroscopy (CRDS) technique [7] to monitor three transient species (C_2 and CH radicals, and H(n = 2) atoms), which are localised within the high temperature region in the plasma ball.

The QCL (*19*) was developed by Cascade Technologies Ltd and operated, in intra-pulse mode [8], within the wavenumber range 1270 - 1278 cm^{-1}, to monitor specific rovibrational transitions of the target molecules CH_4 and C_2H_2. The output frequency was chirped, using a long (2 μs) current pulse, enabling measurement of the entire wavelength resolved spectrum in one pulse. The final spectrum is the average of 5000 wavelength scans. The fast chirp rate of the QCL enables time-resolved absorption measurements also. A guiding (visible) diode laser (*17*) is used to align the (infrared) QCL beam. The latter is passed through a Ge etalon (free spectral range = 0.0481 cm^{-1}) for wavenumber calibration, then directed through the two diamond windows (*24*) that bound the chamber, and focused by a parabolic mirror (*22*) onto a fast, liquid nitrogen cooled, mercury cadmium telluride (MCT) detector (*23*). These optical components are all mounted on a rigid translatable bench that allows sampling over a (vertical) range of ~3 cm while the reactor is held fixed. This design allows measurement of the CH_4 and C_2H_2 column absorptions as a function of height, *d*, above the top surface of the substrate (defined as $d = 0$).

For the CRDS studies, the diamond windows (*24*) are replaced by: bellows (*6*), rigid clamps for the sidearms (*5*), mirror mounts and mirrors (*4*); and the MCT detector is replaced by a photomultiplier (*13*). The flexibility introduced by the bellows again allows vertical translation of the entire optical assembly required for CRDS probing (contained within the dashed line in fig. 2) relative to the fixed reactor body. Different mirrors (Layertec GmbH, reflectivity, $R > 0.999$

at the detected wavelength) are used when measuring different species.

For future reference, 'standard' discharge conditions are defined as: total pressure, p = 150 torr, input power, P = 1.5 kW, and flow rates F of 25 sccm CH_4 (or 25 sccm carbon flow rate), 40 sccm Ar and 500 sccm H_2. When investigating effects of changing the Ar and/or hydrocarbon flow rates, any variation away from these 'standard' conditions is compensated by a corresponding adjustment in the H_2 flow rate so that F_{total} is maintained at 565 sccm.

3. Results and Discussion

3.1 QCL experiments

3.1.1 Spectra

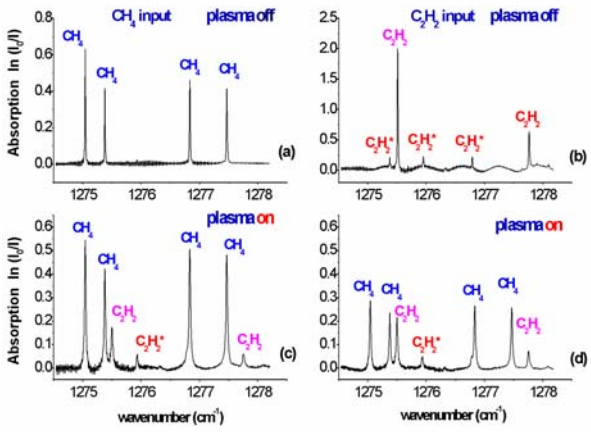

Figure 3 Measured absorption spectra: (a) and (b), CH_4 and C_2H_2 inputs, respectively, without ignition of the plasma; (c) and (d), $CH_4/Ar/H_2$ and $C_2H_2/Ar/H_2$ inputs, respectively, with plasma on.

The stated purities of the CH_4 and C_2H_2 source gases are 99.5% and 98.5%, respectively. To ascertain that the C_2H_2 measured in a $CH_4/Ar/H_2$ plasma or the CH_4 in a $C_2H_2/Ar/H_2$ plasma was not from impurities in the respective feedstock hydrocarbons, 'standard' $CH_4/Ar/H_2$ and $C_2H_2/Ar/H_2$ gas mixtures were flowed through the chamber without igniting the plasma, and the respective absorption spectra measured by scanning the QCL. The spectra so obtained are shown in figs. 3(a) and (b). Reassuringly, only CH_4 absorptions are observed when using CH_4 as the source gas, and only C_2H_2 absorptions when using C_2H_2. When the plasma is on, however, both CH_4 and C_2H_2 absorption lines are observed (figs. 3(c) and (d)), irrespective of the choice of input hydrocarbon. This result provides further clear demonstration of an efficient plasma induced $CH_4 \leftrightarrow C_2H_2$ inter-conversion route.

3.1.2 Vertical profiles

The wavenumber tuning range of the QCL allows us to monitor population in selected rotational levels within the ground vibrational state of CH_4 and the v = 0, v_4 = 1 and v_5 = 1 levels of C_2H_2. The measured d dependences of the CH_4, C_2H_2 and $C_2H_2(v_5 = 1)$ [henceforth C_2H_2*] column absorptions in microwave activated $CH_4/Ar/H_2$ and $C_2H_2/Ar/H_2$ gas mixtures under standard conditions are displayed in figs. 4(a) and (b).

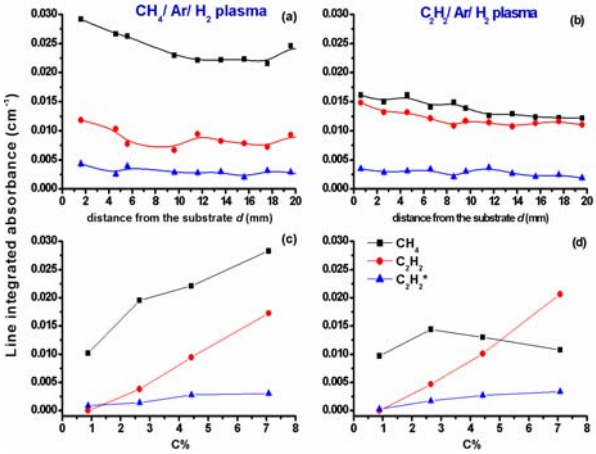

Figure 4 Line integrated absorbances of CH_4, C_2H_2 and C_2H_2*, measured as a function of height d above the substrate for (a) $CH_4/Ar/H_2$ and (b) $C_2H_2/Ar/H_2$ plasmas under standard conditions. (c) and (d) illustrate the way these various absorbances vary with percentage carbon in the respective feedstock mixtures.

These profiles appear rather flat in comparison with those for the C_2 and CH radicals, and the H(n = 2) atoms – see later – for which order of magnitude changes in column densities are observed over similar, or smaller, ranges of d. This indicates the most of the measured absorption due to CH_4, C_2H_2 and C_2H_2* species is from molecules in the cooler regions of the reactor, not in the plasma. This conclusion is reasonable because (i) the absorbers are stable species and the cold region spans a much longer column within the reactor than does the plasma, (ii) the total number density is inversely related to T_{gas} and (iii) the sensitivity factors for the transitions used to probe the ground state species decrease rapidly with increasing temperature [6]. Note also that relatively more CH_4 is detected when using a $CH_4/Ar/H_2$ gas mixture, while more C_2H_2 is measured when using the $C_2H_2/Ar/H_2$

mixture – suggesting that some of the feedstock gas escapes processing under the prevailing operating conditions and stagnates at the column ends. For C_2H_2*, however, the results are similar for both plasmas, consistent with previous suggestions that these vibrationally excited C_2H_2 molecules are formed by reaction, in regions of higher T_{gas} in or near the plasma [6].

3.1.3 Effect of carbon flow rate

Figures 4(c) and (d) show that the C_2H_2 and C_2H_2* absorbances display very similar trends with increasing %C in both $CH_4/Ar/H_2$ and $C_2H_2/Ar/H_2$ plasmas, but that the CH_4 absorbance shows contrasting behaviour. The CH_4 measured when using a $C_2H_2/Ar/H_2$ plasma must derive totally from reaction whereas, in the $CH_4/Ar/H_2$ plasma, part of the CH_4 signal is likely to arise from un-processed feedstock gas (especially at high carbon flow rates) if the conversion of CH_4 to C_2H_2 is not 100% efficient. This likely explains the different behaviours observed at higher CH_4 flow rates.

3.1.4 Temporal behaviour of CH_4, C_2H_2 and C_2H_2* species in $CH_4/Ar/H_2$ and $C_2H_2/Ar/H_2$ plasmas

The temporal resolution of the QCL offers a window through which we can gain dynamical information about the plasma. Fig. 5 shows the measured time (t) dependent variation in CH_4, C_2H_2 and C_2H_2* absorptions after addition of CH_4 to a pre-existing Ar/H_2 plasma.

As figs. 5 and 6 show, the CH_4 and C_2H_2* absorption lines appear first. Absorption due to $C_2H_2(v = 0)$ molecules appears later and increases with a longer time constant. To understand this phenomenon, consider the first few seconds after starting the CH_4 flow (by switching the appropriate MFC at $t = 0$). The gas is fed in at the top of the reactor and has to flow/diffuse down to the region of the plasma ball and the viewing column. The carbon partial pressure in the viewing region will thus gradually rise from zero (at $t = 0$) and at early times will be low – *i.e.* similar to the situation prevailing at low carbon flow rates (recall the data shown in figs. 4(c) and (d)). In the present time dependent studies, any carbon source gas introduced into the pre-existing Ar/H_2 plasma first encounters a region of high H atom number density, [H], and

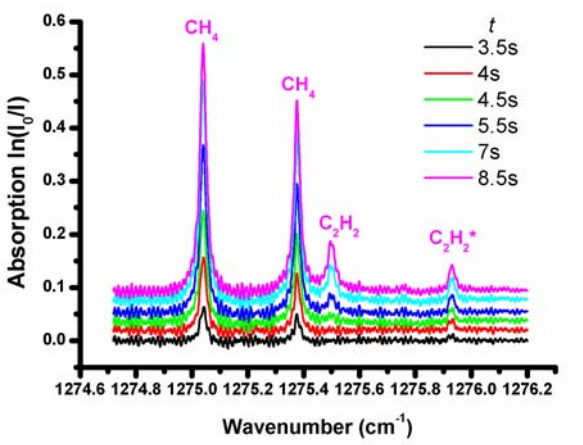

Figure 5 CH_4, C_2H_2 and C_2H_2* absorbances measured as a function of t after introducing 25 sccm CH_4 to a pre-existing Ar/H_2 plasma (maintaining standard F, p and P).

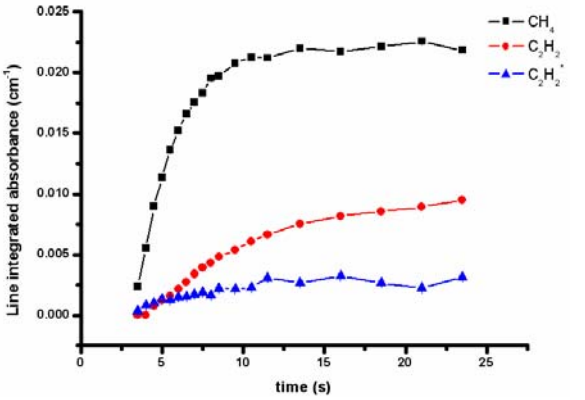

Figure 6 Time dependent build-up of CH_4, C_2H_2 and C_2H_2* line integrated absorbances when CH_4 is added to a pre-existing Ar/H_2 plasma (so as to attain standard conditions at long time).

moderate T_{gas}, at large d, and the equilibria will shift towards CH_4 (as shown by the dashed arrows in fig. 1). Hence the early time observation of CH_4. To be monitored in the present experiments, the gas must reach the viewing column – and thus the region of high T_{gas} associated with the plasma ball. In this region, the $CH_4 \leftrightarrow C_2H_2$ equilibria will shift back towards C_2H_2. The measured time dependences reinforce the view that the exothermicity of this conversion favours population of C_2H_2 products with $v > 0$. Given the relatively slow turn over time of gas in the reactor (volume ~600 cm^3, gas flow rate ~565 sccm), these C_2H_2* products will diffuse away from the 'hot' region, cool, vibrationally relax (through collisions with other gas molecules) and gradually reach local thermal

equilibrium with the surrounding gas. Hence the slower build up of the $C_2H_2(v = 0)$ absorption.

Analogous behaviour is observed when C_2H_2 is used as the input hydrocarbon gas, reflecting the efficiency of the $C_2H_2 \rightarrow CH_4$ conversion when the first C_2H_2 enters the high [H], moderate T_{gas} conditions prevailing at the top of the reactor. These observations provide further evidence (i) that the CH_4 and C_2H_2* species observed at early *t* arise from reactions, not simple transport of the source hydrocarbon, and (ii) for the complete conversion of C_2H_2 to CH_4 at early *t*.

The QCL measurements reveal that, irrespective of the choice of hydrocarbon source gas, the input hydrocarbon will first be converted (substantially or totally, depending on the net carbon flow rate and the choice of hydrocarbon) into CH_4 in the cooler, near inlet region, because of the prevailing favourable high [H] and moderate T_{gas} conditions. Diffusion of the resulting CH_4 towards and into the plasma region (characterised by high [H] and high T_{gas}) results in $CH_4 \rightarrow C_2H_2$*/C_2H_2 conversion. Irrespective of the choice of source gas, therefore, the favoured stable hydrocarbon in and around the plasma ball is predominantly C_2H_2. Thus one should expect the plasma chemistry to be largely insensitive to the choice of hydrocarbon feedstock.

3.2 CRDS experiments

Figures 6 and 7 display illustrative CRDS spectra of $C_2(a, v = 0)$ radicals, monitored via the C_2(d–a) Swan band system, and electronically excited H(n = 2) atoms detected on the H(n = 3 ← n = 2) Balmer-α transition. Analyses of such spectra provide direct measures of the integrated column absorbances, which can be converted to absolute column densities given knowledge of the local gas temperature (determined as T_{gas} ~3000 K for transient species like these that are localised within the plasma ball). Thus, for example, it is possible to map out the variation in column density with *d*, as a function of process conditions. Figure 8 shows one illustrative result, for the case of $C_2(a)$ radicals as a function of CH_4 flow. The marked localisation of radical density clearly contrasts with the 'flat' spatial profiles of the stable hydrocarbons (CH_4 and C_2H_2) shown in fig. 4.

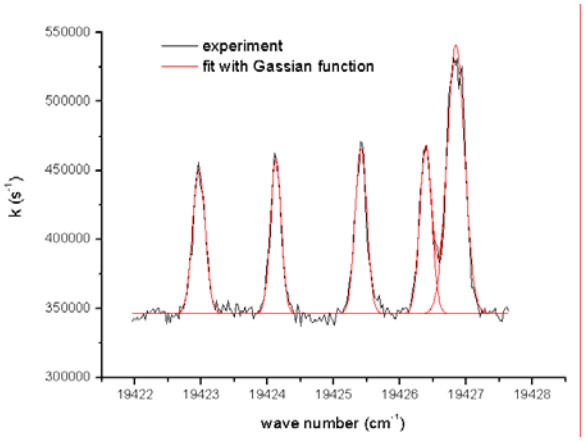

Figure 6 Portion of the C_2(d–a), (0,0)) absorption band measured by CRDS in a microwave activated $CH_4/Ar/H_2$ plasma operating under standard conditions.

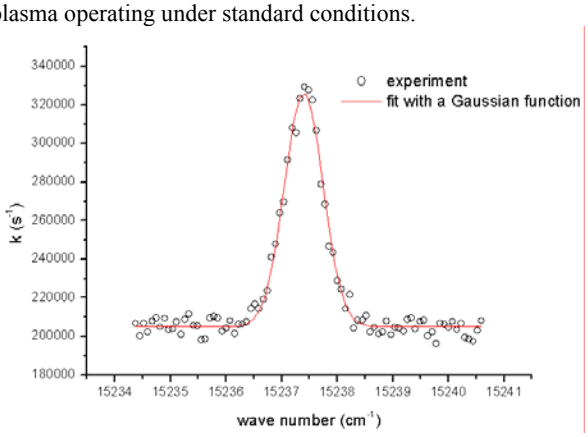

Figure 7 H(n = 3 ← n = 2) Balmer-α absorption line measured by CRDS in a microwave activated $CH_4/Ar/H_2$ plasma operating under standard conditions.

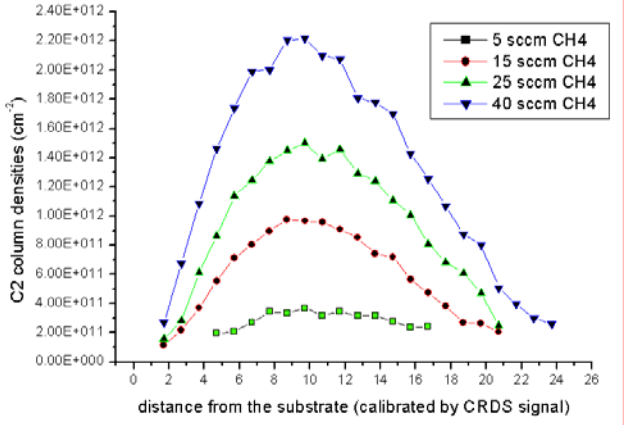

Figure 8 C_2 (a, v = 0) column density profiles measured in microwave activated $CH_4/Ar/H_2$ plasmas operating with the specified CH_4 flow rates and otherwise standard conditions.

Figure 9 compares the *d* dependence of the column densities of three "hot" species (C_2 and CH radicals, and H(n = 2) atoms, each of which is concentrated in the plasma) measured in both $CH_4/Ar/H_2$ and $C_2H_2/Ar/H_2$ plasmas (with the

same input carbon flow rate), as a function of *d*, using spatially resolved CRDS. The radical species display very similar profiles, determined primarily by the temperature distribution within the plasma. The H(n = 2) column density is seen to peak at smaller *d*. H(n = 2) atoms are formed primarily be electron impact excitation of ground state H atoms; the H(n = 2) spatial distribution thus reflects a convolution of the H(n = 1) and the electron density distributions. Of even greater import, in the context of the present work, is the finding that the distribution profile of any one species is essentially identical in the two plasmas – consistent with the reaction schemes and mechanisms described above.

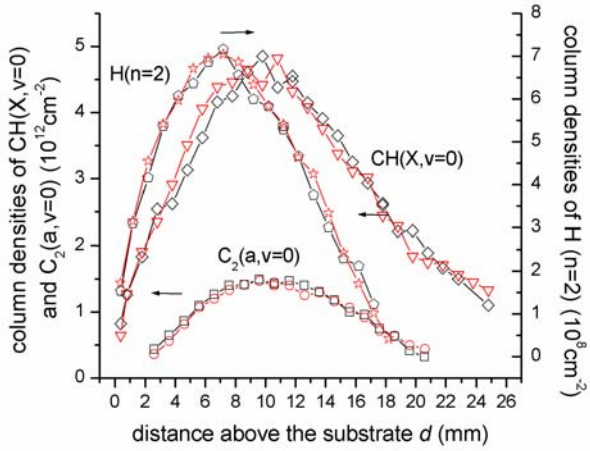

Figure 9 C_2(a, v = 0), CH(X, v = 0) and H(n = 2) column density profiles in $CH_4/Ar/H_2$ and $C_2H_2/Ar/H_2$ plasmas (black and red curves, respectively) under standard operating conditions.

4. Conclusions

This contribution reports the use of two laser absorption spectroscopy techniques (QCL single-path absorption and CRDS) to investigate the aspects of gas phase chemistry prevailing in microwave activated $CH_4/Ar/H_2$ and $C_2H_2/Ar/H_2$ plasmas used for diamond CVD. Inter-conversion between CH_4 and C_2H_2 is clearly observed in both plasmas. The experimental results support the view that inter-conversion occurs via two distinct reaction schemes that prevail in different conditions (and thus different regions of the reactor): In regions of low T_{gas} and high [H], C_2H_2 converts to CH_4 through a sequence of H atom additions, while in regions of abundant [H] and high T_{gas} the equilibrium shifts in the reverse direction and abstraction reactions dominate.

Temporal studies of the dynamical behaviour of CH_4, C_2H_2 and C_2H_2* indicate that the exothermicity associated with steps in the overall $CH_4 \rightarrow C_2H_2$ conversion scheme results in vibrationally excited C_2H_2* products, which relax through collisions to ground state C_2H_2. The measured C_2(a), CH and H(n = 2) profiles measured by CRDS in $CH_4/Ar/H_2$ and $C_2H_2/Ar/H_2$ plasmas are found to be essentially identical, emphasizing the efficiency of $CH_4 \leftrightarrow C_2H_2$ inter-conversion, and the fact that the plasma composition is sensitive to the %C but not the specific choice of hydrocarbon feedstock.

5. Acknowledgements

We are grateful to EPSRC, the Royal Society and Element Six Ltd for financial support of this work, to the ORS for studentship support, and to Drs J.A. Smith and C.M. Western, and K.N. Rosser and E.J. Crichton for their many contributions to this work.

References

[1] D.G. Goodwin and J.E. Butler, in: 'Handbook of Industrial Diamonds and Diamond Films' (eds. M.A. Prelas, G. Popovici and L.K. Bigelow), Marcel Dekker, New York 1998, pp 527-81 and references therein.

[2] M.C. McMaster, W.L. Hsu, M.E. Coltrin, D.S. Dandy and C. Fox, Diam. Rel. Mat. **4**, (1995) 1000.

[3] R.R. Rye, Surf. Sci. **69**, (1977) 653.

[4] J.A. Smith, M.A. Cook, S.R. Langford, S.A. Redman and M.N.R. Ashfold, Thin Solid Films, **368**, (2000) 169.

[5] M.N.R. Ashfold, P.W. May, J.R. Petherbridge, K.N. Rosser, J.A. Smith, Y.A. Mankelevich and N.V. Suetin, Phys. Chem. Chem. Phys. **3**, (2001) 3471.

[6] A. Cheesman, J.A. Smith, M.N.R. Ashfold, N. Langford, S. Wright and G. Duxbury, J. Phys. Chem. A. **110**, (2006) 28.

[7] M.D. Wheeler, S.M. Newman, A.J. Orr-Ewing and M.N.R. Ashfold, J. Chem. Soc. Faraday Trans. **94**, (1998) 337.

[8] G. Duxbury, N. Langford, M.T. McCulloch and S. Wright, Chem. Soc. Rev. **34**, (2005) 1.

Property of accumulated surface charges in a barrier discharge and its external control

T. Sakurai, H. Yoda, T. Terayama and S. Kubota

University of yamanashi,Interdisciplinary Graduate School of Medicine and Engineering, 4-3-11, Takeda, Kofu,400-8511,Japan

Accumulated charges and a transverse electric field on a dielectric barrier in a coplanar barrier discharge are measured by a laser polarization analysis technique using an electro-optic crystal. A spatial and temporal behavior of charges on the surface is analyzed under the comparison with the light intensity emitted from the plasma. In addition, it is found using the same technique that the accumulated charges are modulated by an externally irradiated light beam and the discharge can be controlled with this modulation.

1. Introduction

Plasma has been extensively applied for various fields such as processing, etching and display panel. In these applications, a barrier discharge is widely used. A dielectric surface acts as an electrode and the characteristics of discharge are determined by surface phenomena such as behavior of excited and charged species on the surface.

It is necessary to understand the characteristics of plasma particles on and near the surface in order to discuss the discharge mechanisms and to consider efficient plasma applications. However, the lack of such data near or on the surface is attributed to experimental difficulties.

We have proven that an optical evanescent wave, which is an optical near field appearing on a plane dielectric surface, is very valuable for applications of plasma diagnostics in the vicinity of a dielectric surface. An evanescent laser induced fluorescence (ELIF) [1] and a laser-induced evanescent-mode fluorescence (LIEF) [2]-[4] have been developed to measure the density of the lowest metastable atoms of Ar in the vicinity of barrier surface. Further research works using a cross beam-type LIEF [5] and an optical waveguide type laser absorption [6] have been recently made in order to measure the surface reflectance and the absolute density of metastable atoms on the dielectric surface, respectively. The reflectance measured agreed with an experimental data obtained in ref. [7].

The technique of measuring surface voltage using an electrooptic crystal has been applied to a surface discharge and a plasma display panel (PDP)-like discharge. [8],[9] We have also developed this optical technique using an electro-optic crystal and applied to a dielectric barrier discharge in order to observe spatial and temporal changes of a wall voltage due to accumulated charges.[10]-[12]

In this paper, we describe the estimation of an actual voltage between barrier surfaces using the measured surface charge and the observation of a drift of charges on a barrier surface. In addition, we also describe an external control of the surface charges.

2. Experimental arrangement

The side view of a PDP-like microdischarge device with an electrode gap distance of 100 μm is shown in Fig. 1. The discharge device has no side or back wall and a barrier surface is directly

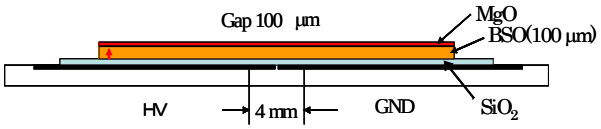

Fig. 1. Side view of discharge device.

connected to a gas filling system. The coplanar electrodes were made of indium tin oxide (ITO) and covered by SiO_2 to a thickness of 30 μm. The electrooptic crystal, z-cut $Bi_{12}SiO_{20}$ (BSO), with a thickness of 100 μm was attached onto the SiO_2 with an adhesive and a thin film of MgO with a thickness of 0.8 μm was evaporated onto the surface of BSO. The surface area of ITO was 22 x 1 mm^2. The device was set in a vacuum chamber.

The experimental arrangement is shown in Fig. 2. The PDP-like microdischarge device shown in Fig. 1 was attached to a glass window

using an optical transparent adhesive and the glass window was connected to the vacuum chamber. After passing through a λ/4 plate and a lens, a semiconductor laser with a circular polarization was transmitted in the z direction perpendicular to the BSO surface. The laser diameter was focused to be about 100 μm at BSO.

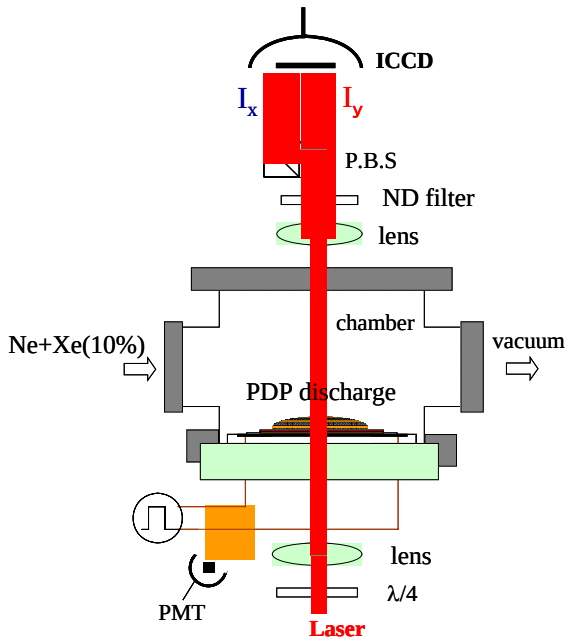

Fig. 2. Experimental arrangement.

The polarization of the transmitted laser beam changes from circular to elliptical depending on voltage on BSO, V_{BSO}. The intensities I_x and I_y in the x- and y- components, respectively, are simultaneously measured with an ICCD camera and the polarization P of the detected laser beam is obtained from $(I_x - I_y)/(I_x + I_y)$. The surface charge density is estimated from V_{BSO} [12].

3. Results and discussion

The surface charge density σ_s in the steady state at 45 μs, much later than the end of discharge, was measured under various pressures of Ne+Xe(10%) gas mixture and is shown in Fig. 3 as a function of total external charge flowing in circuit which was estimated from the time integral of a pulsed discharge current. The breakdown voltage in this experiment is higher than that in a usual PDP, because the pulsed applied voltage has a monopolar waveform and its rise time is about 25 μm, which is longer than the usual case.

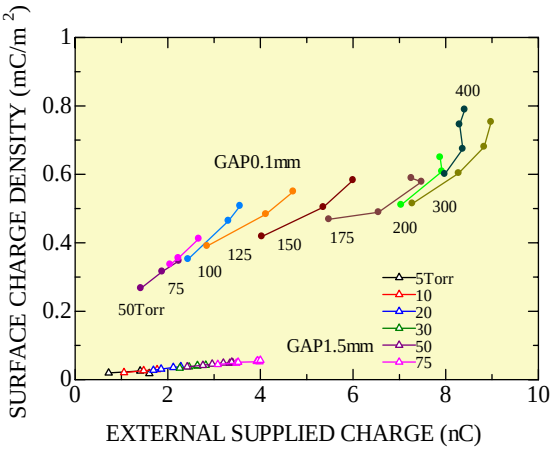

Fig. 3. Surface charge density as a function of total external flowing charges.

In Fig. 3, the result obtained using a macrodevice with coplanar electrodes for which gap distance is 1.5 mm are also plotted. The barrier material for the macrodevice was different from that for the microdevice. An ITO electrode was covered by a glass plate with a thickness of 150 μm. A BSO crystal with a thickness of 100 μm was attached to the glass and the surface of BSO was covered by another glass plate with a thickness of 150 μm. The discharge occurred not on MgO but on the glass surface. The surface area of ITO was 10 x 6 mm^2. Surface charge density σs for a 0.1 mm microgap was one order of magnitude larger than that for a 1.5 mm macrogap.

For the discharge device structure used in this experiment, the charges produced in plasma accumulate not on the surface of BSO but on MgO or glass. However, for the case of the microgap device, each layer of MgO, BSO, SiO_2 and the ITO electrode directly lie in a heap and three capacitances C_M, C_{BSO} and C_S for MgO, BSO and SiO_2, respectively, are in series. Charge density σs estimated from the measured voltage applied to BSO, V_{BSO}, equals the actual charge density accumulated on MgO. Voltage V_S between the top surface of MgO and the ITO electrode is given as a sum of voltage applied on each layer and is given, using V_{BSO}, by

$$V_S = \{(C_{BSO}/C_S) + (C_{BSO}/C_M) + 1\}\, V_{BSO}. \quad (1)$$

Dielectric constant ε of MgO and that of SiO_2 are 9.7 and 4.0, respectively, and C_{BSO}/C_S=4.2 and C_{BSO}/C_M=0.1. Therefore, V_S is given by 5.3 x V_{BSO} for the device used.

A voltage difference on the barrier surface between anode and cathode side, V_{SAC}, is given by V_{SA}-V_{SC}, where V_{SA} and V_{SC} are estimated from V_{BSO} on anode and cathode side, respectively, using eq. (1). These voltages are schematically shown in Fig. 4. The surface

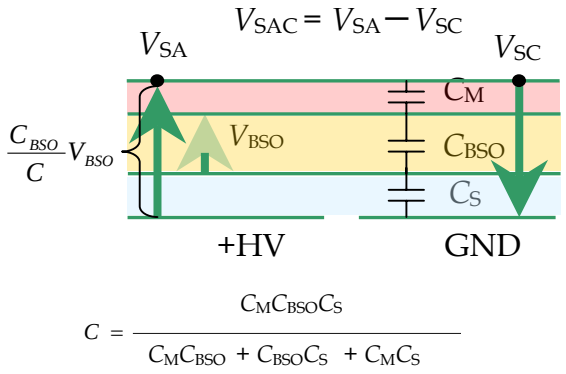

Fig. 4. Voltage at various parts.

voltage difference due to accumulated charges, V_{SAC}(c), obtained from the values shown in Fig. 3 is shown in Fig. 5 as a function of total external supplied charge. The values at the minimum breakdown voltage at a given pressure for both 0.1 and 1.5 mm gap devices are expressed as one smooth function. These results indicate that the surface charges are accumulated to keep the

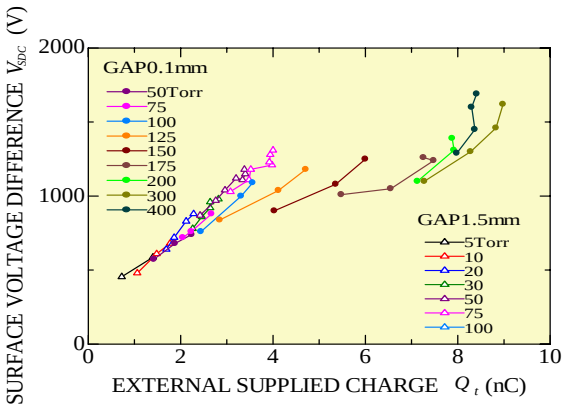

Fig. 5. Surface voltage difference between the ground and high-voltage electrodes on the top barrier surface.

surface voltage difference a fixed value.

An actual voltage difference V_{SAC} is calculated as a sum of V_{SAC}(c) based on the accumulated charges and V_{SAC}(e) based on external applied voltage. For a typical condition at pressure of 200 Torr and applied peak-to-peak voltage of 1500 V, V_{SAC}(c) and V_{SAC}(e) are 1330 and -734 V, respectively. The actual surface voltage difference between electrodes on MgO, V_{SAC}, is 596 V, which is lower than the breakdown voltage under the experimental condition. Next if a negative external voltage is applied between electrodes, the actual surface voltage difference, V_{SAC}, becomes 2064 V, which is much higher than the breakdown voltage.

In next experiment, a pure Ar gas at a pressure of 10 Torr discharged using the microgap device. At this low pressure the standing striation was observed on anode side. The image of a light intensity emitted from plasma was measured by the ICCD camera. The intensity distribution at various time is shown in Fig. 6 (a). For the experiments at pressures higher than 50 Torr, no standing striation observed and the surface charge was uniformly accumulated on the barrier surface under the time resolution of 0.1 ms.

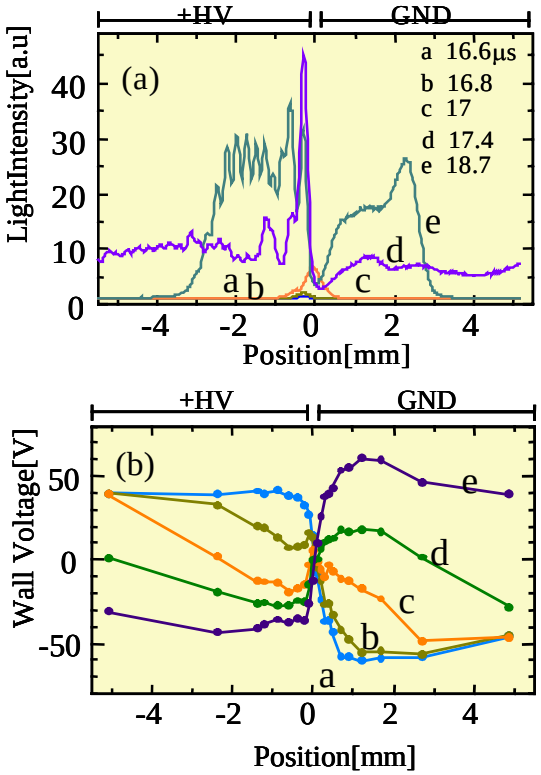

Fig. 6. (a): Intensity distribution emitted by a plasma at various time. (b): Spatiotemporal wall voltage due to the surface charge measured at the same time as shown in (a).

At the same experimental condition as shown in Fig. 6 (a), the spatiotemporal charge distribution was measured. The results are shown in Fig. 6 (b). The figure indicates that

the electrons accumulate near the gap on the anode area at an initial period after the breakdown and the accumulated electrons spread gradually toward outside. The same phenomena for the ion accumulation and its spread is observed on the cathode area, however, the dynamic behaviour of the ion accumulation is slower than that of electrons on the anode side.

Finally the experiment was performed to show that accumulated charges are controlled by an irradiation of laser light. The experimental setup for the discharge and charge measurement were the same as those shown in Fig. 2. In addition to this, a YAG laser with a wavelength of 532 nm, which pulse timing was synchronized to the external applied pulsed voltage for the discharge, irradiated the barrier surface, after passing through the window. The experimental results of the surface voltage modulated by YAG laser irradiation are shown in Fig. 7. In this case, a repetition rate of applied voltage was 20 Hz and YAG laser irradiated only at a half cycle with a delay of 4 ms from the risetime of applied voltage. The surface voltage due to the accumulated charges suddenly decreases with the laser irradiation. This experimental result indicates a possibility of a control of the surface charges using an external irradiation of light.

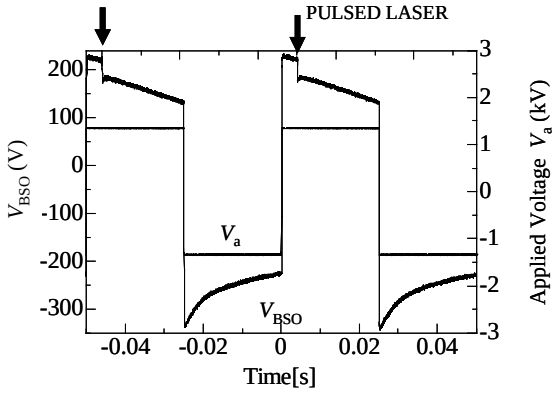

Fig. 7. Experimental results of the surface charge change produced by a pulsed laser irradiation.

3. Conclusion

The spatiotemporal surface charges for a PDP-like microdischarge are measured under various conditions. The surface charges are accumulated to keep the surface voltage difference on the barrier between the ground and high-voltage electrodes a fixed value. Further, the dynamic behaviour of the surface charges is observed for a low pressure discharge with the standing striation. Finally it is indicated that the surface charges accumulated on the barrier can be modulated by a external irradiation of pulsed laser.

Acknowledgement

This work was supported financially in part by a Grant-in-Aid for Science Research on Priority Area (Grant No. 15075204) from the Ministry of Education, Culture, Sports, Science and Technology and also in part by a 2007 Assistance Grant of Hoso Bunka Foundation,

References

[1] T.Sakurai, T.Kubota, Y.Takahara, Y.Inoue and H.Hori, Jpn. J. Appl. Phys. **38,** (1999) L590.

[2] T.Sakurai and M.Toda, Thin Solid Films **374**, (2000) 157.

[3] T.Sakurai, S.Matsuzawa and Y.Kamo, J. Appl. Phys. **91,** (2002) 4806.

[4] T.Ito, H.Nishiyama, K.Terashima, K. Sugimoto, H.Yoshikawa, H.Takahashi and T. Sakurai, J. Phys. D **37,** (2004) 445.

[5] T.Sakurai, Y.Murata and H.Hori, Jpn. J. Appl. Phys. 46, (2007) 378.

[6] T.Sakurai, 2007 IEEE Pulsed Power and Plasma Science Conf., U.S.A. (June 2007) 2E7.

[7] P. Macko and N. Sadeghi, *Plasma Sources Sci. Technol.* **13** (2004) 303.

[8] A. Kumada, M. Chiba and K.Hidaka, *Trans. IEE of Japan* **118A** (1998) 723.

[9] D.C.Jeong, H.S.Bae and K.W.Whang, *J. Appl. Phys.* **97** (2005) 013304.

[10] K.Sugimoto, H.Takahashi, O.Shimomura and T.Sakurai, *J. Phys. D* **36** (2003) 2887.

[11] T.Sakurai, Plasma Sources Sci. Technol. 16 (2007) S101.

[12] T.Sakurai, H.Yoda, T.Terayama, K.Ishii and Y.Murakami, Jpn. J. Appl. Phys. **46** (2007) 3596.

Atomic hydrogen densities in the interaction between hydrogen plasma and carbon detected with Cavity Ring-down spectroscopy

G.J. van Rooij[1], R.S. Al[1], R. Engeln[2], W.J. Goedheer[1], B. de Groot[1], A.W. Kleyn[1,3], W.R. Koppers[1], N.J. Lopes Cardozo[1,2], H.J. van der Meiden[1], D.C. Schram[1,2], A.E. Shumack[1], P.H.M. Smeets[1], W.A.J. Vijvers[1], and J. Westerhout[1]

[1] *FOM-Institute for Plasma Physics Rijnhuizen, Association EURATOM-FOM, P.O.Box 1207, 3430 BE Nieuwegein, The Netherlands, www.rijnhuizen.nl*
[2] *Eindhoven University of Technology, Eindhoven, The Netherlands, www.tue.nl*
[3] *Leiden Institute of Chemistry, Leiden University, Leiden, The Netherlands, www.surfcat.leidenuniv.nl*

Cavity Ring-down spectroscopy is installed at the linear plasma generator Pilot-PSI to determine neutral atom densities in the plasma near a carbon target. This will allow to investigate the importance of neutral particles for the chemical erosion rate of carbon in hydrogen plasma. In this contribution we present the implementation of CRDS at Pilot-PSI and show first results on absolute H(n=2) densities measured in the Pilot-PSI plasma.

1. Introduction

The FOM-Institute for Plasma Physics Rijnhuizen is building the linear plasma generator Magnum-PSI for fundamental research on Plasma Surface Interaction (PSI) in the unexplored regime of plasma conditions as expected in the divertor of ITER [1]. The heart of this device will be a high flux plasma source that is being developed at the forerunner Pilot-PSI. In this device, we have already demonstrated extreme hydrogen plasma conditions: electron densities up to $8 \cdot 10^{20}$ m^{-3} at a temperature of ~2 eV in a magnetic field of 1.6 T [2]. Based on these numbers, Pilot-PSI has become a unique experiment for plasma surface interactions in its own right and is as such used to investigate the erosion of carbon under ITER relevant hydrogen plasma fluxes [3].

Carbon is a candidate material for the ITER divertor. However, chemical erosion by the low temperature hydrogen plasma expected in the divertor might be incompatible with prolonged operation. Erosion studies are traditionally focused on the effect of ionized particles. We are presently undertaking first attempts to assess the importance of neutrals in the erosion processes. This is based on measurements of the neutral atom density with Cavity Ring-down Spectroscopy (CRDS), which is the subject of the present paper. We will describe the implementation of CRDS at Pilot-PSI and present first results on H(n=2) atom densities in the plasma.

2. Experimental

The hydrogen plasma jet in Pilot-PSI (Fig. 1) is produced with a wall stabilized cascaded arc plasma source [2]. Typical operation parameters are: 100 A discharge current, 2 slm gas flow rate, 0.1 bar inlet gas pressure. The plasma expands into a vacuum vessel at ~0.03 mbar where it is confined by a magnetic field up to 1.6 T and directed onto a carbon target at 0.5 m. The carbon targets (Fine Grain Graphite, R 6650, SGL Carbon Group), 30 mm in diameter and 4 mm thick, were clamped on an actively cooled heat sink.

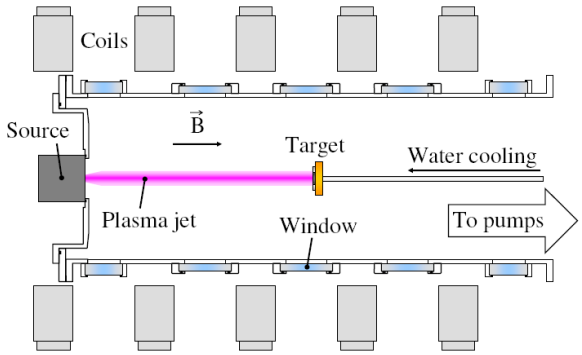

Fig. 1: Schematic layout of the Pilot-PSI linear plasma generator

In order to probe the line integrated H(n=2) number densities, we used light at the Balmer-α wavelength. This was produced with a wavelength-tunable pulsed dye laser (Sirah, Cobra Stretch) pumped with the frequency doubled output of a Nd:YAG laser (LAB-170, Spectra-Physics; 10 Hz, 0.5 J/pulse). The cavity was formed with two high-reflective mirrors (Layertec GmbH, Art. 102314) placed 0.78 m apart. The laser beam was coupled into the cavity without further beam shaping. A 10 nm wide bandpass filter for Balmer-α light was used to block the spontaneous emission of the dye laser. The light leaking out of the cavity was measured with a photomultiplier tube. The cavity was installed either at 40 mm downstream the plasma source or at 18 mm in front of the carbon target. Saturation effects were not observed in a scan of the cavity laser power over two orders of magnitude.

3. Results

Absorption spectra ($1/c\tau$ versus wavelength, with c the speed of light and τ the measured ring down time) recorded at different discharge gas flows at 40 mm from the cascaded arc are presented in Fig. 2.

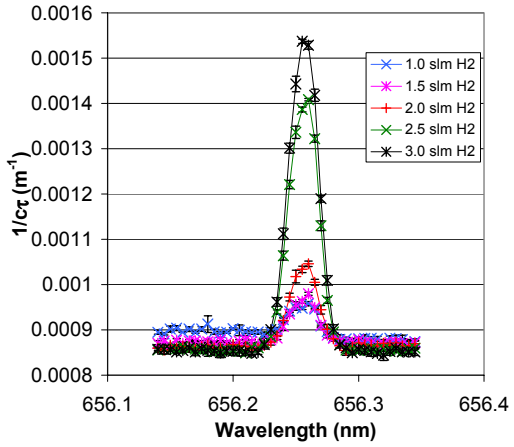

Fig. 2: CRDS absorption spectra at different discharge gas flows at 40 mm downstream the plasma source. The increasing absorption reveals larger H(n=2) column densities at higher gas flows.

These spectra already indicate that the H(n=2) density increases with gas flow. The column density (line integrated density) can be determined from the area under the absorption peak. For this, we write according to Rennick *et al.* [4]:

$$D_{H(n=2)} = dN_{H(n=2)} = \frac{L}{c}\frac{\int \Delta\kappa d\nu}{\int \sigma d\nu},$$

with d the path length through the absorbing species, N the number density of H(n=2), σ the cross section of light absorption (as a function of the light frequency), and L the length of the cavity. The cross section for the Balmer-α transition follows from the average Einstein transition coefficient A_{kj}, which we have taken from Wiese *et al.* [5]:

$$\int \sigma_{jk} d\upsilon = \frac{1}{8\pi} A_{kj} \lambda_{kj}^{\ 2} \frac{g_k}{g_j}.$$

Here, g_k and g_j are the statistical weights of the levels, which are 18 and 8, respectively. The value is $1.7 \cdot 10^{-2}$ $cm^2 s^{-1}$. We use this to calculate the column densities that are plotted in Fig. 3.

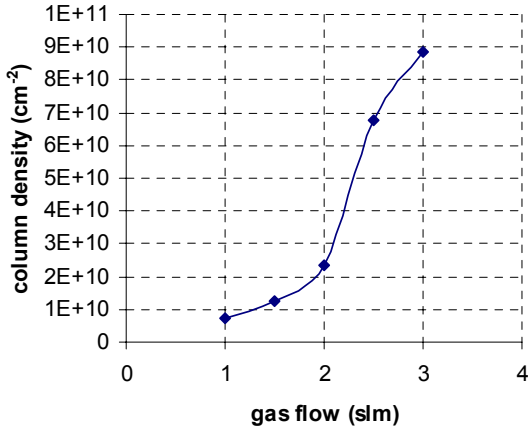

Fig. 3: The column density (line integrated density) at different discharge gas flows. These are calculated from the CRDS absorption spectra in Fig. 2.

This graph shows a sharp increase in H(n=2) column density around a gas flow of ~2.5 slm. This complex dependence is due to the H(n=2) production mechanism, which is expected to be predominantly Molecular Assisted Recombination (MAR): charge exchange [6]

$$H^+ + H_2 \rightarrow H(1s) + H_2^+,$$

followed by dissociative recombination

$$H_2^+ + e \rightarrow H(n\geq 2) + H(1s).$$

Both the ion flux from the source and the molecular background density in the vessel increase with the source gas flow. Thus on the one hand the local rate of H(n=2) formation is increased, at the other hand more recombination has occurred along the distance between source exit and the CRDS detection volume. In addition,

also the (excited) atom flux produced by the source increases with the gas flow.

4. Conclusions and outlook

CRDS was successfully installed at Pilot-PSI. This was demonstrated on the basis of H(n=2) number density measurements in Pilot-PSI in the absence of magnetic fields. Presently, data are collected for magnetized plasmas, near a solid surface that is exposed to the plasma. These will be presented at the conference and will be used to gain insight in the importance of neutrals for carbon erosion yield measurements.

References

[1] A.W. Kleyn *et al.*, Phys. Chem. Chem. Phys. **8** 1761 (2006).
[2] G. J. van Rooij *et al.*, Appl. Phys. Lett. **90** 121501 (2007).
[3] J. Westerhout *et al.*, Phys. Scr. **T128** 18 (2007)
[4] C.J. Rennick *et al*., J. Appl. Phys. **97**, 113306 (2005).
[5] W.L. Wiese *et al.,* Atomic Transition Probabilities, Vol. 1 (National Bureau of Standards, Washington, DC, 1966)
[6] M.J. de Graaf *et al.,* Phys. Rev. E **48** 2622 (1993); N. Ohno *et al.*, Phys. Rev. Lett. **81** 818 (1998).

Spectroscopy and imaging by laser excited terahertz waves

M. Hangyo, M. Tani, S. Nagashima, H. Kitahara, M. Yamaguchi

Institute of Laser Engineering, Osaka University, 2-6 Yamadaoka, Suita, Osaka 569-0871, Japan

Recently, terahertz (THz) technology has developed greatly and has been expected to be used in various fields including basic science, industry, security, biomedical science, etc. In this paper, present status of THz technology using femtosecond lasers has been reviewed based mainly on our results. After explaining the method of emission and detection of THz waves using femtosecond lasers, the THz spectroscopic systems and their applications to characterization of various materials are presented. Next, THz imaging systems are introduced and some examples are described. Future applications of the THz technology to plasma diagnostics are also mentioned.

1. Introduction

Terahertz (THz) waves mean the electromagnetic waves in the frequency region of 0.1 ~ 10 THz (1 THz = 10^{12} Hz) and have been an unexploited region between the microwave and mid-infrared regions until quite recently. This situation is changing rapidly with the invention of emitting and detecting THz waves by various methods. Especially, the methods of THz radiation and detection using femtosecond lasers have a great influence on spreading of terahertz technology [1-3].

There are various types of excitation in the THz region for various materials (solids, liquids, gases) and these materials are characterized by measuring THz spectra. For example, the carrier density and mobility of a doped semiconductor can be deduced from the THz spectra. The gas species are identified by measuring the rotational spectra which can be used as fingerprints of gases.

In this paper, the emission and detection of THz waves by using femtosecond lasers are described. The spectroscopic systems using femtosecond laser excited THz waves named the THz time-domain spectroscopy (THz-TDS) are described [3,4] and their applications to the characterization of materials are shown [3,5]. By the scan of the THz beam [6] or two-dimensional detection using an electro-optic crystal [7,8], THz imaging is possible. The THz imaging systems and their applications are also described. Finally, future applications of THz waves to gas plasma diagnostics are mentioned.

2. THz emission and detection using femtosecond lasers

Figure 1 shows a THz emission and detection system using a femtosecond laser. For emission and detection of THz waves, the semiconductor photoconductive (PC) antennas are frequently used. The basic structure of the PC antenna is metal electrodes with a gap on a semiconductor film or substrate. The low-temperature grown GaAs (LT-GaAs) is appropriate as the film and many research groups use this antenna. The emitter PC antenna is voltage biased and the detector one is connected to a current preamplifier. The gap of an emitter PC antenna is irradiated by ultrashort optical pulses delivered from a mode-locked Ti: sapphire laser (time width ~ 50 fs, wavelength ~ 800 nm, repetition rate ~ 100 MHz). As a result, transient photocurrent flows in the gap and an ultrashort electromagnetic wave pulse is emitted into free space following the Maxwell equations. This pulse travels in free space and is focused to the detector PC antenna, which is triggered by optical pulses split from main optical pulses. The THz field accelerates the photocarrier in the detector PC antenna and the current flows across

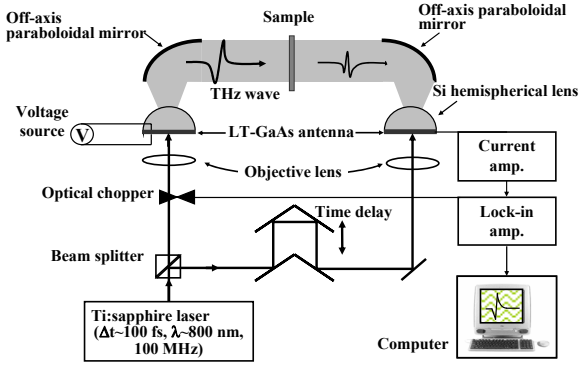

Fig. 1 : THz emission and detection system using a femtosecond laser.

the gap. By changing the time delay in Fig. 1, the waveform of the THz electric field can be obtained. A typical measured waveform is shown in Fig. 2 (a). The pulse has very narrow time width of 0.25 ps. By the Fourier transformation, the power spectrum can be calculated as shown in Fig. 2 (b), showing very broad band emission up to ~ 150 cm^{-1} (4.5 THz).

The PC antenna has flexibility of design and various new function can be added. Figure 3 shows a four-contact electrode PC antenna for polarization control of emitted THz waves [9]. Since the polarization direction of the emitted THz waves is parallel to the direction of the acceleration of photocarriers, the polarization is changed by changing the polarity of the bias voltage applied to the four electrodes as shown in Figs. 3 (a) and (b). Further, the circularly polarized THz waves in the wide frequency region can be obtained by adding a silicon prism. The polarization of THz waves can be analyzed by a similar multi-contact electrode PC antenna used as a detector [10].

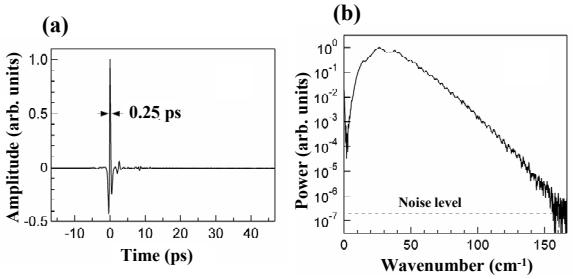

Fig. 2 : (a) Waveform and (b) its power spectrum of THz waves emitted from the PC antenna.

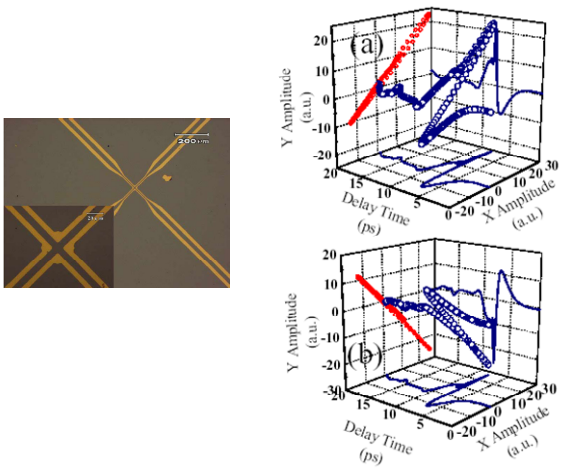

Fig. 3 : Photograph of a four-contact electrode PC antenna and polarization trajectories of THz waves emitted from it.

3. THz time-domain spectroscopy and its applications

The THz time-domain spectroscopy (THz-TDS) is a unique spectroscopic method utilizing the detection of time-domain THz waveforms [4]. In this spectroscopy, a plane-parallel sample with a thickness d is inserted in the THz optical path as shown in Fig. 1 and the waveforms before and after inserting the sample, $E_r(t)$ and $E_s(t)$, are measured. The complex transmittance defined as $\tilde{E}_s(\omega)/\tilde{E}_r(\omega)$, where $\tilde{E}_r(\omega)$ and $\tilde{E}_s(\omega)$ are the complex Fourier transform of $E_r(t)$ and $E_s(t)$, respectively, is a function of the complex refractive index of the sample $\tilde{n}(\omega)=n(\omega)-i\kappa(\omega)$. From the measured complex transmittance, the complex refractive index is deduced. The complex dielectric constant $\tilde{\varepsilon}(\omega)$ and complex electric conductivity $\tilde{\sigma}(\omega)$ can be obtained from $\tilde{n}(\omega)$. These procedures are summarized in Fig. 4. In addition to the standard transmission-type THz-TDS system, various types of THz-TDS system including a magneto-optical THz-TDS system have been developed [11].

As a typical example of the measurement and analysis, the results for a 400-μm thick silicon wafer doped with phosphor is described below [12]. The resistivity of the sample is 1.1 Ωcm. Figure 5 (a) shows the temperature dependence of a waveform of the THz pulse transmitted through the sample together with a reference waveform. The amplitude of the waveform increases with decreasing temperature owing to freezing-out of the carriers. Figs. 5 (b) and (c) are

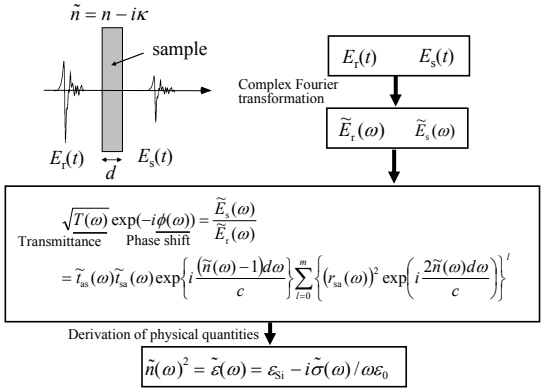

Fig. 4 : Procedures for deducing complex optical constants from the measurement of THz waveforms.

the transmittance and phase shift obtained from the data shown in Fig. 5 (a). Figs. 5 (d) and (e) show the real and imaginary parts of the complex conductivity, showing remarkable changes caused by the changes of the carrier density and mobility. The conductivity spectra can be analyzed by the simple Drude model for free carriers, which is shown in Fig. 6. The temperature dependence of the carrier density and mobility deduced is consistent with the

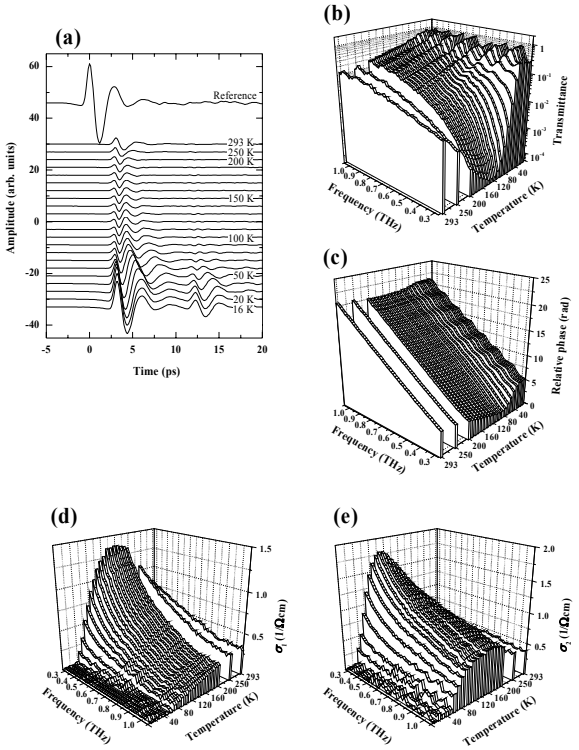

Fig. 5 : Temperature dependence of (a) the THz waveform transmitted through doped silicon, (b) power transmittance, (c) phase shift, (d) real part of the conductivity, and (e) imaginary of the conductivity.

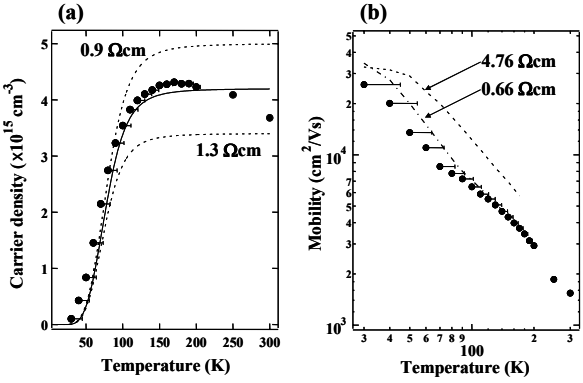

Fig. 6 : (a) Carrier density and (b) mobility deduced from the data shown in Fig. 5 with the Drude model fitting.

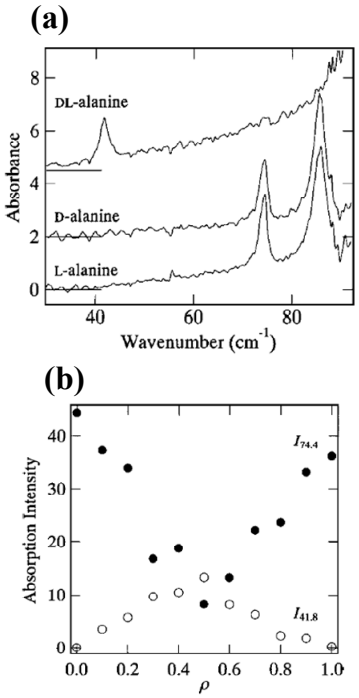

Fig. 7 : (a) THz absorption spectra of L-, D-, and DL-alanine and (b) the dependence of the intensities of the 74.4 and 41.8 cm^{-1} modes on the composition ratio of D-alanine.

values obtained theoretically and by the Hall measurement. This result demonstrates that the carrier density and mobility can be deduced by the THz-TDS without electrical contacts and magnetic field.

We show another example. Figure 7 (a) shows the spectra of polycrystalline L-, D-, and DL-alanine, which are one of the amino acids [13]. The observed sharp lines are assigned mainly to intermolecular vibrations. L- and D-alanine are optical isomers with each other and DL-alanine is a racemic compound. The spectra of L- (D-) alanine and DL-alanine are quite different with each other. Fig. 7 (b) shows the change of the intensities of the 74.4 cm^{-1} line characteristic to L- (D-) alanine and the 41.8 cm^{-1} line characteristic to DL-alanine as a function of the relative D-alanine content ρ for mixtures recrystallized from water solution. The linear change of the intensities indicates that the composition of the L- and D- mixture can be determined from the THz spectra. The THz spectra are also effective for identifying gas species since the gases have their characteristic rotational spectra.

4. THz imaging

THz waves have following unique properties:

(1) Plastics, papers, and ceramics transmit THz waves rather well.

(2) Liquid water absorbs THz waves strongly.

(3) THz waves are safe for human bodies in contrast to ionizing electromagnetic waves such as X rays.

(4) THz waves are not transmitted for long distance in air.

Based on these properties, THz imaging is expected to be used for various purposes [6,14]. For the THz imaging system using femtosecond lasers, two types of imaging method exist: (1) raster scan type imaging, in which the data is obtained at each points successively by scanning a focused beam on a sample, and (2) two-dimensional electro-optic (EO) imaging using an EO crystal and CCD (or C-MOS) camera. The obtained images have good S/N ratio for the former but the long acquisition time is needed, and the image acquisition time is short for the latter but the S/N ratio is relatively low.

The tomographic imaging can be possible using the reflection-type THz-TDS system [15,16]. Figure 8 shows a raster scan-type reflection imaging system. Since waveforms are measured in the time domain, the waves reflected from the interfaces or inner structures of the sample appear in time regions different from the front surfaces of the sample. Therefore, the inner structures of the sample can be imaged by this method. This method is similar to the tomographic imaging using ultrasound. Figure 9 shows a one-dimensional tomographic image of a raw horse mackerel's eye. Some inner structures of a cornea are seen in the image.

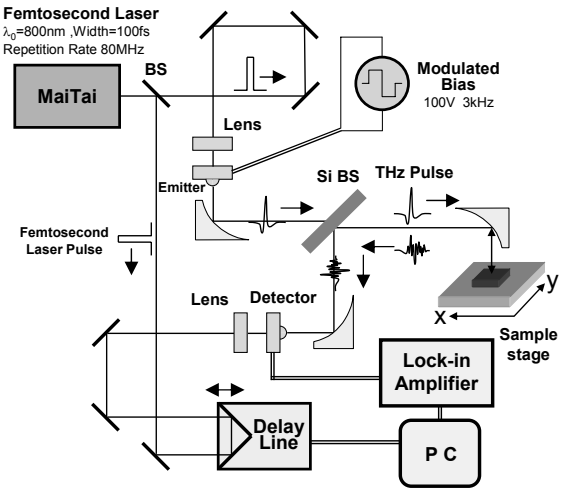

Fig. 8 : Schematic diagram of the reflection-type THz imaging system.

5. Summary

Recent THz technologies using femtosecond lasers including spectroscopy and imaging are described. These technologies are growing rapidly and expected to be used in various fields as shown in Fig. 10. Recently, it is shown that these technologies are also useful for diagnostics of gas plasmas [17,18]. The analysis is essentially the same as that for solid plasmas of carriers in doped semiconductors shown in section 2 in this

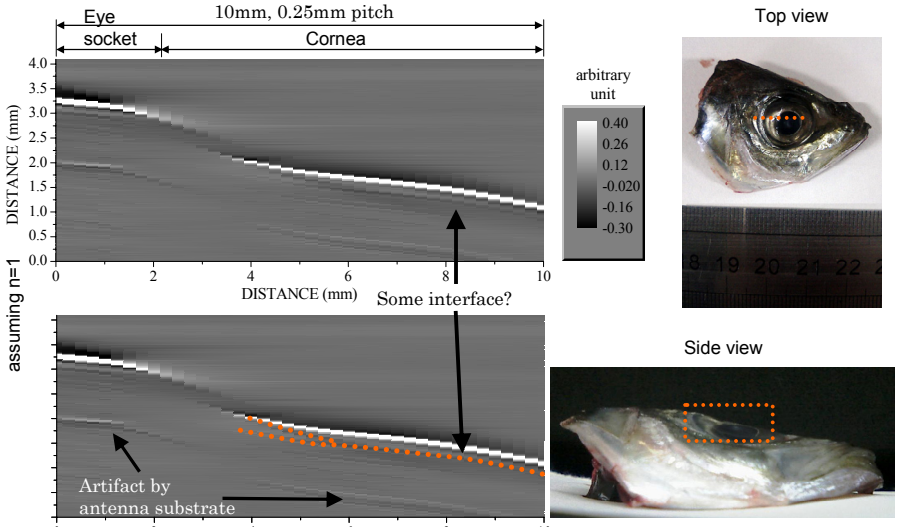

Fig. 9 : THz tomographic image of the raw horse mackerel eye.

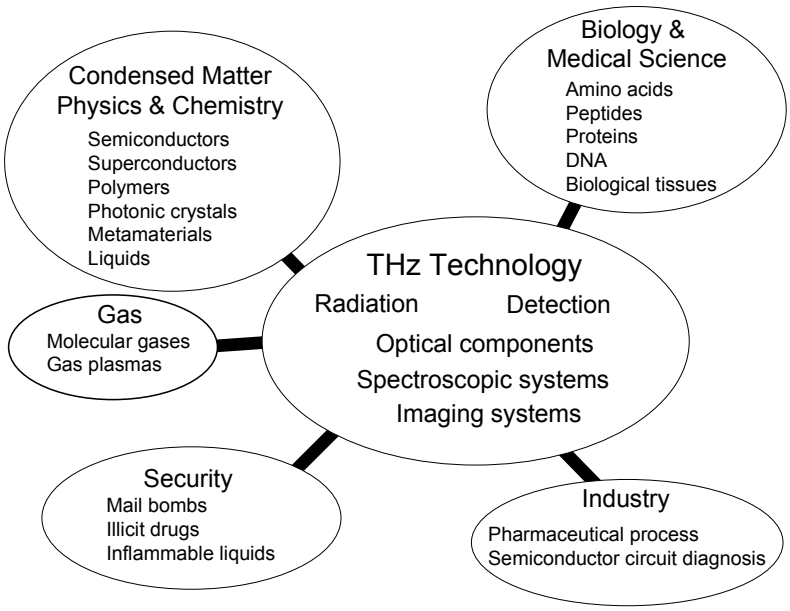

Fig. 10 : Possible applications of THz technology.

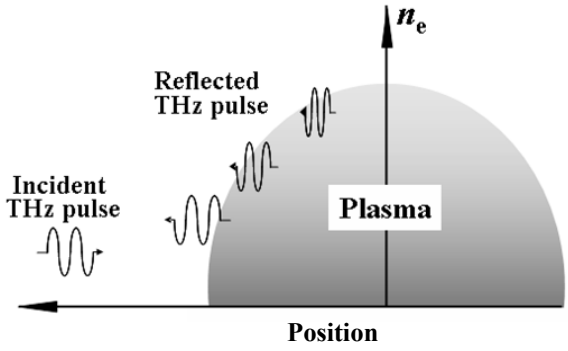

Fig. 11 : Schematic illustration of fusion plasma diagnostics by THz wave pulses.

paper. Reflectometry using pulsed THz waves may be also effective for the diagnostics of high-density plasmas of ITER because the plasma density distribution can be deduced by measuring the reflected waveforms in time domain as shown in Fig. 11 [19-21].

Acknowledgments

This work has been supported partly by Terahertz Optics Project for Medical Application lead by J. Nishizawa, organized by Ministry of Education, Culture, Sports, Science, and Technology, Japan. This work has also been supported partly by a Grant-in-Aid for Scientific Research from the Japan Society for the Promotion of Science.

References

[1] D.H. Auston, K.P. Cheung, P.R. Smith, Appl. Phys. Lett. **45**, (1984) 284
[2] *Sensing with Terahertz Radiation*, *edited by* D. Mittleman (Springer, Berlin, 2003)
[3] *Terahertz Optoelectronics*, *edited by* K. Sakai (Springer, Berlin, 2005)
[4] M. Hangyo, M. Tani, S. Nashima, Meas. Sci. Technol. **13**, (2002) 1727
[5] M. Hangyo, M. Tani, T. Nagashima, Int. J. Infrared and Millimeter Waves **26**, (2005) 1661
[6] B.B. Hu and M.C. Nuss, Opt. Lett. **20**, (1995) 1716
[7] Q. Wu, T.D. Hewitt, X.-C. Zhang, Appl. Phys. Lett. **69**,(1996) 1026
[8] F. Miyamaru *et al*., Jpn. J. Appl. Phys. **43**, (2004) L489
[9] Y. Hirota, R. Hattori, M. Tani, M. Hangyo, Opt. Express **14**, (2006) 4486
[10] E. Castro-Camus *et al*., Appl. Phys. Lett. **86**, (2005) 254102
[11] H. Sumikura, T. Nagashima, H. Kitahara, M. Hangyo : Jpn. J. Appl. Phys. **46**, (2007) 1739
[12] S. Nashima *et al*., J. Appl. Phys. **90**, (2001) 837
[13] M. Yamaguchi *et al*., Appl. Phys. Lett. **86**, (2005) 053903

[14] B. Feruguson, X.-C. Zhang, Nature Materials **1**, (2002) 26
[15] D.M. Mittleman *et al*., Opt. Lett. **22**, (1997) 904
[16] H. Kitahara *et al*., IEEJ Trans. **127-A**, (2007) 391
[17] S.P. Jamison *et al*., J. Appl. Phys. **93**, (2003) 4334
[18] B.H. Kolner *et al*., Appl. Phys. Lett. **87**, (2005) 151501
[19] G. Vayakis *et al*., Nucl. Fusion **46**, (2006) S836
[20] T. Tokuzawa *et al*., *in Abstracts of the 16th Int. Toki Conf.* (NIFS, Toki, 2006) P5-18, 86
[21] M. Hangyo *et al*., to be published in Plasma and Fusion Research

Development of a THz CW gyrotron FU CW III

T. Idehara, La Agusu, H. Mori, S. Kobayashi, T. Saito, I. Ogawa and S. Mitsudo
Research Center for Development of Far Infrared Region, Uiversity of Fukui (FIR FU)
3-9-1 Bunkyo, Fukui-shi 910-8507, Japan
Idehara@fir.fukui-u.ac.jp

The new gyrotron series in FIR FU, so-called Gyrotron FU CW Series is being developed for application to high power THz technologies. Gyrotron FU CW II with an 8 T liquid He free superconducting magnet, the second gyrotron of the series, has been constructed and the operation test was successfully carried out. It will be used for enhancing the sensitivity of 600 MHz proton-NMR by use of Dynamic Nuclear Polarization (DNP). The designed operation mode of the gyrotron is $TE_{2,6}$ at the second harmonic. The corresponding frequency is 394.6 GHz. The real operation frequency is 394.3 GHz at TE_{06} mode, because of fabrication error of the diameter of the cavity. The operation is in complete CW at the output power of around 30 W or higher at the TE_{06} cavity mode. There are many other operation modes at the fundamental and the second harmonic. Typical output power of the fundamental and the second harmonic are higher than 100 W and 20 W, respectively. The thirs gyrotron, Gyrotron FU CW III with 20 T superconducting magnet has already been designed and the construction has been completed. The operation test has started. Such a present status of high frequency gyrotrons in FIR FU covering sub-THz to THz range is introduced.

1 Introduction

Gyrotron FU Series has already achieved high frequency operation up to 0.89 THz by using a 17 T magnet and the second harmonic operation. Recently, a gyrotron in FIR FU with a 21 T pulse magnet achieved the breakthrough of 1 THz. In the gyrotron, a demountable gyrotron tube is installed on the center axis of 21 T pulse magnet. In the operation test, a high voltage pulse is applied to electron gun installed in the region of the maximum field intensity B. When B is changed, many cavity modes are excited at the fundamental and second harmonic of electron cyclotron frequency. The second harmonic radiation is separated from the fundamental by using a high pass filter. Observed frequencies are ranged from 395 GHz to 1,005 GHz. The maximum frequency is achieved by the second harmonic operation of $TE_{6,11}$ cavity mode. Corresponding field intensity B is 19.1 T. Now we are trying to increase the frequency by increasing B.[1)]

For convenience of the application, CW gyrotrons (Gyrotron FU CW Series) is being developed. Gyrotron FU CW I has been developed and succeeded in the CW operation at 300 GHz under high power of 1.8 kW. The next gyrotron, Gyrotrons FU CW II and III are being developed. The parameters are as follows, 400 GHz, 100 W and 1 THz 100 W under CW operation. These gyrotrons will be used for development of high power THz technologies, for example, Plasma diagnostics, DNP-NMR, etc.

2 Gyrotron FU CW II

Just, we have finished the construction of Gyrotron FU CW II and begun the operation test. Fig. 1 shows a cross section of the gyrotron and Photo 1 does the side view.

The gyrotron consists of a 8 T He-free superconducting magnet, a demountable tube, a vacuum pump system and power supplies. The cavity is a simple cylindrical one whose diameter and length are 5.72 mm and 15 mm. The designed frequency is 394.6 GHz at the second harmonic operation of TE_{26} cavity mode. After completing the operation test, the gyrotron will be used for enhancement of NMR sensitivity by use of dynamic nuclear polarization (DNP). 394.6 GHz is corresponding to ESR frequency at the field intensity of around 7.1 T. The frequency of proton NMR at the field is 600 MHz.

We have already succeeded to operate the gyrotron at many fundamental and second harmonics.

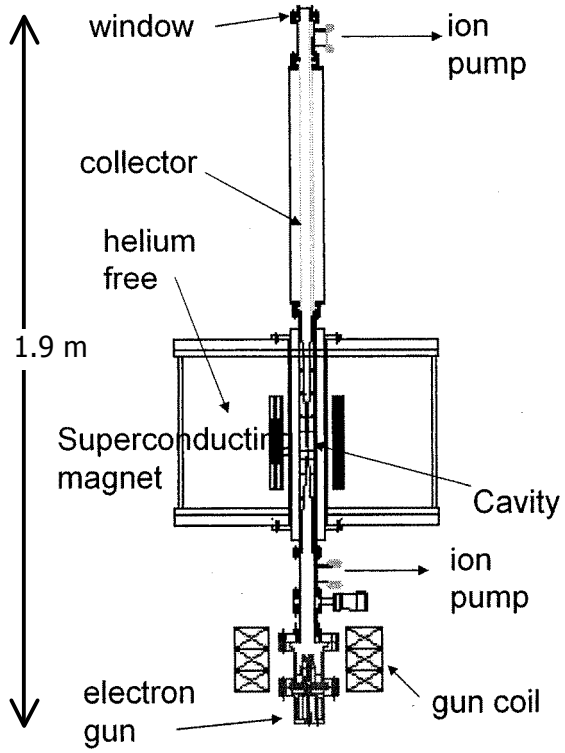

Fig. 1 The cross section of Gyrotron FU CW I

Photo. 1 A side view of Gyrotron FU CW II

First of all, we have measured radiation power from the gyrotron as function of magnetic field intensity. The operation is in a pulsed mode. The repetition rate is 1 Hz and the duty ratio typically 10 to 30 percent. The pulsed output radiation power is sampled and recorded on an XY recorder. Fig. 2 shows the results. In the upper trace, radiation power measured directly after the window is traced as a function of magnetic field intensity, while in the lower trace, radiation power coming out through a high-pass filter with a small circular waveguide is traced as a function of the field intensity. The diameter and the cut−off frequency are 0.7 mm and 251 GHz, respectively. Therefore, the upper trace includes both the fundamental and the second harmonic radiations, while the lower trace only second harmonics. As seen in the figure, the widths of radiation peak in the lower trace (second harmonics) are much narrower than those in the upper trace (mainly fundamentals). Some of the radiation peaks in the lower trace are seen in the upper trace at the same magnetic field intensity. This means that these second harmonic operations occur in single modes without mode competition with any fundamental operation modes. These features are predicted by the computer simulation

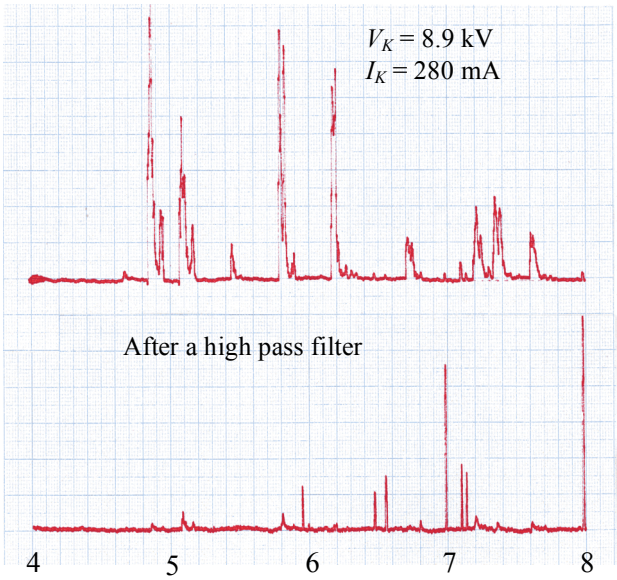

Fig. 2 Radiation power from the gyrotron FU CW II as functions of magnetic field intensity. Upper trace: Radiation power measured just after the output window. Lower trace: Radiation power coming out through the high pass-filter with a thin circular waveguide whose diameter is 0.7 mm. (The corresponding cutoff frequency is 251 GHz.)

demonstrated in our previous paper,[2] and are very important for our high frequency, harmonic gyrotron. Almost all radiation peaks appearing in the both traces correspond to cavity modes whose mode numbers have been identified by observed frequencies.

Next, the operation mode switched from pulsed mode to CW mode. Output power just after the output window for all of observed radiation peaks is measured by use of a water load. The results are shown in Tables 1 and 2. Observed powers are distributed in the ranges of 100 to 200 W for fundamental operations and 10 to 30 W for second harmonic operations. All of these powers are obtained by single mode CW operations even in the cases of second harmonics. Therefore, these are useful and convenient for its application to many new technologies in the sub-THz frequency range.

The frequencies for all of radiation peaks in both the fundamental and the second harmonic operations are measured by a spectrum analyzer with a heterodyne detection system which consists of a synthesizer as a local oscillator and a harmonic mixer. From this measurement, the cavity modes can be identified and listed in both tables. In the tables, azimuthal and radial mode numbers m and n are shown. The results of frequency measurement are shown as f_{meas} in Tables 1 and 2 with the calculated frequencies as f_{cal} for the designed cavity.

Table 1 Operation parameters of gyrotron FU CW II at the fundamentals (n=1). Here, are demonstrated the main field intensity B_0 in T at the cavity region, observed output power P in W, acceleration voltage for electrons V_b in kV, beam efficiency μ in %, measured frequency f_{meas} in GHz and corresponding cavity mode number m,n.

B_0,T	P,W	V_b,kV	μ,%	f_{meas},GHz	$TE_{m,n}$
3.86	130	9.74	5.1	107.48	1,2
4.84	210	9.68	6.8	134.95	2,2
5.10	95	9.68	3.1	141.28	0,2
5.83	100	9.72	3.7	161.34	3,2
6.19	158	9.69	5.3	171.73	1,3
6.74	126	9.71	4.5	186.65	4,2
7.22	180	9.79	8.8	200.43	2,3
7.38	170	9.82	9.6	204.54	0,3
7.62	181	9.81	9.7	211.40	5,2

Table 2 Operation parameters of gyrotron FU CW II at the second harmonics (n=2). Demonstrated operation parameters are the same as those in Table1.

B_0,T	P,W	V_b,kV	μ,%	f_{meas},GHz	$TE_{m,n}$
6.9860	17.9	9.62	0.49	386.03	4,5
7.15	24	13.66	0.52	392.25	2,6
7.19	32	13.675	0.72	394.27	0,6
7.98	5.3	9.62	0.14	440.93	6,5

We have confirm that the measured frequencies are lower than calculated frequencies by about 0.57 percent. This differences come from the fabrication error of the cavity radius. The error is also 0.57 percent and real size of the radius is larger by 14 μm. The frequency of $TE_{0,6}$ mode at the second harmonic opration shown in Table 2 is close to the principally designed frequency, that is, 394.6 GHz of TE_{26} mode. The output power is larger than 30 W. This means that the output power of this mode is available as a radiation source for 600 MHz DNP/ proton-NMR. Many other observed frequencies are also useful for sub-THz spectroscopy, for example, ESR measurement, plasma diagnostics and so on. All frequencies observed up to the present are plotted as functions of magnetic field intensity in Fig. 3.

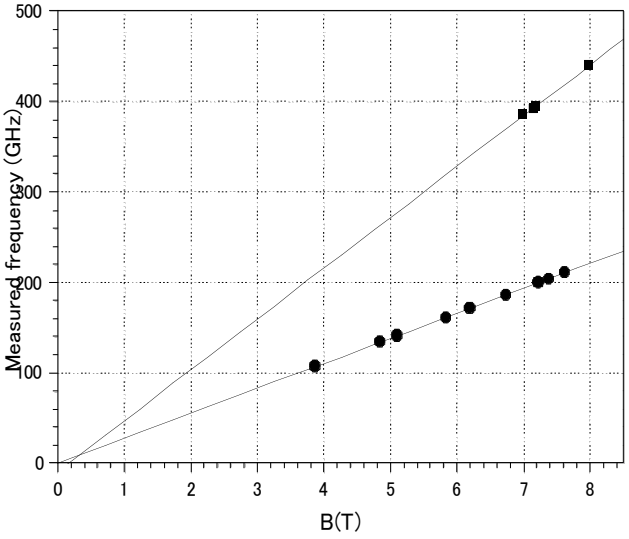

Fig. 3 All of observed frequencies as functions of magnetic field intensity.

The beam efficiency μ is estimated by dividing the measured output power P by the input power of electron beam $V_b \cdot I_b$ and demonstrated in Tables 1 and 2. It ranges from 3 to 10 percent

for fundamental operations and from 0.1 to 0.7 percent for second harmonic operations. The efficiency at the fundamentals is quite high even at low voltage operation lower than 10 kV.

Next, we tried to measure the dependency of output power P on the beam current I_b for several operation modes, $TE_{2,3}$ at the fundamental, $TE_{2,6}$ and $TE_{0,6}$ at the second harmonic. The beam electron energy is kept at the constant values of around 9 keV and 14 keV, respectively. The measurement results are shown in Fig. 4. It seems that output power for all modes is saturated even at low beam current I_b around 300 mA. In the present case, the beam electron energy is low: around 9 keV for fundamentals and around 14 keV for second harmonics. The low saturation level may result from such low beam electron energy. Hopefully, it will be increased by increased beam electron energy V_b.

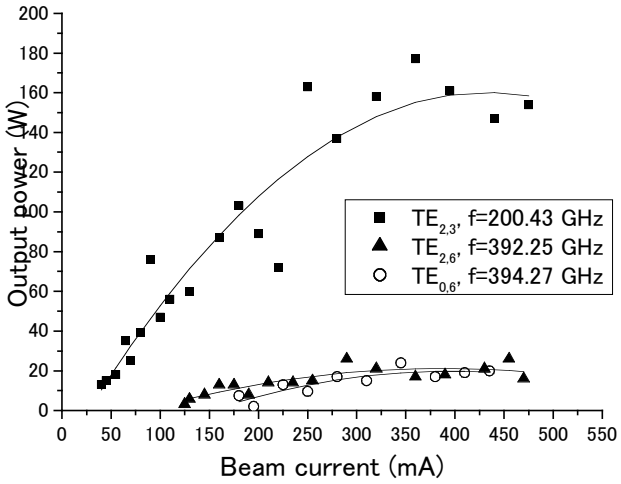

Fig. 4 Observed output power P for $TE_{2,3}$ mode at the fundamental, $TE_{2,6}$ and $TE_{0,6}$ modes at the second harmonics as functions of beam current I_b.

Fig. 5 shows a typical frequency spectrum for $TE_{0,6}$ mode operation at the second harmonic. (The frequency is 394.27 GHz.) A heterodyne detection system with a synthesizer as a local oscillator and a harmonic mixer are used for the measurement. The frequency is quite stable. The fluctuation is an order of 10 kHz. The quality of the spectrum is also excellent. As seen in Fig. 5, the half value width is several kHz and the width for 10 dB lower is around 10 kHz. This means that gyrotron FU CW II can be available for spectroscopy with high frequency resolution.

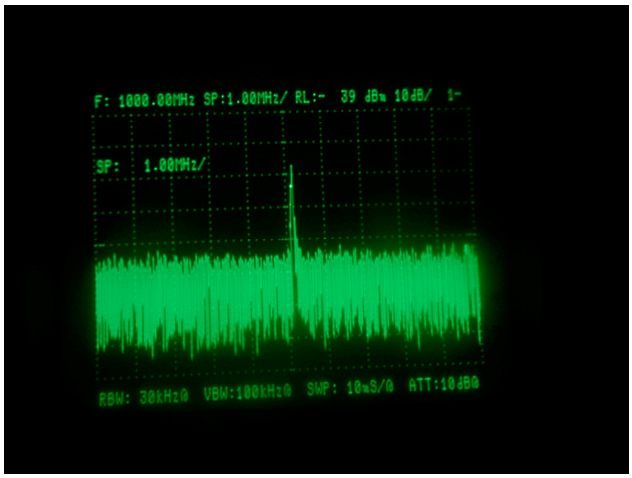

Fig. 5 A frequency spectrum for TE_{06} mode operation at the second harmonic. Horizontal: 1 MHz/div. Vertical: log scale.

3 Gyrotron FU CW III

We have completed the design of a new gyrotron, Gyrotron FU CW III[3]. It consists of 20 T superconducting magnet and a demountable gyrotron tube. The diameter and length of the cavity are 3.9 mm and 10 mm, respectively. The designed operation frequency is increased up to 1.014 THz, which will be achieved by the second harmonic operation of $TE_{4,12}$ cavity mode at the magnetic field intensity of 19.1 T. Expected output power is higher than 0.1 kW. The main parameters are summarized in Table 3. It has been constructed and the operation test already began recently.

Table 3 Main parameters of Gyrotron FU CW III

Total height (electron gun to the window): 2.4 m	
Maximum magnetic field: 20 T (The bore: 50 mm)	
Cavity :	radius: 1.95 mm
	length : 10 mm
	frequency: 1013.7 GHz
	Operating mode: $TE_{4,12}$
	Q-factor : 23720
	Operating magnetic field: 19.1 T
Triode MIG:	Cathode radius: 4.5 mm
	Maximum cathode current: 1 A
	Cathode voltage: 30 kV300 A
	Maximum magnetic field: 20 T
Gun coil :	Maximum input current: 0.183 T

Fig. 6 shows a cross-section of the Gyrotron FU CW III.

Fig. 7 shows a typical result of radiation measurement as a function of magnetic field intensity B. There are many radiation peaks corresponding to cavity modes. Almost all

cavity modes are excited in the fundamental operations.

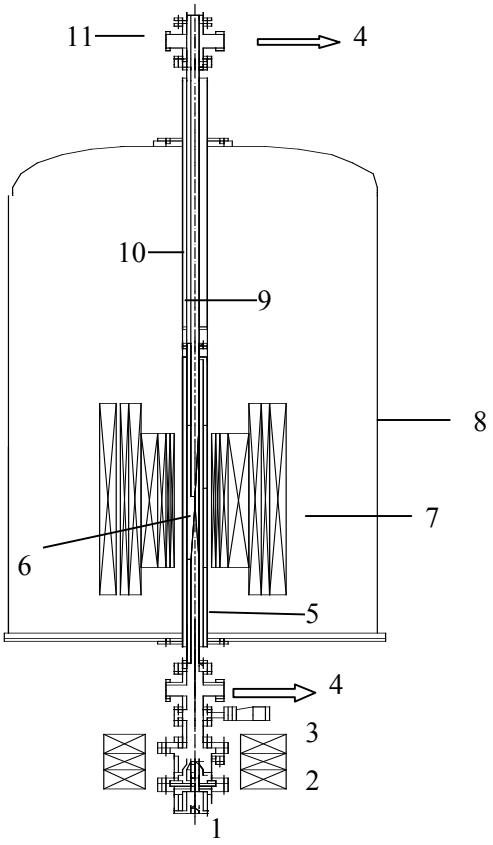

Fig. 6 The cross-sectional view of the cylindrically symmetric 1 THz CW gyrotron tube. The gyrotron tube is approximately 2.5 m long and magnet bore diameter is 5 cm.
1. Electron gun, 2. Gun coil, 3. Gate valve, 4. Tees to the pumping system, 5. Water jacket for cooling the cavity, 6. Cylindrical resonant cavity, 7.Superconducting magnet, 8.Cryostat, 9.Electron collector, 10.Water jacket for cooling the electron collector, 11.Output window

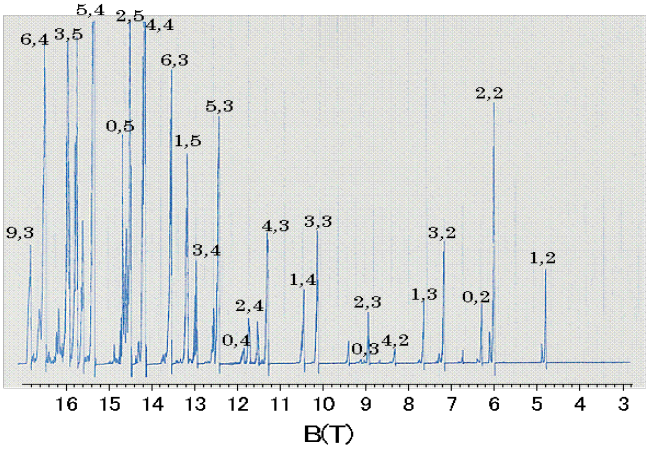

Fig. 7 Radiations coming from the fundamental operations as a function of mafnetic field B

A similar measurement for the second harmonic operations has also been carried out successfully. Fig. 8 summarizes the results. All frequencies expected from the excited cavity mode are plotted as functions of B. The maximum frequency achieved up to the present by the second harmonic operation is 965 GHz in the field range below 18 T. We hope to increase the field intensity up to 20 T for the second harmonic operation.

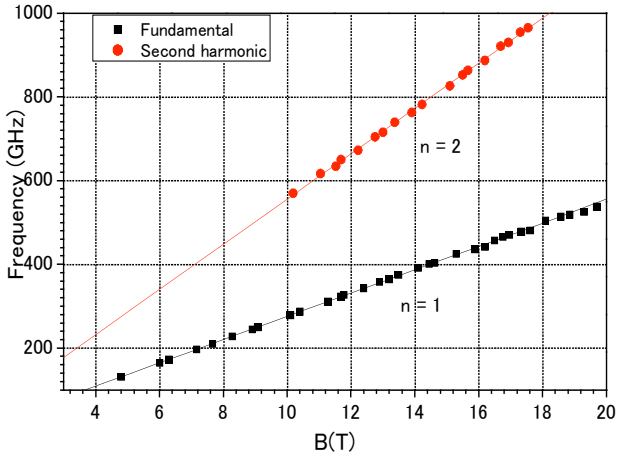

Fig. 8 All frequencies excited up to the present as functions of magnetic field B

4. Summary

THz CW Gyrotron Series in FIR FU are being developed successfully. Developed gyrotron will be used for application to high power THz technologies. The breakthrough of 1 THz CW operation will be achieved soon.

References

1) T. Idehara, H. Tsuchiya, O. Watanabe, La Agusu and S. Mitsudo, Int. J. Infrared and Millimeter Waves 27, 319 (2006).
2) T. Idehara, I. Ogawa, La Agusu, T. Kanemaki, S. Mitsudo, T. Saito, T. Fujiwara and H. Takahashi, Development of 394.6 GHz CW Gyrotron (Gyrotron FU CW II) for DNP/Proton-NMR at 600 MHz, Int. J. Infrared and Millimeter Waves **28**, 433 (2007).
3) La Agusu, T. Idehara, H. Mori, T. Saito, I. Ogawa, and S. Mitsudo, Design of a CW 1 THz gyrotron (Gyrotron FU CW III) using a 20 T superconducting magnet, Int. J. Infrared and Millimeter Waves **28**, 499 (2007).

Development of Light Source for Advanced Lithography

ArF laser part: Toru Suzuki, Kouji Kakizaki, Takashi Matsunaga, Satoshi Tanaka, Yasufumi Kawasuji, Masaya Yoshino, Takahito Kumazaki, Hiroshi Umeda, Hitoshi Nagano, Shinji Nagai, Youichi Sasaki and Hakaru Mizoguchi
Gigaphoton Inc.,400 Yokokura-Shinden Oyama-shi Tochigi 323-8558 JAPAN
and
EUV-source part: Akira Endo, Hideo Hoshino, Takashi Suganuma, Masato Moriya, Tatsuya Ariga, Yoshifumi Ueno, Masaki Nakano, Takeshi Asayama, Tamotsu Abe, Hiroshi Komori,Georg Soumagne, Akira Sumitani and Hakaru Mizoguchi
EUVA (Extreme Ultraviolet Lithography System Development Association), 1200 Manda Hiratsuka, Kanagawa, 254-8567, Japan

In 45nm node, the GT61A ArF laser light source with ultra line narrowed spectrum (<0.35pm), which meets the demand of hyper NA (NA > 1.3) immersion tool, is introduced. It indispensably requires OPC (optical proximity correction) and a narrower process window. The GT61A improves stabilization of spectrum performances by bandwidth control technology; Bandwidth Control Module (BCM) includes high accuracy measurement module which support the narrower bandwidth range and active bandwidth control module. For below 45nm node, a laser produced plasma light source for high volume manufacturing (HVM) EUV lithography is introduced. The light source is based on a short pulse, high power, high repetition rate CO_2 master oscillator power amplifier (MOPA) laser system and a Tin droplet target. In a first step, a 50W@I/F equivalent power light source is demonstrated experimentally. A maximum conversion efficiency of 4.5% and small debris on the corrector mirror position was measured. The CO_2 MOPA laser system is based on commercial high power cw CO_2 lasers, the light source is scalable to more than 100 W EUV in-band power.

1. Introduction

The 193-nm lithography has moved to the mass production phase and its target node is shifting from 65 nm to 45 nm. And the ArF-immersion technology is even spotlighted as the enabling technology for below 45nm node. We developed new GT61A for high NA (>1.3) immersion tool. We have already released an injection lock ArF excimer laser GT40A[1)]/GT60A[2)] since 1Q2005. New GT61A is based on the production proven GT (Giga Twin) platform, which has advanced Injection Lock system.

On the other hand, below 45nm node, EUV lithography is spotlighted because of its short wavelength and its potential resolution ability. A major technical challenge of EUV light source is the in-band power requirement of more than 115W at the intermediate focus. For a laser produced plasma (LPP) source the best selection of the drive laser and the target material is therefore very important. Instead, very high output power due to high amplification efficiency and high beam quality is readily available for cw CO_2 lasers. They are the most frequently used high power lasers for industry applications having low initial and operational cost, as well as robustness and reliability. Since 2002 we have proposed and continue to develop CO2 laser driven LPP EUV light source. In this paper, we introduce recent progress of LPP EUV source development.

Wide spectrum bandwidth of light source produce focus blur by the effect of chromatic aberration of projection lens. Narrower bandwidth is required for smaller design rule. Until now the full width at half maximum (FWHM) metric is widely used to describe the spectrum bandwidth. However bandwidth of 95% energy concentration (E95) metric has better correlation to the lithographic performance parameters.[3)] Figure 1 describes the spectrum specification for different NA of ArF scanners. The slopes below NA = 1 and beyond NA = 1 are different. The reason is that chromatic aberration of projection lens is reduced by the refractive-reflective optics design used for the immersion lithography scanners. As a result E95 less than 0.35pm specification is required for the design rule below 45nm.

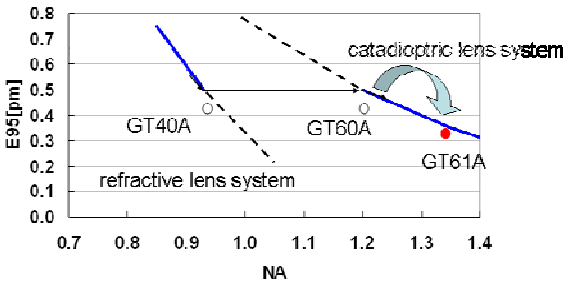

Figure 1. laser E95 specification vs NA

2. ArF laser for hyper NA immersion

2.1 Spectrum Performance Requirement

Generally, the influence of the focus shift on the CD becomes larger in isolated patterns than in dense patterns. Therefore isolated patterns are easy to be influenced by E95 variations. For better understanding of the E95 effect to the CD, CD sensitivity to E95 change for different pattern size is useful.[3] Figure 2 shows the simulation results for the hole patterns. The sensitivity increases as the pattern becomes smaller. To reduce the CD error for smaller design rule, E95 deviation must be suppressed. Change of E95 will also impact upon OPE (Optical Proximity Effect). Laser-to-Laser difference and fluctuation through the laser lifetime could cause variation in OPE tool matching and its stability. To answer these requirements the new laser whose E95 is less than 0.35pm and more stable E95 light source is essentially required.

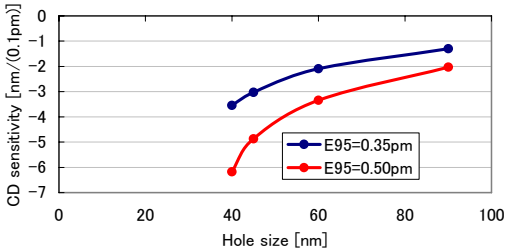

Figure 2. Simulation results of CD sensitivity for the hole pattern

As a answer of these requirement we developed new advanced technologies and installed on the GT61A. They are shown in figure 3. Each technologies are described following sub-chapter.

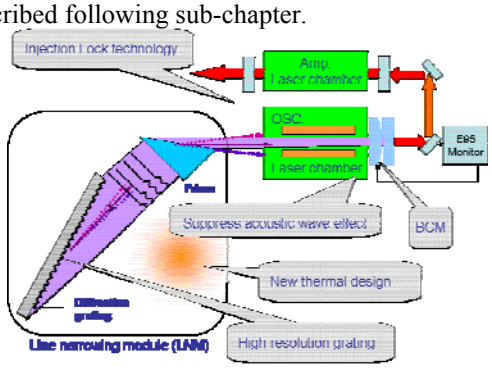

Figure 3. Advance technologies of GT61A

2.2 Low acoustic wave laser chamber

High repetition rate operation of excimer lasers faces two major technical challenges: 1) the occurrence of acoustic waves caused by the discharge in the laser chamber and 2) the huge energy consumption of the large gas flow fans. We succeeded to minimize the acoustic waves up to 6kHz by using computer simulation of acoustic wave generation inside the discharge chamber and measurement of the actual acoustic wave by using Mach-Zehnder interferometric observation at discharge plasma (Figure 4). [4]

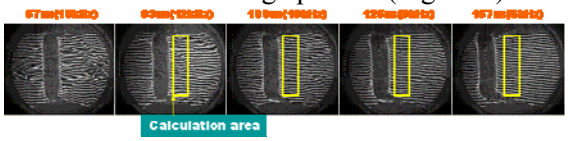

Figure 4. interferometric observation at discharge plasma

2.3 High resolution line narrowing module

In the lithography excimer laser, the module which makes narrow band spectrum is called line narrowing module (LNM). It is a kind of high-resolution monocrometer and works as a rear mirror of laser cavity. For the conventional ArF excimer laser the resolution, ratio between wavelength to bandwidth, of LNM is required about one million. Because GT61A needs to increase the resolution by 30%, new LNM is designed to achieve the less than 0.35pm bandwidth.

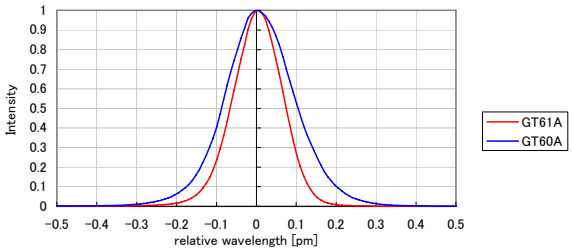

Figure 5. Spectrum profileGT61A: E95 0.25pm, GT60A: E95 0.35pm

In general speaking, when spectrum performance is increased, the efficiency to output the optical energy from the laser is decreased. To prevent this side effect, the improvement of injection lock efficiency and laser power supply without changing the size of laser were performed. Fig. 5 shows the typical spectrum profile of GT61A. Newly designed LNM achieved the E95 of 0.25pm. As a comparison, GT60A's profile is also plotted. Both profiles have good symmetry. The ratio between E95 and FWHM is about 2 for both lasers.

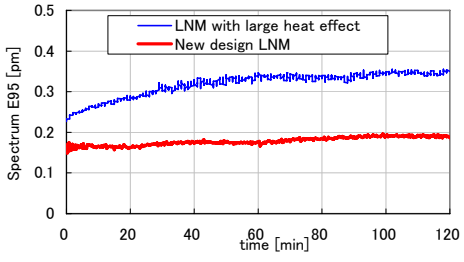

Figure 6. Long-term drift of E95

Figure 6 shows the effectiveness of heat design of new LNM. This test is performed by the 75% duty cycle operation with 60W (10mJ 6KHz), which is highest duty cycle for the laser. Start from the laser's cold condition, firing is started and continued about two hours. Upper line is the case of not good design for the heat. E95 became broader about 0.07pm. New

design LNM (lower line) suppresses long-term drift of the E95. It should be noted that this experiment is done without the E95 feedback control loop.

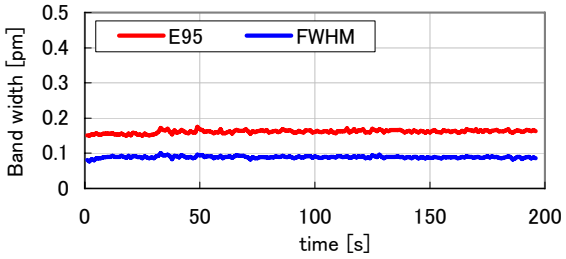

Figure 7. Short-term drift of E95

Also Figure 7 shows short-term drift of E95. It corresponds first two hundreds seconds of Fig. 4. Even such short-term operation within wafer exposure, new LNM maintains good stability. Figure 8 shows the repetition rate dependency of E95.This performance is mainly affected by the acoustic wave intensity in the laser chamber. New chamber design since GT60A shows very good performance.

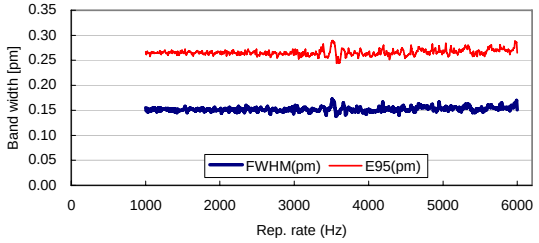

Figure 8. Repetition rate dependency of E95 and FWHM

2.4 High resolution E95 measurement module

The measurement of E95 is more difficult than that of FWHM because it is sensitive to the background light information. The on board spectrometer must be small enough to fit in the laser frame and stable over the lifetime of laser. To meet those requirements, new high resolution E95 measurement module is developed. The deconvolution method, which is same algorithm as the external spectrometer, is used to remove intrinsic error factor[5]. Figure 9 shows the repeatability of new E95 measurement module.

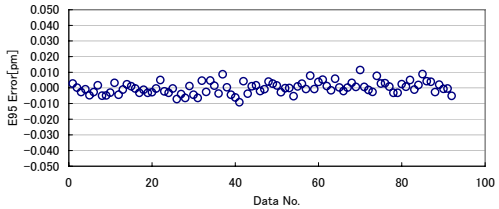

Figure 9. Repeatability of E95 measurement module

2.5 Advenced Bandwidth control module

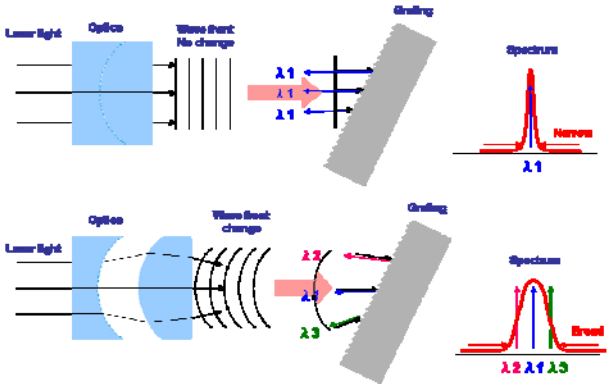

Figure 10. Bandwidth control module

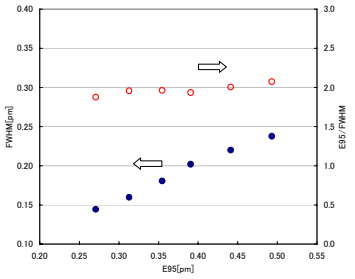

Figure 11. E95 and FWHM relationship for different points

Even the new LNM has good stability of E95, there are still small drift over the lifetime and laser-to-laser differences for the E95. It is important to maintain the same E95 value for every laser, E95 tuning function is essentially important. The new BCM is consist of active optical wave front control system. E95 is rapidly controlled by this BCM. The system is shown in Figure 10 (patent pending).

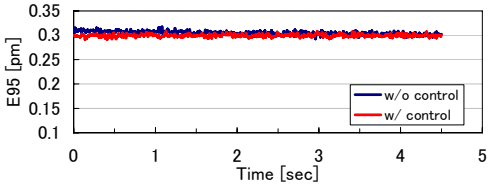

Figure 12-a. Short term (4sec), Target E95 = 0.3pm

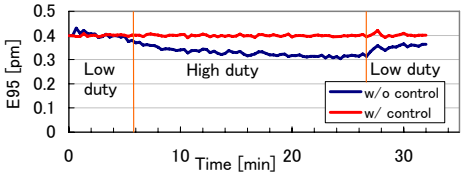

Figure 12-b. Middle term (30 min) ,Target E95 = 0.4pm

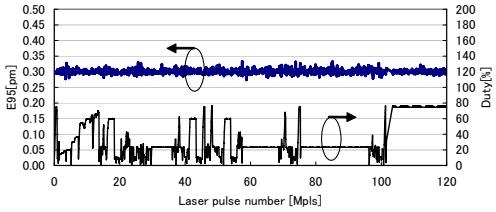

Figure 12-c. Long term (3days) stability of E95

Figure 12-a-b-c shows the BCM performance of GT61A. It describes the E95 changes from 0.25pm to

0.5pm. Filled dot (left axis) shows the FWHM of the spectrum and blanked dot (right axis) shows ratio between E95 and FWHM. This graph shows that the spectrum shape is always same for different E95. These are the BCM data for different time span, short term (four seconds), middle term (thirty minutes), and 3 day gas-life. All graphs show the BCM maintains the same E95 value at any time scale.

2.6 GT61A specification

In Table 1, summary of the specification of GT series lasers.[6] On GT61A longer life time than GT60A/40A is achieved. For the next generation high throughput scanner or double patterning scanner, the development of GT61A-1H which has higher power and high dose stability is planned.

Table 1. Major specification of GT series.

ArF model		GT40A	GT60A	GT61A
Wavelength	nm	193.4	193.4	**193.4**
Power	W	45	60	**60**
Pulse energy	mJ	11.25	10	**10**
Max rep. rate	Hz	4000	6000	**6000**
FWHM	pm	0.2	0.2	**N.A.**
E95	pm	0.5	0.5	**0.35**
Durability(Expected)				
MO Chamber	Bpls	13	13	**20**
PO Chamber	Bpls	19	19	**30**
LNM/ MO LNM	Bpls	-	-	**-**
MM	Bpls	30	30	**30**
FM/ PO FM	Bpls	12	12	**12**
PO RM	Bpls	12	12	**12**

3. LPP EUV light source

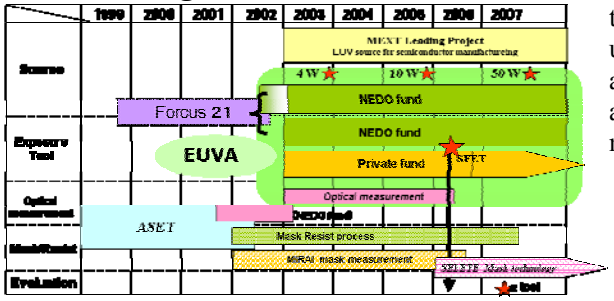

Figure 13. EUV lithography programs in Japan

Since 2003 EUV light source and exposure tool is developed in EUVA under Government fund. Figure 13 shows Japanese EUV lithography development programs. The current Laser Produced Plasma (LPP) light source development status including component development and EUV generation is described.

3.1 CO_2 laser LPP EUV source development

We started LPP EUV source research since the timing of establishment of EUVA in 2003, we concluded that solid-state Nd:YAG laser technology, which is currently limited to kW level output power, cannot be successfully used. Multiplexing of too many laser modules is required, which makes the system layout too complex and too expensive. Instead, very high output power due to high amplification efficiency and high beam quality is readily available for cw CO_2 lasers. They are the most frequently used high power lasers for industry applications having low initial and operational cost, as well as robustness and reliability. RF-excitation is the most commonly employed scheme in axial flow or diffusion cooled slab or waveguide configurations allowing high repetition rates at pulsed operation for laser plasma generation. This CO_2 laser LPP EUV source concept is our original concept [7][8] (patent pending).

3.2 CO_2 drive laser system

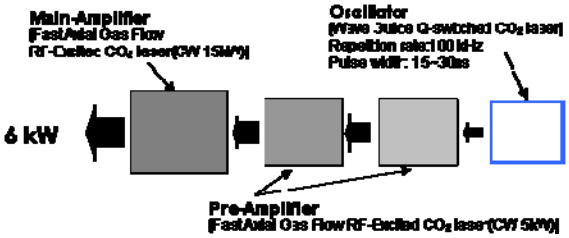

Figure 14. Configuration of the CO_2 MOPA system.

We developed a short pulse CO_2 MOPA (Master Oscillator Power Amplifier) laser system with 15ns pulse width and kW level average power at 100 kHz repetition rate. Figure 14 shows the MOPA configuration. The system consists of a short pulse high repetition rate oscillator and a 3-stage amplifier. The oscillator laser is an EO Q-switched, 15~30 ns, single P(20) line, RF pumped waveguide CO_2 laser with 60 W average power. The repetition rate can be tuned from 10 to 140 kHz. Commercial 5 kW (two units) and 15 kW (one unit) cw CO_2 lasers are used as amplifierswithout cavity mirrors. The two 5 kW lasers are pre-amplifiers and the 15 kW unit is the main-amplifier.

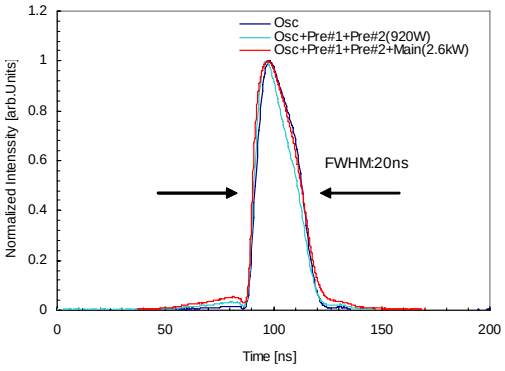

Figure 15. Temporal laser pulse profile.

A pedestal and/or tail of the seed laser pulse will also amplify and reduce the laser gain. The temporal laser pulse profile of the output laser beam was measured to evaluate the pedestal component. In Figure15, “Osc” indicates the temporal laser pulse profile of the EO Q-switched CO_2 oscillator, “Osc+Pre#1+Pre#2” and

"Osc+Pre#1+Pre#2+Main" are the temporal profiles after the "first + second pre-amplifier" and the "first + second pre-amplifier + main amplifier", respectively. A slight 40 ns pedestal exists before the 20 ns main laser pulse. It contains about 6% of the main pulse energy for full amplification.

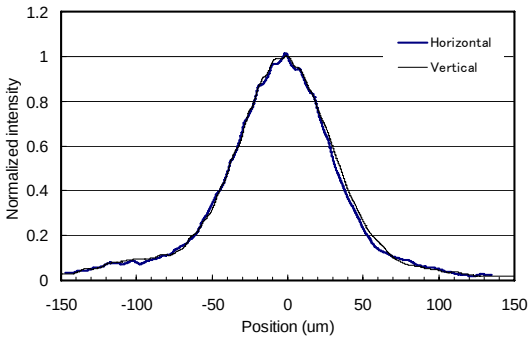

Figure 16. Focusability of the CO_2 laser beam.

The laser beam quality was measured with a ZnSe meniscus lens having a focal length of 127 mm and a slit-scan type beam profiler (Photon Inc., NanoScan). A beam profile of the focused laser output after all three amplifiers is shown in Figure 16. Horizontal and vertical $1/e^2$ beam diameters at the lens focus were 135 μm and 137 μm, respectively. The calculated beam propagation factor M^2 is 1.2. Especially, the beam size is identical before and after amplification, i.e. the amplifiers cause no phase distortion. Figure 17 shows the measured amplification characteristics of the MOPA system, i.e. two pre- and one main amplifier. The input power was measured at the exit of the main amplifier without RF excitation of the amplifiers. The maximum average power is 6kW at 100 kHz repetition rate. The data points are fitted with the Frantz-Nodvik equation.

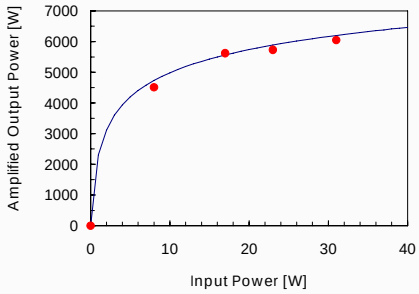

Fig. 17. Amplification characteristics of CO_2 MOPA system.

3.3 Sn Droplet target supply

We develop the Sn droplet supply system based on our Xe droplet supply system. The liquid Sn is ejected through a nozzle into the vacuum chamber. The harmonic oscillation of a piezoelectric transducer (PZT) induces a Rayleigh instability[10] that causes the liquid jet to break up into uniform droplets.

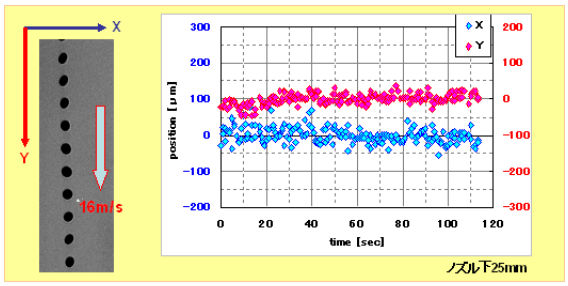

Figure 18. Sn droplet chain and stability

Figure 18 shows a generated Sn droplet chain inside the vacuum chamber. The droplets are generated with a diameter of about 130 μm and a speed of about 17 m/s. Currently, a high speed of 70-m/s Sn droplet supply system is developed for irradiation with the high power CO_2 MOPA system.

3.4 Magnetic field mitigation

The fast ions from a laser produced plasma are controlled by a magnetic field[9]. Figure 19 shows the Faraday cup signal from Nd:YAG laser generated Sn plate target plasma with and without a magnetic field. The Faraday cup signal decreased below the detection limit (about 3 orders) by applying a magnetic field of 1T. For the CO_2 laser, however, the observed sputtering rate is higher than the deposition rate. Since the generated ion number is approximately equal to the amount of debris, (the observed erosion rate is close to zero) it can be concluded that the amount of debris is 1% or less as compared with the Nd:YAG laser.

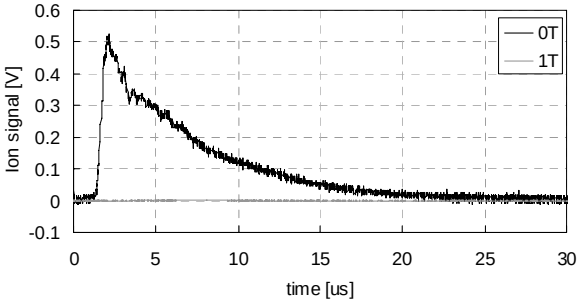

Fig. 19. Faraday cup signal with & w/o magnetic field.

3.5 EUV generation

A preliminary experiment without any system optimization was done with the high power CO_2 MOPA laser and a solid Sn target. The laser output power was 6 kW at a repetition rate of 100 kHz and a rotating Sn disk target was used. The laser incidence angle to the Sn disk normal was 45 degree. The generated EUV in-band energy was measured with a Flying circus 2 energy meter placed at an angle of 15

degree to the target normal. Figure 11 shows the EUV energy of the plasma source into 2 π sr and 2% bandwidth. The average EUV output power at the primary is 130W , 50W equivalent power at intermediate forcus, i.e. the average conversion efficiency of 2.2% was obtained.(Figure 20)

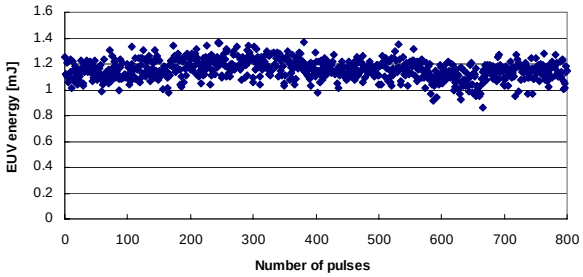

Fig. 20. EUV pulse energy at primary source.

Table 2 lists the IF EUV power as a function of laser power and CE. The assumed EUV transfer efficiency from the primary source to the intermediate focus is 28% for the upper column and 36% for the lower column. An in-band EUV power of 40W is generated with the current laser power of 5 kW at a CE of about 2.2% with 36% transfer efficiency. The required 100 W will be generated from a 7.5 kW CO_2 laser at a CE of 4%. The full CO_2 MOPA system for a 100-W EUV source will have a compact design due to the proper choice of modern laser technology.[11)]

Table 2. Estimated EUV power at the intermediate focus

CE % / Laser kW	2.0	2.2	2.5	3.0	3.5	4.0	4.5
2.5	14	15	18	21	25	28	32
	18	20	23	27	32	36	41
5.0	28	31	35	42	49	56	63
	36	40				72	81
7.5	42	46				84	95
	54	59				108	122
10.0	56	62	70	84	98	112	126
	72	79	90	108	126	144	162

HVM source

Transfer efficiency from primary source to IF

	Total	Debris shield	Collectable angle	Reflectivity	T%	SPF
Case1	0.28	0.8	5sr	0.6	0.9	0.8
Case2	0.36	1	4sr	0.6	0.94	1

4. Conclusion

The GT61A ArF laser light source of the ultra line narrowed spectrum, which meets the demand of hyper NA (NA > 1.3) immersion tool, is introduced. In 45nm node, since it indispensably requires OPC (optical proximity correction) and a narrower process window, improved stabilization of spectrum performances was performed by bandwidth control technology; Bandwidth Control Module (BCM) It also contributes to the reduction of the tool-to-tool differences of the spectrum for every light source.

LPP source based on a high power CO_2 MOPA system and a tin droplet target is demonstrated. A maximum conversion efficiency of 4.5% was measured for a CO_2 laser driven Sn plasma. Debris Mitigation for a CO_2 laser produced Sn plasma system is very promising, since only low Sn deposition on samples has been observed. A laser output power of 6 kW was achieved with a single beam having very good beam quality. The laser power will increase with the correct choice of laser technology. The average EUV output power at the primary is 110W equivalent to 40 W at the intermediate focus. We conclude that the CO_2 laser driven Sn light source is the most promising candidate for HVM EUVL due to its scalability, high efficiency and long collector mirror lifetime.

Injection lock technology is supported by New Energy and industrial technology Development Organization (NEDO) and Ministry of Economy, Trade and Industry (METI) during 2000 - 2002. EUV work was also supported by NEDO.

5. References

(ArF)

1. H. Mizoguchi, et. al.: “High power injection lock laser platform for ArF dry/wet lithography”, SPIE, 5754 (2005) pp. 780-789.
2. H. Mizoguchi, et. al. : “High Power Injection Lock 6kHz 60W Laser for ArF Dry/Wet Lithography”, SPIE, 6154 (2006)
3. K.Huggins, et. al., “Effect of laser bandwidth on OPE in a modern lithography tool”: SPIE, 6154 (2006) pp. 351-362
4. K.Kakizaki et. al.:”Feasibility study of 10kHz-class excimer laser for future generation of ArF immersion lithography”,SEMATECH immersion symposium, TP-03 (Kyoto,2-5 Oct.2006)
5. O.Wakabayashi, et. al.: ” Spectral measurement of ultra line-narrowed F2 laser”, SPIE, 4346 (2001), pp 1066-1073
6. T. Suzuki et. Al.:”Ultra line narrowed injection lock laser light source for higher NA ArF immersion lithography tool”, *Proc. SPIE* 6520-75 (2007)

(EUV)

7. Akira Endo, et. al., "Development Status of HVM Laser Produced Plasma EUV Light Source", Proc. Int. Sematech EUVL Symposium, Barcelona (2006).
8. H. Mizoguchi, et.al., ” Development of CO_2 laser produced Xe plasma EUV light source for microlithography,” *Proc. SPIE*, 6151, 61510S (2006).
9. H. Komori, et. al., “Magnetic field ion mitigation for EUV light sources,” *Proc. SPIE* 5751, 859 (2005)
10. Lord Rayleigh, F.R.S “On the instability of jets” Proc. London mth Soc. 10(4)4-13 (1878)
11. A.Endo, et al.,” Laser-produced EUV light source development for HVM”, Proc. SPIE 6517-23(2007)

Laser absorption and optical emission spectroscopy for the study of argon microdischarge

N. Sadeghi[1], X. Aubert[2], J.F. Lagrange[1], A. Rousseau[2] and G. Xia[1]

[1] *LSP, Université Joseph Fourier & CNRS, 38041Grenoble, France, E-mail: Nader.Sadeghi@ujf-grenoble.fr*
[2] *LPTP, Ecole Polytechnique, CNRS UMR 7648, 91 128 Palaiseau, France*

Argon metastable atoms density, electron density and gas temperature are measured in the plasma of argon formed in a microhollow cathode configuration made of a few hundreds µm diameter hole drilled through a metal/dielectric/metal sandwich. Both stationary and self-pulsing regimes are studied. Argon metastable atoms are produced both by electron impact on ground state atoms and by dissociative recombination of Ar_2^+ ions with electrons.

1. Introduction

Because of their potential application in various fields and their simplicity, there has been a growing interest in microplasmas during the past years. Due to their small dimensions, these plasmas can be operated with a relatively low voltage in the range of a few tens of torr to the atmosphere pressures. In the present work, we study the plasma produced in a microhollow cathode configuration (MHC) made of a few hundreds µm diameter hole drilled through a metal/dielectric/metal sandwich. One of the electrodes acts as cathode (K) and the other as anode (A1). One of the main advantages of this configuration is that it remains stable at very high power loading (100's kW/cm3) without undergoing the glow to arc transition, even at atmospheric pressure. Modelling studies by Boeuf *et al* [1], and verified experimentally by Aubert *et al* [2], have pointed out that this outstanding capability of the MHCD is connected to the transition between an abnormal discharge mode, in which the plasma is confined inside the MHCD hole, and a normal glow discharge mode, in which the plasma largely spreads over the backside surface of the MHCD cathode. Depending on the mean discharge current, the plasma can be in a stable glow regime (region 3 of [3]) or in a self-pulsed regime (region 2 of [3]).

2. Experimental

In this study, the diameter of the MHC hole is 100 or 200 µm and the thickness of the metal and dielectric sheets are 100 and 250 µm, respectively. The discharge is run with argon at 30 to 300 Torr pressure range by applying a voltage around 200 V. Different plasma parameters are deduced using various diagnostic techniques.

To obtain the gas temperature T_g, a trace of nitrogen is added to the feed gas and the recorded N_2 first positive ($B^3\Pi_g$-$A^3\Sigma_u$), or N_2^+ first negative ($B^2\Sigma_u$-$X^2\Sigma_g$) bands are compared to simulated spectra with different rotational temperatures. In the stable glow regime, T_g increases with the gas pressure and discharge current to reach 700 K at 300 Torr and 2.5 mA. In the self-pulsed regime, T_g values as high as 1500 K have been measured during the discharge pulse.

The density of argon Ar*($^3P_2$) metastable atoms inside the MHC hole is deduced from laser absorption experiments, using a frequency tunable 772.42 nm external cavity diode laser. The laser beam crosses the MHC along its axis. Figure 1 shows the experimental set-up for theses measurements. D_1 to D_3 are photodiode detectors, FP is a 20 cm long confocal Fabry-Perot etalon

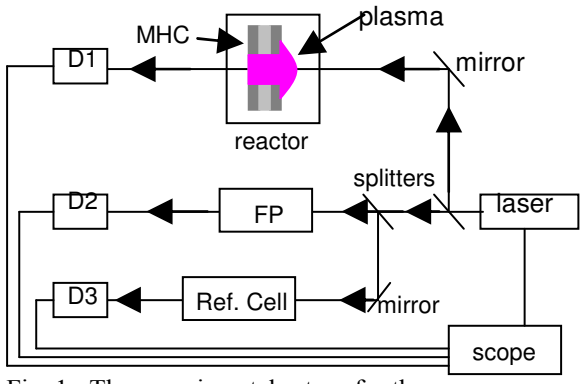

Fig. 1 : The experimental set-up for the argon density measurements.

of 0.375 GHz FSR used for the frequency shift calibration and Ref. Cell is an about 1 torr pressure– 1 mA discharge current argon plasma which provides the precise position of the 772.42 nm line centre. In the self-pulsed regime, the time variations of the Ar*($^3P_2$) metastable density and the 772.42 nm line profile are recorded with a time resolution of about 20 ns.

The electron density inside the MHC hole is deduced from the Stark broadening of the H_β emission line at 486.1 nm, from the trace hydrogen present in the gas.

3. Results and discussion

3.1. Steady state discharge

Figure 2 shows the recorded absorption profiles from the low pressure argon reference cell (1) and from microdischarge run in stable glow regime at 1 mA and 50, 150 and 300 Torr, (2) to (4), respectively. Both collision with neutrals and Stark effect contribute to the

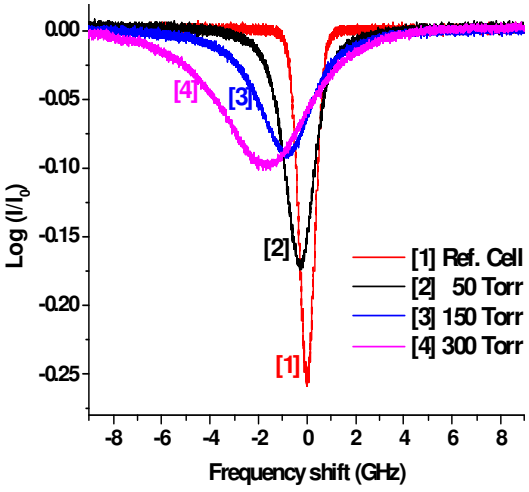

Fig. 2 : Absorption profiles of Ar 772.42 nm line at stable glow regime for 1 mA current (see text).

observed broadening and the red shift of the absorption central frequency and as expected, both increase with pressure. In 200 µm diameter hole, at the steady state, for the discharge current between 0.5 and 2.5 mA, the Ar*($^3P_2$) metastable density ranges between 0.5 and 2 x 10^{19} m^{-3} and the electron densities are in the range of a few 10^{20} m^{-3}.

3.2. Self pulsing regime

In the self-pulsing regime, the peak current can reach up to 100 mA and the resulting peak electron density, which reaches a few 10^{21} m^{-3}, can be deduced from the Stark widths of the both argon 772.42 nm absorption profile and/or hydrogen 486.1 nm line. Figure 3 shows for the 100 µm hole at 100 Torr pressure the absorption line profiles at different times after the peak of the current. At very short times, where the electron density and gas temperatures are very high, the profile if very broad and fully distorted. With increasing time in the afterglow and the decay of the electron density, the width and the red shift of the absorption profile both are reduced. We also observe an evolution on the area under the absorption curves, representative of the Ar*($^3P_2$) metastable densities. Immediately after the discharge pulse, metastable atoms created during the pulse (250 ns curve) are very efficiently destroyed by collision with electrons and their density strongly decays. But as seen from Fig. 3, thanks to a new production source their density increases again in the afterglow and a maximum is reached at a few µs after the

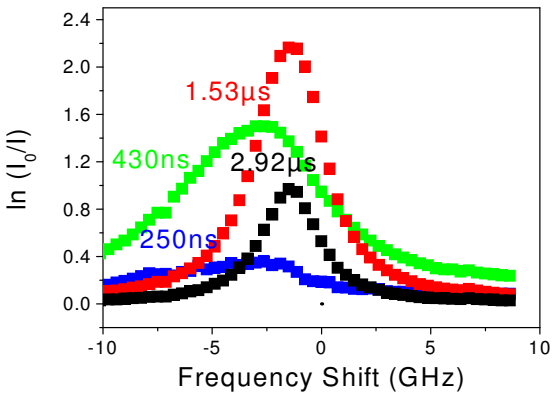

Fig. 3 : Absorption profiles of Ar 772.42 nm line at different times after the current pulse in the 100 µm diameter hole at 100 Torr.

current pulse (depending on the pressure and peak current). This new source of production of metastable atoms comes from the dissociative recombination of argon ions Ar_2^+ with electrons.

References

[1] JP Boeuf, LC Pitchford, KH Schoenbach, Appl. Phys. Lett. **86**, (2005) 071501.

[2] X. Aubert, G. Bauville, J. Guillon, B. Lacour, V. Puech and A. Rousseau, Plasma Sources Science & Technol. **16**, (2007) 23.

[3] A. Rousseau and X. Aubert, J. Phys. D. : Appl. Phys. **39** (2006) 1619.

Collective Thomson Scattering Diagnostics of Plasmas Produced for EUV Light Sources

K. Tomita[1], T. Yamada[1], T. Kagawa[1], K. Uchino[1], S. Katsuki[2], H. Akiyama[2]

[1]*Interdisciplinaly Graduate School of Engineering and sciences, Kyushu University, Fukuoka, Japan*
[2]*Graduate School of Science and Technology, Kumamoto University, Kumamoto, Japan*

Abstract: A collective Thomson scattering diagnostic system for Z-pinch plasmas produced for extreme ultraviolet (EUV) light sources has been developed. Results of measurements gave plasma parameters just after the pinch as the electron density n_e=1.5×10^{24} m^{-3}, the electron temperature T_e=15 eV, and the averaged ionic charge $\bar{Z}$ =7. Furthermore, based on measurements of temporal evolutions of n_e and T_e spatial profiles, the pinched plasma behavior was discussed.

1. Introduction

Extreme ultraviolet (EUV) lithography has been expected as the next generation lithography for 32 nm node design rule. Only a Mo/Si multilayer mirror has reasonable reflectance in the EUV region and it restricts the wavelength range to be at around 13.5 nm with a bandwidth of 2 %. For the practical use, the power necessary in this bandwidth should be more than 115 W at the intermediate focal point [1, 2]. There are two candidates as the EUV light source. One is the discharge produced plasma (DPP) and the other is the laser produced plasma (LPP) [3, 4]. However, these sources have not yet succeeded to radiate the EUV lights in the required band with the necessary power. For both methods, high density (electron density n_e=10^{24} - 10^{26} m^{-3}) and high temperature (electron temperature T_e= 10 - 30 eV) plasmas should be generated using Xe or Sn atoms [5, 6]. In order to produce required EUV lights efficiently, these plasma parameters should be optimized. A prerequisite for such optimization is the quantitative measurements of these parameters.

In the case of DPP, the high density and high temperature plasma is generated through the mechanism of magnetic implosion (pinch) of the pre-produced plasma by applying a high current with a high rise-time. The pinched plasma is alive during a short time (< 50ns) and the plasma size is small (radius < 200 μm). Therefore, a high temporal resolution (<10 ns) and a high spatial resolution (< 100 μm) are required for measurements of DPP sources. A laser Thomson scattering (LTS) method can be expected to fulfill these requirements. The method can yield n_e and T_e values unambiguously.

Depending on the scattering parameter, the Thomson scattering spectrum can be either a coherent (collective) or incoherent [7, 8]. When we use the second harmonics of Nd:YAG laser (λ=532 nm) as the light source, the LTS spectra from the EUV plasmas having aforementioned plasma parameters are in the collective regime. The spectrum of the collective Thomson scattering consists of an ion term and an electron term. The ion term is present very close to the central wavelength of the probing laser, and its expected spectral spread for the EUV plasma is about 100 pm. On the other hand the spectral spread of the electron term is of the order of 10 nm. Taking account of the strong background radiation from the plasma, we determined to measure the ion term, for which we could expect enough SN ratios against the background radiation. One problem to measure the ion term is that the spectral resolution of 10 pm is needed, and the other problem is that the intense wall-scattered laser lights easily overwhelm the ion spectra. In order to overcome these problems, we constructed a newly designed LTS measurement system whose spectral resolution and stray light rejection were enough to resolve fine feature of the ion term. Using the system, we succeeded to evaluate n_e, T_e and $\bar{Z}$ of a Z-pinch type DPP. Furthermore, temporal variations of n_e and T_e spatial profiles were measured and the results were discussed in connection with the evolution of the EUV emission.

2. Experiment

LTS measurements were performed for the EUV source plasma produced in a compact Z pinch device. The experimental arrangement for LTS measurements is shown in Fig. 1. In this experiment, a compact Z pinch device, which consists of a 42 nF capacitor bank, a toroidal ferromagnetic core, and a Z pinch discharge tube, was used. The 42 nF capacitor bank was rapidly charged up to 24 kV by a magnetic pulse compressor and then a current

with an amplitude of 15 kA and pulse duration of 120 ns was delivered to the Z pinch discharge tube. The Z pinch was generated by magnetic pressure due to the current flowing through the tube. More details about the Z pinch device used in this study are described in [3].

The second harmonics of a Nd:YAG laser (Continuum Powerlite 9010 with an injection seeder; spectral spread < 0.1 pm) was used as a light source of LTS measurements. The laser energy (E_L) injected into the plasma was less than 10 mJ, and an achromatic lens (L1, *f*=170 mm) was used to focus the laser beam. The laser spot size at the focusing point was measured by detecting Raman scattering signals from a nitrogen gas at a pressure of 300 Torr. For this experiment, the spatial resolution was set to be 20 μm. The evaluated laser spot diameter was 80 μm (FWHM).

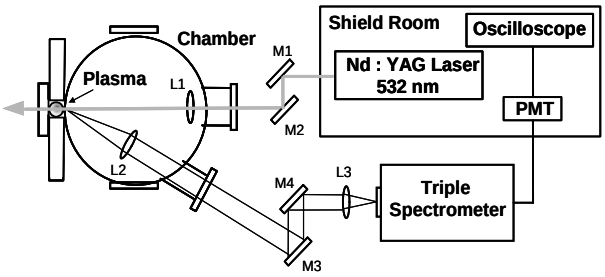

Fig.1 Experimental arrangement.

Scattered lights into the scattering angle of 150 degree from the plasma were focused onto the entrance slit of a triple grating spectrometer (TGS) that is described below, and then dispersed by it. The signal lights passed through an exit slit of the TGS were guided by an optical fiber into an electromagnetically shielded room which was very effective to avoid electromagnetic noise produced by the discharge circuit for the plasma generation. Finally, the signal lights were detected by a photomultiplier tube (Hamamatsu, R943-02).

Because the Z pinch plasmas were generated in a 5 mm diameter discharge tube, strong stray light from probing laser were expected. This stray light would easily overwhelm the ion term if stray light would not be eliminated carefully. Therefore we newly fabricated a triple grating spectrometer (TGS) to eliminate the stray light. The schematic diagram of the TGS is shown in Fig. 2. The structure of the TGS was almost the same as before [9], but its design was different from the previous one to achieve a high spectral resolution. In TGS, three gratings (G1-G3) (58 mm × 58 mm holographic gratings with 1800 Grooves/mm, blazed at 500 nm) were mounted so that lights could be additionally dispersed at each stage. Widths of four slits S1, S2, S3 and S4 were 15 μm, 25 μm, 10 μm and 15 μm, respectively. Two intermediate slits (S2-S3) and final camera lens (L6) (f=250 mm, ϕ=50 mm) were finely translated with a step of 1 μm by stepping motors to change the measurement wavelength. The total inverse dispersion was 0.57 nm/mm and finally we have achieved the spectral resolution of 16 pm and the stray light rejection of 10^{-5} at Δλ=40 pm by this TGS. Figure 3 shows the instrumental function of the TGS measured by using the laser light.

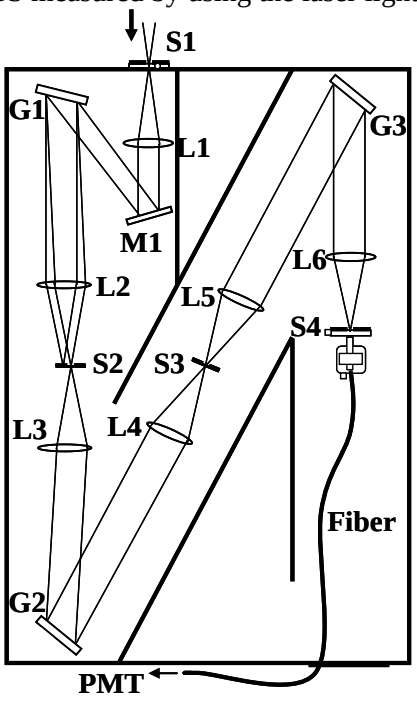

Fig. 2 Schematic diagram of the triple grating spectrometer (TGS). S1-S4: slits, M1: flat mirror, G1-G3: gratings, L1-L6: lenses.

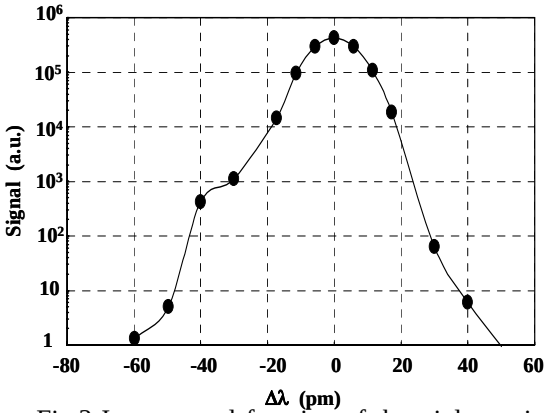

Fig.3 Instrumental function of the triple grating spectrometer.

3. Experimental results and discussions

First, we tried to detect ion term spectra from plasmas produced in a Xe gas. Then, we successfully obtained ion term spectra at a timing 10 ns after the pinch time. However, we found that the spectral resolution of the present system was not enough to resolve ion term spectra of Xe plasmas and was not enough to evaluate plasma parameters from observed spectra. In order to observe clear ion term spectra using the present system, we changed the working gas of the discharge from Xe to Ar, since the ion term spectrum width is inversely proportional to the root of atomic mass number [7, 8]. Argon gas was fed into the discharge tube at the flow rate of 300 cm^3/min. The discharges were generated at a frequency of 10 Hz.

Figure 4 shows an example of the LTS signal and the background radiation signal observed at $\Delta\lambda$=60 pm collected from the Ar gas discharge. It is clear that the LTS signal is almost one order of magnitude larger than the background radiation signal. Figure 5 shows the ion term spectrum measured at 10 ns after the pinch. In order to measure this spectrum, the signals were averaged over a number of 50 laser shots. The error ranges shown in Fig. 5 are the standard deviation of these data from 10 times measurements. In this case, the plasma was flowing to the chamber side along the axis of the discharge (plus side of the z axis). Therefore, the ion term spectrum is Doppler shifted to the blue side by 20 pm. The measured position was z=500 μm. Here, we selected the origin of the z axis (z=0) to be the center of the pinched plasma. From the width of the spectral shift, the plasma velocity can be estimated, and the velocity was 1.2×10^4 m/s to the z direction. Because of the strong stray light signals, the ion term spectrum couldn't be measured at $\Delta\lambda < 25$ pm. However, it is easy to reconstruct the spectral shape of $\Delta\lambda < 25$ pm from the fittings of theoretical curves with the measured part of the ion term spectrum.

The calibration of the LTS signal was done by using the Rayleigh scattering signals from a nitrogen gas at a pressure of 300 Torr. Since the shape, the spectral peak wavelength, and the absolute value of the ion term could be measured, n_e, T_e, and $\bar{Z}$ could be evaluated. It can be seen from Fig. 5 that the solid line is most close to the measured spectrum. So the plasma parameters deduced from the spectrum were $n_e=1.5\times10^{24}$ m^{-3}, $\bar{Z}$ =7, $T_e=T_i$=15 eV. The error ranges for these values were less than $\pm$10.

Temporal variations of n_e and T_e spatial profiles of

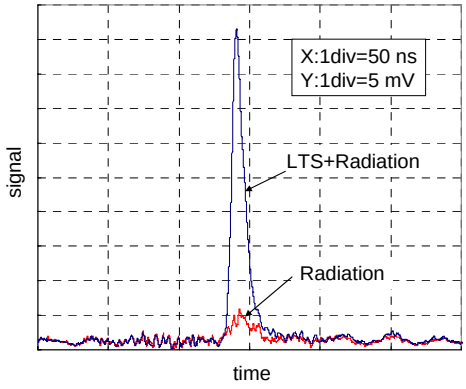

Fig.4 Examples of the LTS signal and the background radiation signal observed at $\Delta\lambda$=60 pm for an Ar plasma.

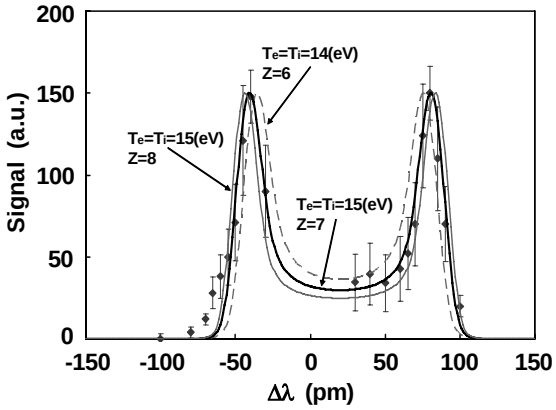

Fig. 5 Observed ion term spectrum from an Ar gas discharge and fitted theoretical curves.

the plasma were measured after the pinch time. Again, the argon gas was used as a working gas. Figure 6 shows spatial distributions of n_e along the z axis at different times after the pinch. T_e profiles are shown in Fig. 7 similarly. The pinched plasma was first formed in the extent of about 1mm along the z axis at 80 ns from the start of the discharge current. Then, the plasma particles were pushed away from the center of the originally formed position (z=0) along the z axis. n_e peaks moved both sides of the z axis and extended to the positions z=±3 mm. As described before, the pinched plasma was formed in the ceramics tube of the diameter of 5 mm. The gas was introduced from left hand side (minus side of the z axis) of Fig. 1 into the tube. The other end of the tube was connected to the large chamber. As the n_e peak moved to the gas-upstream side (z<0), n_e increased and T_e decreased. This can be due to the occurrence of frequent ionization because of the high neutral gas density on the upstream side. On the other hand, as the n_e peak moved to the large chamber (z>0) where the neutral density was low, T_e kept high while

n_e decreased. We contrasted these plasma evolutions with the EUV emission behavior. Then, we found that the EUV lights were radiated on the way that the high temperature plasma moved to the downstream side.

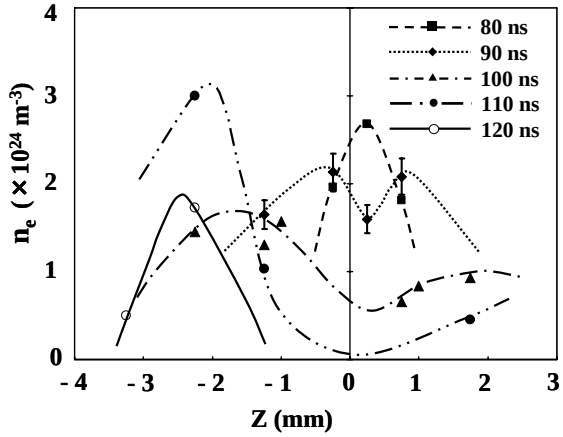

Fig. 6 Temporal evolution of axial n_e profile of the pinched plasma.

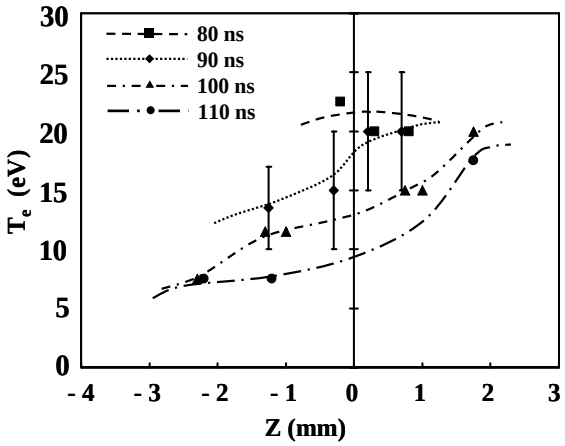

Fig. 7 Temporal evolution of axial T_e profile of the pinched plasma.

Here, we discuss about the validity of evaluated values. First, we assumed T_e=T_i when we deduced the values n_e=1.5×10^{24} m^{-3}, T_e=15 eV, $\bar{Z}$ =7. This assumption can be reasonable because the measurement were performed 10 ns after the pinch time, which was 4 times longer than the electron-ion equipartition time [10]. Second, high density plasmas could be easily perturbed by the absorption of laser light through the process of inverse bremsstrahlung. We estimated possible electron heatings by the laser. The increasing of electron temperature was only 0.3 eV even for the most severe condition of the present study (t=110 ns, z=-2.25 mm: n_e=3.0×10^{24} m^{-3}, T_e=6 eV, $\bar{Z}$ =5, E_L=4 mJ, laser spot size 80 μm), increasing of electron temperature for inverse bremsstrahlung is less than 0.3 eV [11]. So the laser perturbation is not a serious problem in this study.

4. Conclusion

We have developed a collective LTS system for measurements of n_e, T_e, and $\bar{Z}$ of Z pinch plasmas produced for EUV lithography. The system was successfully applied to the diagnostics of pinched plasmas produced in the argon gas. However, in order to apply the LTS system to the Xe plasmas, spatial and spectral resolutions of the system must be improved. Such improvements are now in progress.

References

[1] V. Banine and R. Moors: J. Phys. D: Appl. Phys. **37**, p.3207 (2004).

[2] International Technology Roadmap for Semiconductor Web Site, update 2007, http://public.itrs.net/

[3] S. Katsuki, A. Kimura, Y. Kondo, H. Hotta, T. Namihira, T. Sakukgawa, and H. Akiyama: J. Appl. Phys. **99**, 013305 (2006).

[4] Y. Tao, H. Nishimura, S. Fujioka, A. Sunahara, M. Nakai, T. Okuno, N. Nishihara, N. Miynaga, and Y. Izawa: Appl. Phys. Lett. **86**, 201501 (2005).

[5] E. R. Kieft, J. J. A. M. van der Mullen, and V. Banine: Phys. Rev. E **72**, 026415 (2005).

[6] A. Sasaki, K. Nishimura, F. Koike, T. Kagawa, T. Nishikawa, K. Fujima, T. Kawamura, and H. Furukawa: IEEE Journal of Selected Topics in Quantum Electronics **10**, p.1307 (2004).

[7] J. Sheffield: *Plasma Scattering of Electro-magnetic Radiation*, Academic press (1975).

[8] D.E. Evans, and J. Katzenstein: Rep. Prog. Phys. **32**, p.207 (1969).

[9] S. Hassaballa, M. Yakushiji, Y. K. Kim, K. Tomita, K. Uchino, and K, Muraoka: IEEE Transaction on Plasma Science **32**, p.127 (2004).

[10] L. Spitzer: *Physics of Fully Ionized Gases*, New York (1962).

[11] K. Garloff, M. van den Donker, J. van der Mullen, F. Van Goor, R. Brummans, and J. Jonkers: Phys. Rev. E **66**, 036403 (2002).

CO_2 laser imaging heterodyne and phase contrast interferometer for density profile and fluctuation measurements in LHD

K. Tanaka[1], C. Michael[1], L.N.Vyacheslavov[2], A.L. Sanin[2], T. Akiyama[1], K.Kawahata[1], Y.Ito[1], and S.Okajima[3]

[1] *National Institute for Fusion Science, 322-6 Oroshi-cho, Toki-shi, 509-5292, Japan*
[2] *Budker Institute of Nuclear Physics, 630090, Novosibirsk, Russia*
[3] *Chubu University, 1200 Matsumoto-cho, Kasugai-shi, Aichi 487-8501, Japan*

A CO_2 laser heterodyne imaging interferometer (CO_2 HI) and a CO_2 laser phase contrast imaging interferometer (CO_2 PCI) were installed in LHD. The purpose of CO_2 HI is to measure electron density profile at high density($>1x10^{20}m^{-3}$), where the existing far infrared laser (wavelength 118.9μm) interferometer suffers from fringe jump due to the reduction of signal intensity caused by refraction. In the beginning of 10th LHD experimental campaign (2006~2007), sixty three three of CO_2 HI with 10 channels of YAG HI for vibration compensation, and in the later of 10th LHD experimental campaign. eighty one channels CO_2 HI and 15 channels YAG HI became available. The purpose of CO_2 PCI is to measure turbulent fluctuation, which can contribute to the energy and particle transport. In order to get local fluctuation information, magnetic shear technique was applied with use of 48 (6 by 8)channel two dimensional detector.

1. CO_2 laser heterodyne imaging interferometer

In LHD, we installed a multi channel imaging interferometer[1,2,3]. We use of 10.6 μm CO_2 laser for density measurements. A sufficiently powerful (~8W) and stable laser source is available, and multi channel detector arrays with excellent sensitivity are also available. However, the phase shift due to mechanical vibration is not negligible, so, we subtract the phase shift due to vibration using a co-axial YAG HI.

Recently improved central particle confinement has been achieved in pellet injected discharges in the high density regime ($>10^{20}m^{-3}$) of LHD [4]. It is strongly required to measure the density profile to understand high density transport physics and plasma control in such a high density region is also required. However, the existing 13 channel 118.9 μm far infrared laser interferometer in LHD suffers from fringe jumping at such a high density and many chords fail to measure correctly. This is caused by the reduction of the heterodyne beating signal amplitude when the mixing efficiency gets worse due to the beam bending due to strong density gradient. With the use of a short wavelength CO_2 laser, the fringe jumps due to loss of signal are almost completely avoided, since refraction effects are negligible.

The transmission and detection optics are shown in Fig.1 and the beam paths through the plasma are shown in Fig.2. Two slab beams of the CO_2 and YAG laser are injected, including an edge slab covering the region R=4.038~4.282m, and core slab beam covering the region R=3.730~3.963m,where R is the major radius. And another 30mm diameter circular beam both CO_2 and YAG laser radiation is injected at R=3.705m. This is the local beam for heterodyne detection

In Fig.1 (b), the positions of the lenses and curved mirrors are determined to have an image of the center of the plasma on the detection plane to minimize spherical aberrations. Two 32 channel detector arrays were used for CO_2 HI, one each for the core and edge beams. The detectors are liquid nitrogen cooled photoconductive type HgCdTe. The chord spacing in the plasma is 7.5mm in the core beam and 7.9mm in the edge beam. For vibration compensation, five channels of YAG HI were used for each beam. Slab shaped fiber arrays connected to avalanche photo diodes were used for detection. The chord separation of YAG HI is 30~40mm. In order to compensate the 32 ch CO_2 HI, vibrations were interpolated between YAG HI channels.

The frequency of the CO_2 laser slab beams are shifted by 40MHz using an acoustic optical modulator (AOM) and the frequency of the CO_2 laser circular beam was shifted 41.01MHz by another AOM. The CO_2 slab beams and circular

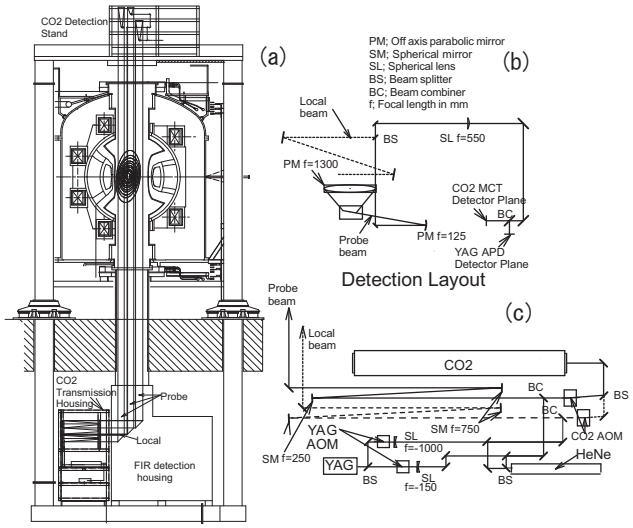

Fig.1 (a) Schematic view of CO_2 laser interferometer (b) edge beam detection optics and (c) transmission optics

beam were mixed on the detection plane and a 10kHz beating signal was obtained for heterodyne detection. Previously, the beating frequency was 1MHz, but, from 10th experimental campaign (2006~2007), the beating frequency was reduced down to 10kHz. This is in order to reduce the cross talk contamination among channels of detector array. This cross talk is due to the voltage drop at the common wiring of the elements. We found that the cross talk is proportional to the signal frequency. Cross talk deforms the measured phase profile especially at edge channels, where the beating signal amplitude is reduced and relative cross talk of the detector is larger. By reducing the beating frequency from 1 MHz down to 10kHz, crosstalk contamination was reduced by a factor 3 ~10. The 10kHz beating signal was sampled at 12.5kHz. This gives an aliased signal at 2.5kHz. The phase shifts are calculated by the digital demodulation technique [5].

The 2.5 kHz band width is enough to follow change of the density due to pellet injection, however, sometimes it is not enough to follow rapid change due to radiation collapse and internal collapse by the MHD event. Recent detector developments succeeded to eliminate cross talk contamination connecting each detector elements directly to bias circuit without common wire. Also if we replace the presently used current mode amplifier with a voltage mode amplifier, cross talk will be reduced, because the current at the common line becomes smaller and results in a smaller voltage drop on the common line. Also, digital correction of cross talk is possible in principle. We plan to reduce cross talk by the above mentioned technique and to operate at around 500kHz to have enough bandwidth to follow the rapid change of density and measure fluctuation behavior.

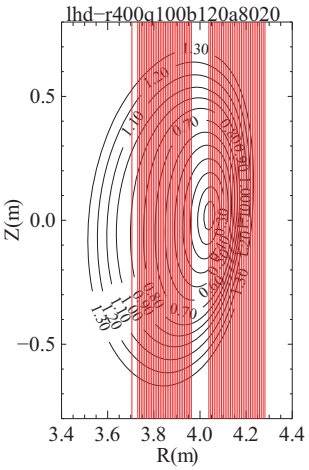

Fig.2 Measured cross section of CO_2 imaging interferometer. Flux surface is mapped one at t=1.2sec of Fig.4

The frequency of YAG slab beam was shifted by 40MHz and the frequency of YAG circular beam was shifted by 40.99MHz using two AOMs. The heterodyne beating signal of the YAG laser interferometer was 990kHz and sampled at 12.5kHz whose down sampled aliased beating frequency was 2.5kHz. The phase shifts were obtained using digital demodulation techniques as well as CO_2 HI. In the previous report [2], unstable YAG HI signals were reported. We concluded this is due to the weak laser power and distorted wave front, which caused low mixing efficiency. This causes residual uncompensated vibration components, which is around 1% of one CO_2 fringe, which corresponds to around $1x10^{18}m^{-3}$ of line averaged density. In addition, it was found that instability of laser oscillation caused an unstable YAG signal. The phase signal of YAG HI sometimes drifted and causes vibration compensation to fail. This drifting is likely due to the temporal change of frequency and spatial coherence of YAG laser. In order to eliminate phase drifting, the probe and local path length was adjusted to be equal. The position of optics of local beam was adjusted in order to make interference phase output constant sweeping the frequency of the CO_2 laser. We improved the stability of the YAG HI.

This system measures phase difference between the channels in the slab beam, however, the edge beam covers the plasma boundary as shown in Fig.2, so that the absolute phase shift due to plasma density can be measured from the phase difference between the each channel and the

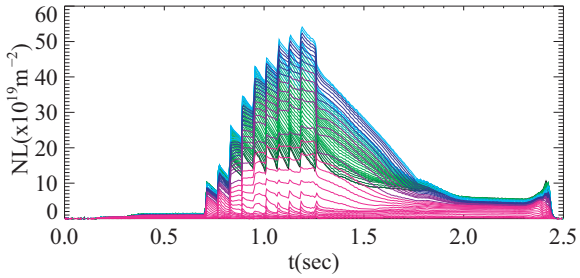

Fig. 3 Example of line density measurements. Mechanical vibration was compensated by YAG laser interferometer

channel at the outside of plasma.

From the later of 10th LHD experimental campaign (2006~2007), additional imaging optics was installed at R=3.36~3.6m, then totally 81 channels of CO_2 HI with 15 channels of YAG HI started to work.

Figure 3 is temporal evolution of line density measured by the CO_2 HI with vibration compensation. Abel inversion to obtain radial density profile was done by using linear least square fitting with regularization of the density gradient. These techniques are well established for tomography reconstruction [5]. The magnetic flux was selected from equilibrium data set to make electron temperature profile of inner and outer magnetic axis identical.

Figure 4 (a) and (b) show an example of the result of flux surface selection showing that both inner and outer $T_e(\rho)$ closely match each other.

Figures 4 (c) and (d) show comparisons of the reconstructed density profile and the electron density profile measure by Thomson scattering.

Presently, the Thomson signal was not calibrated yet absolutely and relatively from Raman or Rayleigh scattering measurements for calibration. So, the absolute value was determined to match the line integrated value of Thomson signal intensity to the line density measured by microwave interferometer, which passed along the same viewing line as the axis of the Thomson scattering system, through at a different toroidal cross section. This calibration factor was obtained shot by shot. Since microwave interferometer suffers from phase jump after pellets are injected, this calibration factor was obtained at low density ($\sim 1\times10^{19}m^{-3}$). Therefore, the YAG laser intensity for Thomson scattering was attenuated to keep linearity of the detector at high density and to use the calibration factor obtained at low density.

Presently, comparison between density profile from Thomson scattering and from CO_2 HI gives rough idea to check validity of two diagnostics. For more precise checking, Thomson calibration experiments are necessary.

Figures 4 (e) and (f) show a comparison of the measured line density profile and the line integration of the reconstructed profile. Both agree reasonably in Fig.4 (e), but a discrepancy can be seen at around R = 3.9m in Fig.4(f). The uncompensated vibration components cannot account for this discrepancy. One of the possible reasons is due to the inappropriate flux surface coordinate. The pressure profile, which was used to calculate the equilibrium, is slightly broad one. and is expressed by $P(\rho)=P_0(1-\rho^2)(1-\rho^8)$, where P_0 is central pressure. This pressure profile reasonably agrees with the measure pressure profile at t=1.2sec, but is much broader than the measured one at t=1.7sec and causes error of magnetic surfaces.

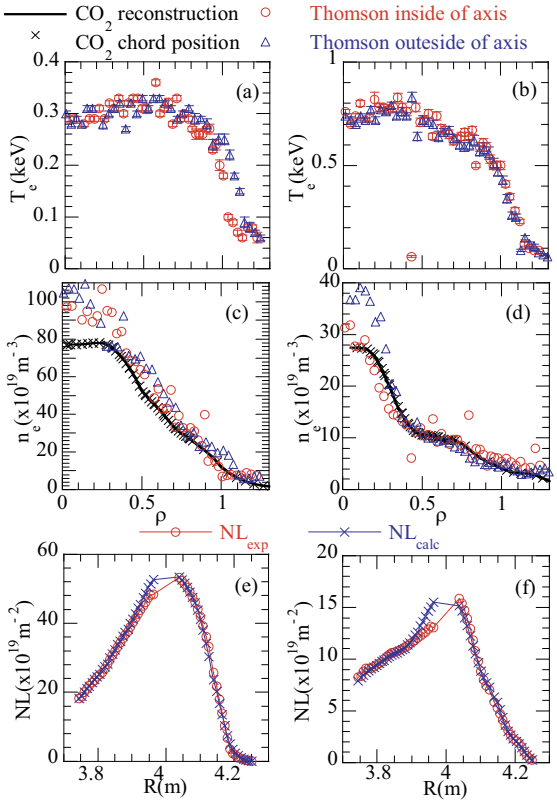

Fig. 4 Measured profiles at around highest central density ((a),(c),(e) t= 1.2 sec) and peaking factor (b),(d),(f) t= 1.7 sec) of the discharge of Fig.2 (a) (b) Temperature profile from Thomson scattering(c), (d) Comparison of profile by CO2 HI Thomson scattering. (e), (f) Measure line density and calculated line density of reconstructed density

At t=1.2sec, the flux surface used for reconstruction is appropriate. So, the discrepancy between CO_2 HI and Thomson scattering might be

due to detector saturation effects on the calibration factor of Thomson scattering. At t=1.7sec, the discrepancy is also due to inappropriate flux surface for reconstruction. The asymmetric inversion procedure, which takes into account of poloidal asymmetry, will help for better reconstruction.

2. CO_2 laser phase contrast imaging interferometer

The CO_2 PCI was installed to measure turbulent electron density fluctuation in order to investigate the turbulence driven anomalous transport in LHD. The phase contrast imaging interferometer measures small phase variation of injected laser beam, which is induced by the turbulence in plasma. This becomes possible giving $\pi/2$ phase difference between scattered and non scattered electromagnetic wave of injected laser by using phase difference plate. The small phase variation can be converted into small intensity variation. The intensity variation can be measured by the sensitive detector [7].

With use of CO_2 laser, the length of scattering volume is larger than plasma size because of small scattering angle, therefore, technique to get local information is required. We applied magnetic shear technique [8,9] to get local measurements. The particularity of our approach is the use of two dimensional (2-D) detector.

Figure 5 illustrates the principle of the measurements. Figure 5 (a) shows a top view of the magnetic field line on the equatorial plane. The strong magnetic shear exists in LHD to

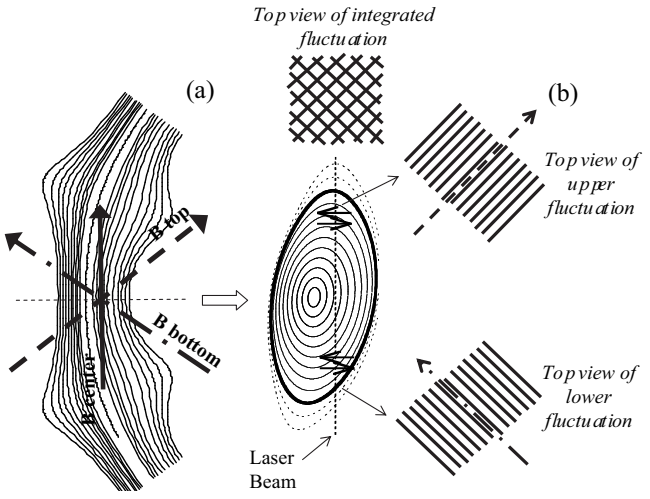

Fig.5 Principle of 2D PCI (a) Top view of LHD (b) toroidal cross section of the measurements and measurements principle

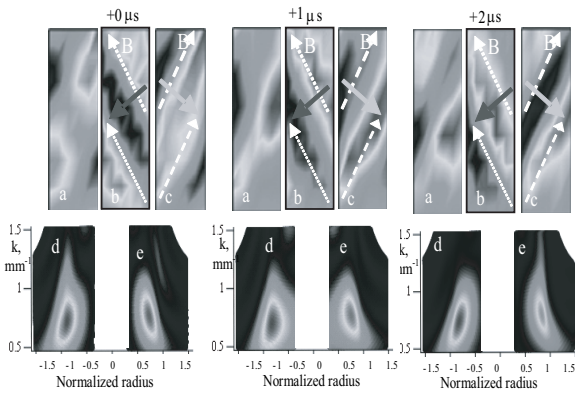

Fig.6 Example of the measurements
(a) Raw PCI image that is the top viewer of integrated fluctuations; fractions of raw image associated with (b) low and (c) upper halves of plasma. The k-spectrum of density fluctuations versus normalized radius in (d) lower and (e) upper halves of plasma.

stabilize interchange instability in the magnetic hill region. The upper and lower field direction is almost orthogonal. Micro turbulence has a long wavelength along magnetic field, of the order of qR, and short wavelength perpendicular to magnetic field, which is of the order of the ion or electron Larmor radius. Thus, the top picture of the fluctuation looks like filament structure and integrated picture looks like grid structure as shown in Fig.5 (b). The idea of this technique is to measure integrated fluctuation picture by phase contrast technique, and resolve fluctuation components into each propagation direction. From the propagation direction, the fluctuation location can be determined by the magnetic field direction, which is perpendicular to propagation direction and can be determined from field calculation.

The eight by six, totally 48 channels two dimensional detector array was used for 2D PCI. Figure 6(a) shows examples of 2D-PCI signals ,which are three successive frames recorded by the array with a 1MHz sampling rate in a plasma with n_e=1.7x10^{19}m^{-3}, T_e=2keV, B_t=1.49T. This system measures fluctuation image 6.1mm (along major radial direction, 8channel sampling) with by 17.5mm (along toroidal direction, 6channel sampling)

To visualize motion of plasma density fluctuations the raw image is digitally split into two parts with negative (b) and positive (c) tilting angle associated with lower and upper halves of the plasma cross-section. Extended along the magnetic field moving objects are clearly seen in

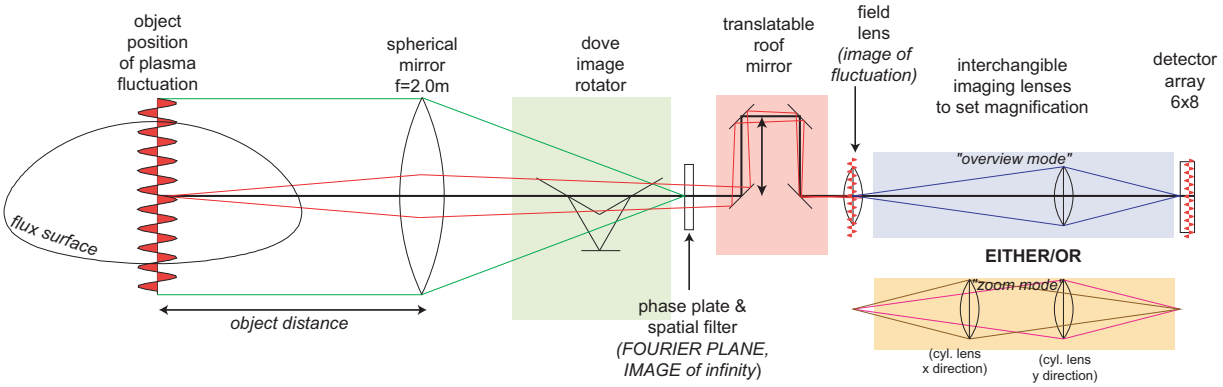

Fig.7 Block layout of detection parti of upgraded optical system.

Fig. 6 (b) and (c). Fluctuations are localized near $\rho = 0.9$ and the width of the peak is larger than the instrumental width determined by calibration with ultra sound waves in air.

In 7th LHD experimental (2003~2004) campaign, the two dimensional PCI was tried first time [10,11] and turbulence character and relation with particle transport were investigated [12,13].

In 9th LHD experimental campaign (2005-2006), upgraded version of 2D PCI was installed to expand the fluctuation wavenumber (k) range and improved spatial resolution [14,15]. The old system used the 42 mm (along major radial direction) by 32 mm (along toroidal direction) $1/e^2$ intensity full width beam passing through CO_2 HI port. The new system used the 80 mm (along major radial direction) by 64 mm (along toroidal direction) $1/e^2$ intensity full width beam and the beam passes through different port. The simultaneous operation of full specification of CO_2 HI and 2D-PCI became possible from 10th experimental campaign. The use of the wider beam improve minimum detectable k.

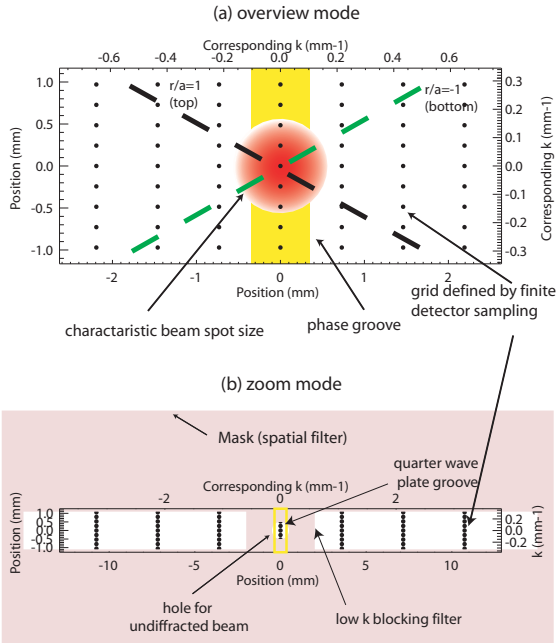

Fig. 8 Array sampling in the *kx* ,*ky* plane, compared with the position in the Fourier plane and phase groove, beam size, and spatial filter.

The spatial sampling is necessary to change dynamic range of k and spatial resolution. Since the layout of the 48 channel detector elements was not changeable, effective spatial sampling was changed by the change of the imaging magnification. With use of cylindrical lens, asymmetric zooming to change ratio of spatial sampling of two orthogonal direction was also possible.

Figure 7 detection systems of new 2-DPCI system. The injected beam was focused on the phase plate, which is the Fourier plane (wave number plane) of fluctuation object. Figure 8 (a) shows sampling of the wavenumber plane. The dot points indicate wavenumber sampling points, which correspond to the detector array elements. The demagnification of the image was 7.8. The yellow region is phase groove, which gives $\pi/2$

phase difference. The signal inside the yellow region can not be detected. The beam spot was also shown. This represents the resolution of wavenumber spectrum. The dotted line indicated angle which is perpendicular to the magnetic field at the last closed flux surface. The most of the signal exists within two dotted lines. Figure 9 (a), (b) shows spatial profile of wavenumber spectrum in old and new over view system. Both systems used symmetric zoom. The plasma parameters of Fig. 9 (a) and (b) are almost identical. The crossing points of doted lines indicate sampling point at each location. The colour area shows accessible region. The measured wavenumber is defined as $k = \sqrt{k_x^2 + k_y^2}$. Since the system measures poloidally dominated wavenumber, propagation direction in laboratory frame is indicated by electron and ion diamagnetic direction.

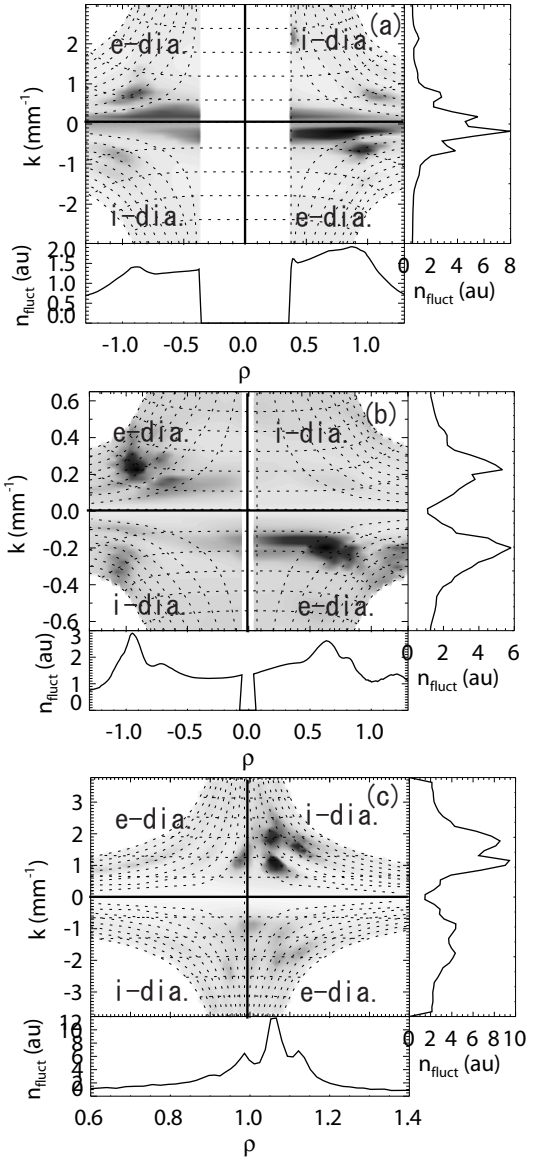

Fig.9 Comparison of *k*-ρ spectra/profiles (a) old overview mode (b) upgrade overview mode and (c) asymmetric zoom mode

As shown in Fig.9(a) old system can show counter propagating components, of which k is around 0.8 mm^{-1} at around ρ =1, which indicates strong velocity shear, but profile of low k (~0.2 mm^{-1}) in the inner region (ρ <1) components are not very clear. In Fig. 9 (b), spatial profile of low k components becomes clear and it propagates electron diamagnetic direction in plasma frame. The new system shows better resolution for low k and measured more inner region of plasma.

With asymmetric zooming, the improvements of spatial resolution for high k components became possible. Figure 8(b) shows sampling in wavenumber plane of asymmetric zoom mode. The demagnification was 2 in the x direction and 7.8 (same as overview mode) in y direction. As shown in Fig. 8 (b), sampling points can be located in the limited area. This makes possible to sample with good spatial and wave number resolution. The maximum detectable propagation angle is $\tan^{-1}(k_{nqy}/\delta k_x)$, where k_{nqy} is Nyquist k of y direction (0.29mm^{-1}) and δk_x is wavenumber resolution in x direction determined by sampling (0.07mm^{-1}). So, zoom mode measures +- 19 degree relative to x axis of k plane. Adjusting x axis to the local magnetic field direction, zoom mode can sample local fluctuation propagating +- 19 degree to normal line to local magnetic field. This angular region corresponds to around 10 % of minor radius. As show in Fig. 7, the dove image rotator [16] was used to adjust local field line. Also translate roof mirror was used to focus the target of the fluctuation. In order to eliminate the fluctuation, which exists outside of the target area in space, spatial filter was also used as show in Fig.8 (b).

Figure 9 (c) shows spatial profile of k spectrum measured by zoom mode. The fluctuation, of which wavenumber is 1~2mm^{-1} exists at ρ = 1.0~1.2 and propagates ion diamagnetic direction.

[1] T. Akiyama et al., Rev. Sci. Instrum. **74**,1683, (2003)

[2] K. Tanaka et al., Rev. Sci. Instrum. **75**,3429, (2004)

[3] K. Tanaka et al., to be published, Journal of Plasma and Fusion Research
[4] Oyabu et al., Phys. Rev. Lett. **97**, 055002-1, (2006)
[5] Y.Jiang et al., Rev. Sci. Instrum. **68**,902, (1997)
[6] M. Anton et al., Plasma Phys. Control. Fusion **38** ,1849, (1996)
[7] H.Weisen et al., *Plasma Phys. Contr. Fusion*,**30**,293,(1988)
[8] P. Devynck *et al.*, Plasma Phys. Controlled Fusion **35**, 63 ,(1993)
[9] S. Kado *et al.*, J. Phys. Soc. Jpn. **65**, 3434 (1996)
[10] A. Sanin et al., Rev. Sci. Instrum. **75**, 3439, (2004)
[11] L. N. VYACHESLAVOV et al., *IEEE Transaction on Plasma Science, **33**,* 464, (2005)
[12] K. Tanaka et al., Nucl. Fusion 46 (2006) 110.
[13] K. Tanaka et al., Fusion Sci. and Tech. 51 (2007) 97.
[14] C. Michael et al., Rev. Sci. Instrum. **77**, 10E923-1(2006)
[15] C. Michael et al.,to be published, Journal of Plasma and Fusion Research
[16] A. E. Smart, J. Phys. E 13, 1166 (1980)

Cotton-Mouton Polarimetry on CHS

T. Akiyama[1], K. Kawahata[1], Y. Itoh[1], S. Okajima[2], K. Nakayama[2], S. Okamura[1], K. Matsuoka[1], M. Isobe[1], S. Nishimura[1], C. Suzuki[1], Y. Yoshimura[1], K. Nagaoka[1], C. Takahashi[1] and CHS experimental Group

[1] *National Institute for Fusion Science, 322-6 Oroshi-cho, Toki-shi, 509-5292, Japan*
[2] *Chubu University, 1200 Matsumoto-cho, Kasugai-shi, Aichi 487-8501, Japan*

A polarimeter based on the Cotton-Mouton effect is one of promising methods for electron density measurements because it is free from fringe jump errors. We have installed a Cotton-Mouton polarimeter with a HCN laser (wavelength of 337 μm), which is combined with an interferometer, on the Compact Helical System (CHS). The Cotton-Mouton effect is measured as the phase difference between probe and reference beams. Since the phase difference is less than only 10 degree, reduction of phase noises is an important issue. Digital complex demodulation technique is adopted for small phase detection. Cross and back talk components have to be suppressed because they causes spurious phase modulations. The line averaged density evaluated from the polarimeter along a plasma center chord is almost consistent with that from the interferometer.

1. Introduction

A polarimeter for electron density measurements in magnetically confined plasmas is expected to be robust even in a high-density range. The reasons are as follows. It is free from fringe jump errors due to smaller phase change than 2π and is immune to mechanical vibrations, which degrade the reliability and resolution of an interferometer. On the other hand, lots of efforts have been paid to increase the signal to noise ratio of the polarimeter because of the small phase change.

There are two types of polarimeters. One is based on the Faraday effect, which is the change in the polarization angle due to the difference in the reflectivities of the right- and left-hand circularly polarized beams. The rotation angle α is given as follows.

$$\alpha = \frac{e^3 \lambda^2}{8\pi\varepsilon_0 m_e^2 c^3} \int n_e B_{//} dl$$

where λ is the wavelength of a probing beam, m_e is the mass of electron, n_e is the electron density and $B_{//}$ is the magnetic field parallel to the direction of the probing beam.

The other type of the polarimeter is based on the Cotton-Mouton (CM) effect, which is the change of the ellipticity due to the difference in the reflectivities of O- and X- mode. The resulting phase difference ϕ_{CM} between O- and X-mode components is described as follows.

$$\phi_{\mathrm{CM}} = \frac{e^4 \lambda^3}{16\pi^3 \varepsilon_0 m_{\mathrm{e}}^3 c^4} \int n_{\mathrm{e}} B_{\perp}^2 dl$$

where $B_{\perp}$ is the magnetic field perpendicular to the direction of the probing beam.

Each magneto-optic effect depends on the particular magnetic field components parallel and perpendicular to the beam propagation in a plasma. Therefore, one of them is chosen according to geometry of the measurement: a beam path, a configuration of the magnetic field. In the case of the electron density measurement along a plasma center chord in a poloidal cross section, only the Cotton-Mouton polarimeter is available because the Faraday effect is too small due to the absence of a magnetic field component parallel to the beam path. On the other hand, polarimeters based on the Faraday effect are usually applied for tangential measurement[1-3].

While polarimeters based on the Faraday rotation, including these for current profile measurement, have been developed in various devices, developments of Cotton-Mouton polarimeters are fewer[4,5]. This paper describes a CM polarimeter using an HCN laser (wavelength of 337 μm) on the Compact Helical System (CHS)[6]. Sec. 2 shows the experimental setup and numerical calculations of the magneto-optic effects in CHS. The estimations of the measurement errors and the measurement results are shown in Sec. 3.

2. Experimental Setup

2.1. Device parameter and the magneto-optic effects in CHS

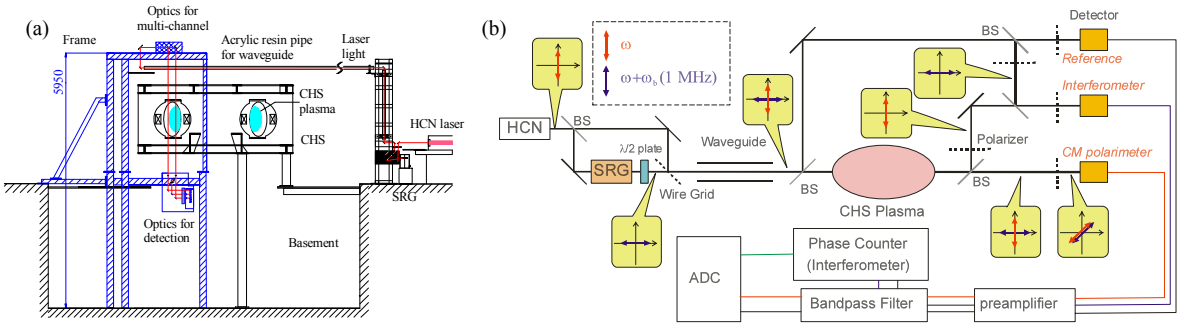

Fig. 1 : (a) CHS and Optical flame of CM polarimeter. (b) The schematic of the optical setup of the CM polarimeter combined with an interferometer with the same chord.

Main features of CHS are briefly introduced here. CHS is a low aspect ration helical device and the maximum magnetic field strength at the magnetic axis is 2 T. The major radius R of the plasma is about 1.0 m. A shape of poloidal cross section is different at each toroidal position with a toroidal period of 8 and an averaged minor radius is about 0.2 m [6]. Probe and reference beams are injected from an upper port and are detected under CHS as shown in Fig.1 (a). The CM polarimeter measures the line averaged electron density along the plasma center chord (in the case of the standard configuration, R_{ax}=0.92 m) in the vertically elongated cross section.

In general, when α and ϕ_{CM} are not small enough, the coupling term between the Faraday and the Cotton-Mouton effect, which leads to phase error, is not neglected. In the above configuration with the electron density profile of $1\times10^{20}(1-\rho^8)$ m^{-3} (ρ: normalized magnetic radius) and a magnetic field strength at the magnetic axis of 1.95 T, the calculated α and ϕ_{CM} are 1.8 degree and 8.2 degree, respectively, and the resulting coupling term can be negligible, 0.09 degree[7].

2.2. Optical Setup

Figure 1(b) shows the schematic illustration of the optical arrangement on CHS. The CM effect is measured as the phase difference between probe and reference beams. The phase measurement has an advantage that it is free from changes in beam intensity due to the output fluctuations of a laser and beam refraction. This is the combined system of the CM polarimeter and the interferometer. The basic idea of the combination is almost the same as that of the polarimeter proposed on W7-X[8]. The light source is the discharge-excited HCN laser[9], whose operational output is about 100 mW (maximum of about 500 mW). Though a slightly longer wavelength is preferable for a good signal-to-noise ratio in the polarimeter, an HCN laser is selected to make the coupling term small and to suppress the beam refraction, which leads to fringe jump errors in the interferometer. Instead, complex demodulation combined with digital filtering[2,10] is adopted to improve the phase resolution.

The HCN laser beam is split into two beams with a Mylar beam splitter, and the frequency of one is shifted with a super rotation grating[11]. The frequency shift ω_b is 1 MHz thank to the high rotation speed (500 rps) of the rotating grating fabricated on the top of the magnetically floating rotor in the turbo molecular pump. After rotating the plane of polarization by $\pi/2$, two laser beams are combined with a wire grid (diameter and spacing of wires are 5 and 12.5 μm, respectively. Graseby Specac Ltd.). In this way an elliptically modulated beam is generated. The laser beam is transmitted with waveguides (inner diameter of 47 mm) made of acrylic resin to CHS. The total transmission efficiency is about 80% (path length is about 15 m). The beam is split into probe and reference beams with a crystal quartz beam splitter, and they are injected into the vacuum vessel through a crystal quartz window. They are detected with Shottky barrier diodes (SBD, Farran Technology). Since only the polarization component parallel to a receiving antenna in the SBD is detected, SBDs are tilted by $\pi/4$, and they obviate polarizers. After passing through an analog band-pass filter and an amplifier, 1-MHz beat signals of the polarimeter's probe and reference are digitized at a frequency of 5 MHz.

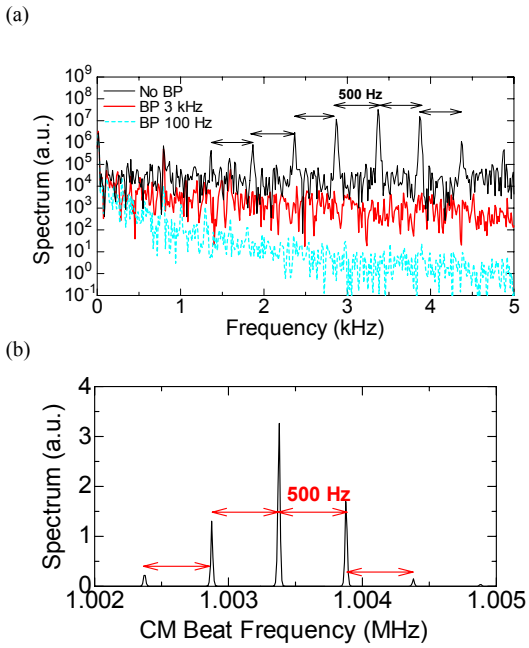

Fig. 2: (a) Spectrum of the 1 MHz beat signal. (b) Spectrum of the phase signal with different band widths of digital band-pass filter.

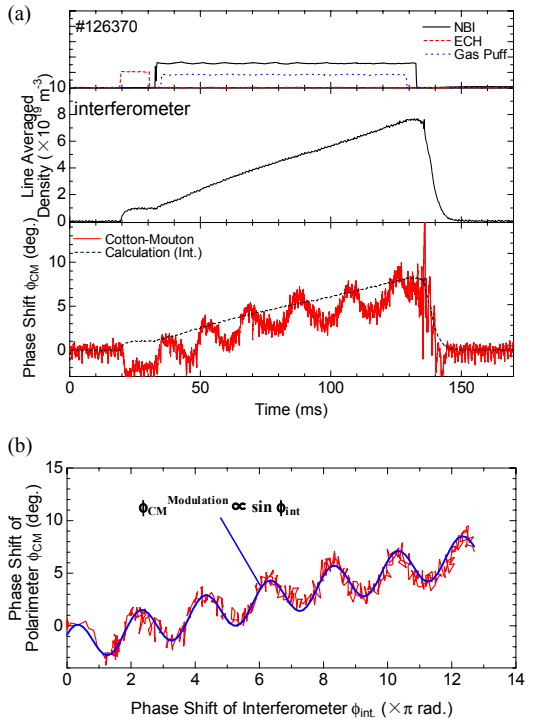

Fig. 3 : (a) Example of measurement results of the CM polarimeter before suppression of back and cross talk components. (b) Modulation components as a function of the phase shift of the interferometer.

Then, complex demodulation is applied to sampled data and the phase difference is extracted. For the interferometric measurement, the probe beam is split after passing through the plasma, and one polarization component (O-mode) is selected with a polarizer. The transverse polarization component is selected from the reference beam and then they are combined. The 1-MHz beat signal is obtained in the same way. The phase shift of the signal ϕ_{int} corresponds to the phase shift of the O-mode component in the plasma. The phase shift is detected with a phase counter made at the National Institute for Fusion Science (NIFS)[12].

3. Experimental Results

3.1. Resolutions

The response time of CM polarimeter is determined by a bandwidth of the digital band-pass filter. For example, the standard deviations are about 0.50 deg. and 0.17 deg. (correspond to line averaged electron densities of 6.1×10^{18} m^{-3} and 2.1×10^{18} m^{-3}) with response times of 0.32 ms and 3.2 ms, respectively. Figure 2(a) shows the spectrum of the phase signals with different bandwidths of the band-pass filter. There are noises with a period of 500 Hz. The noises are attributed to the frequency noises of the 1-MHz beat signal shown in Fig. 2(b). Side band frequencies with a period equal to the rotation period 500 Hz of the grating of the SRG.

In the complex demodulation technique, product of beat signals of I_{probe} and the complex conjugation of I_{ref} is calculated and then 1-MHz component in phase is removed[11]. When there are side-band frequencies, the noises with the frequency differences between the main and noise frequencies remain in the phase signal like Fig. 2(a). These side-band noise frequencies are expected to be caused by the misalignment between the rotor axis and the grating[12]. To improve the resolution, it is necessary to replace the grating or to adopt a twin laser system.

3.2. Source of errors

Figure 3(a) shows an example of measurement results of the CM polarimeter. While the line averaged electron density ramped up monotonically, the phase shift due to the CM effect was modulated. Hence, the modulations were apparently spurious and the phase was found to be correlated with that of the interferometer as shown in Fig. 3(b). As pointed out in refs. 5 and 13, multi-reflection between the detector and optical components (called 'back-talk') causes spurious oscillations in the phase difference of the polarimeter. In addition,

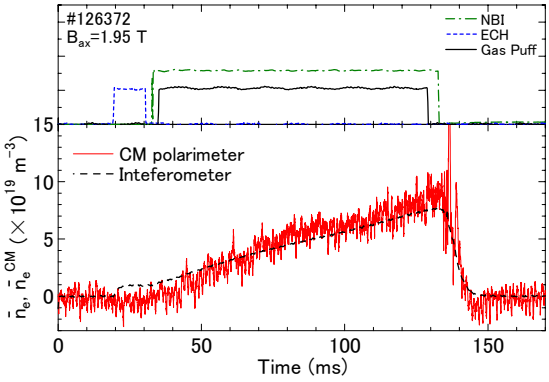

Fig. 4 : Measurement results after suppression of the cross and back talk components.

electrical cross-talk between beat signals of the polarimeter and the interferometer also causes oscillations. When the beat signal of the polarimeter is contaminated with small friction of that of the interferometer $A\sin(\omega_b t+\phi_{int.})$, the measured phase shift ϕ_{CM}^{Mod} is approximately given as follows.

$$\begin{aligned} I_{pola} &= \sin(\omega_b t+\phi_{CM}) + A\sin(\omega_b t+\phi_{int.}) \\ &= \sin\omega_b t(\cos\phi_{CM} + A\cos\phi_{int.}) \\ &\quad + \cos\omega_b t(\sin\phi_{CM} + A\sin\phi_{int.}) \\ &\propto \sin(\omega_b t+\phi_{CM}^{Mod}) \\ \phi_{CM}^{Mod} &= \tan^{-1}\left(\frac{\sin\phi_{CM} + A\sin\phi_{int.}}{\cos\phi_{CM} + A\cos\phi_{int.}}\right) \\ &\approx \phi_{CM} + A\sin\phi_{int.} \quad (A<<1, \phi_{CM}<<1) \end{aligned}$$

The extracted phase signal contains the sinusoidal components with the phase difference due to a plasma. This is the reason that ϕ_{CM} was modulated with a phase of the interferometer.

The back-talk was reduced by inserting an attenuator in front of the SBD because the multi-reflection passed through it several times and became small. The electrical cross-talk was improved by changing the electrical circuit in the band-pass filter.

3.3. Plasma measuement

Figure 4 shows measurement results of the polarimeter and the interferometer after suppression of the cross and back talk components. The combined interferometer works successfully, and agrees with that measured with the existing 2-mm wave interferometer (not shown). The line averaged density $\bar{n}_e^{CM}$ evaluated from the polarimeter is almost consistent with that of the interferometer. The response time of the polarimeter in Fig.4 is 0.32 ms. However, there are still slight differences between them. Possible reasons include changes in the magnetic field due to a finite β effect, changes in the electron density profile ($(1-\rho^8$ is supposed to convert ϕ_{CM} to $\bar{n}_e^{CM}$), and residual cross- and back-talk components. In particular, $\bar{n}_e^{CM}$ remains at zero in the low but finite density range at the beginning of the discharge. Since $\bar{n}_e^{CM}$ in the low-density range sometimes seems to go negative, the first and the second speculations cannot explain the discrepancy in the low-density range. Though the third might seem the most possible at present, the frequencies of the residual oscillation are different (about one-quarter) from these removed. Therefore, the explanation based on cross- and back-talk remains in question.

4. Summary

We developed a Cotton-Mouton polarimeter with an HCN laser for the electron density measurement on CHS. This system is combined with an interferometer. The present standard deviation of the electron density derived from the polarimeter is 6.1×10^{18} m^{-3} with a response time of 0.32 ms; the noises are mainly caused by beat frequency noises. The back and cross talk components cause significant spurious phase modulations. Measurement results of the polarimeter after suppressing the back and cross talk components show good agreement with those of the interferometer.

References

[1] Y. Kawano *et al.* , Rev.Sci. Instrum., **72**, 1068 (2001)
[2] T. Akiyama *et al.* , Rev.Sci. Instrum., **74**, 2695 (2003)
[3] H. Park *et al.* , Rev. Sci. Instrum. **70**, 710 (1999).
[4] V.F. Shevchenko *et al.* , Plasma Phys. Rep. **22**, 28 (1996)
[5] Ch. Fuchs and H.J.Hartfuss, Phys. Rev. Let. **81**, 1626 (1998)
[6] S. Okamura *et al.* ,Nucl. Fusion, **39**, 1337 (1999)
[7] T. Akiyama *et al.*, Rev. Sci. Instrum. **77**, 10F118 (2006).
[8] Ch. Fuchs, Diagnostics Proposal on Cotton-Mouton Polarimeter (sub-mm/IR) for W7-X, 9/2000
[9] Digest of 11th int. Conf. on IR and MM Waves, Pisa, 249 (1986)
[10] Y. Jiang *et al.* , Rev.Sci. Instrum., **68**, 902 (1997)
[11] T. Maekawa *et al.* , Rev.Sci. Instrum., **62**, 304 (1991)
[12] Y. Itoh *et al.*, Fusion Engineering and Design, **56-57**, 965 (2001)
[13] D. Elbèze *et al.* , Rev. Sci. Instrum. **75**, 3405 (2004)

Developments of the interfero-polarimeter for the new Tore Supra FIR reflected channels

C. Gil, D. Elbeze, A. Barbuti, M. Taglione

Association Euratom-CEA, Département de Recherche sur la fusion Contrôlée,
CEA/Cadarache F-13108 Saint Paul Lez Durance, France E-mail : christophe.gil@cea.

On Tore Supra, the interfero-polarimeter diagnostic has been upgraded by doubling the number of channels. The associated developments are discussed in this paper:
Cooled specific internal optical components such as corner cube mirrors have been installed.
As a two-detector technique is used for polarimetric measurements, the beam transport has been designed to reduce the effects of the misalignments and a cold double detector has been tested.
An experiment has been settled to characterize without plasma the oscillations affecting the polarimetry.
The electronic has been renewed to reduce the fringe jumps on the interferometer.

Introduction

On Tore Supra (TS), five FIR channels, designed for long pulse plasma operations, have been installed to double the existing traversing ones, in order to increase the spatial resolution of the electron and current density measured by the interfero-polarimeter diagnostic [1-2] (figure 1). The electron density is evaluated by the phase measurement of 100KHz signals, created by a two-colour (119µm and 195µm) Mach-Zender interferometer [3]. The current is evaluated from the Faraday angles, which are measured by a two detector polarimetric technique based on the amplitude and phase measurements of the 195µm beam [4].

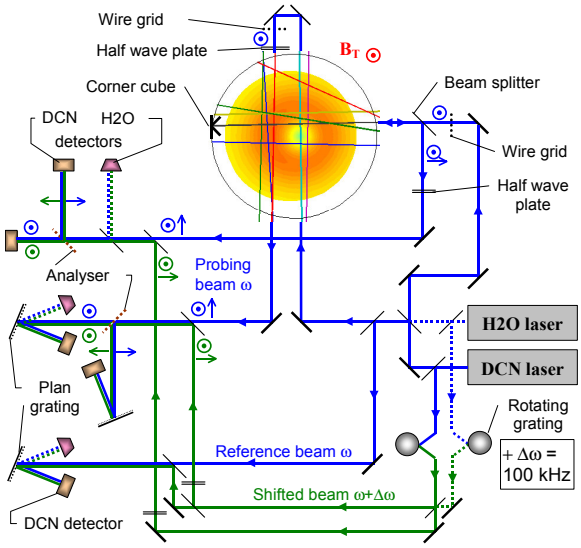

Fig 1: Layout of the combined interfero-polarimeter

We discuss here about some of the diagnostic developments that optimize its exploitation.

Cooled components.

The new channel geometries are similar to those of the intended ITER polarimeter. Inside the tokamak, the beams are reflected on water-cooled copper corner cube mirrors (CC), developed to endure the long duration plasma radiations ($0.3MW/m^{2}$·1000s) [1]. Figure 2 shows the CC evolution after a one-year plasma campaign, where a 700 nm deposit had been measured [4], and after four years. No significant change could be observed, neither on the surface look, which shows the same triangular inner deposit independent from the magnetic lines, nor on the measured reflectivity.

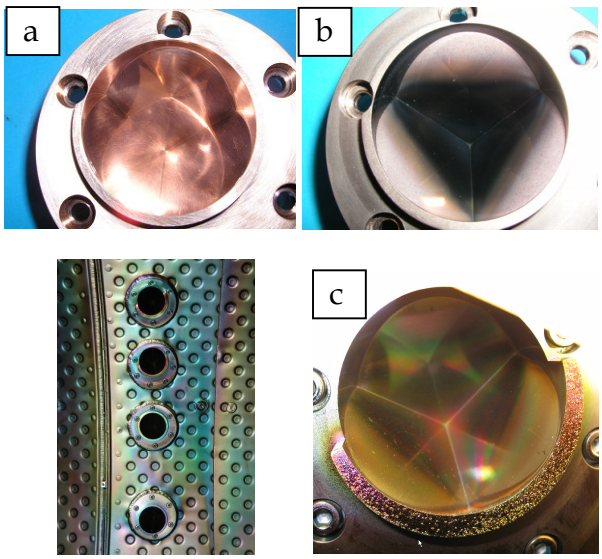

Fig 2: Corner cube mirrors screwed on the internal panel
a: new , b : after a one year campaign, c : after 4 years

Optimization of the polarization measurement

When using a two-detector technique, the polarization of the beam is evaluated as a function of the ratio of the two measured amplitudes. The advantages of this method are that it doesn't need the superposition of beams, it is very easy to use with interferometry and it gives full information on the elliptic polarization by amplitude and phase characterization. But it is very sensitive to differential changes of alignment during plasma. To reduce this effect, special care has been taken for the new reflected channels; The separating grid has been positioned as near as possible from the detectors and the distances after the grid are equal, so that any change of alignment, prior to the grid, induces the same changes of amplitude on the detectors (figure 3)

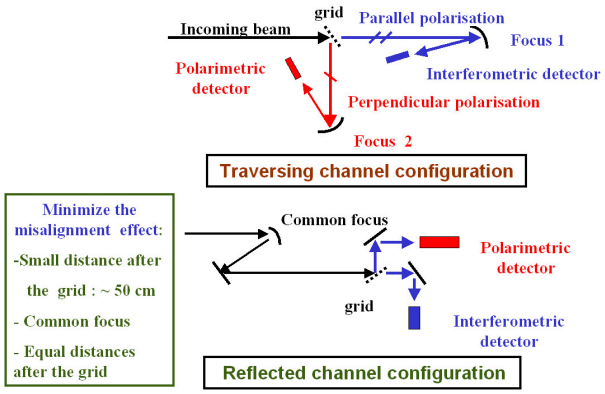

Fig 3: Improvement of the two-detector technique

This concept can be even more optimized by installing the grid few millimetres in front of the two detectors. A prototype of this type has been mounted and tested on TS (figure 4).

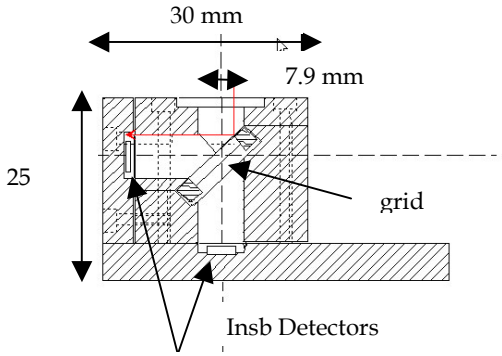

Fig 4: Design of the double detector

As the detectors are Helium cooled bolometers, the double detector is fixed inside the cryostat. The cold grid is composed of a 1 µm thick Mylar® film upon which 1µm wires, 1µm spaced, have been deposited.

This solution is very promising to simplify the design of a polarimeter and indeed it proved on TS to be very easy to use and align. But the present design of the copper mounting must be improved to eliminate a disturbing depolarization, which occurs prior to the grid [7].

Study of the Faraday angle oscillations

The Faraday angles are mostly less than 10° on TS and need to be measured with a good precision (<0.06°) in order to reconstruct the current density [5].

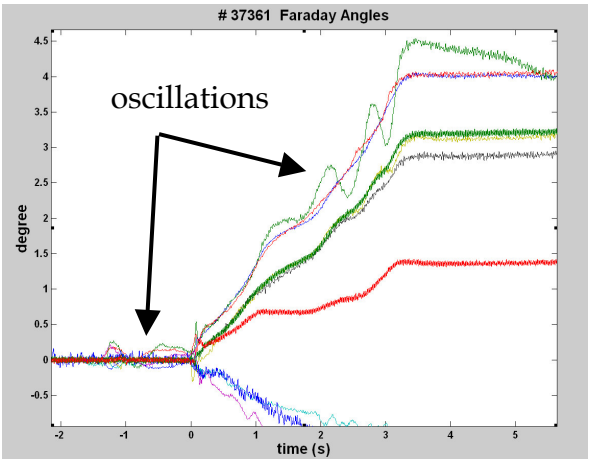

Fig 5: Oscillations during a shot

Figure 5 shows that oscillations larger than 0.1° still affect the measurements on TS. They are due to interferences with a third beam, which is issued from spurious reflections on the optical components (figure 6) [6]. Efforts have been made to reduce the effect by protecting the critical components but as the oscillations are seen only when the absolute phase of the probe beam is varying they can only be estimated during the plasma shots.

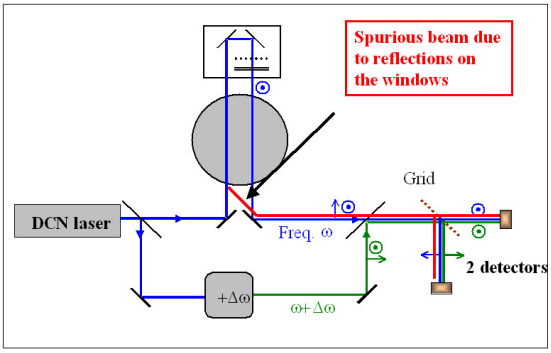

Fig 6: Three beam interferences

To overcome this difficulty, we plan to include a phase variator on the beam path before it is split in different channels.

A prototype has been successfully tested. It consists of a 2 mm thick natural quartz plate, with its optical axis and its rotation axis perpendicular to the incident plane. Results are shown on figure 7 and show that a 45° rotation is sufficient to characterize the oscillations.

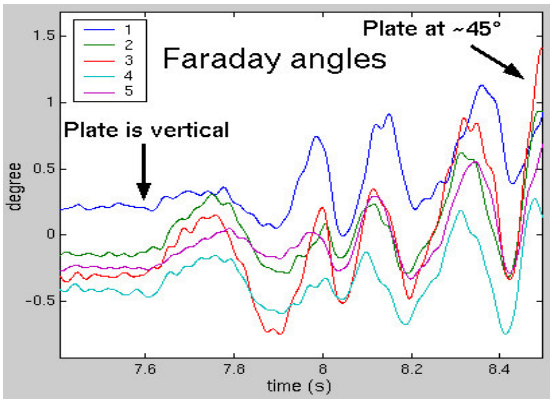

Fig 7: Created oscillations without plasma

Next step will be to automate the rotation and thus to be able, in addition to minimize the oscillations, to correct the Faraday angles, versus the phase measured by interferometry. Eventually, this type of device could be used on ITER to control the Faraday angles, provided that an absolute phase is measured.

Real time fringe jump corrections

The electronic for interferometry has been improved. At these wavelengths, the critical issue is that the phase varies on several periods and thus the signal must be continuously probed to avoid the so called jumps of fringes on the measure. The possible perturbations may come from the RF heating that induces strong noise and from the plasma refraction when the disruptions or the pellet injections occur. This leads to dramatic decreases of the amplitude of the sinusoid and even stops the phase counting for a while.

On TS, to measure the phase, the sinusoidal signals are transformed in square signals, driven by zero crossing time measurements. These signals are sent to another card that calculates the time delay between the probe fronts J and the reference fronts K. A Field Programmable Gate Array semiconductor is used, which can be programmed in VHDL language. There are 5 parallel processes, which are internally governed by a 20MHz clock and this leads to a 1/200 fringe precision. The algorithm uses slow counters J and K that are incremented at each front and 20MHz counters to calculate the delay between successive fronts. Figure 8 shows a Matlab simulation of the reconstruction of the phase:

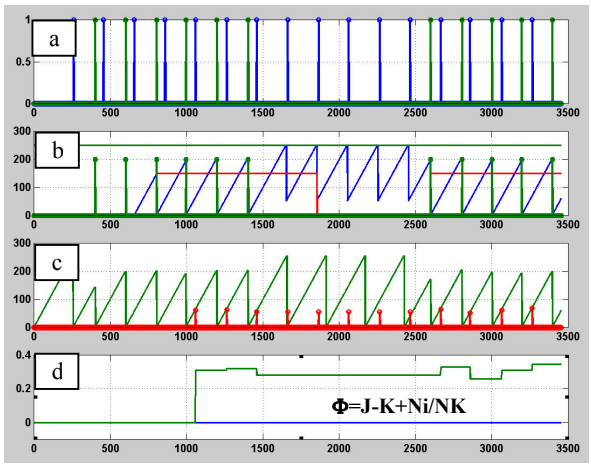

Fig 8: 5 J loss phase simulation and corrections
a: fronts from the K reference and the J plasma beams
b: 20Mhz counters of the J delays with corrections
c : in red counter Ni of the J-K phase difference
d: green: reconstructed phase Φ blue : slow J-K

One can see on b that a temporary loss of signal J is detected by the counter when it reaches the maximum plausible value and this leads to

corrections of counter J , so that the phase is not disturbed. That enables an as fast as 10 µs correction, providing that during this time the phase has not changed.

The efficiency of the algorithm has been verified during plasma. Figure 9 shows a correction of the phase during an ICRH heating breakdown.

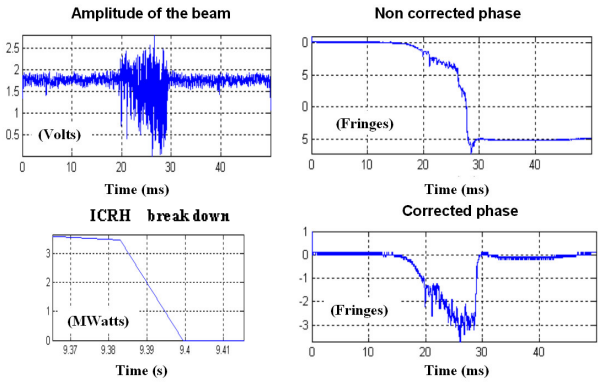

Fig9: 100kz beam analysis and phase corrections during an HF breakdown

As the amplitude is temporary too small for the zero crossing detection, fringes jumps occur, which would be difficult to correct by soft afterwards because meanwhile the effective phase varies. On the contrary, the correction algorithm perfectly reconstructs the phase.

Conclusions and prospects:

The ten-channel interfero-polarimeter is now an on going diagnostic on TS and is fully used for the electron and current density studies.

Improvements on interferometry have been made to reinforce the reliability of the phase measurement when disturbing events occur.

To improve the precision of polarimetry, which is still insufficient, regarding to the specifications to determine precisely the current, different promising techniques are tested.

These efforts will be continued to improve the TS measurements.

Since long duration plasmas are operated on TS, with significant densities of radiation, it could also be of interest to use the diagnostic to validate the needed techniques that optimize the measurements and the relevant components as well, to contribute to prepare the future polarimeters like the ITER one.

References:

[1] C. Gil and al: Fusion engineering and design vol 56-57 (2001) p 969-973

[2]C. Gil, D. Elbeze and al: Retro-Reflected Channels of the Tore Supra FIR Interfero-Polarimeter for the long Pulse Operation, Fusion Engineering and Design, In Press, March 2007.

[3]J.L Bruneau and C.Gil: 14th IRMMW conf – Wuzburg,RFA 1989 p 264-265

[4] E. Joffrin and al: Polarimetry on Tore Supra, EUR-CEA-FC-1553 –1995

[5] T. Aniel and al : Proc EPS 2002

[6] D. Elbeze, C. Gil and al: Rev Sci instr, 75 ,3405 (2004)

[7] C.Gil and al: 32th IRMMW-15 th THz conf – Cardiff ,GB, 2007 , to be published

Density profile measurement by using the multi-channel interferometer in GAMMA 10

M. Yoshikawa, T. Matsumoto, Y. Shima, S. Negishi, Y. Miyata, T. Imai,
A. Itakura, J. Kohagura, Y. Nakashima, H. Hojo, T. Cho,
and GAMMA 10 Group

Plasma Research Center, University of Tsukuba, Tsukuba, Ibaraki 305-8577, Japan

The tandem mirror GAMMA 10 utilizes an electron cyclotron resonance heating (ECRH) for forming a confinement potential. In order to study the plasma confinement improvement by the confinement potential formation, we have constructed a multi-channel microwave interferometer. This system can measure electron density and density fluctuation radial profiles in a single plasma shot. It is one of the powerful tools for understanding of E_r shear effects. We show the clear results for density fluctuation suppression by the effect of the electric field formation and potential formation with applying the plug ECRH.

1. Introduction

The tandem mirror GAMMA 10 (Fig. 1) utilizes an electron cyclotron resonance heating (ECRH) for forming a confinement potential. The advance in the potential formation leads to a finding of remarkable effects of radially sheared electric fields dE_r/dr on turbulence suppression and transverse-loss reduction. The radial transport barrier is explained by the formation of a strong E_r shear or peaked vorticity W with the direction reversal of $E_r \times B$ sheared flow near the potential Φ_C peak for the turbulence suppression [1-8]. In order to study the plasma confinement improvement by the confinement potential formation, we have constructed a new multi-channel microwave interferometer [9]. This system can measure electron density and density fluctuation radial profiles in a single plasma shot. It is one of the powerful tools for understanding of E_r shear effects.

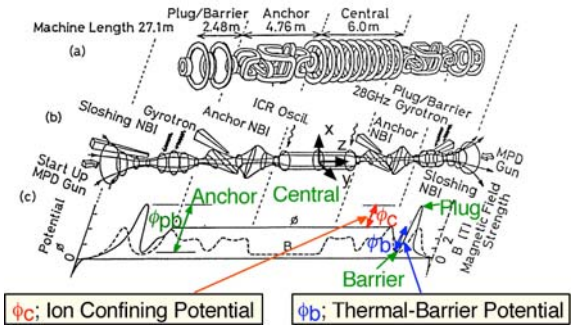

Fig. 1: Schematic view of GAMMA 10 tandem mirror.

In this paper, we show the multi-channel microwave interferometer and clear results for density fluctuation suppression by the effect of the electric field formation and potential formation with applying the plug ECRH.

2. Experimental Apparatus

GAMMA 10 is an effectively axisymmetrized minimum-B anchored tandem mirror with a thermal barrier at both end-mirrors [1-4,6,9-15]. The device consists of an axisymmetric central mirror cell, anchor cells with minimum-B configuration, and plug/barrier cells with axisymmetric mirrors. In the tandem mirror GAMMA 10, the plasma confinement is achieved by not only a magnetic mirror configuration but also high potentials at the both end regions. The main plasma confined in GAMMA 10 is produced and heated by ion cyclotron range of frequency (ICRF) power deposition. The potentials are produced by means of ECRH at the plug/barrier region. Neutral beam injection (NBI) is also utilized at the plug/barrier cell to produce the sloshing ion. The typical electron density, electron and ion temperatures are about 2×10^{12} cm^{-3}, 0.08 keV and 5 keV, respectively. Vertical axis x, z and horizontal axis y are shown in Fig. 1. The mid plane of GAMMA 10 device is set to z = 0. The central axis is x and y = 0.

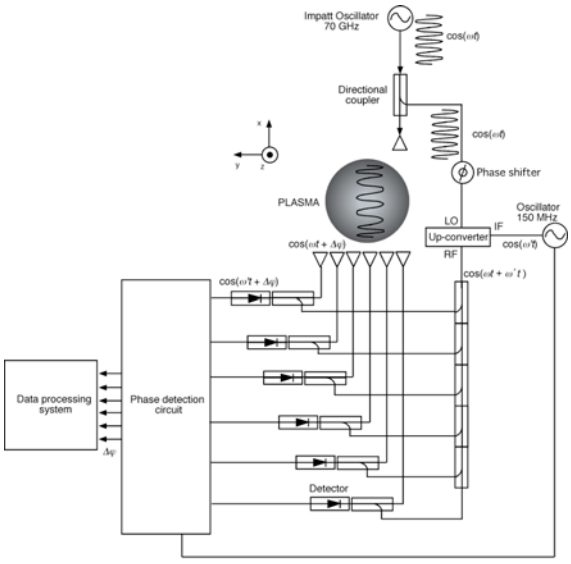

Fig. 2: Schematic diagram of the multi-channel microwave interferometer.

A new multi-channel microwave interferometer (Fig. 2) for measuring the plasma density profile and density fluctuation profile in a single plasma shot [9]. It is designed using Gaussian-beam propagation theory and ray tracing code. The system is configured as a heterodyne interferometer consisting of a 70 GHz (1 W) Impatt oscillator and a 150 MHz oscillator. The probe microwave beam is injected into the plasma without a lens system from the upper port of GAMMA 10. The probe beam extends and is received by 6 horns settled at the measuring position of y = -1.7 cm (ch. 1), -3.7 cm (ch. 2), -6.3 cm (ch. 3), -9.3 cm (ch. 4), -11.4 cm (ch. 5), and -14.4 cm (ch. 6) at the bottom outside the port of GAMMA 10. The spatial resolution of the system is approximately 3 cm. The line-integrated electron density of each position is calculated numerically. We combined the data of the movable interferometer of the measured position of y = 6 cm and those of the multi-channel interferometer in order to obtain radial line density profiles. The Abel inversion technique is used for obtaining the electron density radial profile.

Gold neutral (Au^0) beam probe (GNBP) [13] is used for the potential measurement and the E_r shear study. It consists of a gold negative ion source of a spattering type, a beam transport region of the gold negative ion, a neutralizing gas box, a beam transport region of the primary gold neutral beam, a micro channel plate (MCP) ion detector and sweeping circuits of beam injection angle.

3. Density profile measurements

The plasma is produced at 50.5 ms and sustained by ICRF. Barrier-ECRH is applied between 155 and 175 ms to create thermal barrier potential and plug-ECRH is applied between 160 and 170 ms to create confining potentials. NBI is injected between 159 and 163 ms. The electron density in the central cell is measured by the movable interferometer and the newly installed multi-channel microwave interferometer in a single plasma shot. Figure 3 shows the line density and diamagnetism between 152 and 163 ms. The diamagnetism raises with the applying plug-ECRH and

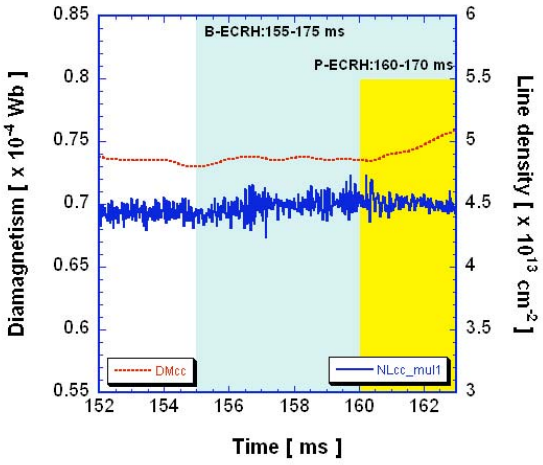

Fig. 3: The line density and diamagnetism between 152 and 163 ms.

electron density slightly increase with applying the barrier-ECRH. The fluctuation on the line density decreases with application of plug-ECRH. Figures 4(a) and 4(b) show the electron density radial profiles before applying plug-ECRH at 152-152.5 ms, and that during applying plug-ECRH at 162-162.5 ms, respectively. Electron density is about 2.3×10^{12} cm^{-3}. The radial density fluctuation is small in Fig. 4(b), while clear radial density fluctuation is observed in Fig. 4(a). Then it is shown that a clear density fluctuation suppression by the formation of the confinement potential with applying the plug-ECRH.

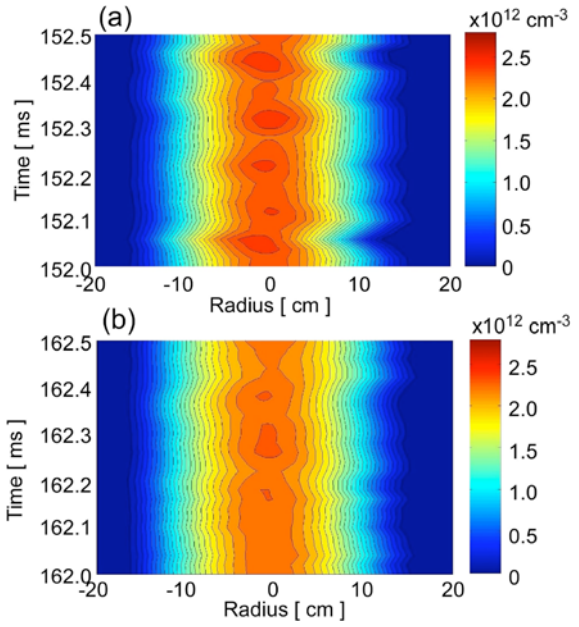

Fig. 4: (a) and (b) show the electron density radial profiles before applying plug-ECRH at 152-152.5 ms, and that during plug-ECRH at 162-162.5 ms, respectively.

Figures 5(a), 5(b), and 5(c) show the FFT spectra of noise level (dotted lines), before (hair lines), 152 - 153 ms, and during (bold lines), 162 - 163 ms, applying plug-ECRH for ch. 1, ch. 4, and ch. 6, respectively. In the spectrum on each channel before applying plug-ECRH, some strong peaks are observed. The coherent mode near the frequency of 13 kHz corresponds to the diamagnetic drift. During the application of plug-ECRH, the spectrum of each channel shows the lower fluctuation in all observing channels except for ch. 4 and ch. 5. Measured position of ch. 4 and ch. 5 corresponds to the lower value of the dE_r/dr shier position.

This is the first clear results of the density fluctuation suppression by the confinement potential formation that is also the dE_r/dr shier formation. However it is middle dE_r/dr shier produced plasma. Then we plan to study more detail of the density fluctuation suppression mechanisms in the higher electric dE_r/dr shier plasma.

4. Summary

We have constructed a new multi-channel microwave interferometer, in order to study the effect of the confinement potential and electric field shier formation. Then the fluctuation suppression by the formation of confinement

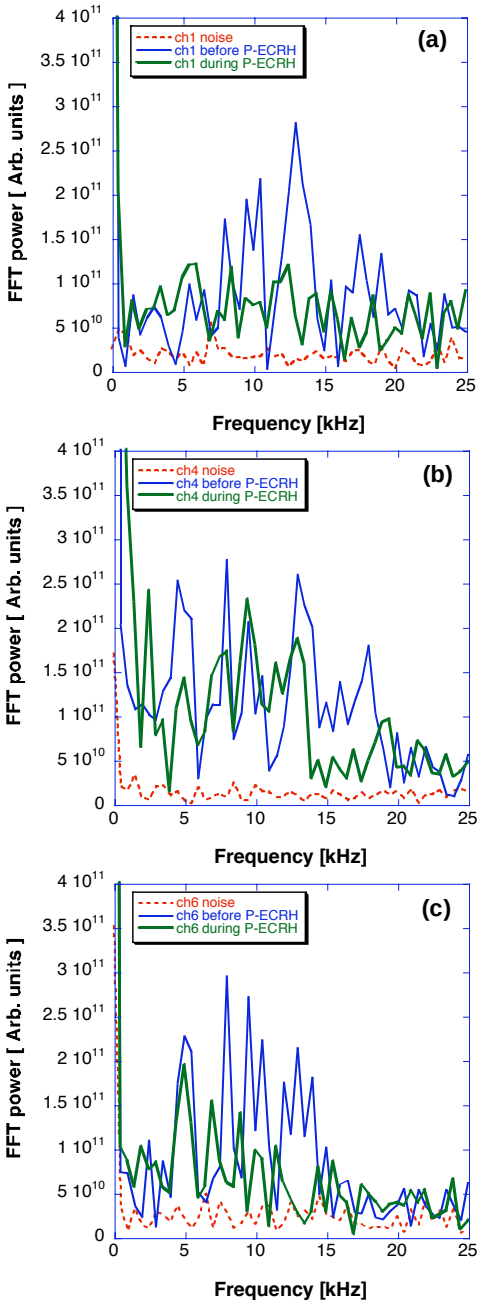

Fig. 5: (a), (b), and (c) show the FFT spectra of noise level (dotted lines), before (hair lines) and during (bold lines) applying plug-ECRH for ch. 1, ch. 4, and ch. 6, respectively.

potential is clearly observed by using the multi-channel microwave interferometer for the first time. We have a powerful tool for studying the improvement of the plasma potential confinement experiments.

Acknowledgements

This work was partly supported by Ministry of Education, Culture, Sports, Science and Technology, Grant-in-Aid for Scientific Research in Priority Areas, No 16082203. This work is performed with the support and under the auspices of the NIFS Collaborative Research Program, No NIFS04KOAP009.

References

[1] T. Cho *et al.*, Phys. Rev. Lett. **94**, 085002 (2005).
[2] T. Cho *et al.*, Nucl. Fusion **45**, 1650 (2005).
[3] T. Cho *et al.*, Phys. Rev. Lett. **97**, 055001 (2006)
[4] T. Cho *et al.*, *21th IAEA Fusion Energy Conf.* (Chengdu, 2006) IAEA/EX/P7-14.
[5] R. F. Post, Nucl. Fusion **27**, 1579 (1987).
[6] A.Mase, *et al.*, Phys. Rev. Lett. **64** (1990) 2281.
[7] M. B. Chaudhry, *et al*., J. Phys. Soc. Jpn. **57** (1988) 3043.
[8] M. Kwon *et al.*, Trans. Fusion Sci. Tech. **43**, 23 (2003).
[9] M. Yoshikawa, *et al*., Rev. Sci. Instrum. **77**, 10E906 (2006).
[10] M. Yoshikawa, *et al*., Trans. Fusion Technol. 35, 273 (1999).
[11] M. Yoshikawa, *et al*., Surface Rev. Lett. 9, 555 (2002).
[12] M. Yoshikawa, *et al*., Trans. Fusion Sci. Tech. 43, 189 (2003).
[13] K. Ishii *et al.*, Rev. Sci. Instrum. **60**, 3270 (1989).
[14] M. Yoshida *et al.*, Rev. Sci. Instrum. **74**, 1909 (2003).
[15] T. Cho *et al.*, Phys. Rev. A **45**, 2532 (1992)

Cavity Ring Down Spectroscopy
- a sensitive and versatile optical diagnostic -

Richard Engeln

Department of Applied Physics, Plasma and Materials Processing,
Eindhoven University of Technology, P.O. Box 513, 5600 MB Eindhoven,
The Netherlands

In recent years the cavity ring down absorption technique has emerged as a versatile and sensitive optical diagnostic technique, that has been applied e.g. for trace gas detection and for combustion and plasma studies. The advantage over normal absorption spectroscopy results from (i) the intrinsic insensitivity of the CRD technique to light source intensity fluctuations, and (ii) the extremely long effective path-lengths (many kilometres) that can be realized in stable optical cavities. In this contribution an historical overview of the CRD technique is given and various CRD detection schemes are described.

1. An historical overview

Cavity Ring Down (CRD) spectroscopy is a direct absorption technique that combines a good detection sensitivity with a rather simple and straightforward experimental setup. Application of direct absorption techniques is advantageous in a variety of research fields, since quantitative concentration data as well as absolute frequency dependent absorption cross-sections can be extracted from the measurements. For these reasons, sensitive absorption spectroscopic techniques are still gaining in interest. Among the variety of techniques that have been developed, the Cavity Ring Down (CRD) absorption technique has proven to be a valuable addition to other detection techniques like Laser Induced Fluorescence (LIF), Infrared Laser Absorption Spectroscopy (IRLAS) or Resonance Enhanced Multi Photon Ionisation (REMPI). The CRD technique is based on the measurement of a rate of absorption rather than the magnitude of absorption of a light pulse confined in a closed optical cavity with a high Q factor [1]. The advantage over normal absorption spectroscopy results from (i) the intrinsic insensitivity of the CRD technique to light source intensity fluctuations, and (ii) the extremely long effective path-lengths (many kilometers) that can be realized in stable optical cavities.

Use of CRD spectroscopy for sensitive absorption measurements with pulsed lasers was first demonstrated by O'Keefe and Deacon in 1988[2]. Since then, trace gas detection by means of CRD absorption spectroscopy has been demonstrated via the measurement of OH and CH_3 in flames and discharges[3, 4] and via the detection of trace amounts of atomic mercury vapor and ammonia in ambient air[5], to just name a few. Successful application of CRD for the measurement of absolute oscillator strengths of weak (forbidden) transitions of stable molecules has, for instance, been demonstrated on overtone transitions of HCN in the visible region of the spectrum[6] and on the Herzberg bands of molecular oxygen in the near UV [7, 8]. The CRD technique has also been used to determine pre-dissociation lifetimes of the $A^2\Sigma^+(v'=1)$ state of the SH radical[9]. The CRD detection technique is also shown to be a viable diagnostic for density measurements of Si, SiH and SiH_3 in a remote Ar-H_2-SiH_4 plasma [10, 11, 12] and C, CH, C_2 and C_2H_2 in Ar-H_2-CH_4 and Ar-H_2-C_2H_2 plasma [13, 14, 15]. In other experiments, explicit use has been made of the pulsed nature of the CRD detection method, due to which the absorbing species only need to be present in the ring down cavity for a short period of time. CRD is therefore well suited for absorption measurements in repetitive sources like pulsed molecular beams [16, 17, 18], laser vaporization sources [19] and pulsed discharges [20, 21]. A nice example in which the pulsed nature of the technique has been explicitly used is the study of growth processes during the plasma deposition of thin layers. Often the surface reaction probability β of the species has been obtained indirectly or under process conditions different from the actual plasma deposition

process. With time-resolved cavity ring down (τ-CRD) β is obtained *during* plasma deposition: the CRD method is used to map an increased radical density due to a pulsed rf bias to the substrate in addition to a continuously operated remote SiH_4 plasma. This yields simultaneously information on the surface reaction probability β and the density of the radicals under specific plasma conditions. , here particularly for the case of high rate deposition of hydrogenated amorphous silicon (a-Si:H) [22, 23].

To date, several absorption detection schemes based on the CRD principle have been reported and reviewed [24, 25, 26]. The time-resolved CRD detection scheme has been mentioned before, for the study of plasma-surface interactions. Furthermore, CRD absorption can also be performed on transparent solid samples. An obvious way to proceed is to place a transparent solid sample, containing for instance a thin film of the material to be studied, at Brewster's angle in the ring down cavity, thereby minimizing reflection losses. An approach that is experimentally found to be superior is to place the transparent solid sample in the cavity in such a way that all separate cavities are optically stable. Although there will be a significant reflection at each interface, these are not experienced as overall cavity losses; with a 3 mm thick optically flat ZnSe window placed in the ringdown cavity, we found the losses per passage through the sample to be below 340 ppm around 8.5 μm, even though the reflection per surface is on the order of 20 %. With a 20 to 30 nm thick C_{60} film deposited on this ZnSe window, the absorption line (one of the four F_{1u} IR fundamental absorptions) centred at 8.46 μm was recorded with a free electron laser using the CRD detection scheme [27]. Also, defect-related absorption measurements have been reported in amorphous silicon thin films. Defects located in the bulk and defects located in the surface/interface region of a-Si:H were distinguished through their different spectral dependences [28 , 29]. An even more recent application combines evanescent wave spectroscopy with CRD spectroscopy. Here, in the optical cavity a transparent optical element is inserted in which the light pulse experiences one or more total internal reflections (TIR). In undergoing these TIRs, the evanescent wave probes the volume in front of the optical element over a depth typically in the order of the wavelength of the light. The CRD spectrum shows the losses of the light pulse due to the losses of the evanescent wave plus the overall (broadband) losses in the CRD cavity [30, 31].

There is no intrinsic limitation to the spectral region in which CRD can be applied, provided mirrors with a sufficiently high reflectivity, detectors with a sufficiently fast time-response, and tunable (pulsed) light sources are available. The detection of oxygen via the Schumann-Runge band around 197 nm [32] and the detection of CO on the spin-forbidden Cameron band [6] shows the applicability of CRD spectroscopy down to and even below 200 nm. Using a state-of-the-art narrow band tunable infrared laser system, Rakestraw and co-workers reported the first CRD experiment in the IR spectral region out to 3500 nm [33]. Using a free-electron laser, CRD absorption experiments were performed at even longer wavelengths, and the detection of ethylene in the 10-11 μm region was demonstrated [34].

Quantitative information is most readily extracted from the CRD measurements when the line width of the light source can be neglected relative to the width of the absorption line. If this is no longer valid, one can still extract the correct absorption coefficient from the measured transients, provided the spectral intensity distribution of the light source is known [5, 35 , 36]. As a consequence, one does not necessarily need a narrow band laser to perform a CRD experiment. One might just as well use a polychromatic light source and extract the spectral information after spectrally dispersing the light exiting the cavity. For this the temporal shape of the ring down transient for a specific frequency-(interval) has to be recorded and analyzed. A monochromator with suitable detector or a time-resolved optical multi-channel analyzer could for instance be used. Another possibility, i.e. to couple the polychromatic light pulse exiting the cavity into a Michelson interferometer, has been shown to work as well [37].

In view of the limited duty cycle, the pulsed nature of the CRD detection method is actually a drawback when absorption measurements are performed on static samples; in a typical CRD experiment with a 10-50 Hz repetition rate laser and cavities with ring-down times of 1-50 μs, one

effectively measures only during a small fraction of the time. For this reason, as well as for the reason of compactness, the use of continuous (diode) lasers has been experimented with in a variety of experimental schemes [24, 38, 39, 40]. As in these experiments the spectral resolution is in principle only limited by the width of the longitudinal cavity modes[41], i.e. the spectral resolution can even be better than the band width of the laser, (extremely) high resolution CRD absorption spectroscopy can be performed in these cw-CRD detection schemes.
In the remaining part of this contribution I will discuss the principles of several CRD spectrometers, in which resp. pulsed lasers (section 2.1), cw lasers (section 2.2), and incoherent broadband cw light sources (section 2.3) are used.

2. Principles of cavity ring down spectroscopy

2.1. Pulsed cavity ring down detection scheme

In a typical CRD experiment a short light pulse is coupled into a stable optical cavity, formed by two highly reflecting plano-concave mirrors. The fraction of light that enters the cavity on one side, rings back and forth many times between the two mirrors. The time behaviour of the light intensity

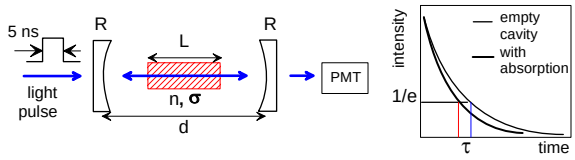

Fig. 1: Principle scheme of a pulsed CRD experiment

inside the cavity can be monitored by the small fraction of light that is transmitted through the other mirror (see Fig. 1). If the only loss factor in the cavity is the reflectivity loss of the mirrors, one can show that the light intensity inside the cavity decays exponentially in time with a decay constant τ, the `ring down time', given by:

$$\tau = \frac{d}{c\left|\ln R\right|} \qquad (1)$$

Here d is the optical path length between the mirrors, c is the speed of light and R is the reflectivity of the mirrors. If R is close to unity, the approximation

$$\tau = \frac{d}{c(1-R)} \qquad (2)$$

can be made.

If there is additional loss inside the cavity due to the presence of absorbing and light scattering species, the light intensity inside the cavity will still decay exponentially in time provided the absorption follows Beer's law. The ring down time can now be written as:

$$\tau(\nu) = \frac{d}{c\left(1-R+\sum \sigma_i(\nu)\times\int_0^d N_i(x)dx\right)} \qquad (3)$$

and the sum is over all light scattering and absorbing species with frequency dependent cross-sections $\sigma_i(\nu)$ and a line-integrated number density. The product of the frequency dependent absorption cross-section with the number density $N_i(x)$ is commonly expressed as the absorption coefficient $\kappa_i(\nu,x)$. In an experiment it is most convenient to record $1/(c\,\tau(\nu))$ as a function of frequency, i.e. to record the total cavity loss as a function of frequency, as this is directly proportional to the absorption coefficient, apart from an offset, which is mainly determined by the finite reflectivity of the mirrors.

2.2. cw cavity ring down detection schemes

The use of continuous wave (cw) lasers, especially diode lasers, in CRD experiments has several advantages over pulsed lasers. Diode lasers are relatively cheap and small plug-and-play lasers, which have the highest possible duty cycle with powers in the preferable range (<10 mW). Furthermore, the use of narrow band cw lasers in CRD schemes makes it possible to measure line profiles accurately. However, CRD with cw lasers is experimentally more elaborate than conventional pulsed CRD. In order to couple light into the high Q factor optical cavity, the single mode cw laser has to be mode-matched to one of the narrow modes of the optical cavity. To satisfy this mode-matching condition several cw-CRD detection schemes have been developed [24]. In almost all these schemes the light coupling into the cavity is repetitively interrupted, and a transient is recorded. Despite that high sensitivities have been reported, the complexity of the cw-CRD detection schemes has prevented a widespread implementation.
In the last ten years, several experimentally less elaborate cw-CRD detection schemes have been introduced. Techniques based on this principle do

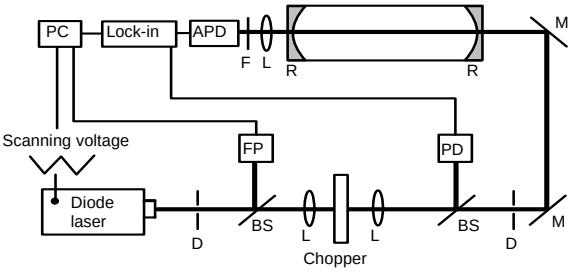

Fig.2: Schematic view of a PSCRD spectrometer.

not require any optical switching or fast digitizers to record ring down transients; thus these techniques allow continuous sampling of the cavity. One of these less elaborate detection schemes was introduced in 1996 [38] and was called *phase shift cavity ring down (PSCRD)*. This technique is based on the ideas of Herbelin *et al.* [42], who used an intensity modulated cw laser beam to measure the reflectivity of mirror coatings. During a PSCRD-experiment the absorption spectrum is extracted from a measurement of the magnitude of the phase shift that intensity modulated continuous laser light experiences upon passing through a high-finesse optically stable cavity. It has been shown in [38] that the phase shift, ϕ_ν, that is recorded during a PSCRD experiment is related to the ring down time of the cavity, τ_ν, as follows: $\tau_\nu = \tan\phi_\nu / \omega$, in which ω is the angular modulation frequency of the intensity. The absorption is then obtained using the following formula:

$$\kappa(\nu) = \frac{\omega}{c}\left(\frac{1}{\tan\phi_\nu} - \frac{1}{\tan\phi_\nu^0}\right). \qquad (4)$$

Here, ϕ_ν^0 is the phase shift introduced by the empty cavity (mainly determined by the reflectivity of the mirrors). In Fig. 2 the schematic view of a PSCRD spectrometer is shown. In this figure D stands for diaphragm, BS for beam splitter, FP for Fabry-Perot, L for lens, (A)PD for (avalanche) photodiode detector, M for mirror, and R for the high reflective mirrors that build up the CRD cavity. The phase shift is recorded with a lock-in amplifier.

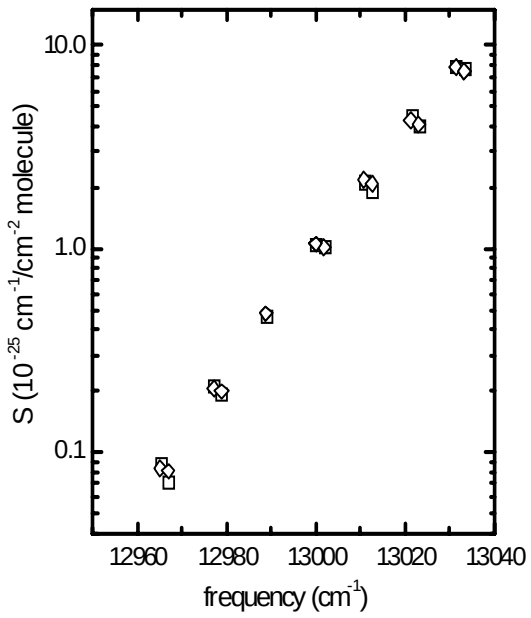

Fig. 3: The measured absolute line strengths for O_2 transitions in the A-band (open square) and the line intensities of the 2001 HITRAN database (open diamond)

Although the PSCRD scheme is very simple, the use of this detection scheme for the determination of absolute absorption cross-sections is only reported by Lewis *et al.*, who measured the integrated cross-sections of the C-H ($\Delta\nu$=5) and ($\Delta\nu$=6) vibrational overtones [43, 44]. Whereas Lewis *et al.* found good agreement between their PSCRD measurements and FT-VIS measurements on the C-H ($\Delta\nu$=5) transition, DeMille *et al.* [45] measured the C-H ($\Delta\nu$=6) overtone absorptions using CRD and found that the cross sections obtained by PSCRD were about 30 % lower. The reason for this discrepancy is not evident, but they concluded that caution against absolute absorption cross-sections determined using PSCRD has to be taken. In [46] it has been shown that the discrepancy could well be explained by the presence of amplified spontaneous emission (ASE) in the laser beam To show the accurateness of the technique, the line strengths of several transitions in the atmospheric A-band of molecular oxygen have been measured and compared with the line strengths given in the HITRAN data base (see Fig. 3). After the correction for ASE, the measured line strengths are on the average 4% different from the HITRAN values (note the dynamical range over which the line strengths are recorded).

2.3. Broadband cavity ring down detection schemes

The aforementioned CRD detection schemes use narrow band coherent light sources. However, there have been several reports on the use of broadband incoherent light sources in CRD spectrometers [47, 48]. In [47] a multiplex version of the phase shift cavity ring down (PSCRD) technique is reported. The intensity of a high pressure cw xenon arc is used to excite the ring down cavity of the PSCRD spectrometer. A Fourier Transform (IFS 66) spectrometer is used to analyze the light exiting the ring down cavity. The spectrally integrated phase shift is recorded as function of the optical path length difference in the Michelson interferometer of the FT spectrometer. The absorption information is obtained from the ratio of the Fourier transform of the in- and out-of phase component of the intensity modulated light exiting the cavity. In this way a FT-PSCRD spectrometer is formed which combines the advantages of a FT spectrometer and the phase shift continuous wave CRD technique. The increased sensitivity of the FT-PSCRD spectrometer as compared to a standard FT spectrometer is obtained through the increased absorption path length, which can be several kilometres in a ring down cavity with a length of 0.5 m. The light is modulated by means of a photo elastic modulator (PEM). Fiedler et al. [48] have introduced incoherent broad-band cavity-enhanced absorption spectroscopy (IBBCEAS) in which the narrow band laser is replaced by a short-arc Xe-lamp. The frequency selectivity is obtained by dispersing the light, after passing the cavity, by means of a monochromator, which is equipped with a diode array. Recently they reported a similar experiment in which the monochromator is replaced by a FT spectrometer [49].

Acknowledgement

The author likes to thank J.H. van Helden, E. Hamers, W.M.M. Kessels, M.C.M. van de Sanden and D.C. Schram for their contributions to (parts of) the work presented here.

References

[1] Cavity-Ringdown Spectrosocpy: An Ultratrace-Absorption Measurement Technique, edited by K W Busch and M A Busch (American Chemical Society, Washington, DC, 1999)

[2] A. O'Keefe, D.A.G. Deacon, Rev. Sci. Instrum. **59** (1988) 2544

[3] J.J.L. Spaanjaars, J.J. ter Meulen, and G. Meijer, J. Chem. Phys. **107** (1997) 2242

[4] P. Zalicki, Y. Ma, R.N. Zare, E.H. Wahl, J.R. Dadamio, T.G. Owano, and C.H. Kruger, Chem. Phys. Lett. **234** (1995) 269

[5] R.T. Jongma, M.G.H. Boogaarts, I. Holleman, and G. Meijer, Rev. Sci. Instrum. **66** (1995) 2821

[6] R.T. Jongma, M.G.H. Boogaarts, and G. Meijer, J. Mol. Spectrosc. **165** (1994) 303

[7] D.L. Huestis, R.A. Copeland, K. Knutsen, T.G. Slanger, R.T. Jongma, M.G.H. Boogaarts, and G. Meijer, Can. J. Phys. **72** (1994) 1109

[8] T.G. Slanger, D.L. Huestis, P.C. Cosby, H. Naus, and G. Meijer, J. Chem. Phys. **105** (1996) 9393

[9] M.D. Wheeler, A.J. Orr-Ewing, M.N.R. Ashfold, and T. Ishiwata, Chem. Phys. Lett. **268** (1997) 421

[10] W.M.M. Kessels, J.P.M. Hoefnagels, M.G.H. Boogaarts, D.C. Schram, and M.C.M. van de Sanden, J. Appl. Phys. **89** (2001) 2065.

[11] W.M.M. Kessels, A. Leroux, M.G.H. Boogaarts, J.P.M. Hoefnagels, M.C.M. van de Sanden, and D.C. Schram, J. Vac. Sci. Technol. **A 19** (2001) 467.

[12] M.G.H. Boogaarts, P.J. Böcker, W.M.M. Kessels, D.C. Schram, and M.C.M. van de Sanden, Chem. Phys. Lett. **326** (2000) 400

[13] J. Benedict, M. Wisse, R.V. Woen, R. Engeln, and M.C.M. van de Sanden, J. Appl. Phys. **94** (2003) 6932

[14] J.B. Wills, J.A. Smith, W.E. Boxford, J.M.F. Elks, M.N.R. Ashfold, A.J. Orr-Ewing, J. Appl. Phys. **92** (2002) 4213

[15] C.J. Rennick, R. Engeln, J.A. Smith, A.J. Orr-Ewing, M.N.R. Ashfold, Yu. A. Mankelevich, J. Appl. Phys. **97** (2005) 113306

[16] A. O'Keefe, J.J. Scherer, A.L. Cooksy, R. Sheeks, J. Heath, and R.J. Saykally, Chem. Phys. Lett. **172** (1990) 214

[17] J.J. Scherer, J.B. Paul, C.P. Collier, and R.J. Saykally, J. Chem. Phys. **102** (1995) 5190

[18] M.G.H. Boogaarts and G. Meijer, J. Chem. Phys. **103** (1995) 5269

[19] D. Kraus, R.J. Saykally, and V.E. Bondybey, Chem. Phys. Lett. **295** (1998) 285

[20] M. Kotterer and J.P. Maier, Chem. Phys. Lett. **266** (1997) 342

[21] H. Linnartz, T. Motylewski, and J.P. Maier, J. Chem. Phys. **109** (1998) 3819

[22] W. M. M. Kessels, R. J. Severens, A. H. M. Smets, B. A. Korevaar, G. J. Adriaenssens, D. C. Schram, and M. C. M. van de Sanden, J. Appl. Phys., **89** (2001) 2404

[23] J.P.M. Hoefnagels, A.A.E. Stevens, M.G.H. Boogaarts, W.M.M. Kessels, and M.C.M. van de Sanden, Chem. Phys. Lett. **360** (2002) 189.

[24] G. Berden, R. Peeters, G. Meijer, Int. Rev. Phys. Chem. **19** (2000) 565

[25] S. S. Brown, Chem. Rev. **103** (2003) 5219

[26] M. D. Wheeler, S. M. Newman, A. J. Orr-Ewing, M. N. R. Ashfold, J. Chem. Soc. Faraday Trans. **94** (1998) 337

[27] R. Engeln, G. von Helden, A.J.A. van Roij, and G. Meijer, J. Chem. Phys. **110** (1999) 2732

[28] A.H.M. Smets, J.H. van Helden, and M.C.M. van de Sanden, J. Non-Cryst. Solids **610** (2002) 299

[29] I.M.P. Aarts, B. Hoex, A.H.M. Smets, R. Engeln, W.M.M. Kessels, M.C.M. van der Sanden, Appl. Phys. Lett. **84** (2004) 3079

[30] A.C.R. Pipino, J.T. Woodward, C. W. Meuse, and V. Silin, J. Chem. Phys. **120** (2004) 1585

[31] A.C.R. Pipino, Phys. Rev. Lett. **83** (1999) 3093

[32] M. Sneep, S. Hannemann, E.-J. van Duijn, W. Ubachs, Opt. Lett. **29** (2004) 1378

[33] J.J. Scherer, D. Voelkel, D.J. Rakestraw, J.B. Paul, C.P. Collier, R.J. Saykally, and A. O'Keefe, Chem. Phys. Lett. **245** (1995) 273

[34] R. Engeln, E. van den Berg, G. Meijer, L. Lin, G.M.H. Knippels, and A.F.G. van der Meer, Chem. Phys. Lett. **269** (1997) 293

[35] P. Zalicki and R.N. Zare, J. Chem. Phys. **102** (1995) 2708

[36] J.T. Hodges, J.P. Looney, and R.D. van Zee, Appl. Opt. **35** (1996) 4112

[37] R. Engeln and G. Meijer, Rev. Sci. Instr. **67** (1996) 2708

[38] R. Engeln, G. von Helden, G. Berden, and G. Meijer, Chem. Phys. Lett. **262** (1996) 105

[39] D. Romanini, A.A. Kachanov, N. Sadeghi, and F. Stoeckel, Chem. Phys. Lett. **264** (1997) 316

[40] R Engeln, G. Berden, R. Peeters, and G. Meijer, Rev. Sci. Instrum. **69** (1998) 3763

[41] K.K. Lehmann and D. Romanini, J. Chem. Phys. **105** (1996) 10263

[42] J.M. Herbelin, J.A. McKay, M.A. Kwok, R.H. Ueunten, D.S. Urevig, D.J. Spencer, D.J. Benard, Appl. Opt. **19** (1980) 144

[43] E.K. Lewis, C.J. Moehnke, C.E. Manzanares, Chem. Phys. Lett. **394** (2004) 25.

[44] E.K. Lewis, D. Reynolds, X. Li, G. de Villele, C. Leduc, D.L. Cedeño, C. Manzanares I, Chem. Phys. Lett. **334** (2001) 357

[45] S. DeMille, R.H. deLaat, R.M. Tanner, R.L. Brooks, N.P.C. Westwood, Chem. Phys. Lett. **366** (2002) 383.

[46] J.H. van Helden, D.C. Schram, R. Engeln, Chem. Phys. Lett. **400** (2004) 320.

[47] E. Hamers, D.C. Schram, R. Engeln, Chem. Phys. Lett. **365** (2002) 237

[48] S.E. Fiedler, A. Hese, A.A. Ruth, Chem. Phys. Lett. **371** (2003) 284

[49] A.A. Ruth, J. Orphal, S.E. Fiedler, Appl. Opt. **46** (2007) 3611

Laser Diagnostics of Debris from Laser-Produced Tin Plasma for EUV Light Source

T. Okada [1], D. Nakamura[1] , A. Takahashi[2] , K. Tamaru [1] , T. Akiyama [1]

[1] *Kyushu University, 744 Motookka, Fukuoka, 819-0395, Japan*
[2] *Kyushu University, 3-1-1 Maedashi, Fukuoka, 812-8582, Japan*

We describe the emission characteristics of extreme ultraviolet light and the generation of debris from laser-produced Sn plasmas. A CO_2 laser-produced Sn plasma provides higher spectral purity and conversion efficiency than a Nd:YAG laser-produced Sn plasma. The generation of Sn atoms, ions and droplets was studied by the laser-induced spectroscopy (LIF), a Faraday cup and a crystal quartz microbalance. The sputtering by the fast ions and its mitigation were also investigated by LIF.

1. Introduction

The extreme ultraviolet EUV light source has been under development for the next generation lithography system, which is scheduled on the international technology roadmap for semiconductors as the most promising technology for the 32 nm and below technology nodes. The most important requirement on the source for EUV lithography is to deliver sufficient in-band (2% bandwidth around 13.5 nm) EUV power. In a practical EUV lithography system, as for EUV power, an average output power of more than 180 W is required at the intermediate focus. Taking into account the transfer efficiency from the EUV source to the intermediate focus, an EUV emission power of more than 300 W is required at the EUV sources [1]. Such high power EUV light sources have been under development using the CO_2 laser-produced tin (Sn) plasma (Sn-LPP) [2,3].

In the case of Sn-LPP, however, the generation of debris is quite severe. Therefore, the mitigation of debris is also one of the most important subjects, in order to develop a practical EUV lithography system. Debris typically consists of droplets, neutral atoms and fast ions. Several techniques have been proposed for the mitigation of debris, including a magnetic field trap of ions [4], a gas curtain, foil trap techniques, and so on. In order to establish the guideline for the optimum design of the mitigation system, detailed knowledge on the behavior of debris is required.

In this paper, we investigate the generation of debris from Sn thin film targets. The generation of Sn atoms was studied by the two dimensional laser-induced spectroscopy (2D-LIF). The dynamics of ions were measured with Faraday cups and the sputtering of a substrate by the fast ions form the plasma was visualized by 2D-LIF and the mitigation of the fast ions by a gas curtain was also investigated.

2. Experimental setup

A Nd:YAG laser (Spectra-Physics PRO-230) or a TEA CO_2 laser was used as a driver laser for the production of Sn plasmas. A flat Sn plate, Sn thin films on glass substrates and Sn wires were used as the target materials for the plasma production. The laser beam perpendicularly hit the target that was placed in a vacuum chamber evacuated at a pressure of 10^{-3} Pa. In the experiment on the mitigation of the fast ions, the chamber was filled with H_2 gas.

The emission characteristics of the EUV light was measured by a X-ray CCD camera through a transmission grating spectrometer. Plasma emission images were captured by a gated and intensified CCD camera through a band-pass filter with transmission at 317.5 nm of the $5p^2\,{}^3P_2$ – $6s\,{}^3P^o_1$ transition. In the case of LIF imaging for Sn atoms, a planar sheet laser beam from a tunable dye laser pumped by the third harmonics of a Q-switched Nd:YAG laser was passed perpendicular to the target normal. Sn atoms were excited by the dye laser beam tuned on 286.3 nm for the $5p^2\,{}^3P_0$ – $6s\,{}^3P^o_1$ transition. The resultant fluorescence image at 317.5 nm was observed through the band-pass filter.

In order to study the kinetics of the fast ions, Faraday cups were used for the time of flight

measurements and the 2D-LIF system was adopted to study the sputtering process by the fast ions from the plasma.

3. Results

3.1. EUV emission characteristics

Figure 1 (a) and (b) show the normalized EUV spectra from CO_2 and Nd:YAG laser-produced Sn plasmas at different irradiation intensities. In the case of the Nd:YAG LPP, the intensities at a shorter wavelength around 8 nm rapidly increased with the laser intensity. The emission around 13.5 nm attributes to the charge state from Sn^{+7} to Sn^{+12}, and the emission around 8 nm attributes to the charge state of Sn^{+15} [5]. Therefore, the Nd:YAG laser-produced plasma is too hot to obtain the emission around 13.5 nm.

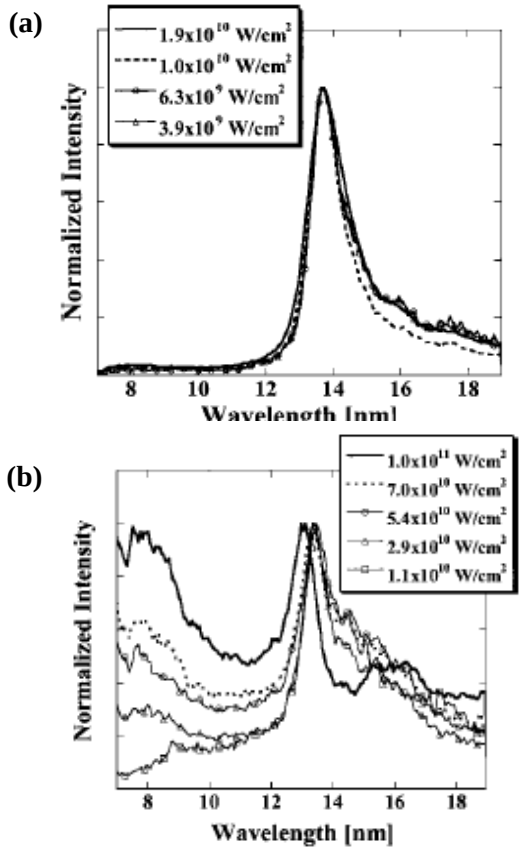

Fig. 1 EUV spectra from (a) CO_2 and (b) Nd:YAG laser-produced Sn plasmas.

In the case of the CO_2 LPP, on the other hand, the EUV spectral shapes remain unchanged over the laser intensity examined. It is apparent that the spectral purity of the CO_2 LPP at an intensity $1.9x10^{10}$ W/cm^2 is compared with that of the Nd:YAG LPP at the similar intensity. In fact, the peak conversion efficiency of the CO_2 laser-produced Sn plasma was higher than that of the Nd:YAG laser-produced Sn plasma. Thus, the CO_2 laser-produced Sn plasma is superior to the Nd:YAG laser-produced plasma from the view point of the generation of EUV light.

3.2. Sn atoms from mass-limited target

When a Sn plate was used as a target, a various types of debris including Sn atoms, Sn ions and droplets are emitted from the plasma. It is supposed that the debris limit the lifetime of a collecting optics in a practical EUV lithography system. In order to mitigate the debris problem, it is thought that a mass-limited Sn-based target is effective, especially for the suppression of the Sn atoms and droplets. Here, we evaluated the effect of the limited-mass effect on the production of the neutral atoms by 2D-LIF.

Examples of the spatial distribution of the Sn atoms from a Sn thin film target with a thickness of 60 nm on a BK7 substrate is shown in Fig. 2(a), along with that from the Sn plate target in Fig. 2(b) for comparison. Those were taken at a delay time of 7 μs after Nd:YAG laser irradiation. The gray solid arrow shows the contour of the

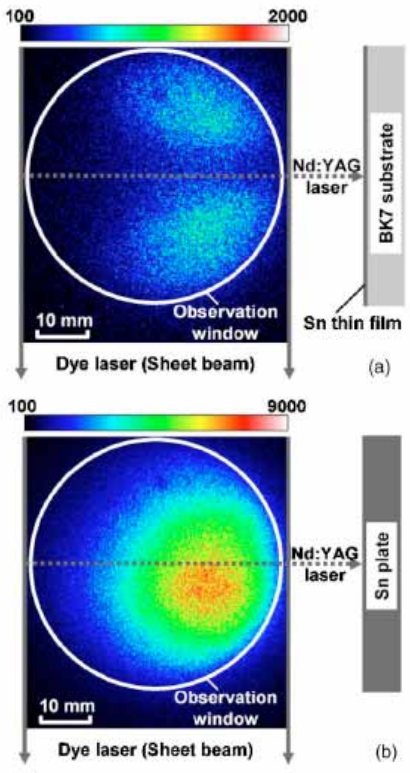

Fig. 2 Spatial distributions of Sn atoms at 7 μs after plasma production from 60 nm thick Sn film (a) and Sn plate (b).

sheet beam, and the center of the sheet was about 40 mm from the target. The optical axis of the Nd:YAG laser is shown by the gray dotted arrows and was perpendicular to the target surface. In the case of the flat plate target, Sn atoms distributed symmetrically with respect to the target normal and peaked along target normal. In the case of the thin film target, on the other hand, LIF signal intensities around the beam axis of the Nd:YAG laser are much lower than in the surrounding area, indicating the depletion of neutral Sn atoms. It is thought that Sn atoms on the Nd:YAG laser beam are fully ionized. Thus it is clearly demonstrated that the mass-limited target is quite effective to suppress the emission of the neutral Sn atoms [6].

3.3. Sn ions

The fast Sn ions from the plasma causes the sputtering of the collection mirror facing to the plasma and results in the limited life-time of the optical system. The kinetic energy of the Sn ions was measured with Faraday cups. It was found that the CO_2 laser-produced plasma generates the more energetic ions than the Nd:YAG laser-produced plasma at a lower irradiation power. As an irradiation power increased, the faster ions were generated. The ions having kinetic energy of more than 10 keV were easily generated.

Next, in order to study the influence of the fast ions on a mirror substrate, the interaction between the dummy mirror and the ions was visualized by 2D-LIF. The experimental arrangement for 2D-LIF visualization is shown in Fig. 3. A Si substrate which was a dummy substrate for a collecting optics made by multilayer of Mo and Si, was placed at 40 mm from a Sn target. Nd:YAG laser beam was irradiated on the Sn target perpendicularly. The

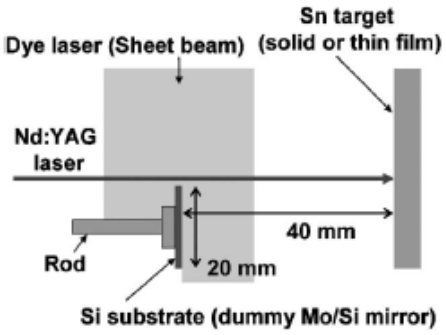

Fig. 3 2D-LIF arrangement for visualization of sputtering by the fast Sn ions.

Sn ions from the plasma hit the Si substrate and causes the sputtering. Under the present experimental condition, the surface of the Si substrate was covered with the layer of Sn atoms that were also from the plasma. Therefore, by observing Sn atoms near the surface of the Si substrate by 2D-LIF, we can investigate the influence of the fast ions on the sputtering of the dummy mirror.

Figure 4 shows the snapshots of the spatial distributions of Sn atoms in front of the Si substrate at different delay times after ablation. The sputtered Sn atoms can be seen at 300 ns in front of the Si substrate placed at 40 mm from a target. The sputtered Sn atoms expanded from the substrate with a kinetic energy of about 10 eV. On the other hand, the Sn atoms which directly flew from the plasma can reach the Si substrate only at 3 μs, as shown in Figs. 4(f) - 4(g) where Sn atoms directly flown from the plasma can be seen in the right hand side of each image. The kinetic energy of the ions which sputtered Sn atoms in Fig. 4(b) corresponds to about 11 keV, based on the flight time of 300 ns and assuming that the species are the Sn ions. This kinetic energy agreed well with that measured with a Faraday cup [6].

3.4. Mitigation of ions

In order to investigate the mitigation of debris, we have investigated the mitigation of the fast ions generated from Sn plasma by H_2 gas. The mitigation of the fast Sn atoms by H_2 gas were study by observing the sputtering of the dummy mirror substrate by the fast Sn ions. Figure 5 shows the spatial distribution of the sputtered Sn atoms at a delay time of 1 μs after plasma production in different H_2 gas pressure from 1.3 to 93 Pa. It is clearly seen that the sputtering was suppressed by increasing H_2 pressure.

Based on the similar images at a delay time of 500 ns after plasma production, the relative density of Sn atoms at 0.5 mm from the Si substrate is plotted as a function of H_2 gas pressure. Since the relative density is proportional to the number density of the sputtered atoms, it provides the direct assessment about the influence of the fast ions on the damage of the mirror substrate. The density decreased almost exponentially with gas pressure. At 66.6 Pa, the sputtered Sn atoms almost disappeared, and the fast ions were almost mitigated by the

collision with H_2 gas. The column density that is required to decelerate the fast ions to sufficiently lower kinetic energy so that the sputtering does not take place can be estimated to 3.8×10^{20} $1/m^2$, taking the 1/e point as a reference.

4. Conclusion

We have investigated the EUV emission characteristics from Nd:YAG and CO_2 laser-produced Sn plasmas. The CO_2 LPP has higher conversion efficiency and spectral purity of EUV light. The generation of Sn atoms and Sn ions from the laser-produced Sn plasmas were studied. A mass-limited target is quite effective to suppress the generation of neutral Sn atoms. The sputtering caused by the fast ions from the Sn plasmas and the mitigation of the ions were also investigated by 2D-LIF.

References

[1] U. Stamm, J. Phys. D **37,** (2004) 3244.

[2] H. Tanaka, K. Akinaga, A. Takahashi, T.Okada, Jpn. J. Appl. Phys. **43**, (2004) L585.

[3] H. Tanaka, A. Matsumoto, K. Akinaga, A. Takahashi, T. Okada, Appl. Phys. Lett. **87**, (2005) 041503.

[4] H. Komori, Y. Imai, G. Soumagne, T. Abe, T. Suganuma, Akira Endo, Proc. SPIE **5751**, (2005) 859.

[5] W. Svendsen and G. O'Sullivan, Phys. Rev. A **50**, (1994) 3710.

[6] H. Tanaka, Y. Hashimoto, K. Tamaru, A. Takahashi, T. Okada, Appl. Phys. Lett. **89**, (2006) 181109.

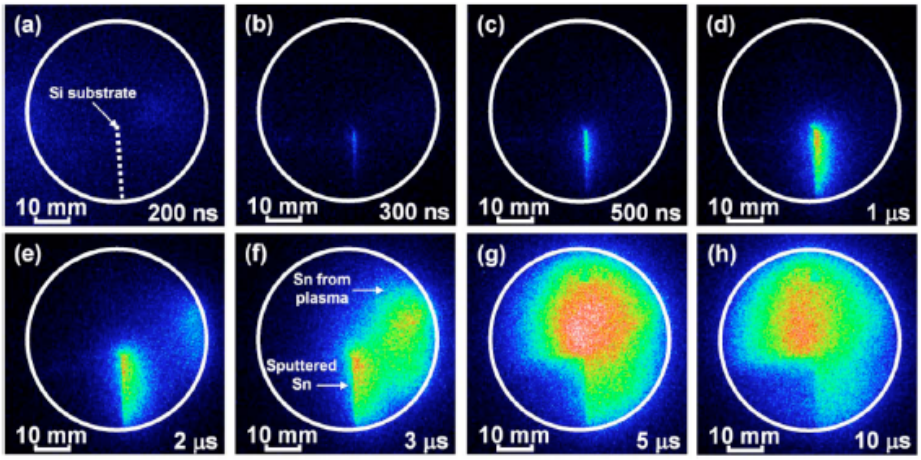

FIG. 4. LIF images near surface of dummy Si substrate at different delay times after plasma production.

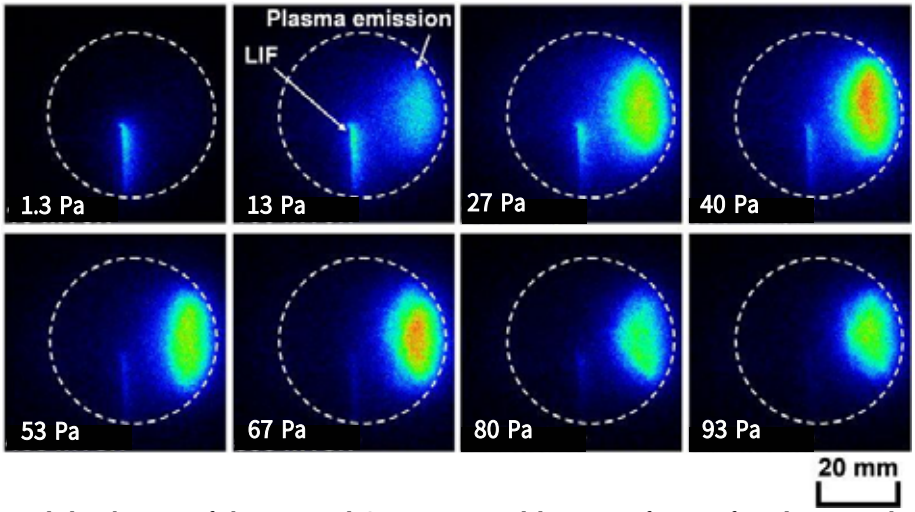

Fig. 5 Spatial distributions of the sputtered Sn atoms at a delay time of 1 μs after plasma production in different H_2 gas pressure from 10 to 700 mTorr.

Eclipse Laser Photodetachment Method: Its Development and Various Applications to Plasma Diagnostics

S. Kajita[1], S. Kado[2]

[1] *Japan Atomic Energy Agency, Mukouyama 801-1, Naka, Ibaraki 311-0193, Japan*
[2] *High Temperature Plasma Center, The University of Tokyo, Kashiwanoha, Kashiwa, Chiba 277-8568 Japan*

A newly developed eclipse laser photodetachment method can be applied to the measurement of the sheath thickness and collection region of photodetached electrons, which are important parameters to check the validity of the measurement in magnetized plasmas, as well as H^- density measurement with avoiding crucial overestimation due to probe surface ablation. In this paper, several applications of the eclipse-LPD are reviewed in terms of its capability to avoid probe surface ablation and to measure the electron sheath thickness. Furthermore, the radial transport effect on H^- density profile in the divertor simulator MAP-II is discussed based on the measurement and numerical simulation.

1. Introduction

Negative ions have possibility of playing important roles in various applications including in negative ion sources for neutral beam injection heating, in a divertor region for experimental fusion reactors and in processing plasmas. A laser photodetachment (LPD) technique has been verified as a reliable method to measure negative ion density locally and absolutely at least in un-magnetized plasmas [1].

In the present paper, a newly developed eclipse laser photodetachment method, which has been originally developed for avoiding crucial overestimation due to the probe ablation phenomena induced by direct laser irradiation to the probe surface [2], is presented. It is found that the eclipse-LPD also has a capability of measuring important physical parameters, the electron sheath thickness and the collection region of photodetached electrons (PDEs), by use of the variation of the temporal evolution of the signals [3]. The measurements of these parameters are very important to check the validity of the measurement method in magnetized plasmas in particular because it can affect the measurement results of H^- velocity and density.

In Sec. 2, the phenomena and the mechanism of the probe ablation problems, and the effects of the eclipse-LPD on the ablation problems are presented. In Sec. 3, measurements of the electron sheath thickness and the length of the collection area of PDEs by use of eclipse-LPD are provided. In Sec. 4, behaviour of H^- in the divertor simulator MAP-II is investigated based on the measurement and particle simulation of H^-.

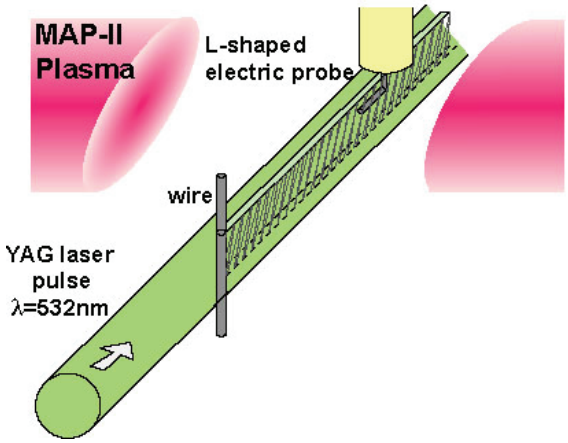

Fig. 1 : A schematic diagram of the experimental setup for the eclipse laser photodetachment method. A thin screening object (wire) is located in the laser channel to avert the direct laser irradiation to the probe tip surface.

2. Ablation free measurement method

Briefly, we here describe about the experimental device MAP-II [4]. The plasma is generated by DC arc discharge and cylindrical plasma 2 m in length is formed with the help of the magnetic field (0.02 T). Low temperature high density hydrogen/helium plasmas are formed; typically the electron density and temperature are 10^{17}-5×10^{18} m^{-3}, <5 eV, respectively.

In Ref. [5], an anomaly large signal has been identified in pure hydrogen plasmas when the laser pulse energy was higher than several

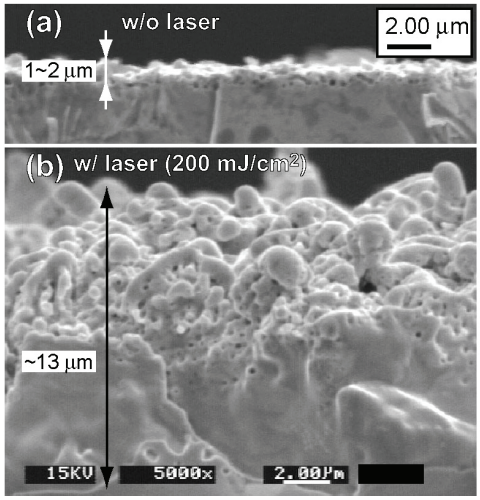

Fig. 2 : SEM images of tungsten cross sections [7]. (a) without laser irradiation, (b) with laser irradiation. The bursting of the holes/bubbles causes the probe surface ablation even when the laser pulse energy is lower than the ablation threshold.

hundreds mJ/cm^2. It becomes more significant when the other gas species that can damage or contaminate the probe surface exists in plasmas. Until now, it has been identified that helium and hydrocarbon gases considerably reduce the threshold to arise the ablation problems [6].

The mechanism to arise the ablation is not so simple. In helium mixed plasmas, for instance, it has been recognized that sub-micron holes/bubbles can easily formed on the surface by the exposure to helium plasma/ion as shown in Fig. 2(a) because the interaction between the lattice vacancy and helium atoms is very strong. Figure 2(b) is the case when the 18000 laser pulses (200 mJ/cm^2) are irradiated together with the helium plasma [7]. The synergetic effects of laser pulse and plasma irradiation lead to the enhancement of the surface roughness. It has been suggested that the holes/bubbles can reduce the ablation threshold with bursting of the helium holes/bubbles in which highly pressurized helium is packed [8].

Figure 3 shows the laser power dependence of excess electron current for the conventional LPD and eclipse-LPD methods in helium-hydrogen mixture plasmas. In the conventional LPD method, the anomalous ablation signal superposes on the LPD signal. On the other hand, the signal is improved in the eclipse-LPD method and its laser power dependence can be well explained by the theoretical photodetachment rate shown as a dotted line in Fig. 3. It has been

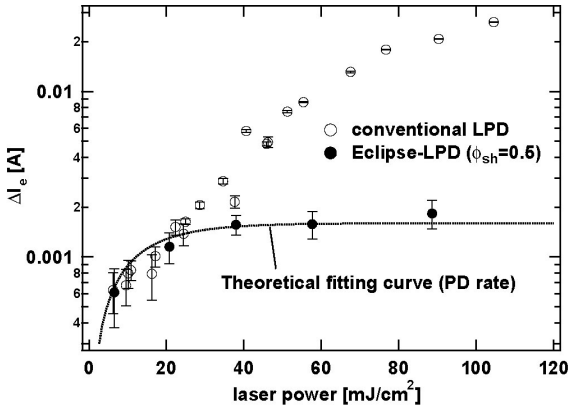

Fig. 3 : Laser power dependence of the excess electron current for conventional LPD and eclipse LPD. The anomalous large signals are improved and well fitted with theoretical photodetachment (PD) rate in the eclipse-LPD case.

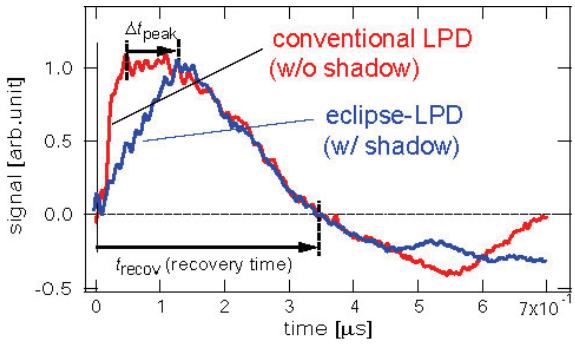

Fig. 4 : Typical temporal evolutions of conventional and eclipse LPD methods. In eclipse LPD method, the peak time of the signal is slightly delayed because of the shadow formed by the screening object in which no excess electrons are produced.

confirmed that H^- density is accurately evaluated from the LPD signal intensity when some conditions are satisfied, even when a part of the collection region of PDEs is overlapped by the shadow [2]. Thus, it can be said that the eclipse-LPD is an ablation-free LPD method that can be used to evaluate the negative ion density at a sufficient laser pulse energy as well as a filament shaped heated probe that has been also developed as an ablation free LPD method by cleaning the probe tip surface [6].

3. Measurement of electron sheath thickness and collection area of photodetached electrons

Figure 4 shows typical temporal evolutions of the conventional and eclipse-LPD signals. In the eclipse-LPD, the signal peak time is slightly delayed compared to that of the conventional

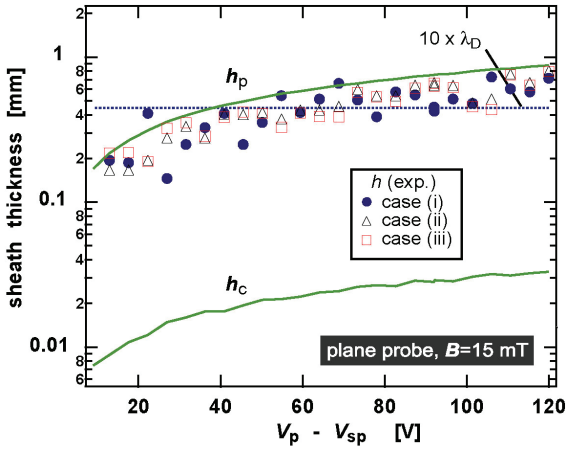

Fig. 5 : Comparisons of experimentally obtained electron sheath thickness formed around a plane probe in magnetized plasmas. Cases (i) , (ii) and (iii) show the electron sheath thicknesses evaluated from three different ways, indicating that they deduced the consistent value with each other. Theoretical sheath thicknesses using Child-Langmuir law (plane and cylindrical geometries) are shown as solid lines, and ten times the Debye length is shown as a dotted line.

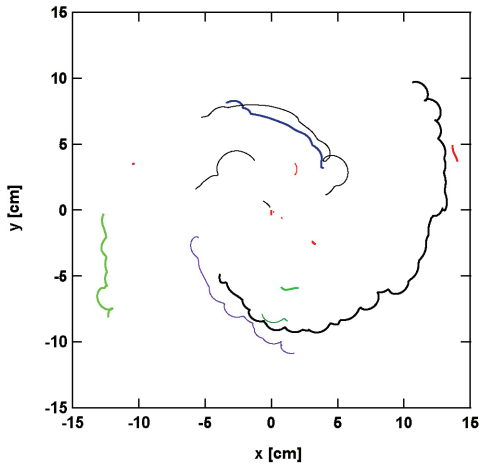

Fig. 6 : Typical calculated trajectories of negative ions. Negative ions are gradually transported to the peripheral region due to the elastic collisions with the help of the electric field.

LPD signal. The peak time shift Δt_{peak} corresponds the time in which photodetached electron swarm reaches the electron sheath edge. The drift velocity of the swarm, v_d, can be evaluated from the signal recovery time, t_{recov}, in which the signal recovers to the initial value. Thus, the electron sheath thickness h can be evaluated by use of these two parameters as follows [3]:

$$h = \frac{(d_{sh}/2 - r_p)t_{recov} - (R_L - r_p)\Delta t_{peak}}{\Delta t_{peak} + t_{recov}}, \quad (1)$$

where d_{sh} is the width of the shadow for eclipse and r_p is the probe tip radius. Moreover, in addition to Eq. (1), h can be obtained in two other independent ways by measuring the shifts of the recovery time and of the peak time [3].

Figure 5 shows the probe bias dependence of the electron sheath thickness along the magnetic field line formed around the plane probe. The cases (i) , (ii) and (iii) show the results from three different ways including Eq. (1), indicating that they deduced the consistent value with each other. The electron Larmor radius is sufficiently smaller than the probe tip size, so that this corresponds to a magnetized regime. Because the electron current is limited only along the magnetic field line, the experimentally obtained electron sheath thickness corresponds to the Child-Langmuir sheath thickness in plane parallel geometry.

Moreover, eclipse-LPD method can measure the length of the collection region of PDEs, L_{PDE}. Since there is concern that the collection area expands along the magnetic field in magnetized plasmas, it is necessary to check whether the collection region of PDEs remains inside the laser beam channel for the purpose of confirming the validity of the LPD method in magnetized plasmas. By use of eclipse-LPD, L_{PDE} has been measured in various magnetized regimes in Ref. [9]. Even in strongly magnetized plasmas, it has been verified that L_{PDE} is shorter than the laser size, so that negative ion density can be accurately measured under the experimental conditions including strongly magnetized regime.

4. H^- density measurement in the divertor simulator MAP-II

For investigating the behavior of H^- in magnetized plasmas, H^- density profile was measured in MAP-II. Moreover, the trajectory of negative ion is calculated by numerically solving the equation of motion including the effect of collisions [10]. The effects of Coulomb collisions are taken into account in each time step, and elastic collisions and collisional extinction are taken into account by Monte Carlo method.

Figure 6 shows the typical calculated trajectories of negative ions. The calculation continued until the particles disappeared due to the extinction processes by collision and parallel

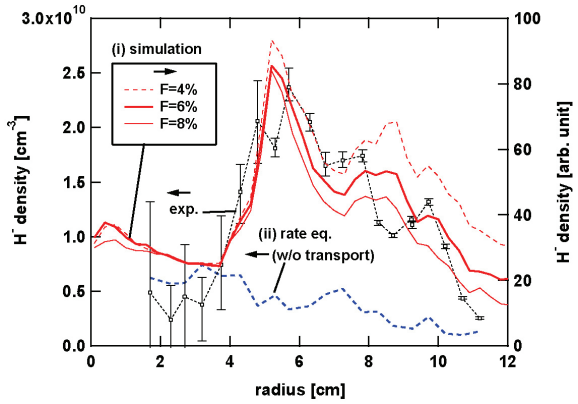

Fig. 7 : A comparison of calculated H^- density profiles with measured H^- density profile. Case (i) and cases (ii) represent, respectively, the calculation results from the rate equation without transport effects and particle simulation.

transport; some trajectories are very short, while the others have rather long trajectory. It is shown that the negative ions can be transported to radially exterior region where the lifetime of negative ions are fairly long with the help of the electric field and the elastic collisions.

Figure 7 shows the comparisons between the experimentally and numerically obtained density profiles of H^-. It is found from the experiments that H^- density has a hollow profile having a peak at the peripheral region, though the electron density and temperature have a peak at the center of the plasma column. The hollow profile could not reproduced from the rate equation of H^- shown as case (i) in Fig. 7 balancing the local production and extinction rates. Case (ii) in Fig. 7 shows the H^- density profile obtained from the particle simulation in which the radial transport effect is included. It is assumed that the degree of dissociation F is uniform in space, and calculations are performed at F=4, 6 and 8%. In the simulation, the H^- radial profile agrees well with the measured one.

In linear discharge devices like divertor simulator, two-separated regions like negative ion sources are naturally formed. In other words, ro-vibrationally excited hydrogen molecules are produced in the central region, while the lifetime of the negative ions are fairly long in the peripheral region. Furthermore, the potential well, which may be formed by ambipolar diffusion process across the magnetic field, is formed in plasmas, so that the produced negative ions are transported to the peripheral region. This transport effect can enhance the negative ion density at the peripheral region.

Acknowledgement

One of the Authors (S. Kajita) thanks Dr. N. Ohno and Prof. S. Takamura for helpful comments and discussion. He also thanks MAP-II experimental group members for excellent supports and collaboration.

References

[1] M. Bacal, Rev. Sci. Instrum., **71** (2000) 3981.
[2] S. Kajita, S. Kado, S. Tanaka, Plasma Sources Sci. and Technol., **14** (2005) 566.
[3] S. Kajita, S. Kado, A. Okamoto *et al.*, Phys. Rev. E, **70** (2004) 066403.
[4] S. Kado, Y. Iida, S. Kajita, *et al.*, J. Plasma Fusion Res., **81** (2005) 810.
[5] M. Bacal, G. M. Hamilton, Phys. Rev. Lett., **42** (1979) 1538.
[6] S. Kajita, S Kado, A. Okamoto *et al.*, Jpn. J. Appl. Phys., **44** (2005) 8661.
[7] S. Kajita, D. Nishijima, N. Ohno *et al.*, J. Plasma Fusion Res., **81** (2005) 745.
[8] S. Kajita, D. Nishijima, N. Ohno *et al.*, J. Appl. Phys., **100** (2006) 103304.
[9] S. Kajita, S. Kado, S. Tanaka, Contrib. Plasma Phys., **46** (2006) 373.
[10] S. Kajita, S. Kado, N. Ohno *et al.*, submitted to Phys. Plasmas.

A LIF polarization spectroscopy by use of a Stark-electric quadrupole interference for electric field vector measurement in plasmas

K. Takiyama[1], S. Furukawa[1], S. Namba[1], T. Oda[2]

[1] *Graduate School of Engineering, Hiroshima University, Higashi-Hiroshima 739-8527, Japan*
[2] *Faculty of Engineering, Hiroshima Kokusai Gakuin University, Hiroshima 739-0321, Japan*

We have developed a high-sensitive method to measure electric field vector in plasmas by use of interference between Stark and electric quadrupole amplitudes. The method relies on the circular polarization of a laser-induced fluorescence (LIF) from He atoms excited through the interference term in the crossed electric and magnetic fields in plasmas. The strength and polarity of electric field are obtained from measurements of the absolute value and sign of the degree of polarization, respectively. To study the effect of magnetic fields on the interference the excitation spectra of LIF were observed in the magnetron discharge plasma under a magnetic field of 2 kG. Based on the results, the application to magnetically confined plasma edge will be also discussed.

1. Introduction

Laser-induced fluorescence (LIF) methods utilizing the Stark effect have been extensively developed to directly measure electric field distributions because of their high sensitivity and high spatial resolution [1-3]. We have developed a high-sensitive method, which relies on polarization of LIF on atomic helium involving excitation of the forbidden transitions (He I: $2^1S \rightarrow n^1D$, where n=3, 4,…) caused by electric quadrupole moment (QDP) and Stark mixing between ^1P and ^1D levels due to the presence of an electric field. The electric field can be determined only from the degree of polarization, which is a function of electric field [2]. There are two types of the method, which utilizes atomic polarization, called alignment or orientation, formed among magnetic sublevels of the initial state in the fluorescence process. Atoms in the alignment state emit the linearly polarized LIF in the direction perpendicular to the quantization axis. The degree of polarization P_L is proportional to E^2 when E is relatively weak, because it is based on the quadratic Stark effect (LP method). This can be applied to plasmas regardless of the existence of the magnetic field [4, 5]. When the magnetic field **B** perpendicular to the electric field **E** exists (**E**⊥**B** configuration), the anisotropic population, orientation, is created among Zeeman sublevels of the excited states, because the Stark-electric quadrupole interference (SQIF) is involved in the laser excitation process [6]. The anisotropy is observed by the circularly polarized light radiating in the magnetic field direction. The polarization has been observed for the first time in a hollow cathode discharge plasma with a weak **B** perpendicular to **E**, in which the Zeeman splitting Δ_{Zeeman} is less than the spectral width of laser Δ_{Laser} [7]. It has been found in the experiment that the polarity of electric field vector can be detected as well as the strength (CP-method). The feasibility of the CP method was demonstrated by the measurement of potential well created in The inertial electrostatic confinement plasma, applying weak magnetic field (5 G): an extremum of the potential curve was successfully detected with high spatial resolution [8]. It was also verified that the sensitivity was an order of magnitude higher than that of the LP method.

In this work, the experiment is carried out in the magnetron discharge plasma under strong magnetic fields, $\Delta_{Laser} < \Delta_{Zeeman}$, to investigate the effect of Zeeman splitting on SQIF. Based on the present results obtained as well as the previous work [9], the possibility of the application to the electric field measurement in the edge region of the magnetic confinement plasma is examined.

2. Principle of the CP method

In **E**⊥**B** configuration, the relationship between electric field E and degree of circular polarization P_C is described in the following. The excitation and observation geometry is shown in Fig. 1, where the laser light propagates along

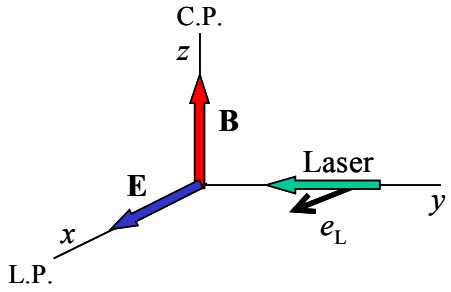

Fig. 1 Geometry for LIF. e_L: laser polarization

the y-axis and the polarization vector is perpendicular (e_L//x) to the magnetic field. The circularly polarized LIF is observed in the magnetic field direction (z-axis). Fig. 2 shows the Zeeman sublevels of the relevant energy levels of He atoms, laser induced fluorescence processes and the relative transition rates obtained considering quantization axis and selection rules. Symbols S and Q stand for matrix elements of the Stark transition and QDP transition, respectively. In this case, the interference of both transitions occurs, because Stark transition and QDP transition share a Zeeman sublevels (+2 or -2) of the final state (n^1D) in the laser excitation, as shown in Fig. 2(a). Then, the asymmetric distribution proportional to the forbidden excitation rates is formed. The distribution will bring about very large difference in population between m=+2 and -2, when S and Q are close in strength.

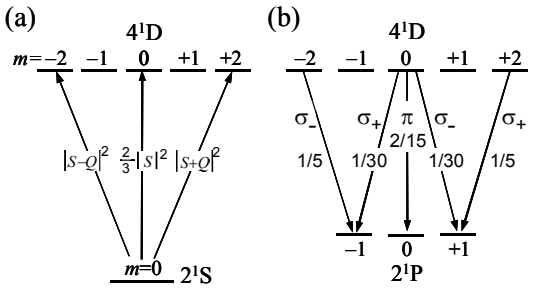

Fig. 2 Relative transition probabilities of (a) excitation and (b) fluorescence for the various magnetic sublevels of He I when $\boldsymbol{E}\perp\boldsymbol{B}$. S and Q represent matrix elements of the Stark and quadrupole transitions, respectively.

The degree of circular polarization of LIF P_C is defined as,

$$P_C = \frac{I_L - I_R}{I_L + I_R}. \qquad (1)$$

Here, I_L and I_R are intensities of circularly polarized LIF components observed in the experiments, which are given by the excitation rates and relative fluorescence rates appeared in Fig. 2(b).

$$I_L = \frac{1}{5}\times|Q+S|^2 + \frac{1}{30}\times\frac{2}{3}|S|^2 \ ,$$
$$I_R = \frac{1}{5}\times|Q-S|^2 + \frac{1}{30}\times\frac{2}{3}|S|^2 \ . \qquad (2)$$

Finally, P_C is related to E,

$$P_C = \frac{2(S/Q)}{1+\frac{10}{9}(S/Q)^2} \ , \qquad (3)$$

where, S^2/Q^2=0.75 (E^2/C^2) and C=0.24 kV/cm in case of n=4 [2]. It should be noted that since P_C contains a linear term of S, a matrix element of the Stark transition, the polarity changes when the direction of the electric field is inverted.

3. Experiments

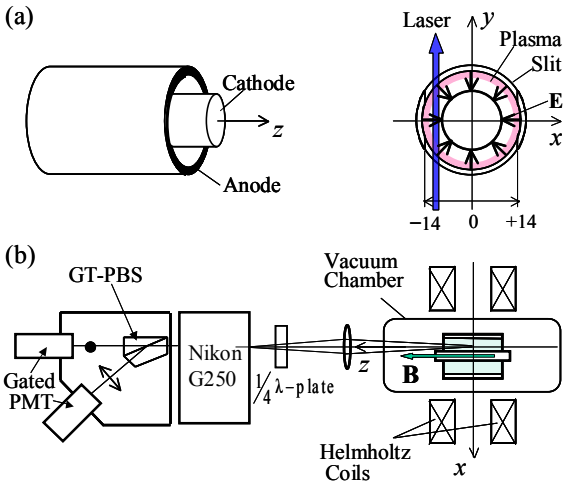

Fig. 3 (a) Schematic view of electrodes for magnetron discharge. (b) Geometry for LIF observation and detection system of circularly polarized light.

The structure of discharge electrodes is shown in Fig. 3(a). A rod cathode (a diameter of 20 mm) is inserted in a cylindrical anode (inner diameter of 30 mm and length of 60 mm). The magnetic field of 2 kG was applied in the z-direction by a Helmholtz coil (Fig. 3 (b)). The magnetron discharge plasma was generated in the gap between the electrodes. The radial electric field is generated perpendicular to the magnetic field in the sheath around the cathode.

The excitation of the forbidden transition (2^1S-4^1D, 397.2 nm) was made by the polarized

laser light with e_L//x by a tuneable dye laser (397.2 nm) with a pulse width of 5 ns in the sheath region. Circularly polarized components of LIF (4^1D-2^1P, 492.2 nm) were measured along the *z*-axis. The excitation spectrum of each polarized component was measured by scanning the laser wavelength. Spatial distribution of the LIF was measured by moving the discharge vessel along the *x*-axis.

4. Results and discussion

The excitation spectra of left-circularly (σ_+ light) and right-circularly (σ_- light) polarized LIF components were observed in the sheath by scanning the laser wavelength covering all the Zeeman splitting, as shown in Fig. 4. Both components are largely different in intensity and peak position. Additionally, the interval between their peaks approximately equals four times the Zeeman splitting. The intensities of both components I_L and I_R are obtained as the integrated ones for respective experimental data points. Then, P_C is obtained from the intensities using Eq. (1). By substituting this value in Eq. (3), S/Q and E are estimated to be 5.2 and 1.46 kV/cm, respectively. Using the value of S/Q, excitation rates and relative fluorescence intensities in Fig. 2, theoretically calculated excitation spectra were drawn by solid lines in Fig. 4, assuming that the spectral shape for laser absorption was a Gaussian with a Doppler width of 3.5 pm. It becomes clear that the anisotropic distribution (orientation) among the Zeeman sublevels of excited state 4^1D is formed in proportion to the excitation rates at E=1.46 kV/cm.

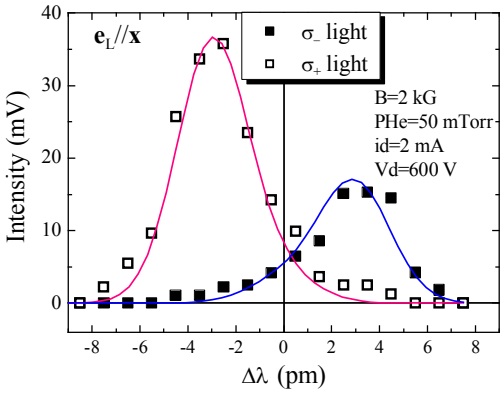

Fig. 4 Excitation spectra of circularly polarized LIF components measured under B=2 kG. Solid lines represent theoretically calculated excitation spectra.

Fig. 5 shows the spatial distribution of electric field observed in the sheath, where E decreases gradually towards the anode from the negative electrode. However, we could not observe the plasma region localizing on the anode wall, which is out of the observation range. Then, assuming the electric field to be zero at –14 mm, the potential difference between the electrodes was roughly estimated to be 550 V, the value of which is reasonably close to the discharge voltage of 600 V.

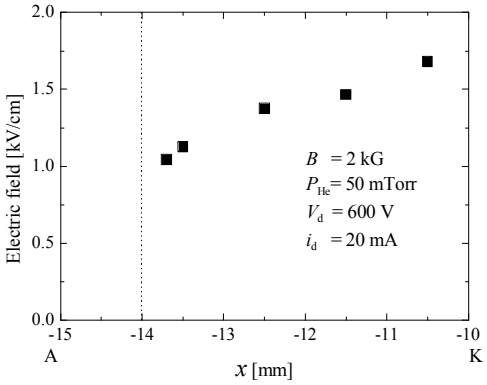

Fig. 5 Spatial distribution of electric field. K: cathode A: anode

In this excitation configuration, the two transitions to the Zeeman sublevels with m=+2 and -2 in 4^1D states of which the level spacing is four times the Zeeman splitting are associated with the SQIF. Since the spectral width of the laser (~1 pm) for this experiment is comparable to the Zeeman splitting at B= 2.0 kG, the probability of the simultaneous excitation of both transitions should be very small, even if the Doppler width of absorption spectrum is considered when the laser tunes to the wavelength corresponding to the transition to m=+2 or -2. Therefore, the above result shows that SQIF will take place, even when the selective excitation to a magnetic sublevel with either +2 or -2 is performed. The electric field measurement with high performances in sensitivity and spatial resolution using SQIF becomes possible by the simultaneous excitation of 2^1S to two Zeeman sublevels with opposite sign of 4^1D using a two-colour laser system, when the strong magnetic field exists.

5. Applications to magnetic confinement plasmas

A possible configuration for applying our methods to the electric field measurement in the

edge of the magnetic confinement plasma is shown in Fig. 6. In the case (a) in which only a radial electric field (macro-field) exists, the electric field can be measured by both methods, because P_C and P_L are dependent on E. On the other hand, ion micro-fields, shown in Fig. 6(b), are detectable by the LP method, but not by the CP method, because the sum of the vectors at a given point in isotropic micro-fields gives zero.

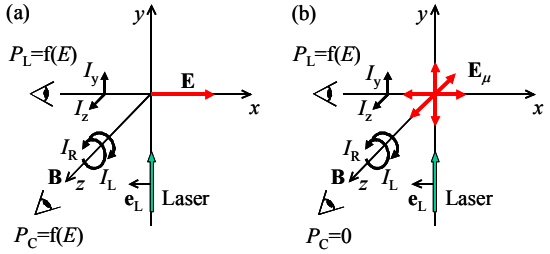

Fig. 6 Possible geometry for electric field measurements in magnetic confinement plasmas. (a) Radial macroscopic field and (b) Isotropic micro-field.

Thus, the macro-field is detectable by either LP or CP method. In the LP method, however, it might be troublesome to discriminate the macro-field from the observed electric field, as the micro-field become larger with increasing the electron density. The detection limit of E by the LP method for n=4 is around 100 V/cm, the corresponding micro-field of which is generated at the electron density of 2×10^{12} cm^{-3}. On the other hand, by use of the CP method it can be expected to detect the macro-field with sufficient S/N ratio, since the method is the micro-field free and the lower limit in sensitivity is 10 V/cm.

When the CP method is applied to the high-density plasma, the depolarization of the fluorescence should also be considered. The dependence of collisional depolarization rate on electron density has already been measured [9]. Since the decay of the degree of polarization is very small up to 10^{12} cm^{-3}, the electric field is obtained with high accuracy. Even in the case of $n_e>10^{12}$ cm^{-3}, if the electron density is known, it is possible to obtain the electric field with the help of the simulation of LIF waveform by a time-dependent CR-model [10], as long as the polarization does not disappear.

4. Summary

To study the effect of magnetic fields on the SQIF the excitation spectra of circularly polarized LIF were observed in the magnetron discharge plasma under a magnetic field of 2 kG. It was found that the anisotropic distribution (orientation) was formed among the Zeeman sublevels of the excited state 4^1D in proportion to the forbidden excitation rates which depends on E in plasmas. The potential difference between the electrodes, obtained from the spatial distribution of electric fields measured in the sheath, reasonably agreed to the discharge voltage. Thus, it was demonstrated that it was possible to use the SQIF for measuring the electric field in plasmas by the simultaneous excitation of 2^1S to two Zeeman sublevels in 4^1D using a two-colour laser system under strong magnetic fields.

Based on the above results, a possible configuration was examined for the application to the magnetically confined plasma edge. It was suggested that the macro-field could be detected with sufficient S/N ratio by the CP method.

Acknowledgments

This work was supported by a Grant-in-Aid for Scientific Research from the Japanese Ministry of Education, Culture, Sports, Science and Technology.

References

[1] C. A. Moore, G.P. Davis and R. A. Gottscho, Phys. Rev. Lett. **52** (1984) 538.

[2] T. Oda and K. Takiyama, Proc. 7th Int. Sympo. Laser-Aided Plasma Diagnostics, Fukuoka, Japan, (1995) p. 227.

[3] U. Czarnetskii, D. Luggenhölscher and H.,F. Döbele, Phys. Rev. Lett. **81** (1998) 4592.

[4] M. Watanabe, K. Takiyama and T. Oda, Rev. Sci. Instrum. **70** (1999) 903.

[5] K. Takiyama, M. Watanabe, T. Oda, J. Nucl. Mater. **266-269** (1999) 953.

[6] L. R. Hunter, W. A. Walker, and D. S. Weiss, Phys. Rev. Lett. **56**, 823 (1986).

[7] K. Takiyama et al., Proc. Int. Sympo. Plasma Polarization Spectroscopy, NIFS-PROC, **57** (2004) p. 399

[8] S. Furukawa at al., (these Proceedings).

[9] S. Furukawa et al., Proc. 28th ICPIG, Prague, Czech Republic, (2007) p. 1562.

[10] K. Takiyama et al., Proc. 8th Int. Sympo. Laser-Aided Plasma Diagnostics, Doorwerth, The Netherlamds, (1997) p. 81.

LAPD13 Time Table

Time	Session	9/17(Mon.)	9/18(Tue.)	9/19(Wed.)	9/20(Thu.)	9/21(Fri.)
7			Breakfast (7:00-8:30)	Breakfast (7:00-8:30)	Breakfast (7:00-8:30)	Breakfast (7:00-8:30)
8			Registration (8:00-8:45)			
9	**AM1** 8:45- 10:30 (18, 19) or 10:20(20, 21)		**8:45 Opening** **9:00 (Akazaki Lecture) U. Czarnetzki** **9:50 (G1) S. Nielsen**	**8:45 (G4) M. Kantor** **9:25 (T3) M. Walsh** **9:50 (T4) T. Kondoh** **10:15 (S3) J. Brotankova**	**8:45 (G5) V.Schulz von der Gathen** **9:25 (T5) M. Ashfold** **9:50 (S4) T. Sakurai** **10:05 (S5) G. van Rooij**	**8:45 (G9) K.Tanaka** **9:25 (T9) T. Akiyama** **9:50 (S9) C. Gil** **10:05 (S10) M. Yoshikawa**
10			Coffee (10:30-10:50)	Coffee (10:30-10:50)	Coffee (10:20-10:40)	Coffee (10:20-10:40)
11	**AM2** 10:50-12:10(18) or 12:00(19) or 10:40-12:25(20) or 12:30(21)		**10:50 (G2) A. Mase** **11:30 (T1) H.K. Park**	**10:50 -12:00 Pre-poster (2)**	**10:40 (G6) M. Hangyo** **11:20 (T6) S. Okajima**	**10:40 (G10) R. Engeln** **11:20 (T10) T. Okada**
12			**11:55 (S1) N.C. Luhmann,**		**11:45 (T7) T. Idehara** **12:10 (S6) B. Graham**	**11:45 (S11) S. Kajita** **12:00 (S12) K. Takiyama** **12:15 Closing**
13			Lunch/Break (12:10-15:35)	Excursion to Kamikochi (with Lunch and Dinner) (12:30-19:30)	Lunch/Break (12:25-15:45)	
14						
15						
16	**PM1** 15:45(20) or 15:35(18) -18:00		**15:35 (G3) S. Kado** **16:15 (T2) A. Reighard** **16:40 (S2) A. Kono**		**15:45 (G7) H. Mizoguchi** **16:25 (G8) K. Tachibana** **17:05 (T8) M. Bowden**	**Presentation Time** **Akazaki: 50 min.** **General: 40 min.** **Topical: 25 min.** **Short: 15 min**
17			**16:55 -18:00 Pre-poster (1)**		**17:30 (S7) N. Sadeghi** **17:45 (S8) K. Tomita**	
18		Registration (18:00-) Reception (19:00-21:00)	Dinner (18:15-19:45)		Banquet (18:30-21:30)	
19						
20	**PM2** (20:00-22:00)		**20:00 -22:00 Poster (1)**	**20:00 -22:00 Poster (2)**		
21						
22						